Transactions of the ASME, Journal of Heat Transfer (ISSN 0022-1481) is published bi-monthly (Feb., Apr., June, Aug., Oct., Dec.) by The American Society of Mechanical Engineers, Three Park Avenue, New York, NY 10016. Periodicals postage paid at New York, NY and additional mailing offices. POSTMASTER: Send address changes to Transactions of the ASME, Journal of Heat Transfer, c/o THE AMERICAN SOCIETY OF MECHANICAL ENGINEERS, 22 Law Drive, Box 2300, Fairfield, NJ 07007-2300.
CHANGES OF ADDRESS must be received at Society headquarters seven weeks before they are to be effective. Please send old label and new address.

Journal of Heat Transfer

Published Bimonthly by ASME

VOLUME 126 • NUMBER 1 • FEBRUARY 2004

TECHNICAL PAPERS

(**Contents continued on inside back cover**)

This journal is printed on acid-free paper, which exceeds the ANSI Z39.48-1992 specification for permanence of paper and library materials. ♾™
♲ 85% recycled content, including 10% post-consumer fibers.

Journal of Heat Transfer Volume 126, Number 1 FEBRUARY 2004

The ASME Journal of Heat Transfer is abstracted and indexed in the following:

Applied Science and Technology Index, AMR Abstracts Database, Chemical Abstracts, Chemical Engineering and Biotechnology Abstracts (Electronic equivalent of Process and Chemical Engineering), Civil Engineering Abstracts, Compendex (The electronic equivalent of Engineering Index), Corrosion Abstracts, Current Contents, E & P Health, Safety, and Environment, Ei EncompassLit, Engineered Materials Abstracts, Engineering Index, Enviroline (The electronic equivalent of Environment Abstracts), Environment Abstracts, Environmental Engineering Abstracts, Environmental Science and Pollution Management, Fluidex, Fuel and Energy Abstracts, Index to Scientific Reviews, INSPEC, International Building Services Abstracts, Mechanical & Transportation Engineering Abstracts, Mechanical Engineering Abstracts, METADEX (The electronic equivalent of Metals Abstracts and Alloys Index), Petroleum Abstracts, Process and Chemical Engineering, Referativnyi Zhurnal, Science Citation Index, SciSearch (The electronic equivalent of Science Citation Index), Theoretical Chemical Engineering

Analysis of Multiplicity Phenomena in Longitudinal Fins Under Multi-Boiling Conditions

Rizos N. Krikkis
University of Thessaly,
Department of Mechanical and Industrial Engineering,
Thermal Engineering Section,
Pedion Areos 38334, Volos, Greece

Stratis V. Sotirchos
Professor,
Department of Chemical Engineering,
University of Rochester, Rochester, NY 14627, USA
Research Director
Institute of Chemical Engineering and High Temperature Chemical Processes,
P.O. Box 1414,
Stadiou St., Platani, 26 500 Patras, Greece

Panagiotis Razelos
Mem. ASME
Professor Emeritus,
College of Staten Island,
CUNY, New York, USA

A numerical bifurcation analysis is carried out in order to determine the solution structure of longitudinal fins subject to multi-boiling heat transfer mode. The thermal analysis can no longer be performed independently of the working fluid since the heat transfer coefficient is temperature dependent and includes the nucleate, the transition and the film boiling regimes where the boiling curve is obtained experimentally for a specific fluid. The heat transfer process is modeled using one-dimensional heat conduction with or without heat transfer from the fin tip. Furthermore, five fin profiles are considered: the constant thickness, the trapezoidal, the triangular, the convex parabolic and the parabolic. The multiplicity structure is obtained in order to determine the different types of bifurcation diagrams, which describe the dependence of a state variable of the system (for instance the fin temperature or the heat dissipation) on a design (Conduction-Convection Parameter) or operation parameter (base Temperature Difference). Specifically the effects of the base Temperature Difference, of the Conduction-Convection Parameter and of the Biot number are analyzed and presented in several diagrams since it is important to know the behavioral features of the heat rejection mechanism such as the number of the possible steady states and the influence of a change in one or more operating variables to these states. [DOI: 10.1115/1.1643088]

Keywords: Boiling, Enhancement, Finned Surfaces, Heat Transfer

Introduction

The study of extended surfaces operating under multi-boiling conditions has actually begun with the pioneer work of Westwater and co-workers [1–4]. The authors pointed out that the methods of fin design, so far developed, could not be used for the boiling case because the heat transfer coefficient was assumed uniform over the fin surface. Indeed if we assume for instance that the working fluid is water at atmospheric pressure, where the fin base TD is maintained at $\Delta T_b = 100°C$ and the fin tip TD is, say $\Delta T_e = 18.1°C$ then the ratio of the tip to base heat transfer coefficients can be obtained as

$$\frac{h_e}{h_b} = \frac{h(18.1°C)}{h(100°C)} = \frac{30116}{301} \approx 100$$

From the above argument it is evident the boiling heat transfer coefficient is highly nonuniform so that a different approach to the problem had to be taken. The authors therefore determined experimentally the heat transfer coefficient and used successfully a one-dimensional model, including the effects of radiation, for the prediction of the extended surfaces heat duty. Moreover, using the methodology of Wilkins [5], they obtained the optimum profile for pin fins under multi-boiling conditions. The experiments conducted by Haley and Westwater [2] confirmed the simultaneous and adjacent existence of different types of boiling on the fin surface for R-113 and isopropyl alcohol. This particular characteristic of the fin, the operation under multi-boiling conditions constitutes an efficient and powerful heat transfer enhancement mechanism since the TD at the base of the fin is not limited to the TD corresponding to the peak of the boiling curve, as it would have been in the absence of the fin and as a result the heat fluxes measured were significantly increased. Similar theoretical as well as experimental investigations were carried out at the Institute for High Temperatures of the Russian Academy of Sciences by Petukhov, Kovalev and co-workers [6–10]. Of particular interest is the work of Kovalev and Rybchinskaya [9] who examined the simultaneous effects of multi-boiling heat transfer and internal heat generation on the performance of a cylindrical pin fin. Specifically when both mechanisms are present, for a given base heat flux the existence of four different base TD values are possible (see Fig. 1 in [9]).

Since the prediction of the heat duty under multi-boiling conditions is attractive many analytical solutions for simple (constant thickness) profiles can be found in the literature. Lai and Hsu [11] proposed a simple model for the determination of the length of the nucleate boiling section on a longitudinal fin of rectangular profile and the base heat dissipation of the fin. The authors divided the fin in several sections and each section was subjected to a different boiling mode. A global temperature and heat flux distribution was obtained by requiring that the temperature and its derivative at the base of one segment to match the corresponding values at the tip of the next segment. The same approach was adopted by Unal, [12,13] in order to obtain closed form solutions for simple profile configurations. Liaw and Yeh [14,15] conducted, in Part I of their work, both a theoretical and an experimental investigation for a constant thickness profile longitudinal and pin fin with a heat transfer coefficient of the form of Eq. (11) for negative and positive exponents. The analytical solution was expressed in terms of the hypergeometric function. Both cases with and without heat transfer from the tip were examined. In addition they carried out a linear stability analysis for the transition boiling mode and its unstable nature was revealed from the resulting negative eigenvalues. In Part II the authors considered multi-boiling heat transfer conditions for the same fins and used the previous obtained analytical solution and the methodology of Lai and Hsu [11] in order to determine the temperature distribution through the fin, which compared well with the experimental data for water and isopropyl alcohol. Recently Lee and co-workers [16–19], conducted a linear stability analysis for pin fins under two and three mode boiling

Contributed by the Heat Transfer Division for publication in the JOURNAL OF HEAT TRANSFER. Manuscript received by the Heat Transfer Division November 20, 2002; revision received September 23, 2003. Associate Editor: G. S. Dulikravich.

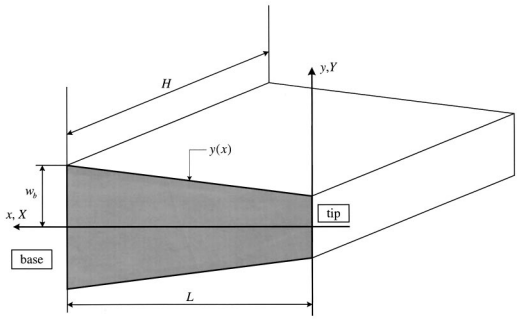

Fig. 1 Longitudinal fin geometry

using polynomial as well as trigonometric basis eigenfunctions. Their analysis was extended to include radial and longitudinal fins while the theoretical results were supported by experiments.

Bifurcation phenomena are common in chemical reaction engineering and a multitude of mathematical tools has been used for its investigation Aris [20]. The singularity theory, Golubitsky and Schaeffer [21], provides an efficient tool for the bifurcation analysis of physical systems described by a single algebraic equation and has been successfully employed by Balakotaih and Luss [22,23] in the investigation of the multiplicity of a number of lumped-parameter systems and by Witmer et al. [24] in the investigation of a distributed diffusion and reaction problem. The two-point BVP of conduction-convection in a fin under multi-boiling conditions is similar to the reaction-diffusion BVP encountered in chemical engineering and the solution methodologies proposed by Michelsen and Villadsen, [25], Kubíček and Hlaváček [26,27], Hsuen and Sotirchos [28–30], are generally applicable to the problem at hand. A complete picture of the bifurcation structure of the conduction-convection multi mode boiling system is still lacking, although many investigators have considered the fundamental mechanisms. This is because knowledge of the singular points of a system of equations provides local information about its multiplicity, but, by constructing the complete loci of the limit and hysteresis points of the solution diagram, global information may be obtained as well.

In the present study a one-dimensional conduction model is employed for the numerical bifurcation analysis of longitudinal fins of several profiles subjected to multi-boiling heat transfer conditions. The multiplicity structure is obtained in order to determine the different types of bifurcation diagrams, which describe the dependence of a state variable of the system (for instance the fin temperature or the heat dissipation) on a design (CCP) or operation parameter (base TD). Specifically the effects of the base TD, of CCP and of the Biot number are analyzed and presented in several diagrams since it is important to know the behavioral features of the heat rejection mechanism such as the number of the possible steady states and the influence of a change in one or more operating variables to these states.

Statement of the Problem

Consider a uniform density longitudinal fin depicted schematically in Fig. 1 with symmetric profile $Y=Y(X)$ and constant thermal conductivity k. The fin has length H base thickness $2w$, tip thickness $2w_e$ and height L. The base of the fin is maintained at constant temperature T_b with the surrounding liquid at boiling temperature T_∞. The analysis is based on the following modified Murray [32] and Gardner [33] assumptions:

1) One-dimensional heat conduction.
2) The temperature at the fin base is uniform.
3) There are no heat sources or sinks in the fin.
4) The length of the fin H is much larger than either w or L.
5) The temperature of the boiling liquid is uniform.

Table 1 Taper ratio and exponents for the profiles considered

Profile	λ	n
Rectangular	1.00	0
Trapezoidal	0.50	1
Triangular	0.05	1
Convex Parabolic	0.05	3/2
Parabolic	0.05	2

6) The heat transfer coefficient h at any point on the nonisothermal fin surface is the same as it would be obtained if the surface surrounding the point was at the same temperature (''local assumption,'' Haley and Westwater [2]).

On the basis of the above assumptions the conservation of energy yields the following differential equation that must be satisfied by the fin temperature in dimensionless form:

$$\frac{d^2\Theta}{dx^2}=\frac{u^2h_r\Theta-y'\Theta'}{y},\quad 0\leqslant x\leqslant 1 \tag{1}$$

where

$$h_r=\frac{h(\Theta\Delta T_{\rm ref})}{h_{\rm ref}} \tag{2}$$

is the reduced heat transfer coefficient. The corresponding boundary conditions are

$$\Theta(1)=\Theta_b \tag{3}$$

$$\Theta'(0)=\frac{h_eL}{k}\Theta(0)=\left(\frac{h_e}{h_{\rm ref}}\right)u{\rm Bi}^{1/2}\Theta_e\,. \tag{4}$$

The equation that describes the profile of the fin is

$$y(x)=Y/w=\lambda+(1-\lambda)x^n \tag{5}$$

The values of the taper ratio λ and the profile exponent n considered in the present study are summarized in Table 1. It can be seen from Eq. (1) that the dimensionless temperature Θ and its derivative Θ′ have the form:

$$\Theta=\Theta(x;u,{\rm Bi},\Theta_b),\quad \Theta'=\Theta'(x;u,{\rm Bi},\Theta_b) \tag{6a,b}$$

The heat dissipated by the fin, after introducing dimensionless variables becomes

$$Q=\frac{q_f}{2k\Delta T_{\rm ref}}=\frac{w}{L}\Theta'(1)=\frac{{\rm Bi}^{1/2}\Theta'(1)}{u}={\rm Bi}^{1/2}D \tag{7}$$

where the heat flux parameter D is defined as

$$D=\Theta'(1)/u \tag{8}$$

It has been pointed out by Razelos and Georgiou [34], that the condition that will economically justify the use of fins is: ''the ratio of heat dissipated by the fin to be much larger in comparison with the heat that would have been dissipated from the surface $2wH$, in the absence of the fin.'' This ratio is the effectiveness (or removal number) and it is equal to

$$N_r=\frac{q_f}{q_b}=\frac{2k\Delta T_{\rm ref}Q}{(2w)h_b\Delta T_b}=\frac{D}{{\rm Bi}^{1/2}}\left(\frac{h_{\rm ref}/h_b}{\Theta_b}\right) \tag{9}$$

Of particular interest is the fin's reduced heat flux in terms of the critical heat flux as a measure of the fin performance

$$Q_r=\frac{q_f/A_b}{q_{\rm CHF}}=\frac{q_f/(2w)}{q_{\rm CHF}}=\left(\frac{q_{\rm ref}}{q_{\rm CHF}}\right){\rm Bi}^{-1/2}D \tag{10}$$

where $q_{\rm ref}=h_{\rm ref}\Delta T_{\rm ref}$

Table 2 Constants and exponents for the boiling heat transfer coefficients in Eq. (12)

Fluid	a_1	a_2	a_3	A_1	A_2	A_3	ΔT_{n-t} [°C]	ΔT_{t-f} [°C]
Water	1.81	−3.46	−0.5	157.6	7.55×10^8	3100	18.52	66.04
Isopropanol	2.0	−2.50	0.0	28	4.70×10^7	254	24.17	127.91
R-113	2.0	−4.00	0.0	16	3.00×10^9	194	23.92	62.71

The Heat Transfer Coefficient

A power-law function is usually used to express the heat transfer coefficient for the three boiling regimes [8,13,15] as an approximation to experimental data

$$h_j = A_j (T - T_\infty)^{a_j}, \quad j = 1,2,3 \tag{11}$$

The TD at the knots for the nucleate-transition and for the transition-film section are calculated respectively as

$$\ln \Delta T_{j+1-j} = \frac{\ln(A_j / A_{j+1})}{a_{j+1} - a_j}, \quad j = 1,2 \tag{12}$$

The boiling constants and exponents for water, isopropyl alcohol and R-113 are summarized in Table 2. Many algorithms for the numerical solution of ODE are based on the Taylor expansion and require continuity of the derivatives up to a high order. Equations (11) have discontinuous derivatives at the knot TD and may produce unreliable results in the neighborhood close to the knot TD. In addition the sharp transition from one boiling section to the other is not experimentally observed (Haley and Westwater [2], Dhir and Liaw [31]) and continuous boiling curves were prepared from available experimental data [2,8] and used in the present study.

Results and Discussion

The mathematical model presented in the previous sections is used here to study the multiplicity characteristics of a longitudinal fin under multi-boiling heat transfer mode. The second order, two-point BVP described by Eq. (1) was first transformed into a first order IVP which was then solved using a single-shooting technique (Ascher et al. [35], Keller [36]). Because of the dependency of the boiling heat transfer coefficient on the TD, Eq. (1) is nonlinear and multiple steady states exist at certain operating conditions. With multiple steady states we mean more than one temperature distributions for the fin that satisfy Eq. (1). This is clearly demonstrated in Fig. 2 where for a given base TD ΔT_b there exist three different tip TD ΔT_e for $u > 0.2$ for example. In Fig. 2 the tip TD is plotted against the base TD with water as the boiling liquid for a rectangular profile fin with an insulated tip. At each axis the corresponding knot TD ΔT_{n-t} and ΔT_{t-f} are also plotted and the corresponding boiling regimes (that is nucleate, transition and film) are also indicated. In this way a grid is generated which defines the boiling modes on the $(\Delta T_e, \Delta T_b)$ plane. Thus for a given base TD we can immediately identify the operating regime(s) of the base and the tip of the fin. From Eqs. (6) it is evident that the temperature distribution of the fin depends on the following parameters: the CCP, the Biot number and the dimensionless base TD Θ_b. For the construction of the $\Delta T_e - \Delta T_b$ diagram a working fluid, a fin profile and a reference TD are being selected while the CCP is kept constant and the BVP described by Eq. (1) is solved repeatedly for each value of the CCP. Hence a family of curves similar to those depicted in Fig. 2 is obtained where u is the free parameter. A closer examination of Fig. 2 reveals the following boiling modes:

- single-mode boiling when $\Delta T_b < \Delta T_{n-t}$
- two-mode boiling when $\Delta T_{n-t} < \Delta T_b < \Delta T_{t-f}$ and $\Delta T_e < \Delta T_{n-t}$ that is transition and nucleate (TN) or when $\Delta T_{t-f} < \Delta T_b$ and $\Delta T_{n-t} < \Delta T_e < \Delta T_{t-f}$ that is film and transition (FT)
- three-mode boiling (FTN) when $\Delta T_{t-f} < \Delta T_b$ and ΔT_e takes values in the three boiling regimes

Another expected result is that as $\mathrm{Bi} \to 0$, $u \to 0$, which means that $k \to \infty$ and the tip TD asymptotically equals the base TD: $\Delta T_e \simeq \Delta T_b$. For the further discussion of the bifurcation characteristics of the multi-boiling heat transfer mode the Turning Points (TP) [37–39], on the $\Delta T_e - \Delta T_b$ diagram will be introduced.

Solution Diagrams and Temperature Distributions. On the TP change of the stability characteristics of the system is taking place and on the $(\Delta T_e, \Delta T_b)$ plane these TP are numerically determined from the relation

$$\left(\frac{\partial \Delta T_b}{\partial \Delta T_e} \right)_u = 0 \tag{13}$$

and they are denoted with the symbol (○) in Fig. 2. Generally two TP exist in each curve with $u = \text{const.}$, the upper and the lower respectively. The upper TP $(\Delta T_e)^u_{\mathrm{TP}}$, $(\Delta T_b)^u_{\mathrm{TP}}$ corresponds to the upper steady-state temperature distribution while the lower TP $(\Delta T_e)^l_{\mathrm{TP}}$, $(\Delta T_b)^l_{\mathrm{TP}}$ corresponds to the lower steady state temperature distribution (see Fig. 3). For example for $u > 0.2$ there exist two TP while for $u < 0.2$ no TP exist since the base TD is a single

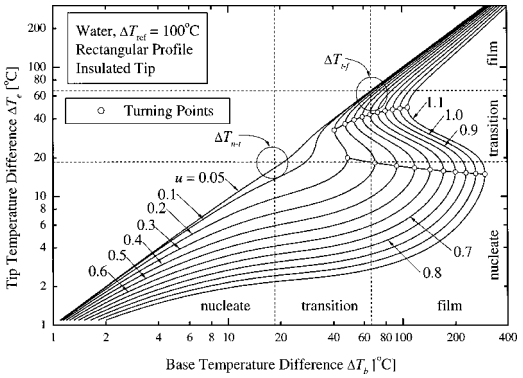

Fig. 2 Loci of the turning points on the $(\Delta T_e, \Delta T_b)$ plane with the CCP as a parameter

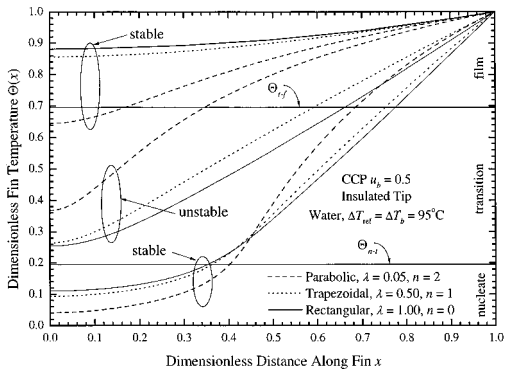

Fig. 3 Stable and unstable temperature distributions for the rectangular, the trapezoidal and the parabolic profile

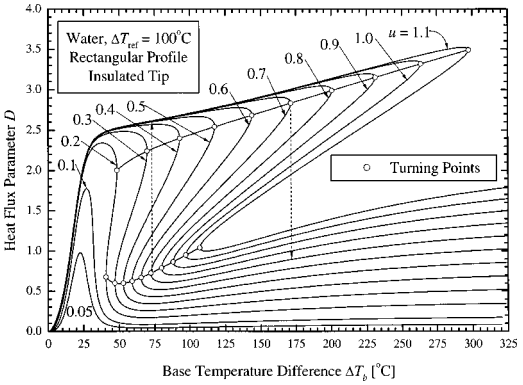

Fig. 4 Hysteresis curves for the rectangular profile with insulated tip

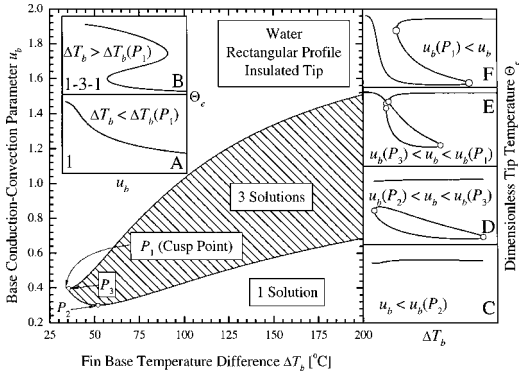

Fig. 5 Loci of the turning points on the $(u_b, \Delta T_b)$ plane for the rectangular profile

value function of the tip TD and for that cases the fin can operate only on single-mode boiling. The TP define the values of the base TD for which multiple steady states exist. That is only when the condition

$$(\Delta T_e)^u_{\mathrm{TP}} < \Delta T_b < (\Delta T_b)^l_{\mathrm{TP}} \tag{14}$$

is satisfied more than one (in fact three) temperature distributions exist. Moreover the TP separate the $\Delta T_e - \Delta T_b$ curves into the following three branches:

- upper steady state branch: $\Delta T_e > (\Delta T_e)^u_{\mathrm{TP}}$
- unstable steady state branch: $(\Delta T_e)^l_{\mathrm{TP}} < \Delta T_e < (\Delta T_e)^u_{\mathrm{TP}}$
- lower steady state branch: $\Delta T_e < (\Delta T_e)^l_{\mathrm{TP}}$

For example when the fin base operates at the transition regime, that is $\Delta T_{n-t} < \Delta T_b < \Delta T_{t-f}$ (i.e., two-mode boiling) there exist three operating points: one on the lower stable branch for which the tip TD corresponds to nucleate boiling, one on the unstable branch for which the tip TD corresponds to the transition boiling and one on the upper stable branch with the tip TD corresponding to the transition boiling. Therefore, for two-mode boiling although two operating points are on the same boiling regime (i.e., transition) only one of them is stable. Furthermore when the fin base operates at the film regime, that is $\Delta T_{t-f} < \Delta T_b$ (i.e., three-mode boiling) there exist three operating points: one on the lower stable branch for which the tip TD corresponds to nucleate boiling, one on the unstable branch for which the tip TD corresponds to the transition boiling and one on the upper stable branch with the tip TD corresponding on the film boiling. Therefore the TP are the limiting stable operating points. Hence with the aid of Fig. 2 we can recognize the mode of heat transfer mechanism (single-boiling or multi-boiling), the multiplicity pattern (one solution or three solutions) and the stability characteristics of each solution (stable or unstable).

Figure 4 represents the hysteresis curves. These are the curves of the dimensionless base heat dissipation as a function of the base TD with the CCP as the free parameter, which correspond to the same states of Fig. 2. It is interesting to notice that in general there exist three base TD for a given value of the heat flux parameter and for a given D there exist three base TD values as it was first observed by Haley and Westwater [2]. Since the unsteady states are not realizable by the system it is then expected at TP the state variables D and Θ_e to move to another stable operating point rather than trace the unstable branch. This behavior is indicated in Fig. 4 for the curve with $u=0.7$ and for a rectangular profile with an insulated tip. During say a heating run when the upper TP is reached that is $\Delta T_b = (\Delta T_b)^u_{\mathrm{TP}}$ then the system state variables will move in the direction of the arrow of the dashed line which connects the upper TP with the lower stable branch. A similar behavior is expected during a cooling run. When the lower TP is reached, $\Delta T_b = (\Delta T_b)^l_{\mathrm{TP}}$ the state variables will move from the lower stable branch to the upper stable branch in the direction indicated by arrow of the dashed line, which connects the two branches.

The existence of three (two stable and one unstable) temperature distributions $\Theta(x)$ along the fin height is demonstrated in Fig. 3 for three different profiles. The rectangular $(\lambda=1, n=0)$, the trapezoidal $(\lambda=0.5, n=1)$ and the parabolic profile $(\lambda=0.05, n=2)$ for the value of the CCP $u_b=0.5$. The two dimensionless knot temperatures the nucleate-transition $\Theta_{n-t} = \Delta T_{n-t}/\Delta T_b = 0.1949$ and the transition-film $\Theta_{t-f} = \Delta T_{t-f}/\Delta T_b = 0.6952$ are also plotted as horizontal lines. The upper steady state temperature distributions for the rectangular and the trapezoidal profile show that the fin is operating under single-mode boiling, both the base and the tip TD are in the film regime. For the parabolic profile, however, the operation is being under two-mode boiling (FT) since the tip TD just enters the transition regime. For all the profiles the unsteady states are under two-mode boiling (FT), while the lower stable one is under three-mode boiling (FTN). It should be emphasized here that the stability analysis of a certain steady state, obtained from Eq. (1), to small perturbations leads to the solution of a corresponding Sturm–Liouville problem in order to obtain the eigenvalues and the eigenfunctions. In such an eigensystem all eigenvalues are real and distinct (no complex eigenvalues exist), but a finite number may be positive in which case the corresponding steady state is unstable. Numerical solution of the Sturm–Liouville problem confirmed that the upper and lower solutions in Fig. 3 are stable (all eigenvalues were negative), while in the intermediate solution the first eigenvalue was positive and therefore this solution is unstable.

The locus of the TP on the (p_i, p_j) plane, where p_i and p_j are two of the model parameters divides the plane into two regions with different number of solutions. Figure 5 presents loci of TP on the $(u_b, \Delta T_b)$ plane for the rectangular profile with an insulated tip. It is seen that its locus of TP divides the $(u_b, \Delta T_b)$ plane into two regions, one where a unique (type A) solution exists and another one with three (type B) solutions. The number of solutions in each region is noted in Fig. 5 inside a frame while each solution locus together with the multiplicity pattern are given in the two inserted graphs, on the left, inside Fig. 5. Its locus of TP exhibits a cusp point (CP), which is also indicated in Fig. 5 as point P_1 and it is numerically calculated from the following relations:

$$\left(\frac{\partial u_b}{\partial \Theta_e}\right)_{\Delta T_b} = \left(\frac{\partial^2 u_b}{\partial^2 \Theta_e}\right)_{\Delta T_b} = 0 \tag{15}$$

As the base TD increases the CCP increases (except a small region of the lower branch between 35°C and 50°C), while the multiplicity region increases in size. When a different parameterization for the representation of the solution locus is selected. For example if u_b is considered as a parameter the solution locus on

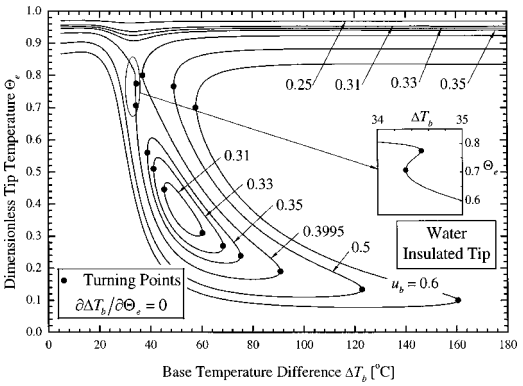

Fig. 6 Loci of the turning points on the $(\Theta_e, \Delta T_b)$ plane for the rectangular profile with parameter the base CCP u_b

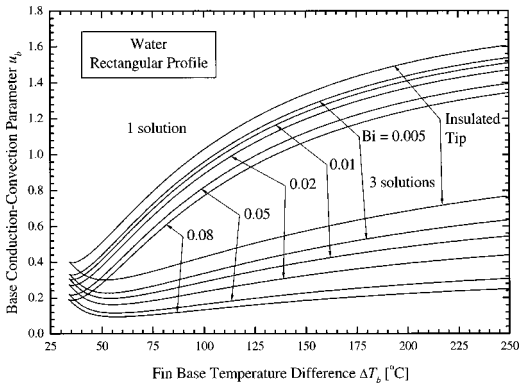

Fig. 8 The effect of Biot number on the locus of the turning points on the $(u_b, \Delta T_b)$ plane for the rectangular profile

the $(\Theta_e, \Delta T_b)$ plane is represented by the four inserted graphs (type C, D, E, and F) on the right hand side of Fig. 5 with the corresponding TP (○). Point P_2 corresponds to the birth of an isola on the $(\Theta_e, \Delta T_b)$ plane while P_3 represents the point where the isola comes in contact with the upper branch of the solution diagram. The complete solution locus on the $(\Theta_e, \Delta T_b)$ plane is shown on Fig. 6. It should be noted here that the following relationship holds between u and u_b:

$$\frac{u}{u_b} = \left(\frac{h_{\text{ref}}}{h_b}\right)^{1/2}. \tag{16}$$

The effect of the profile on the solution diagrams shows a significant reduction on the CCP TP is observed especially for the upper branch. The reduction of the CCP causes in turn a significant reduction on the multiplicity size, while the CP CCP decreases and the CP base TD remains almost unchanged as Fig. 7 shows.

The Effect of the Biot Number on the Solution Diagrams The effect of the Biot number will be considered only for the rectangular profile since for the other profiles the heat transfer area at the tip is significantly decreased and consequently the heat transfer from the tip is unimportant. As the Biot number increases the TP CCP is decreasing which results in a decreased multiplicity region as it is presented in Fig. 8. The Biot number also affects the CP and specifically the CCP decreases while the base TD increases as it is shown in Fig. 14. Figure 9 shows the remarkable effect of the Biot number on the hysteresis curves. Comparing with the insulated tip case the upper TP has increased by 80°C while the maximum heat dissipation is increased by 20% approximately. For the lower TP however only an increase of about 10°C is observed in the base TD TP while the increase in the heat dissipation is of the order of 5%. In addition as the Biot number increases the curve on the upper TP becomes sharper.

Fin Performance and Comparison With Experimental Data Figure 10 shows the effectiveness N_r for the rectangular profile fin where values as high as 96 can be reached. At the same time the dimensionless heat flux in terms of the critical heat flux Q_r in Fig. 11 reaches 5.8. This clearly demonstrates that the use of an extended surface under multi-boiling conditions constitutes a powerful heat transfer enhancement mechanism. In Fig. 12 and in Fig. 13 a comparison between the calculated and the experimental data of Liaw and Yeh [15] are presented since for the rectangular profile fin and the corresponding cylindrical pin fin the governing equations are identical. For water the agreement is generally better

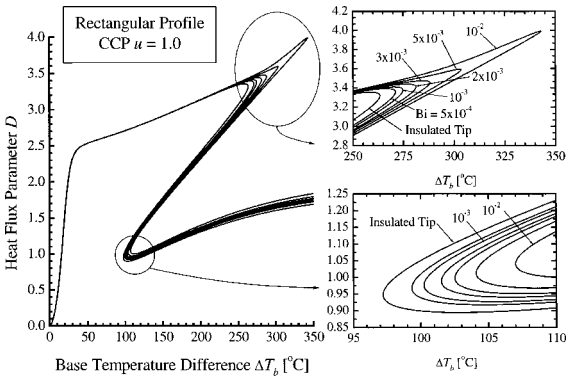

Fig. 9 The effect of the Biot number on the hysteresis curves for the rectangular profile

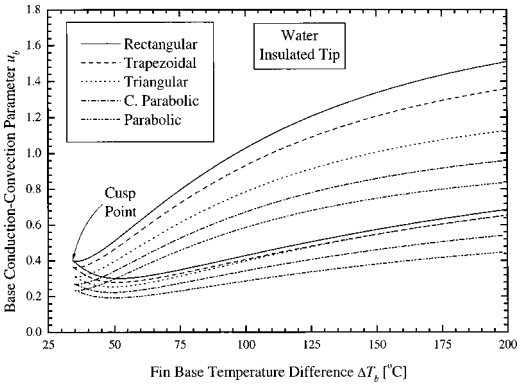

Fig. 7 Loci of the turning points on the $(u_b, \Delta T_b)$ plane for the five profiles

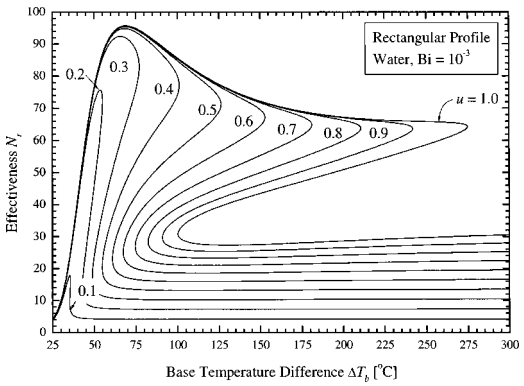

Fig. 10 The removal number N_r as a function of the base TD and the CCP for the rectangular profile fin

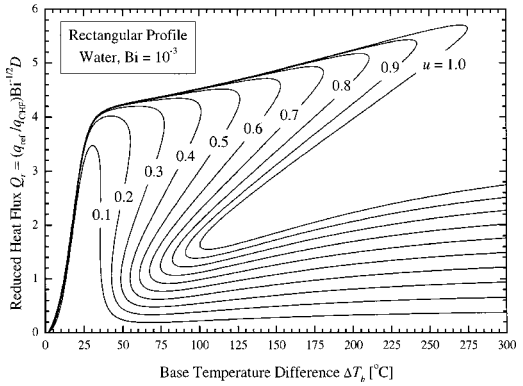

Fig. 11 The reduced heat flux Q_r of the base TD and the CCP for the rectangular profile fin

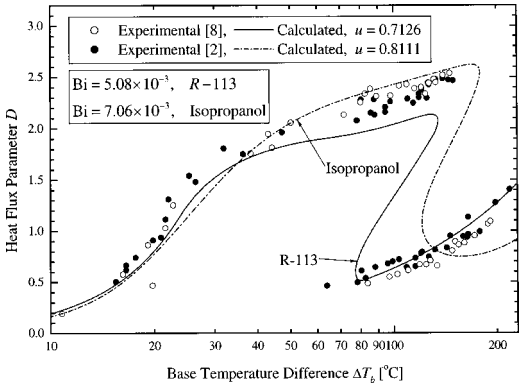

Fig. 14 Comparison of the calculated and measured heat flux data for isopropanol and R-113 for a cylindrical pin fin

and the lower branch is well represented by the model. For the case of isopropyl alcohol an additional comparison with the experimental results of Haley and Westwater [2] is depicted in Fig. 14, where the experimental data of Petukhov et al. [8] for the R-113 are also presented. Generally the heat flux predicted by the one-dimensional theoretical analysis is reasonable although the agreement is better for lower values of the Biot number (in the experiments performed by Haley and Westwater [2] and Petukhov et al. [8] the Biot number is almost one order of magnitude lower than the corresponding Biot number of the experiments of Liaw and Yeh [15]). As the Biot number increases probably two-dimensional effects become important. It is worth noticing that for a given fin volume the dimensionless fin heat dissipation curves and the effectiveness exhibit a maximum. This characteristic behavior is a consequence of the variable boiling heat transfer coefficient. Therefore, using the solution structure, the limit points and the hysteresis points of the present study the operating conditions under which the heat dissipation is maximized can be obtained and the framework for the optimum design of fins operating under multi-boiling conditions can be developed.

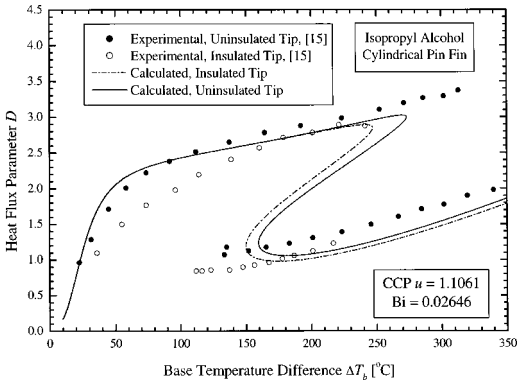

Fig. 12 Comparison of the calculated and measured heat flux data for isopropyl alcohol for a cylindrical pin fin

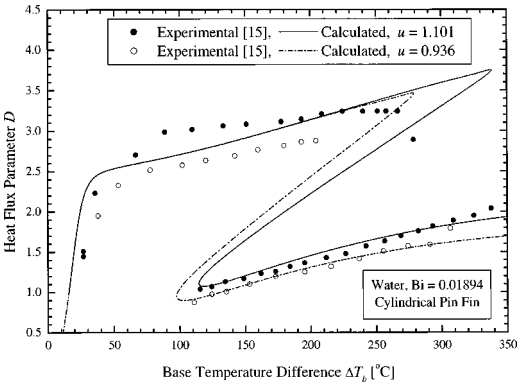

Fig. 13 Comparison of the calculated and measured heat flux data for water for a cylindrical pin fin

Conclusions

In the present study a numerical bifurcation analysis has been carried out for longitudinal fins under multi-boiling heat transfer mode. Five profiles were considered: the rectangular, the trapezoidal, the triangular, the convex parabolic and the parabolic one. The theoretical model is based on the one dimensional heat conduction with and without heat transfer from the tip. In addition comparison with experimental data for water, isopropanol and R-113 available in the literature shows that the agreement between the model and the measurements is reasonable. Important conclusions are as follows:

1) The base TD ΔT_b, the CCP u and the Biot number Bi are the important operating variables of the boiling system under consideration.
2) The taper ratio λ and the profile exponent n have a significant effect on the fin heat dissipation and on the size of the multiplicity region.
3) The Biot number has an important effect on the stable operating range and on the maximum heat dissipation for a rectangular profile fin. Moreover, as the Biot number increases the multiplicity region increases.
4) The use of an extended surface can be very beneficial since the removal number can take values up to 100 while the heat flux developed shows almost a six-fold increase under conditions presented in this study.

Nomenclature

a_j = boiling exponents, Eq. (11), [-]
A_j = dimensional boiling constants, Eq. (11), [W/(m^{2}K)]
Bi = $(h_{\text{ref}}w/k)$ Biot number, [-]
D = function defined by Eq. (8), [-]
h = heat transfer coefficient, [W/(m^{2}K)]
H = fin length, [m]
k = fin thermal conductivity, [W/(mK)]
L = fin height, [m]
N_r = effectiveness, [-]
O = order of magnitude, [-]
q_f = fin heat loss per unit length, [W/m]
Q = dimensionless fin heat dissipation, [-]
Q_r = reduced fin heat flux, [-]
T = temperature, [K]

X = coordinate, Fig. 1, [m]
x = (X/L) dimensionless distance along fin, [-]
Y = coordinate, Fig. 1, [m]
u = $(L\mathrm{Bi}^{1/2}/w)$ conduction-convection parameter, [-]
w = fin semi-thickness, [m]

Greek Symbols

ΔT = $(T-T_\infty)$ temperature difference, [K]
Θ = $[(T-T_\infty)/(T_{\mathrm{ref}}-T_\infty)]$ dimensionless fin temperature, [-]
λ = (w_e/w_b) tip to base fin semi-thickness ratio, [-]

Subscripts

b = fin base
e = fin tip
f = fin, film boiling regime
n = nucleate boiling regime
r = reduced value (i.e., $h_r=h/h_{\mathrm{ref}}$)
ref = reference value
t = transition boiling regime
TP = turning point
∞ = ambient boiling liquid

Superscripts

$(')$ = derivative with respect to x
l = lower steady state
u = upper steady state

Abbreviations

BVP = Boundary Value Problem
CCP = Conduction-Convection Parameter
CP = Cusp Point
IVP = Initial Value Problem
LAI = Length of Arc Idealization
ODE = Ordinary Differential Equation
TD = Temperature Difference
TP = Turning Point(s)

References

[1] Haley, K. W., and Westwater, J. W., 1965, ''Heat Transfer From a Fin to a Boiling Liquid,'' Chem. Eng. Sci., **20**, pp. 711.
[2] Haley, K. W., and Westwater, J. W., 1966, ''Boiling Heat Transfer From Single Fins,'' *Proc. 3rd International Heat Transfer Conference*, AIChE-ASME, **3**, pp. 245–253.
[3] Klein, G. J., and Westwater, J. W., 1973, ''Heat Transfer from Multiple Spines to Boiling Liquids,'' AIChe J., **17**(5), pp. 1050–1056.
[4] Shih, C.-C., and Westwater, J. W., 1974, ''Spheres, Hemispheres and Discs as High-Performance Fins for Boiling Heat Transfer,'' Int. J. Heat Mass Transfer, **17**, pp. 125–133.
[5] Wilkins, J. E. Jr., 1960, ''Minimum Mass Thin Fins for Space Radiators,'' *Proc. Heat Transfer and Fluid Mechanics Institute*, **228**, Stanford University Press.
[6] Petukhov, B. S., Kovalev, S. A., Zhukov, V. M., and Kazakov, G. M., 1971, ''Measurement of Local Heat Transfer on a Nonisothermal Surface,'' High Temp., **9**(6), pp. 1159–1161.
[7] Petukhov, B. S., Kovalev, S. A., and Zhukov, V. M., 1973, ''Local Boiling Heat Transfer on Nonisothermal Surfaces,'' Heat Transfer-Sov. Res., **5**(6), pp. 154–162.
[8] Petukhov, B. S., Kovalev, S. A., Zhukov, V. M., and Kazakov, G. M., 1972, ''Study of Heat Transfer During the Boiling of a Liquid on the Surface of a Single Fin,'' Heat Transfer-Sov. Res., **4**(4), pp. 148–156.
[9] Kovalev, S. A., and Rybchinskaya, G. B., 1978, ''Prediction of the Stability of Pool Boiling Heat Transfer to Finite Disturbances,'' Int. J. Heat Mass Transfer, **21**, pp. 694–700.
[10] Kovalev, S. A., Zhukov, V. M., and Usatikov, S. V., 2000, comment on the paper by Lin, W. W., Yang, J. C., and Lee, D. J., 2000, ''Metastable Pin Fin Boiling,'' Int. J. Heat Mass Transfer, **43**(9), pp. 1629–1635; Int. J. Heat Mass Transfer, **44**(18), pp. 3575–3577.
[11] Lai, F.-S., and Hsu, Y.-Y., 1967, ''Temperature Distribution in a Fin Partially Cooled by Nucleate Boiling,'' AIChE J., **13**(4), pp. 817–821.
[12] Unal, H. C., 1985, ''Determination of the Temperature Distribution in an Extended Surface With a Non-Uniform Heat Transfer Coefficient,'' Int. J. Heat Mass Transfer, **28**(12), pp. 2279–2284.
[13] Unal, H. C., 1987, ''An Analytic Study of Boiling Heat Transfer From a Fin,'' Int. J. Heat Mass Transfer, **30**(2), pp. 341–349.
[14] Liaw, S. P., and Yeh, R. H., 1994, ''Fins With Temperature Dependent Surface Heat Flux-I. Single Heat Transfer Mode,'' Int. J. Heat Mass Transfer, **37**(10), pp. 1509–1515.
[15] Liaw, S. P., and Yeh, R. H., 1994, ''Fins With Temperature Dependent Surface Heat Flux-II. Multi-boiling Heat Transfer,'' Int. J. Heat Mass Transfer, **37**(10), pp. 1517–1524.
[16] Lin, W. W., and Lee, D. J., 1996, ''Boiling on a Straight Pin Fin,'' AIChE J., **42**(10), pp. 2721–2728.
[17] Lin, W. W., and Lee, D. J., 1998, ''Boiling on a Plate Fin and Annular Fin,'' Int. Commun. Heat Mass Transfer, **25**(8), pp. 1169–1180.
[18] Lin, W. W., Yang, J. C., and Lee, D. J., 1999, ''Boiling on a Conical Spine,'' Exp. Heat Transfer, **12**, pp. 175–191.
[19] Lin, W. W., Yang, J. C., and Lee, D. J., 2000, ''Metastable Pin Fin Boiling,'' Int. J. Heat Mass Transfer, **43**(9), pp. 1629–1635.
[20] Aris, R., 1975, *The Mathematical Theory of Diffusion and Reaction in Permeable Catalysts*, Vols. 1 and 2, Clarendon Press, Oxford.
[21] Golubitsky, M., and Scaeffer, D., 1985, *Singularities and Groups in Bifurcation Theory*, Vols. 1 and 2, Springer, New York.
[22] Balakotaiah, V., and Luss, D., 1982, ''Structure of the Steady State Solutions of Lumped-Parameter Chemically Reacting Systems,'' Chem. Eng. Sci., **37**, pp. 1611–1623.
[23] Balakotaiah, V., and Luss, D., 1982, ''Global Analysis of the Multiplicity Features of Multi-Reaction Lumped Multi-Parameter Systems,'' Chem. Eng. Sci., **39**, pp. 865–881.
[24] Witmer, G., Balakotaiah, V., and Luss, D., 1986, ''Finding Singular Points of Two-Point Boundary Value Problems,'' J. Comp. Phys., **65**, pp. 244–250.
[25] Michelsen, M. L., and Villadsen, J., 1972, ''Diffusion and Reaction on Spherical Catalysts: Steady State and Local Stability Analysis,'' Chem. Eng. Sci., **27**, pp. 751–762.
[26] Kubíček, M., and Hlaváček, V., 1971, ''Solution of Non-Linear Boundary Value Problems-III. A Novel Method: Differentiation With Respect to an Actual Parameter,'' Chem. Eng. Sci., **26**, pp. 705–709.
[27] Kubíček, M., and Hlaváček, V., 1974, ''Solution of Non-Linear Boundary Value Problems-VIII. Evaluation of Branching Points Based on Shooting Method and GPM Technique,'' Chem. Eng. Sci., **29**, pp. 1695–1699.
[28] Hsuen, H. K. D., and Sotirchos, S. V., 1989, ''Multiplicity Analysis of Intraparticle Char Combustion,'' Chem. Eng. Sci., **44**(11), pp. 2639–2651.
[29] Hsuen, H. K. D., and Sotirchos, S. V., 1989, ''Multiplicity Analysis of Char Combustion With Homogeneous CO Oxidation,'' Chem. Eng. Sci., **44**(11), pp. 2653–2665.
[30] Hsuen, H. K. D., and Sotirchos, S. V., 1991, ''Multiplicity and Stability Phenomena in Diffusion Flames,'' Chem. Eng. Sci., **46**(12), pp. 3165–3175.
[31] Dhir, V. K., and Liaw, S. P., 1989, ''Framework for a Unified Model for Nucleate and Transition Pool Boiling,'' ASME J. Heat Transfer, **111**, pp. 739–746.
[32] Murray, M. W., 1938, ''Heat Transfer Through an Annular Disk or Fin of Uniform Thickness,'' ASME J. Appl. Mech., **60A**, pp. 278.
[33] Gardner, K. A., 1945, ''Efficiency of Extended Surfaces,'' Trans. ASME, **69**(8), pp. 621–631.
[34] Razelos, P., and Georgiou, E., 1992, ''Two-Dimensional Effects and Design Criteria for Convective Extended Surfaces,'' Heat Transfer Eng., **13**(3), pp. 38–48.
[35] Ascher, U. M., Mattheij, R. M. M., and Russel, R. D., 1995, *Numerical Solution of Boundary Value Problems for Ordinary Differential Equations*, 2nd ed., SIAM, Philadelphia, PA.
[36] Keller, H. B., 1992, *Numerical Methods for Two-Point Boundary-Value Problems*, Dover, New York.
[37] Seydel, R., 1994, *Practical Bifurcation and Stability Analysis. From Equilibrium to Chaos*, Springer-Verlag, New York.
[38] Govaerts, W. J. F., 2000, *Numerical Methods for Bifurcations of Dynamical Equilibria*, SIAM, Philadelphia, PA.
[39] Iooss, G., and Joseph, D. D., 1990, *Elementary Stability and Bifurcation Theory*, 2nd ed., Springer-Verlag, New York.

Heat Transfer Mechanisms During Flow Boiling in Microchannels

Satish G. Kandlikar
e-mail: sgkeme@rit.edu
Thermal Analysis and Microfluidics Laboratory,
Department of Mechanical Engineering,
Rochester Institute of Technology,
Rochester, NY 14623

The forces due to surface tension and momentum change during evaporation, in conjunction with the forces due to viscous shear and inertia, govern the two-phase flow patterns and the heat transfer characteristics during flow boiling in microchannels. These forces are analyzed in this paper, and two new nondimensional groups, $\mathbf{K_1}$ *and* $\mathbf{K_2}$*, relevant to flow boiling phenomenon are derived. These groups are able to represent some of the key flow boiling characteristics, including the CHF. In addition, a mechanistic description of the flow boiling phenomenon is presented. The small hydraulic dimensions of microchannel flow passages present a large frictional pressure drop in single-phase and two-phase flows. The small hydraulic diameter also leads to low Reynolds numbers, in the range 100–1000, or even lower for smaller diameter channels. Such low Reynolds numbers are rarely employed during flow boiling in conventional channels. In these low Reynolds number flows, nucleate boiling systematically emerges as the dominant mode of heat transfer. The high degree of wall superheat required to initiate nucleation in microchannels leads to rapid evaporation and flow instabilities, often resulting in flow reversal in multiple parallel channel configuration. Aided by strong evaporation rates, the bubbles nucleating on the wall grow rapidly and fill the entire channel. The contact line between the bubble base and the channel wall surface now becomes the entire perimeter at both ends of the vapor slug. Evaporation occurs at the moving contact line of the expanding vapor slug as well as over the channel wall covered with a thin evaporating film surrounding the vapor core. The usual nucleate boiling heat transfer mechanisms, including liquid film evaporation and transient heat conduction in the liquid adjacent to the contact line region, play an important role. The liquid film under the large vapor slug evaporates completely at downstream locations thus presenting a dryout condition periodically with the passage of each large vapor slug. The experimental data and high speed visual observations confirm some of the key features presented in this paper.*
[DOI: 10.1115/1.1643090]

Keywords: Boiling, Bubble Growth, Heat Transfer, Interface, Microscale

Introduction

It has been well recognized that the flow boiling heat transfer consists of a nucleate boiling component and a convective boiling component, e.g., Schrock and Grossman [1]. The convective boiling component results from the convective effects, whereas the nucleate boiling component results from the nucleating bubbles and their subsequent growth and departure at the heated surface. The nucleate boiling and the convective boiling mechanisms cannot be distinguished precisely, as they are closely interrelated.

The nucleation, growth and subsequent departure of bubbles from a heated wall constitute the major stages of a bubble ebullition cycle in pool boiling. The heat transfer mechanisms associated with pool boiling include: transient conduction, film vaporization, microconvection, contact line heat transfer, and to a lesser degree, the vaporization condensation, and Marangoni convection. The bubble dynamics under flow boiling conditions are affected in such a way as to shift toward smaller nucleation cavity sizes and smaller departure bubble diameters. In this paper, the forces governing the liquid vapor interface in microchannels during flow boiling are analyzed and two new dimensionless groups are identified. The role of nucleate boiling is re-examined and the heat transfer mechanisms are discussed. The high-speed flow visualization conducted by the author and his co-workers and the experimental heat transfer data from literature are used in arriving at the mechanistic description of the flow boiling phenomena in microchannels.

In this paper, the channel classification proposed by Kandlikar and Grande [2] is used. This classification should be used as a mere guide indicating the size range, rather than rigid demarcations based on specific criteria. In reality, the effects will depend on fluid properties and their variation with pressure changes. Undoubtedly, the actual flow conditions, such as single phase liquid or gas flow, or flow boiling or flow condensation, will present different classification criteria. The classification by Kandlikar and Grande is based on rarefaction effects for common gases around 1 atmospheric pressure. At smaller dimensions below about 10 μm, molecular effects begin to be important, again subject to specific operating conditions. Molecular nanochannels are still very large compared to the molecular dimensions, but the intermolecular forces begin to play an important role especially in the near wall region. In two-phase applications, recently Kawaji and Chung [3] reported significant departure for their 100 μm microchannels from the linear relationship between volumetric quality versus void fraction proposed by Ali et al. [4] for narrow channels.

Conventional channels: >3 mm
Minichannels: 3 mm$\geq D_h >$200 μm
Microchannels: 200 μm$\geq D_h >$10 μm
Transitional Channels: 10 μm$\geq D_h >$0.1 μm (100 nanometer, nm, or 1000 Å)
Transitional Microchannels: 10 μm$\geq D_h >$1 μm
Transitional Nanochannels: 1 μm$\geq D_h >$0.1 μm
Molecular Nanochannels: 0.1 μm$\geq D_h$

Review of Available Non-Dimensional Groups Related to Two-Phase Flow and Interfacial Phenomena

Before deriving the relevant new non-dimensional groups in microchannels, the existing groups commonly applied in the two-

Contributed by the Heat Transfer Division for publication in the JOURNAL OF HEAT TRANSFER. Manuscript received by the Heat Transfer Division February 20, 2003; revision received September 24, 2003. Associate Editor: M. K. Jensen.

Table 1 Non-dimensional Groups relevant to two-phase flow studies in microchannels

Non-dimensional number	Significance	Relevance to Microchannels
	Groups based on Empirical Considerations	
Martinelli parameter, X $X^2=\left(\left\|\frac{dp}{dz}\right\|_F\right)_L \Big/ \left(\left\|\frac{dp}{dz}\right\|_F\right)_G$	Represents the Ratio of frictional pressure drops with liquid and gas flow. It has been employed successfully in two-phase pressure drop models in simple as well as complex geometries	Because of its success in predicting pressure drop in compact evaporator geometries, it is expected to be a useful parameter in microchannels as well.
Convection Number, Co $\mathrm{Co}=[(1-x)/x]^{0.9}[\rho_G/\rho_L]^{0.5}$	Co is a modified Martinelli parameter, introduced by Shah [5] in correlating flow boiling data	Its direct usage beyond flow boiling correlation may be limited.
Boiling number, Bo $\mathrm{Bo}=\frac{q}{G\,h_{fg}}$	Heat flux is non-dimensionalized with mass flux and latent heat. It is not based on any fundamental considerations.	Since it combines two important flow parameters, q and G, it will be used in empirical treatment of flow boiling.
	Groups based on Fundamental Considerations	
Bond number, **Bo** $\mathbf{Bo}=\frac{g(\rho_L-\rho_G)D^2}{\sigma}$	**Bo** represents the ratio of buoyancy force to surface tension force. Used in droplet atomization and spray applications.	Since the effect of gravitational force is expected to be small, **Bo** is not expected to play an important role in microchannels.
Eötvös Number, Eo $\mathrm{Eo}=\frac{g(\rho_L-\rho_G)L^2}{\sigma}$	Eötvös number is similar to the Bond number, except that the characteristic dimension L could be D_h or any other physically relevant parameter.	Similar to **Bo**, Eo is not expected to be important in microchannels except at very low flow velocities and vapor fractions.
Capillary number, **Ca** $\mathbf{Ca}=\frac{\mu\,V}{\sigma}$	**Ca** represents the ratio of viscous to surface tension forces. It is useful in analyzing the bubble removal process.	**Ca** is expected to play a critical role as both the surface tension and the viscous forces are important in microchannel flows.
Ohnesorge Number, **Z** $Z=\frac{\mu}{(\rho\,L\,\sigma)^{1/2}}$	**Z** represents the ratio of the viscous force to the square root of the product of the inertia and the surface tension forces. It is used in analyzing liquid droplets and droplet atomization processes.	The combination of the three forces into one masks the individual effects of each force. Although Z may come out as an important variable, it may not be suitable in the early stages of microchannel research.
Weber Number, We $\mathrm{We}=\frac{L\,G^2}{\rho\,\sigma}$	We represents the ratio of the inertia to the surface tension forces. For flow in channels, D_h is used in place of L.	We I useful in studying the relative effects of surface tension and inertia forces on flow patterns in microchannels.
Jakob Number, Ja $\mathrm{Ja}=\frac{\rho_L}{\rho_V}\frac{c_{p,L}\,\Delta T}{h_{fg}}$	Ja represents the ratio of the sensible heat for a given volume of liquid to heat or cool through ΔT in reaching its saturation temperature, to the latent heat required in evaporating the same volume of vapor.	Ja may be used as an important parameter in studying the effects of liquid superheat prior to initiation of nucleation in microchannels. It may also be useful in studying the subcooled boiling conditions.

phase and flow boiling applications are reviewed in this section. Non-dimensional groups are useful in arriving at key basic relations among system variables that are valid for different fluids under different operating conditions. Some of these groups have been derived empirically, often on the basis of experimental data. Fundamental considerations of the governing forces and their mutual interactions lead to non-dimensional groups that provide important insight into the physical phenomena. A listing of both types of non-dimensional groups, based on empirical considerations and on theoretical analysis of forces, is given in Table 1. A brief description of their significance along with their relevance to flow boiling in microchannels is also included in the table.

The non-dimensional groups based on empirical considerations have been proposed in literature on the basis of extensive data analysis. Their extension to other systems requires rigorous validation, often requiring modifications of constants or exponents. Convection number and boiling number fall under this category. Although the Martinelli parameter is derived from fundamental considerations of the gas and the liquid phase friction pressure gradients, it is used extensively as an empirical group in correlating experimental results on pressure drop, void fraction, and is some cases, heat transfer as well.

It can be seen from Table 1 that among the groups derived from fundamental considerations, Capillary number, Ca, and Weber number, We, are important in microchannel two-phase flows. They represent the ratios of viscous and surface tension forces, and inertia and surface tension forces respectively. The ratio of inertia to viscous forces, represented by Reynolds number, Re, is extensively used in single phase flows; it is also expected to have an important role in two-phase flows, as the single-phase heat transfer and pressure drop characteristics are often found to be useful in predicting the two-phase flow behavior.

The Bond number represents the ratio of the gravitational to surface tension forces on a droplet or a bubble. Departure bubble diameter is sometimes used as the characteristic dimension in the definition of the Bond number in pool boiling. Since the gravitational forces are expected to be small compared to the surface tension and viscous forces, usefulness of Bond number in microchannel application is limited.

Additionally, there are a number of non-dimensional groups used in literature for correlating different boiling phenomena. For example, Stephan and Abdelsalam [6] utilized eight dimensionless groups in developing a comprehensive correlation for saturated pool boiling heat transfer. Similarly, Kutateladze [7] combined the critical heat flux with other parameters through dimensional analysis to obtain a non-dimensional group. However, only those non-dimensional groups that are derived from some basic considerations are reviewed here.

Forces Acting on a Liquid-Vapor Interface Due to Evaporation Momentum Change, Inertia and Surface Tension. The non-dimensional groups employed so far in literature for analyzing the flow patterns during flow boiling have been similar to those employed in the adiabatic two-phase flow applications. The Jakob number is used in analyzing the bubble growth phenomenon. The Weber number has been recently introduced in flow pattern maps for microchannels and minichannels. The effect of heat flux appears only in the Boiling number, which is used in heat transfer correlations along with the density ratio; the Boiling number has not been used in flow pattern maps.

Heat flux has a significant effect on the two-phase structure during flow boiling. A higher heat flux results in a more rapid bubble growth leading to quickly filling the channel with a vapor slug. The forces generated due to rapid evaporation become significant for microchannels, as the growing bubbles interact with the channel walls. Further discussion on this aspect is presented in the following sections.

As a nucleating bubble grows, the difference in the densities of

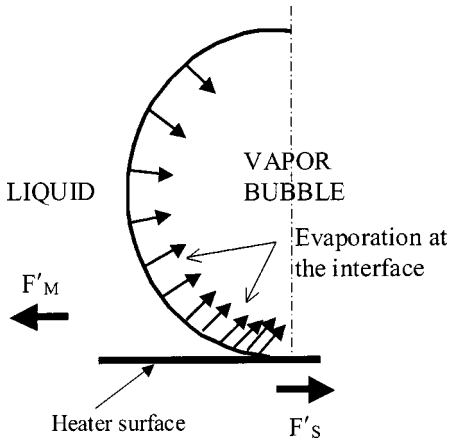

Fig. 1 Forces acting on a vapor bubble growing on a heater surface in a liquid pool, only half of a symmetric bubble shown

the two phases causes the vapor phase to leave at a much higher velocity than the corresponding liquid velocity toward the receding and evaporating interface. The resulting change in momentum due to evaporation introduces a force on the interface. The magnitude of this force is highest near the heater surface due to a higher evaporation rate in the contact line region between the bubble base and the heater surface as illustrated in Fig. 1.

For the case of saturated flow boiling, the heat flux at the wall results in an evaporation mass flux of q/h_{fg}. The resulting momentum change introduces a force on the liquid interface that can be expressed as described below per unit characteristic dimension, either based on the bubble diameter as shown in Fig. 1, or based on the channel diameter as shown in Fig. 2. This force was first introduced by Kandlikar [8] in developing a CHF model based on the force balance at the contact line at the base of a bubble on the heater surface.

Thus force per unit length due to momentum change caused by evaporation at the interface is given by

$$F'_M = \frac{qD}{h_{fg}} \frac{q}{h_{fg}} \frac{1}{\rho_G} = \left(\frac{q}{h_{fg}}\right)^2 \frac{D}{\rho_G} \tag{1}$$

where D is the characteristic dimension.

The other forces acting on the interface are due to the inertia of the flow and the surface tension in the contact line region. The forces per unit length are given by the respective equations below.

The stress resulting from the inertia forces is given by ρV^2. The resulting force per unit length due to the inertia is then given by

$$F'_I = \rho_L V^2 D = \frac{G^2 D}{\rho_L} \tag{2}$$

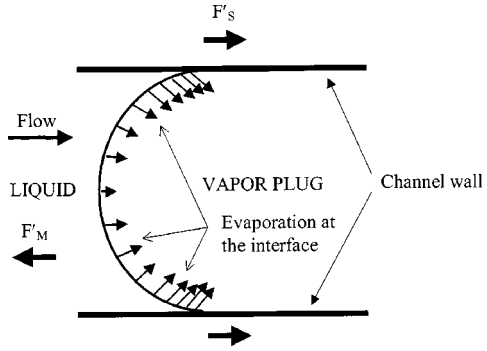

Fig. 2 Forces acting on a liquid-vapor interface that covers the entire channel cross section

Similarly, the force per unit length due to the surface tension force is given by

$$F'_S = \sigma \cos\theta \tag{3}$$

where θ is the appropriate contact angle, advancing or receding, depending on the direction of the motion of the liquid into or away from the interface respectively.

The net gravitational force (due to buoyancy) may be represented in a similar manner as

$$F'_g = (\rho_L - \rho_G) g D^2 \tag{4}$$

The gravitational force is generally quite small compared to the forces due to inertia and the momentum change during flow boiling in microchannels.

The viscous forces are not considered here, although they are important in determining the flow stability in microchannels. Their effect is represented through the Capillary number and the Reynolds number.

New Non-Dimensional Groups Relevant to Flow Boiling in Microchannels. The relative magnitudes of the forces due to evaporation momentum, inertia, and surface tension, introduced in Eqs. (1–3), influence the two-phase structure during flow boiling. The ratios of these forces, taken two at a time, yield the relevant non-dimensional groups in flow boiling.

New Non-Dimensional Group $\mathbf{K_1}$. This group represents the ratio of the evaporation momentum force, Eq. (1), and the inertia force, Eq. (2). It is given by

$$\mathbf{K_1} = \frac{\left(\frac{q}{h_{fg}}\right)^2 \frac{D}{\rho_G}}{\frac{G^2 D}{\rho_L}} = \left(\frac{q}{G h_{fg}}\right)^2 \frac{\rho_L}{\rho_G} \tag{5}$$

The non-dimensional group $\mathbf{K_1}$ includes the Boiling number and the liquid to vapor density ratio. The Boiling number alone does not represent the true effect of the evaporation momentum, and its coupling with the density ratio is important in representing the evaporation momentum force.

A higher value of $\mathbf{K_1}$ indicates that the evaporation momentum forces are dominant and are likely to alter the interface movement. As an example, consider the bubble growth shown in Fig. 3 inside a 200 μm square microchannel, Steinke and Kandlikar, [9]. Each frame in Fig. 3 is 8 ms apart. The bubble grows rapidly aided by the evaporation at the liquid-vapor interface. The high evaporation rate causes the interface to move rapidly downstream. The upstream interface also experiences the force due to evaporation momentum and the increased pressure inside the bubble, causing it to move against the flow direction in one of the channels as shown. The flow reversal occurs at high heat fluxes and has been observed in 1 mm square minichannels as well by Kandlikar et al. [10] and Kandlikar [11]. Further discussion on the actual values of $\mathbf{K_1}$ employed in microchannels and minichannels is presented in later sections.

New Non-Dimensional Group $\mathbf{K_2}$. This new group represents the ratio of the evaporation momentum force, Eq. (1), and the surface tension force, Eq. (3). It is given by

$$\mathbf{K_2} = \frac{\left(\frac{q}{h_{fg}}\right)^2 \frac{D}{\rho_G}}{\sigma} = \left(\frac{q}{h_{fg}}\right)^2 \frac{D}{\rho_G \sigma} \tag{6}$$

The contact angle is not included in the above ratio. The actual force balance in a given situation may involve more complex dependence on contact angles and surface orientation. However, it should be recognized that the contact angles play an important role in bubble dynamics and contact line movement and need to be included in a comprehensive analysis. The non-dimensional group $\mathbf{K_2}$ governs the movement of the interface at the contact

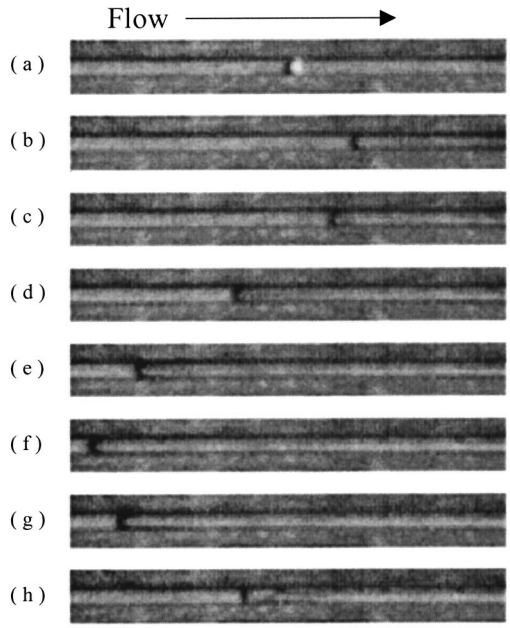

Fig. 3 Rapid bubble growth causing reversed flow in a parallel microchannel. Water flow is from left to right, single channel shown, t=(a) 0 ms, (b) 8 ms, (c) 16 ms, (d) 24 ms, (e) 32 ms, (f) 40 ms, (g) 48 ms, and (h) 56 ms, Steinke and Kandlikar [9].

line. The high evaporation momentum force causes the interface to overcome the retaining surface tension force. This group was effectively used by Kandlikar [8] in developing a model for CHF in pool boiling. The characteristic dimension D was replaced with the departure bubble diameter. The resulting expression for the CHF in pool boiling from a smooth planar surface oriented at an angle of φ with the horizontal was obtained as

$$q_{\mathrm{CHF}}=h_{fg}\rho_G^{1/2}\left(\frac{1+\cos\theta}{16}\right)\left[\frac{2}{\pi}+\frac{\pi}{4}(1+\cos\theta)\cos\phi\right]^{1/2}\times[\sigma g(\rho_L-\rho_G)]^{1/4} \quad (7)$$

Alternatively, the value of $\mathbf{K_2}$ at CHF for the case of pool boiling may be written as

$$\mathbf{K}_{2,\mathrm{CHF}}=\left(\frac{q_{\mathrm{CHF}}}{h_{fg}}\right)^2\frac{D}{\rho_G\sigma}=\left(\frac{1+\cos\theta}{16}\right)^2\left[\frac{2}{\pi}+\frac{\pi}{4}(1+\cos\theta)\cos\phi\right]\times\left[\frac{g(\rho_L-\rho_G)}{\sigma}\right]^{1/2}D \quad (8)$$

The characteristic dimension D is simply half of the critical wavelength, (alternatively, it may be taken as the departing bubble diameter), given by

$$D=2\pi\left[\frac{\sigma}{g(\rho_L-\rho_G)}\right]^{1/2} \quad (9)$$

Thus, $\mathbf{K}_{2,\mathrm{CHF}}$ for pool boiling is given by

$$\mathbf{K}_{2,\mathrm{CHF}}=2\pi\left(\frac{1+\cos\theta}{16}\right)^2\left[\frac{2}{\pi}+\frac{\pi}{4}(1+\cos\theta)\cos\phi\right] \quad (10)$$

In other words, the non-dimensional number $\mathbf{K_2}$ has a unique value for CHF in pool boiling and depends on the contact angle and the orientation angle of the heater with respect to the horizontal. This group is expected to be important in CHF analysis during flow boiling in microchannels and minichannels as well.

The experimental CHF data of Vandervort et al. [12] during flow boiling is plotted with $\mathbf{K}_{2,\mathrm{CHF}}$ as a function of the hydraulic diameter for three different mass fluxes. The result is shown in Fig. 4. The value of $\mathbf{K}_{2,\mathrm{CHF}}$ for each mass flux set is seen to be quite constant, considering the scatter present in the original data. This is quite remarkable, and further, as expected, a dependence of the respective $\mathbf{K}_{2,\mathrm{CHF}}$ values on the mass flux is seen since $\mathbf{K}_{2,\mathrm{CHF}}$ does not include the inertia related forces. Further CHF modeling needs to include the mass flux effect. Incidentally, $\mathbf{K}_{2,\mathrm{CHF}}$ is seen to increase with mass flux as one would expect.

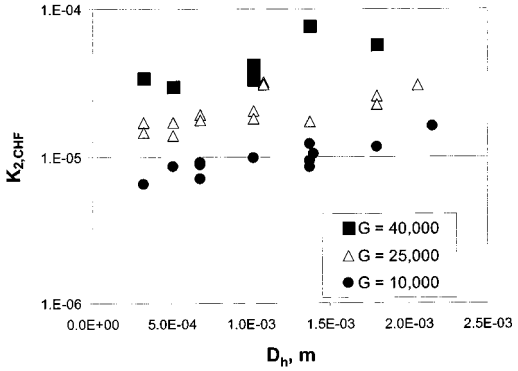

Fig. 4 Variation of $K_{2,CHF}$ with diameter for flow boiling CHF data of Vandervort et al. [12] for different values of G in kg/m^2 s

As a first attempt, applying a mass flux correction factor $\mathbf{K}_{1,\mathrm{CHF}}^{0.75}$ to $\mathbf{K}_{2,\mathrm{CHF}}$ nearly collapses the data of Vandervort et al. [12] for different mass fluxes on a single horizontal line. Figure 5 shows the resulting plot. Considering the scatter in the CHF data due to measurement uncertainties, the agreement is very encouraging. However, further experimental data need to be included in the comparison, and additional property effects (including contact angles) need to be considered while developing a CHF model for flow boiling in microchannels.

Importance of Weber Number and Capillary Number in Microchannel Flow Boiling. The Weber number, We, and the Capillary number, Ca, should prove to be useful in determining the transition boundaries between different flow patterns. We and Ca are believed to influence the CHF phenomenon as well. These groups are commonly employed in analyzing the gas-liquid adiabatic flows. They may prove to be useful in refining the mass flux and viscous effects on CHF in the $\mathbf{K}_{2,\mathrm{CHF}}\,\mathbf{K}_{1,\mathrm{CHF}}^{0.75}$ group shown in Fig. 5. Further work on this can be undertaken after reliable experimental data become available for CHF in microchannels with a wide variety of fluids.

Ranges of Non-Dimensionless Parameters Employed in Microchannel and Minichannel Flow Boiling Experiments in Literature. A large body of experimental data is available for flow boiling in conventional sized channels. There are only a handful

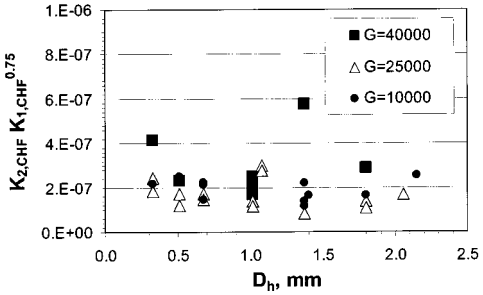

Fig. 5 Variation of $K_{2,CHF}$ $K_{1,CHF}^{0.75}$ with diameter for flow boiling CHF data of Vandervort et al. [12] for different values of G in kg/m^2 s

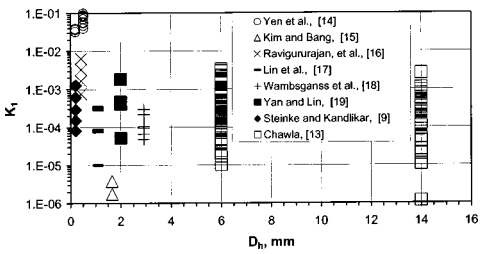

Fig. 6 Ranges of the new non-dimensional parameter K_1 employed in various experimental investigations

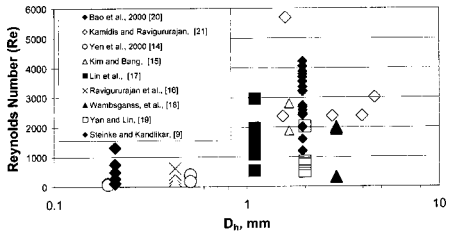

Fig. 10 Ranges of Reynolds Number, Re, employed in various experimental investigations

of reliable experimental data sets available for minichannels and microchannels, e.g., [9] and [13–21], although more are emerging in literature as the interest continues to grow in this field. It is interesting to look at the ranges of dimensionless parameters employed in these experiments as a function of hydraulic diameter.

Figures 6–10 show the ranges of non-dimensional parameters employed in several investigations. The ranges of $\mathbf{K_1}$ over the channel hydraulic diameters employed in literature are shown in Fig. 6. The 6 and 15-mm diameter data for R-11 by Chawla [13] covers a wide range of $\mathbf{K_1}$. Looking into the experimental data sets, it is seen that the higher end values of $\mathbf{K_1}$ correspond to the nucleate boiling dominant region, while the lower end values of $\mathbf{K_1}$ indicate the convective boiling dominant region. The large diameter data sets cover a wide range, whereas it is seen that most of the minichannel and microchannel data sets fall toward the higher end of $\mathbf{K_1}$ values. Especially the data set of Yen et al. [14] is seen to fall at the very high end. Higher values of $\mathbf{K_1}$ are indicative of a relatively higher heat flux for a given mass flux value, and also of the increased importance of the evaporation momentum force.

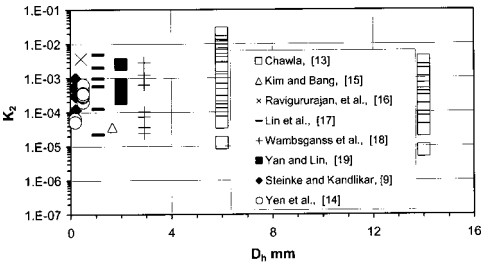

Fig. 7 Ranges of the new non-dimensional parameter K_2 employed in various experimental investigations

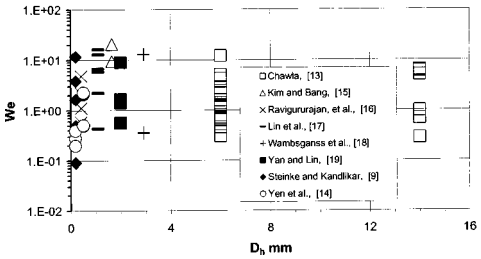

Fig. 8 Ranges of Weber Number, We, employed in various experimental investigations

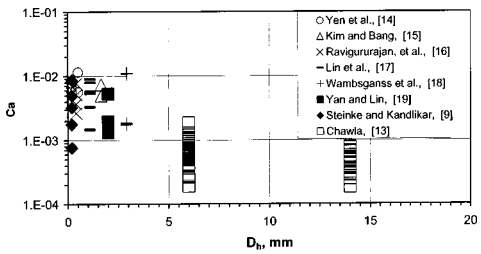

Fig. 9 Ranges of Capillary Number, Ca, employed in various experimental investigations

Figure 7 shows a similar plot for $\mathbf{K_2}$ plotted against D_h. The maximum value of $\mathbf{K_2}$ (not shown in the plot as no data are available) is indicative of the CHF location. There are very few studies available on CHF in Minichannels, and practically none for the microchannels. This is an area where further research is warranted.

Figure 8 shows the range of We in the data sets analyzed here. No appreciable differences are noted, and the data sets do not show any shift in the We range indicative of any change in the experimental conditions for smaller hydraulic diameter channels. Although We does not appear to be a significant parameter in this plot, it may be representative of the inertia effects that are important in modeling the CHF in flow boiling.

The Capillary number is expected to be important in the microchannel flows as both the viscous and the surface tension forces are expected to be important. Figure 9 shows the variation of Ca range with hydraulic diameter for representative data sets. It can be seen that there is a systematic shift toward higher values of Ca for smaller channel diameters. This indicates that the viscous forces become more important than the surface tension forces under flow boiling conditions in microchannels. This is somewhat of an unexpected result, as one would believe the dominance of the surface tension forces at smaller channel dimensions.

Finally, Fig. 10 shows the range of all liquid flow Reynolds numbers employed in the data sets. As the channel diameter is decreased, a clear shift toward lower Reynolds number is seen. This points to the increased importance of the viscous forces in microchannels. Combining this observation with the discussion on the Capillary number in the above paragraph, it can be concluded that the viscous forces are extremely important in microchannel flows. The effect of lower Re on flow boiling heat transfer modeling will be discussed in the section on heat transfer coefficient prediction.

Influence of Channel Hydraulic Diameter on Flow Boiling Heat Transfer Mechanisms

Flow Patterns. Flow boiling in a channel is studied from the subcooled liquid entry at the inlet to a liquid-vapor mixture flow at the channel outlet. As the liquid flows through a microchannel, nucleation occurs over cavities that fall within a certain size range under a given set of flow conditions. Assuming that cavities of all sizes are present on the heater surface, the wall superheat necessary for nucleation may be expressed from the equations developed by Hsu and Graham [22] and Sato and Matsumura [23]:

$$\Delta T_{\mathrm{sat,ONB}} = \frac{4\sigma T_{\mathrm{sat}} v_{fg} h}{k h_{fg}} \left[1 + \sqrt{1 + \frac{k h_{fg} \Delta T_{\mathrm{sub}}}{2\sigma T_{\mathrm{sat}} v_{fg} h}} \right] \qquad (11)$$

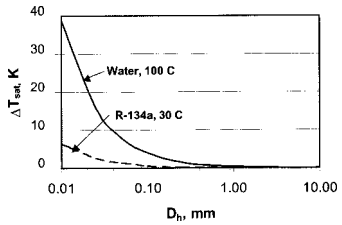

Fig. 11 Wall superheat required to initiate nucleation in a channel with hydraulic diameter D_h for saturated liquid conditions

For a conservative estimate, $\Delta T_{sub}=0$ is taken in estimating the local superheat at the onset of nucleate boiling. Since the single phase liquid flow is in the laminar region, the Nusselt number is given by

$$\mathrm{Nu}=\frac{hD_h}{k}=C \tag{12}$$

where C is a constant dependent on the channel geometry and the wall thermal boundary condition. Combining Eqs. (11) and (12) with zero subcooling, we get,

$$\Delta T_{sat,ONB}=\frac{8\sigma T_{sat}v_{fg}C}{D_h h_{fg}} \tag{13}$$

Taking the case of a constant wall temperature boundary condition, representative of microchannels in a large copper block, the variation of ΔT_{sat} with D_h is plotted in Fig. 11 for water at a saturation temperature of 100°C and for R-134a at 30°C. For channels larger than 1 mm, the wall superheat is quite small, but as the channel size becomes smaller, larger superheat values are required to initiate nucleation. For water in a 200 μm channel, a wall superheat of 2°C is required before nucleation can begin. The actual nucleation wall superheat may increase due to the absence of cavities of all sizes, while it may reduce due to (a) the presence of dissolved gases in the liquid, Kandlikar et al., [24], (b) corners in the channel cross section, and (c) pressure fluctuations.

From the above discussion, for channels smaller than 50 μm, the wall superheat may become quite large, in excess of 10°C with water, and above 2–3°C for refrigerants. Flow boiling in channels smaller than 10 μm will pose significant challenges. The buildup of wall superheat presents another issue that is discussed in the following paragraph.

Once the nucleation begins, the large wall superheat causes a sudden release of energy into the vapor bubble, which grows rapidly and occupies the entire channel. A number of investigators have considered this vapor slug as an elongated bubble. The rapid bubble growth pushes the liquid-vapor interface on both caps of the vapor slug at the upstream and the downstream ends, and leads to a reversed flow in the parallel channel case as the liquid on the upstream side is pushed back, and the other parallel channels carry the resulting excess flow. Kandlikar et al. [10] observed this reversed flow in 1-mm square parallel channels, while Steinke and Kandlikar [9] report a rapid flow reversal inside individual channels in a set of six parallel microchannels, $D_h=200$ μm. Reversed flow was also observed by Peles et al. [26]. Kandlikar and Balasubramanian [25] observed only a small reverse displacement of the interface in a 197 μm x 1054 μm single microchannel. Due to the relatively high inlet ''stiffness'' of the water supply loop, the single microchannel does not show as dramatic reversed flow behavior as the parallel microchannels. (In case of parallel channels, the other channels act as the upstream sections for any given channel). Figure 3 by Steinke and Kandlikar [9] shows a sequence of bubble formation and reversed flow (from right to left) in a channel. The images are 8 ms apart and show a bubble from its nucleation stage, as it occupies the entire channel, and eventually

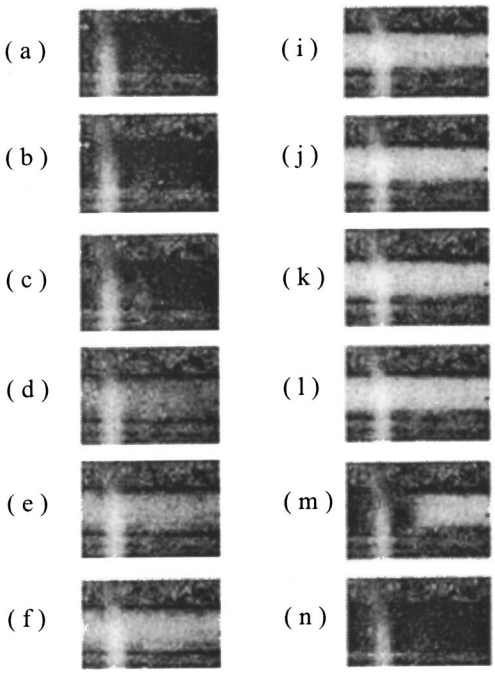

Fig. 12 High speed flow visualization of water boiling in a 197 μm×1054 μm channel showing rapid dryout and wetting phenomena with periodic passage of liquid and vapor slugs, each successive frame is 5ms apart, Kandlikar and Balasubramanian [25]

becomes a vapor slug that expands in both directions. The flow patterns are seen as periodic, with small nucleating bubbles growing into large bubbles that completely fill the tube and lead to rapid movement of the liquid-vapor interface along the channel.

Figure 12 shows the periodic dryout and rewetting through an image sequence obtained with a flow of water in a single channel, 197 μm×1054 μm in cross-section, by Kandlikar and Balasubramanian [25]. Here the bubble growth is extremely rapid, and the moving interface could not be precisely imaged. However, the flow goes from all liquid flow in frames (a) and (b) to a thin film in frames (c)-(d)-(e). In frames (f)-(l), the liquid film has been completely evaporated, and the channel walls are under a dryout condition. The liquid front is seen to pass through the channel in frame (m), followed by all liquid flow in the last frame. The periodic wetting and rewetting phenomena were also observed by Hetsroni et al. [27] for parallel microchannels of 103–129 μm hydraulic diameters.

Other flow patterns reported by Steinke and Kandlikar [9] include slug flow, annular flow, churn flow and dryout condition. A number of investigators, including Hetsroni et al. [27] and Zhang et al. [28] have also reported these flow patterns. The long vapor bubble occurring in a microchannel is similar to annular flow with intermittent slugs of liquid between two long vapor trains.

The periodic phenomena described above is seen to be very similar to the nucleate boiling phenomena, with the exception that the entire channel acts like the area beneath a growing bubble, going through periodic drying and rewetting phases. The transient heat conduction under the approaching rewetting film and the heat transfer in the evaporating meniscus region of the liquid-vapor interfaces in the contact line region exhibit the same characteristics as the nucleate boiling phenomena.

Dynamic Advancing and Receding Contact Angles. The contact angles are believed to play an important role during dryout and rewetting phenomena during flow boiling in a microchannel. These angles are important in the events leading to the CHF as

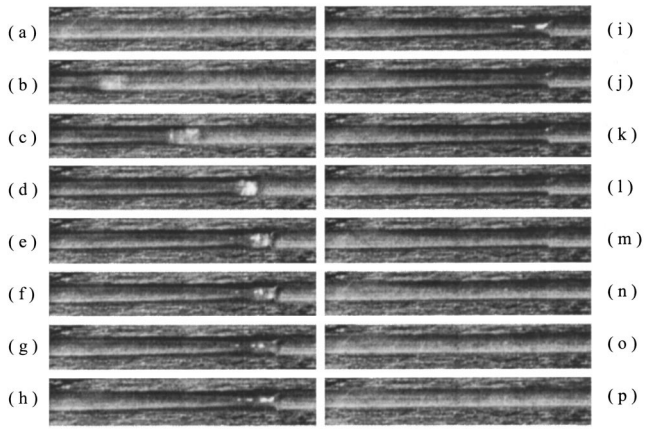

Fig. 13 Changes in contact angle at the liquid front during flow reversal sequence, water flowing in a parallel microchannel with $D_h=200$ μm, Steinke and Kandlikar [9]

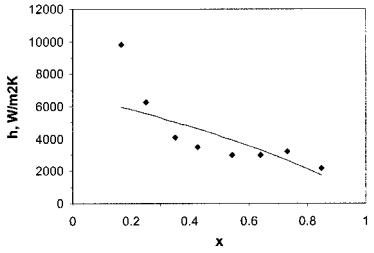

Fig. 14 Comparison of the Kandlikar [1,2,35] correlation and Eqs. (15) and (16) for the Nucleate Boiling Dominant Region with Yen et al. [14] data in the laminar region, plotted with heat transfer coefficient as a function of local vapor quality x, R-134a, $D_h=190$ μm, $\mathrm{Re}_{LO}=73$, $G=171$ kg/m^2 s, $q=6.91$ kW/m^2

well. The pool boiling CHF model by Kandlikar [8] incorporates these angles as seen from Eq. (7). During normal bubble growth, the dynamic receding contact angle comes into play. During the rewetting process, the liquid front is advancing with its dynamic advancing contact angle. As the CHF is approached, or as the flow reversal takes place due to flow instabilities, the liquid front changes its shape from the dynamic advancing angle to the dynamic receding angle. This event was captured by Steinke and Kandlikar [9] using high-speed imaging techniques and is displayed in Fig. 13 for the flow of water in a set of six parallel microchannels, each with a 200 μm square cross section.

The events in Fig. 13 show the changes in the contact angles. The liquid front is moving forward from left to right in frames (a)-(d). In frame (d), it stops moving forward. Note the dynamic advancing contact angle in this frame, which is greater than 90 deg. During frames (d)-(i), it experiences rapid evaporation at the right side of the front interface and changes to the receding contact angle value, which is less than 90 deg. The liquid slug subsequently becomes smaller, making way to the vapor core with its residual liquid film in frames (i)-(m). Eventually, the liquid film dries out completely as seen in frames (n)-(p). Additional studies on the contact angle changes at evaporating interfaces are reported by Kandlikar [29]. More detailed experiments are needed to further understand the precise effect of contact angles on CHF.

Heat Transfer Coefficients during Flow Boiling in Microchannels

As the channel size becomes smaller, the Reynolds number also becomes smaller for a given mass velocity, and the flow patterns exhibit characteristics similar to a bubble ebullition cycle as discussed in the previous sections. It is therefore expected that the flow boiling correlation for the nucleate boiling dominant region should work well here.

Consider the flow boiling correlation by Kandlikar [30,31].

$$h_{TP}=\text{larger of}\begin{cases}h_{TP,\mathrm{NBD}}\\ h_{TP,\mathrm{CBD}}\end{cases} \tag{14}$$

$$h_{TP,\mathrm{NBD}}=0.6683Co^{-0.2}(1-x)^{0.8}f_2(\mathrm{Fr}_{LO})h_{LO}+1058.0Bo^{0.7}(1-x)^{0.8}F_{Fl}h_{LO} \tag{15}$$

$$h_{TP,\mathrm{CBD}}=1.136Co^{-0.9}(1-x)^{0.8}f_2(\mathrm{Fr}_{LO})h_{LO}+667.2Bo^{0.7}(1-x)^{0.8}F_{Fl}h_{LO}$$

where Fr_{LO} is the Froude number with all flow as liquid. Since the effect of Froude number is expected to be small in microchannels, the function $f_2(\mathrm{Fr}_{LO})$ is taken as 1.0. The single-phase, all-liquid flow heat transfer coefficient h_{LO} is given by appropriate correlations given by Petukhov and Popov [32], and Gnielinski [33], depending on the Reynolds number in the turbulent liquid flow. The values of the fluid-dependent parameter F_{Fl} can be found in [34] or [35].

For microchannels with the all-liquid flow in the laminar region, the corresponding all-liquid flow Nusselt number is given by

$$\mathrm{Nu}_{LO}=\frac{h_{LO}D_h}{k_L}=C, \tag{16}$$

where the constant C is dependent on the channel geometry and the wall thermal boundary condition.

Kandlikar and Steinke [34] showed that the use of Eq. (16) for h_{LO} is appropriate in Eq. (15) when the all-liquid flow is in the laminar region. The use of turbulent flow correlation by Gnieliski was found to be appropriate for $\mathrm{Re}>3000$, while for $\mathrm{Re}<1600$, the use of laminar flow correlation yielded good agreement. In the transition region, a linear interpolation was recommended between the limiting Re_{LO} values of 1600 and 3000.

With further reduction in the Reynolds number, $\mathrm{Re}<300$, Kandlikar and Balasubramanian [35] showed that the flow boiling mechanism is nucleate boiling dominant and the use of only the nucleate boiling dominant expression in Eq. (15) for $h_{TP,\mathrm{NBD}}$ is appropriate in the entire range of vapor quality. Thus, Kandlikar and Balasubramanian [35] recommend the following scheme:

$$h_{TP}=h_{TP,\mathrm{NBD}} \quad \text{for } \mathrm{Re}_{LO}<300 \tag{17}$$

Using the above scheme, a recent data set published by Yen et al. [14] was tested. Figure 15 shows a comparison between the experimental data and the above correlation scheme. Here $\mathrm{Re}_{LO}=73$, and only the nucleate boiling dominant part of the correlation in Eq. (15) is used. At such low Reynolds numbers, the convective boiling does not become the dominant mechanism in the entire vapor quality range. In this plot, the first few points show a very high heat transfer coefficient. This is due to the sudden release of the high liquid superheat following nucleation that causes rapid bubble growth in this region as seen in Fig. 14 as well. Steinke and Kandlikar [36] observed a similar behavior with their water data as shown in Fig. 15.

The flow boiling mechanism is quite complex in microchannels as seen from the experimental data and flow visualization studies. Although simple models available in literature, e.g., [37], present a good analysis under certain idealized conditions, phenomena such as rapid bubble growth, flow reversal, and periodic dryout introduce significantly greater complexities. Effect of parallel channels on heat transfer is another area where little experimental work is published.

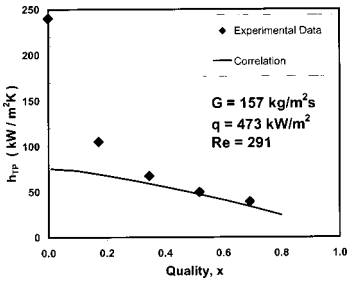

Fig. 15 Comparison of the Kandlikar [1,2,35] correlation and Eqs. (15) and (16) for the Nucleate Boiling Dominant Region with Steinke and Kandlikar 36 data in the laminar region, plotted with heat transfer coefficient as a function of local vapor quality x, water, $D_h = 207\ \mu$m, $Re_{LO} = 291$, $G = 157$ kg/m^2 s, $q = 473$ kW/m^2

Heat Transfer Mechanism during Flow Boiling in Microchannels

Based on the above discussion, the heat transfer mechanisms can be summarized as follows:

1. When the wall superheat exceeds the temperature required to nucleate cavities present on the channel walls, nucleate boiling is initiated in a microchannel. Absence of nucleation sites of appropriate sizes may delay nucleation. Other factors such as sharp corners, fluid oscillations, and dissolved gases affect the nucleation behavior. The necessary wall superheat is estimated to be $2-10°$C for channels smaller than $50-100\ \mu$m hydraulic diameter with R-134a and water respectively at atmospheric pressure conditions.
2. Immediately following nucleation, a sudden increase in heat transfer coefficient is experienced due to release of the accumulated superheat in the liquid prior to nucleation. This leads to rapid evaporation, sometimes accompanied by flow reversal in parallel channels.
3. The role of the convective boiling mechanism is diminished in microchannels. The nucleate boiling plays a major role as the periodic flow of liquid and vapor slugs in rapid succession continues. The wall dryout may occur during the vapor passage. The wetting and rewetting phenomena have marked similarities with the nucleate boiling ebullition cycle. The dryout period becomes longer at higher qualities and/or at higher heat fluxes. The nucleate boiling heat transfer suffers further as the liquid film completely evaporates (dryout) during extended periods of vapor passage.
4. As the heat flux increases, the dry patches become larger and stay longer, eventually reaching the CHF condition.

Closing Remarks. Although it is desirable to have a good mathematical description of the heat transfer mechanism during flow boiling in microchannels, the rapid changes of flow patterns, complex nature of the liquid film evaporation, transient conduction, and nucleation make it quite challenging to develop a comprehensive analytical model. Further, the conduction in the substrate, parallel channel instability issues, header-channel interactions, and flow maldistribution in parallel channels pose additional challenges. The usage of the new non-dimensional groups $\mathbf{K_1}$ and $\mathbf{K_2}$ in conjunction with the Weber number and the Capillary number is expected to provide a better tool for analyzing the experimental data and developing more representative models. The scale change in hydraulic diameter introduces a whole new set of issues in microchannels that need to be understood first from a phenomenological standpoint.

Conclusions

Flow boiling in microchannels is addressed from the perspective of interfacial phenomena. The following major conclusions are derived from this study:

1. After reviewing the non-dimensional groups employed in the two-phase applications, the forces acting on the liquid-vapor interface during flow boiling are investigated, and two new non-dimensional groups $\mathbf{K_1}$ and $\mathbf{K_2}$ are derived. These groups represent the surface tension forces around the contact line region, the momentum change forces due to evaporation at the interface, and the inertia forces.
2. In a simple first-cut approach, the combination of the non-dimensional groups, $\mathbf{K_2 K_1^{0.75}}$ is seen to be promising in representing the flow boiling CHF data by Vandervort et al. [12]. Further analysis and testing with a larger experimental data bank with a wide variety of fluids is recommended in developing a more comprehensive model for CHF. In additon, the influence of We, and Ca on the CHF needs to be studied further.
3. The nucleation criterion in flow boiling indicates that the wall superheat required for nucleation in microchannels becomes significantly large ($>2-10°$C) as the channel hydraulic diameter becomes smaller, about $50-100\ \mu$m depending on the fluid. The presence of dissolved gases in the liquid, sharp corners in the cross section geometry, and flow oscillations will reduce the required wall superheat, while the absence of cavities of appropriate sizes may increase the nucleation wall superheat.
4. Considerable similarities are observed between the flow boiling in microchannels and the nucleate boiling phenomena with the bubbles nucleating and occupying the entire channel. The process is seen to be very similar to the bubble ebullition cyle in pool boiling.
5. Heat transfer during flow boiling in microchannels is seen to be nucleate boiling dominant.
6. A description of the heat transfer mechanisms during flow boiling in microchannels is provided based on the above observations. Some of the key features, such s rapid bubble growth, flow reversal, nucleate boiling dominant heat transfer have been confirmed with high speed video pictures and experimental data.
7. Further experimental research is needed to generate more data for developing more accurate models and predictive techniques for flow boiling heat transfer and CHF in microchannels.

Nomenclature

- A = area, (m^2)
- Bo = Bond number, Table 1
- Bo = Boiling number, Table 1
- C = a constant
- Ca = capillary number, Table 1
- Co = convection number, $(\rho_G/\rho_L)^{0.5}((1-x)/x)^{0.8}$
- c_p = specific heat, (J/kg K)
- d = diameter, (m)
- dP/dz = pressure gradient, N/m^3
- D_h = hydraulic diameter, (m)
- Eo = Eötvös number, Table 1
- F_{Fl} = Fluid dependent parameter in Kandlikar [1,2] correlation, $=1$ for water, $=1.60$ for R-134a
- Fr = Froude number, $=G^2/(\rho_L^2 gD)$
- F' = force per unit length, (N/m)
- f = friction factor
- G = mass flux, (kg/m^{2}s)
- g = gravitational acceleration, (m/s^2)
- h = heat transfer coefficient, (W/m^{2}K)
- h_{fg} = latent heat of vaporization, (J/kg)
- Ja = Jakob number, Table 1
- $\mathbf{K_1}$ = new non-dimensional constant, eq. (5)
- $\mathbf{K_2}$ = new non-dimensional constant, eq. (6)
- k = thermal conductivity, (W/m K)

L, l = length (m)
$\dot{m}$ = mass flow rate (kg/s)
Nu = Nusselt number ($=hD_h/k$)
P = pressure (Pa)
q = heat flux (W/m^2)
Re = Reynolds number ($=GD_h/\mu$)
T = temperature (°C)
ΔT = temperature difference (K)
V = velocity (m/s)
v = specific volume (m^3/kg)
We = Weber number, Table 1
w = channel width (m)
X = Martinelli parameter, Table 1
x = vapor mass fraction
Z = Ohnesorge number, Table 1

Greek

ϕ = orientation with respect to horizontal (°)
μ = dynamic viscosity (Ns/m^2)
θ = contact angle (°)
ρ = density (kg/m^3)
σ = surface tension (N/m)

Subscripts

CHF = critical heat flux
F = friction
CBD = convection dominated region
G = gas or vapor
g = due to gravity
I = inertia
L = liquid
LO = all flow as liquid
fg = latent quantity, difference between vapor and liquid properties
M = due to momentum change
NBD = nucleate boiling dominant region
ONB = onset of nucleate boiling
S = surface tension
sat = saturation
sub = subcooled
TP = two-phase

References

[1] Schrock, V. E., and Grossman, L. M., 1959, ''Forced Convection Boiling Studies,'' *Forced Convection Vaporization Project*—Issue No. 2, Series No. 73308—UCX 2182, Nov. 1, 1959, University of California, Berkeley, CA.

[2] Kandlikar, S. G., and Grande, W. J., 2002, ''Evolution of Microchannel Flow Passages—Thermohydraulic Performance and Fabrication Technology,'' Heat Transfer Eng., **25**(1), pp. 3–17.

[3] Kawaji, M., and Chung, P. M.-Y., 2003, ''Unique Characteristics of Adiabatic Gas-Liquid Flows in Microchannels: Diameter and Shape Effects on Flow Patterns, Void Fraction and Pressure Drop,'' Paper No. ICMM2003-1013, *Proceedings of the First International Conference on Microchannels and Minichannels*, ASME, NY, pp. 115–127.

[4] Ali, M. I., Sadatomi, M., and Kawaji, M., 1993, ''Two-Phase Flow in Narrow Channels between Two Flat Plates,'' Can. J. Chem. Eng., **71**(5), pp. 449–456.

[5] Shah, M. M., 1982, ''Chart Correlation for Saturated Boiling Heat Transfer: Equations and Further Study,'' ASHRAE Trans., **88**, Part I, pp. 185–196.

[6] Stephan, K., and Abdelsalam, M., 1980, ''Heat Transfer Correlation for Natural Convection Boiling,'' Int. J. Heat Mass Transfer, **23**, pp. 73–87.

[7] Kutateladze, 1948, ''On the Transition to Film Boiling under Natural Convection,'' Kotloturbostroenie, No. 3, pp. 10–12.

[8] Kandlikar, S. G., 2001, ''A Theoretical Model To Predict Pool Boiling CHF Incorporating Effects Of Contact Angle And Orientation,'' ASME Journal of Heat Transfer, **123**, pp. 1071–1079.

[9] Steinke, M. E., and Kandlikar, S. G., 2003, ''Flow Boiling and Pressure Drop in Parallel Microchannels,'' Paper No. ICMM2003-1070, *First International Conference on Microchannels and Minichannels*, ASME, NY, pp. 567–579.

[10] Kandlikar, S. G., Steinke, M., Tian, S., and Campbell, L., 2001, ''High-Speed Photographic Observation of Flow Boiling of Water in Parallel Mini-Channels,'' Paper # NHTC01-11262, *ASME National Heat Transfer Conference*, ASME, New York.

[11] Kandlikar, S. G., 2002, ''Fundamental Issues Related To Flow Boiling In Minichannels and Microchannels,'' Exp. Therm. Fluid Sci., **26**(2–4), pp. 389–407.

[12] Vandervort, C. L., Bergles, A. E., and Jensen, M. K., 1994, ''An Experimental Study of Critical Heat Flux in very High Heat Flux Subcooled Boiling,'' Int. J. Heat Mass Transfer, **37**, Suppl 1, pp. 161–173.

[13] Chawla, J. M., 1967, ''Wärmeübergang und Druckabfall in waagrechten Rohren bei der Strömung von verdampfenden Kältemitteln,'' *VDI-Forschungsheft*, No. 523.

[14] Yen, T.-H., Kasagi, N., and Suzuki, Y., 2002, ''Forced Convective Boiling Heat Transfer at Low Mass and Heat Fluxes,'' *Proceedings of the International Symposium on Compact Heat Exchangers*, Grenoble, Edizioni ETS, pp. 190.

[15] Kim, J., and K. Bang, 2001, ''Evaporation Heat Transfer of Refrigerant R-22 in Small Hydraulic-Diameter Tubes,'' *Proceedings of 4th International Conference on Multiphase Flow*.

[16] Ravigururajan, T. S., Cuta, J., McDonald, C. E., and Drost, M. K., 1996, ''Effects of Heat Flux on Two-Phase Flow Characteristics of Refrigerant Flows in a Micro-Channel Heat Exchanger,'' *Proceedings of National Heat Transfer Conference*, HTD-329, pp. 167–178.

[17] Lin, S., P. A. Kew, and K. Cornwell, 2001, ''Flow Boiling of Refrigerant R141B in Small Tubes,'' *Transactions of IchemE*, **79**, Part A, pp. 417–424.

[18] Wambsganss, M. W., France, D. M., Jendrzejczyk, J. A., and Tran, T. N., 1993, ''Boiling Heat Transfer in a Horizontal Small-Diameter Tube,'' ASME Journal of Heat Transfer, **115**, pp. 963–972.

[19] Yan, Y., and Lin, T., 1998, ''Evaporation Heat Transfer and Pressure Drop of Refrigerant R-134a in a Small Pipe,'' Int. J. Heat Mass Transfer, **41**, pp. 4183–4194.

[20] Bao, Z. Y., Fletcher, D. F., Hayes, B. S., 2000, ''Flow Boiling Heat Transfer of Freon R11 and HCFC123 in Narrow Passages,'' Int. J. Heat Mass Transfer, **43**, pp. 3347–3358.

[21] Kamidis, D. E., and T. S. Ravigururajan, 1999, ''Single and Two-Phase Refrigerant Flow in Mini-Channels,'' *Proceedings of 33rd National Heat Transfer Conference*.

[22] Hsu, Y. Y., and Graham, R. W., 1961, ''An Analytical and Experimental Study of the Thermal Boundary Layer and Ebullition Cycle in Nucleate Boiling,'' NASA TN-D-594.

[23] Sato, T., and Matsumura, H., 1964, ''On the Conditions of Incipient Subcooled Boiling with Forced Convection,'' Bull. JSME, **7**(26), pp. 392–398.

[24] Kandlikar, S. G., Steinke, M. E., and Balasubramanian, P., 2002, ''Single-Phase Flow Characteristics and Effect of Dissolved Gases on Heat Transfer Near Saturation Conditions in Microchannels,'' Paper No. IMECE2002-39392, *International Mechanical Engineering Conference and Exposition 2002*, ASME, New York.

[25] Kandlikar, S. G., and Balasubramanian, P., 2003, ''High Speed Photographic Observation of Flow Patterns During Flow Boiling in a Single Rectangular Minichannel,'' Paper No. HT2003-47175, *Proceedings of the ASME Summer Heat Transfer Conference*.

[26] Pelles, Y. P., Yarin, L. P., and Hetsroni, G., 2001, ''Steady and Unsteady Flow in a Heated Capillary,'' Int. J. Multiphase Flow, **27**(4), pp. 577–598.

[27] Hetsroni, G., Segal, Z., and Mosyak, A., 2000, ''Nonuniform Temperature Distribution in Electronic Devices Cooled by Flow in Parallel Microchannels,'' *Packaging of Electronic and Photonic Devices*, EEP- Vol. **28**, ASME, New York, pp. 1–9.

[28] Zhang, L., Koo, J., Jiang, L., Asheghi, M., Goodson, K. E., Santiago, J. G., and Kenney, T. W., 2002, ''Measurements and Modeling of Two-Phase Flow in Microchannels with Nearly Constant Heat Flux Boundary Conditions,'' J. Microelectromech. Syst., **11**(1), pp. 12–19.

[29] Kandlikar, S. G., 2001, ''A Photographic Insight into the Motion of Liquid-Vapor Interface of a Liquid Droplet on a Heated Surface,'' Paper #IMECE01, paper presented at the ASME IMECE 2001, ASME, New York.

[30] Kandlikar, S. G., 1990, ''A General Correlation for Two-phase Flow Boiling Heat Transfer Coefficient Inside Horizontal and Vertical Tubes,'' ASME Journal of Heat Transfer, **112**, pp. 219–228.

[31] Kandlikar, S. G., 1991, ''Development of a Flow Boiling Map for Subcooled and Saturated Flow Boiling of Different Fluids in Circular Tubes,'' ASME Journal of Heat Transfer, **113**, pp. 190–200.

[32] Petukhov, B. S., and Popov, V. N., 1963, ''Theoretical Calculations of Heat Exchange in Turbulent Flow in Tubes of an Incompressible Fluid with Variable Physical Properties,'' High Temp., **1**(1), pp. 69–83.

[33] Glienski, V., 1976, ''New Equations for Heat and Mass Transfer in Turbulent Pipe and Channel Flow,'' Int. Chem. Eng., **16**, pp. 359–368.

[34] Kandlikar, S. G., and Steinke, M. E., 2003, ''Predicting Heat Transfer During Flow Boiling in Minichannels and Microchannels,'' ASHRAE Trans., **109**, Part 1.

[35] Kandlikar, S. G., and Balasubramanian, P., 2003, ''Extending the Applicability of the Flow Boiling Correlation at Low Reynolds Number Flows in Microchannels,'' Paper ICMM2003-1075, presented at the *First International Conference on Microchannels and Minichannels*, ASME, New York, pp. 603–608.

[36] Kandlikar, S. G., and Steinke, M. E., 2003, ''Flow Boiling and Pressure Drop in Parallel Flow Microchannels,'' First International Conference on Microchannels and Minichannels, April 24–25, 2003, Rochester, NY, USA, Paper No. ICMM 2003-1070, S. G. Kandlikar, ed., ASME, pp. 567–579.

[37] Jacobi, A. M., and Thome, J. R., 2002, ''Heat Transfer Model for Evaporation of Elongated Bubble Flows in Microchannels,'' ASMR Journal of Heat Transfer, **124**, pp. 1131–1136.

Single-Side Heated Monoblock, High Heat Flux Removal Using Water Subcooled Turbulent Flow Boiling

Ronald D. Boyd Sr.[1]
e-mail: ronald_boyd@pvamu.edu
Fellow

Penrose Cofie

Hongtao Zhang

Ali Ekhlassi

Thermal Science Research Center (TSRC),
College of Engineering,
P.O. Box 4208,
Prairie View A&M University,
Prairie View, TX 77446-4208

Plasma-facing components for fusion reactors and other high heat flux heat sinks are subjected to a peripherally nonuniform heat flux. The monoblock test section under study is a single-side heated square cross-section heat sink with a circular coolant channel bored through the center. The heated length of the test section is 180 mm. The inside diameter and outside square sides are 10 mm and 30 mm, respectively. It was subjected to a constant heat flux on one side of the outside surfaces, and the remaining portion was not heated. The exit water subcooling varied from 55 to 101°C, the exit pressure was maintained at 0.207 MPa, and the mass velocity was 0.59 Mg/m^2s. The results consist of three-dimensional wall temperature distributions and a display of two-dimensional quasi-boiling curves. These results are among the first full set of three-dimensional wall temperature measurements for a single-side heated monoblock flow channel which contains the effects of conjugate heat transfer for turbulent, subcooled flow boiling. In the single-phase region, good predictability resulted when the thermal hydraulic diameter was used.
[DOI: 10.1115/1.1643092]

Keywords: Boiling, Forced Convection, Heat Transfer, Three-Dimensional, Two-Phase

Introduction

Since plasma-facing component (PFC) design requirements and goals are evolving, the development of an experimental conjugate multi-dimensional, flow boiling data base will provide the basis for flow boiling correlation modification and adaptation. This would include single-side heating effects as well as subcooled turbulent flow boiling effects. The results would (1) be used for detail PFC and other high heat flux heat sink (HHFHS) flow channel and substrate design studies, and (2) lead to cost-effective and robust designs. The optimized design of single-side heated PFCs and HHFHS is dependent on using conjugate heat transfer to find the local distribution of inside channel wall temperature and heat flux.

Conjugate heat transfer modeling [1,2] has proven useful in forming baselines and identifying important parameters affecting peaking factors and data reduction for the spectrum of high heat fluxes found in a wide variety of applications. For various applications requiring different fluids, the results show the following: (1) the coexistence of three flow boiling regimes at some axial locations inside the single-side heated flow channel, (2) the correlational dependence of the inside wall heat flux and temperature (fluid independent), and (3) inaccuracies that could arise in some data reduction procedures (fluid independent). However, for PFC and other HHFHS (e.g., in boilers and electronic components) applications, work is still needed to expand conjugate heat transfer analyses from simple circular and complex laboratory geometries [3,4] to prototypic geometries. This will lead to improved predictability of peaking factors and prototypic conditions.

International efforts are vigorously proceeding in the investigation of heat transfer and related critical heat flux (CHF) in single-side heated flow channels. Some examples of recent single-side heating efforts include the following: (1) the international round-robin monoblock CHF swirl-flow tests by Youchison et al. [5]; (2) CHF in multiple square channels by Akiba et al. [6]; (3) CHF comparison of an attached-fin hypervapotron and porous coated surface by Youchison et al. [7]; (4) CHF enhancements due to wire inserts by Youchison et al. [8]; (5) post-CHF with and without swirl flow in a monoblock by Marshall [9]; (6) CHF JAERI data base compilation by Boscary et al. [3,10]; (7) post-CHF enhancement factors by Marshall et al. [11]; (8) CHF peaking factor empirical correlations by Inasaka and Nariari [12], and Akiba et al. [13]; (9) CHF correlation modification to account for peripheral non-uniform heating by Celata et al. [14]; (10) comparison of single-side heating with uniform heating by Boyd [15]; (11) single-and two-phase subcooled flow boiling heat transfer in smooth and swirl tubes by Araki et al. [16]; (12) smooth tube heat transfer, CHF and post-CHF by Becker et al. [17]; and (13) turbulent heat transfer analysis by Gartner et al. [18].

Monoblock Test Section

The configuration under study consists of a single-side heated monoblock (with square outside surfaces) test section with a circular coolant channel bored through the center. A detailed description of the test section is shown in Fig. 1. The overall length of the test section, including the inlet and outlet reduced diameter sections, is 360 mm. The main section of the test section available for heating is 200 mm long with a nominal outside width and height of 30 mm and an inside diameter of 10 mm. The actual directly heated length (L_H) was 180 mm. Water was the coolant. The inlet temperature can be set at any level in the range from 20.0 to 130.0°C and the exit pressure can be set at any level in the range from 0.2 to 4.0 MPa. The mass velocity can be set at any level in the range from 0.3 to 10.0 Mg/m^2s. Thermocouples were placed at forty-eight locations inside the solid portion of the test section. For each of four axial stations, a set of three (at three different radii) thermocouples were embedded at each of the four circumferential measurement locations (0, 45, 135, and 180 deg, where 0 deg corresponds to the portion of the plane of symmetry close to the heated surface) in the wall of the test section.

[1]Distinguished Professor of Mechanical Engineering, Honeywell Endowed Professor of Engineering, and TSRC Director.

Contributed by the Heat Transfer Division for publication in the JOURNAL OF HEAT TRANSFER. Manuscript received by the Heat Transfer Division April 14, 2002; revision received October 6, 2003. Associate Editor: M. K. Jensen.

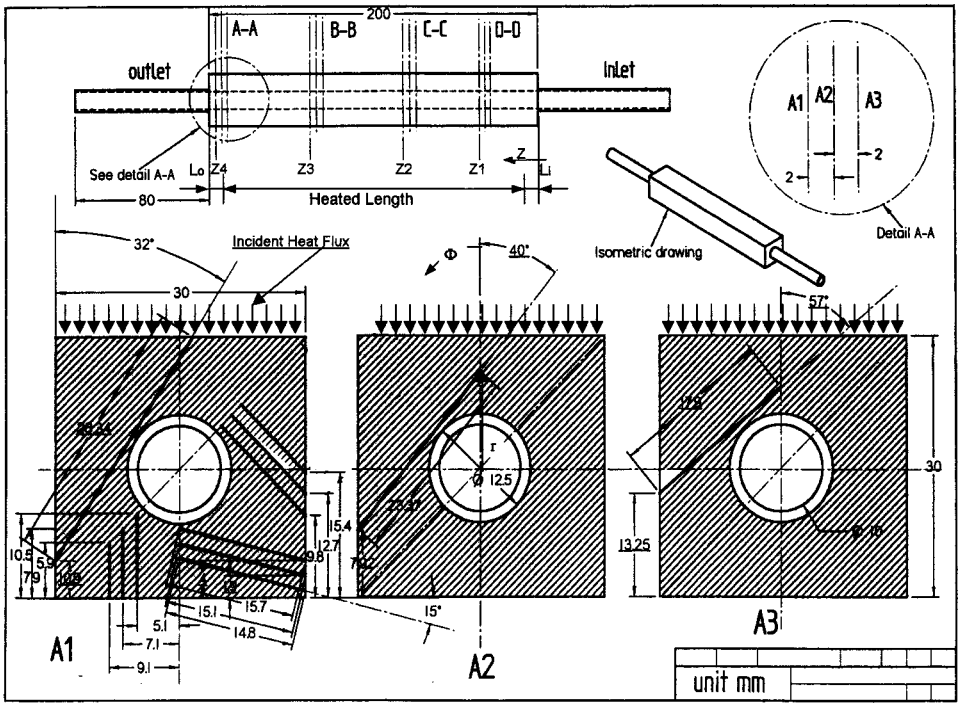

Fig. 1 Locations of thermocouples (TCs) inside the monoblock test section in planes #A1, #A2, and #A3. The TC wells are the solid black lines with specified lengths and angles.

The mass velocity, exit pressure, and exit subcooling range used for the present case were 0.59 Mg/m^2s, 0.207 MPa (T_{sat} = 121.3°C), and 55 to 101°C, respectively. Type-J thermocouples were used and calibrated to within ±0.1°C with a precision calibrator. For these conditions, the basic fluid flow is a turbulent (Re=9,400) and highly developing flow with a reciprocal Graetz number (Gz^{-1}) less than 3.3×10^{-4}. A detail description of the test facility, experimental, and measurement details are given elsewhere by Boyd et al. [19].

The test sections were made of Type AL-15 Glidcop Grade Copper. Also shown in Fig. 1 are four axial stations labeled A-A, B-B, C-C, and D-D, which are axial locations of thermocouple (TC) wells for in-depth wall temperature measurements. The purpose is to measure the axial distribution of the wall temperature for a given applied heat flux. Since the geometry of the TC wells is identical at all four axial stations, a detail description will be given for only one axial station. The A-A axial station has 12 TC wells: 10 in plane A1, one in plane A2, and another in plane A3. Planes A2 and A3 are axially displaced upstream from plane A1 by 2 mm and 4 mm, respectively. Finally, the lengths L_i (=16 mm) and L_o (=4 mm) shown in Fig. 1 are variable lengths whose sum must equal 20 mm for a given experimental setup.

The TCs at station A-A will give both radial and circumferential distributions of the local wall temperature. Hence, a combination of all axial stations will produce a three-dimensional distribution of the wall temperature as a function of the applied heat flux; and, the water flow regime will vary from single-phase at the inlet to subcooled pre or post-CHF at the exit. The applied heat flux comes from a 350.0 kW DC power supply which provides resistive heating to the test section via a grade G-20 graphite flat heater (see Fig. 2). The heater was placed over a 1.0 mm thick aluminum nitride layer which in turn rests on the test section shown in Fig. 2. The power supply provides power to the heater element in the experimental set-up through a copper bus duct/cabling system [19].

Results

Robust PFC and HHFHS designs must be based on accurate three-dimensional conjugate flow boiling analyses and optimizations of the local wall temperature and hence on the local flow boiling regime variations. Such analyses must have three-dimensional data as a basis for comparison, assessment, and flow boiling correlation adaptation for localize boiling. As an initial part of an effort to begin to provide such data, selected results are presented for the above noted conditions for the (1) three-dimensional variations of the wall temperature as functions of the circumferential (ϕ), radial (r), and axial (Z) coordinates, and (2) net incident steady-state heat flux as a function of the local wall

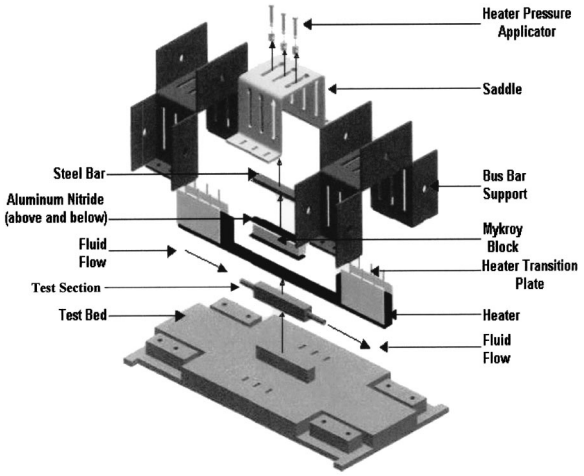

Fig. 2 High heat flux monoblock test section expanded assembly

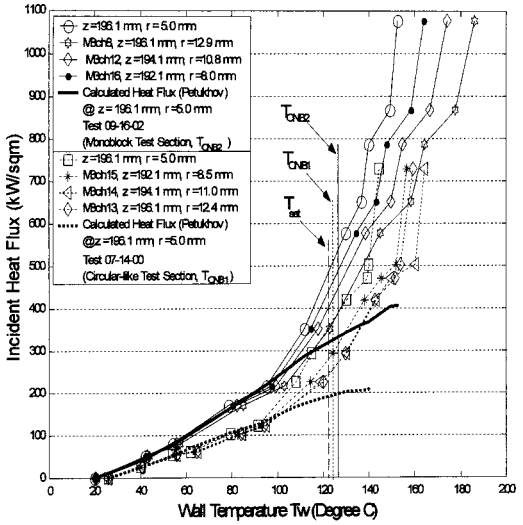

Fig. 3 Measured two-dimensional quasi-boiling curves for the single-side heated monoblock and single-side heated circular test sections at $\phi=0$ deg and for specified axial locations (near $Z=Z_4=196.1$ mm)

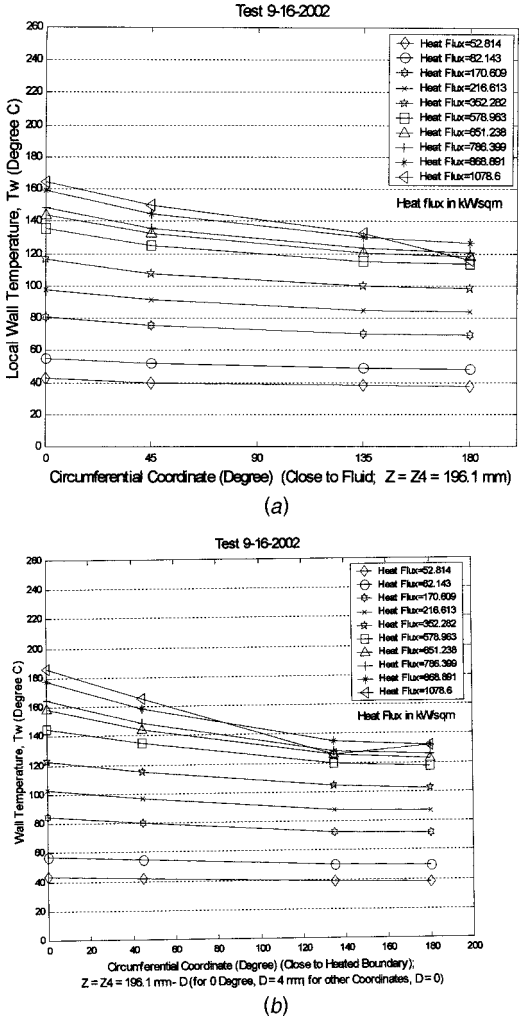

Fig. 4 (*a*) Circumferential wall temperature profiles from the thermocouples nearest to the fluid/solid boundary as a function of net incident heat flux, at $Z=Z_4=196.1$ mm; (*b*) Circumferential wall temperature profiles from the thermocouples nearest to the heated boundary (i.e., away from the fluid/solid boundary) as a function of the net incident heat flux.

temperature (two-dimensional quasi-boiling curves). The net incident heat flux relationship with the locally measured wall temperature will be discussed first.

Incident Heat Flux/Wall Temperature Relationship. Experimental results show the relationship between the incident heat flux (q_o) and the wall temperature (T_w) at different three-dimensional coordinates. This relationship between q_o and T_w would be directly related to the two-dimensional local boiling curve if the radius at which this relationship was considered was equal to the inside radius of the flow channel. The present work will lead eventually to the development of these two-dimensional boiling curves.

Single-Side Heated Monoblock. The relationship between the steady state, net incident heat flux and the local wall temperature is presented in Fig. 3 for $Z=Z_4$. The solid curves connecting the data are complete in that they show evidence of an influence from the three basic subcooled flow boiling regimes (partially nucleate boiling, fully developed flow boiling, and local film boiling) of the boiling curve. Measured data are shown for three radial locations ($r=8.0$, 10.8, and 12.9 mm) and are used to extrapolate the local inside ($r=5$ mm) wall temperature of the coolant channel. Both the saturation temperature and the temperature for the onset of nucleate boiling (T_{ONB2}) are shown [20]. Further, Petukhov's [21] correlation was used for the single-phase heat transfer predictions at the inside boundary of the coolant channel. For the single-side heated geometry predictions, all fluid properties were evaluated at the local bulk temperature, and the thermal hydraulic [22] diameter (D_T) was used in the Nusselt number. D_T is defined as $a \cdot D_i$, where a is a constant which accounts for single-side heating effects ($a=1.2$ for the monoblock and 2.0 for the circular cylinder). Good agreement occurs except near ONB.

One observes a progressive increase of the slope of the q_o versus T_w curves in Fig. 3 as the radius decreases or as the inside fluid-solid boundary is approached. The set of three data points on each curve beyond ONB denotes entry into the region of fully developed nucleate flow boiling. The occurrence of a significant boiling event at $\phi=0$ deg and $Z=Z_4$ (which is nominally 196.1 mm) is denoted by a decrease in the slope of the curves beyond these points as q_o increases further. The reduction in the slope suggests an as yet undetermined event which could be significant bubble coalescence or a stable entry into the local post-CHF regime. As the heat flux was increased further, a loud hammer-like sound also began and increased in amplitude as the heat flux was further increased. In addition, moderate local wall temperature fluctuations (about 10°C) begin with a modest increase in the incident heat flux (850 to 870 kW/m^2). These periodic fluctuations increased in magnitude to about 18.0°C as q_o was increased beyond 1.0 MW/m^2. It is interesting to note that these periodic steady conditions resulted in an increase in the slope of the $T_w - q_o$ curve and hence resulted in locally stable, steady, periodic conditions in which the local mean and peak wall temperatures were almost constant.

Comparisons With the Single Side Heated Circular Tube. Figure 3 shows a comparison of two single-side heated geometries (1) a monoblock test section heated on one of its four outside surfaces, and (2) a ''circular-like'' (approximating a circular tube) test section heated on one-half of its outside circumference. For this comparison, the mass velocity was 0.59 Mg/m^{2}s and the measurements were made near the end of the heated length of the test sections. The cross-sectional aspect ratio (R_o) for the single-side heated monoblock test section is defined as the ratio of the heated width to the inside diameter of the flow channel. R_o for the single-side heated ''circular-like'' tube is the ratio of the outside diameter to the inside diameter. For both geometries, R_o is 3. It should be

noted that R_o is neither a peaking factor nor a similarity parameter for this comparison. Rather, it is used in the present work only for (1) to convenience of design, and (2) to demonstrate the obvious difference which has not been always apparent to some investigators. As expected at a given level of heat flux, the wall temperatures in the circular-like test section are typically higher than those in the monoblock test section. Correspondingly at a given power level, the local monoblock test section wall temperature is higher than that for the circular tube. Further, the fully developed flow boiling region extended over a broader heat flux range for the circular tube test section when compared with the monoblock test section. Near the fluid-solid boundary, the on-set to fully developed boiling occurred at a slightly higher temperature for the single-side heated circular tube than for the single-side heated monoblock flow channel. As can be seen, there is also good agreement between the data for the circular configuration and single-phase predictions except near ONB (i.e., ONB1).

Three-Dimensional Variations for a Single-Side Heated Monoblock. The circumferential variations of the wall temperature are presented in Figs. 4(*a*) and 4(*b*) for ten levels of the net incident heat flux, q_o. These figures show such variations close to the inside fluid-solid boundary and the outside (partially heated) boundaries, respectively. Comparing the two sets of plots, one observes that the circumferential wall temperature variations are basically similar except at the highest heat flux. However, there is a larger variation near the partially heated boundary. Since there are only four circumferential locations for each set of measurements, these distributions will not show the exact local circumferential slopes but the quantitative trends at the four locations are evident. The locus of the data in Fig. 4 displays approximately the correct boundary condition of a zero circumferential temperature gradient as ϕ approaches 180 deg for most levels of q_o. The zero temperature gradient is not directly apparent at $\phi=0$ deg from the lines (used only for convenient data point identification) connecting the data points. However, this data is amenable to this boundary condition; and, the data interpretation improves when this condition is used. Close to the fluid-solid boundary, the temperature is almost constant between $\phi=135$ and 180 deg. As ϕ increases, the local wall temperature decreases sharply and then gradually decreases as expected. The gradual decrease is due to the large value of R_o. As R_o decreases, this circumferential variation will increase [15].

At all heat flux levels, the temperature variations between $\phi=0$ and 45 deg are usually much less for the circular tube than for the monoblock. This implies that for a given heat flux level above that needed for local boiling, a larger portion of the single-side heated circular tube inside wall experiences boiling in the circumferential direction than the single-side heated monoblock.

Figure 5 displays the radial temperature profiles at $\phi=45$ deg and shows significant variations with respect to r. As can be seen by comparing Figs. 4(*a*) and 4(*b*) at identical values of q_o, the radial variation at $\phi=0$ deg is larger than at other circumferential locations. These radial temperature profiles may be useful in estimating the local heat flux and wall temperature on the inside flow channel surface.

Finally, Fig. 6 shows the remaining portion of the three-dimensional variations via the axial wall temperature profiles. The curves are for test section locations along the heated portion of the plane of symmetry ($\phi=0$ deg) and close to the heated boundary. These local axial wall temperature profiles show that the wall temperature in the axial direction increases with the axial coordinate up to the third axial station ($Z=Z_3=147.1$ mm), beyond which the local wall temperature decreases. Although small, axial variations occurred between Z_2 ($=98$ mm) and Z_3 ($=147.1$ mm) at all power levels. These variations will increase for monoblock test section wall and prototypic PFC substrate thicknesses smaller than the 10 mm nominal value for the present case.

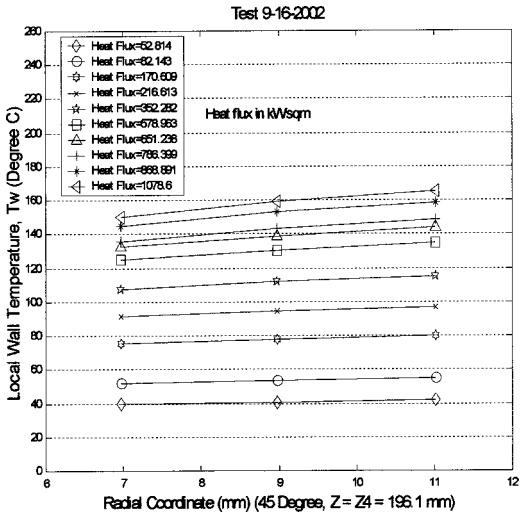

Fig. 5 Radial wall temperature profiles for the flow channel at $\phi=45$ deg and $Z=Z_4=196.1$ mm as a function of the net incident heat flux

Conclusions

The optimized design of single-side heated plasma-facing components (PFCs) and other high heat flux heat sinks is dependent on knowing the local distribution of inside wall heat flux and temperature in the flow channels. This knowledge will result in a reliable description of the different heat transfer regimes at the inside wall of the cooling channel. The inside wall heat flux can be obtain from selectively chosen local wall temperatures close to the inside boundary of the flow channel. To this end, three-dimensional thermal measurements for a single-side heated monoblock test section were made and show (1) the three-dimensional variation of the wall temperature close to both the heated and fluid-solid surface boundaries, as well as at an intermediate location (2) two-dimensional quasi-boiling curves, and (3) good agreement with the Petukhov [21] correlation in the single-phase region when the thermal hydraulic diameter [1,22] is used. These results (1) are among the first full set of three-dimensional wall temperature measurements for single-side heated monoblock flow channels which contain the effect of conjugate heat transfer from turbulent, subcooled flow boiling, and (2) provide a unique two-

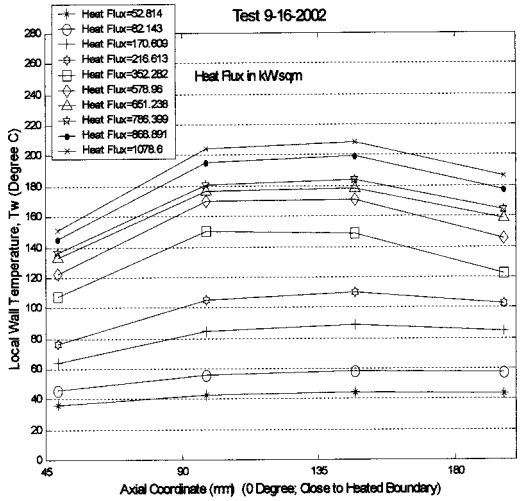

Fig. 6 Axial wall temperature profiles from the TCs at $\phi=0$ deg, and close to the heated boundary as a function of the net incident heat flux

phase, turbulent, flow boiling data base for single-side heated flow channels which can be used for comparisons with future computational fluid dynamic and heat transfer predictions and existing correlations.

Acknowledgments

The authors are appreciative to the Department of Energy (DOE) for its support of this work under contract #DEFGO3-97ER54452. The authors are also appreciative to Mrs. Vivian Pope for supporting many aspect of this work. Finally, the authors are appreciative to Richard Martin for completing the schematic for the test section assembly.

Nomenclature

A_H = outside heated surface area$=tL_H$ for the monoblock test section and $5tL_H$ for the circular-like test section (m^2)
a = dimensionless constant with different values for different single-side heating and geometric configurations
D = correction for the axial coordinates ($Z=Z_j-D$) for TCs at $\phi=0$ deg and in test section planes #A2 ($D=2$ mm) and #A3 ($D=4$ mm)
D_i = inside coolant channel diameter (m)
D_T = thermal hydraulic diameter, $a\cdot D_i$ (m)
G = mass velocity (kg/m^{2}s)
Gz = Graetz number, Re Pr $(L_H/\mathrm{Di})^{-1}$
h = local heat transfer coefficient (W/m^{2}K)
k_f = fluid thermal conductivity (W/mK)
L_H = heated length (m)
L_i = unheated inlet length (m)
L_o = unheated exit length (m)
Pr = Prandtl number
Nu_{D_T} = local Nusselt Number, hD_T/k_f
q_o = net incident flux based on A_H (kW/m^2)
Re = Reynolds Number, GD_i/μ
r = radial coordinate (m)
t = heater width (m)
TC = thermocouple
T_{sat} = saturation temperature (°C)
T_w = local wall temperature (°C)
Z = axial coordinate or measurement location (mm)
Z_j = axial coordinate location for axial sections A-A ($Z=Z_4=196.1$), B-B ($Z=Z_3=147.1$), C-C ($Z=Z_2=98.0$), and D-D ($Z=Z_1=49.0$), where $j=1$, 2, 3, or 4 (mm)

Greek Symbols

μ = dynamic viscosity (kg/ms)
ϕ = circumferential coordinate (deg)

References

[1] Boyd, R.D., 1999, ''Single-Side Conduction Modeling for High Heat Flux Coolant Channels,'' Fusion Technol., **35**, pp. 8–16.
[2] Marshall, T.D., Youchison, D.L., and Cadwallader, L.C., 2001, ''Modeling the Nukiyama Curve for Water-Cooled Fusion Divertor Channels,'' Fusion Technol., **35**, pp. 8–16.
[3] Boscary, J., Araki, M., and Akiba, M., 1997, ''Critical Heat Flux Database of JAERI for High Heat Flux Components for Fusion Applications,'' JAERI-Data/Code 97-037, Japan Atomic Energy Research Institute.
[4] Liu, W., Nariari, H., and Inasaka, F., 2000, ''Prediction of Critical Heat Flux for Subcooled Flow Boiling,'' Int. J. Heat Mass Transfer, **43**, pp. 3371–3390.
[5] Youchison, D.L., Schlosser, J., Escourbiac, F., Ezato, K., Akiba, M., and Baxi, C.B., 1999, ''Round Robin CHF Testing of an ITER Vertical Target Swirl Tube,'' 18th IEEE/NPSS Symposium on Fusion Engineering, Albuquerque, NM, pp. 385–387.
[6] Akiba, M., Ezato, K., Sato, K., Suzuki, S., and Hatano, T., 1999, ''Development of High Heat Flux Components in JAERI,'' 18th IEEE/NPSS Symposium on Fusion Engineering, Albuquerque, NM, pp. 381–384.
[7] Youchison, D.L., Nygren, R.E., Griegoriev, S., and Driemeyer, D.E., 1999, ''CHF Comparison of an Attached-Fin Hypervapotron and Porous-Coated Channels,'' 18th IEEE/NPSS Symposium on Fusion Engineering, Albuquerque, NM, pp. 388–391.
[8] Youchison, D.L., Cadden, C.H., Driemeyer, D.E., and Wille, G.W., 1999, ''Evaluation of Helical Wire Inserts for CHF Enhancement,'' 18th IEEE/NPSS Symposium on Fusion Engineering, Albuquerque, NM, pp. 119–122.
[9] Marshall, T., 1998, ''Experimental Examination of the Post-Critical Heat Flux and Loss of Flow Accident Phenomena for Prototypical ITER Divertor Channels,'' Ph.D. thesis, Rensselaer Polytechnic Institute, Troy, NY.
[10] Boscary, J., Araki, M., and Akiba, M., 1997, ''Analysis of the JAERI Critical Heat Flux Data Base for Fusion Application,'' JAERI-Data/Code 97-037, Japan Atomic Energy Research Institute.
[11] Marshall, T.D., Watson, R.D., McDonald, J.M., and Youchison, D.L., 1995, ''Experimental Investigation of Post-CHF Enhancement Factor for a Prototypical ITER Divertor Plate with Water Coolant,'' *Symposium on Fusion Engineering*, IEEE, pp. 206–209.
[12] Inasaka, R., and Nariari, H., 1996, ''Critical Heat Flux of Subcooled Flow Boiling in Swirl Tubes Relevant to High-Heat-Flux Components,'' Fusion Technol., **29**, p. 487.
[13] Akiba, M., et al., 1994, ''Experiments on Heat Transfer of Smooth and Swirl Tubes Under One-Sided Heating Conditions,'' presented at the US/Japan Workshop, Q182, on Helium-Cooled High Heat Flux Components Design, General Atomics Corporation, San Diego, CA.
[14] Celata, G.P., Cumo, M., and Mariani, A., 1996, ''A Mechanistic Model for the Prediction of Water-Subcooled-Flow-Boiling Critical Heat Flux at High Liquid Velocity and Subcooling,'' Fusion Technol., **29**(4), p. 499.
[15] Boyd, R.D., 1994, ''Similarities and Differences Between Single-Side and Uniform Heating for Fusion Applications—I: Uniform Heat Flux,'' Fusion Technol., **25**, pp. 411–418.
[16] Araki, M., et al., 1994, ''Experiment on Heat Transfer of the Smooth and the Swirl Tubes Under One-Side Heating Conditions, Department of Fusion Engineering Research,'' Japan Atomic Energy Research Institute (JAERI) Report.
[17] Becker, K.M., et al., 1988, ''Heat Transfer in an Evaporator Tube with Circumferentially Non-Uniform Heating,'' Int. J. Multiphase Flow, **14**(5), pp. 575–586.
[18] Gärtner, D., et al., 1974, ''Turbulent Heat Transfer in a Circular Tube with Circumferentially Varying Thermal Boundary Conditions,'' Int. J. Heat Mass Transfer, **17**, pp. 1003–1018.
[19] Boyd, R.D., Cofie, P., Li, Q.Y., and Ekhlassi A., 2000, ''A New Facility for Measurements of Three-Dimensional, Local Subcooled Flow Boiling Heat Flux and Related Critical Heat Flux,'' International Mechanical Engineering Congress and Exposition (IMECE), **HTD-866**-4, ASME International, New York, pp. 199–208.
[20] Bergles, A.E., and Rohsenow, W., 1964, ''The Determination of Forced-Convection Surface-Boiling Heat Transfer,'' ASME J. Heat Transfer, p. 365.
[21] Petukhov, B.S., 1970, ''Heat Transfer and Friction in Turbulent Pipe Flow with Variable Physical Properties,'' Adv. Heat Transfer, **6**, pp. 503–564.
[22] Boyd, R.D., and Meng, X., 1996, ''Local Subcooled Flow Boiling Model Development,'' Fusion Technol., **29**, pp. 459–467.

Modeling and Numerical Prediction of Flow Boiling in a Thin Geometry

Ranganathan Kumar
e-mail: Rnkumar@mail.ucf.edu
University of Central Florida,
Orlando, FL 32816

Charles C. Maneri

T. Darton Strayer

Lockheed Martin Corporation,
Schenectady, NY 12301

An analysis capability to examine the two-phase bubbly flow in high pressure boiling systems has been developed. The models have been adapted from the literature for a narrow high aspect ratio geometry using the measurements obtained in a companion paper. Three-dimensional computational results have been compared with cross-section averaged and line-averaged void fractions measured with a gamma densitometer, and local void fraction measured with a hot-film anemometer. These comparisons have been made over a wide range of flow inlet conditions, wall heating and system pressure. Comparisons are found to be good when the flow is bubbly, but at high void fractions, where the flow is churn-turbulent or annular, the two-field modeling approach does not perform adequately. This result emphasizes the need for multiple field modeling.
[DOI: 10.1115/1.1643754]

Keywords: Boiling, Heat Transfer, Modeling, Multi-Phase

Introduction

The two-phase flow analysis developed over the years can be grouped into two categories: fluid mixture and two-fluid. Researchers have used the two-fluid approach successfully since it is readily adaptable to multi-dimensional analysis. In particular, Lahey and Drew [1–3] have shown that mechanistic closure models developed for the Computational Fluid Dynamics (CFD) predictions of bubbly flow match the void distribution and turbulence quantities measured by Serizawa [4] in tubes very well. There is a need to extend these models for boiling flows in thin geometry applications. Very thin tubes and thin ducts in the millimeter range are now employed in compact evaporators and in the micrometer range in ink jet printers and other Micro Electro Mechanical Systems (MEMS). In these narrow geometries, the micron-size bubbles originating at the heated surface are quickly confined in the space as they grow. When these bubbles span the narrow space, they start elongating with a spherical cap and a cylindrical tail in the case of a tube, and a planar cap in the case of a thin duct. Therefore, the geometry plays a major role in bubble development. The three parameters of importance in any thin geometry are Eotvos number, Morton number and Weber number [5,6] for the development of the drag model and the non-drag model such as the lift force.

In the literature, the closure conditions or models have been developed and tested based on measurements in air-water systems. Some of these models that are primarily developed for dilute bubbly flows have not been tested in high-pressure heated systems. At high pressure, a higher frequency of bubbles is present and the flow can stay bubbly at void fractions as high as 60 percent [6,7], although in thin geometries, the bubbles may behave like slugs at much lower void fractions. Therefore, the integrated effects of the closure models acting at a bubbly interface in a high-pressure heated system have not been validated using a numerical code.

The present work is undertaken to apply the lift and drag models developed for high-pressure systems in a companion paper [6] along with the other available momentum models in the literature, and heat partitioning at the wall in a numerical code. The primary objective is to evaluate integrated model predictions in a modeling fluid in a rectangular geometry for which unique measurements are available. Rectangular geometries present better optical access for the measurements, and capture three-dimensional effects. Limited model verification will be done using specific experiments in a refrigerant fluid, R-134a (SUVA) in thin high aspect ratio geometry. The experimental facility, instrumentation and measurement procedures have been explained in detail in [6]. The ability to predict local flow field parameters for many conditions of interest will be established by comparison of three-dimensional results with detailed local and average void fraction and pressure drop measurements. Shortcomings of two-field modeling beyond the bubbly flow regime will be demonstrated and discussed.

Ensemble Averaging Process. In the two fluid approach, the ensemble averaged conservation equations are written for each phase. Ensemble averaging is more appropriate for general two-phase flows since it preserves both spatial and temporal flow variations. Closure conditions used in the current analysis were developed within the cell model averaging framework developed by Drew [8]. The ensemble average is obtained by examining the set of realizable flows occurring at $\underline{x}$, resulting from a sphere (bubble) center occupying different positions $\underline{z}$ within the cell. If f is some microscopic process, the dependence on the ensemble for this case is denoted by $f(\underline{x},t;\underline{z})$. In this model, flow realizations of a single bubble contained within the averaging cell are calculated as

$$\overline{f}=\int_{V_{\text{cell}}}\int\int f(\underline{x},t;\underline{z})\wp(\underline{x},t;\underline{z})dV \tag{1}$$

where $\underline{x}$ is the fixed flow observation point located within the volume dV, $\underline{z}$ is the location of the bubble center located within the cell, and $\wp$ is the probability of a particular flow realization. A phase indicator function is defined as

$$X_i(x,t)=\begin{cases}1 & \text{for phase } i \text{ at } (x,t)\\ 0 & \text{otherwise}\end{cases} \tag{2}$$

The ensemble-averaged equations are obtained by first multiplying the single-phase equations by the phase indicator function. This leads to averaged quantities such as

$$\overline{\rho}_i=\frac{\overline{\rho_i X_i}}{\overline{X_i}}=\frac{\overline{\rho_i X_i}}{\alpha_i}$$

Contributed by the Heat Transfer Division for publication in the JOURNAL OF HEAT TRANSFER. Manuscript received by the Heat Transfer Division November 20, 2002; revision received October 16, 2003. Associate Editor: D. B. R. Kenning.

$$\overline{f_i} = \frac{\overline{f_i X_i \rho_i}}{\alpha_i \overline{\rho_i}} \tag{3}$$

These concepts are used in deriving the ensemble-averaged Navier-Stokes equations as given in Eqs. (4)–(6). More details are provided in [8].

Governing Equations. In the averaging of Navier-Stokes equations, microscale flow phenomena (individual interface interactions) are filtered out and the resulting averaged equations are used to predict the desired macroscale flow behavior (such as local void distributions) once the appropriate closure conditions are included. As with all averaging processes, some physical information is lost during averaging. Therefore, closure conditions or constitutive equations must be introduced, the form of which must be determined through analysis of the interfacial physics. These relations or ''models'' are described in detail later in the section, ''Closure Models.''

The two-fluid model entails solving phasic equations of mass, momentum, and energy conservation to determine the flow variables. Each phase has a unique value for every flow variable. Pressure is assumed to be common to both phases. The conservation equations are given below.

Conservation of Phasic Mass.

$$\frac{\partial}{\partial x^k}(\alpha_i \rho_i u_i^k) = \underline{\sum_{j \neq i} (\Gamma_{ji} - \Gamma_{ij})} \tag{4}$$

Conservation of Phasic Momentum.

$$\frac{\partial}{\partial x^k}(\alpha_i \rho_i u_i^k u_i^l) = -\alpha_i \frac{\partial p}{\partial x^l} + \frac{\partial}{\partial x^k}\left\{ \alpha_i u_i \left(\frac{\partial u_i^l}{\partial x^k} + \frac{\partial u_i^k}{\partial x^l} \right) \right\} + \underline{M_i^l} + \underline{\sum_{j \neq i} D_{ij}(u_j^l - u_i^l)} + \Gamma_{ji} u_j^l - \Gamma_{ji} u_i^l \tag{5}$$

Conservation of Phasic Energy.

$$\frac{\partial}{\partial x^k}(\alpha_i \rho_i u_i^k h_i) = \frac{\partial}{\partial x^k}\left(\alpha_i k_i \frac{\partial T_i}{\partial x^k} \right) + \underline{Q_i} + \underline{\sum_{j \neq i} (\Gamma_{ji} h_j^{\text{int}} - \Gamma_{ij} h_i^{\text{int}})} \tag{6}$$

The subscript, *i*, denotes the field. In bubbly flow, there are only two fields, representing the two phases, liquid and vapor. The representation given in Eqs. (4)–(6) lends itself well to a multifield formulation, which would be necessary if multiple flow regimes are encountered in the same problem. In bubbly flow, there is only the liquid-vapor interface. The double subscript in the mass transfer term, Γ_{ij}, denotes a quantity transferred from the phase indicated by the first index (donor phase) to the phase indicated by the second index (receptor phase). For example, an evaporative mass generation term in bubbly flow is indicated by $\Gamma_{l\text{-}v}$ (liquid-vapor). The superscript *k* is the repeated index. $D_{ij}(u_j^l - u_i^l)$ represents the interfacial drag force; M_i^l, the nondrag forces including Reynolds stresses; Q_i, the net heat transfer to phase *i* due to interfacial, wall and volumetric heating sources. The thermodynamic variables, temperature and enthalpy are related by $C_{P_i} = \partial h_i / \partial T_i$. From the definition of volume fraction, $\Sigma \alpha_i = 1$. Flow toward the interface from either field is in the positive direction and away from the interface in the negative direction. For heat transfer at an interface, this convention results in vapor generation being a positive phase change and condensation a negative one when referenced to the liquid side.

The interfacial and wall quantities in the governing equations are given by closure relationships, which are expressed in terms of the primary flow field parameters, *u*, *v*, *w*, *T*, *h*, α, and *p*. Pressure, *p*, is common to both phases. In addition to the closure relationships, solution of the governing equations requires the following boundary conditions.

At the inlet to the duct, the following values are set for each phase: three velocity components, density, volume fraction, temperature, and enthalpy. In addition, *k* and ε are also given in the liquid phase as given in the next section. A pressure boundary condition is specified across the exit plane of the duct. No slip boundary conditions are used on the walls of the duct. Along the wall, nonzero heat fluxes are specified. Setting the system pressure and the fluid properties completes the flow specification.

k-ε Transport Equations. If the liquid phase is turbulent, transport equations for the turbulent kinetic energy and the dissipation of kinetic energy (*k* and ε) are solved in the liquid field. The dispersed vapor phase is assumed to be laminar. The turbulence structure in the liquid phase must be carefully modeled, since it is known that the two-phase turbulence can significantly affect the lateral void distribution. The conservation equations will be considered closed if the turbulent stress is modeled. The form of the *k-ε* transport equations used here is a simple extension of the single-phase model to two-phase flows. The eddy viscosity hypothesis is valid and has been used with modifications made for bubble-induced turbulence as explained later. The turbulence equations are given below. Although the subscript, *i*, can be used to represent any continuous field, in the bubbly flow case, *i* in Eqs. (7)–(9) represents only the liquid phase.

Turbulence Kinetic Energy Equation.

$$\nabla.(\rho_i \alpha_i u_i k_i) = \nabla.\left\{ \alpha_i \left(\mu_i + \frac{\mu_i^T}{\sigma_i} \right) \nabla k_i \right\} + P_i + G_i - \rho_i \alpha_i \varepsilon_i \tag{7}$$

where the shear production and buoyancy production terms, P_i and G_i, are given by

$$P_i = \alpha_i \mu_{\text{eff}} \nabla u.(\nabla u + \nabla u^T); \quad G_i = \alpha_i \frac{\mu_{\text{eff}}}{\sigma_T} \beta_i (g.\nabla T) \tag{8}$$

Turbulence Dissipation Equation.

$$\nabla.(\rho_i \alpha_i u_i \varepsilon_i) = \nabla.\left\{ \alpha_i \left(\mu_i + \frac{\mu_i^T}{\sigma_\varepsilon} \right) \nabla \varepsilon_i \right\} + C_1 \frac{\varepsilon_i}{k_i}(P_i + G_i) - C_2 \rho_i \alpha_i \frac{\varepsilon_i^2}{k_i} \tag{9}$$

Numerical Procedure. The system of governing differential equations is discretized using a finite volume formulation in which first order hybrid upwinding is used for the convection terms. The discretized equations are solved in a segregated fashion using the SIMPLEC algorithm [9] on a collocated grid. Pressure velocity coupling is enforced using the algorithm developed by Rhie and Chow [10], and coupling between the phases is accomplished using a modified algorithm developed by Spalding [11] for two phases and adapted for a nonstaggered grid in the commercial code, CFDS-FLOW3D [12].

Several different grid spacings were examined and the numerical results presented herein are generated with nonuniformly spaced grids ($16 \times 25 \times 37$). This grid was found to be adequate for the experimental conditions reported and was constructed to ensure that corner nodes had a $\Delta y / \Delta z$ ratio of 1 in the transverse plane. Solution convergence was measured by examining the mass, momentum and energy residuals in the continuous liquid field. Additional measures of convergence included global mass and energy balances, and numerical solution invariance.

Jump Conditions

Mass Jump Condition. The phases are coupled via interfacial transfer terms underlined in Eqs. (4)–(6). These terms are related by what are called the jump conditions. The continuity jump condition arises from a mass balance, and it states that mass cannot

accumulate on the interface. This condition is met since the mass transfer terms are written as source and sink terms in the opposite phases ($\Gamma_{l-\nu} = -\Gamma_{\nu-l}$).

Energy Jump Condition. The energy jump condition dictates that latent heat and work against surface tension balance the net flux of energy to the interface. The jump condition is then met by assuming that all interfacial heat transfer goes into latent heat of phase change, and that no energy goes into sensible heating or accumulates at the interface. During phase change, mass is assumed to start at the bulk enthalpy/temperature of the donor phase and to end at the saturation state of the receptor phase. The energy jump condition thus allows the mass transfer rate to be determined from the interfacial heat transfer. At the wall, the bubble interface is a hybrid in that the part of the interface in contact with the wall is treated differently than the remainder of the interface. The energy jump condition is expressed as

$$q_{i_{l-\nu}} + q_{i_{\nu-l}} + q_E - (\Gamma_{l-\nu} + \Gamma_w) h_{fg} = \varepsilon^{\sigma}_{i_{l-\nu}} \tag{10}$$

where the right hand side is the interfacial energy source due to surface tension. Since the bubbles are assumed to be rigid, there is no contribution from the right hand side. With the first two terms in Eq. (10) replaced in terms of their respective heat transfer coefficients and temperature differences, the phase change terms are written as

$$\Gamma_l = -(\Gamma_{l-\nu} + \Gamma_w)$$

$$= -A^m_{\nu-l}\{H_{l-\nu}(T_l - T_s) + H_{\nu-l}(T_\nu - T_s)\} - \frac{q_E}{h_{fg}} \tag{11}$$

$$\Gamma_w = \frac{q_E}{h_{fg}}; \quad \Gamma_\nu = \Gamma_{l-\nu} + \Gamma_w \tag{12}$$

Momentum Jump Condition. The momentum jump condition is given by

$$M_{l-\nu} + M_{\nu-l} + \Gamma_{l-\nu} v_{i_{l-\nu}} + \Gamma_{l-\nu} v_{i_{\nu-l}} + \Gamma_w u_{l_{wn}} - \Gamma_w u_{\nu_{wn}} = m^{\sigma}_{i_{l-\nu}} \tag{13}$$

The momentum jump condition dictates that the net force acting on the interface (summation of the underlined forces in all fields) is balanced by surface tension effects. As a first approximation, for rigid bubbles, the right hand side is zero, and no net momentum is stored at the interface. Mass leaves a donor phase at the velocity of the donor phase and arrives in the receptor phase with its velocity unchanged. As with the energy treatment of phase change, for a bubble at the wall, the region of the interface in contact with the wall is treated differently from the remainder of the interface. Since only vapor generation occurs at the wall and the wall is rigid, the velocities induced in the liquid and vapor on the wall side of the bubble are different from the velocities acting over the remainder of the bubble surface. The induced velocities on the wall side act primarily normal to the wall. Although an axial component exists, it is assumed to be negligible compared to the normal component. Therefore, the phase change momentum terms in Eq. (5) are written as

$$\Gamma_l v_{i_l} = -\Gamma_{l-\nu} v_{i_{l-\nu}} - \Gamma_w u_{l_{wn}}$$

$$\Gamma_\nu v_{i_\nu} = -\Gamma_{l-\nu} v_{i_{\nu-l}} - \Gamma_w u_{l_{wn}} \tag{14}$$

The velocities at the wall node are given as

$$u_{l_{wn}} = \frac{\Gamma_w}{\rho_l A'''} = \frac{q_E}{\rho_l h_{fg} A'''}$$

$$u_{\nu_{wn}} = \frac{\Gamma_w}{\rho_\nu A'''} = \frac{q_E}{\rho_\nu h_{fg} A'''} \tag{15}$$

Using Eqs. (14) and (15), the momentum jump condition in Eq. (13) can be written as

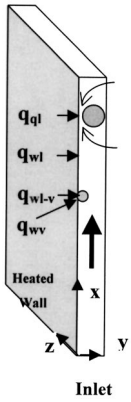

Fig. 1 Flow geometry and heat partitioning representation at the wall (figure not drawn to scale)

$$M_{l-\nu} + M_{\nu-l} + \Gamma_{l-\nu}(v_{i_{l-\nu}} - v_{i_{\nu-l}}) - \left(\frac{\rho_l - \rho_\nu}{\rho_l \rho_\nu}\right)\frac{q_E^2}{h_{fg}^2 A'''} = 0 \tag{16}$$

The interfacial phase change term and the velocities are known. This allows the source term, $M_{l-\nu}$ to be written in terms of the $M_{\nu-l}$.

Closure Models

The underlined terms in Eqs. (4)–(6) are models that are reintroduced into the flow equations after physical information is lost during the averaging process. These models represent phase-to-phase and phase-to-wall interactions. The majority of these bubbly flow models have been taken from the literature in air-water flows in tubes. These models have been adapted in high-pressure systems and applied locally. The drag was derived for the noncircular geometry and the lift model was presented in terms of Eotvos number in [6]. The other models described here for the analysis of phase distribution and phase separation are presented by Lahey and Drew [2] for bubbly upflows and downflows in pipes and more complex geometry conduits.

Heat Transfer Models

Heat Partitioning at the Wall. At the wall node, the heat input from the wall and initial vapor generation are introduced into the flow field. The models discussed here are based on a wall partition model developed by Kurul [13] for subcooled nucleate boiling. The gist of the model is that heat is apportioned to the fluid via various mechanisms such as sensible heating and forced boiling. All mechanisms receive heat simultaneously with the relative distribution being set by heat transfer coefficient models. Using the heat transfer coefficients and the saturation temperatures, a wall temperature is calculated so that the sum of the energy going into each heating mechanism sums to the boundary value.

Referring to Fig. 1, the input heat generation, q_{wtot}, is partitioned as

$$q_{wtot} = q_{wl-\nu} + q_l + q_{w\nu} \tag{17}$$

where $q_{wl-\nu}$ is the energy that goes directly into boiling, $q_{w\nu}$ is the energy transferred directly to the bubble. The last term would be significant only in dryout situations. The energy transferred to the liquid, q_l is further partitioned into two separate modes of heat transfer, namely

$$q_l = q_{ql} + q_{wl} \tag{18}$$

where the first term is the quenching mode of heat transfer which is the energy that heats up the cooler liquid that replaces the bubble after it departs the wall or collapses. The second term is the energy transferred to the liquid outside the influence area of

Table 1 Heat transfer coefficients in the wall-partitioning model

Model	Comments
$H_{wl}=0.023\frac{k_l}{d_h}\left(\frac{\rho_l d_h u_l}{\mu_l}\right)^{0.8}\left(\frac{c_{p_l}\mu_l}{k_l}\right)^{1/3}$	Dittus-Boelter outside bubble area. K in Eq. (19) is taken as 4.0 [14]
$H_{ql}=2\left(\frac{f\rho_l k_l c_{p_l}}{\pi}\right)^{1/2}$; $f=\left(\frac{4}{3d_b}g\frac{\Delta\rho}{\rho_l}\right)^{1/2}$	Adjusted form of quenching model given in [14]. f is the bubble departure frequency given in [15]
$H_\nu=\frac{k_\nu}{\delta_\nu}$ where $\delta_\nu=$ effective thermal layer$=\beta_1 d_b$ $F_\nu=\beta_2 N''\pi d_b^2/4$ in Eq. (19); $(\pi/4)\beta_2/\beta_1=1$	Energy transferred from wall to vapor. $F^{d\nu}$ is a fraction of the wall area underneath the bubble where the liquid is totally evaporated [13]
$N''=\min\left(\frac{\Delta\rho g}{\sigma}\left(2374\frac{\Delta T_s}{T_s}\right)^{1.8}\left(1-\frac{\Delta T_{\text{sonb}}}{\Delta T_s}\right)^{1.8}, N''_{\max}\right)$, where $\Delta T_{\text{sonb}}=180\left(\frac{2\sigma T_s\Delta\rho}{h_{fg}\rho_l\rho_\nu}\right)\frac{1}{k_l}\left[0.023\frac{k_l}{d_h}\left(\frac{Gd_h}{\mu_l}\right)^{0.8}\left(\frac{c_{p_l}\mu_l}{k_l}\right)^{1/3}\right]$	Modified nucleation site density from [13]. $N''_{\max}$ is the maximum bubble packing limit, $2/3^{0.5}d_b^2$ T_{sonb} is the nucleation inception superheat [16]. $\Delta T_{\text{sonb}}=T_{\text{sonb}}-T_s$

the bubbles. In the subcooled boiling region, this energy acts to heat the liquid adjacent to the wall. The wall temperature, T_w, can be determined in terms of heat transfer coefficients and ΔT as given in the next equation.

$$q_{wtot}=H_{wl}\left(1-KN''\frac{\pi d_b^2}{4}\right)A'''(T_w-T_l)+H_{ql}KN''\frac{\pi d_b^2}{4}A'''(T_w-T_l)+H_\nu F_\nu d_b A'''(T_w-T_\nu)+fN''\frac{\pi d_b^3}{6}\rho_\nu h_{fg}A''' \quad (19)$$

The fourth term in Eq. (19) is the fraction of the wall heat generation going directly into boiling. fN'' is the rate at which bubbles form and depart per unit surface area, and $\rho_\nu h_{fg}$ is the heat content per unit volume. As seen in Eq. (19) and in Table 1, the nucleation site density, N'', is an integral part of the heat partition model.

Each of the energy terms in the partition model in Eq. (19) is a function of the nucleation site density. The nucleation site density and quenching models given in Table 1 were adjusted to be consistent with the experimental results found in the literature [14]. These results showed that only 2–3% of the wall heat goes into boiling, 5–10% goes into single phase convective heat transfer, and the remaining 87–93% is associated with the quenching mode.

The wall superheat is given in Table 1, assuming that the temperature gradient away from the wall is linear, and that the bubble nuclei on cavities in the heated wall persists only if the lowest liquid temperature on the surface of the bubble nuclei exceeds the vapor temperature given by the Clausius-Clapeyron relationship [16].

Interfacial Heat Transfer. The total transfer rate is the sum of the wall heat transfer (which is zero in the interior of the domain) and the interfacial heat transfer. Expressions for heat transfer coefficients are given in Table 2.

Momentum Models

Drag Force. Most of the available correlations for drag have been developed for a single bubble in an infinite medium. When bubbles are confined by walls, they start elongating with a planar cap in the case of a high aspect ratio geometry. The bubbles may look like Taylor bubbles in the narrow dimension, whereas they may seem circular in the other two dimensions. The cell model is valid for dispersed flows only, and for nondilute flows, the closure needs to be done on a more phenomenological basis. In our companion paper, Kumar et al. [6] took a phenomenological approach in developing a drag model given in Table 3. They measured bubble rise velocity and bubble sizes in different groups based on Morton number. The bubbly regimes were identified based on the bubble shape and rise behavior. Small bubbles obey the Stokes' law in the viscous regime, whereas large bubbles become oblate. The rise velocity for large bubbles slightly decreases because the wake behind the bubble becomes turbulent. Kumar et al. [6] developed a drift velocity in a multiple bubble system and expressed the drag force in terms of relative velocity between the phases and the equivalent bubble diameter. The spherical bubbles grow in size, and become planar as they are constrained by the walls in the narrow dimension. Since the three-dimensional and planar bubbles are dynamically equivalent, it is reasonable to use the drag equation given in Table 3 for planar bubbles as well, with d_B taken as the spherical equivalent bubble diameter given in Table 4.

Lift Force. Under the influence of the trailing vortex street, the nose of an elongated bubble confined in a narrow space will

Table 2 Interfacial heat transfer coefficients

Model	Comments
$H_{l-\nu}=\frac{k_l}{d_b}\left[2.0+0.6\left(\frac{\rho_l d_b\lvert\underline{v}_\nu-\underline{v}_l\rvert}{\mu_l}\right)^{1/2}\left(\frac{c_{p_l}\mu_l}{k_l}\right)^{1/3}\right]$	Flow around a sphere by Ranz and Marshall [17]
$H_{\nu-1}=K\frac{2k_\nu}{d_b}$	K is taken to be large to ensure that the droplet and the bubble are saturated and not superheated

Table 3 Bubbly drag and lift models

Model	Comments
Vapor Drag	Derivation is given in [6] for a multiple bubble system based on ideas developed for a single bubble rise model.
$F_D = C_D N A_P \rho_l \frac{u_R^2}{2}$;	NA_P = total projected area of the vapor phase
$C_D = \frac{4}{3}\frac{d_B}{V_{gj}^{B^2}}(1-\alpha^2)\frac{\Delta\rho}{\rho_l}g$	N = bubble number density
Drift velocity in a multiple bubble system	U_V and U_{DI} are rise velocities in the viscous and distorted-inertial regimes. $n=8$ (empirical from the data of [6]). Subscript *mb* indicates multiple bubbles.
$V_{gj}^B = \{(U_V(1-\alpha))^{-n} + (U_{DI} f_{DI})^{-n}\}^{-1/n}$;	U_{DI} is derived from an analogy that exists between the propagation velocity of surface waves and rise velocity of bubbles in infinite media [18].
$U_V = \frac{g\Delta\rho d_b^2}{K_b \mu_l}$;	
$K_b = K_M\left(\frac{d_b}{d_\infty}\right)^{0.425}$;	
$d_\infty = 2\left\{\frac{\sigma}{\Delta\rho g}\right\}^{1/2}$	
$K_M = 60(1-e^{-5.3\times 10^{10}\mathrm{Mo}_{mb}})$;	
$\mathrm{Mo}_{mb} = \frac{\mathrm{Mo}}{(1-\alpha)^4}$;	
$\mathrm{Mo} = \frac{g\mu_l^4\Delta\rho}{\rho_l\sigma^3}$	
$U_{DI} = \left[g\frac{d_b}{2}\frac{\Delta\rho}{\rho_l} + \frac{2\sigma}{\rho_l d_b}\right]^{1/2}$;	f_{DI} accounts for the multiple bubble effects [19].
$f_{DI} = \frac{(1-\alpha)^{5/2}\left\{1+\frac{0.46}{\mathrm{Mo}^{1/8}}\right\}}{1+\frac{0.46}{\mathrm{Mo}^{1/8}}(1-\alpha)^{9/7}}$	
Vapor Lift	Original lift model was derived by [20]. The lift coefficient changes sign and is based on Eo [6]. [5] and [21] have also postulated the change of sign in lift.
$F_L = -C_L\rho_l\alpha u_R \times (\nabla \times u_R)$	
$C_L = \begin{cases} 0.1 & \mathrm{Eo}<3 \\ 0.33[1-0.41\sqrt{\mathrm{Eo}}] & 3\leq \mathrm{Eo}\leq 9 \\ -0.075 & \mathrm{Eo}>9 \end{cases}$; $\mathrm{Eo} = g\Delta\rho d_b^2/\sigma$	

move from side to side. The lift force exerted from the edges at different points on this large slug-like bubble is nonuniform because of the bubble shape that tends to keep the slug oscillating.

The spiraling motion of the bubble depending on its size is well established for large size tubes. The lift force captures the influence of the liquid velocity gradient on the bubbles, thereby impacting the transverse distribution of the void fraction profile. The intrinsic fluctuating bubble motion can be described in terms of the Eotvos number, Eo [5,6], and the magnitude of the fluctuation increases with Eo. At low Eo, the tendency of the bubble is to move toward the wall, and at high Eo, the bubble migrates to the center. The functional form of the lift is the same for shear-induced lift in small Eo and lift induced by the vortex motion behind the deformed bubble in large Eo, and is given in Table 3.

Miscellaneous Momentum Models. Apart from the drag and lift forces, lubrication wall force and turbulence dispersion force are two of the models that affect the transverse distribution of void

Table 4 Bubble diameter and interfacial area density models

Model	Comments
Departure Bubble Size (wall nodes only)	Expression for nucleation inception wall superheat, ΔT_{sonb}, is given in Table 1. The kernel, d_o, is Levy's bubble diameter [22]. The model is based on [23].
$d_b = \min[d_o, d_o \exp\{-(\Delta T_{\mathrm{sub}}/45\Delta T_{\mathrm{sonb}})^{0.5}\}]$	
$d_o = 0.0315(\sigma d_h/\tau_w)^{1/2}$	
Bulk bubble size (all nodes not including wall nodes)	The void fraction dependent coefficient to Levy's model was proposed by [6] based on their bulk size measurements. α_o is set to 0.8.
$d_b = d_0\left\{1+\frac{21.64\alpha}{(\alpha_0-\alpha)^{0.29}}\right\}$	
Interfacial area density	The interfacial area density for the bubble is given for an equivalent spherical particle [18].
$A''' = 6\alpha/d_b$	

Table 5 Miscellaneous momentum models

Model	Comments
Lubrication wall force $M_l=\left[C_{w1}+C_{w2}\left(\frac{d_b}{y}\right)\right]\frac{\rho_l\alpha}{d_b}\lvert(u_v-u_l).n_x\rvert^2 n_y$ x and y are the streamwise and thickness directions respectively, n_x, n_y are the unit.	For bubbles flowing near a wall, a lateral force acts to move the bubbles toward the center of the channel. This wall force is derived from potential flow theory [24,25]. $C_{w1}, C_{w2}=-0.1, 0.12$.
Turbulence dispersion $M_{td}=-0.1\rho_l k_l \nabla\alpha$	The impact of this model in dispersing the bubbles and affecting the inception of transition is significant [26].
Wall shear $\tau_w=T_m u_P;\ T_m=\rho_l C_\mu^{1/4} k_P^{1/2}\kappa/\ln(Ey_P^+)$ E=9.0; P is the wall node, $\kappa=0.4$; $C_\mu=0.09$	The wall shear formulation uses a low-of-the-wall approach in two-phase flow, which has been validated by [27].
Turbulent viscosity $\mu_T=\rho_{cl}C_\mu k_l^2/\varepsilon_l+\rho_l C_{\mu b} d_b \alpha u_R;\ C_{\mu b}=0.6$ (shear-induced + bubble-induced viscosity)	The second term is due to the additional turbulence caused by bubble agitation [28]. This linear superposition is valid for dilute flows.

fraction in the narrow space. In addition to these models, the wall shear and the bubble-induced turbulence viscosity are important for accurate prediction of pressure drop. These models are mostly taken from the literature and are provided with brief descriptions in Table 5.

Experimental Measurements

The test facility and instrumentation have been described in detail elsewhere [6,29] and only a brief description is provided here for completeness. A refrigerant loop and the test section have been designed to conduct fundamental two-phase flow experiments for model validation. The test section is designed to have flat sides to allow optical access and to afford simplified measurement capability. It has a length of 1.2 m, a width of 57.2 mm and a thickness of 2.5 mm. The data analyzed in [6] are used in this paper for model validation. An instrument scanning mechanism positions a gamma densitometer system (GDS) along three axes: the *x*-axis (vertical, or streamwise position), the *y*-axis (horizontal scans along the test section narrow dimension perpendicular to the wall), the *z*-axis (horizontal scans across the width of the test section). A hot-film anemometer is also used to obtain local measurements of void fraction. Wall heating is provided by transparent Indium tin oxide conductive films coated on the quartz walls in three strips in the width direction. The power to each of the three window heater strips is independently controlled, and experiments can be performed with step power changes in the width direction. This capability is important for the three-dimensional validation of the numerical code, and is demonstrated by comparison of the predictions with void measurements for two nonuniformly heated conditions (Table 6).

The uncertainty in the various measurements is discussed in our companion paper by Kumar et al. [6]. Simultaneous measurements with multiple instruments were performed to confirm data trends, and cross-qualify void fraction and bubble size measurements. The uncertainty in the void fraction was calculated to be ± 0.025.

Integrated Modeling Effects Versus Experiments

In this section, an integrated model prediction is performed to test the various models as a group, and determine how they interact and change the overall flow prediction in the duct. To this end, the goal of this analysis is to predict the local conditions, and average conditions as a subcooled single-phase flow at the inlet passes through different types of bubble motion within the bubbly flow regime. Several representative test cases (see Table 6) at different pressures, flow rates, inlet subcooling and non-uniform wall heating have been predicted and compared against the data. Comparisons include: (a) cross-section averaged void fractions using the gamma densitometer (GDS) wide beam measurements at each non-dimensional axial *x*-location; (b) narrow dimension *y*-distribution of void fraction averaged along the width using GDS; (c) width dimension *z*-distribution of void averaged along the narrow space using GDS; (d) narrow dimension *y*-distribution point measurements of void using a hot-film anemometer (HFA); and (e) incremental pressure drop. Not all the measurements were available for all the cases.

Plot (a) of Figs. 2 and 3 show that the single phase subcooled liquid enters the test section and heats up until sufficient wall superheat is reached to initiate nucleation. The onset of nucleation is indicated by the formation of the bubbles near the heated walls. The point at which nucleation begins is strongly dependent on the subcooled boiling models employed. Following the onset of nucleation, the void fraction increases in the axial direction.

The lateral distribution of the vapor phase is determined by the dynamic balance among the following forces: (a) the lift force, which moves the vapor toward the wall or away from it depending on the bubble size, (b) the lubrication force which pushes the vapor away from the wall, and (c) turbulent dispersion which tends to distribute the void across the duct. Therefore, the void distribution in the narrow dimension (*y*-axis) varies according to the bubble size and shape, and basically determines the topology of the bubbly flow regime. The fluid enters the duct subcooled so that when bubbles first form, they exist in the vicinity of the heated wall where the fluid is either superheated or saturated. Since the fluid core is subcooled, bubbles that venture into the core due to turbulent dispersion tend to collapse. As the core fluid heats up to the saturation point, more and more bubbles can exist in the core. However, if the bubbles are spherical, the lift force

Table 6 Test conditions

Case	flow rate (kg/hr)	pressure (MPa)	Net Power kW	inlet subcooling (°C)	Uniformity of heating in the width direction (maximum/average ratio)
1	266	2.4	6.03	33.2	1
2	106	1.4	1.082	25.8	1.0*
3	532	1.4	2.647	3.6	1
4	532	1.4	5.062	3.6	1
5	266	2.4	2.964	7	1
6	532	2.4	5.722	2.1	1
7	2128	2	20.034	5.4	1
8	1064	1.7	9.951	15	1.5
9	318	2.4	3.382	8.3	1.5
10	366	2.4	6.601	26.3	1.33

*Only the third window is heated

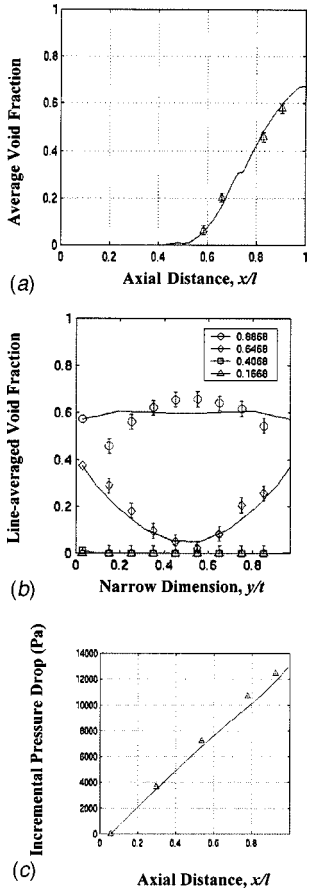

Fig. 2 Comparison plots for Case 1: 266 kg/hr; 2.4 MPa; 6.03 kW; 33.2°C subcooling: (*a*) Comparison of predicted cross section average void fraction with GDS measurement; (*b*) Comparison of predicted line-average void distribution in narrow dimension with GDS measurement at different *x*/*l*; and (*c*) Comparison of predicted and measured incremental pressure drop. Solid lines and symbols represent predictions and measurements, respectively. Boxed numbers represent *x*/*l*.

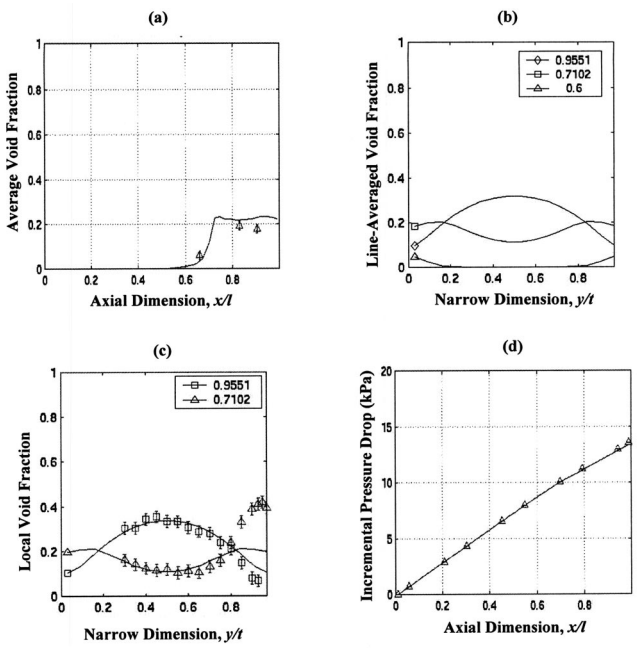

Fig. 3 Comparison plots for Case 2: 106 kg/hr; 1.4 MPa; 1.082 kW; 25.8°C subcooling: (*a*) Comparison of predicted cross section average void with GDS measurement; (*b*) Predicted line-average void distribution in narrow dimension at different *x*/*l* (no GDS data available); (*c*) Comparison of predicted and local void in narrow dimension with HFA measurement at different *x*/*l*; and (*d*) Comparison of predicted and measured incremental pressure. Note that solid lines and symbols represent predictions and measurements, respectively. Boxed numbers represent *x*/*l*.

tends to move them toward the wall or keep them in the vicinity of the wall depending on the bubble size. The line-averaged void predictions in Fig. 2(*b*) and the local predictions in Fig. 3(*c*) both show this wall-peaked behavior.

As the bubbles grow in size, surface tension forces can no longer maintain a spherical geometry; consequently, the bubbles become distorted, and the lift force reverses direction causing the bubbles to move towards the center of the duct. The bubble size at which the spherical surface begins to oscillate and become distorted is proportional to $\sqrt{\sigma/(\Delta\rho g)}$ [30]. The proportionality constant has been empirically determined and incorporated in the current lift model in terms of Eotvos number. This bubble size is therefore the critical value for which a reversal in the lift force would be initiated. Although the transition from wall-peaked to center-peaked profiles is well predicted by the models, the local peak at the wall at $x/l=0.71$ in Fig. 3(*c*) is underpredicted. This is probably because the departure size is not adequately modeled to represent the local subcooling.

The line-averaged void in Plot (b) and the local void in Plot (c) are similar in Fig. 3, suggesting that the bubbles are unconfined between the walls, and, therefore, are well dispersed in both *y* and *z*-directions. Typically, in SUVA, the minimum bubble size is, on average, 0.2 mm and 0.3 mm at 2.4 MPa and 1.4 MPa, respectively, about one-tenth the thickness of the duct. Therefore, two-dimensional and three-dimensional analyses at low void fractions would result in similar point and line-averaged distributions. This need not be the case at high power for which the bubbles would bridge the space between the walls.

The cases in Figs. 4 and 5 represent higher flow and higher inlet temperature (lower inlet subcooling). For these cases, the void inception occurs earlier in the duct. The core gets quickly saturated, and the bubbles grow in size and begin to span the narrow gap. The peak in the void distribution moves from the vicinity of the wall to the center of the duct at $x/l\sim0.4$ as seen in both the experimental and predicted results. Near $x/l\sim0.5$, the flow deviates significantly from a typical dispersed bubbly flow. Beyond $x/l=0.5$, the cross-section average void and the pressure drop in Figs. 4(*a*) and 4(*e*) are seen to be overpredicted. In general, the void distribution for Case 3 (Fig. 4) is well predicted by the models, although there exists some discrepancy at the transition between the wall-peaked and the center-peaked profiles. For the condition in Fig. 5, the pressure, the flow rate and the inlet subcooling were maintained constant, and the wall power was nearly doubled. The void fraction increases and the bubbles grow via interfacial evaporation and coalescence, becoming confined and planar and growing in the width dimension. The churn-turbulent regime sets in earlier. At $x/l=0.71$, as shown by the void profile from the hot film anemometer (Fig. 5(*d*)), the local void fraction in the vapor core is greater than 0.9 and the flow is locally annular. The vapor behaves like a continuous phase, separated by a thin liquid film at the wall. The bubbly models no longer describe the dynamic behavior of the interface between two continuous fluids, and therefore should not be expected to predict the void profiles well.

For the two cases discussed here in Figs. 4 and 5 near the same axial location, the point measurements of void fraction are higher than the line-averages. Such a trend is reasonably well established by the numerical results, although the predictions are flatter compared to the data. This shows that at higher void fractions, the

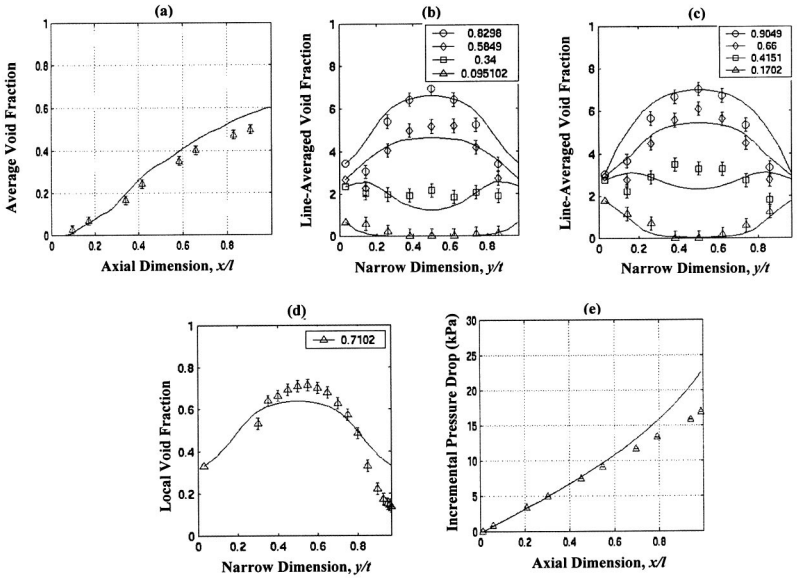

Fig. 4 Comparison plots for Case 3: 532 kg/hr; 1.4 MPa; 2.647 kW; 3.6°C subcooling: (*a*) Comparison of predicted cross section average void fraction with GDS measurements; (*b*), (*c*) Comparison of predicted line-averaged void in *y* with GDS measurements; (*d*) Comparison of predicted local void distribution in *y* with HFA measurements; and (*e*) Comparison of predicted and measured incremental pressure drop. Solid lines and symbols represent predictions and measurements respectively. Boxed numbers represent *x*/*l*.

bubbles are confined between the walls, and tend to stay away from the edges. A two-dimensional analysis overpredicts the void fraction and pressure drop further, stressing the importance of conducting a three-dimensional analysis even for symmetric wall heating.

Figures 6 and 7 show the void comparisons at high-pressure (2.4 MPa). Predictions are fairly good for these cases even at high void fractions because bubbly flows can persist up to and sometimes beyond ~0.6 at high pressures [3,27]. It is shown in [6] that there is usually a significant increase in bubble frequency in the refrigerant fluid, SUVA, as the system pressure is increased with all other flow conditions held constant. Figure 8 shows a flow condition at a mass flux several times that of the previous cases considered. At such high mass fluxes, the bubbles are smaller and the flow stays bubbly at high void fractions. Once again, the line and cross-section averaged void predictions are excellent so long as the flow stays predominantly bubbly.

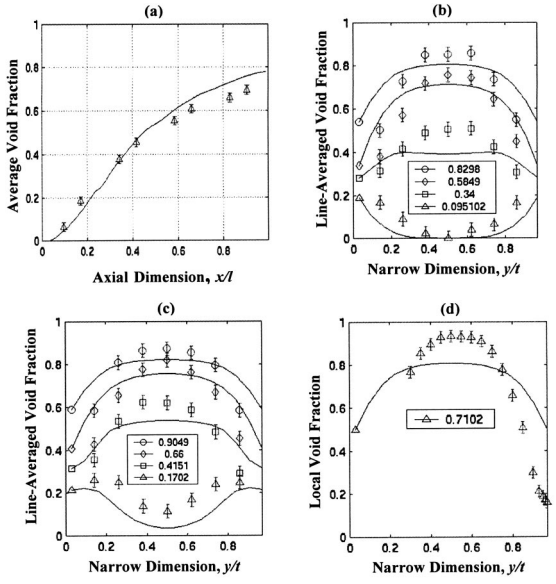

Fig. 5 Comparison plots for Case 4: 532 kg/hr; 1.4 MPa; 5.062 kW; 3.6°C subcooling: (*a*) Comparison of predicted cross section average void fraction with GDS measurements; (*b*) and (*c*) Comparison of predicted line-averaged void in *y* with GDS measurements; and (*d*) Comparison of predicted and measured local void fraction using HFA. Solid lines and symbols represent predictions and measurement respectively. Boxed numbers represent *x*/*l*.

The predictions for the experimental results for complex wall heating are shown for Cases 8 through 10 shown in Figs. 9–11. These plots include line-averaged void fraction in the width dimension yielding the *z*-profiles parallel to the walls. This type of void measurement using the gamma densitometer carried the highest uncertainty since the gamma beam traversed only a thin flow passage. For this case (Fig. 9(*e*, *f*)), the heat flux peaked closer to one edge in the widthwise direction. Both the narrow and width dimension void profiles are predicted very well. At $x/l \sim 0.89$ and $z/w \sim 0.7$ (Fig. 9(*d*)), the void fraction reaches a peak of 0.8 where the flow is locally annular. These local conditions, for which the current bubbly models are not valid, overpredict both the average void and pressure drop slightly. The same edge peaked heat flux is used for Case 9 at a relatively high mass flux, as shown in Fig. 10. Here, the stratification of void is high coincident with the peak heat flux, as expected. Once again for this case, beyond $x/l \sim 0.67$, the local void is too high to be predicted by the bubbly models. In Case 10 (Fig. 11), the heat flux peaks at the center. Since the inlet subcooling is quite high for this case, the flow is bubbly almost throughout the test section, except possibly near the exit. The averaged void fraction and the pressure drop are well predicted. Near the exit at $x/l \sim 0.93$, the line-averaged profile is wall-peaked in the narrow dimension (Fig. 11(*c*)), whereas the local profiles (Fig. 11(*d*, *e*)) are center-peaked.

Although only 10 cases are analyzed and shown here, a total of 71 bubbly R-134a cases were run with fixed coefficients in the models given in Tables 1–5. Both pressure drop and cross-section averaged void fraction were predicted within 5%. Some of the cases known to be in the churn-turbulent or annular regime were

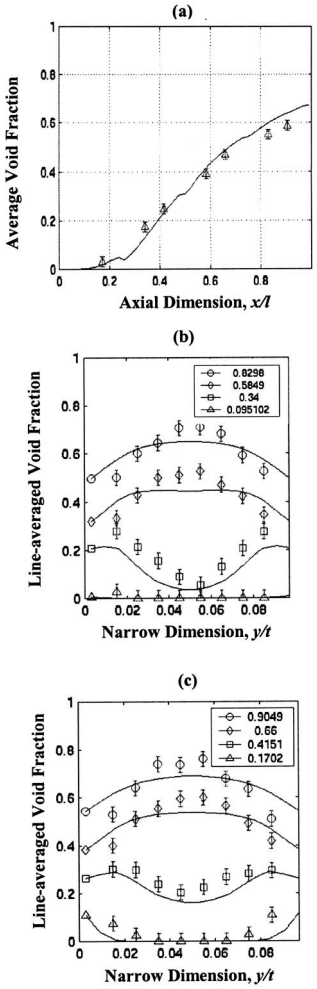

Fig. 6 Comparison plots for Case 5: 266 kg/hr; 2.4 MPa; 2.964 kW; 7.0°C subcooling: (*a*) Comparison of predicted cross section average void fraction with GDS measurement; (*b*) and (*c*) Comparison of predicted average void distribution in narrow dimension with GDS measurement. Solid lines and symbols represent predictions and measurements respectively. Boxed numbers represent *x/l*.

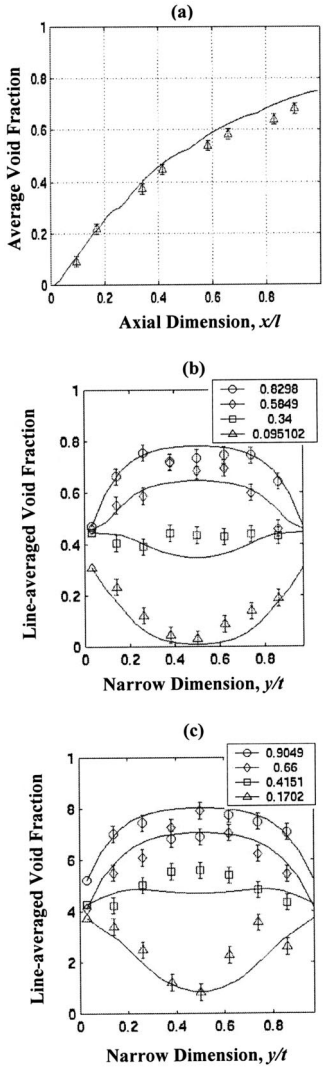

Fig. 7 Comparison plots for case 6: 532 kg/hr; 2.4 MPa; 5.722 kW; 2.1°C subcooling: (*a*) Comparison of predicted cross section average void fraction with GDS measurement; (*b*) and (*c*) Comparison of predicted average void distribution in narrow dimension with GDS measurement. Solid lines and symbols represent predictions and measurements respectively. Boxed numbers represent *x/l*.

excluded from this suite of 71 cases. However, several cases with confined and elongated capped bubbles at high void fractions were included. Some of these cases contributed to the scatter in the local void prediction. The line-averaged void fraction was predicted fairly well in both directions. In general, the collective set of models has demonstrated great ability in predicting the three-dimensional behavior of the high-pressure bubbly flow for a variety of flow conditions and wall heat flux distributions.

Summary and Conclusions

A set of bubbly flow models capable of predicting both three-dimensional local and global two-phase flow characteristics has been developed. This approach, based on a set of ensemble averaged equations, utilizes physically based closure conditions adapted for high-pressure systems. Moreover, an attempt has been made to develop modeling coefficients as functions of appropriate physical parameters such as Eotvos number, Morton number, and Weber number. While efforts have been made to capture the two-phase flow physics using mechanistic models, due to the complexity of the flow, some of the models may be considered phenomenological. This is still a major step in assembling closure models for CFD work in high pressure boiling two-phase flow through narrow spaces. This initial work needs to be expanded and benchmarked with data over other complex geometries.

The integrated model set presented herein is able to predict heated bubbly flows in high-pressure boiling systems. These models have been validated by comparing local void predictions with experimental measurements obtained with a gamma densitometer and a hot film anemometer. The integrated effects of these models have also been validated by comparing cross-section averaged and line-averaged void fraction, as well as cumulative pressure drop at various axial locations. A total of 10 representative cases were chosen from the experimental database and provided here for comparison, encompassing a wide range of inlet flow conditions, system pressure and wall heating.

In each of these cases, there is overall good agreement between predicted and measured void fractions for any type of wall heating as long as the flow stays in the bubbly regime locally, establishing the validity of the overall modeling approach. However, at high void fraction conditions, the bubbles scale the narrow space and elongate, and the vapor behaves more like a continuous phase

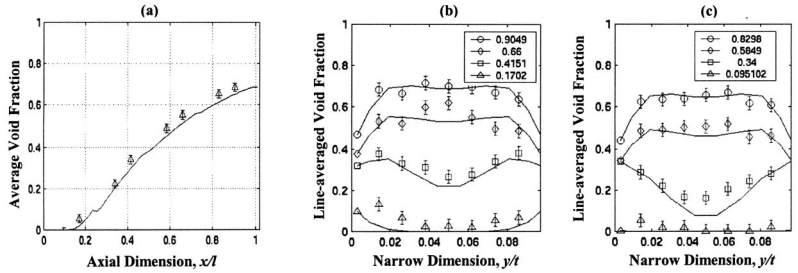

Fig. 8 Comparison Plots for case 7: 2128 kg/hr; 2.0 MPa; 20.034 kW; 5.4°C subcooling: (*a*) Comparison of predicted cross section average void with GDS measurement; (*b*) and (*c*) Comparison of predicted line-averaged void fraction with GDS measurement. Solid lines and symbols represent predictions and measurements respectively. Boxed numbers represent *x*/*l*.

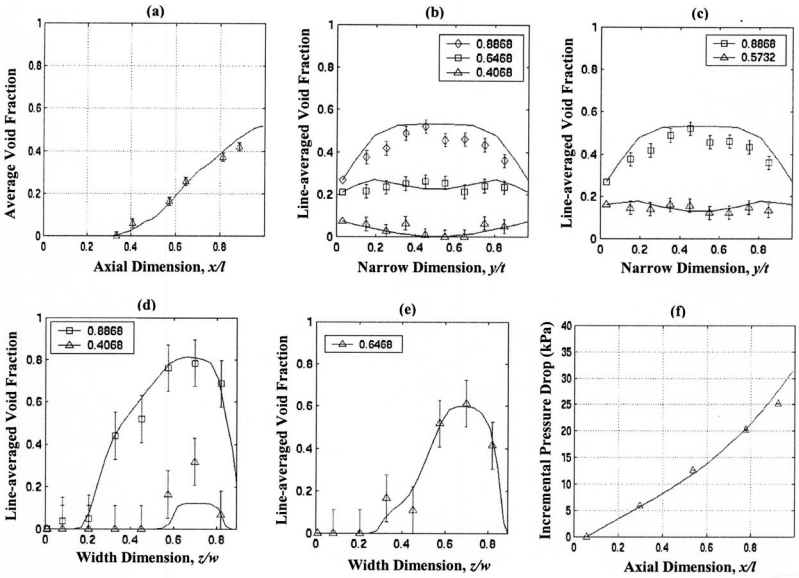

Fig. 9 Comparison plots for case 8: 1064 kg/hr; 1.7 MPa; 9.951 kW; 15.0°C subcooling: (*a*) Comparison of predicted cross section average void with GDS measurement; Plots (*b*) and (*c*) Comparison of predicted line-averaged void fraction with GDS measurement in *y* (thickness); (*d*) and (*e*) Comparison of predicted line-averaged void fraction with GDS measurements in width dimension; and (*f*) Comparison of predicted and incremental pressure drop. Solid lines and symbols represent predictions and measurements, respectively. Boxed numbers represent *x*/*l*.

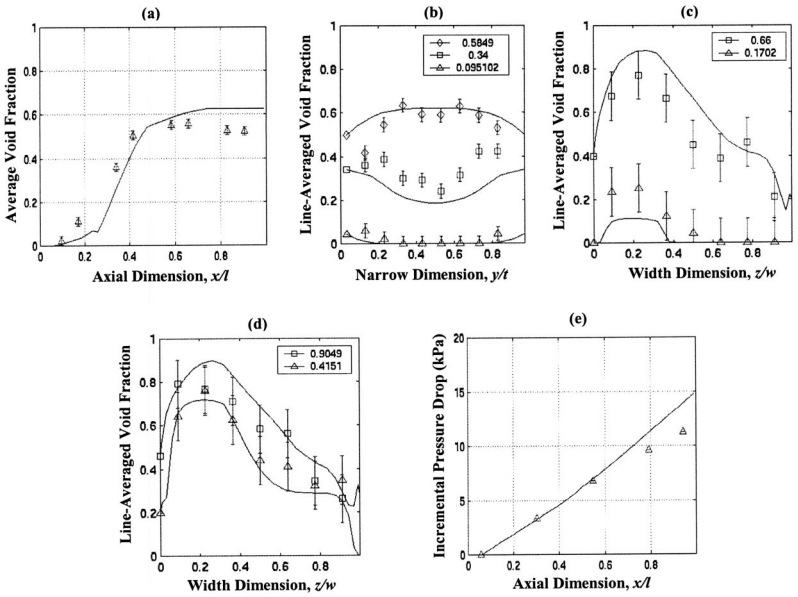

Fig. 10 Comparison plots for case 9: 318 kg/hr; 2.4 MPa; 3.382 kW; 8.3°C subcooling: (*a*) Comparison of predicted cross section average void with GDS measurement; (*b*) Comparison of predicted line-averaged void fraction with GDS measurement in *y* (thickness); (*c*) and (*d*) Comparison of predicted line-averaged void fraction with GDS measurements in *z* (width); and (*e*) Comparison of predicted and incremental pressure drop. Solid lines and symbols represent predictions and measurements respectively. Boxed numbers represent *x*/*l*.

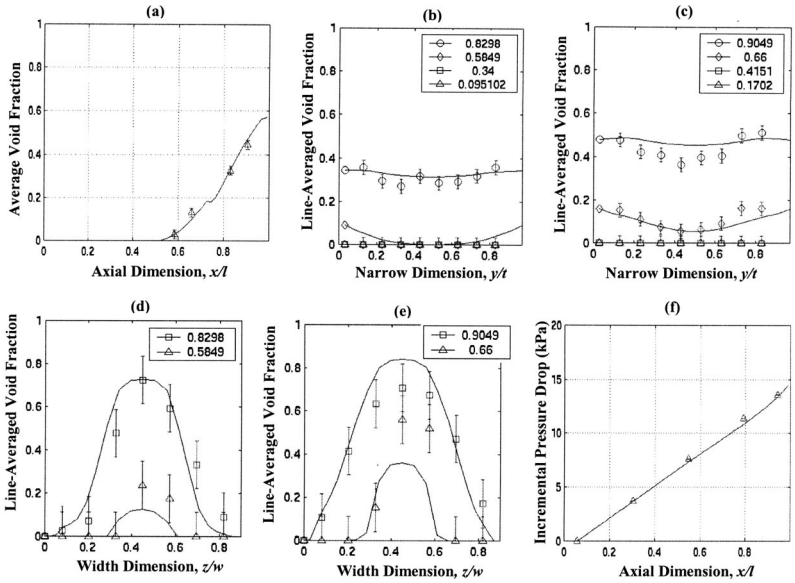

Fig. 11 Comparison plots for case 10: 366 kg/hr; 2.4 MPa; 6.601 kW; 26.3°C subcooling: (*a*) Comparison of predicted cross section average void with GDS measurement; (*b*) and (*c*) Comparison of predicted line-averaged void fraction with GDS measurement in *y* (thickness); (*d*) and (*e*) Comparison of predicted line-averaged void fraction with GDS measurements in *z* (width); and (*f*) Comparison of predicted and incremental pressure drop. Solid lines and symbols represent predictions and measurements respectively. Boxed numbers represent *x*/*l*.

than a dispersed phase. The flow transitions into churn-turbulent and possibly even locally annular. The void fraction and the pressure drop are overpredicted, and the current models used for the liquid-vapor interface are not valid. This overprediction at high void fractions highlights the deficiencies in the two-field modeling approach and the need for handling various types of interfaces through a multi-field modeling approach which allows a continuous and a dispersed field within the same phase [1–30].

Acknowledgment

We gratefully acknowledge B. W. Siebert and R. F. Kunz for their efforts in the numerical implementation of the models.

Nomenclature

A''' = interfacial area density, 1/mm
A_P = projected area of a single bubble, m^2
C_D = drag coefficient
d = diameter (bubble or droplet), mm
D = tube diameter, mm
d_o = bubble diameter corresponding to Levy's model
d_h = hydraulic diameter, mm
E = entrainment rate
Eo = Eotvos number, $\mathrm{Eo}=g\Delta\rho d_{d\nu}^2/\sigma$
f = liquid bridge breakup frequency
f_B = bubble frequency, 1/s
f_i = interfacial friction factor
f_{sp} = single-phase friction factor
F_D = drag force per unit volume, N/m^3
G = mass flux, kg/m^2s
h = enthalpy, kJ/kg
H = heat transfer coefficient
I = interfacial momentum terms
k = thermal conductivity or turbulent kinetic energy or repeated index
L = length of the duct, m
Mo = Morton number, $\mathrm{Mo}=g\mu_l^4\Delta\rho/\rho_l\sigma^3$
N = bubble number density, m^{-3}
P = pressure, MPa
Re = Reynolds number
t = thickness of the duct, mm
T_S = saturation temperature, °K
u = velocity vector
u_R = relative velocity between phases, m/s
U_B = single bubble rise velocity, m/s
U_V = rise velocity in the viscous subregime
U_{DI} = rise velocity in the distorted-inertial subregime
V_B = bubble volume, m^3
V_{gj}^B = drift velocity for a single bubble, m/s
V_{gj} = drift velocity in a multiple-bubble system, m/s
w = width of the duct, mm
We = weber number
x = flow direction
y = lateral or thickness direction
z = width direction
α = volume fraction
$\overline{\alpha}$ = cross-section averaged volume fraction
δ = liquid film thickness, mm
ε = turbulent kinetic energy dissipation
Γ = mass transfer rate
ρ = density, kg/m^3
$\Delta\rho$ = density difference between liquid and vapor phases, kg/m^3
ΔT_{sub} = (T_s-T_l), °K
ΔT_{sonb} = nucleation inception wall superheat, °K
μ = dynamic viscosity, kg/m/s
σ = surface tension, N/m
τ_w = wall shear stress, MPa

Subscripts

f, l = liquid saturation
g = vapor saturation
i = interface
ij = donor phase i to receptor phase j
lf = liquid film
w = wave

References

[1] Drew, D. A., 1992, ''Analytical Modeling of Multiphase Flows,'' *Boiling Heat Transfer*, R. T. Lahey, ed., Elsevier, pp. 31–84.

[2] Lahey, R. T., and Drew, D. A., 2001, ''The Analysis of Two-Phase Flow and Heat Transfer Using a Multidimensional, Four Field, Two-Fluid Model,'' Nucl. Eng. Des., **204**, pp. 29–44.

[3] Lahey, R. T., 1996, *A CFD Analysis of Multidimensional Two-Phase Flow and Heat Transfer Phenomena: Process, Enhanced and Multiphase Heat Transfer* (A. E. Bergles-Festschrift), Begell House, Inc., New York.

[4] Serizawa, A., 1974, ''Fluid Dynamic Characteristics of Two-Phase Flow,'' Ph.D. thesis, Kyoto University, Japan.

[5] Tomiyama, A., 1998, ''Struggle with Computation Bubble Dynamics,'' *Proc. of the Int. Conf. on Multiphase Flow*, ICMF'98, Lyon, June 8–12, pp. 1–18.

[6] Kumar, R., Trabold, T. A., and Maneri, C. C., 2003, ''Experiments and Modeling in Bubbly Flows at Elevated Pressures,'' ASME J. Fluids Eng., **125**, pp. 469–478.

[7] Hosler, E. R., 1968, ''Flow Patterns in High Pressure Two-Phase (Steam-Water) Flow with Heat Addition,'' AIChE Symp. Ser., **64**, pp. 54–66.

[8] Drew, D. A., and Passman, S. L., 1998, *Theory of Multicomponent Fluids*, Springer-Verlag, New York.

[9] Patankar, S. V., 1980, *Numerical Heat Transfer and Fluid Flow*, Hemisphere Publishing Inc., NY.

[10] Rhie, C. M., and Chow, W. L., 1983, ''Numerical Study of the Turbulent Flow Past and Airfoil with Trailing Edge Separation,'' AIAA J., **21**(11), pp. 1525–1532.

[11] Spalding, D. B., 1980, ''Mathematical Methods in Nuclear Reactor Thermal-Hydraulics,'' *Proceeding of ANS Meeting on Nuclear Reactor Thermal-Hydraulics*, R. T. Lahey, ed., pp. 1979–2023.

[12] *FLOW3D Release 3.2 User's Manual*, 1992, Computational Fluid Dynamics Services, AEA Industrial Technology, Harwell Laboratory, Oxford, UK.

[13] Kurul, N., 1990, ''Multidimensional Effects in Two-Phase Flow Including Phase Change,'' Ph.D. thesis, Rensselaer Polytechnic Institute.

[14] Del Valle, M. V. H., and Kenning, D. B. R., 1985, ''Subcooled Flow Boiling at High Heat Flux,'' Int. J. Heat Mass Transfer, **28**, pp. 1907–1920.

[15] Ceumern-Lindenstjerna, W. C., 1977, ''Bubble Departure and Release Frequencies During Nucleate Pool Boiling of Water and Aqueous NaCl Solutions,'' *Heat Transfer in Boiling*, Academic Press and Hemisphere.

[16] Davis, E. J., and Anderson, G. H., 1966, ''The Incipience of Nucleate Boiling in Forced Convection Flow,'' AIChE J., **12**, pp. 774–780.

[17] Ranz, W. E., and Marshall, W. R., 1952, Chem. Eng. Prog., **48**, pp. 141–146.

[18] Mendelson, H. D., 1967, ''The Prediction of Bubble Terminal Velocities from Wave Theory,'' AIChE J., **13**, pp. 250–253.

[19] Ishii, M., and Zuber, N., 1979, ''Drag Coefficient and Relative Velocity in Bubbly, Droplet or Particulate Flows,'' AIChE J., **25**, pp. 843–855.

[20] Drew, D. A., and Lahey, R. T., 1987, ''The Virtual Mass and Lift force on a Sphere in Rotating and Straining Inviscid Flow,'' Int. J. Multiphase Flow, **13**(1), pp. 113–121.

[21] Zun, I., 1987, ''Transition from Wall Void Peaking to Core Void Peaking in Turbulent Bubbly Flow,'' *Proc. ICHMT Conf. on Transport Phenomena in Multiphase Flow*, Dubrovnik, Yugoslavia.

[22] Levy, S., 1967, ''Forced Convection Subcooled Boiling-Prediction of Vapor Volumetric Fractions,'' Int. J. Heat Mass Transfer, **10**, pp. 951–965.

[23] Tolubinsky, V. I., and Kostanchuk, D. M., 1970, ''Vapor Bubbles Growth Rate and Heat Transfer Intensity at Subcooled Water Boiling,'' *Fourth Int. Heat Transf. Conf., Paris-Versailles*, **5**, p. 132.8.

[24] Maneri, C. C., 1970, ''The Motion of Plane Bubbles in Inclined Ducts,'' Ph.D. thesis, Polytechnic Institute of Brooklyn, Brooklyn, NY.

[25] Antal, S. P., Lahey, R. T., and Flaherty, J. E., 1991, ''Analysis of Phase Distribution in Fully Developed Laminar Bubbly Two-Phase Flow,'' Int. J. Multiphase Flow, **17**, pp. 635–652.

[26] Lopez de Bertodano, M., 1992, ''Turbulent Bubbly Two Phase Flow in a Triangular Duct,'' Ph.D. thesis, Rensselaer Polytechnic Institute, Troy, NY.

[27] Marie, J. L., 1987, ''Modeling of the Skin Friction and Heat Transfer in Turbulent Two-Component Bubbly Flow in Pipes,'' Int. J. Multiphase Flow, **113**, pp. 309–325.

[28] Sato, Y., Sadatomi, M., and Sekoguchi, K., 1981, ''Momentum and Heat Transfer in Two-Phase Bubble Flow,'' Parts I and II. Int. J. Multiphase Flow, **7**, pp. 167–190.

[29] Kirouac, G. J., Trabold, T. A., Vassallo, P. F., Moore, W. E., and Kumar, R., 1999, ''Instrumentation Development in Two-Phase flow,'' Exp. Thermal Science, **20**, pp. 79–93.

[30] Haberman, W. L., and Morton, R. K., 1953, ''An Experimental Investigation of the Drag and Shape of Air Bubbles Rising in Various Liquids,'' David Taylor Model Basin Report 802.

Effect of Ethoxylation and Molecular Weight of Cationic Surfactants on Nucleate Boiling in Aqueous Solutions

Juntao Zhang

Raj M. Manglik
Mem. ASME
e-mail: Raj.Manglik@uc.edu

Thermal-Fluids and Thermal Processing Laboratory,
Department of Mechanical, Industrial and Nuclear Engineering,
University of Cincinnati,
Cincinnati, OH 45221-0072

Saturated, nucleate pool boiling on a horizontal, cylindrical heater and the associated bubble dynamics in aqueous solutions of cationic surfactants of different molecular weight and ethoxylation or ethylene oxide (EO) content, are experimentally investigated. Boiling curves ($q''_w \propto \Delta T_{sat}$) for different concentrations and photographic records of the salient features of the ebullient behavior are presented, along with a characterization of interfacial properties (surface tension and contact angle). The surfactant additive significantly alters the nucleate boiling in water and enhances the heat transfer. The enhancement increases with concentration, with an optimum obtained in solutions at or near the critical micelle concentration (c.m.c.) of the surfactant. The photographic and visual observations indicate a markedly different boiling behavior than that of water, as well as between pre- and post-c.m.c. solutions. A lower molecular weight surfactant tends to reduce surface tension faster, and show better enhancement performance than its higher molecular weight counterpart. With EO groups in its molecular chain the surfactant solution becomes more hydrophilic, and the higher wettability tends to suppress nucleation, thereby weakening the boiling process. Also, enhancement in pre-micellar solutions is shown to depend on the dynamic surface tension, and the number of EO groups in and molecular weight of the surfactant. [DOI: 10.1115/1.1643755]

Keywords: Additives, Enhancement, Heat Transfer, Interface, Phase Change, Surface Tension

Introduction

Nucleate boiling is an important thermal management process with a broad spectrum of applications because relatively small temperature differences result in high heat transfer rates. Extensive research on numerous facets of boiling heat transfer has been reported in the literature [1]. In recent years, enhancement of nucleate boiling heat transfer has received much attention, and different active and passive techniques have been documented in several reviews [2–4]. Among these, the use of additives, which include surfactants or surface-active substances that significantly alter the surface tension of the boiling liquid even at very low concentrations, has been the focus of some current research. The reviews by Wasekar and Manglik [5–6] provide an extended discussion of several issues associated with enhanced boiling heat transfer in surfactant solutions.

Surfactants are long-chain compounds with a molecular structure made up of a hydrophilic head and a hydrophobic tail, which adsorb at the liquid-vapor interface with their polar head towards the aqueous solution and the hydrocarbon tail directed towards the vapor. Based on the nature of the hydrophilic part of the molecule, which is ionizable, polar, and polarizable, surfactants are generally categorized as anionics, nonionics, cationics, and zwitterionics. Their surface tension relaxation is a diffusion-rate dependent process, and is typically found to depend on the type of surfactants, its diffusion-adsorption kinetics, micellar dynamics, ethoxylation, and bulk concentration levels [7–8]. The time scale for complete surface tension relaxation tends to be smallest for lower molecular weight compounds. For boiling applications with small surface age interface, however, the dynamic surface tension relaxation process rather than the equilibrium condition is perhaps the more critical determinant [7–8]. Furthermore, as pointed out by Hoffmann and Rehage [9], it should be noted that dilute solutions of ionic and nonionic surfactants usually behave as Newtonian liquids, and their viscosity is always close to that of the solvent[1] [10].

Several studies have investigated enhanced pool boiling in aqueous surfactant solutions under atmospheric conditions [11–19], and a variety of different predictive parameters and mechanisms have been proposed to describe the complex phase-change process. The primary determinants of the general boiling problem can essentially be classified under three broad categories: heater, fluid, and heater-fluid interface [20]. For nucleate boiling in aqueous surfactant solutions, the associated potential mechanisms that may be involved are depicted as a conjugate problem in Fig. 1. Besides the effects of heater geometry, its surface characteristics and wall heat flux level, bulk concentration of additive, surfactant chemistry (ionic nature and molecular weight), dynamic surface tension, surface wetting and nucleation cavity distribution, marangoni convection, surfactant adsorption and desorption, and foaming are considered to have a significant influence [5–6,19,21]. Also, the bubble dynamics (inception and gestation →growth→departure) is found to be considerably altered with reduced departure diameters, increased frequencies, and decreased coalescence [14,17–19]. A direct correlation of the heat transfer with suitable descriptive parameters for these effects, however, remains elusive because of the complex nature of the problem. In an earlier study [19], a case has been made for the dynamic σ relaxation and surfactant molecular weight as determinants of the nucleate boiling heat transfer, which is further investigated in this paper.

Contributed by the Heat Transfer Division for publication in the JOURNAL OF HEAT TRANSFER. Manuscript received by the Heat Transfer Division June 2, 2003; revision received October 17, 2003. Associate Editor: D. B. R. Kenning.

[1]The measured shear-rate and temperature dependent viscosity in this study, though not presented here, showed insignificant change from those for water [10].

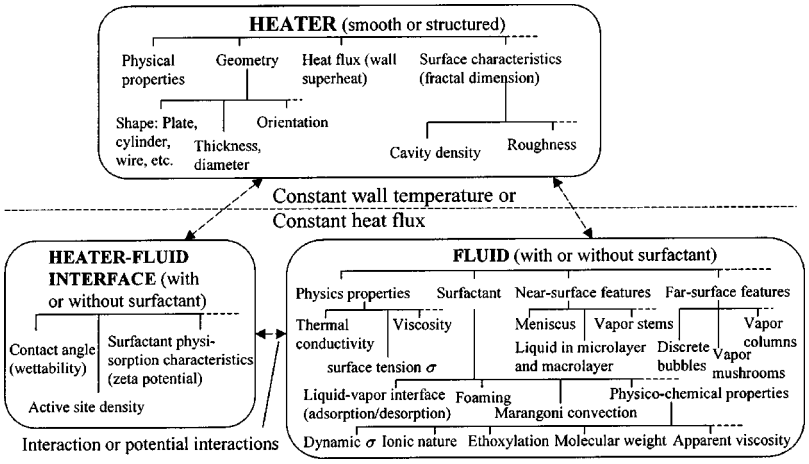

Fig. 1 The conjugate problem in modeling nucleate boiling of aqueous surfactant solutions

Furthermore, the presence of the ethoxy or ethylene oxide (EO) group in its molecular-chain, increases the overall size of the polar head and makes the surfactant more hydrophilic [22]. This increases surface wettability due to the adsorption of surfactant molecules on the solid surface [23]. The concomitant influence on the active nucleation site density and dynamic contact angle should therefore be taken into consideration in nucleate boiling of aqueous surfactant solutions. Wang and Dhir [24] have systematically studied the effect of pure liquid wettability on the active nucleation site density in pool boiling. They correlated their data for active site density as a function of the wall superheat and contact angle, and pointed out that the fraction of the nucleated cavities decreases as the wettability of the surface improves. Similarly, as reviewed by Kenning [25], increased surface wettability results in fewer nucleation sites that produce larger bubbles at lower frequencies. The presence of EO group in surfactants also changes the critical packing parameter (CPP)[2], which is a key determinant of their micellar structure and critical micelle concentration (c.m.c.)[3] in their aqueous solutions [26,27]. The micelle formation in highly ethoxylated surfactants consistently yields vesicular mesophases, which results in a reduction in c.m.c. at elevated temperatures [27,28]. On the other hand, molecules of CTAB (a non-ethoxylated cationic) cannot pack into a cone truncated by surfaces of high and opposite curvature as needed to direct the vesicular mesostructure [28]; instead, lamellar mesophases are commonly formed in bulk and thin-film samples.

This paper investigates the dependence of saturated nucleate pool boiling heat transfer of aqueous cationic surfactant solutions on the additives' ethoxylation and molecular weight. Four cationic surfactants, namely, dodecyltrimethylammonium chloride (DTAC), cetyltrimethyl-ammonium bromide (CTAB), oleylmethylbis[2-hydroxyethyl]ammonium chloride (Ethoquad O/12 PG), and octadecylmethyl[15-polyoxyethylene]ammonium chloride (Ethoquad 18/25), were employed. They have different molecular weights and number of EO groups, and their chemical composition and relevant physico-chemical properties are listed in Table 1. Both the dynamic and equilibrium surface tension of their aqueous solutions of varying concentrations ($C>0\rightarrow>$c.m.c.) as well as their contact angle variations are recorded, to characterize their vapor-liquid and solid-liquid interfacial behaviors. Pool boiling curves for the incipience to fully developed nucleate boiling regimes are presented, along with a photographic documentation of the bubbling activity. Also, the influences of the additive chemistry (ethoxylation and molecular weight), pre- and post-micellar bulk concentration, wall heat flux, and dynamic surface tension relaxation are highlighted.

[2]CPP is the ratio between the cross-sectional area of the hydrocarbon tail part and that of the polar head group of the surfactant molecule.

[3]It is the concentration at which micelles (colloid-sized clusters or aggregates of monomers) start to form.

Table 1 Physico-chemical properties of cationic surfactants

Surfactant (Chemical Name)	DTAC (Dodecyltrimethylammonium chloride)	CTAB (Cetyltrimethylammonium bromide)	Ethoquad O/12 PG (Oleylmethylbis[2-hydroxyethyl] ammonium chloride)	Ethoquad 18/25 (Octadecylmethyl[15-polyoxyethylene] ammonium chloride)
Chemical formula	$C_{15}H_{34}ClN$	$C_{19}H_{42}BrN$	RN(CH3)/(CH2CH2OH)2Cl, R=oleyl	RN(+)(CH3)[(CH2CH2O)mH][(CH2 CH2O)nH] Cl(−), R=C18H37
Ionic nature	Cationic	Cationic	Cationic	Cationic
EO group[a]	0	0	2	15
Appearance	White powder	White powder	Yellow viscous liquid	Yellow viscous liquid
Molecular weight	263.9	364.5	403	994
Manufacturer	Sigma-Aldrich	Sigma-Aldrich	AkzoNobel	AkzoNobel
Purity	⩾99%	≈99%	⩾99%	⩾99%
Melting point	>246°C	>230°C	-	-
Solubility (20°C)	50 mg/mL	10% (w/v)	>25% (w/v)	-
Specific Gravity	-	-	0.986 (25°C)	1.058 (25°C)
Viscosity (cp)[b] (pure liquid)	-	-	-	1750 (23°C), 110 (90°C)
Surface Tension (mN/m) (25°C)	-	-	40.3 (0.1%), 40.7 (1.0%)	50 (0.4%)

[a]Ethoxy or ethylene oxide group
[b]Brookfield viscometer

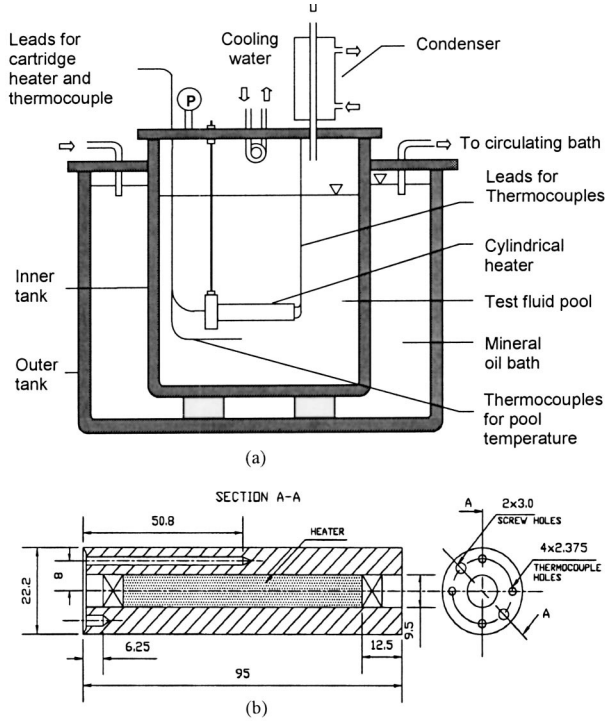

Fig. 2 Schematic of experimental facility: (*a*) pool boiling apparatus; and (*b*) cross-sectional view of cylindrical heater assembly.

Pool Boling Experiment Setup

The experimental setup used for the pool boiling studies is shown schematically in Fig. 2(*a*). The inner glass tank, which contains the surfactant solution pool and the cylindrical heater, is encased in an outer glass tank that has circulating mineral oil fed from a constant-temperature recirculating bath (not shown in figure) to maintain the test pool at its saturation temperature. A water-cooled reflux condenser, along with a second coiled-tube water-cooled condenser, helps condense the generated vapor and maintain an atmospheric-pressure pool. A pressure gage (± 0.0025 bar precision) is mounted on top of the boiling vessel to monitor the pressure in the pool throughout the experiments. The heating test section (shown in Fig. 2(*b*)) consists of a horizontal, gold plated, hollow copper cylinder of 22.2 mm outer diameter; the 0.0127 mm thick gold plating mitigates any surface degradation and oxidation from chemicals in the test fluids. A 240 V, 1500 W cartridge heater, with insulated lead wires, is press-fitted in the hollow cylinder with conductive grease to fill any remaining air gaps and provide good heat transfer to the inside of the tube. The cartridge heater is centrally located inside the copper tube, and the gaps at each end are filled with silicone rubber to prevent water contact.

The heater-wall and pool-bulk temperature measurements were recorded using copper-constantan precision (± 0.5°C) thermocouples, interfaced with a computerized data acquisition system with an in-built ice junction and calibration curve. A variac-controlled AC power supply, a current shunt (0.15 Ω with 1% accuracy), and two high-precision digital multimeters (for current and voltage measurements) provided the controls and measurements of the input electric power. At each incremental value of power input or heat load, the dissipated wall heat flux q''_w and the wall superheat ΔT_w were computed from the measured values of V, I, the four wall thermocouple readings ($T_{i,r}$), and saturation temperature of the pool from the following set of equations:

$$q''_w = (VI/A) \tag{1}$$

$$T_w = \left\{ \sum_{i=1}^{4} \left[T_{i,r} - (q''_w r_o/k)\ln(r_o/r) \right] \Big/ 4 \right\} \tag{2}$$

$$\Delta T_w = (T_w - T_{\text{sat}}) \tag{3}$$

The maximum experimental uncertainties in q''_w and ΔT_w, based on a propagation of error analysis [29], were 1.44% and 0.5% respectively. Details of the experimental procedure, uncertainty analysis, and the extended validation of test measurements with boiling data for water are given in [6].

Surface Tension and Contact Angle Measurement

Surface tension measurements were made by the maximum bubble pressure method using a twin orifice computerized surface tensiometer (SensaDyne QC6000, CSC Scientific Company). Dry air at 3.4 bar is slowly bubbled through a parallel set of small and large glass orifice probes of 0.5 and 4.0 mm diameter, respectively, which are immersed in the test fluid pool in a small beaker to produce a differential pressure signal proportional to the fluid surface tension. The temperature of the test fluid is measured using a well-calibrated thermistor (± 0.1°C precision, 0–150°C) attached to the orifice probes. The aqueous solution container is immersed in a constant temperature bath in order to control and maintain its desired temperature. The time interval between the newly formed interface and the point of bubble break-off is referred to as ''surface age,'' and it gives the measure of bubble growth time that corresponds to the dynamic surface tension value at a given operating bubble frequency. Thus, by altering the air-bubble frequencies through the probes, both static or equilibrium and dynamic surface tension can be measured. Detailed descriptions of the solution preparation, instrument calibration, and validation procedures, along with measurement uncertainties can be found in [7,10,30]. The maximum uncertainties in the measurement of concentration, temperature, and surface tension were found to be ± 0.4% for powder form additives, ± 5% for additives in liquid form, and ± 0.5% and ± 0.7%, respectively. The liquid-solid contact angle was measured by the sessile drop method, using a Kernco GI Contact Angle Meter/Wettability Analyzer. The measurement uncertainty in this case is estimated to be a max of ± 1.4%.

Photographic Observations

The growth of nucleating vapor bubbles and their motion near the cylindrical heater surface were recorded by a PULNiX TMC-7 high-speed color CCD camera with shutter speeds of up to 0.1 micro-second. The CCD camera is interfaced with a PC through a FLASHBUS MV Pro image capture kit that has high-speed (~500 frames/s) PCI-based bus-mastering capabilities (up to 132 Mbytes/s). It delivers consecutive frames of video in real time into the system memory while keeping the CPU free to operate on other applications. Furthermore a FUJI 12.5–75 mm micro lens was used on the CCD camera to facilitate high quality close-up photography.

Results and Discussion

The variations with concentration of both the equilibrium and dynamic surface tension values of the four cationic surfactant solutions at 23°C are graphed in Fig. 3. While dynamic σ (represented by a typical surface age of 50 ms) is always larger than the corresponding equilibrium value (surface age 17–59 s), both are seen to decrease with increasing surfactant concentration to asymptotically attain a constant value beyond the critical micelle concentration (c.m.c.). The c.m.c. for the four surfactants at 23°C (obtained from the asymptotic intersection point of the equilibrium adsorption isotherm) are ~6000 wppm for DTAC, ~400 wppm for CTAB, ~600 wppm for Ethoquad O/12 PG, and ~2300 wppm for Ethoquad 18/25. For aqueous CTAB solutions, the σ

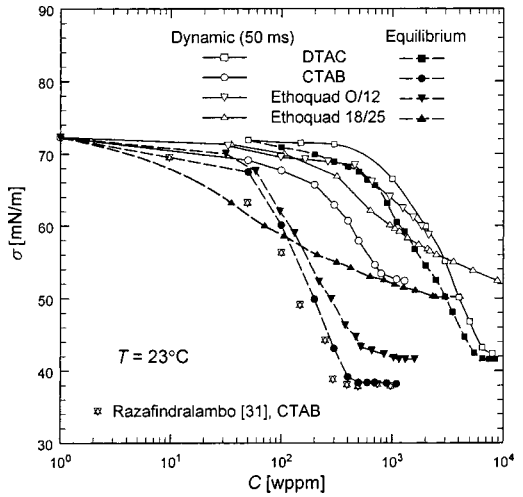

Fig. 3 Equilibrium and dynamic surface tension measurements for aqueous surfactant solutions at 23°C

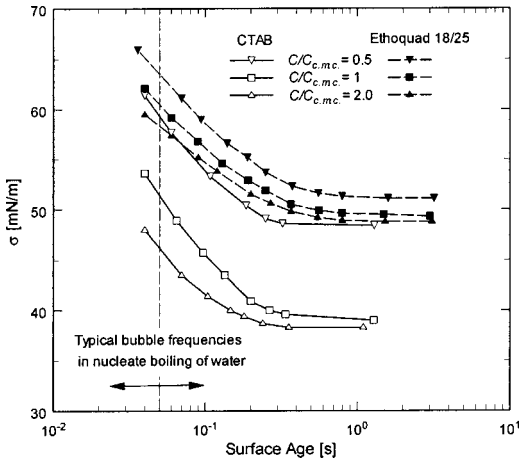

Fig. 5 Dynamic surface tension relaxation for aqueous solutions of CTAB and Ethoquad 18/28 at room temperature (23°C)

$-C$ data compare quite well with the Razafindralambo et al. [31] results at 20°C, and so does the c.m.c. with the 392.5 wppm value at 25°C reported by Holmberg et al. [27].

The dynamic and equilibrium σ values for the different surfactant solutions at an increased bulk temperature of 80°C are presented in Fig. 4. The dynamic measurements are, once again, for a bubble surface age of 50 ms, which is representative of bubble frequencies typically encountered in nucleate boiling of water. The surfactant adsorption at the bubble vapor-liquid interface is a time-dependent process that gives rise to the dynamic surface tension behavior; this, however, eventually reduces to the equilibrium condition after a long time period [7–8, 30]. The variation of σ with surface age in Fig. 5 clearly illustrates this. Also, a lower molecular weight surfactant diffuses faster than its higher molecular weight counterpart, and this is seen in the faster σ relaxation of CTAB in comparison with that for Ethoquad 18/25 in Fig. 5. The presence of EO groups in Ethoquad 18/25 makes its polar head more bulky and lowers its mobility. A similar trend is obtained at elevated temperature [10]. As such, the dynamic σ isotherms at 80°C are atypical of the additive adsorption-desorption kinetics during atmospheric pressure boiling of aqueous surfactant solutions.[4] The equilibrium σ at c.m.c., on the other hand, represents the maximum possible surface tension reduction for the solutions at 80°C. In general, it is observed that the process of micelle formation takes place over a range of concentrations [26,32], and in the present measurements, they are found to be ~4500 wppm for DTAC, ~500 wppm for CTAB, ~850 wppm for Ethoquad O/12 PG, and ~500 wppm for Ethoquad 18/25.

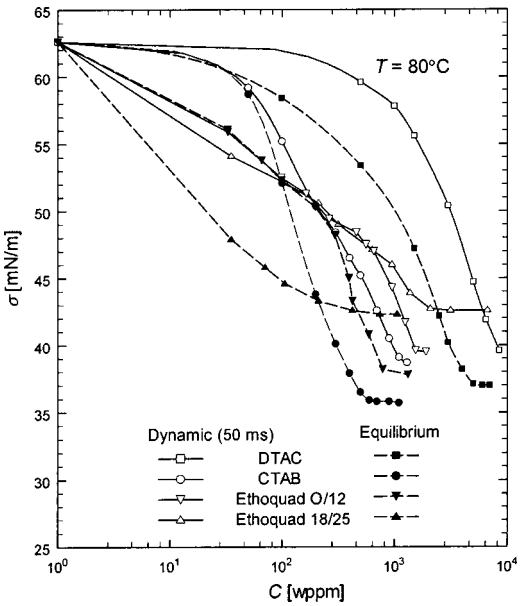

Fig. 4 Equilibrium and dynamic surface tension measurements for aqueous surfactant solutions at 80°C

The results in Fig. 4, when compared with the respective values at 23°C in Fig. 3, indicate overall reductions in σ at the higher temperature (80°C), which are due to increased surfactant diffusivity with increased temperature [26–27]. These reductions, however, are not uniform over both the dynamic and equilibrium conditions. The degree of variation depends on the surfactant ionic nature and molecular structure among some other factors [7,26–27,30], and it reflects completely different adsorption-diffusion kinetics at elevated temperature during short and long transients. Another salient feature is that surfactants with EO groups in their hydrocarbon chain show larger reductions in σ with increasing temperature (Ethoquads versus DTAC and CTAB). The surfactant's molecular-chain geometry and packing essentially determine the aggregate/micelle structure, and it is well known [27] that the polyoxyethylene chain compresses as the temperature increases. This leads to an increased CPP (critical packing parameter) value, which lowers the c.m.c. as well as the surface tension [27]. The temperature effect on c.m.c. is even stronger for surfactants with larger number of EO groups, as the polar head size increases with increasing number of ethylene oxide units, and because they tend to form vesicle micelles instead of spherical or lamellar micelles [28], thereby exhibiting a totally different temperature dependence [7,30,33]. However, the $\sigma-T$ variation generally tends to be linear for a surfactant at a given concentration [10].

The pool boiling data for different concentration aqueous solution of CTAB and Ethoquad 18/25, typically representative of the four cationics, are presented in Figs. 6 and 7, respectively. While CTAB is a higher molecular weight cationic surfactant, Ethoquad 18/25 has an even higher molecular weight but with a relatively high ethoxylation of 15 EO groups (Table 1). The impact of their different chemistry is clearly seen in the respective nucleate boiling curves for their aqueous solutions. All data graphed in Figs. 6 and 7 are for decreasing heat flux unless indicated otherwise.

The data for CTAB (Fig. 6) show considerable heat transfer

[4]While 80°C is the upper limit for QC-6000 surface tensiometer, the surface tension data at real boiling temperature can be obtained by extrapolation of surface tension data with temperature, which typically has a linear relationship [10].

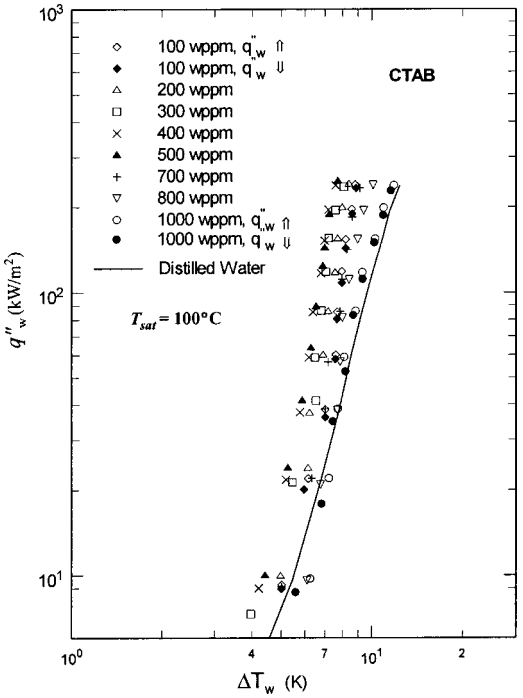

Fig. 6 Nucleate pool boiling data for aqueous solutions of CTAB

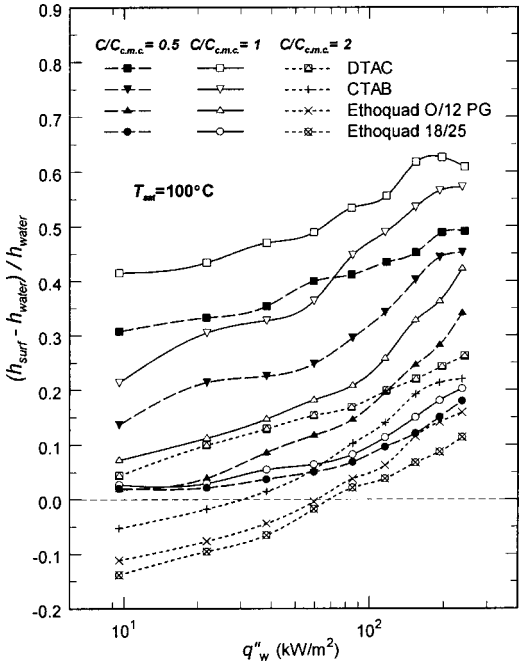

Fig. 8 Variation of the relative heat transfer performance of aqueous cationic surfactant solutions with heat flux and additive concentration (decreasing q''_w)

enhancement with increasing concentration, as represented by the characteristic leftward shift in the boiling curve relative to that for distilled water. Also, there was early incipience or onset of nucleate boiling (ONB) (observed visually with onset of bubbling activity): for $C=400$ wppm, ONB was seen at $q''_w \cong 8.5$ kW/m^2 or $\Delta T_w \cong 3.7$ K, as compared to that for distilled water at $q''_w \cong 12.83$ kW/m^2 or $\Delta T_w \cong 5.13$ K. The optimum heat transfer enhancement is seen to be obtained with 400–500 wppm solutions ($\sim$c.m.c. for CTAB at 80°C). But with $C>$c.m.c., the enhancement decreases and the heat transfer even deteriorates below that in distilled water in high concentration ($\geqslant$800 wppm) solutions, particularly at low heat fluxes. A similar dependence on C with a different cationic surfactant (Habon G, $M=500$) is seen in the Hetsroni et al. [18] data, as well as those for anionic and nonionic surfactant solutions reported in other studies [16,17,19].

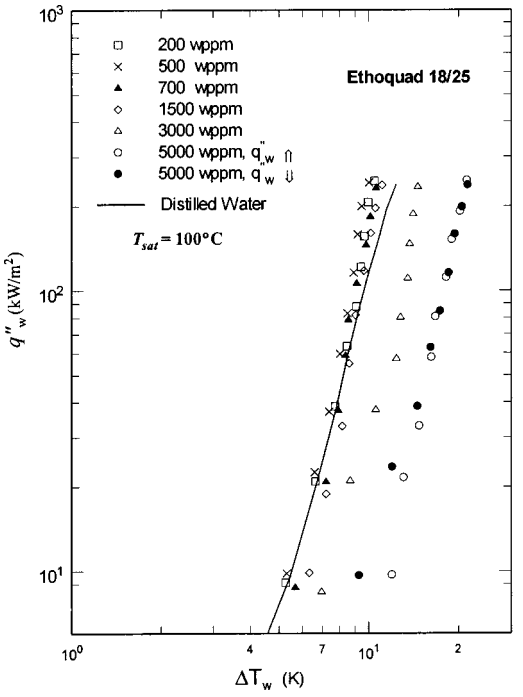

Fig. 7 Nucleate pool boiling data for aqueous solutions of Ethoquad 18/25

The boiling curves for aqueous Ethoquad 18/25 solutions in Fig. 7 display a somewhat different behavior, with considerably less enhancement. In fact significant enhancement is seen only at higher heat fluxes, and, once again, the peak performance is with $C\sim$c.m.c. ($\sim$500 wppm). With higher concentrations ($C>$c.m.c.), there is a rightward shift in the boiling curve, and substantially lower heat transfer coefficients than those for distilled water are obtained when $C\geqslant 3000$ wppm. This is also accompanied with delayed incipience and thermal hysteresis or temperature overshoot, as seen in the increasing and decreasing $q''_w - \Delta T_w$ data for 5000 wppm solution; such hysteresis was not seen in lower ($C<$c.m.c.) concentration solutions. This boiling behavior is akin to that normally observed in highly wetting liquids [1,25,34].

The effects of heat flux and surfactant concentration on the nucleate boiling heat transfer are further highlighted in Fig. 8, where the relative increase in the heat transfer coefficient from that of water for all four cationic surfactants are graphed. Besides depicting the improved heat transfer in solutions with $0<C\leqslant$c.m.c., it clearly shows the decrease in the enhancement in high concentration ($C>$c.m.c.) solutions. In fact, at low heat fluxes there is even a degradation in heat transfer compared to that for water in all surfactant solutions except in those with DTAC. With a maximum enhancement of 63% in 4000 wppm aqueous DTAC solution, the performance is seen to be dependent upon the wall heat flux, concentration, and surfactant molecular weight and EO group content. The enhancement is significantly greater in aqueous solutions of DTAC and CTAB (non-ethoxylated cationics) as compared to that in Ethoquad O/12 PG and Ethoquad 18/25 (ethoxylated cationics) solutions. As pointed out previously [7,19], the process of micelle formation and the molecular dynam-

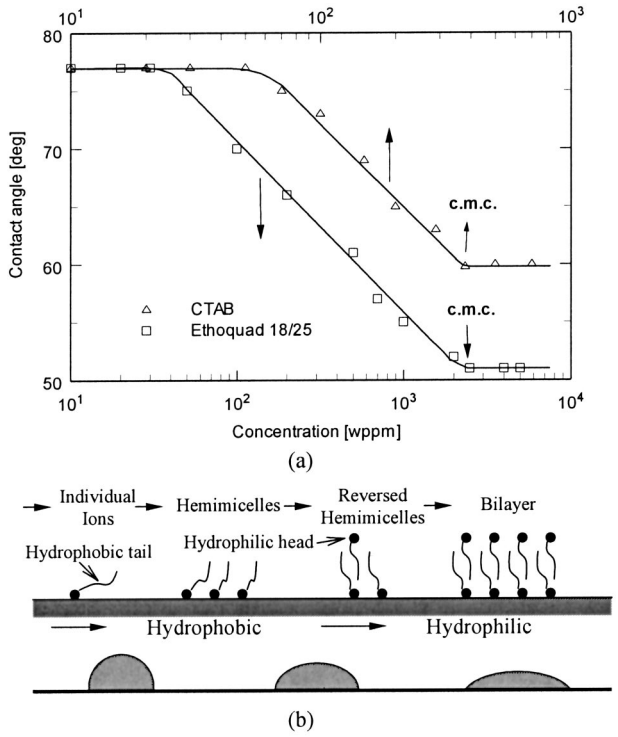

Fig. 9 Surface wettability characteristics [10]: (*a*) measured contact angle for aqueous CTAB and Ethoquad 18/25 solutions; and (*b*) corresponding surfactant adsorption surface state.

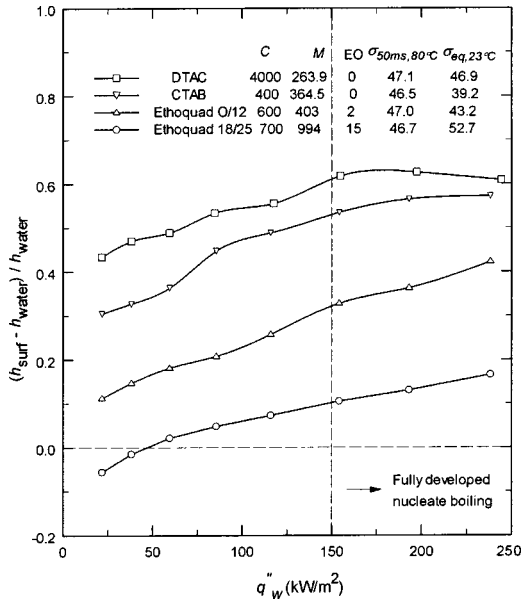

Fig. 10 Effect of surfactant molecular weight and its ethoxylation on the heat transfer coefficient enhancement

ics in a concentration sublayer at the vapor-liquid interface characterizes the resultant optimum heat transfer enhancement in surfactant solutions with $C \sim$ c.m.c.. The presence of EO group in their hydrocarbon chain (ethoxylation) alters the solution's surface wettability [22–23], and this is clearly seen from the contact angle measurements [10] for CTAB and Ethoquad 18/25 graphed in Fig. 9(*a*). The later has significantly lower contact angles with increasing C, particularly when $C \geqslant$ c.m.c.. This is a direct consequence of the surfactant chemistry and its physisorption dynamics [35], and the altered surface wettability probably accounts for the boiling deterioration in Ethoquad O/12 PG and Ethoquad 18/25 solutions at $C >$ c.m.c. concentrations.

Figure 10 provides further insights on the role of surfactant ethoxylation, molecular weight, and dynamic surface tension of their solutions on the heat transfer enhancement. The normalized pool boiling heat transfer coefficient data for DTAC (4000 wppm), CTAB (400 wppm), Ethoquad O/12 PG (600 wppm), and Ethoquad 18/25 (700 wppm) solutions are graphed. While their respective concentration is different, the dynamic surface tension value (nominally representative of nucleate boiling bubble frequencies) of their aqueous solutions at 80°C is the same ($\sim$47 mN/m) in each case. In the measured range of heat fluxes, the heat transfer enhancement is seen to be in the order of DTAC $>$CTAB$>$Ethoquad O/12 PG$>$Ethoquad 18/25, which is in the reverse order of their respective molecular weights and number of EO groups. It also shows a boiling deterioration at low heat flux ($q''_w < 50$ kW/m^2) for Ethoquad 18/25. Within the typical time transients for bubble growth in nucleate boiling of surfactant solutions, the faster diffusion of lower molecular weight surfactants leads to a larger number of surfactant molecules approaching the growing bubble interface. They, therefore, reduce the surface tension faster and increase the bubble growth and departure frequencies to yield better heat transfer performance. Also, in this dynamic ebullient and additive adsorption process, a measure of the dynamic surface tension is perhaps the more appropriate scaling property instead of the equilibrium value.

The enhanced boiling performance can be related to the ebullient characteristics, and typical photographic records are presented in Fig. 11. They represent the boiling behavior in water, and CTAB and Ethoquad 18/25 solutions (non-ethoxylated and ethoxylated surfactants, with number of EO groups$=0$ and 15, respectively) of three different concentrations ($C/C_{\text{c.m.c.}}=0.5$, 1, and 2) at two different heat flux levels ($q''_w=20$, and 50 kW/m^2). In comparison to that in water, boiling in CTAB solutions is more vigorous and is characterized by clusters of smaller-sized, more regularly shaped bubbles that originate at the underside of the cylindrical heater. These bubbles then slide along the heater surface at departure, thereby knocking off much smaller bubbles growing on the top surface of the heater. This process was observed to increase with heat flux and the consequent higher bubble departure frequency. Also, because of the considerable reduction in σ for CTAB solutions, much smaller-sized bubbles are nucleated in a cluster of active nucleation sites, especially at lower heat fluxes. They have a significantly higher bubble departure frequency, with virtually no coalescence of either the neighboring or sliding bubbles that come in contact with others around the heater's periphery when $C <$ c.m.c. However, when $C \geqslant$ c.m.c., some foaming patches begin to occur, the liquid only coverage of the heater surface increases, and slightly larger bubbles are formed, all of which indicate a surface wetting condition change. A foam layer, whose thickness increases with heat flux, is also seen to form at the free surface of the pool. This boiling history is very similar to that also seen in anionic and nonionic surfactant solutions [17,36].

Boiling in Ethoquad 18/25, on the other hand, shows much smaller-sized bubbles in pre-c.m.c. solutions, and considerably fewer and larger-sized bubbles are formed with increasing concentrations (Fig. 11). This presents a contrastingly different behavior from not only that of water but also that of CTAB, and is perhaps due to the surfactant's high degree of ethoxylation. The presence of large number of EO groups in their hydrocarbon chains totally changes the surface wettability at the solid-water interface. This is quite evident from the measured contact angle data presented in Fig. 9.

The observed ebullience and boiling data cannot be explained by the reduced dynamic surface tension alone. If this were so, then smallest-sized bubbles would be seen in $C \geqslant$ c.m.c. solutions, where the surface tension reaches the lowest possible value. In-

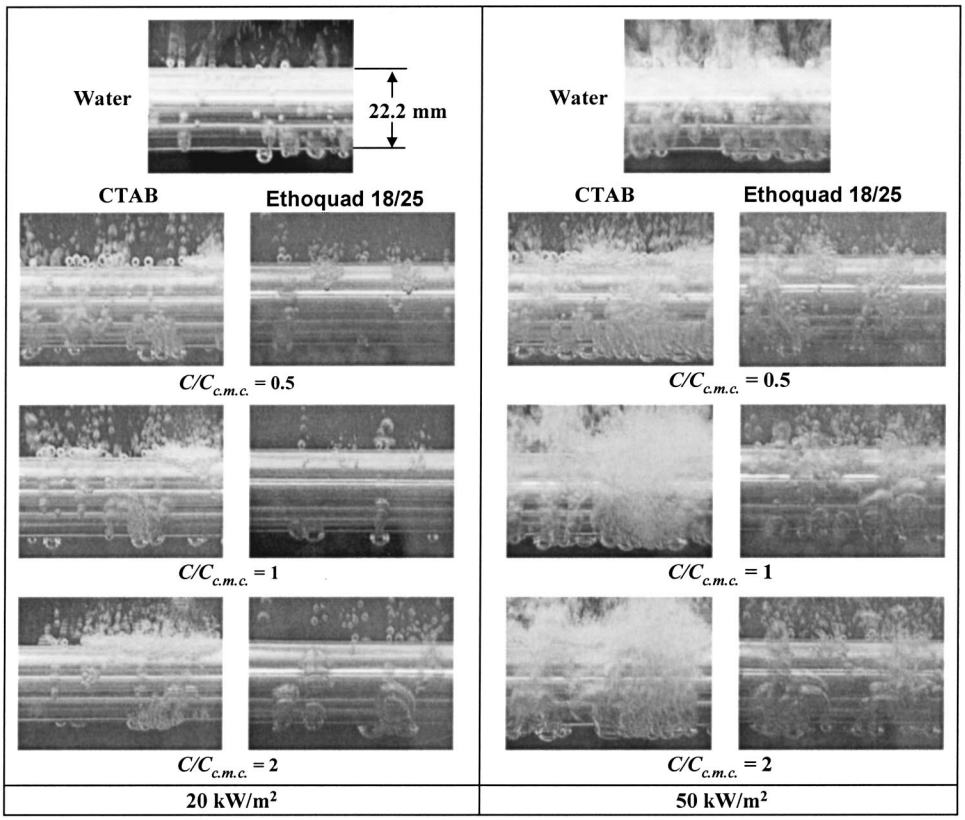

Fig. 11 Ebullient behavior in nucleate boiling of distilled water, and aqueous CTAB and Ethoquad 18/25 solutions of different concentrations ($C/C_{c.m.c}$=0.5, 1, and 2) at q''_w=20 kW/m² and 50 kW/m²

stead, because of the adsorption of surfactants and their different orientations in the adsorption layer (Fig. 9(*b*)), the heater surface wettability increases with increasing concentration. Fewer bubbles are thus nucleated that have relatively larger departure diameters. As pointed out by Fuerstenau [35], the adsorption isotherm and corresponding surface state can be divided into four regimes that are associated with the aggregation mode of adsorbed ions at the solid-water interface: (1) at low concentrations, surfactant adsorption takes place as individual ions[5]; (2) there is a sharp increase in the adsorption density due to self-association of adsorbed surfactant ions and the formation of hemimicelles; (3) the surfactant ions adsorb as reverse hemimicelles, with their polar heads oriented both toward the surface and liquid, and the surface becomes increasingly hydrophilic; and (4) as the c.m.c. is approached, the adsorption becomes independent of the bulk concentration in solution, and the surfactant molecules form a bilayer on the surface to make it strongly hydrophilic. The measured contact angle data in Fig. 9(*a*) correlate well with this characterization schematically illustrated in Fig. 9(*b*). The reason that Ethoquad 18/28 shows more hydrophilic behavior that CTAB at lower concentrations is because of its bulky polar head that occupies larger portion of the heater surface, and the variation in ebullience at the heater surface (Fig. 11) also reflects this wettability change.

Conclusions

With the addition of small amounts of cationic surfactants, the saturated pool boiling behavior of water is altered significantly, In general, besides the heat flux (or wall superheat) levels, the relative extent of enhancement is seen to be governed by several additive-chemistry based factors and the interfacial adsorption-desorption kinetics. These include the dynamic σ reduction of the solution, micellar structure of the surfactant, its degree of ethoxylation (which influences both surface tension and wettability or contact angle), and its molecular weight and ionic nature (which influence coverage, inter-molecular repulsion or lack thereof at the vapor-liquid and solid-liquid interfaces, and σ relaxation time). The salient features that describe the heat transfer performance can be summarized as follows:

1. The heat transfer in saturated nucleate boiling of aqueous cationic surfactant solutions is enhanced considerably, and it generally increases with q''_w and additive concentration up to a $C \leqslant$ c.m.c. Depending on C and q''_w, the heat transfer coefficient is found to increase by as much as 63% over that for pure water for DTAC (a low molecular weight cationic) solutions. With $C >$ c.m.c., the enhancement decreases and the heat transfer can even deteriorate below that for water depending upon q''_w and the surfactant chemistry. High concentration solutions of the ethoxylated cationic Ethoquad 18/25 (15 EO groups), for example, show considerable heat transfer deterioration as well as incipience thermal hysteresis that is typically found in highly wetting fluids.
2. The boiling process in non-ethoxylated surfactant solutions was observed to be characterized by an early incipience of regularly shaped smaller-sized bubbles, with a reduced tendency for coalescence and relatively higher bubble departure frequencies. The presence of EO groups in the molecular chain of the surfactant, which changes the surface wettability and alters the active nucleation site density and their distribution, tends to promote the inception of smaller-diameter bubbles in pre-micellar concentrations and suppress the nucleation process in post-micellar solutions. The

[5]Adsorption takes place with polar heads of the surfactant ions oriented toward the surface that yields a hydrophobic surface with most surfactants except for high molecular weight ones, whose bulky polar head would occupy a larger surface area.

different boiling mechanisms between non-ethoxylated and ethoxylated surfactants can essentially be related to the different physisorption of surfactant molecules at solid-water interface, which is reflected in the surface wettability variations as a function of surfactant concentration.

3. Except for their surface tension, aqueous cationic surfactant solutions do not exhibit any significant change in the solvent's thermo-physical properties. Both the equilibrium and dynamic σ, as well as c.m.c. are temperature dependent, where the degree of variation depends on the ethoxylation, molecular packing, and micellar structure of the surfactant.
4. Because of the highly dynamic nature of nucleate boiling in surfactant solutions, the measure of dynamic surface tension is seen to be an effective scaling property for the heat transfer data. The faster diffusion of lower molecular weight surfactants tends to reduce the surface tension faster in a short period of time, which is reflected in the better heat transfer performance of their solutions.
5. Besides the dynamic surface tension relaxation, the additive physico-chemical properties, which alter the surface wetting of aqueous solutions due to the interfacial physisorption of surfactant molecules, are shown to be critical parameters in predicting their enhanced nucleate pool boiling heat transfer performance.

Acknowledgments

This study was supported in part by the National Science Foundation (Grant No. CTS-9502128), Ohio Board of Regents, and the University Research Council. Manish Bahl, Satish Vishnubhatla, and S. Sethu Raghavan provided technical assistance in acquiring some rheology and interfacial data. Also, the valuable suggestions of Dr. D.B.R. Kenning, Oxford University, UK, are gratefully acknowledged.

Nomenclature

A = heater surface area ($=2\pi r_o L$) [m^2]
C = concentration [wppm]
h = boiling heat transfer coefficient [kW/m^2K]
I = current [A]
k = thermal conductivity of heater material [kW/m K]
L = length of heated cylinder [m]
M = molecular weight [kg/kmol]
q''_w = wall heat flux [W/m^2, or kW/m^2]
r = radius of wall thermocouple location [m]
r_o = cylindrical heater radius [m]
T = temperature [°C, or K]
ΔT_w = wall superheat [K]
V = voltage [V]

Greek Symbols

σ = surface tension [mN/m]

Subscripts

o = outer surface
r = radial location
sat = saturation
surf = pertaining to aqueous surfactant solution
w = at heater wall
water = pertaining to pure water

References

[1] Kandlikar, S. G., Shoji, M., and Dhir, V. K., eds., 1999, *Handbook of Phase Change: Boiling and Condensation*, Taylor & Francis, Philadelphia, PA.
[2] Thome, J. R., 1990, *Enhanced Boiling Heat Transfer*, Hemisphere, New York, NY.
[3] Bergles, A. E., 1997, "Enhancement of Pool Boiling," Int. J. Refrig., **20**, pp. 545–551.
[4] Manglik, R. M., 2003, "Heat Transfer Enhancement," in *Heat Transfer Handbook*, A. Bejan, and A. D. Klaus, eds., Wiley, New York, Chap. 14.
[5] Wasekar, V. M., and Manglik, R. M., 1999, "A Review of Enhanced Heat Transfer in Nucleate Pool Boiling of Aqueous Surfactant and Polymeric Solutions," J. Enhanced Heat Transfer, **6**, pp. 135–150.
[6] Wasekar, V. M., and Manglik, R. M., 2001, "Nucleate Pool Boiling Heat Transfer in Aqueous Surfactant Solutions," Thermal-Fluids & Thermal Processing Laboratory Report No. TFTPL-4, University of Cincinnati, Cincinnati, OH.
[7] Manglik, R. M., Wasekar, V. M., and Zhang, J., 2001, "Dynamic and Equilibrium Surface Tension of Aqueous Surfactant and Polymeric Solutions," Exp. Therm. Fluid Sci., **25**, pp. 55–64.
[8] Iliev, Tz. H., and Dushkin, C. D., 1992, "Dynamic Surface Tension of Micellar Solutions Studied by the Maximum Bubble Pressure Method," Colloid Polym. Sci., **270**, pp. 370–376.
[9] Hoffmann, H., and Rehage, H., 1986, "Rheology of Surfactant Solutions," in *Surfactant Solutions-New Methods of Investigation*, R. Zana, ed., **22**, Marcel Dekker, New York, pp. 209–239.
[10] Manglik, R. M., Bahl, M., Vishnubhatla, S., and Zhang J., 2003, "Interfacial and Rheological Characterization of Aqueous Surfactant Solutions," Thermal-Fluids and Thermal Processing Laboratory Report No. TFTPL-9, University of Cincinnati, Cincinnati, OH.
[11] Morgan, A. I., Bromley, L. A., and Wilke, C. R., 1949, "Effect of Surface Tension on Heat Transfer in Boiling," Ind. Eng. Chem., **41**, pp. 2767–2769.
[12] Jontz, P. D., and Myers, J. E., 1960, "The Effect of Dynamic Surface Tension on Nucleate Boiling Coefficients," AIChE J., **6**(1), pp. 34–38.
[13] Tzan, Y. L., and Yang, Y. M., 1990, "Experimental Study of Surfactant Effects on Pool Boiling Heat Transfer," ASME J. Heat Transfer, **112**, pp. 207–212.
[14] Wu, W.-T., Yang, Y.-M., and Maa, J.-R., 1995, "Enhancement of Nucleate Boiling Heat Transfer and Depression of Surface Tension by Surfactant Additives," ASME J. Heat Transfer, **117**, pp. 526–529.
[15] Ammerman, C. N., and You, S. M., 1996, "Determination of Boiling Enhancement Mechanism Caused by Surfactant Addition to Water," ASME J. Heat Transfer, **118**, pp. 429–435.
[16] Wu, W.-T., Yang, Y.-M., and Maa, J.-R., 1998, "Nucleate Pool Boiling Enhancement by means of Surfactant Additives," Exp. Therm. Fluid Sci., **18**, pp. 195–209.
[17] Wasekar, V. M., and Manglik, R. M., 2000, "Pool Boiling Heat Transfer in Aqueous Solutions of an Anionic Surfactant," ASME J. Heat Transfer, **122**, pp. 708–715.
[18] Hetsroni, G., Zakin, J. L., Lin, Z., Mosyak, A., Pancallo, E. A., and Rozenblit, R., 2001, "The Effect of Surfactants on Bubble Growth, Wall Thermal Patterns and Heat Transfer in Pool Boiling," Int. J. Heat Mass Transfer, **44**, pp. 485–497.
[19] Wasekar, V. M., and Manglik, R. M., 2002, "The Influence of Additive Molecular Weight and Ionic Nature on the Pool Boiling Performance of Aqueous Surfactant Solutions," Int. J. Heat Mass Transfer, **45**, pp. 483–493.
[20] Nelson, R. A., Kenning, D. B. R., and Shoji, M., 1996, "Nonlinear Dynamics in Boiling Phenomena," Japan Heat Transfer Society Journal, **35**(136), pp. 22–34.
[21] Wasekar, V. M., and Manglik, R. M., 2003, "Short-Time-Transient Surfactant Dynamics and Marangoni Convection Around Boiling Nuclei," ASME J. Heat Transfer, **125**(5), pp. 858–866.
[22] Barry, B. W., and Wilson, R., 1978, "C. M. C., Counterion Binding and Thermodynamics of Ethoxylated Anionic and Cationic Surfactants," Colloid Polym. Sci., **256**, pp. 251–260.
[23] Ashayer, R., Grattoni, C. A., and Luckham, P. F., 2000, "Wettability Changes During Surfactant Flooding," 6^{th} *International Symposium on Evaluation of Reservoir Wettability and Its Effect on Oil Recovery*, Socorro, New Mexico, USA.
[24] Wang, C. H., and Dhir, V. K., 1993, "Effect of Surface Wettability on Active Nucleation Site Density During Pool Boiling of Water on a Vertical Surface," ASME J. Heat Transfer, **115**, pp. 659–669.
[25] Kenning, D. B. R., 1999, "What Do We Really Know About Nucleate Boiling," in *IMechE Trans*: 6^{th} *UK National Heat Transfer Conference*, Edinburgh, 15–16 September, pp. 143–167.
[26] Rosen, M. J., 1989, *Surfactants and Interfacial Phenomena*, 2nd Ed., Wiley, New York, NY.
[27] Holmberg, K., Jönsson, B., Kronberg, B., and Lindman, B., 2003, *Surfactants and Polymers in Aqueous Solution*, 2nd Ed., Wiley, New York, NY.
[28] Lu, Y., Fan, H., Stump, A., Ward, T. L., Rieker, T., and Brinker, C. J., 1999, "Aerosol-Assisted Self-Assembly of Mesostructured Spherical Nanoparticles," Nature (London), **398**, pp. 223–226.
[29] Moffatt, R. J., 1988, "Describing the Uncertainties in Experimental Results," Exp. Therm. Fluid Sci., **1**(1), pp. 3–17.
[30] Bahl, M., Zhang, J., and Manglik, R. M., 2003, "Measurement of Dynamic and Equilibrium Surface Tension of Surfactant Solutions by the Maximum Bubble Pressure Method," CD-ROM Paper No. HT2003-47137, Proceedings of 2003 ASME Summer Heat Transfer Conference, ASME, New York, NY.
[31] Razafindralambo, H., Blecker, C., Delhaye, S., and Paquot, M., 1995, "Application of the Quasi-Static Mode of the Drop Volume Technique to the Determination of Fundamental Surfactant Properties," J. Colloid Interface Sci., **174**, pp. 373–377.

[32] Adamson, A. W., 1976, *Physical Chemistry of Surfaces*, 3rd ed., Wiley, New York.
[33] Partearroyo, M. A., Alonso, A., Goni, F. M., Tribout, M., and Paredes, S., 1996, ''Solubilization of Phospholipid Bilayers by Surfactants Belonging to the Triton X Series: Effect of Polar Group Size,'' J. Colloid Interface Sci., **178**, pp. 156–159.
[34] Bergles, A. E., 1988, ''Fundamentals of Boiling and Evaporation,'' in *Two-Phase Flow Heat Exchangers*, S. Kakac, A. E. Bergles, and O. Fernandes, eds., Kluwer, Dordrecht, The Netherlands, pp. 159–200.
[35] Fuerstenau, D. W., 2002, ''Equilibrium and Nonequilibrium Phenomena Associated with the Adsorption of Ionic Surfactants at Solid-Water Interfaces,'' J. Colloid Interface Sci., **256**, pp. 79–90.
[36] Zhang, J., and Manglik, R. M., 2003, ''Visualization of Ebullient Dynamics in Aqueous Surfactant Solutions,'' ASME J. Heat Transfer, **125**(4), p. 547.

The Effect of Support Grid Features on Local, Single-Phase Heat Transfer Measurements in Rod Bundles

Mary V. Holloway

Heather L. McClusky

Donald E. Beasley
Fellow, ASME

Department of Mechanical Engineering,
Clemson University,
Clemson, SC 29634

Michael E. Conner
Westinghouse Nuclear Fuel,
5801 Bluff Road,
Columbia, SC 29250

Locally averaged heat transfer measurements in a rod bundle downstream of support grids with and without flow-enhancing features are investigated for Reynolds numbers of 28,000 and 42,000. Support grids with disk blockage flow-enhancing features and support grids with split-vane pair flow enhancing features are examined. Grid pressure loss coefficients and feature loss coefficients are determined based on pressure drop measurements for each support grid design. Results indicate the greatest heat transfer enhancement downstream of the support grid designs with disk blockages. In addition, the local heat transfer measurements downstream of the split-vane pair grid designs indicate a region of decreased heat transfer below that of the hydrodynamically fully developed value. This decreased region of heat transfer is more pronounced for the lower Reynolds number case. A correlation for the local Nusselt numbers downstream of the standard support grid designs is developed based on the blockage of the support grid. In addition, a correlation for the local Nusselt numbers downstream of support grids with flow-enhancing features is developed based on the blockage ratio of the grid straps and the normalized feature loss coefficients of the support grid designs. The correlations demonstrate the tradeoff between initial heat transfer enhancement downstream of the support grid and the pressure drop created by the support grid. [DOI: 10.1115/1.1643091]

Keywords: Bundles, Enhancement, Forced Convection, Heat Transfer, Swirling

Introduction

The core of a pressurized water reactor is constructed from an array of nuclear fuel rods positioned by support grids. Forced convection to water flowing primarily parallel to the rods is used to transport the thermal energy from the surfaces of the rods to the bulk fluid. Figure 1 shows a laboratory scale rod bundle consisting of a 5×5 array of simulated fuel rods. Typical operating conditions for pressurized water reactors are predominantly in the single-phase flow regime. Thus, single-phase heat transfer is an important consideration in the evaluation of any rod bundle design. Flow-enhancing features can be implemented into the design of the support grid to alter the hydrodynamics in the rod bundle in an effort to improve the heat transfer characteristics of the rod bundle. The present study measures the local, single-phase heat transfer coefficients for different support grid designs in 5×5 laboratory scale rod bundles. In addition, the pressure drop measurements for rod bundles with different support grid designs are obtained. Correlations for local heat transfer downstream of both standard support grid designs and support grids with flow-enhancing features are developed.

Support grids are used in nuclear rod bundles to precisely position and support the fuel rods. Examples of different support grid designs are shown in Fig. 2. Rod support features formed out of the grid strap are used to position and hold the rods on a constant pitch. The presence of the support grids increases the pressure drop of the rod bundle assembly. However, the support grids also enhance the heat transfer performance of the rod bundle by increasing the local heat transfer coefficients. The design of the support grid must be optimized based on the pressure drop and heat transfer enhancement it provides.

Contributed by the Heat Transfer Division for publication in the JOURNAL OF HEAT TRANSFER. Manuscript received by the Heat Transfer Division December 23, 2002; revision received October 3, 2003. Associate Editor: K. S. Ball.

A standard support grid design is shown in Fig. 2(*a*). ''Standard'' support grid designs, also called honeycomb or eggcrate grids in other investigations, consist only of the grid straps with rod support features to position and hold the rods in place. Rehme [1] includes illustrations of different standard support grid designs, including details of the rod support features. In a standard support grid, the local heat transfer coefficients within and just downstream of the grid are increased due to increased flow velocity and turbulence caused by the flow blockage of the grids as well as by the destruction and redevelopment of boundary layers. The standard support grid design is used as a baseline design and flow-enhancing features may be attached to such a base strap design. The flow-enhancing features may improve the hydrodynamic characteristics and heat transfer performance of the rod bundle by increasing flow blockage, improving mixing in the rod bundle, and/or creating swirling flow in rod bundle subchannels. One type of flow-enhancing feature is disk blockages attached to the downstream edge of the support grid. Figures 2(*b*) and (*c*) are support grid designs that have disk blockage features. A commonly used flow-enhancing feature is split-vane pairs attached to the downstream edge of the support grid and arranged at an angle of approximately 30 deg relative to the axial flow in alternating up/down and left/right vane configurations, as shown in Fig. 2(*d*). The split-vane pairs increase the lateral mixing between subchannels and can create swirling flow in the rod bundle subchannels. A subchannel is the flow area between four adjacent rods in a square array. Figure 3 illustrates a typical subchannel of a rod bundle containing a split-vane pair.

Several previous investigations have focused on the fluid dynamics of swirling flow created downstream of a support grid with split-vane pairs. Herer [2] and Yang and Chung [3] experimentally investigated velocity and turbulence intensity downstream of a split-vane pair grid design using laser Doppler velocimetry. Yang and Chung [3] reported axial turbulence intensities of approximately 15% downstream of a split-vane pair grid. Karoutas et al.

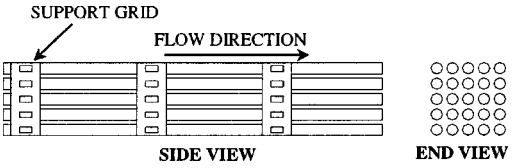

Fig. 1 Schematic diagram of 5×5 rod bundle assembly

[4] investigated axial and lateral velocities downstream of a split-vane pair grid by comparing laser Doppler velocimetry measurements to computational fluid dynamics (CFD) simulations. Swirling flow in the subchannel was predicted using CFD and confirmed using the laser Doppler velocimetry measurements. A computational study of the hydrodynamic flow fields downstream of support grids with different vane types and configurations, including split-vane pair grid designs, was performed by In [5]. Swirling flow in the subchannel and cross-flow between subchannels downstream of the split-vane pair grid design were noted. McClusky et al. [6,7] experimentally investigated the development of swirling flow in a rod bundle subchannel. The swirling flow was characterized based on lateral velocity fields obtained from particle image velocimetry. The vortex created from the split-vane pair was found to be consistent with a Lamb-Oseen vortex [8], but had unique axial development as a result of the subchannel geometry [6]. The development of swirling flow in the rod bundle subchannels can have a significant impact on the heat transfer characteristics of the rod bundle.

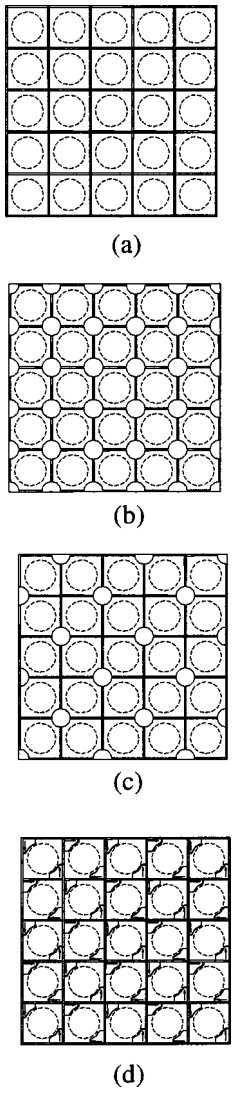

Fig. 2 Representative drawings of support grid designs for the following: (*a*) grids A, E, and G; (*b*) grid B; (*c*) grid C; and (*d*) grids D, F, and H.

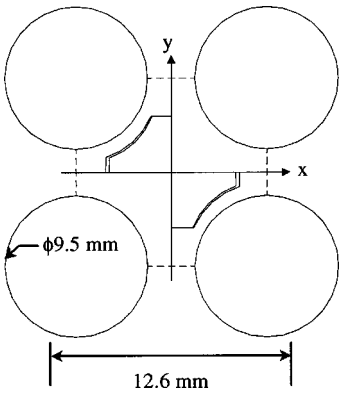

Fig. 3 Typical rod bundle subchannel with split-vane pair

The decaying, swirling flows created from split-vane pairs can increase the critical heat flux in a rod bundle geometry with two-phase flow (de Crecy [9]). Additionally, the decaying, swirling flow structure may be useful in improving the single-phase heat transfer performance of the rod bundle. No previous experimental investigations of heat transfer downstream of split-vane pair grid designs are known. Insight into the heat transfer characteristics of swirling flow in a rod bundle may be gained by examining the fundamental research area of decaying, swirling flow in a pipe. The swirling flow in the following investigations was created using tangential injection methods. Blum and Oliver [10] and Hay and West [11] found heat transfer enhancement in swirling pipe flow above that of nonswirling pipe flow. Chang and Dhir [12] identified two main mechanisms for heat transfer enhancement in the swirling pipe flow. The radial pressure gradient in the swirling flow increased the axial velocities near the wall of the pipe which caused an increase in the heat transfer rate from the wall. In addition, high turbulence levels created by the swirling flow were shown to enhance the mixing and thus enhance the heat transfer. Thus the swirling flow structure in a rod bundle subchannel is expected to enhance the single-phase heat transfer coefficients for some distance downstream of the support grid. This paper examines how changes in the hydrodynamic flow fields caused by flow enhancing features such as split-vane pairs affect the heat transfer performance of the rod bundles.

Table 1 identifies the test grids examined in the present study. The grid blockage ratio, ε, is defined as the ratio of the projected area of the support grid to the open flow area. Values of the grid blockage ratio for the grids used in the present study are given in Table 1. In addition, the base strap design (the support grid design of the strap with no flow-enhancing features) and a brief description of the test grid are included. An end view of the standard grid designs, grids A, E, and G, is shown in Fig. 2(*a*). The differences between these grid designs include different grid blockage ratios and the grid strap length along the flow direction.

The two disk grid designs tested are shown in Fig. 2(*b*) and Fig. 2(*c*). Figure 2(*b*) is an end view of grid B that has 5.8 mm diameter disks attached on the downstream edge of the grid strap at every intersection point. Figure 2(*c*) is an end view of grid C that has 5.8 mm diameter disks attached on the downstream edge of the grid strap at alternating intersection points. An end view representation of the split-vane pair grid designs is shown in Fig. 2(*d*). Grids D, F, and H are split-vane pair support grid designs. The vanes on these support grids form an angle of approximately 30 deg with the axial flow direction. The vane designs for

Table 1 Description of test grids

Grid ID	Grid Blockage Ratio ε	Base Grid Strap	Description
A	0.20	A	Standard egg-crate type grid. No vanes or flow blockage
B	0.43	A	Flow blockage created by 5.8 mm disks attached to downstream edge of grid at every intersection point.
C	0.31	A	Flow blockage created by 5.8 mm disks attached to downstream edge of grid at alternating intersection points.
D	0.40	A	Split-vane pair grid with vane angle of approximately 30 deg.
E	0.14	E	Standard egg-crate type grid. No vanes or flow blockage
F	0.36	E	Split-vane pair grid with vane angle of approximately 30 deg.
G	0.20	G	Standard egg-crate type grid. No vanes or flow blockage. Grid has longer strap length compared to grids A and E.
H	0.47	G	Split-vane pair grid with vane angle of approximately 30 deg.

the three different split-vane pair support grids are not identical, but all are designed to create swirling flow in the rod bundle subchannels.

The present study investigates how the addition of flow-enhancing features to the support grid design affects the single-phase heat transfer in 5×5 rod bundles. A heated copper sensor is utilized to measure the locally averaged single-phase heat transfer coefficients at various axial locations downstream of the support grids. Pressure drop for all of the rod bundle assemblies is measured. Correlations for heat transfer rates downstream of standard support grid designs are developed. In addition, an innovative approach is implemented to develop a general heat transfer correlation for flow downstream of support grid designs with flow-enhancing features. For this correlation, the pressure drop associated with the grid strap design is separated from the pressure drop associated with the flow enhancing features. These two pressure drop characteristics of the grids are used to predict the heat transfer downstream of the support grid designs.

Experimental Facility

The closed loop facility used to measure heat transfer and pressure drop in the 5×5 rod bundles is shown in Fig. 4. Filtered water is circulated through the facility using a 15 hp variable speed pump. The constant head tank used in conjunction with the variable speed pump ensures a constant flow rate through the test section. A heat exchanger placed in the constant head tank is used to hold the water temperature between 18 and 20°C. As shown in Fig. 4, two 90 deg bends occur in the flow loop piping directly before the inlet of the test section. These 90 deg bends cause tangential disturbances to the otherwise axial flow. A flow straightener plate is positioned at the inlet of the test section to redirect the momentum of the fluid in the axial direction.

The test section is constructed from Lexan and has a square inner flow area of 42.25 cm^2. The 5×5 rod bundle consists of 9.5 mm rods separated on a square array by a pitch of 12.6 mm. The hydraulic diameter of the rod bundle subchannel is 11.8 mm. The rods are held in place by three support grids placed 508 mm apart. The first support grid is located 90 mm from the test section inlet. The first two support grids in the rod bundle are standard support grids. These grids have no flow-enhancing features and are used to condition the flow. The third grid in the rod bundle assembly is the test grid. The four different types of grid designs tested in the present study are shown in Fig. 2.

The flow rate through the facility is measured using a Sponsler turbine-type flowmeter (model SP3-CP-PHIL-A-4X) with a range from 0 to 2.46 m^3/min and a manufacturer stated accuracy of $\pm2\%$. Two volumetric flow rates of 0.36 and 0.54 m^3/min are investigated in the present study. These volumetric flow rates correspond to nominal axial velocities of 2.44 and 3.66 m/s, respectively. The corresponding Reynolds numbers investigated in the present study are $Re_{Dh}=28{,}000\pm1200$ and $Re_{Dh}=42{,}000\pm1700$. A Kline-McClintock sensitivity approach (as described in [13]) was performed to determine the uncertainty of the Reynolds number.

Pressure Drop Measurements. The pressure drop over several axial spans in the rod bundle is measured for each of the support grid designs listed in Table 1. The test section is equipped with pressure taps at the axial locations shown in Fig. 5. The positioning of the three support grids relative to the test section is also indicated in this figure. Three different pressure drop measurements are made using three Schaevitz pressure transducers. The pressure drop across a grid, Δp_{grid}, is measured over a span of $\Delta z_{\text{grid}}=302$ mm that includes a grid. The pressure drop across the rods, Δp_{rod}, is measured over a span of $\Delta z_{\text{rod}}=206$ mm. In addition, the pressure drop across a complete 508 mm grid span, Δp_{span}, is measured to provide a cross check for the pressure measurements. The absolute uncertainty in the pressure drop measurement is ±300 Pa calculated using a root-sum-squares method [13] based on error contributions from the pressure transducer calibration, calibration measurement standard resolution, and data acquisition errors.

Heat Transfer Measurements. Heat transfer coefficients are measured for axial locations both upstream and downstream of the test grids for $Re_{Dh}=28{,}000$ and $Re_{Dh}=42{,}000$ using a rod instrumented with a heated copper sensor. A drawing of the copper sensor is shown in Fig. 6. The sensor is 9.5 mm in diameter and is 28.6 mm long. The copper sensor is heated with a concentrically inserted cartridge heater, providing a constant heat flux input to the inner surface of the copper sensor. Use of copper as the sensor material reduces variations in surface temperature and heat flux at the outer surface of the copper. Four 36-gauge E-type thermocouples are embedded in 90 deg increments around the circumference of the sensor on a diameter of 7.9 mm. The thermocouples are attached at a depth of 19 mm with epoxy into holes with a

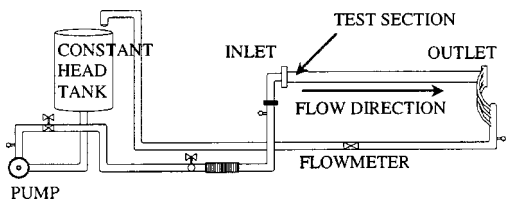

Fig. 4 Drawing of experimental facility

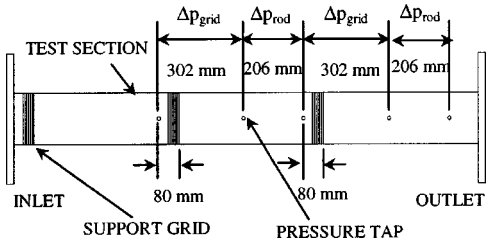

Fig. 5 Pressure tap locations

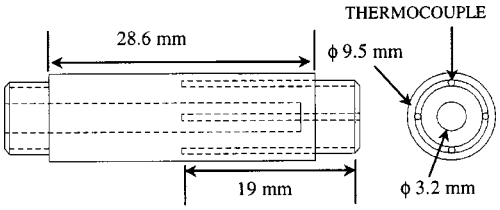

Fig. 6 Drawing of heated copper sensor

diameter of 0.74 mm. To decrease conduction losses from the ends of the heated copper sensor, an insulating Delrin cylinder is attached to each end of the copper sensor. Zircaloy extension rods are attached to each Delrin cylinder to complete an instrumented rod in the rod bundle assembly. Each instrumented rod extends past the inlet and outlet of the test section. This allows for the copper sensor to be positioned at different axial locations without disassembly of the rod bundle.

The heat transfer coefficient is determined based on the measured DC power input to the cartridge heater, the surface area of the sensor, and the temperature difference between the surface of the heated copper sensor and the bulk fluid temperature,

$$h = q/A_s(T_s - T_m). \tag{1}$$

The locally averaged heat transfer coefficients obtained are averaged both temporally and spatially. Spatially, the measurement method yields heat transfer coefficients that are averaged around the circumference and over the length of the copper sensor. The DC power is determined by independently measuring the voltage and current supplied to the cartridge heater using two Hewlett Packard multimeters (Model #34401A). The typical operating power for the heated copper sensor in the present study is approximately 70 W. The power is held to within ± 0.1 W during each series of heat transfer measurements. During each individual measurement period, the power fluctuates less than ± 0.05 W. Two instrumented rods are placed within the rod bundle and used to measure the temperature difference between the heated copper sensor and the bulk fluid temperature. The copper sensor in one of the rods is heated using the cartridge heater, while the sensor in the second rod is not heated and is used to measure the bulk fluid temperature in the test section. A differential temperature calibration was performed for each thermocouple pair to directly measure this temperature difference. The typical uncertainty in a calibrated thermocouple pair, based on a root-sum-square method of combining measurement error and the calibration error ($t_{\nu,95}S_{yx}$), is ± 0.10°C. A Hewlett Packard nanovoltmeter (Model #34420A) is used to measure the differential voltage of each thermocouple pair. The estimated relative uncertainty in the measured Nusselt number determined using a Kline-McClintock sensitivity approach [13] is $\pm 4.8\%$. This measurement uncertainty was calculated as

$$u_{\mathrm{Nu}} = \pm \sqrt{\left(\frac{\partial \mathrm{Nu}}{\partial h}u_h\right)^2 + \left(\frac{\partial \mathrm{Nu}}{\partial D_h}u_{D_h}\right)^2 + \left(\frac{\partial \mathrm{Nu}}{\partial k}u_k\right)^2}, \tag{2}$$

with error contributions to the uncertainty in Nusselt number as listed below.

$$u_h \quad \pm 1000 \ \mathrm{W/m^2K}$$

$$u_{Dh} \quad \pm 0.25 \ \mathrm{mm}$$

$$u_k \quad \pm 0.0016 \ \mathrm{W/mK}$$

$$u_{\mathrm{Nu}}{}^* \quad \pm 22 \ (\pm 4.8\%)$$

*based on nominal values of $h = 23{,}000$ W/m^{2}K, $k = 0.601$ W/mK

Further discussion of the design of the heated copper sensor, the temperature measurement technique, and the uncertainty analysis can be found in Armfield [14] and Armfield et al. [15].

Table 2 Pressure drop measurements for $\mathrm{Re}_{Dh} = 28{,}000$

Grid ID	Δp_{grid} (Pa)	Δp_{rod} (Pa)	K_g	K_s	K_{feat}	K_{feat}/K_g
A	4960	1550	0.91	0.91	-	-
B	7790	1860	1.71	0.91	0.80	0.47
C	5960	1650	1.19	0.91	0.29	0.24
D	5720	1790	1.05	0.91	0.14	0.13
E	4340	1550	0.70	0.70	-	-
F	4930	1720	0.81	0.70	0.11	0.14
G	6170	1650	1.26	1.26	-	-
H	6860	1720	1.46	1.26	0.20	0.14

The determination of the surface temperature of the heated copper sensor based on the measured temperature difference between the heated sensor and the bulk fluid temperature is an inverse heat transfer problem. A two-dimensional finite-difference conduction model is used to determine the temperature distribution within the heated copper sensor. The steady-state conduction model has a global energy balance of better than 99.9 percent. The conduction model is used to determine the surface temperature of the heated sensor based on the measured temperature difference and the power input into the heated sensor. In addition, it is used to estimate the power lost by conduction to the Delrin insulating supports. This estimated power loss is less than 2 percent.

Results and Discussion

Pressure Drop Results. Pressure drop measurements for nominal axial Reynolds numbers of 28,000 and 42,000 are obtained for the grid and rod spans of eight different support grid designs. Tables 2 and 3 present pressure drop across the grid span, Δp_{grid}, pressure drop across the rod span, Δp_{rod}, grid loss coefficient, K_g, strap loss coefficient, K_s, feature loss coefficient, K_{feat}, and the normalized feature loss coefficient, K_{feat}/K_g, for $\mathrm{Re}_{Dh} = 28{,}000$ and $\mathrm{Re}_{Dh} = 42{,}000$, respectively. The pressure drop measured across the grid span, Δp_{grid}, includes contributions of pressure drop from both the grid and the rods. For the standard support grid designs, the standard deviation of the measured pressure drop values across the rod span provided in Tables 2 and 3 is 3.6 percent; this small standard deviation both confirms that the rod span pressure drop is consistent among the grids and provides indication of the replication error of the pressure drop measurements. The friction factor

$$f = \Delta p_{\mathrm{rod}} \frac{\mathrm{D_e}}{\Delta z_{\mathrm{rod}}} \left(\frac{\rho V^2}{2}\right) \tag{3}$$

is within 8 percent of that predicted using the Moody diagram (with Reynolds number based on the hydraulic diameter of the rod bundle, D_e). This indicates that the flow is hydrodynamically fully developed over the rod span pressure measurement location for the standard support grid designs. Grids with flow enhancing features consistently have larger pressure drops along the rod span. For example, the measured pressure drop data for the rod spans for grids having split-vane pairs (Grids D, F, and H) are 10

Table 3 Pressure drop measurements for $\mathrm{Re}_{Dh} = 42{,}000$

Grid ID	Δp_{grid} (Pa)	Δp_{rod} (Pa)	K_g	K_s	K_{feat}	K_{feat}/K_g
A	10200	3170	0.83	0.83	-	-
B	16400	3930	1.60	0.83	0.76	0.48
C	12510	3410	1.13	0.83	0.29	0.26
D	11860	3790	0.95	0.83	0.11	0.12
E	9000	3240	0.64	0.64	-	-
F	10310	3590	0.76	0.64	0.12	0.16
G	12690	3380	1.16	1.16	-	-
H	14340	3520	1.38	1.16	0.22	0.16

percent larger than those for the standard grids; this suggests that the pressure drop for the rod span is greater for the swirling flow produced by the split-vane pairs.

The contribution of the pressure drop due solely to the grid, Δp_g, is calculated by assuming the pressure drop across the rods is directly proportional to the measurement span of the pressure drop

$$\Delta p_g = \Delta p_{\text{grid}} - \frac{\Delta z_{\text{grid}}}{\Delta z_{\text{rod}}} \Delta p_{\text{rod}} \tag{4}$$

where Δp_{rod} is the value measured for each individual test. Equation (4) neglects the effect the flow-enhancing features have on the rod span pressure drop. The loss coefficients for each grid design are calculated based on the pressure drop of the grid. The grid loss coefficient is defined as

$$K_g = \frac{\Delta p_g}{1/2\rho V^2} \tag{5}$$

This grid loss coefficient represents the nondimensional pressure loss in the rod bundle assembly contributed by the grid. In order to characterize the pressure losses from the flow-enhancing features, a feature loss coefficient is calculated for the grids with flow-enhancing features. Since the grids with flow-enhancing features are constructed from one of three standard strap designs (grids A, E, and G), the feature loss coefficient can be defined based on the loss coefficient for the grid, K_g, and the loss coefficient for the standard strap design, K_s

$$K_{\text{feat}} = K_g - K_s \tag{6}$$

This feature loss coefficient isolates the pressure losses associated with the flow-enhancing features attached to the grid strap.

The pressure drop results presented in Tables 2 and 3 identify similar trends for both Reynolds numbers tested. As shown in Table 2, the grid loss coefficients at $\text{Re}_{Dh}=28{,}000$ for the standard grid designs A, E, and G are 0.91, 0.70, and 1.26, respectively. The differences in grid loss coefficients for these standard grid designs can be attributed to differences in form drag and friction drag between the standard grid designs. For a standard support grid design, the pressure losses due to form drag can be directly related to the blockage ratio of the grid. Grid E, with the smallest grid blockage ratio, has the smallest grid loss coefficient. Grids A and G have the same blockage ratios; however, the loss coefficient for grid G is higher than that for grid A due to the increased friction loses created by the longer strap length of grid G.

Comparisons of the pressure drop results for support grids with the base grid strap design A, grids A, B, C, and D, are used to identify general trends in the pressure drop characteristics of each support grid type. As reported in Table 2, the loss coefficient for the standard grid design, grid A, is lower than the loss coefficients for grid designs with flow-enhancing features. It should be noted that although the grid blockage ratios for grid B and grid D are approximately equal, the grid loss coefficient for grid D, $K_g = 1.05$, is significantly smaller than that of grid B, $K_g = 1.71$. The difference in grid loss coefficient can be explained by examining the shape of the flow-enhancing features attached to the two grids; grid D has split-vane pair flow enhancing features that are more streamlined than the blunt disk blockage features of grid B. The feature loss coefficients, K_{feat}, of Table 2 highlight the differences in the pressure drop of Grid B and D due to bluntness of the two flow-enhancing feature geometries. It is evident that the pressure losses for a support grid with fundamentally different flow-enhancing feature designs cannot be predicted based solely on blockage ratio.

The feature loss coefficient normalized by the grid loss coefficient indicates the percentage of the total pressure losses that are contributed by the flow-enhancing features. Thus, the normalized feature loss coefficient, K_{feat}/K_g, allows a direct comparison between all of the grid designs to determine the effect of the flow-enhancing features on the pressure losses. As shown in Table 2, the ratio of the loss coefficients for the split-vane pair grids designs, grids D, F, and H, range from 0.13 to 0.14. This small range indicates that the effect of the vanes on the pressure losses for the three split-vane pair grid designs is essentially constant. The ratios of loss coefficients for grids B and C, with disk blockage flow enhancing features, are 0.47 and 0.24, respectively.

Pressure drop results for $\text{Re}_{Dh}=42{,}000$ are presented in Table 3. For corresponding grids, the grid loss coefficients for this higher Reynolds number are smaller than those for the lower Reynolds number tabulated in Table 2. The same general trends identified for the lower Reynolds number hold for the higher Reynolds number cases. The normalized feature loss coefficients, K_{feat}/K_g, for the split-vane pair grid designs range from 0.12 to 0.16. Although this range is slightly higher than that reported for the lower Reynolds number case, the effect of the vanes on the pressure losses for the three split-vane pair grid designs is essentially the same. The normalized feature loss coefficients for grids B and C are 0.48 and 0.26, which correspond with those reported for $\text{Re}_{Dh}=28{,}000$.

Heat Transfer Correlations. Previous investigations have related the pressure drop in a rod bundle to the grid blockage ratio, ε. Rehme [1,16] reports that the grid loss coefficient for a standard grid is predicted by

$$K_g = K_v \varepsilon^2 \tag{7}$$

where K_v is a modified loss coefficient that has a weak dependency on Reynolds number for the range of Reynolds numbers tested in the present investigation. Marek and Rehme [17] measured heat transfer in both smooth and rough rod bundles downstream of a standard spacer grid using a triangularly arrayed three-rod bundle cooled with air and determined the maximum heat transfer enhancement from a standard support grid to be a function of the blockage ratio

$$\frac{\text{Nu}}{\text{Nu}_0} = 5.55\varepsilon^2 + 1 \tag{8}$$

where Nu_0 is the fully-developed Nusselt number.

Correlations for standard support grid designs have been proposed to predict the axial development of local heat transfer averaged around the circumference of the rod. The decay of the heat transfer coefficient with z/D_h can either take the form of an exponential decay or a power law. Yao et al. [18] used an exponential decay function to correlate heat transfer downstream of a standard support grid design

$$\frac{\text{Nu}}{\text{Nu}_0} = 1 + 5.55\varepsilon^2 e^{-0.13z/D_h} \tag{9}$$

The initial heat transfer enhancement reported by Marek and Rehme [17] (Eq. 8) was used to account for the initial effect of flow blockage on heat transfer, and the decay rate was based on previous heat transfer measurements. Kidd et al. [19] measured local heat transfer coefficients in an electrically heated seven-rod hexagonally arrayed rod bundle cooled with air and used a power law relationship to correlate heat transfer downstream of a standard support grid design

$$\text{Nu} = \gamma \, \text{Re}^{\beta_1}{}_{D_h} \left(\frac{z}{D_h} \right)^{\beta_2} \tag{10}$$

The effect of Prandtl number is included in the γ coefficient. Kidd et al. [19] reported coefficients of $\gamma = 0.041$, $\alpha = 0.77$, and $\beta = -0.15$ for air at Reynolds numbers between 38,000 and 63,000. A hexagonal support grid with no flow-enhancing features (i.e., a standard grid) was used to develop this correlation. Results from Yao et al. [18] and Kidd et al. [19] indicate that either power law functions or exponentially decaying functions can be used to accurately capture the heat transfer development downstream of a support grid.

Yao et al. [18] developed a correlation for the expected heat transfer enhancement downstream of a support grid design with split-vane pairs. The correlation

$$\frac{\mathrm{Nu}}{\mathrm{Nu}_0}=(1+5.55\varepsilon^2 e^{-0.13z/D_h})(1+A_v^2\tan^2\phi e^{-0.034z/D_h})^{0.4} \tag{11}$$

is a combination of the normalized Nusselt number downstream of a standard support grid design and the expected heat transfer augmentation caused by swirling flow in the rod bundle subchannel. The spatial decay rate of the angular momentum of swirling flow in a pipe as reported by Kreith and Sonju [20] was used to model the expected effect of swirl on the heat transfer decay rate in the rod bundle. No heat transfer data downstream of a split-vane pair grid design was available for comparison to the correlation at the time it was developed. The blockage ratio, ε, is the total blockage ratio of the grid including the blockage of the base grid strap and the split-vane pairs.

To date, no general correlation has been developed to predict heat transfer downstream of support grids with fundamentally different flow-enhancing feature designs. In the present study, correlations for the local heat transfer coefficient downstream of both standard support grid designs and support grids with flow-enhancing features are developed. Both exponential and power fits of the local heat transfer data are investigated. The initial heat transfer enhancement just downstream of the support grid with flow-enhancing features is determined based on measured pressure drop characteristics.

The initial heat transfer enhancement just downstream of a standard support grid design can be predicted by using either a grid loss coefficient, K_g, or a grid blockage ratio, ε. The primary initial heat transfer enhancement mechanism just downstream of the support grid is due to the increased flow velocity that is created from the decrease in flow area around the support grid. This decrease in flow area is directly related to the pressure losses due to form drag of the support grid. For a standard support grid design, the grid blockage ratio provides an indication of the form drag of the support grid; whereas, the grid loss coefficient indicates both the form and friction drag losses. Since the initial heat transfer enhancement is directly correlated with the form drag (and not friction drag) of the support grid, the grid blockage ratio is a more appropriate correlating parameter for the heat transfer enhancement downstream of a standard support grid design. A correlation of the form

$$\frac{\mathrm{Nu}}{\mathrm{Nu}_0}=1+C_1\varepsilon_s^2 e^{-\alpha z/D_h} \tag{12}$$

is used to correlate the local heat transfer development downstream of a standard support grid design. For future convenience, the grid blockage ratio, ε_s, used in the correlation is the strap blockage ratio. Since the standard support grid designs have no flow-enhancing features, ε and ε_s are identical for standard support grid designs. The correlation presented in Eq. (12) is of the same form as that of Eq. (9) (Yao et al. [18]). For comparison purposes, a correlation for flow downstream of a standard support grid design is also developed based on a power law equation. The correlation is of the form

$$\frac{\mathrm{Nu}}{\mathrm{Nu}_0}=1+\kappa\left(\frac{z}{D_h}\right)^{\lambda} \tag{13}$$

For support grid designs with flow-enhancing features, it is assumed that the initial heat transfer enhancement contributed by the flow-enhancing features is directly related to the feature loss coefficient, K_f. Therefore, the heat transfer enhancement above the base strap design heat transfer can be predicted based on the normalized feature loss coefficient, K_{feat}/K_g. The total heat transfer enhancement downstream of a support grid design with flow-enhancing features can be expressed based on a superposition of the heat transfer enhancement of the base strap design and the heat transfer enhancement from the flow-enhancing features. The heat transfer enhancement downstream of a support grid with flow-enhancing features is expressed as

$$\frac{\mathrm{Nu}}{\mathrm{Nu}_0}=1+\left[C_1\varepsilon_s^2+C_2\left(\frac{K_{\mathrm{feat}}}{K_g}\right)\right]e^{-\alpha z/D_h} \tag{14}$$

A correlation of this form represents the tradeoff between heat transfer enhancement and pressure losses for flow downstream of a support grid in a rod bundle.

Heat Transfer Results. The locally averaged heat transfer coefficients for water flowing primarily parallel to rod bundles at nominal axial Reynolds numbers of 28,000 and 42,000 are presented. The Reynolds number investigated in the present study is an order of magnitude lower than that occurring in the core of a nuclear reactor. However, comparisons of flow fields obtained downstream of split-vane pair grid designs and CFD simulations at in-core conditions indicate that the overall flow structures and decay rate of the swirl are similar [7]. The heat transfer performance downstream of eight different support grids is discussed. The heat transfer coefficients are measured for rods located in the interior of the 5×5 rod bundle. No systematic effect of the interior rod location on local heat transfer coefficients is found; thus no distinction between rod locations is made for the different interior rod locations tested. Results for the standard grid designs are presented as local Nusselt numbers as well as local Nusselt numbers normalized by the hydrodynamically fully developed Nusselt number. Results for the support grids with flow-enhancing features are presented as local Nusselt numbers normalized by the hydrodynamically fully developed Nusselt number. Local heat transfer measurements obtained using the present method have been previously documented for several of the support grids used in the present study (Armfield [15] and Armfield et al. [21]). Discussion of pressure loss coefficients, generalized heat transfer correlations, and a more extensive heat transfer analysis are included in the present study.

An unheated starting length is inherently present using the heated copper sensor to measure locally averaged heat transfer coefficients. The sensor is the only portion of the rod that is heated; therefore, there is a developing thermal boundary layer at each axial measurement location. The flow can become hydrodynamically fully developed but will never be thermally fully developed. The measured heat transfer coefficient is higher when the sensor is placed in the hydrodynamically fully developed region of the flow than it would be if measured for identical hydrodynamic conditions in a rod bundle with thermally fully developed conditions. Normalization of the measured heat transfer rate with the measured hydrodynamically fully developed value of the heat transfer rate is used to compare heat transfer enhancement between different support grid designs. Hay and West [11] used this type of normalization to compare heat transfer results obtained in swirling pipe flow that had a disturbance in the thermal boundary layer at the heat flux sensor location. Guellouz and Tavoularis [22] also used this type of normalization to report circumferential variations in heat transfer around a rod in fully developed flow in a rod bundle. In the present study, the temperature of the copper sensor, and thus the local heat transfer coefficients, are determined by the local hydrodynamic conditions at the sensor location. Therefore, a comparison among the measured local heat transfer coefficients obtained in the present study can be used to demonstrate differences in the hydrodynamic development of the flow fields downstream of different support grid designs.

The locally averaged heat transfer coefficients are measured for axial locations ranging from $z/D_h=1.4$ to $z/D_h=33.6$ downstream of each support grid. The axial location of $z/D_h=0$ corresponds to the downstream edge of the test grid. The local heat transfer coefficients downstream of a support grid decay from a maximum value just downstream of the grid to the hydrodynami-

cally fully developed value some distance downstream of the grid. Results from the present study indicate that the hydrodynamically fully developed value of heat transfer is achieved well before the end of the 508 mm span separating two support grids. The local heat transfer coefficient is measured upstream of the test grid at $z/D_h = -9.6$ to determine the hydrodynamically fully developed value of heat transfer for each bundle assembly. This upstream measurement location should be undisturbed by grid effects (Yao et al. [18]) and represent a measure of the hydrodynamically fully developed heat transfer coefficient. Results from the present study confirm that this measurement location is sufficiently distant from both the second conditioning grid and the third test grid to obtain a measurement of the hydrodynamically fully developed value of heat transfer.

Previous experimental measurements of fully developed heat transfer in rod bundles [19,23] indicate that the fully developed value of heat transfer depends on the Prandtl number and the Reynolds number (based on hydraulic diameter). For example, Dingee and Chastain [23] investigated heat transfer in water-cooled, electrically heated rod bundles in triangular and square arrays with several pitch-to-diameter (P/D) ratios and determined that the fully developed value of heat transfer is well predicted by the Colburn equation when the concept of equivalent diameter (hydraulic diameter) for different pitch-to-diameter ratios was used. The Colburn equation is

$$\mathrm{Nu} = C\,\mathrm{Re}^{0.8}\mathrm{Pr}^{0.33} \tag{15}$$

where C is 0.023. Kidd et al. [19] measured local heat transfer coefficients in an electrically heated seven-rod hexagonally arrayed rod bundle cooled with air. The fully developed value of the heat transfer coefficient was found to be within 12.5 percent of the Dittus-Boelter equation (with heating)

$$\mathrm{Nu} = 0.023\mathrm{Re}^{0.8}\mathrm{Pr}^{0.4} \tag{16}$$

In the present investigation, the Prandtl number is held constant; therefore, the hydrodynamically fully developed value of heat transfer is a function of Reynolds number only and should be independent of the support grid design used. Results from grids A through H tested in the present study indicate that the support grid design does not affect the hydrodynamically fully developed value of heat transfer.

For each Reynolds number, the measured hydrodynamically fully developed heat transfer coefficients for all of the support grid designs (A-H) are averaged to determine the hydrodynamically fully developed value of heat transfer for the rod bundle. For $\mathrm{Re}_{Dh}=28{,}000$, the hydrodynamically fully developed value of heat transfer is 11,256 $\mathrm{W/m^2K}$ with a standard deviation of $\pm 380\ \mathrm{W/m^2K}$ (± 2.0 percent). For $\mathrm{Re}_{Dh}=42{,}000$, the hydrodynamically fully developed value of heat transfer is 15,034 $\mathrm{W/m^2K}$ with a standard deviation of $\pm 603\ \mathrm{W/m^2K}$ (± 2.7 percent). The measured hydrodynamically fully developed values of heat transfer are 22 percent higher than the Dittus-Boelter equation (Eq. 16) for $\mathrm{Re}_{Dh}=28{,}000$ and 18 percent higher than the Dittus-Boelter equation for $\mathrm{Re}_{Dh}=42{,}000$.

The local Nusselt numbers downstream of standard support grid designs are shown in Figs. 7 and 8. Figure 7 presents the Nusselt numbers downstream of standard support grids A and G which have a grid blockage ratio, ε (and ε_s), of 0.20. Results for $\mathrm{Re}_{Dh}=28{,}000$ and $\mathrm{Re}_{Dh}=42{,}000$ are shown. In addition, error bars representing the experimental uncertainty of ± 4.8 percent are shown. As discussed in the pressure drop results section, Grid G has a larger grid loss coefficient than grid A due to increased friction drag. For each Reynolds number, the local Nusselt number development downstream of grid A and grid G are essentially identical within the uncertainty of the experimental measurements, which suggests that the local Nusselt numbers are not a strong function of pressure drop resulting from skin friction. For $\mathrm{Re}_{Dh}=28{,}000$, the Nusselt number decays from approximately $\mathrm{Nu}=245$ just downstream of the support grid to the hydrodynamically fully developed value of $\mathrm{Nu}=220$ by an axial location of approximately six hydraulic diameters downstream of the support grid. For $\mathrm{Re}_{Dh}=42{,}000$, the Nusselt number decays from a value of approximately $\mathrm{Nu}=320$ just downstream of the support grid to the hydrodynamically fully developed value of $\mathrm{Nu}=294$ by approximately six hydraulic diameters downstream of the support grid. Exponential curve fits of the data obtained for the standard support grid designs (Grids A, E, and G) indicate appropriate values for the correlation of heat transfer downstream of a standard support grid design, Eq. (12), are $C_1=6.5$ and $\alpha=0.8$. The correlation for the local Nusselt number downstream of a standard support grid

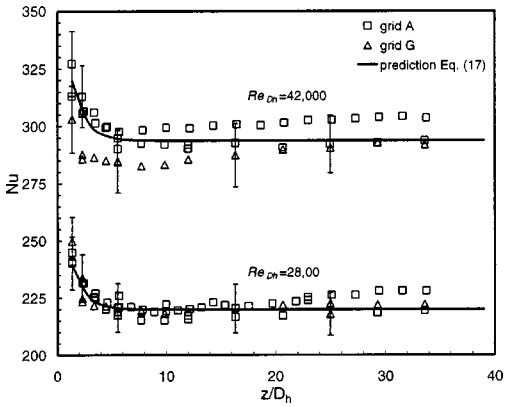

Fig. 7 Nusselt numbers for standard grids A and G $\varepsilon=\varepsilon_s=0.20$

$$\mathrm{Nu} = \mathrm{Nu}_0(1 + 6.5\varepsilon_s^2 e^{-0.8z/D_h}) \tag{17}$$

is included in Fig. 7. This correlation can also be expressed in normalized form as

$$\frac{\mathrm{Nu}}{\mathrm{Nu}_0} = 1 + 6.5\varepsilon_s^2 e^{-0.8z/D_h} \tag{18}$$

These correlations are valid for axial locations between $z/D_h = 1.4$ to $z/D_h = 33.6$.

Figure 8 presents the Nusselt numbers downstream of the standard support grid E which has a grid blockage ratio of 0.14. Error bars representing the experimental uncertainty of ± 4.8 percent are included. In addition, the correlation for local Nusselt numbers downstream of a standard support grid design, Eq. (17), is shown. The local Nusselt numbers downstream of grid E are accurately predicted by the correlation. For all three of the standard support grid designs, grids A, G, and E, there is an initial heat transfer enhancement just downstream of the grid which is caused prima-

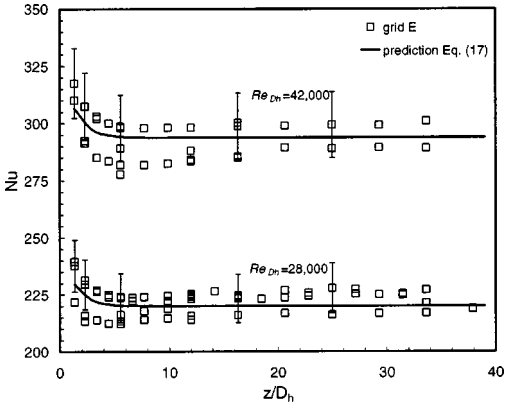

Fig. 8 Nusselt numbers for standard grid E $\varepsilon=\varepsilon_s=0.14$

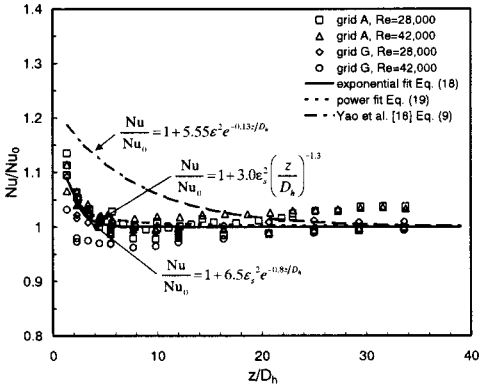

Fig. 9 Nusselt number normalized by hydrodynamically fully developed Nusselt number for standard grids A and G, $\varepsilon = \varepsilon_s = 0.20$

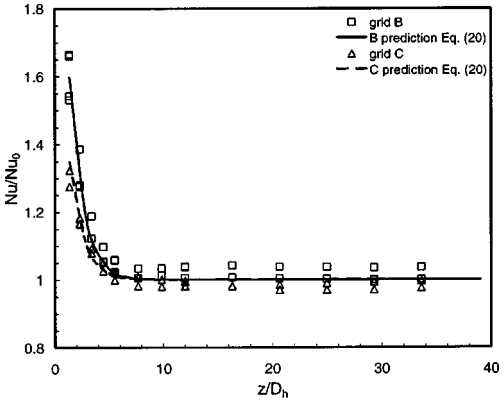

Fig. 10 Nusselt number normalized by hydrodynamically fully developed Nusselt number for support grids with disk blockage, grids B and C, $Re_{Dh}=28{,}000$, $\varepsilon_s = 0.20$

rily by the increased flow velocity created by the grid blockage. This initial heat transfer enhancement decays to the hydrodynamically fully developed value of heat transfer by approximately six hydraulic diameters downstream of the grid. This indicates that the hydrodynamic flow field is not affected by the presence of the standard support grids beyond six hydraulic diameters downstream of the grid.

Normalized Nusselt numbers for the standard support grid designs A and G are shown in Fig. 9. Reynolds numbers of 28,000 and 42,000 are included for each grid design. The local normalized Nusselt numbers for the standard support grid designs show no Reynolds number dependence over the range of Reynolds numbers tested. Figure 9 presents both of the heat transfer correlations for normalized Nusselt number downstream of standard support grid design, the exponential decay correlation, Eq. (18), and the power fit correlation

$$\frac{\mathrm{Nu}}{\mathrm{Nu}_0} = 1 + 3.0\varepsilon_s^2 \left(\frac{z}{D_h} \right)^{-1.3} \tag{19}$$

Equation (19) is valid from a range of $z/D_h = 1.4$ to $z/D_h = 33.6$. The correlation for standard support grid designs presented by Yao et al. [18], Eq. (9), is also shown in Fig. 9. The heat transfer correlations, Eq. (18) and Eq. (9), are of the same basic form; however, the values for the coefficients and decay rates are not the same. As shown in Fig. 9, the correlation from Yao et al. [18] captures the heat transfer just downstream of the grid reasonably well; however, the decay rate of the correlation does not match well with the current experimental data. The Yao et al. [18] correlation was developed based on heat transfer measurements from rod bundles with fully heated rods cooled by gas (air or helium), while the correlation developed in the present investigation, Eq. (18) was developed based on measurements in water using a heated copper sensor and otherwise isothermal conditions. The variation in Prandtl number as well as the different thermal boundary conditions contributes to the different decay rates between the two correlations.

As can be seen in Fig. 9, both the power law correlation, Eq. (19), and the exponential decay correlation, Eq. (18), accurately capture the heat transfer behavior downstream of the standard support grid designs. The value of the decay rate for the power fit correlation, $\lambda = -1.3$, is used to gain additional insight into the measurements obtained using the heated copper sensor with an unheated starting length. Yang and Chung [3] report that, in general, the correlation for the turbulence intensity decay downstream of a support grid in a rod bundle is of the same form as that for grid generated turbulence. Comte-Bellot and Corrsin [24] report the decay of turbulence intensity downstream of grid generated turbulence as proportional to $(z/M)^{-1.3}$, where M is the mesh size of the grid. The decay rate of heat transfer downstream of standard support grid designs, as measured using the heated copper sensor in the present study, is the same as the decay rate of grid generated turbulence. For the current measurement technique, the primary mechanism for the decay of heat transfer downstream of the support grid from $z/D_h = 1.4$ to $z/D_h = 6.0$ is consistent with the decay of turbulence intensity. The decay rate of $\lambda = -1.3$ accurately captures the initial decay of the heat transfer data for all of the support grid designs tested.

Normalized heat transfer results for the support grid designs with disk blockages and split-vane pair flow-enhancing features, grids B, C, D, F, and H, are used to determine the coefficients in the heat transfer correlation for support grid designs with flow-enhancing features, Eq. (14). Exponential curve fits of the experimental data indicate that appropriate coefficients for the correlation are $C_1 = 6.5$, $C_2 = 3.2$, and $\alpha = 0.8$. Based on the present experimental heat transfer measurements, the correlation for heat transfer downstream of support grids with flow-enhancing features is

$$\frac{\mathrm{Nu}}{\mathrm{Nu}_0} = 1 + \left[6.5\varepsilon_s^2 + 3.2 \left(\frac{K_{\mathrm{feat}}}{K_g} \right) \right] e^{-0.8z/D_h}. \tag{20}$$

This correlation represents a superposition of the heat transfer augmentation caused by a standard support grid strap (Eq. 18) and the heat transfer augmentation caused by the flow-enhancing features. This correlation is valid from a range of $z/D_h = 1.4$ to $z/D_h = 33.6$. The local normalized Nusselt numbers obtained at a Reynolds number of 28,000 for grids B and C are shown in Fig. 10. Grids B and C have normalized grid feature loss coefficients (K_{feat}/K_g) of 0.47 and 0.24, respectively. The correlation developed for the heat transfer downstream of support grids with flow-enhancing features, Eq. (20), is shown in the figure for each data series. The correlation accurately predicts the heat transfer just downstream of the support grid design for both of the grid designs. In addition, the decay of the local normalized Nusselt numbers is well predicted.

Figure 11 presents the local Nusselt numbers normalized by the hydrodynamically fully developed Nusselt number for grid F, a split-vane pair grid design with a normalized feature loss coefficient, K_{feat}/K_g, of 0.15. Results for Reynolds numbers of 28,000 and 42,000 are presented. The correlation developed in Yao et al. [18], Eq. (11), for the heat transfer augmentation downstream of a split-vane pair grid design is shown in the figure. In this correlation, the blockage ratio, ε, includes the blockage of both the base strap and split-vane pairs. As shown in Fig. 11, the Yao et al. [18] correlation does not capture the data measured downstream of the split-vane pair grid in the present investigation. This correlation overpredicts the initial heat transfer enhancement by approxi-

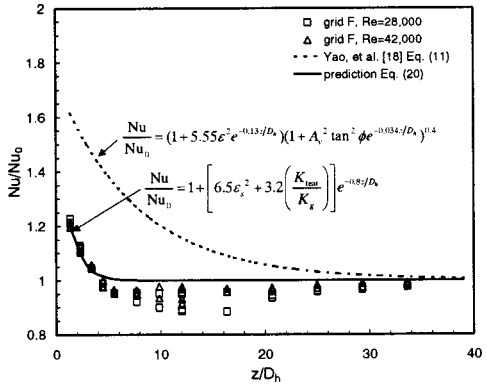

Fig. 11 Nusselt number normalized by hydrodynamically fully developed Nusselt number for grid F, $\varepsilon_s=0.14$, $K_{feat}/K_v=0.15$

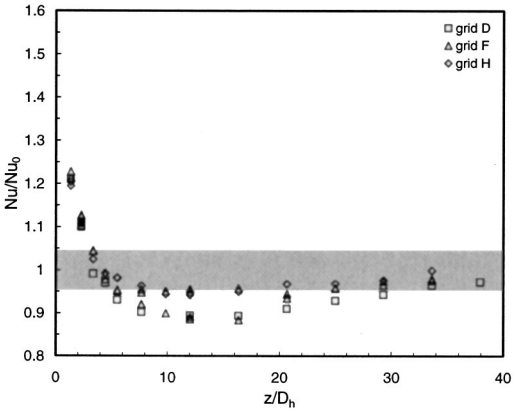

Fig. 12 Nusselt number normalized by hydrodynamically fully developed Nusselt number for grids D, F, H, $Re_{Dh}=28{,}000$

mately 30 percent. In addition, the decay rate of the correlation differs from the decay rate of the normalized Nusselt numbers obtained using the heated copper sensor of the present study. It should be noted that the Yao correlation compared well to bundle data with fully heated rods. Possible explanations for the different decay rates between the experimental data and the Yao et al. [18] correlation were discussed previously for the standard grid designs. The difference in the Prandtl number and thermal boundary conditions as a result of the locally heated rod section in the present test could also contribute to the difference in initial heat transfer enhancement.

Of significant importance is a comparison of measured heat transfer coefficients between grids with different blockage ratios. At an axial distance of $z/D_h=1.4$ just downstream of the grid, the contribution of the swirling flow to the local Nusselt number in the Yao et al. [18] correlation, Eq. (11), is negligible. Therefore, a comparison of the heat transfer predicted using the Yao et al. [18] correlation, Eq. (9), applied to different grid designs may be performed. It should be noted, however, that this correlation was developed based on data obtained downstream of standard support grid designs. A comparison of the initial heat transfer enhancement obtained from Eq. (9) for grids B, C, and F results in a predicted value for grid F that falls between the values of B and C, which are the disc grid and alternating disc grid, respectively. However, data in Figs. 10 and 11 show that the initial heat transfer enhancement for grid F is actually below that of both grids B and C. This indicates that the blockage ratio alone (used as the correlating parameter in the Yao et al. [18] correlation) may not be an appropriate parameter for comparing the heat transfer enhancement from support grid designs with fundamentally different flow-enhancing feature designs.

The new correlation developed for flows downstream of a support grid design with flow enhancing features, Eq. (20), is also shown in Fig. 11. A comparison of this correlation with the experimental results indicates that the initial heat transfer enhancement downstream of a support grid with split-vane pairs is accurately represented using the feature loss coefficient and the grid strap blockage ratio. Incorporating the effect of streamlined features by implementing the feature loss coefficient provides improved initial heat transfer results over predictions based solely on grid blockage. Initially, the decay of the local heat transfer, between $z/D_h=1.35$ and $z/D_h=6.0$ is well predicted by the correlation equation. However, at axial locations between approximately 6 and 25 hydraulic diameters downstream of the support grid, there is a decrease in the local heat transfer below that of the hydrodynamically fully developed value. This trend of decreased heat transfer values over certain axial regions appears in other split-vane pair grid designs and will be discussed in more detail.

The normalized Nusselt numbers downstream of the split-vane pair grid designs, grids D, F, and H, are shown in Figs. 12 and 13 for Reynolds numbers of 28,000 and 42,000, respectively. The shaded areas in both Figs. 12 and 13 represent the expected range of values for the measured hydrodynamically fully developed value of heat transfer based on the experimental uncertainty of $\pm 4.8\%$. As shown in Fig. 12, the normalized Nusselt numbers clearly fall below the hydrodynamically fully developed values for both grid D and grid F from between approximately 6 and 25 hydraulic diameters downstream of the support grid. Mills [25] documented decreased regions of the local heat transfer for a pipe flow with a bellmouth entrance. The decreased region of heat transfer in the pipe flow documented by Mills [25] was attributed to boundary layer transition and growth for the flow downstream of the bellmouth entrance. The decreased region of heat transfer in the present study, which has been observed only downstream of the split-vane pair grid designs, indicates that the hydrodynamic conditions created by the swirling flow have adversely affected the local heat transfer. Axial velocity deficits or a migration of the swirling flow structure from the center of the rod bundle subchannel towards one of the rods are possible causes for the decreased region of heat transfer in some of the split-vane pair grid designs. Vortex migration of a swirling flow in a rod bundle subchannel has been previously documented in McClusky et al. [6]. At a Reynolds number of 42,000, as shown in Fig. 13, there is a similar region of decreased heat transfer. However, the amount of decrease below the hydrodynamically fully developed value is less for $Re_{Dh}=42{,}000$ compared to $Re_{Dh}=28{,}000$. This indicates that the hydrodynamic disturbances causing the decreased region of

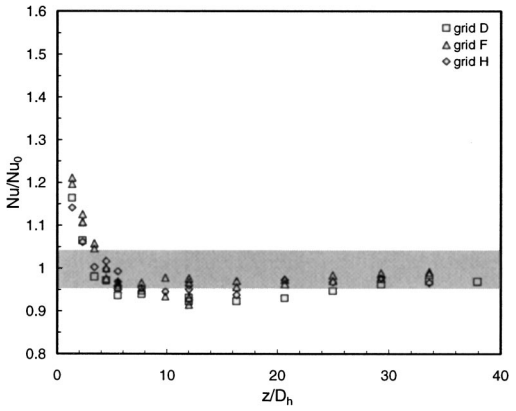

Fig. 13 Nusselt number normalized by hydrodynamically fully developed Nusselt number for grids D, F, H, $Re_{Dh}=42{,}000$

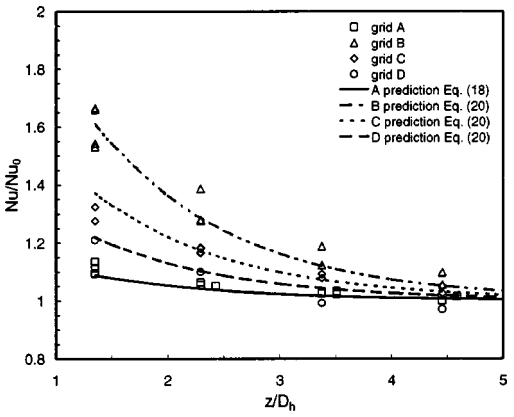

Fig. 14 Nusselt number normalized by hydrodynamically fully developed Nusselt number for grids A, B, C, and D, Re_{Dh} =28,000, ε_s=0.20

heat transfer downstream of support grids with split-vane pair features may be lessened or not present for higher Reynolds number operating conditions.

The local normalized Nusselt numbers for the first five hydraulic diameters downstream of grids A, B, C, and D are shown in Fig. 14. Grids A, B, C, and D all have a base strap design of grid A. Therefore, this figure provides a comparison between the heat transfer performance of a standard grid and grids with flow-enhancing features. The correlation for flow downstream of a support grid with flow-enhancing features, Eq. (20), is included in Fig. 14. For the standard support grid design, grid A, the normalized feature loss coefficient is equal to zero, therefore Eq. (20) reduces to Eq. (18), which is the correlation developed for flow downstream of a standard support grid. As shown in Fig. 14, grid B has the highest heat transfer just downstream of the grid. Grid C has the second highest heat transfer just downstream of the support grid. The split-vane pair design, grid D, has a heat transfer performance below that of grids B and C but above that of the standard grid design, grid A. Results indicate that the pressure losses created by the flow-enhancing features are a direct indicator of the local, single-phase heat transfer performance of the support grid design.

The heat transfer measurement technique implemented in the present study incorporates simplifications to the in-core operating conditions of a pressurized water reactor. Specifically, only a section of a single rod in the bundle is heated. Implementing the measurement technique has provided documentation of the following:

1) pressure drop versus initial heat transfer enhancement for different grid designs
2) effect of friction pressure losses versus form pressure losses on heat transfer enhancement
3) comparison of different flow enhancing features
4) evaluation of existing heat transfer correlations in literature for support grids with flow enhancing features
5) development of new correlation to predict heat transfer for various support grid designs based on pressure losses

Conclusions

Single-phase heat transfer and pressure drop in a rod bundle downstream of support grid designs with and without flow-enhancing features have been investigated in the present study for Reynolds numbers of 28,000 and 42,000. The locally averaged heat transfer downstream of eight different support grid designs has been documented using a heated copper sensor. Results indicate that pressure drop measurements can be used to develop general heat transfer correlations for the local heat transfer downstream of support grid designs. A correlation for the heat transfer in a rod bundle downstream of a standard support grid design based on the grid blockage ratio has been developed. In addition, a correlation for the local heat transfer downstream of support grid designs with flow-enhancing features has been developed based on the grid strap blockage ratio and the normalized flow-enhancing feature loss coefficient. The flow-enhancing features investigated in the present study include blunt disk blockages and split-vane pairs. Since the correlation is based on pressure drop measurements, it is expected to be applicable to a general support grid design with attached flow-enhancing features. Future work in the area of local heat transfer measurements in a rod bundle includes implementing a fully heated rod bundle to document the effect of a different thermal boundary condition on the local heat transfer development. In addition, documenting the effect of Prandtl number on the downstream development of the heat transfer as well as measurements at higher Reynolds numbers are needed.

Acknowledgments

This material is based in part upon work supported under a National Science Foundation Graduate Research Fellowship to the first author.

Nomenclature

A_s = surface area
A_f = open flow area in rod bundle
A_{sc} = area of subchannel
A_{sp} = projected area of spacer grid
A_v = projected area of vanes
C = coefficient in heat transfer correlations
D = rod diameter
D_e = hydraulic diameter of rod bundle, $=4A_f/P_{rb}$
D_h = hydraulic diameter of typical subchannel, $=4A_{sc}/P_{sc}$
f = friction factor
h = heat transfer coefficient
k = thermal conductivity
K_{feat} = feature loss coefficient
K_g = grid loss coefficient
K_s = loss coefficient of base strap design
K_v = modified loss coefficient
Nu = Nusselt number, $=hD/k$
Nu_0 = fully-developed Nusselt number
P = rod pitch
Pr = Prandtl number
P_{rb} = wetted perimeter of rod bundle
P_{sc} = wetted perimeter of subchannel
q = convective heat transfer
Re = Reynolds number, $=VD/\nu$
S_{yx} = Standard error of fit of calibration equation
$t_{\nu,95}$ = Student t distribution (95%)
T_m = bulk fluid temperature
T_s = surface temperature
u = contribution to uncertainty
V = velocity
z = axial coordinate direction
α = coefficient in Eq. (12, 14)
β_1, β_2 = coefficients in Eq. (10)
C_1 = coefficient in Eq. (12, 14)
C_2 = coefficient in Eq. (14)
Δp_{grid} = pressure drop across grid span
Δp_g = grid pressure drop
Δp_{rod} = pressure drop across rod span
Δp_{span} = pressure drop across complete span between two grids
Δz_{grid} = axial distance across grid span between pressure taps = 302 mm

Δz_{rod} = axial distance across rod span between pressure taps = 206 mm
ε = grid blockage ratio, $= A_{sp}/A_f$
ε_s = blockage ratio of base grid strap with no flow-enhancing features
γ = coefficient in Eq. (10)
κ = coefficient in Eq. (13)
λ = coefficient in Eq. (13)
ν = kinematic viscosity
ρ = density
ϕ = vane angle

References

[1] Rehme, K., 1973, "Pressure Drop Correlations for Fuel Element Spacers," Nucl. Technol., **17**, pp. 15–23.
[2] Herer, C., 1991, "3D Flow Measurements in Nuclear Fuel Rod Bundles Using Laser Doppler Velocimetry," *ASME Fluid Measurement and Instrumentation Forum*, **108**, ASME International, New York, pp. 95–99.
[3] Yang, S. K., and Chung, M. K., 1998, "Turbulent Flow Through Spacer Grids in Rod Bundles," ASME J. Fluids Eng., **120**, pp. 786–791.
[4] Karoutas, Z., Gu, C. Y., and Scholin, B., 1995, "3-D Flow Analyses for Design of Nuclear Fuel Spacer," *Proceedings of the 7th International Meeting on Nuclear Reactor Thermal-Hydraulics NURETH-7*, **1**, pp. 3153–3174.
[5] In, K. W., 2001, "Numerical Study of Coolant Mixing Caused by the Flow Deflectors in a Nuclear Fuel Bundle," Nucl. Technol., **134**, pp. 187–195.
[6] McClusky, H. L., Holloway, M. V., Beasley, D. E., and Conner, M. E., 2002, "Development of Swirling Flow in a Rod Bundle Subchannel," ASME J. Fluids Eng., **124**, pp. 747–755.
[7] McClusky, H. L., Holloway, M. V., Conover, T. A., Beasley, D. E., Conner, M. E., and Smith, L. D., III, 2003, "Mapping of the Lateral Flow Field in Typical Subchannels of a Support Grid with Vanes," ASME J. Fluids Eng., **125**(6), pp. 987–996.
[8] Saffman, P. G., 1992, *Vortex Dynamics*, Cambridge University Press.
[9] de Crecy, F., 1994, "The Effect of Grid Assembly Mixing Vanes on Critical Heat Flux Values and Azimuthal Location in Fuel Assemblies," Nucl. Eng. Des., **149**, pp. 233–241.
[10] Blum, H. A., and Oliver, L. R., 1966, "Heat Transfer in a Decaying Vortex System," *Proceedings of the 1966 ASME HTD Winter Annual Meeting*, **62**, pp. 1–8.
[11] Hay, N., and West, P. D., 1975, "Heat Transfer in Free Swirling Flow in a Pipe," ASME J. Heat Transfer, **97**, Series C, No. 3, pp. 411–416.
[12] Chang, F., and Dhir, V. K., 1995, "Mechanisms of Heat Transfer Enhancement and Slow Decay of Swirl in Tubes Using Tangential Injection," Int. J. Heat Fluid Flow, **16**, pp. 78–87.
[13] Figliola, R. S., and Beasley, D. E., 1998, *Theory and Design for Mechanical Measurements, 3rd Edition*, John Wiley & Sons.
[14] Armfield, M. V., 2001, "Effects of Support Grid Design on Local, Single-Phase Turbulent Heat Transfer in Rod Bundles," Master's Thesis, Clemson University, Clemson, SC, USA.
[15] Armfield, M. V., Langford, H. M., Beasley, D. E., and Conner, M. E., 2000, "Average Heat Transfer Coefficient Measurements in a Fuel Bundle: Method Development," *Proceedings of the ASME Heat Transfer Division*, HTD-366-2, ASME International, New York, pp. 163–170.
[16] Rehme, K., 1976, "Pressure Drop of Spacer Grids in Smooth and Roughened Rod Bundles," Nucl. Technol., **33**, pp. 314–317.
[17] Marek, J., and Rehme, K., 1979, "Heat Transfer in Smooth and Roughened Rod Bundles Near Spacer Grids," *Presented at the ASME Winter Annual Meeting Dec 2–7*, 1979, pp. 163–170.
[18] Yao, S. C., Hochreiter, L. E., and Leech, W. J., 1982, "Heat-Transfer Augmentation in Rod Bundles Near Grid Spacers," ASME J. Heat Transfer, **104**, pp. 76–81.
[19] Kidd, G. J., Hoffman, H. W., and Stelzman, W. J., 1968, "The Temperature Structure and Heat Transfer Characteristics of an Electrically Heated Model of a Seven-Rod Cluster Fuel Element," ASME Paper 68-WA/HT-33.
[20] Kreith, F., and Sonju, O. K., 1965, "The Decay of a Turbulent Swirl in a Pipe," J. Fluid Mech., **22**, pp. 257–271.
[21] Armfield, M. V., Langford, H. M., Beasley, D. E., and Conner, M. E., 2001, "Single-Phase Turbulent Rod Bundle Heat Transfer," *Proceedings of 2001 ASME International Mechanical Engineering and Exposition*, IMECE2001/HTD-24116, pp. 1–8.
[22] Guellouz, M. S., and Tavoularis, S., 1992, "Heat Transfer in Rod Bundle Subchannels with Varying Rod-Wall Proximity," Nucl. Eng. Des., **132**, pp. 351–366.
[23] Dingee, D. A., and Chastain, J. W., 1956, "Heat Transfer from Parallel Rods in Axial Flow," *Reactor Heat Transfer Conference of 1956*, TID-7529 (Pt. 1), Book 2, pp. 462–501.
[24] Comte-Bellot, G., and Corrsin, S., 1966, "The Use of a Contraction to Improve the Isotropy of Grid-Generated Turbulence," J. Fluid Mech., **25**, pp. 657–682.
[25] Mills, A. F., 1962, "Experimental Investigation of Turbulent Heat Transfer in the Entrance Region of a Circular Conduit," J. Mech. Eng. Sci. **4**, No. 1 pp. 63–77.

Laminar Forced Convection Heat Transfer in the Combined Entry Region of Non-Circular Ducts

Y. S. Muzychka
Asst. Prof.
Faculty of Engineering and Applied Science,
Memorial University of Newfoundland,
St. John's, NF, Canada, A1B 3X5

M. M. Yovanovich
Distinguished Professor Emeritus,
Fellow ASME
Department of Mechanical Engineering,
University of Waterloo,
Waterloo, ON, Canada, N2L 3G1

A new model for predicting Nusselt numbers in the combined entrance region of non-circular ducts and channels is developed. This model predicts both local and average Nusselt numbers and is valid for both isothermal and isoflux boundary conditions. The model is developed using the asymptotic results for convection from a flat plate, thermally developing flows in non-circular ducts, and fully developed flow in non-circular ducts. Through the use of a novel characteristic length scale, the square root of cross-sectional area, the effect of duct shape on Nusselt number is minimized. Comparisons are made with several existing models for the circular tube and parallel plate channel and with numerical data for several non-circular ducts. Agreement between the proposed model and numerical data is within ± 15 percent *or better for most duct shapes.*
[DOI: 10.1115/1.1643752]

Keywords: Forced Convection, Heat Transfer, Heat Exchangers, Internal, Laminar, Modeling

Introduction

Heat transfer in the combined entry region of non-circular ducts is of particular interest in the design of compact heat exchangers. In these applications passages are generally short and usually composed of cross-sections such as triangular or rectangular geometries in addition to the circular tube or parallel plate channel. Also, due to the wide range of applications, fluid Prandtl numbers usually vary between $0.1<\mathrm{Pr}<1000$, which covers a wide range of fluids encompassing gases and highly viscous liquids such as automotive oils.

A review of the literature reveals that the only models available for predicting heat transfer in the combined entry region are those of Churchill and Ozoe [1,2] for the circular duct and Baehr and Stephan [3] and Stephan [4] for the circular duct and parallel plate channel. Recently, Garimella et al. [5] developed empirical expressions for the rectangular channel, while numerical data for polygonal ducts were obtained by Asako et al. [6]. Additional data for the rectangular, circular, triangular, and parallel plate channel are available in Shah and London [7], Kakac et al. [8], Rohsenow et al. [9], and Kakac and Yener [10]. A complete review of design correlations is presented later. In addition, data are reported for the circular annulus in [7]. The models reported in this paper are applicable to the annulus, but only for the special cases where both surfaces of the annulus are at the same wall temperature or wall flux condition.

The present work will develop a new model using the Churchill and Usagi [11] asymptotic correlation method. In this method, the special asymptotic solutions of the combined entry problem are used to develop a more general model for predicting heat transfer coefficients in non-circular ducts.

Governing Equations

In order to fully appreciate the complexity of the combined entry problem, the governing equations for each of the three fundamental forced covection problems are reviewed. These are as follows: combined entry or simultaneously developing flow, the thermal entrance problem or Graetz flow, and thermally fully developed flow.

Contributed by the Heat Transfer Division for publication in the JOURNAL OF HEAT TRANSFER. Manuscript received by the Heat Transfer Division March 14, 2003; revision received October 2, 2003. Associate Editor: N. K. Anand.

Combined Entry, $0<\mathrm{Pr}<\infty$. In cartesian coordinates the governing equations for an incompressible and constant property fluid in the combined thermal entrance region are [7]:

$$\frac{\partial u}{\partial x}+\frac{\partial v}{\partial y}+\frac{\partial w}{\partial z}=0 \tag{1}$$

$$u\frac{\partial w}{\partial x}+v\frac{\partial w}{\partial y}+w\frac{\partial w}{\partial z}=-\frac{1}{\rho}\frac{dp}{dz}+\nu\left(\frac{\partial^2 w}{\partial x^2}+\frac{\partial^2 w}{\partial y^2}\right) \tag{2}$$

$$u\frac{\partial T}{\partial x}+v\frac{\partial T}{\partial y}+w\frac{\partial T}{\partial z}=\alpha\left(\frac{\partial^2 T}{\partial x^2}+\frac{\partial^2 T}{\partial y^2}\right) \tag{3}$$

The pressure gradient may be written

$$-\frac{1}{\rho}\frac{dp}{dz}=w_c\frac{dw_c}{dz} \tag{4}$$

where $w_c=w_c(z)$ is the velocity of the inviscid core. The above equations are subject to the no slip condition $w_{\mathrm{wall}}=0$, the boundedness condition $w(x,y,z)\neq\infty$ along the duct axis, and the initial condition $w(x,y,0)=\overline{w}$. In cartesian coordinates, one additional equation is required to relate the two components of transverse velocity. To date, very few solutions to this set of equations, Eqs. (1–4), have been obtained.

Fully Developed Hydrodynamic Flow, $\mathrm{Pr}\rightarrow\infty$. In cartesian coordinates the governing equation for fully developed laminar flow in a constant cross-sectional area duct is

$$\frac{\partial^2 w}{\partial x^2}+\frac{\partial^2 w}{\partial y^2}=\frac{1}{\mu}\frac{dp}{dz} \tag{5}$$

which represents a balance between the pressure and viscous forces.

If the velocity field develops quickly, then the energy equation in cartesian coordinates for thermally developing laminar flow in ducts of constant cross-sectional area is given by

$$\frac{\partial^2 T}{\partial x^2}+\frac{\partial^2 T}{\partial y^2}=\frac{w}{\alpha}\frac{\partial T}{\partial z} \tag{6}$$

where $w=w(x,y)$ is the fully developed velocity profile. This is the classic Graetz problem for a non-circular duct.

When the flow becomes thermally fully developed the energy equation may be written in terms of the mixing cup temperature $T_m(z)$, Kays and Crawford [12]

$$\frac{\partial^2 T}{\partial x^2}+\frac{\partial^2 T}{\partial y^2}=\frac{w}{\alpha}\frac{dT_m}{dz} \tag{7}$$

for the uniform wall flux (UWF) condition, and

$$\frac{\partial^2 T}{\partial x^2}+\frac{\partial^2 T}{\partial y^2}=\frac{w}{\alpha}\left(\frac{T_w-T}{T_w-T_m}\right)\frac{dT_m}{dz} \tag{8}$$

for the uniform wall temperature (UWT) condition, where

$$T_m(z)=\frac{1}{\overline{w}A}\int\int_A wT\,dA \tag{9}$$

Later, a model is developed which utilizes a number of limiting approximate solutions to these equations. These are as follows: fully developed flow, thermally developing flow, and laminar boundary layer flow.

A dimensionless heat transfer coefficient or Nusselt number may be defined as

$$\mathrm{Nu}_{\mathcal{L}}=\frac{\overline{q}_w(z)\,\mathcal{L}}{k(\overline{T}_w(z)-T_m(z))}=\frac{h\mathcal{L}}{k} \tag{10}$$

where $T_m(z)$ is the bulk fluid temperature, $\overline{T}_w(z)$ is the average wall temperature, and $\overline{q}_w(z)$ is the average wall heat flux at any point along the duct. For UWT, T_w = Constant and for UWF, q_w = Constant.

In terms of the solutions to Eqs. (1–4), the Nusselt number, $\mathrm{Nu}_{\mathcal{L}}$, may be defined as follows:

$$\mathrm{Nu}_{\mathcal{L}}=\mathcal{L}\frac{\frac{1}{P}\oint -\left.\frac{\partial T}{\partial n}\right|_w ds}{\frac{1}{P}\oint T_w\,ds-\frac{1}{\overline{w}A}\int\int_A w\,T\,dA} \tag{11}$$

where $\partial T/\partial n$ represents the temperature gradient at the duct wall with respect to an inward directed normal, ds is the differential of arc length, $\mathcal{L}$ is an arbitrary characteristic length scale to be determined later, A is the cross-sectional area and P is the wetted perimeter of the duct. Traditionally, $\mathcal{L}=4A/P$, the hydraulic diameter of the duct. Finally, the flow length averaged Nusselt number is related to the local Nusselt number through

$$\overline{\mathrm{Nu}}=\frac{1}{z}\int_0^z \mathrm{Nu}(z)\,dz \tag{12}$$

Literature Review

A review of the literature reveals that very little work has been done in the area of modeling heat transfer in the combined entrance region of non-circular ducts. Only the circular duct and parallel plate channel have models or correlations which cover a wide range of Prandtl number and dimensionless duct length. Even for these common channel shapes, the expressions are only valid for particular boundary conditions and flow conditions.

Stephan, see [3], developed a correlation for the circular tube which is valid for all values of the dimensionless duct length z^* and for $0.1<\mathrm{Pr}<\infty$.

The Stephan correlation (see [3]) has the following form:

$$\mathrm{Nu}_{m,T}=\frac{\mathrm{Nu}(\mathrm{Pr}\to\infty)}{\tanh(2.432\mathrm{Pr}^{1/6}(z^*)^{1/6})} \tag{13}$$

where

$$\mathrm{Nu}(\mathrm{Pr}\to\infty)=\frac{3.657}{\tanh(2.264(z^*)^{1/3}+1.7(z^*)^{2/3})}+\frac{0.0499}{z^*}\tanh(z^*) \tag{14}$$

A solution for the circular tube based upon the Karman-Pohlhausen integral method was first developed by Kays [13] and later corrected by Kreith [14]. It is given by the following expression which is only valid for small values of the parameter z^*:

$$\mathrm{Nu}_{m,T}=\frac{1}{4z^*}\ln\left(\frac{1}{1-2.65(z^*)^{1/2}\mathrm{Pr}^{-1/6}}\right) \tag{15}$$

which is valid for $\mathrm{Pr}>2$ and $z^*<0.001$.

For the case of a parallel plate channel, Stephan [4] correlated numerical results in the following way:

$$\mathrm{Nu}_{m,T}=7.55+\frac{0.024(z^*)^{-1.14}}{1+0.0358\mathrm{Pr}^{0.17}(z^*)^{-0.64}} \tag{16}$$

which is valid for $0.1<\mathrm{Pr}<1000$. Shah and Bhatti, see Ref. [8], obtained the following expression for the local Nusselt number from the correlation developed by Stephan [4]

$$\mathrm{Nu}_{z,T}=7.55+\frac{0.024(z^*)^{-1.14}(0.0179\mathrm{Pr}^{0.17}(z^*)^{-0.64}-0.14)}{(1+0.0358\mathrm{Pr}^{0.17}(z^*)^{-0.64})^2} \tag{17}$$

Sparrow [15] using the Karman-Pohlhausen integral method, obtained the following approximate analytical expression for the Nusselt number

$$\mathrm{Nu}_{m,T}=\frac{0.664}{\sqrt{z^*}\mathrm{Pr}^{1/6}}(1+6.27(\mathrm{Prz}^*)^{4/9})^{1/2} \tag{18}$$

which is valid for $\mathrm{Pr}>2$ and $z^*<0.001$.

Churchill and Ozoe [1,2] developed Eqs. (19,20), for the local Nusselt number for the UWF and UWT conditions, where $\mathrm{Gz}=\pi/(4z^*)$ is the Graetz number, in the combined entrance region of a circular duct. These models were developed using the asymptotic correlation method of Churchill and Usagi [11] and are valid for all Prandtl numbers $0<\mathrm{Pr}<\infty$, but only for the circular duct.

$$\frac{\mathrm{Nu}_{z,T}+1.7}{5.357[1+(\mathrm{Gz}/97)^{8/9}]^{3/8}}=\left[1+\left(\frac{\mathrm{Gz}/71}{[1+(\mathrm{Pr}/0.0468)^{2/3}]^{1/2}[1+(\mathrm{Gz}/97)^{8/9}]^{3/4}}\right)^{4/3}\right]^{3/8} \tag{19}$$

$$\frac{\mathrm{Nu}_{z,H}+1}{5.364[1+(\mathrm{Gz}/55)^{10/9}]^{3/10}}=\left[1+\left(\frac{\mathrm{Gz}/28.8}{[1+(\mathrm{Pr}/0.0207)^{2/3}]^{1/2}[1+(\mathrm{Gz}/55)^{10/9}]^{3/5}}\right)^{5/3}\right]^{3/10} \tag{20}$$

In all of the above models, the characteristic length is $\mathcal{L}=D_h$. Later it will be shown that a more appropriate length scale should be used.

Only a limited set of numerical data are available for the combined entrance region. In addition to numerical data for the circular duct and the parallel plate channel for a range of Prandtl numbers, a small set of data are available for the rectangular and triangle ducts for $\mathrm{Pr}=0.72$. All of the available data and models for the combined entrance region are reviewed by Kakac and Yener [10].

Finally, numerical data were obtained by Asako et al. [6] for the polygonal ducts for a range of Prandtl numbers, while Garimella et al. [5] obtained empirical data for the rectangular channel in the laminar-transition-turbulent regions for a number of aspect ratios.

At present, no single model is available which can predict the data for both the circular duct or parallel plate channel. Further, no

correlating equations are available for any of the numerical data related to non-circular ducts. In the sections which follow, a new model is proposed which serves these needs.

Model Development

A model which is valid for most non-circular ducts will now be developed using an approach similar to that proposed by Churchill and Ozoe [1,2]. Churchill and Ozoe [1,2] developed a model for the circular duct which is valid for all Prandtl numbers over the entire range of dimensionless duct lengths, by combining a composite model for the Graetz problem with a composite model for laminar forced convection from a flat plate. With some additional modification, Churchill and Ozoe [1,2] were able to apply these models for all Prandtl numbers. The present approach is limited to the range $0.1<\mathrm{Pr}<\infty$, which is valid for most flows found in heat exchangers.

The model development will be presented in several steps. First, each characteristic region: fully developed flow ($L \gg L_h, L_t$), Graetz flow ($L \gg L_h, L \ll L_t$), and laminar boundary layer flow ($L \ll L_h, L_t$) will be examined in detail to show how each region is dealt with in non-circular ducts. Next a model is developed for a range of Prandtl numbers, duct lengths, thermal boundary condition, and Nusselt number type, i.e., local or average value. Finally, the model is compared with published data from numerous sources. Much of these data have been collected and organized by Shah and London [7]. Since much of the published data appears in graphical form in the original sources, tabulated values from [7] are used for comparison. In most cases these data were obtained from the original authors, when available.

Fully Developed Flow. The fully developed flow limit for both hydrodynamic and thermal problems has been addressed by Muzychka [16] and reported in Yovanovich and Muzychka [17] and Muzychka and Yovanovich [18,19]. Additional results appear in Muzychka and Yovanovich [20,21] and Yovanovich et al. [22]. These references [17–22] provide models for the classic Graetz problem and the hydrodynamic entrance problem for forced flow, and for natural convection in vertical ducts of non-circular cross-section. In addition, Refs. [20], [21] applied scaling principles to all of the fundamental internal flow problems.

An important result of Yovanovich and Muzychka [17] is that the characteristic length scale for non-circular ducts in laminar flows should not be the hydraulic diameter, but rather, the square root of the cross-sectional area of the duct. This conclusion was drawn from dimensional analysis performed on an arbitrarily shaped duct with validation provided by examination of the analytical and numerical data from the literature. Bejan [23] also arrived at the same conclusion using his constructal theory of organization in nature.

Yovanovich and Muzychka [17] showed that when the friction factor-Reynolds number product is based upon the square root of cross-sectional area, the vast number of data were reduced to a single curve which was merely a function of the aspect ratio of the duct or channel. They also showed that this curve was accurately represented by the first term of the exact series solution for the rectangular duct cross-section. This result is given by

$$f\,\mathrm{Re}_{\sqrt{A}} = \frac{12}{\sqrt{\epsilon}(1+\epsilon)\left[1-\dfrac{192\epsilon}{\pi^5}\tanh\left(\dfrac{\pi}{2\epsilon}\right)\right]} \tag{21}$$

For most rectangular channels it is sufficient to choose $0.01<\epsilon<1$, since the rectangular channel approaches the parallel plate for $\epsilon<0.01$. A plot of this model with data for many duct shapes is provided in Fig. 1. Figure 2 shows a broader comparison with several other non-circular ducts.

The aspect ratio in Figs. 1 and 2 is taken to be a measure of the slenderness of the non-circular duct. In most cases, it is merely the width to length ratio of the duct. However, in cases such as the circular annulus, annular sector, and the trapezoid, it is defined as the mean channel spacing divided by the mean channel width. This alternative definition was chosen since these shapes contain the parallel plate channel limit when aspect ratio becomes small.

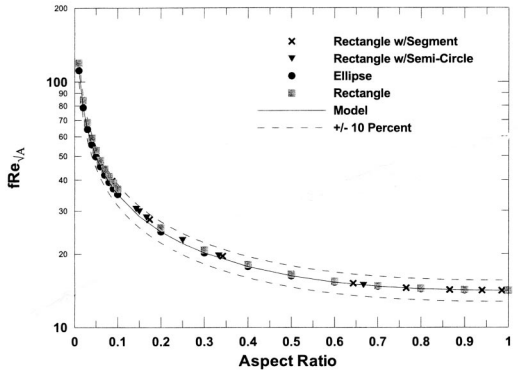

Fig. 1 $f\,\mathrm{Re}_{\sqrt{A}}$ **for singly connected geometries, data from Ref. [7]**

Next, Muzychka and Yovanovich [18] applied the same reasoning to the fully developed Nusselt number in non-circular ducts, leading to the development of a model for the classic Graetz problem.

Figures 3 and 4 compare the data for many duct shapes obtained from Shah and London [7]. When the results are based upon the square root of cross-sectional area two distinct bounds are formed for the Nusselt number. The lower bound consists of all duct shapes which have re-entrant corners, i.e., angles less than 90 deg, while the upper bound consists of all ducts with rounded corners and/or right angled corners. A model has been developed

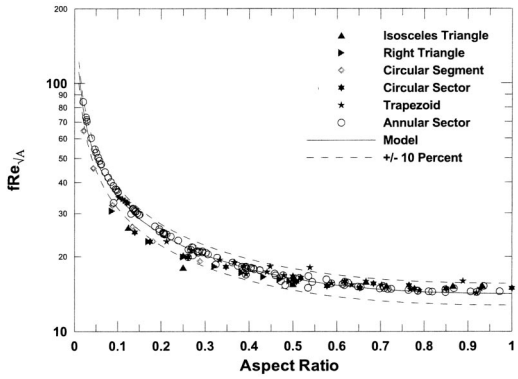

Fig. 2 $f\,\mathrm{Re}_{\sqrt{A}}$ **for other singly connected geometries, data from Ref. [7]**

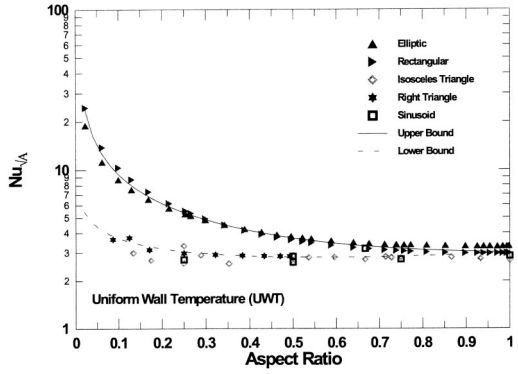

Fig. 3 Fully developed flow Nu_T**, data from Ref. [7]**

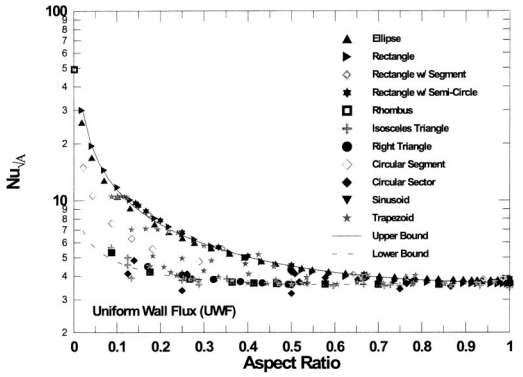

Fig. 4 Fully developed flow Nu_H, data from Ref. [7]

which accurately predicts the data for both thermal boundary conditions and both upper and lower bounds. The resulting expression which is related to Eq. (21) is

$$\mathrm{Nu}_{\sqrt{A}} = C_1\left(\frac{f\,\mathrm{Re}_{\sqrt{A}}}{8\sqrt{\pi}\epsilon^{\gamma}}\right) \tag{22}$$

where C_1 is equal to 3.24 for the (UWT) boundary condition and 3.86 for the (UWF) boundary condition. These results are the exact solutions for fully developed flow in a circular tube when the characteristic length scale is the square root of cross-sectional area. The parameter γ is chosen based upon the geometry. Values for γ which define the upper and lower bounds in Figs. 3 and 4 are fixed at $\gamma = 1/10$ and $\gamma = -3/10$, respectively. Almost all of the available data are predicted within ± 10 percent by Eq. (22), with a few exceptions.

Graetz Flow. If the velocity distribution is fully developed and the temperature distribution is allowed to develop, the classic Graetz problem results. In the thermal entrance region, the results are weak functions of the shape and geometry of the duct. This behavior is characterized by the following approximate analytical expression first attributed to Leveque, see [24]:

$$\mathrm{Nu} \propto \left(\frac{C^*}{z^*}\right)^{1/3} \tag{23}$$

where C^* is the dimensionless mean velocity gradient at the duct wall and z^* is the dimensionless axial location. Thus, if C^* is made a weak function of shape, then Nu will be a weaker function of shape due to the one third power.

In the thermal entrance region of non-circular ducts the thermal boundary layer is thin and it may be assumed to be developing in a region where the velocity gradient is linear. For very small distances from the duct inlet, the effect of curvature on the boundary layer development is negligible. Thus, the we may treat the duct wall as a flat plate. The governing equation for this situation is given by

$$Cy\frac{\partial T}{\partial z} = \alpha\frac{\partial^2 T}{\partial y^2} \tag{24}$$

where the constant C represents the mean velocity gradient at the duct wall. For non-circular ducts, this constant is defined as:

$$C = \overline{\left.\frac{\partial w}{\partial n}\right|}_w = \frac{1}{P}\oint \left.\frac{\partial w}{\partial n}\right|_w ds \tag{25}$$

For hydrodynamically fully developed flow, the constant C is related to the friction factor-Reynolds number product

$$\frac{f\,\mathrm{Re}_{\mathcal{L}}}{2} = \overline{\left.\frac{\partial w}{\partial n}\right|}_w \frac{\mathcal{L}}{\overline{w}} = C^* \tag{26}$$

where $\mathcal{L}$ is an arbitrary length scale.

If the following parameters are defined:

$$\overline{y} = \frac{y}{\mathcal{L}} \quad z^* = \frac{z/\mathcal{L}}{\mathrm{Re}_{\mathcal{L}}\mathrm{Pr}} \quad \theta = T - T_o \quad \mathrm{Re}_{\mathcal{L}} = \frac{\overline{w}\mathcal{L}}{\nu}$$

the governing equation becomes

$$C^*\overline{y}\frac{\partial\theta}{\partial z^*} = \frac{\partial^2\theta}{\partial\overline{y}^2} \tag{27}$$

The governing equation may now be transformed into an ordinary differential equation for each wall condition using a similarity variable [22]

$$\eta = \frac{\overline{y}}{(9z^*/C^*)^{1/3}} \tag{28}$$

Both the UWT and UWF conditions are examined. Solution to the Leveque problem is discussed in Bird et al. [24]. The solution for local Nusselt number with the UWT condition yields:

$$\mathrm{Nu}_{\mathcal{L}} = \frac{3\sqrt{3}\,\Gamma(2/3)}{2\,\pi}\left(\frac{f\,\mathrm{Re}_{\mathcal{L}}}{18z^*}\right)^{1/3} \approx 0.4273\left(\frac{f\,\mathrm{Re}_{\mathcal{L}}}{z^*}\right)^{1/3} \tag{29}$$

while the solution for the local Nusselt number for the (UWF) condition yields:

$$\mathrm{Nu}_{\mathcal{L}} = \Gamma(2/3)\left(\frac{f\,\mathrm{Re}_{\mathcal{L}}}{18z^*}\right)^{1/3} \approx 0.5167\left(\frac{f\,\mathrm{Re}_{\mathcal{L}}}{z^*}\right)^{1/3} \tag{30}$$

The average Nusselt number for both cases may be obtained from Eq. (12), which gives

$$\overline{\mathrm{Nu}}_{\mathcal{L}} = \frac{3}{2}\mathrm{Nu}_{\mathcal{L}} \tag{31}$$

The solution for each wall condition may now be compactly written as

$$\mathrm{Nu}_{\mathcal{L}} = C_2C_3\left(\frac{f\,\mathrm{Re}_{\mathcal{L}}}{z^*}\right)^{1/3} \tag{32}$$

where the value of C_2 is 1 for local conditions and 3/2 for average conditions, and C_3 takes a value of 0.427 for UWT and 0.517 for UWF.

The Leveque approximation is valid where the thermal boundary layer develops in the region near the wall where the velocity profile is linear. The weak effect of duct geometry in the entrance region is due to the presence of the friction factor-Reynolds number product, f Re, in the above expression, which is representative of the average velocity gradient at the duct wall. The typical range of the f Re group is $6.5 < f\,\mathrm{Re}_{D_h} < 24$, Shah and London [7]. This results in $1.87 < (f\,\mathrm{Re}_{D_h})^{1/3} < 2.88$, which illustrates the weak dependency of the thermal entrance region on shape and aspect ratio. Further reductions are achieved for similar shaped ducts by using the length scale $\mathcal{L} = \sqrt{A}$, i.e., see Figs. 1 and 2.

A model which is valid over the entire range of dimensionless duct lengths for $\mathrm{Pr} \to \infty$, was developed by Muzychka and Yovanovich [18] by combining Eq. (22) with Eq. (32) using the Churchill and Usagi [11] asymptotic correlation method. The form of the proposed model for an arbitrary characteristic length scale is

$$\mathrm{Nu}(z^*) = \left(\left\{C_2C_3\left(\frac{f\,\mathrm{Re}}{z^*}\right)^{1/3}\right\}^n + (\mathrm{Nu}_{fd})^n\right)^{1/n} \tag{33}$$

Now using the result for the fully developed friction factor, Eq. (21), and the result for the fully developed flow Nusselt number, Eq. (22), with $n \approx 5$ a new model [19] was proposed having the form

Table 1 Coefficients for general model

Boundary Condition		
UWT	$C_3=0.409,\ C_1=3.24$	$f(\mathrm{Pr})=\dfrac{0.564}{[1+(1.664\mathrm{Pr}^{1/6})^{9/2}]^{2/9}}$
UWF	$C_3=0.501,\ C_1=3.86$	$f(\mathrm{Pr})=\dfrac{0.886}{[1+(1.909\mathrm{Pr}^{1/6})^{9/2}]^{2/9}}$
Nusselt Number Type		
Local	$C_2=1$	$C_4=1$
Average	$C_2=3/2$	$C_4=2$
Shape Parameter		
Upper Bound	$\gamma=1/10$	
Lower Bound	$\gamma=-3/10$	

$$\mathrm{Nu}_{\sqrt{A}}(z^*)=\left[\left\{C_2C_3\left(\frac{f\,\mathrm{Re}_{\sqrt{A}}}{z^*}\right)^{1/3}\right\}^5+\left\{C_1\left(\frac{f\,\mathrm{Re}_{\sqrt{A}}}{8\sqrt{\pi\epsilon}^{\gamma}}\right)\right\}^5\right]^{1/5} \tag{34}$$

where the constants C_1, C_2, C_3, and γ are given in Table 1. These constants define the various cases for local or average Nusselt number and isothermal or isoflux boundary conditions for the Graetz problem. The constant C_3 was adjusted from that found by the Leveque approximation to provide better agreement with the data.

Laminar Boundary Layer Flow. Finally, if both hydrodynamic and thermal boundary layers develop simultaneously, the results are strong functions of the fluid Prandtl number. In the combined entrance region the behavior for very small values of z^* may be adequately modeled by treating the duct wall as a flat plate. The characteristics of this region are

$$\mathrm{Pr}\to 0 \quad \frac{\mathrm{Nu}_z}{\sqrt{\mathrm{Re}_z}}=0.564\mathrm{Pr}^{1/2} \tag{35}$$

$$\mathrm{Pr}\to \infty \quad \frac{\mathrm{Nu}_z}{\sqrt{\mathrm{Re}_z}}=0.339\mathrm{Pr}^{1/3} \tag{36}$$

for the UWT condition [2], and

$$\mathrm{Pr}\to 0 \quad \frac{\mathrm{Nu}_z}{\sqrt{\mathrm{Re}_z}}=0.886\mathrm{Pr}^{1/2} \tag{37}$$

$$\mathrm{Pr}\to \infty \quad \frac{\mathrm{Nu}_z}{\sqrt{\mathrm{Re}_z}}=0.464\mathrm{Pr}^{1/3} \tag{38}$$

for the UWF condition [1].

Composite models for each wall condition were developed by Churchill and Ozoe [1,2] using the asymptotic correlation method of Churchill and Usagi [11]. The results may be developed in terms of the $\mathrm{Pr}\to 0$ behavior or the $\mathrm{Pr}\to\infty$ behavior. For internal flow problems, the appropriate form is chosen to be in terms of the $\mathrm{Pr}\to 0$ characteristic which introduces the Peclet number $\mathrm{Pe}=\mathrm{Re}\,\mathrm{Pr}$:

$$\frac{\mathrm{Nu}_z}{(\mathrm{Re}_z\mathrm{Pr})^{1/2}}=\frac{C_o}{\left[1+\left(\dfrac{C_o\mathrm{Pr}^{1/6}}{C_\infty}\right)^n\right]^{1/n}}=f(\mathrm{Pr}) \tag{39}$$

where C_o and C_∞ represent the coefficients of the right hand side of Eqs. (35–38). The correlation parameter n may be found by solving Eq. (39) at an intermediate value of Pr where the exact solution is known, i.e., $\mathrm{Pr}=1$. This leads to $n=4.537$ for the UWT condition and $n=4.598$ for the UWF condition. For simplicity, $n=9/2$ is chosen for both cases.

The average Nusselt number for both cases may now be obtained from Eq. (12), which gives:

$$\overline{\mathrm{Nu}_{\mathcal{L}}}=2\,\mathrm{Nu}_{\mathcal{L}} \tag{40}$$

The solution for each wall condition may now be compactly written as

$$\mathrm{Nu}_{\mathcal{L}}=\frac{C_4}{\sqrt{z^*}}f(\mathrm{Pr}) \tag{41}$$

where the value of $C_4=1$ for local conditions and $C_4=2$ for average conditions, and $f(\mathrm{Pr})$ are defined as

$$f(\mathrm{Pr})=\frac{0.564}{[1+(1.664\mathrm{Pr}^{1/6})^{9/2}]^{2/9}} \tag{42}$$

for the UWT condition, and

$$f(\mathrm{Pr})=\frac{0.886}{[1+(1.909\mathrm{Pr}^{1/6})^{9/2}]^{2/9}} \tag{43}$$

for the UWF condition. The preceding results are valid only for small values of the parameter z^*.

General Model. A new model for the combined entrance region may now developed by combining the solution for a flat plate with the model for the Graetz flow problem developed earlier. The proposed model takes the form

$$y(z)=(\{y_{z\to 0}(\mathrm{Pr})\}^m+\{y_{z\to 0}^n+y_{z\to\infty}^n\}^{m/n})^{1/m} \tag{44}$$

which is similar to that proposed by Churchill and Ozoe [1,2] for the circular duct. This model is a composite solution of the three asymptotic solutions just discussed.

This results in the following model for simultaneously developing flow in a duct of arbitrary cross-sectional shape

$$\mathrm{Nu}_{\sqrt{A}}(z^*)=\left[\left(\frac{C_4f(\mathrm{Pr})}{\sqrt{z^*}}\right)^m+\left(\left\{C_2C_3\left(\frac{f\,\mathrm{Re}_{\sqrt{A}}}{z^*}\right)^{1/3}\right\}^5+\left\{C_1\left(\frac{f\,\mathrm{Re}_{\sqrt{A}}}{8\sqrt{\pi\epsilon}^{\gamma}}\right)\right\}^5\right)^{m/5}\right]^{1/m} \tag{45}$$

The parameter m was determined to vary between 2 and 7 for all of the data examined. Values for the blending parameter were found to be weak functions of the duct aspect ratio and whether a local or average Nusselt number was examined. However, the blending parameter was found to be most dependent upon the fluid Prandtl number.

A simple linear approximation was determined to provide better accuracy than choosing a single value for all duct shapes. Due to the variation in geometries and data, higher order approximations offered no additional advantage. Therefore, the linear approxima-

tion which predicts the blending parameter within 30 percent was found to be satisfactory. Variations in the blending parameter of this order will lead to small errors in the model predictions, whereas variations on the order of 100 percent or more, i.e., choosing a fixed value, produce significantly larger errors. The resulting fit for the blending parameter m is

$$m = 2.27 + 1.65\mathrm{Pr}^{1/3} \tag{46}$$

The above model is valid for $0.1 < \mathrm{Pr} < \infty$ which is typical for most low Reynolds number flow heat exchanger applications.

Finally, the following model was developed by Muzychka and Yovanovich [18,20] for the apparent friction factor in the entrance region. It is given here for completeness as follows:

$$f_{\mathrm{app}}\,\mathrm{Re}_{\sqrt{A}} = \left[\left(\frac{12}{\sqrt{\epsilon}\,(1+\epsilon)\left[1 - \frac{192\epsilon}{\pi^5}\tanh\left(\frac{\pi}{2\epsilon}\right)\right]} \right)^2 + \left(\frac{3.44}{\sqrt{z^+}} \right)^2 \right]^{1/2} \tag{47}$$

It predicts most of the non-circular friction data within ± 10 percent.

Comparisons of Model With Data

Comparisons with the available data from [7] are provided in Tables 2–6 and Figs. 5–11. Good agreement is obtained with the data for the circular duct and parallel plate channel. Note that comparison of the model for the parallel plate channel was obtained by considering a rectangular duct having an aspect ratio of $\epsilon = 0.01$. This represents a reasonable approximation for this system. The data are also compared with the models of Churchill and Ozoe [1,2] and Stephan [3,4] for the circular duct and parallel plate channel in Figs. 5–8.

The model is compared with the data by determining the percent difference between the data and the model predictions. Maximum and minimum values of the percent difference are given in Tables 2–6 for each set of data.

The numerical data for the the UWT circular duct fall short of the model predictions at low Pr numbers. However, all of the models are in excellent agreement with the integral formulation of

Table 2 Comparison of model and data for circular duct [7] (min/max—% diff)

Pr	$\mathrm{Nu}_{z,T}$	$\mathrm{Nu}_{m,T}$	$\mathrm{Nu}_{z,H}$
0.7	−6.59/−0.07	−14.69/3.87	−0.08/3.98
2.0	−8.43/−0.07	−19.07/1.34	−0.07/5.19
5.0	−8.65/−0.07	−24.41/−0.60	−0.20/5.40
∞		−1.24/8.57	−1.60/5.27

Table 3 Comparison of model and data for parallel plate channel [7] (min/max—% diff)

Pr	$\mathrm{Nu}_{m,T}$	$\mathrm{Nu}_{z,H}$
0.1	−13.33/6.32	N/A
0.7	−5.17/7.43	−1.59/5.32
2.0	−0.24/7.43	−1.79/4.49
5.0	−0.02/13.75	−0.05/6.01
∞	1.60/10.0	−9.93/7.03

Table 4 Comparison of model and data for square duct [7] (min/max—% diff)

Pr	$\mathrm{Nu}_{z,H}$	$\mathrm{Nu}_{m,H}$
0.1	−0.45/11.32	−8.14/11.42
1.0	−2.19/2.56	−6.72/4.82
10	−1.96/1.52	−1.15/5.07
∞	−2.76/1.73	

Table 5 Comparison of model and data for rectangular duct [7]: Pr=0.72, (min/max—% diff)

$\epsilon = b/a$	$\mathrm{Nu}_{m,T}$	$\mathrm{Nu}_{z,H}$	$\mathrm{Nu}_{m,H}$
1	−20.7/1.21	−0.18/13.14	−3.75/14.8
1/2	−18.5/7.48	−0.11/13.13	−2.42/14.6
1/3	−16.5/7.43	−0.05/13.4	−0.42/13.16
1/4	−14.6/6.73	−0.04/12.04	−0.33/13.5

Table 6 Comparison of model and data for equilateral triangular ducts [7] (min/max—% diff)

Pr	$\mathrm{Nu}_{z,T}$	$\mathrm{Nu}_{m,T}$	$\mathrm{Nu}_{z,H}$	$\mathrm{Nu}_{m,H}$
0.72	−14.17/−1.85	−11.1/12.27	−1.50/4.19	−8.92/4.84
∞		−12.11/−6.81	−7.24/−2.09	

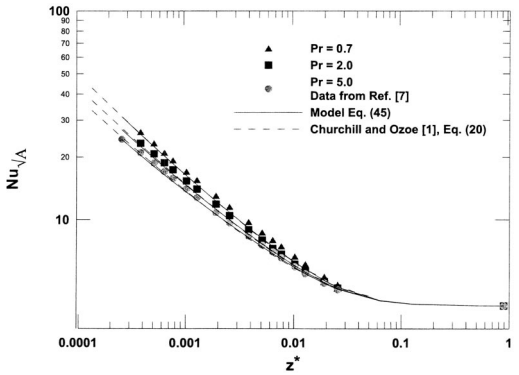

Fig. 5 Simultaneously developing flow in a circular tube $\mathrm{Nu}_{H,z}$, data from Ref. [7]

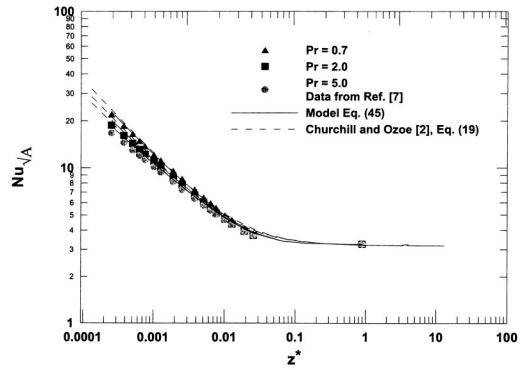

Fig. 6 Simultaneously developing flow in a circular tube $\mathrm{Nu}_{T,z}$, data from Ref. [7]

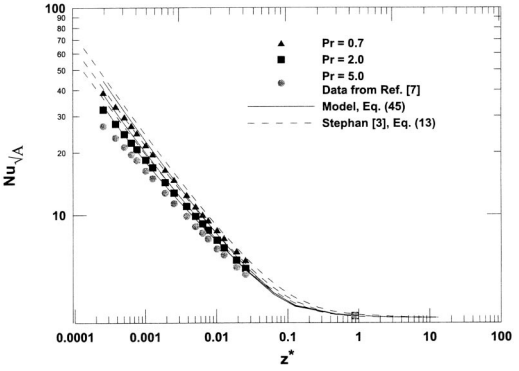

Fig. 7 Simultaneously developing flow in a circular tube $\mathrm{Nu}_{T,m}$, data from Ref. [7]

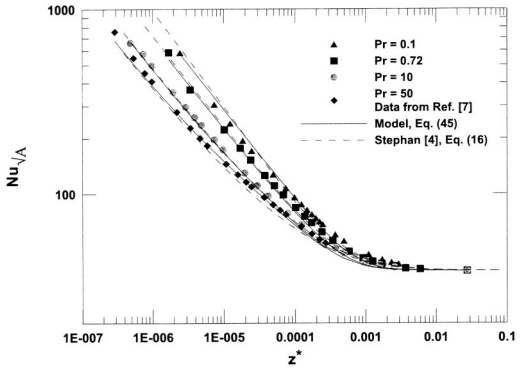

Fig. 8 Simultaneously developing flow in channel $Nu_{T,m}$, data from Ref. [7]

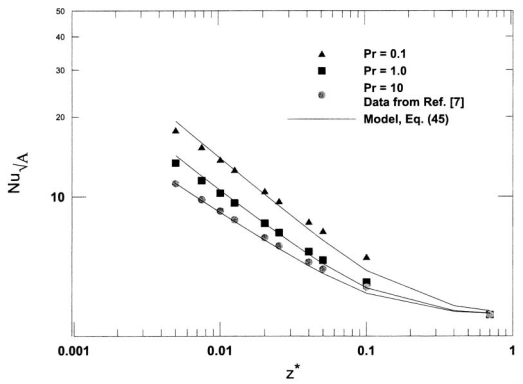

Fig. 11 Simultaneously developing flow in square duct $Nu_{H,m}$, data from Ref. [7]

Kreith [14]. Good agreement is also obtained for the case of the square duct for all Prandtl numbers. Comparisons of the model with data for the rectangular duct at various aspect ratios, see Table 5, and the equilateral triangular duct, see Table 6, show that larger discrepancies arise. Also included in Tables 2–6 are the results of Muzychka and Yovanovich [19] for the case of $Pr \rightarrow \infty$.

The data used for comparison in Tables 5 and 6 were obtained by Wibulswas [25]. In this work, the effects of transverse velocities in both the momentum and energy equations were ignored. Comparison of the data for the square duct at $Pr = 1.0$ obtained by Chandrupatla and Sastri [26] which includes the effects of transverse velocities with the data of Wibulswas [25] for $Pr = 0.72$ shows that the discrepancy is likely due to the data and not the model.

The accuracy for each case may be improved considerably by using the optimal value of the parameter m. However, this introduces an additional parameter into the model which is deemed unnecessary for purposes of heat exchanger design. The proposed model predicts most of the available data for the combined entry problem to within ± 15 percent and may be used to predict the heat transfer characteristics for other non-circular ducts for which there are presently no data.

The present model also agrees well with the published models of Churchill and Ozoe [1,2], Eqs. (19,20), and the models of Stephan [3,4], Eqs. (13,16), for the tube and channel. It is evident from Figs. 5–8 that the present model provides equal or better accuracy to the existing expressions.

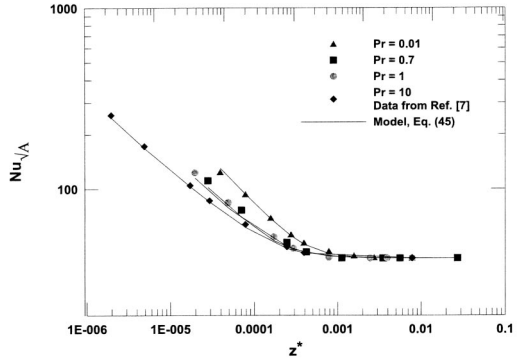

Fig. 9 Simultaneously developing flow in channel $Nu_{H,z}$, data from Ref. [7]

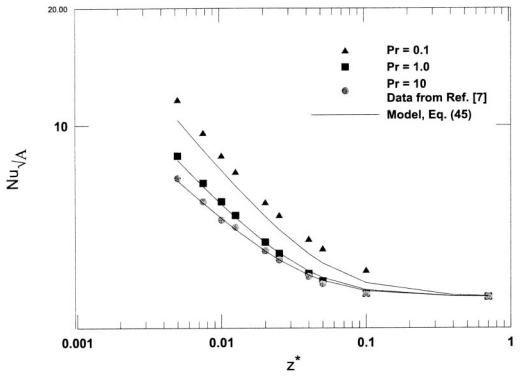

Fig. 10 Simultaneously developing flow in square duct $Nu_{H,z}$, data from Ref. [7]

Summary and Conclusions

A general model for predicting the heat transfer co-efficient in the combined entry region of non-circular ducts was developed. This model is valid for $0.1 < Pr < \infty$, $0 < z^* < \infty$, both uniform wall temperature (UWT) and uniform wall flux (UWF) conditions, and for local and mean Nusselt numbers. Model predictions agree with numerical data to within ± 15 percent for most non-circular ducts and channels. The model was developed by combining the asymptotic results of laminar boundary layer flow and Graetz flow for the thermal entrance region. In addition, by means of a novel characteristic length, the square root of cross-sectional area, results for many non-circular ducts of similar aspect ratio collapse onto a single curve.

Acknowledgments

The authors acknowledge the support of the Natural Sciences and Engineering Research Council of Canada (NSERC) under a post-doctoral research fellowship for the first author and research grants for both authors.

Nomenclature

A = flow area, m^2
a = major axis of ellipse or rectangle, m
b = minor axis of ellipse or rectangle, m
C = constant
C_i = constants, $i = 1..5$
D = diameter of circular duct, m
D_h = hydraulic diameter of plain channel, $\equiv 4A/P$
f = friction factor $\equiv \overline{\tau}/(1/2\rho\overline{w}^2)$
Gz = Graetz number, $\equiv \pi/4z^*$
h = heat transfer coefficient, W/m^2K

k = thermal conductivity, W/mK
L = length of channel, m
L_h = hydrodynamic entry length, m
L_t = thermal entry length, m
L^* = dimensionless thermal length, $\equiv L/\mathcal{L}\,\mathrm{Re}_{\mathcal{L}}\mathrm{Pr}$
$\mathcal{L}$ = characteristic length scale, m
m = correlation parameter
$\dot{m}$ = mass flow rate, kg/s
n = inward directed normal
$\mathrm{Nu}_{\mathcal{L}}$ = Nusselt number, $\equiv h\mathcal{L}/k$
P = perimeter, m
p = pressure, Pa
Pr = Prandtl number, $\equiv \nu/\alpha$
q = heat flux, W/m^2
Q = heat transfer rate, W
r = radius, m
$\mathrm{Re}_{\mathcal{L}}$ = Reynolds number, $\equiv \overline{w}\mathcal{L}/\nu$
s = arc length, m
T = temperature, K
T_m = bulk temperature, K
T_w = wall temperature, K
u, v, w = velocity components, m/s
w = axial velocity, m/s
$\overline{w}$ = average velocity, m/s
x, y, z = cartesian coordinates, m
z = axial coordinate, m
z^+ = dimensionless position for hydrodynamically developing flows, $\equiv z/\mathcal{L}\,\mathrm{Re}_{\mathcal{L}}$
z^* = dimensionless position for thermally developing flows, $\equiv z/\mathcal{L}\,\mathrm{Re}_{\mathcal{L}}\mathrm{Pr}$

Greek Symbols

α = thermal diffusivity, m^2/s
ϵ = aspect ratio, $\equiv b/a$
γ = shape parameter
$\Gamma(\cdot)$ = Gamma function
μ = dynamic viscosity, Ns/m^2
ν = kinematic viscosity, m^2/s
ρ = fluid density, kg/m^3
τ = wall shear stress, N/m^2
θ = temperature excess, $T-T_b$, K

References

[1] Churchill, S. W., and Ozoe, H., 1973, "Correlations for Laminar Forced Convection with Uniform Heating in Flow Over a Plate and in Developing and Fully Developed Flow in a Tube," ASME J. Heat Transfer, **95**, pp. 78–84.

[2] Churchill, S. W., and Ozoe, H., 1973, "Correlations for Laminar Forced Convection in Flow Over an Isothermal Flat Plate and in Developing and Fully Developed Flow in an Isothermal Tube," ASME J. Heat Transfer, **95**, pp. 416–419.

[3] Baehr, H., and Stephan, K., 1998, *Heat Transfer*, Springer-Verlag.

[4] Stephan, K., 1959, "Warmeubergang und Druckabfall bei Nicht Ausgebildeter Laminar Stromung in Rohren und in Ebenen Spalten," *Chem-Ing-Tech*, **31**, pp. 773–778.

[5] Garimella, S., Dowling, W. J., Van derVeen, M., Killion, J., 2000, "Heat Transfer Coefficients for Simultaneously Developing Flow in Rectangular Tubes," *Proceedings of the 2000 International Mechanical Engineering Congress and Exposition*, Vol. 2, pp. 3–11.

[6] Asako, Y., Nakamura, H., and Faghri, M., 1988, "Developing Laminar Flow and Heat Transfer in the Entrance Region of Regular Polygonal Ducts," Int. J. Heat Mass Transfer, **31**, pp. 2590–2593.

[7] Shah, R. K., and London, A. L., 1978, *Laminar Flow Forced Convection in Ducts*, Academic Press, New York, NY.

[8] Kakac, S., Shah, R. K., and Aung, W., 1987, *Handbook of Single Phase Convective Heat Transfer*, Wiley, New York.

[9] Rohsenow, W. M., Hartnett, J. P., and Cho, Y. I., eds., 1988, *Handbook of Heat Transfer*, McGraw-Hill, New York.

[10] Kakac, S., and Yener, Y., 1983, "Laminar Forced Convection in the Combined Entrance Region of Ducts," in *Low Reynolds Number Heat Exchangers*, S. Kakac, R. K. Shah and A. E. Bergles, eds., Hemisphere Publishing, Washington, pp. 165–204.

[11] Churchill, S. W., and Usagi, R., 1972, "A General Expression for the Correlation of Rates of Transfer and Other Phenomena," *American Institute of Chemical Engineers*, **18**, pp. 1121–1128.

[12] Kays, W. M., and Crawford, M. E., 1993, *Convective Heat and Mass Transfer*, McGraw-Hill, New York, NY.

[13] Kays, W. M., 1955, "Numerical Solutions for Laminar Flow Heat Transfer in Circular Tubes," Trans. ASME, **77**, pp. 1265–1274.

[14] Kreith, F., 1965, *Principles of Heat Transfer*, 2nd ed., International Textbook Co., Scranton, PA.

[15] Sparrow, E. M., 1955, "Analysis of Laminar Forced Convection Heat Transfer in Entrance Region of Flat Rectangular Ducts," *NACA Technical Note 3331*.

[16] Muzychka, Y. S., 1999, "Analytical and Experimental Study of Fluid Friction and Heat Transfer in Low Reynolds Number Flow Heat Exchangers," Ph.D. thesis, Uinversity of Waterloo, Waterloo, ON.

[17] Yovanovich, M. M., and Muzychka, Y. S., 1997, "Solutions of Poisson Equation within Singly and Doubly Connected Domains," AIAA Paper 97-3880, presented at the National Heat Transfer Conference, Baltimore MD.

[18] Muzychka, Y. S., and Yovanovich, M. M., 1998, "Modeling Fricton Factors in Non-Circular Ducts for Developing Laminar Flow," AIAA Paper 98-2492, presented at the 2nd Theoretical Fluid Mechanics Meeting, Albuquerque, NM.

[19] Muzychka, Y. S., and Yovanovich, M. M., 1998, "Modeling Nusselt Numbers for Thermally Developing Laminar Flow in Non-Circular Ducts," AIAA Paper 98-2586, presented at the 7th AIAA/ASME Joint Thermophysics and Heat Transfer Conference, Albuquerque, NM.

[20] Muzychka, Y. S., and Yovanovich, M. M., 2002, "Laminar Flow Friction and Heat Transfer in Non-Circular Ducts and Channels: Part I—Hydrodynamic Problem," *Compact Heat Exchangers: A Festschrift on the 60th Birthday of Ramesh K. Shah*, Grenoble, France, August 24, 2002, G. P. Celata, B. Thonon, A. Bontemps, and S. Kandlikar, eds., pp. 123–130.

[21] Muzychka, Y. S., and Yovanovich, M. M., 2002, "Laminar Flow Friction and Heat Transfer in Non-Circular Ducts and Channels: Part II—Thermal Problem," *Compact Heat Exchangers: A Festschrift on the 60th Birthday of Ramesh K. Shah*, Grenoble, France, August 24, 2002, G. P. Celata, B. Thonon, A. Bontemps, and S. Kandlikar, eds., pp. 131–139.

[22] Yovanovich, M. M., Teertstra, P. M., and Muzychka, Y. S., 2001, "Natural Convection Inside Vertical Isothermal Ducts of Constant Arbitrary Cross-Section," AIAA Paper 01-0368, presented at the 39th Aerospace Sciences Meeting and Exhibit, Reno, NV, January 8–11.

[23] Bejan, A., 2000, *Shape and Structure, From Engineering to Nature*, Cambridge University Press, Cambridge, UK.

[24] Bird, R. B, Stewart, W. E., and Lightfoot, E. N., 1960, *Transport Phenomena*, Wiley, New York, NY.

[25] Wibulswas, P., 1966, "Laminar Flow Heat Transfer in Noncircular Ducts," Ph.D. thesis, London University.

[26] Chandrupatla, A. R., and Sastri, V. M. K., 1977, "Laminar Forced Convection Heat Transfer of a Non-Newtonian Fluid in a Square Duct," Int. J. Heat Mass Transfer, **20**, pp. 1315–1324.

Fluctuating Temperature Measurements on a Heated Cylinder Placed in a Cylinder Near-Wake

Z. J. Wang

Y. Zhou
e-mail: mmyzhou@polyu.edu.hk

X. W. Wang

W. Jin

Department of Mechanical Engineering,
The Hong Kong Polytechnic University,
Hung Hom, Kowloon, Hong Kong

The local time-averaged temperature $\overline{\theta_s}$ and its fluctuating component θ_s on the surface of a heated circular cylinder immersed in a cylinder near-wake were measured using a fiber-optic Bragg grating (FBG) sensor. Three cylinder center-to-center spacing, i.e., $L/d=5.20$, 2.50, and 1.18, were investigated. In order to validate the FBG sensor measurement, a thermocouple and a single hot-wire were employed to measure $\overline{\theta_s}$ on the heated cylinder and streamwise fluctuating velocity u in the near-wake of the downstream cylinder, respectively. The FBG sensor measurement of $\overline{\theta_s}$ is in good agreement with that simultaneously obtained by the thermocouple. The measured θ_s is closely correlated to the hot-wire measurement; the θ_s-spectrum exhibits a pronounced peak at the vortex shedding frequency, as identified in E_u, for each L/d. The results suggest that the FBG sensor can be used to measure reliably both time-averaged and fluctuating temperatures. The heat transfer characteristics of the heated cylinder are examined for different L/d and further compared with the case of an isolated cylinder. [DOI: 10.1115/1.1643910]

Keywords: Cylinder, Experimental Flow, Heat Transfer, Measurement Techniques, Sensors, Temperature, Wakes

1 Introduction

The flow behind two inline circular cylinders has been investigated extensively in the past due to its practical significance in many branches of engineering [1–4]. Representative applications include tube bank heat exchanger, adjacent tall buildings, bundled transmission lines, and piles of offshore platforms [5–7]. This flow depends to a great extent on the ratio, L/d, where L is the center-to-center cylinder spacing and d is the cylinder diameter. The flow may be classified into three flow regimes [2,4,8]. For large spacing ($L/d>3.4\sim3.8$), a vortex street is observed between the cylinders. Vortex shedding from the downstream cylinder is synchronized with that from the upstream cylinder, and a binary vortex street is formed behind the downstream cylinder [2,9]. At intermediate spacing, i.e., $1.2\sim1.8<L/d<3.4\sim3.8$, the shear layers separating from the upstream cylinder re-attach on the downstream cylinder and the vortex street is observed only behind the downstream cylinder. For very small spacing, i.e., $L/d<1.2\sim1.8$, the shear layers separating from the upstream cylinder roll up behind, without reattaching on, the downstream cylinder, forming a vortex street downstream [8].

The study of the heat transfer characteristics of a heated circular cylinder placed behind another cylinder is of particular relevance to heat exchangers. As discussed earlier, as L/d varies, the flow around the downstream cylinder may be divided as three distinct regimes. One may expect heat transfer characteristics on this cylinder to be different between the flow regimes. A thorough understanding of the characteristics is crucial for optimizing the performance of heat exchangers. It is well known that the flow separation point may oscillate circumferentially as the boundary layer separates from a circular cylinder [10–12]. Naturally, the surface temperature fluctuates and local heat transfer from the cylinder to fluid varies azimuthally [13–15], resulting in the nonuniform circumferential distribution of the time-averaged temperature. Experimental investigations of the heat transfer problem around two inline circular cylinders have been concentrated mainly on the measurement of the global and local heat transfer coefficients, usually obtained by measuring the local heat flux and simultaneously the temperature difference between the cylinder surface and ambient flow [1]. The data of the local fluctuating surface temperature and in particular its relationship with L/d are however scarce in spite of its significance in understanding the physics of heat transfer. One objective of this work is therefore to investigate the dependence on L/d of the local fluctuating surface temperature.

A number of well-established techniques are available for temperature measurements [16]. Morris [17] classified these techniques into eight categories based on their operating principle, i.e., thermal expansion method, thermocouples, resistive sensors, quartz thermometers, radiation thermometers, thermograph (thermal imaging), acoustic thermometers, and fiber optic temperature sensors. Most of these techniques are suitable either for a particular situation or for the measurement of the time-averaged temperature. For example, thermograph provides the static temperature distribution over a surface. Radiation thermometers are noninvasive, though largely suitable for a high temperature situation. Acoustic thermometers cater for needs to measure cryogenic temperature [17]. Fluctuating temperatures may be measured using thermocouples, resistive sensors [17–19]. Thermocouples suffer from a poor dynamic response and consequently are generally used to measure the time-averaged temperature or fluctuating temperature of a low frequency [16]. In the presence of a flow, this technique may be intrusive to the flow. Resistive sensors, such as fine wires used in the gas flow or thin metal films for solid surfaces, have good dynamic responses [20]. However, both thermocouples and resistive sensors are prone to corruption by a neighboring electromagnetic field. Therefore, another objective of this work is to seek an alternative technique to measure both time-averaged and fluctuating temperatures on the surface of a heated circular cylinder in a cross flow.

The fiber-optic technique is relatively new for temperature sensors [17,19]. A typical application of fiber-optic temperature sen-

Contributed by the Heat Transfer Division for publication in the JOURNAL OF HEAT TRANSFER. Manuscript received by the Heat Transfer Division June 26, 2003; revision received November 19 2003. Associate Editor: P. M. Ligrani.

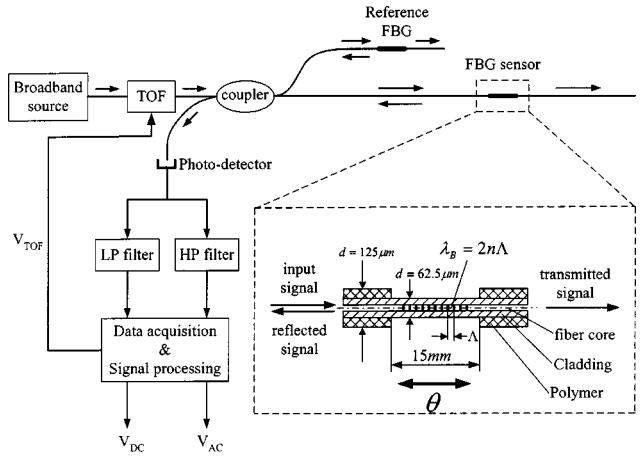

Fig. 1 Fiber-optic Bragg grating sensing system (adapted from Kersey et al. [23]; Ho et al. [26]). TOF denotes a tunable optical filter, and LP and HP stand for low pass and high pass, respectively.

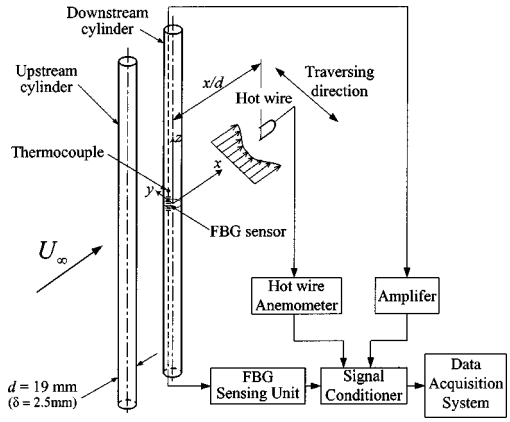

Fig. 2 Experimental arrangement

sors is to monitor or measure the average temperature or temperature distribution of large surfaces or long objects [19,21,22]. With the introduction of a grating on an optic fiber [23], the resulting fiber-optic Bragg grating (FBG) sensor is capable of the measurement of fluctuating strain on a structure. Zhou et al. [24] and Jin et al. [25] have successfully applied this sensor to measure dynamic strain, due to vortex-excitation, on a flexural slender cylinder. Ho et al. [26] recently demonstrated that the sensor can be used to provide both static and dynamic measurands. It is intended presently to apply this sensor for the measurement of both time-averaged and fluctuating temperature, which induces strain on a structure. The FBG sensor has many unique advantages. For example, its diameter can be as small as 80 μm. Therefore, its attachment to the structure would not seriously compromise the flow around the structure. Furthermore, it is immune to corruption by neighboring electromagnetic field and also causes no disturbance to the temperature field. In view of these advantages, the technique is most attractive for temperature measurements on a cylinder in a cross flow.

2 Concept of FBG Sensing System

The FBG sensing system was built in-house [26], consisting of a sensing FBG, a reference FBG, a broadband light source, a tunable optical filter (TOF), a fiber coupler, a photo-detector, a low pass electrical filter, a high-pass electrical filter and the data acquisition and signal processing unit (Fig. 1). Light from the broadband source first passes through TOF and then split into two by the fiber coupler, one to the sensing FBG and the other to the reference FBG. Light reflected from the two FBGs is combined by the same coupler and is fed into the photo-detector. The photo-detector converts optical signal to electrical signal that is further processed to give two outputs, one (V_{DC}) for time-averaged temperature measurement and the other (V_{AC}) for dynamic temperature measurement.

The FBGs are formed inside the core of an optical fiber by introducing a periodic change in the refractive index along the fiber (Fig. 1). Assuming the input signal to be broadband light incident on the grating, a narrow band signal is reflected back at the Bragg resonance wavelength $\lambda_B = 2n\Lambda$ [23], where Λ is the grating pitch and n the averaged fiber refractive index. When an optical fiber built with an FBG sensor is bounded on the surface of the structure along the cylinder span, the fiber and the FBG sensor will follow the surface temperature of the cylinder. Any perturbation, say due to applied temperature variation, θ, of the grating results in a variation in Λ and n, and therefore a shift $\Delta\lambda_B$ in λ_B. The value of $\Delta\lambda_B$ is related to θ by $\Delta\lambda_B = K\theta$, where K is a scale factor and can be determined by a calibration process. The FBG system, dynamically dependent on the characteristics of the TOF and the FBG sensors [24–25], can measure fluctuating strain/temperature up to 20 kHz for a single FBG sensor [26]. The dynamic characteristics of the FBG system have also been validated in [24–25]. Using a wavelength detector, $\Delta\lambda_B$ can be converted into the variation of light intensity. The intensity variation is subsequently converted into an electric current or voltage through a photo-detector. Therefore, θ is related to that of the electric signal.

The time-averaged temperature measurement is carried out by scanning the TOF and recording the TOF control voltages $V_{TOF} = V_r$ and $V_{TOF} = V_s$, which correspond to the center wavelength of the TOF aligned to the Bragg wavelengths of the reference and sensing FBGs, respectively. The Bragg wavelength of the reference grating is maintained as a constant, while that of the sensing grating varies with θ. The differential voltage $V_s - V_r$ is proportional to the difference between the two Bragg wavelengths and is therefore to the applied time-averaged temperature.

The dynamic temperature measurement is performed by the following procedure: after the aforementioned scan is completed, the TOF control voltage, V_{TOF}, is tuned to and held at a constant value $V_o = V_s + \Delta V_s$, corresponding to a maximum slope point on the reflection spectrum of the sensing FBG. Around this operating point, the sensor response is linear and most sensitive to a small dynamic temperature. Any dynamic temperature applied to the sensing grating is transformed linearly into a light intensity variation that is converted into a time varying voltage (V_{AC}) at the photo-detector output. The ΔV_s value is determined by the spectral characteristic of the sensing grating. By repeating the scanning-and-holding process, the time-averaged and dynamic temperatures can be measured alternatively. The scanning and holding times can be adjusted and should be selected carefully to optimize the measurement performance.

3 Experimental Details

3.1 Experimental Setup. Experiments were conducted in a suction-type wind tunnel with a 0.5 m long working section (0.35 m$\times$0.35 m). The streamwise velocity is uniform to within 0.05% and the free stream turbulence intensity is 0.2%. Two identical brass circular tubes with outer diameter $d = 19.0$ mm and wall thickness $\delta = 2.5$ mm were arranged in line and vertically mounted in the mid-plane of the working section (Figs. 2 and 3). They spanned the full height of the tunnel, resulting in a blockage of about 5.4% and an aspect ratio of 18.4. The downstream cylinder was located at 250 mm away from the exit plane of the tunnel contraction. Its location was fixed throughout experiments; L/d was adjusted by varying the upstream cylinder position in the streamwise direction. The structural rigidity of the test cylinder is very large, the vortex-induced cylinder vibration being negligible.

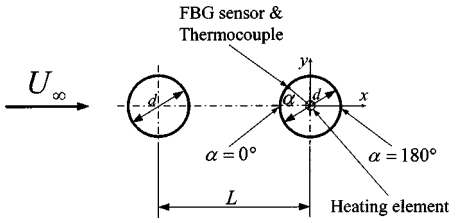

Fig. 3 Schematic of test cylinders

This is crucial since the present FBG sensing system is also sensitive to dynamic strain [24–26], which may contaminate the fluctuating temperature signal.

Three cylinder spacing ratios were investigated, i.e., $L/d = 5.20$, 2.50, and 1.18, respectively. These ratios were chosen because the corresponding flow structures were representative of different flow regimes [3,4]. The downstream cylinder was electrically heated using the heating element of a 3.0 mm diameter, which was positioned at the center of the cylinder tube and spanned the full cylinder length (Fig. 3), thus resulting in an azimuthally uniform heating power distribution. The time-averaged temperature around the cylinder surface varies, implying a nonconstant heat flux body. However, the variation is smaller than 2% of the global mean temperature. We may therefore consider the cylinder to be an approximately constant heat flux body. The heating power was unchanged throughout the entire experiments. Measurements were carried at the free stream velocity $U_\infty = 7.2$ m/s, corresponding to the Reynolds number Re ($\equiv U_\infty d/\nu$, where ν is the fluid kinematic viscosity) = 9080.

3.2 Fluctuating Surface Temperature Measurement. An optical fiber of a 125 μm diameter was buried with heat-conducting silicone in a groove of about 125 μm deep along the downstream cylinder span. The fiber, flush with the cylinder surface using heat-conducting silicone, was built with a fiber-optic Bragg grating of about 1 cm in length. The grating was located at the mid-span of the cylinder and measured the time-averaged temperature $\overline{\theta_s}$ and its fluctuating component θ_s on the cylinder surface. The dynamic response of the FBG sensor may be adversely affected by the thermal inertia of silicone between the cylinder surface and sensing grating. This silicon layer, whose thermal conductivity is excellent, is extremely thin, about 29 μm. Therefore, the possible thermal lag effects should not downgrade to a significant extent the dynamic response of the FBG sensor. By rotating the cylinder, the circumferential distribution of temperature was measured. Kieft et al. [27] showed that heat added to a horizontal circular cylinder could result in a difference in the vortex strength between upper and lower vortices (Re = 75). The two cylinders were presently vertically mounted, avoiding possible buoyancy effects on the cross-flow distribution of velocity/temperature profiles. It has been confirmed in a single cylinder case that the distribution of $\overline{\theta_s}$ at $R = 9080$ was symmetrical about the centerline. Therefore, $\overline{\theta_s}$ and θ_s were measured from $\alpha = 0$ deg to 180 deg only (Figs. 2 and 3).

In order to validate the FBG sensor measurement, $\overline{\theta_s}$ was simultaneously measured using a type-*K* (nickel-chromium/nickel-aluminum) thermocouple of 0.3 mm diameter placed at the same α as the FBG sensor but 2 cm ($\approx 1d$) away in the spanwise direction. The thermocouple was riveted in the same groove with FBG sensor and flushed with the cylinder surface using heat-conducting silicone. The thermocouple measurement was carried out for an isolated cylinder arrangement only at Re = 7600. As the boundary layer separates from the cylinder, the vortex cell is characterized by a typical spanwise extent of $1 \sim 3d$ [12,28]. Therefore, the time-averaged surface temperature captured by the thermocouple should be the same as that by the FBG sensor.

3.3 Hot-Wire Measurements. The wake fluctuating velocity u was monitored by a single Tungsten hotwire placed at $x/d = 2$ and $y/d = 1.5$, where x and y are the stream-wise and lateral coordinates, respectively, whose origin was chosen at the center of the downstream cylinder (Figs. 2 and 3). At this location, the reversible flow effect on the hotwire measurement should be negligible. The hotwire was operated at an overheat ratio of 1.6 with a constant temperature anemometer.

The signals u, θ_s, and $\overline{\theta_s}$ were simultaneously measured and amplified and then digitized using a 12-bit A/D board and a personal computer at a sampling frequency of 3.5 kHz per channel. At Re = 9080, the frequency of vortex shedding from the inline cylinders does not exceed 100 Hz for L/d investigated. Therefore, a sampling frequency of 3.5 kHz is considered to be adequate. Correspondingly, the cutoff frequency was set at 1.8 kHz. The duration of each record was 20 sec, which has been verified to be sufficiently long for the root mean square (rms) value, $\theta_{s,\mathrm{rms}}$, of θ_s to reach approximately constant, with a variation smaller than 1.0%.

3.4 Laser-Induced Fluorescence (LIF) Flow Visualization. Experiments were carried out in a water tunnel with a square working section (0.15 m × 0.15 m) of 0.5 m long. The water tunnel is a recirculating single reservoir system. A centrifugal pump delivers water from the reservoir to the tunnel contraction. The area ratio of the contraction is 10:1 over a length of 0.6 m. A honeycomb is used to remove any large-scale irregularities prior to the contraction. The flow variation is controlled by a regulator valve, up to a maximum velocity of about 0.32 m/s in the working section, which is made up of four 20 mm thick Perspex panels.

Two inline acrylic circular tubes of an identical diameter of 10 mm were horizontally, with the upstream cylinder placed 0.20 m downstream of the exit plane of the tunnel contraction. The spacing ratios were identical to those in the wind tunnel experiments. The tubes spanned the full width of the tunnel, resulting in a blockage of 6.7%. Dye (Rhodamine 6G 99%) was chosen to be the flow marker. For each cylinder, dye was introduced through two injection pinholes of 0.5 mm in diameter at the mid-span of the cylinder. The two pinholes were located at 90 deg, clockwise and anti-clockwise, respectively, from the forward stagnation point. A thin laser sheet, which was generated by laser beam sweeping, provided illumination vertically at the mid-plane of the working section. A Spectra-Physics Stabilite 2017 Argon Ion laser with a maximum power output of 4 watts was used to generate the laser beam. A digital video camera recorder (Sony DCR-PC100E) was used to record the dye-marked vortex streets at a framing rate of 25 frames per sec. Flow visualization was conducted at Re = 450.

4 Results and Discussions

4.1 Flow Structures. Figure 4 presents typical flow patterns from the LIF flow visualization for three typical flow regimes, which reconfirm previous reports that the flow structure around two inline circular cylinders depends to a great extent on L/d [2,4,8]. For example, at $L/d = 5.20$ (Fig. 4(*a*)), both cylinders generate vortices and vortex shedding from the downstream cylinder is synchronized with that from the upstream cylinder. At $L/d = 2.50$, the shear layers separating from the upstream cylinder reattach on the downstream cylinder; the vortex street is observed only behind the downstream cylinder (Fig. 4(*b*)). At $L/d = 1.18$, the shear layers separating from the upstream cylinder overshoot the downstream cylinder, forming one vortex street (Fig. 4(*c*)).

4.2 Time Histories and Spectra. Figure 5 presents time histories of the measured θ_s (upper trace), along with the simultaneously measured u (lower trace), at $\alpha = 85$ deg. The same scales are used for the θ_s (or u) signals at different L/d to facilitate comparison. At $L/d = 5.20$ (Fig. 5(*a*)), θ_s appears closely correlated with the u signal, both exhibiting a quasi-periodic fluctuation. The corresponding power spectral density function E_{θ_s}

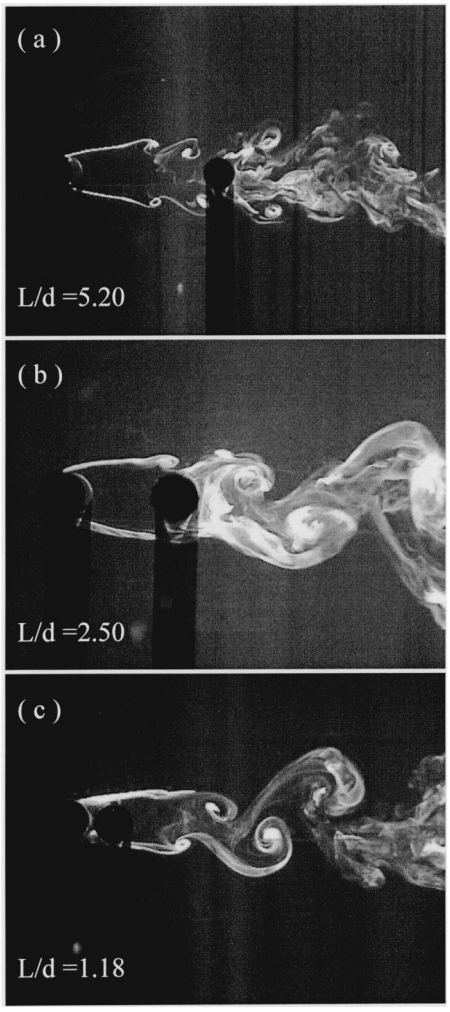

Fig. 4 Laser-induced fluorescence flow visualization in the water tunnel behind two inline cylinders: (*a*) $L/d=5.20$; (*b*) 2.50; and (*c*) 1.18. Re=450. Flow is left to right.

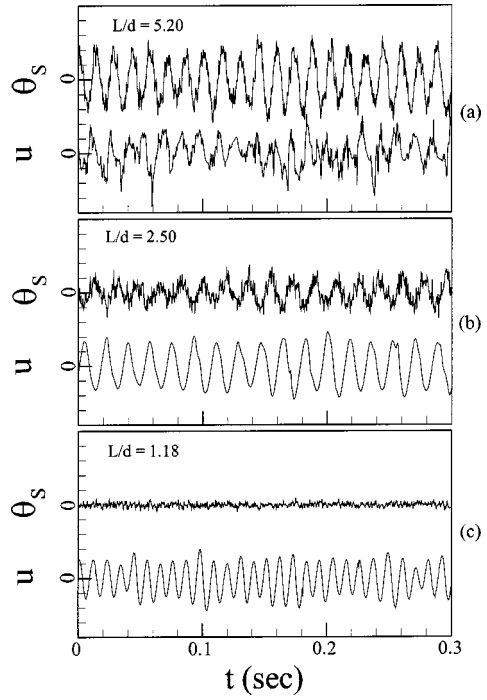

Fig. 5 Time histories of u (the hot wire was placed at $x/d=2$ and $y/d=1.5$) and θ_s at $\alpha=85$ deg. Time $t=0$ is arbitrary; (*a*) $L/d=5.20$; (*b*) $L/d=2.50$; and (*c*) $L/d=1.18$. The same scales are used in (*a*), (*b*), and (*c*) for u and θ_s.

(Fig. 6(*a*)) of θ_s and E_u (Fig. 6(*b*)) of u both display one pronounced peak at $f_s^*=0.177$, apparently due to vortex shedding. The observation is expected because of the association of heat with shedding vortices in the near wake, thus providing a validation for the FBG sensor measurement. Some minor peaks occur at higher frequencies, up to 6 or more multiples of f_s^* in E_{θ_s}, due to the higher harmonics of f_s^* or the effects of flow separation from the other side of the cylinder. The observation suggests that the FBG sensor has a small thermal inertia and its dynamic response is adequate to resolve the fluctuating temperature on the cylinder surface due to vortex shedding.

As L/d decreases to 2.50, the behavior of the θ_s signal (Fig. 5(*b*)) is similar to that at $L/d=5.20$, though the maximum amplitude of the quasi-periodic fluctuation is appreciably reduced. The corresponding E_{θ_s} and E_u (Fig. 6) show one major peak at $f_s^*=0.153$, suggesting a reduced vortex frequency, compared with that ($f_s^*=0.177$) at $L/d=5.20$. The difference in f_s^* is not surprising in view of the drastically distinct flow structures (Figs. 4(*a*) and 4(*b*)) between the two cases.

When L/d is further reduced to 1.18, the θ_s signal (Figs. 5(*c*)) becomes quite different from those at $L/d=5.20$ and 2.50; its fluctuation is greatly impaired. This is also reflected by the significantly reduced major peak in E_{θ_s} (Fig. 6(*a*)), which linked to vortex shedding. This observation is consistent with the reported flow characteristics around two inline cylinders. At such small cylinder spacing, vortices behind the downstream cylinder originate from the free shear layer separating from the upstream cylinder (Fig. 4(*c*)), not from the shear layer around the downstream cylinder [29]. As a result, the fluctuation of the local heat transfer coefficient should be limited, thus leading to a minimum fluctuation in θ_s and a small peak at f_s^* in E_{θ_s}. Note that the peak in E_{θ_s} and E_u occurs at $f_s^*=0.247$ for $L/d=1.18$, which is significantly higher than at $L/d=2.50$ or 5.20. The variation in f_s^* with L/d is

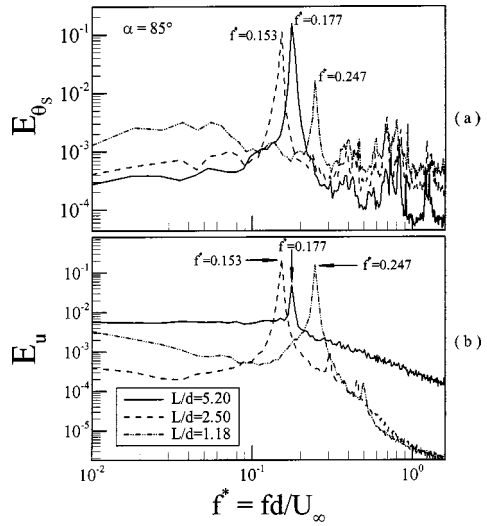

Fig. 6 Power spectral density function E_{θ_s} of the fluctuating surface temperature θ_s at $\alpha=85°$ and E_u of the streamwise fluctuating velocity u: (*a*) E_{θ_s}; and (*b*) E_u. The hot wire was located at $x/d=2$ and $y/d=1.5$. ——, $L/d=5.20$; — — —, $L/d=2.50$; ·····, $L/d=1.18$.

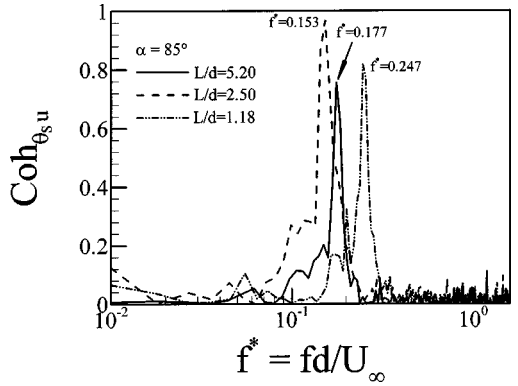

Fig. 7 Spectral coherences $Coh_{\theta_s u}$ between the fluctuating surface temperature θ_s at $\alpha=85$ deg and the streamwise fluctuating velocity u. The hot wire was located at $x/d=2$ and $y/d=1.5$. ——, $L/d=5.20$; — — —, $L/d=2.50$; ·····, $L/d=1.18$.

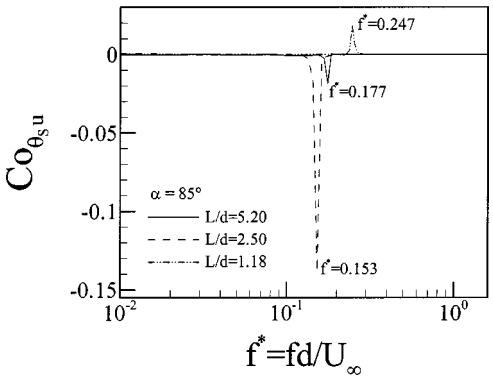

Fig. 8 Co-spectrum $Co_{\theta_s u}$ between the fluctuating surface temperature θ_s at $\alpha=85$ deg and the streamwise fluctuating velocity u. The hot wire was located at $x/d=2$ and $y/d=1.5$. —, $L/d=5.20$; — — —, $L/d=2.50$; ·····, $L/d=1.18$.

qualitatively consistent with previous report at $\mathrm{Re}=3.5\times10^4$ by Igarashi [2]. He observed that f_s^* was minimum f_s^* $(=0.15)$ at $L/d=2.06\sim2.94$. This frequency was increased to 0.27 at $L/d=1.03$; for $L/d>2.94$, f_s^* went up slowly as L/d increased, though not exceeding that of an isolated cylinder.

Interestingly, the u-signal at $L/d=2.50$ or 1.18 is rather smooth, displaying laminar-like characteristic. Generally, at $\mathrm{Re}=9080$, the laminar boundary layer separates from an isolated cylinder [30]. (The readers are cautioned that flow separation from the cylinder surface is complex; for example, the laminar-turbulent transition, boundary layer reattachment and turbulent separation may occur depending on initial conditions.) This does not seem to be altered in the presence of an upstream cylinder as long as no vortex is generated between the cylinders. On the other hand, u appears quite spiky or turbulent at $L/d=5.20$. This is probably attributed to the fact that the near-wake at $5d$ downstream of the upstream cylinder is turbulent.

It should be pointed out that the FBG sensor is sensitive to any applied dynamic strains. The present FBG sensing system *per se* could not seclude strain disturbance [26]. Great care has been taken to minimize such contamination. The present test cylinder, fix-supported at both ends, may vibrate due to vortex excitation forces, which produces a structural dynamic strain [31]. This strain may be reflected on the FBG sensor measurement [24], thus contaminating the temperature signal. A test was thus conducted at identical conditions (section 3) except the cylinder was unheated. The corresponding signal measured by the FBG sensor reflects the structural vibration and background noise. Its amplitude was greatly reduced, compared with the heated cylinder. Furthermore, the corresponding E_{θ_S} did not show any peak, thus indicating a negligible effect of the structural vibration and other non-temperature based perturbations on the temperature measurement. Based on the test data, the signal-to-noise ratio of the present temperature measurement was estimated to be 2 to 6.

The spectral coherence $Coh_{\theta_s u}$ $[\equiv(Co^2_{\theta_s u}+Q^2_{\theta_s u})/E_{\theta_s}E_u$, where $Co_{\theta_s u}$ and $Q_{\theta_s u}$ are the cospectrum and quadrature spectrum of θ_s and u, respectively] provides a measure of the degree of correlation between the Fourier components of θ_s and u. Figure 7 presents the $Coh_{\theta_s u}$ between θ_s at $\alpha=85$ deg and u for each L/d. $Coh_{\theta_s u}$ at f_s^* is 0.76 at $L/d=5.20$, 0.97 at $L/d=2.50$ and 0.82 at $L/d=1.18$, indicating a high level of correlation between θ_s and u. $Coh_{\theta_s u}$ at $L/d=1.18$ is smaller than at $L/d=2.50$, conforming to the fact that vortices do not originate from the boundary layer around the downstream heated cylinder (Fig. 4(*c*)). On the other hand, Fig. 4(*a*) indicates that at $L/d=5.20$ the vortex street behind the downstream cylinder results from interaction between vortices generated by the upstream cylinder and the shear layers separating from the downstream cylinder. The interaction weakens the correlation between the coherent velocity and θ_s, resulting in the relatively small $Coh_{\theta_s u}$ at f_s^*. The co-spectrum $Co_{\theta_s u}$ exhibits a negative peak at f_s^* for $L/d=5.20$ and 2.50; in contrast, $Co_{\theta_s u}$ displays a positive peak at f_s^* for $L/d=1.18$ (Fig. 8). The observation is reasonable. For $L/d=5.20$ and 2.50, when the shear layer separates from the downstream cylinder, the streamwise velocity measured by the hot-wire at $x/d=2$ and $y/d=1.5$ is increasing, giving rise to a positive u. Meanwhile, the shear layer takes heat away from the cylinder surface, resulting in a negative θ_s. As a result, θ_s and u tend to be anti-phased, as confirmed by the spectral phase at f_s^* (not shown), and the peak at f_s^* in $Co_{\theta_s u}$ is negative. At $L/d=1.18$, vortices originate from the shear layer separation from the upstream cylinder (Fig. 4(*c*)); there should be no direct connection between vortex shedding and θ_s. Instead, the flow reversal due to the rolling up of the shear layer on the lower side of the downstream cylinder should have a dominant effect on local heat transfer on the upper side of the cylinder, thus resulting in a positive peak in $Co_{\theta_s u}$.

4.3 Time-Averaged Temperature. In order to further validate the FBG sensor measurement, a type-*K* thermocouple was simultaneously used with the FBG sensor to measure the local time-averaged temperature $\overline{\theta_s}$ on an isolated cylinder. For the purpose of comparison, the measured temperature is normalized by the global mean surface temperature, $\Theta=1/n\Sigma_{i=1}^{n}\overline{\theta_s}(i)$, where $\overline{\theta_s}(i)$ represents the measured local time-averaged surface temperature and n is the total number of $\overline{\theta_s}$ measured around the cylinder surface. Figure 9 presents both FBG sensor and thermocouple measurements of $\overline{\theta_s}/\Theta$ on the isolated cylinder at $\mathrm{Re}=7600$. The FBG-measured Θ is about 30°C, almost identical to that measured by the thermocouple. In fact, the FBG and thermocouple-measured $\overline{\theta_s}$ distributions, varying from 28°C to 32°C, are very close to each other. The good agreement between the techniques provides a validation for the time-averaged temperature measurement by the FBG sensor. Since the temperature variation and the sensing grating are linearly related, i.e., $\Delta\lambda_B=K\theta$, where K is a constant (section 2), the FBG sensor does not need calibrating for the measurements of a range of temperature/strain [24–26,32]. The good agreement in the time-averaged temperature between the FBG and thermocouple measurements implicitly provides a validation for dynamic temperature measurements provided that the FBG system has an adequate dynamic response. The global mean temperatures measured by the thermocouple and the FBG sensor are nearly the same, i.e., $\Theta\approx30$°C. The discrepancy in the recirculation region, i.e.,

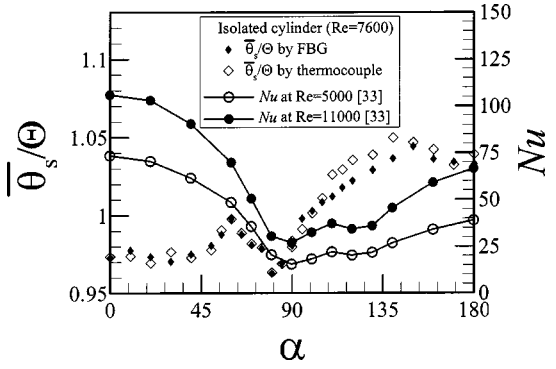

Fig. 9 Circumferential distributions of $\overline{\theta_s}/\Theta$ and Nu (from Adachi et al. [33]) on an isolated cylinder. ♦, $\overline{\theta_s}/\Theta$ measured using the FBG sensor; ◇, $\overline{\theta_s}/\Theta$ measured using a type-*K* thermocouple; ○, Nu at Re=5000; ●, Nu at Re=11000.

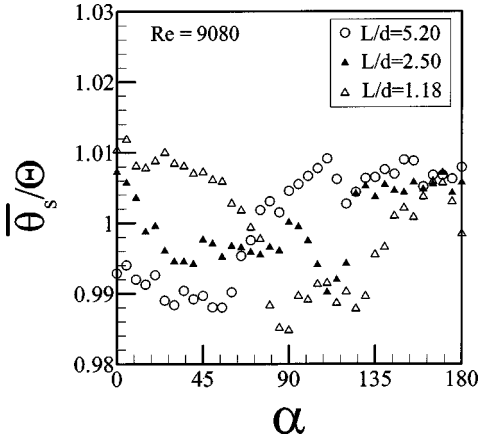

Fig. 10 Circumferential distributions of the local time-averaged surface temperature $\overline{\theta_s}/\Theta$ measured using the FBG sensor. ○, $L/d=5.20$; ▲, $L/d=2.50$; △, $L/d=1.18$. Re=9080.

α=105 deg–140 deg, could be ascribed to experimental uncertainties. A rather conservative estimate indicates a 5% experimental uncertainty in the FBG-measured $\overline{\theta_s}$. The experimental uncertainty of a thermocouple in measuring $\overline{\theta_s}$ depends on thermocouple materials, geometrical dimension, construction of the junction and installation, etc. [17,19] and is presently estimated to be 10%. Given the dynamic nature in the recirculation region and the poor frequency response of a thermocouple, the FBG sensor measurement should be trustworthier.

Figure 9 also compares measured $\overline{\theta_s}/\Theta$ with previously reported local Nu ($=hd/k$, where h is the local heat transfer coefficient and k is the thermal conductivity of fluid) around the cylinder at Re=5000 and 11,000 [33]. Nu displays a maximum at α=0 deg and a minimum at $\alpha\approx$90 deg, while $\overline{\theta_s}/\Theta$ reaches a local maximum at α=60 deg and a minimum at $\alpha\approx$80 deg. A difference between the $\overline{\theta_s}$ and Nu distributions is not unexpected. Firstly, the Nu data were obtained on the assumption of a constant heat flux body. This is strictly speaking not true for the present heated cylinder in cross flow (see section 3.1). Secondly, the flow around the cylinder surface depends on initial conditions such as Re and experimental setup, which are not identical for the two cases. The circumferential distribution of $\overline{\theta_s}/\Theta$ is, nevertheless, largely in qualitatively agreement with the Nu data. In the front body of the cylinder, heat transfer is adversely affected by the growing laminar boundary layer as α increases and thus Nu gradually decreases. Accordingly, $\overline{\theta_s}/\Theta$ rises, showing a local maximum at α=60 deg, and then drops appreciably, reaching the minimum at $\alpha\approx$80 deg. This drop is suspected to be connected to the occurrence of flow separation. Flow separation from the cylinder surface is highly complex. For example, the flow separation point oscillates circumferentially on the cylinder surface [10–12,34], and the laminar-turbulent transition, boundary layer reattachment and turbulent separation may occur depending on initial conditions. The averaged flow separation point may not be at α =60°; instead, it is more likely at $\alpha\approx$80 deg, which coincides with the maximum temperature fluctuation, as shown later in section 4.4, and also approximately with the minimum Nu (Fig. 9). For $\alpha>$80°, $\overline{\theta_s}/\Theta$ climbs steadily up to $\alpha\approx$145 deg because the residence time of fluid in the recirculation region increases towards the trailing stagnation point.

Figure 10 presents the distribution of $\overline{\theta_s}/\Theta$ on the cylinder surface in the presence of an upstream cylinder. The measured $\overline{\theta_s}/\Theta$ at $L/d=5.20$ differs from that of an isolated cylinder; $\overline{\theta_s}/\Theta$ displays a minimum near $\alpha\approx$55 deg, followed by a steady climb up to $\alpha\approx$115 deg. Evidently, the boundary layer development over the upstream surface of the downstream cylinder is affected by the impingement of vortices shed from the upstream cylinder. Our flow visualization data (Fig. 4(*a*)), with the caveat of a lower Re, suggest the impingement of vortices at $\alpha\approx$60 deg. The impingement may enhance the local Nu, leading to the minimum $\overline{\theta_s}/\Theta$. The following climb in $\overline{\theta_s}/\Theta$ could be attributed to the growing boundary layer. The maximum $\overline{\theta_s}/\Theta$ occurs at $\alpha\approx$110 deg, where flow separation from the downstream cylinder probably occurs. Similarly to a single cylinder, there is a subsequent drop between $\alpha\approx$110 deg and 130 deg in $\overline{\theta_s}/\Theta$ due to an increase in Nu. The observation suggests that the impingement of vortices could act to delay the occurrence of flow separation from the downstream cylinder. This will have an adverse effect on heat transfer between the cylinder and fluid, and offset the positive effect on heat transfer by the vortex impingement.

At $L/d=2.50$, $\overline{\theta_s}/\Theta$ appears steadily decreasing from the leading stagnation point (α=0 deg), resulting from the reattachment of the free shear layer separating from the upstream cylinder (Fig. 4(*b*)). The reattachment may perturb the laminar boundary sublayer, which is responsible for the main thermal resistance associated with the convective heat transfer [35], thus enhancing the local heat transfer of the downstream cylinder. One minor peak occurs near α=90 deg, which may indicate the probable flow separation point. There is a rapid decrease in $\overline{\theta_s}/\Theta$ from α=90 deg to 110 deg due to increased turbulence associated with flow separation, and then a rapid climb because of the effect of the recirculation region (120 deg~180 deg).

At $L/d=1.18$, the downstream cylinder is located in the recirculation region of the upstream cylinder [2]. The $\overline{\theta_s}/\Theta$ value decreases slowly from α=0 deg to 90 deg, compared with that at $L/d=2.50$ and 5.20, because of the long residence time of fluid between the cylinders. At such small L/d, the shear layer separating from the upstream cylinder overshoots the downstream cylinder to form a vortex street (see Fig. 4(*c*)). As a result, local heat transfer should be maximum near α=90 deg, which is nearest to the free shear layer blowing over. For 90 deg$<\alpha\leqslant$180 deg, $\overline{\theta_s}/\Theta$ is considerably smaller than that at $L/d=5.20$ and 2.50. It is possible that the flow reversal, due to vortex shedding, in the recirculation region could play a major role in heat transfer from the downstream cylinder.

The effect of cylinder spacing on heat transfer from the downstream cylinder is well summarized by the dependence of Θ on L/d (Fig. 11). The measured Θ was 36.0°C, 27.2°C and 30.3°C for $L/d=1.18$,2.50 and 5.20, respectively, the corresponding $\overline{\theta_s}$ varying from 35.5°C to 36.4°C, 26.9°C to 27.4°C, and 29.9°C to 30.6°C, respectively. Apparently, heat transfer is worst at very small L/d. At $L/d=2.50$, Θ is minimum. Since the heating power was unchanged throughout the entire experiments, the result indicates that the best performance of convective heat transfer occurs

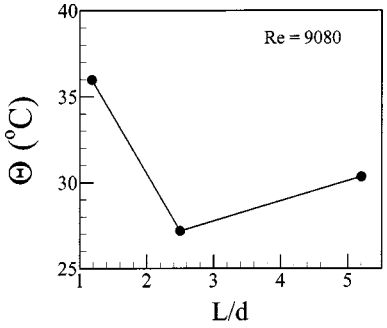

Fig. 11 Influence of L/d on the global mean surface temperature Θ of the downstream cylinder

in this flow regime. As L/d increases further, Θ climbs slowly probably resulting from a delayed flow separation, due to vortex impingement, from the downstream cylinder.

4.4 Circumferential Distribution of $\theta_{s,\mathrm{rms}}$. The circumferential distribution of $\theta_{s,\mathrm{rms}}$ for each L/d is given in Fig. 12, along with that around an isolated cylinder measured at the same Re. The $\theta_{s,\mathrm{rms}}/\Theta$ of an isolated cylinder displays a maximum at $\alpha\approx 82$ deg, which should be the flow separation point. The assertion is consistent with previous reports that the separation point varied from $\alpha=75°$ to 85° for $\mathrm{Re}=1.06\times10^5$ [11]. The mean location is dependent upon Re [34]. For example, Higuchi et al. [12] found that the separation point oscillated between 87 deg and 95 deg at $\mathrm{Re}=1.96\times10^5$, while Achenbach [10]'s investigation indicated that boundary layer separation occurred at 78 deg for $\mathrm{Re}=10^5$ and shifted to 94 deg for $\mathrm{Re}=3\times10^5$. The minimum $\theta_{s,\mathrm{rms}}/\Theta$ occurs at the leading and trailing stagnation points. The present observation conforms to Scholten and Murray [15]'s heat flux measurement, which indicated a large fluctuation in the heat flux on the cylinder surface at $\alpha=85$ deg ($\mathrm{Re}=21580$). The circumferential distribution of $\theta_{s,\mathrm{rms}}$ on the downstream cylinder surface is similar to that of an isolated cylinder. The maximum $\theta_{s,\mathrm{rms}}/\Theta$ occurs at $\alpha\approx85$ deg~90 deg. The minimum $\theta_{s,\mathrm{rms}}/\Theta$ occurs at $\alpha=0$ deg and 180 deg. It is evident that the maximum $\theta_{s,\mathrm{rms}}/\Theta$ increases with L/d (Fig. 12), and in all cases is substantially smaller than that in an isolated cylinder case.

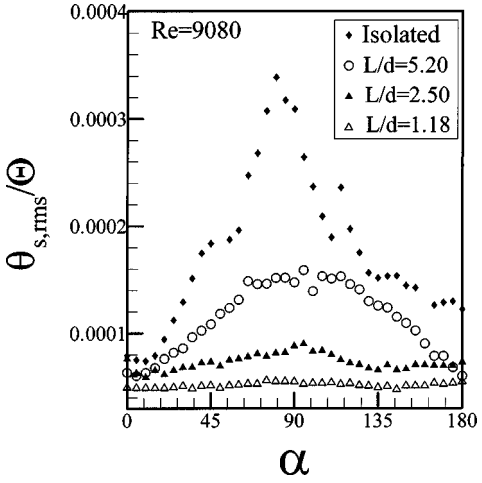

Fig. 12 Circumferential distribution of the rms value $\theta_{s,\mathrm{rms}}/\Theta$ of the fluctuating surface temperature θ_s. Re=9080. ♦, Isolated cylinder; ○, $L/d=5.20$; ▲, $L/d=2.50$; △, $L/d=1.18$.

5 Conclusions

To our knowledge, this is the first attempt to measure simultaneously the time-averaged and fluctuating surface temperatures on a heated cylinder immersed in the wake of an upstream cylinder using the FBG sensor. Three L/d ratios, 5.20, 2.50, and 1.18, were investigated. The measurements were compared with those obtained for an isolated cylinder. The investigation leads to the following conclusions:

1) The local time-averaged surface temperature $\overline{\theta_s}/\Theta$ measured using the FBG sensor is in good agreement with that simultaneously obtained by a K-type thermocouple. Furthermore, the measured fluctuating temperature θ_s/Θ is closely correlated to the hot-wire measurement. The power spectrum E_{θ_s} exhibits a prominent peak at f_s^*, as identified in E_u, for each L/d; the spectral coherence at f_s^* ranges between about 0.8 to almost 1. The observation is consistent with the fact that in the near-wake heat is associated with vortices shed from the heated cylinder. The results suggest that the FBG sensor can provide reliable measurements for both time-averaged and fluctuating surface temperatures on cylinders in a cross flow. The sensor is characterized by small thermal inertia and its dynamic response is excellent [25]. The major limitation of its dynamic response comes from heat conduction between the fiber and surroundings material. In addition, The FBG sensor can be used reliably up to 600°C [36].

2) The circumferential distribution of the local time-averaged surface temperature $\overline{\theta_s}/\Theta$, measured using the FBG sensor, is qualitatively consistent with the reported flow characteristics around two tandem cylinders in cross-flow, which provides further validation for the proposed technique. For relatively large cylinder spacing, $L/d=5.20$, the flow separation point appears shifted from $\alpha\approx85$ deg in an isolated cylinder case to $\alpha\approx110$ deg, as a result from the vortex impingement on the upstream surface of the cylinder. As L/d decreases to 2.50, there is an appreciable dip in $\overline{\theta_s}/\Theta$ at $\alpha\approx30$ deg~90 deg, due to the re-attachment of the shear layer separated from the upstream cylinder, which may lead to an increase in the local Nu on the downstream cylinder. At very small L/d, 1.18, $\overline{\theta_s}/\Theta$ increases from $\alpha=0$ deg to 90 deg. However, it appears decreasing from $\alpha=90°$ to 180°, due to the enhanced backflow effects of the vortices generated from the upstream cylinder. The global mean surface temperature Θ is minimum at $L/d=2.50$, indicating a higher global Nu in this flow regime.

3) The circumferential distribution of $\theta_{s,\mathrm{rms}}$ displays a maximum at $\alpha\approx85$ deg~90 deg for two cylinders in tandem. This location slightly deviates from that of an isolated cylinder ($\alpha\approx80$ deg). The maximum value of $\theta_{s,\mathrm{rms}}/\Theta$ increases with L/d and reaches the maximum for an isolated cylinder.

Acknowledgment

The authors wish to acknowledge support by the Central Research Grant of The Hong Kong Polytechnic University through Grants G-T408, G-YD21 and G-T444.

Nomenclature

$Co_{\theta_s u}$ = cospectrum of θ_s and u
$Coh_{\theta_s u}$ = spectral coherence between θ_s and u
d = diameter of circular cylinder (mm)
$E_\beta(f)$ = spectrum of fluctuation β (β represents either θ_s or u), normalized so that $\int_0^\infty E_\beta(f)df=1$
f = frequency in spectrum analysis (Hz)
f_s = vortex shedding frequency of a stationary cylinder (Hz)
h = convection heat transfer coefficient ($\mathrm{W/m^2K}$)
k = thermal conductivity of fluid (W/mK)
L = center-to-center cylinder spacing (mm)
Nu = Nusselt number$=hd/k$
$Q_{\theta_s u}$ = quadrature spectrum of θ_s and u

Re = Reynolds number$\equiv U_\infty d/\nu$
S_t = Strouhal number$\equiv f_s d/U_\infty$
u = streamwise fluctuating velocity (m/sec)
U_∞ = free-stream velocty (m/sec)
x, y = co-ordinates in streamwise and lateral directions, respectively

Greek Symbols

α = circumferential angle on the cylinder, $\alpha=0$ deg and 180 deg corresponds to the leading and trailing stagnation points, respectively
δ = cylinder wall thickness (mm)
λ_B = optical fiber Bragg grating resonance wavelength (nm)
ν = fluid kinematic viscosity
θ_s = fluctuating surface temperature. An over bar represents time-averaged value (°C)
$\theta_{s,\mathrm{rms}}$ = root mean square values of θ_s (°C)
Λ = optical fiber Bragg grating pitch (nm)
Θ = global mean surface temperature$=1/n\Sigma_{i=1}^{n}\overline{\theta_s}(i)$, where $\overline{\theta_s}(i)$ represents the measured local time-averaged surface temperature and n is the total number of $\overline{\theta_s}$ measured around the cylinder surface (°C)

Superscript

* = dimensionless parameter normalized by d and U_∞

References

[1] Kostic, Z. G., and Oka, S. N., 1972, ''Fluid Flow and Heat Transfer With Two Cylinders in Cross Flow,'' Int. J. Heat Mass Transfer, **15**, pp. 279–299.
[2] Igarashi, T., 1981, ''Characteristics of the Flow Around Two Circular Cylinders Arranged in Tandem,'' Bull. JSME, **24**(188), pp. 323–331.
[3] Hiwada, M., Mabuchi, I., and Yanagihara, H., 1982, ''Fluid Flow and Heat Transfer Around Two Circular Cylinders,'' Bull. JSME, **25**(209), pp. 1737–1745.
[4] Zdravkovich, M. M., 1987, ''The Effects of Interference Between Circular Cylinders in Cross Flow,'' J. Fluids Struct., **1**, pp. 239–261.
[5] Mahir, N., and Rockwell, D., 1996, ''Vortex Formation From a Forced System of Two Cylinders, Part 1: Tandem Arrangement,'' J. Fluids Struct., **10**, pp. 473–489.
[6] Meneghini, J. R., Saltara, F., Siqueira, C. L. R., and Ferrari, Jr., J. A., 2001, ''Numerical Simulation of Flow Interference Between Two Circular Cylinders in Tandem and Side-by-Side Arrangement,'' J. Fluids Struct., **15**, pp. 327–350.
[7] Buyruk, E., Barrow, H., and Owen, I., 1995, ''The Influence of Adjacent Tubes on Convection Heat Transfer From a Heated Tube in Cross-Flow,'' *In Fourth UK National Conference on Heat Transfer*, I. Mech. E. Conference Trans., pp. 135–139.
[8] Zdravkovich, M. M., and Pridden, D. J., 1977, ''Interference Between Two Circular Cylinders; Series of Unexpected Discontinuities,'' Journal of Industrial Aerodynamics, **2**, pp. 255–270.
[9] Arie, M., Kiya, M., Tamura, H., and Mori, H., 1983, ''Pressure Fluctuations on Two Circular Cylinders in Tandem Arrangement,'' ASME J. Fluids Eng., **105**, pp. 161–167.
[10] Achenbach, E., 1968, ''Distribution of Local Pressure and Skin Friction Around a Circular Cylinder in Cross-Flow Up to $\mathrm{Re}=5\times10^6$,'' J. Fluid Mech., **34**(4), pp. 625–639.
[11] Dwyer, H. A., and Mccroskey, W. J., 1973, ''Oscillating Flow Over a Cylinder at Large Reynolds Number,'' J. Fluid Mech., **61**(4), pp. 753–767.
[12] Higuchi, H., Kim, H. J., and Farell, C., 1989, ''On Flow Separation and Reattachment Around a Circular Cylinder at Critical Reynolds Numbers,'' J. Fluid Mech., **200**, pp. 149–171.
[13] Giedt, W. H., 1949, ''Investigation of Variation of Point Unit Heat-Transfer Coefficient Around a Cylinder Normal to an Air Stream,'' Trans. ASME, May, pp. 375–381.
[14] Krall, K. M., and Eckert, E. R. G., 1973, ''Local Heat Transfer Around a Cylinder at Low Reynolds Number,'' J. Heat Transfer, **95**, pp. 273–275.
[15] Scholten, J. W., and Murray, D. B., 1998, ''Unsteady Heat Transfer and Velocity of a Cylinder in Cross Flow: Part 1—Low Freestream Turbulence,'' Int. J. Heat Mass Transfer, **41**(10), pp. 1139–1148.
[16] Valvano, J. W., 1992, ''Temperature Measurements,'' Adv. Heat Transfer, **22**, pp. 359–436.
[17] Morris, A. S., 1993, *Principles of Measurement and Instrumentation*, Second ed., Redwood Books Ltd, Trowbridge, Wiltshire, Great Britain.
[18] Morrison, R., 1984, *Instrumentation Fundamentals and Applications*, John Wiley & Sons, New York.
[19] Michalski, L., Eckersdorf, K., and McGhee, J., 1991, *Temperature Measurement*, John Wiley & Sons Ltd. Baffins Lane, Chichester, West Sussex PO19 1UD, England.
[20] Marton, L., and Marton, C., 1981, *Methods of Experimental Physics: Volume 18, Fluid Dynamics*, Part B, Academic Press, Inc. (London) LTD.
[21] Sandberg, C., and Haile, L., 1987, ''Fiber Optic Application in Pipes and Pipelines,'' IEEE Trans. Ind. Appl., **IA-23**(6), p. 1061.
[22] Grattan, K. T. V., 1987, ''The Use of Fibre Optic Techniques for Temperature Measurement,'' Meas. Control, **20**(6), pp. 32–39.
[23] Kersey, A. D., Davis, M. A., Patrick, H. J., LeBlanc, M., Koo, K. P., Askins, C. G., Putnam, M. A., and Friebele, E. J., 1997, ''Fiber Grating Sensors,'' J. Lightwave Technol., **15**, pp. 1442–1462.
[24] Zhou, Y., So, R. M. C., Jin, W., Xu, H. G., and Chan, P. K. C., 1999, ''Dynamic Strain Measurements of a Circular Cylinder in a Cross Flow Using a Fibre Bragg Grating Sensor,'' Exp. Fluids, **27**, pp. 359–367.
[25] Jin, W., Zhou, Y., Chan, P. K. C., and Xu, H. G., 2000, ''A Fibre-Optic Grating Sensor for the Study of Flow-Induced Vibrations,'' Sens. Actuators, **79**, pp. 36–45.
[26] Ho, H. L., Jin, W., Chan, C. C., Zhou, Y., and Wang, X. W., 2002, ''A Fiber Bragg Grating Sensor for Static and Dynamic Measurands,'' Sens. Actuators A, **96**, pp. 21–24.
[27] Kieft, R. N., Rindt, C. C. M., Steenhoven, A. A., and van Heijst, G. J. F., 2003, ''On the Wake Structure Behind a Heated Horizontal Cylinder in Cross-Flow,'' J. Fluid Mech., **486**, pp. 189–211.
[28] King, R., 1977, ''A Review of Vortex Shedding Research and Its Application,'' Ocean Eng., **4**, pp. 141–171.
[29] Zdravkovich, M. M., 1977, ''Review of Flow Interference Between Two Circular Cylinders in Various Arrangements,'' ASME J. Fluids Eng., **99**, pp. 618–633.
[30] Zdravkovich, M. M., 1997, *Flow Around Circular Cylinders*, Vol. 1. Oxford University Press.
[31] Zhou, Y., Wang, Z. J., So, R. M. C., Xu, S. J., and Jin, W., 2001, ''Free Vibrations of Two Side-by-Side Cylinders in a Cross Flow,'' J. Fluid Mech., **443**, pp. 197–229.
[32] Shi, C. Z., Chan, C. C., Zhang, M., Ju, J., Jin, W., Liao, Y. B., Zhang, Y., and Zhou, Y., 2002, ''Simultaneous Interrogation of Multiple Fiber Bragg Grating Sensors for Dynamic Strain Measurements,'' J. Optoelectron. Adv. Mater., **4**, pp. 937–941.
[33] Adachi, T., Okamoto, S., and Adachi, M., 1979, ''The Effect of Sound on the Rate of Heat Transfer From a Cylinder Placed Normal to an Air Stream,'' Bull. JSME, **22**, pp. 1407–1415.
[34] Chen, S. S., 1987, *Flow-Induced Vibration of Circular Cylindrical Structures*, Hemisphere Publishing Corporation, Washington.
[35] Holman, J. P., 1997, *Heat Transfer*, 8th ed., Mcgraw-Hill Companies, New York, pp. 248–255, 303.
[36] Krohn, D. A., 2000, *Fiber Optic Sensors: Fundamentals and Applications*, Research Triangle, ISA, NC, USA.

X. Y. Chen
K. C. Toh
C. Yang
J. C. Chai
e-mail: mckchai@ntu.edu.sg

Nanyang Technological University,
School of Mechanical and Production Engineering,
Nanyang Avenue,
Singapore 639798

Numerical Computation of Hydrodynamically and Thermally Developing Liquid Flow in Microchannels With Electrokinetics Effects

Developing fluid flow and heat transfer with temperature dependent properties in microchannels with electrokinetic effects is investigated numerically. The electrokinetic effect on liquid flow in a parallel slit is modeled by the general Nernst-Planck equation describing anion and cation distributions, the Poisson equation determining the electrical potential profile, the continuity equation, and the modified Navier-Stokes equation governing the velocity field. A Finite-Volume Method is utilized to solve the proposed model.
[DOI: 10.1115/1.1643909]

Keywords: Heat Transfer, Microscale, Modeling

1 Introduction

Fluid flow and heat transfer in microchannels have become an important research area due to their wide applications, such as microchannel heat sink in electronics cooling, MEMS based fluidic devices, ranging from sensors such as pH and temperature, to fluid actuators, such as pumps, mixers, and valves as well as Lab-on-a-Chip or Bio-chip systems for drug delivery, chemical analysis, and biomedical diagnosis. Fundamental understanding of the fluid flow and heat transfer characteristics in microchannels is crucial to the optimum design and process control of these microfluidic devices. However, many experimental observations of microchannel flow behavior, such as nonlinear pressure distributions [1], early transition from laminar flow to turbulent flow [2], and dependence of flow characteristics on channel dimension [3] and fluid type (e.g., polar or non-polar fluids) [4], still cannot be adequately explained by conventional theories.

A possible explanation of the observed anomalous dependence of flow characteristics on the channel size and fluid properties might be attributed to the electrokinetic effect. In the literature, a variety of analytical and numerical studies have been reported to investigate the electrokinetic effect on fully developed liquid flow characteristics in microchannels of various geometric domains. Yang and Li [5,6] considered a pressure-driven flow in rectangular microchannels. A two-dimensional electric potential model was proposed, and was solved both analytically using the Debye-Hückel linear approximation [5] and numerically [6]. A Green's function approach was developed to obtain a close-form solution of the flow field. Moreover, Yang et al. [7] examined liquid convective heat transfer in a rectangular microchannel, and found that the heat transfer characteristics could be significantly influenced by the presence of the electrical double layer (EDL). Mala et al. [8] investigated the effect of the EDL on liquid flow and heat transfer between two parallel plates. Ng and Poh [9] also investigated the effect of the EDL on flow and heat transfer in rectangular microchannels. On the experimental side, verification of the electrokinetic (or electroviscous) effect on liquid flow in microchannels was reported by Li and co-workers [10,11]. In these studies, the fluid flow and heat transfer are assumed to be hydrodynamically and thermally fully developed.

To the best knowledge of the present authors, there is no study on the effect of the EDL in the developing (both hydrodynamic and thermal) region of a pressure-driven flow. As shown by Yang et al. [7], in the developing microchannel flow regime the Boltzmann equilibrium distributions cannot be assumed. Furthermore, the fluid properties, such as viscosity, conductivity and dielectric constant of the fluid are all temperature dependent. When the fluid is heated, some of these parameters, which have great effect on the fluid flow and heat transfer, cannot be assumed as constants.

In this article, a mathematical model is developed to study the electrokinetic effect on liquid flow and heat transfer in a parallel slit including the general Nernst-Planck equation describing anion and cation distributions, the Poisson equation determining the electrical potential profile, the continuity equation, and the modified Navier-Stokes equations governing the velocity field. The Finite-Volume method (FVM) of Patankar [12] is used to solve the system of coupled governing equations. A new streaming potential for developing flow is presented. The characteristics of the pressure-driven flow in the presence of the electroviscous effect are examined. Some fluids properties are temperature dependent.

The remainder of this article is divided into four sections. The mathematical formulation of the problem is presented in the next section. This is followed by a section describing the physical model, boundary conditions and material properties. The numerical method used to solve the governing equations is also discussed in this section. Next, the numerical results are discussed. Finally, some remarks are given to conclude the article.

2 Mathematical Models

The concept of electrokinetic (or electroviscous) effect on pressure-driven flow in microchannels has been well established [13]. In brief, it is well known that most surfaces acquire a certain amount of electrostatic charges when brought in contact with aqueous solutions. The most likely charging mechanism is due to the asymmetric dipoles of water molecules that reside at the solid-liquid interface [14]. If the liquid contains a very small amount of ions (this is unavoidable in reality due to impurities), the presence of such surface charges on the microchannel surface causes both counter-ions and co-ions in the liquid to be preferentially redis-

Contributed by the Heat Transfer Division for publication in the JOURNAL OF HEAT TRANSFER. Manuscript received by the Heat Transfer Division March 19, 2003; revision received October 16, 2003. Associate Editor: P. S. Ayyaswamy.

tributed, leading to the formation of the EDL [13]. Conceptually, the EDL can be divided into an inner compact layer and an outer diffuse layer. The inner layer, usually of several Angstroms, is immediately next to the charged surface and contains a layer of immobile counter-ions that are strongly attracted to the surface. In contrast, ions in the diffuse layer are less affected by the charged surface and hence are mobile. The boundary between the compact layer and the diffuse layer is usually referred to as the shear plane, where the electrical potential is measurable and is called the zeta potential, ζ [13].

According to the theory, the electrical potential in the diffuse part of the EDL is governed by the Poisson equation, which in Cartesian tensor notation is expressed as

$$\frac{\partial}{\partial x_j}\left(\varepsilon_r \frac{\partial \psi}{\partial x_j}\right) = -\frac{\rho_e}{\varepsilon_0} \tag{1}$$

The net charge density ρ_e in Eq. (1) is given by

$$\rho_e = e(Z_+ n_+ + Z_- n_-) \tag{2}$$

Equation (1) is also valid in the core region where the net charge density is zero. In thermodynamic equilibrium where the chemical potential is balanced by the electrical potential, it can be shown that both n_+ and n_- follow the Boltzmann distributions [13],

$$n_\pm = n_0 \exp\left(-Z_\pm \frac{e\psi}{k_b T}\right) \tag{3}$$

However, in the presence of developing flow, the n_+ and n_- ionic number concentration distributions are described by the more general Nernst-Planck equations [15] as

$$\frac{\partial(u_j n_\pm)}{\partial x_j} = \frac{\partial}{\partial x_j}\left(D_\pm \frac{\partial n_\pm}{\partial x_j}\right) + \frac{\partial}{\partial x_j}\left(Z_\pm n_\pm \frac{eD_\pm}{k_b T}\frac{\partial \psi}{\partial x_j}\right) \tag{4}$$

The conventional Navier-Stokes equation that governs fluid flow is modified to account for EDL. As mentioned earlier, the electrical net charge density, ρ_e in the diffuse part of the EDL is not zero. When liquid flows in a microchannel under an applied hydraulic pressure, the nonzero electrical charges are carried downstream, resulting in an electrical current called the streaming current. Corresponding to this streaming current, there is an electrokinetic potential called the streaming potential. This flow-induced streaming potential is a potential difference that builds up along a microchannel. Such a streaming potential interacts with the net charge density arising from the difference between the counter-ions and co-ions in the diffuse part of the EDL, and resulting in the movement of ions in the direction opposite to the pressure-driven flow direction. These ions pull the liquid molecules along, leading to a reduced flow rate. If the reduced flow rate is compared with the flow rate predicted by the conventional fluid mechanics theory, the effect of the presence of the EDL is akin to that of a liquid having a higher viscosity. Such phenomenon is referred to as the electrokinetic (or electroviscous) effect [13]. The continuity, momentum and energy equations are presented next. Continuity equation

$$\frac{\partial(\rho u_j)}{\partial x_j} = 0 \tag{5}$$

Modified Navier-Stokes equation

$$\frac{\partial(\rho u_j u_i)}{\partial x_j} = \frac{\partial}{\partial x_j}\left(\mu \frac{\partial u_i}{\partial x_j}\right) + \frac{\partial}{\partial x_j}\left(\mu \frac{\partial u_j}{\partial x_i}\right) - \frac{2}{3}\frac{\partial}{\partial x_i}\left(\mu \frac{\partial u_k}{\partial x_k}\right) - \frac{\partial p}{\partial x_i} + \rho_e E_{sx} \delta_{i1} \tag{6}$$

where the Kronecker Delta δ_{i1} is given by

$$\delta_{i1} = \begin{cases} 1 & i = 1 \\ 0 & i \neq 1 \end{cases} \tag{7}$$

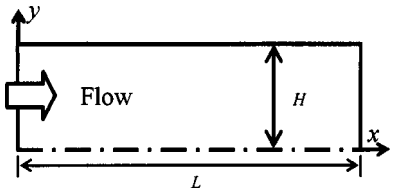

Fig. 1 Computational domain

Energy equation

$$\frac{\partial(\rho C_p u_j T)}{\partial x_j} = \frac{\partial}{\partial x_j}\left(k \frac{\partial T}{\partial x_j}\right) + \frac{1}{2}\mu \dot{\gamma}^2 \tag{8}$$

where

$$|\dot{\gamma}| = \sqrt{\left[\left(\frac{\partial u_i}{\partial x_j} + \frac{\partial u_j}{\partial x_i}\right)^2 - \frac{4}{3}\left(\frac{\partial u_k}{\partial x_k}\right)^2\right]} \tag{9}$$

In Eq. (6), E_{sx} is the electrical field generated by the streaming potential which is not known yet. To obtain the streaming potential in developing flow, a general expression for the axial component of the local electrical current density is expressed as [15]

$$i_x = u_1 \rho_e - \sum D_i Z_i e \frac{\partial n_i}{\partial x_1} + \lambda E_{sx} \tag{10}$$

Under steady-state situation, the electric current over a cross-section is zero. Integrating Eq. (10) over a cross-sectional area gives

$$\int_{A_c}\int \left[u_1 \rho_e + \lambda E_{sx} - e\left(D_+ Z_+ \frac{\partial n_+}{\partial x_1} + D_- Z_- \frac{\partial n_-}{\partial x_1}\right)\right] dA = 0 \tag{11}$$

Equation (11) shows that for a developing electrokinetic flow, the electric current not only includes the streaming (term 1) and conduction (term 2) currents, which are present in the fully developed flow, but also has an additional term to account for an induced current due to ionic concentration gradient. Solving Eq. (11) yields the expression for the streaming potential gradient

$$E_{sx} = \frac{\int_{A_c}\int \left[u_1 \rho_e - \left(D_+ Z_+ \frac{\partial n_+}{\partial x_1} + D_- Z_- \frac{\partial n_-}{\partial x_1}\right)\right] dA}{-\int_{A_c}\int (\lambda_+ n_+ + \lambda_- n_-) dA} \tag{12}$$

3 Problem Description

The effects of EDL on developing flow and heat transfer between two flat plates are investigated. Figure 1 shows a schematic sketch of the physical situation. The height of the channel $2H$, is 6 μm and the length of the channel L, is 20 μm. An infinitely diluted aqueous 1:1 electrolyte (NaCL) solution is considered in this study. The inlet temperature of the solution is kept at 25°C. The temperatures of the two plates are kept at 85°C. The velocity at the inlet is assumed uniform with a Reynolds number Re, of 1.0. Two bulk ion concentrations of the solution and corresponding zeta potentials are considered. These are taken as 10^{-5} M (6.022×10^{21}), 100 mV and 10^{-6} M (6.022×10^{20}), 150 mV respectively. These values are chosen based on the experimental observation of Mala et al. [16]. Due to symmetry only the top half of the geometry is modeled (as shown in Fig. 1). For the temperature range examined in this article, the density changes by less than 3%. As a result, buoyancy effect is not included in this study.

3.1 Boundary Conditions. The mathematical equations derived above are subject to the boundary conditions at inlet, outlet, wall and symmetric centerline as specified below.

Table 1 Constants in properties versus temperature correlations

x	a_x	b_x	c_x	d_x
0	999.84	8958.9	-0.58166	2.414×10^{-5}
1	18.225	-40535	6.3556×10^{-3}	247.8
2	-7.92×10^{-3}	0.11243	-7.964×10^{-6}	140.0
3	-5.545×10^{-5}	-1.014×10^{-4}		
4	1.498×10^{-7}			
5	-3.933×10^{-10}			
6	1.816×10^{-2}			

Table 2 Properties used in this paper

Variable	Unit	Value
D_+*	$m^2\,s^{-1}$	1.334×10^{-9}
D_-*	$m^2\,s^{-1}$	2.032×10^{-9}
e	C	1.60219×10^{-19}
k_b	$J\,K^{-1}$	1.38066×10^{-23}
ε_r*		79
ε_0	$CV^{-1}\,m^{-1}$	8.85419×10^{-12}
λ_+*	$m^2\,Smol^{-1}$	50.08×10^{-4}
λ_-*	$m^2\,Smol^{-1}$	76.31×10^{-4}

*at 298 K.

(a) Momentum and Energy Equations.

$$\text{Inlet:}\quad u_1=u_{in},\quad u_2=0,\quad T=298\ \text{K} \tag{13a}$$

$$\text{Outlet:}\quad \text{mass conservation},\quad \frac{\partial u_2}{\partial x_1}=0,\quad \frac{\partial T}{\partial x_1}=0 \tag{13b}$$

$$\text{Wall:}\quad u_1=u_2=0\quad T=358\ \text{K} \tag{13c}$$

$$\text{Symmetry:}\quad \frac{\partial u_1}{\partial x_2}=0\quad u_2=0\quad \frac{\partial T}{\partial x_2}=0 \tag{13d}$$

(b) Poisson Equation.

$$\text{Inlet:}\quad \psi=0 \tag{14a}$$

$$\text{Outlet:}\quad \frac{\partial \psi}{\partial x_1}=0 \tag{14b}$$

$$\text{Wall:}\quad \psi=\zeta \tag{14c}$$

$$\text{Symmetry:}\quad \frac{\partial \psi}{\partial x_2}=0 \tag{14d}$$

(c) Nernst-Planck Equations.

$$\text{Inlet:}\quad n_\pm=n_0 \tag{15a}$$

$$\text{Outlet:}\quad \frac{\partial n_\pm}{\partial x_1}=0 \tag{15b}$$

$$\text{Wall:}\quad n_\pm=n_0\exp\left(-Z_\pm\frac{e\zeta}{k_bT}\right) \tag{15c}$$

$$\text{Symmetry:}\quad \frac{\partial n_\pm}{\partial x_2}=0 \tag{15d}$$

3.2 Properties of Water. Properties of water are allowed to vary with temperature. The functional relations of density, specific heat, thermal conductivity and viscosity with temperature are [17]:

$$\rho=\frac{a_0+a_1T+a_2T^2+a_3T^3+a_4T^4+a_5T^5}{1+a_6T} \tag{16}$$

$$C_P=b_0+b_1T+b_2T^2+b_3T^3 \tag{17}$$

$$k=c_0+c_1T+c_2T^2 \tag{18}$$

$$\mu=d_0 10^{d_1/(T-d_2)} \tag{19}$$

In Eqs. (16) through (19), thermal conductivity k is in W/m·K, viscosity μ is in Pa·s, specific heat is in J/kg·K and temperature T is in K except for Eq. (16) where it is in °C respectively. The various constants are listed in Table 1. The dielectric constant of water [18] is calculated using

$$\varepsilon_r=0.0007T^2-0.3949T+88.281 \tag{20}$$

where temperature T is in °C. The ionic conductivities and diffusion coefficients are also temperature dependent. These increase 2–3% per degree when the temperature is above 25°C [18], 2.5% is used in this paper. Table 2 lists the data of these parameters at 25°C, and other constant used in this study.

3.3 Numerical Method. In this article, the FVM of Patankar [12] is used to solve the equations listed in section 2. Since a detailed discussion of the FVM is available in Patankar [12], only a very brief description of the major features of the FVM used is given here.

In the FVM, the domain is divided into a number of control volumes such that there is one control volume surrounding each grid point. The grid points are located in the centers of control volumes. The governing equation is integrated over each control volume to derive an algebraic equation containing the grid point values of the dependent variable. The discretization equation then expresses the conservation principle for a finite control volume just as the partial differential equation expresses it for an infinitesimal control volume. The resulting solution implied that the integral conservation of quantities such as mass, momentum and energy is satisfied for any control volume and of course, for the whole domain. The power-law scheme is used to model the combined convection-diffusion effect in the transport equations. The SIMPLER algorithm of Patankar [12] is used to resolve the pressure-velocity coupling. The resulting algebraic equations are solved using a line-by-line Tri-Diagonal Matrix Algorithm.

4 Results and Discussions

A grid independence study is carried out using 240×140 and 480×280 control volumes in the axial and transverse directions respectively. In order to resolve the sharp changes inside the EDL region, significant numbers of control volumes are concentrated in the near-wall region. The EDL thickness [7] is calculated as $1/\sqrt{2z^2e^2n_0/\varepsilon_0\varepsilon_r k_bT}$. In this article, in the 240×140 grid system, 80 control volumes are used to discretize a region equal to five times the EDL thickness. The number of control volumes in the same region is doubled to 160 when 480×280 control volumes are used. The fully developed f Re and Nu are compared with analytic values (with constant properties and without EDL effects). The fully developed f Re and Nu obtained using the coarse (240×140) grid are 95.9 and 7.55 respectively. The exact solutions are 96 and 7.54 respectively. The errors in the f Re and Nu are around 0.1% of the respective exact values. A further grid test is carried out with EDL effects. In this test, the zeta potential, ion concentration and Reynolds number are kept as 150 mV, 10^{-6} and 1.0, respectively. The fully developed f Re predicted using these grid sizes differ by less than 1% (40.7 and 40.3 respectively). The results presented in this article are obtained using the coarse grid of 240×140 control volumes.

Wherever possible, appropriate dimensionless forms of the variables are used to present the results. Some of the variables are:

$$\text{Non-dimensional coordinates:}\quad X=\frac{x}{H}\quad Y=\frac{y}{H} \tag{21}$$

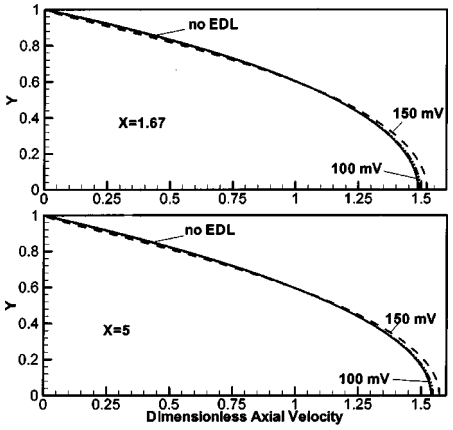

Fig. 2 Velocity distributions at different locations

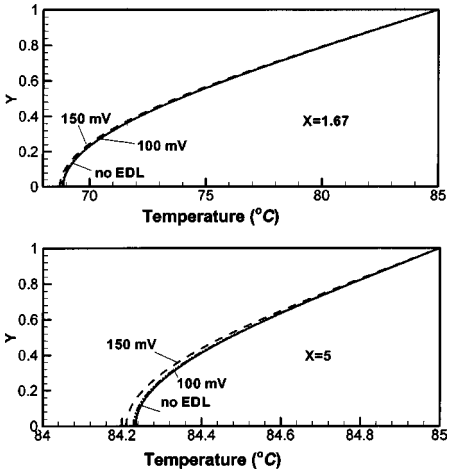

Fig. 3 Temperature distributions at different locations

$$\text{Dimensionless velocity:} \quad U = \frac{u}{u_{in}} \tag{22}$$

$$\text{Dimensionless ionic concentration:} \quad N_{\pm} = \frac{n_{\pm}}{n_0} \tag{23}$$

$$\text{Friction factor:} \quad f \equiv \frac{-(\partial p/\partial x)D_h}{\rho u_{in}^2/2} \tag{24}$$

$$\text{Reynolds number} \quad \mathrm{Re} \equiv \frac{\rho u_{in} D_h}{\mu} \tag{25}$$

$$\text{Hydraulic diameter:} \quad D_h \equiv \frac{4A}{P} = 4H \tag{26}$$

$$\text{Dimensionless electrical potential:} \quad \Psi = \frac{Ze\psi}{k_b T} \tag{27}$$

$$\text{Nusselt number:} \quad \mathrm{Nu} = \frac{hD_h}{k} = \frac{\left.\dfrac{\Delta T}{\Delta Y}\right|_{\text{wall}} D_h}{T_{\text{wall}} - T_{\text{bulk}}} \tag{28}$$

4.1 Velocity Distributions. The axial velocity distributions with and without EDL effect at two different axial locations are shown in Fig. 2. Although the flow evolution patterns are similar for the two cases, the effect of EDL on the developing flow is clearly demonstrated. As discussed earlier, due to the interaction between the streaming potential and the net charge density in the EDL near the channel wall, there exists an electrostatic body force exerting on the ions in an opposite direction to the flow. Consequently, compared with the case of no EDL effect, such electrostatic force would impede the fluid flow, resulting in smaller velocities in the EDL regime. Because of the liquid viscosity, the electrokinetic effect occurring in the neighborhood of the wall would extend to the rest of the channel via hydrodynamic shear stress. It however should be pointed out here that for a proper comparison the same Reynolds number of $\mathrm{Re}=1.0$ (also the same mean velocity) is used in the computations of the two cases, i.e., with and without the presence of the EDL effect. To maintain constant mass flow rate, the velocity in the central region of the channel appears larger than that without consideration of the EDL effect. Hence, the results in this study are presented differently from those reported in the literature [7] where the pressure difference between inlet and outlet is usually given instead of the mean velocity or the Reynolds number. With the pressure difference specified, the EDL effect results in a decrease of the velocities across the entire channel, and thus a reduction of the flow rate. Moreover, the presence of the EDL in the developing flow decreases the fluid velocities in the EDL regime, resulting in velocity distributions which deviate from the conventional patterns.

The effect of different ion concentrations and zeta potentials can also be found in Fig. 2. Larger zeta potential and lower ion concentration lead to larger resistance near the wall, which induces lower velocity near the wall. From the results, it can be seen that the effect of the zeta potential on the velocity is nonlinear.

4.2 Temperature Distributions. Figure 3 shows the temperature distributions at two different axial locations. The lower flow velocities near the wall (due to the EDL) lead to lower heat transfer coefficients. As a result, the heat transfer from the wall to the fluid is less than that without EDL. So temperatures in the fluid with the EDL effects are lower than that without the EDL effect. It is also shown in Fig. 3 that the temperature for 10^{-5} M ion concentration and 100 mV zeta potential is larger than that for 10^{-6} M ion concentration and 150 mV zeta potential. This can be explained as follows: lower ion concentrations in the fluid and higher zeta potentials on the wall enhance the EDL effect, which leads to lower velocity and hence lower heat transfer coefficients near the wall. Therefore the temperature near the center of the channel for 150 mV zeta potential is smaller.

4.3 Electrical Potential, Ions Concentration Distributions. Figures 4–6 show the dimensionless electrical potential distributions, the dimensionless counter-ion and co-ion ions concentration distributions in the fluid for different ion concentrations and zeta potentials respectively. For clarity, the Y axis starts at $Y=0.5$, and not at the symmetry line of $y=0$. Both the electrical potential and

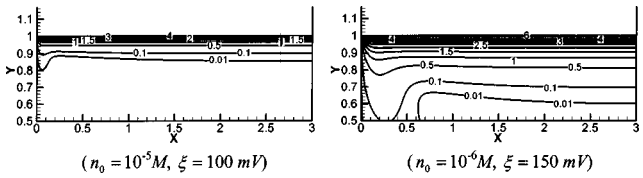

Fig. 4 Dimensionless electrical potential distributions

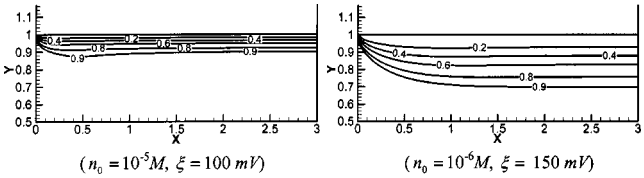

Fig. 5 Dimensionless co-ion concentration distributions

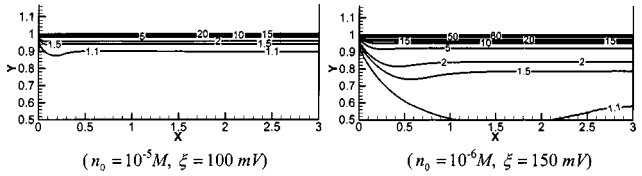

Fig. 6 Dimensionless counter-ion concentration distributions

ion concentrations vary along the flow direction; hence the development of the EDL field resembles that of the hydrodynamic boundary layer. From Figs. 4 to 6, it can be found that, in the fully developed region, when the bulk ion concentrations of the solution and corresponding zeta potentials are 10^{-5} M, 100 mV, the thickness of the region where the ion concentrations are changing is only about 12% of the channel height. When the bulk ion concentration of the solution and corresponding zeta potential are 10^{-6} M and 150 mV, the thickness increases considerably. This indicates that the EDL effects are larger for lower concentration aqueous solutions. It also can be found in Fig. 6 that the developing length for 150 mV zeta potential is larger than that of 100 mV.

4.4 Local *f* Re Distributions. The local *f* Re distributions along the channel with and without the EDL effect are depicted in Fig. 7. Three sets of zeta potentials namely, $\zeta=0$ (no EDL), $\zeta=100$ mV, and $\zeta=150$ mV are considered. According to the definition given in Eqs. (24) and (25), for a given u_{in}, μf Re is proportional to the pressure gradient, $\partial p/\partial x$. The dependency of *f* Re on μ is removed by using the inlet temperature as the reference temperature in calculating *f* Re. As discussed earlier, the presence of the EDL decreases the fluid velocities. Hence, to maintain the same u_{in}, higher $\partial p/\partial x$ is needed, and correspondingly larger *f* Re is expected. This trend is amply demonstrated in Fig. 7. As expected, the *f* Re increases as the zeta potential increases. The fluid viscosity decreases with increasing temperature, which reduces the *f* Re. So, as shown in Fig. 7, when the fluid flow approaches the fully developed region, the *f* Re for the three cases are all less than 50, which are much smaller than the exact value according to the conventional fluid mechanics theory for constant properties of 96. The same drop in *f* Re is also observed for hydrodynamically and thermally developing flow in microchannels with temperature dependent properties without the EDL effect [19].

4.5 Local Nu Number Distributions. Figure 8 shows the local Nu number distribution along the axial direction with and without the EDL effect. It is shown that when approaching the fully developed region, the Nu number for the three cases are all larger than the theoretical value for constant viscosity without considering viscous dissipation of 7.54. When the fluid flows through the channel, it is heated by the wall, the viscosity decreases as the temperature increases. So the velocities near the wall are higher than that under constant viscosity, which leads to larger heat transfer coefficient. Hence, the higher Nu number is achieved. But as discussed earlier, the EDL effect decreases the heat transfer coefficient, so the Nu number for the two cases with the EDL effects are smaller than that without the EDL effects. It is also seen that the smaller ion concentrations and higher zeta potentials lead to smaller Nu number.

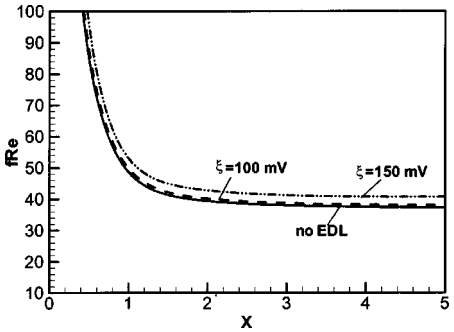

Fig. 7 Local *f* Re distributions

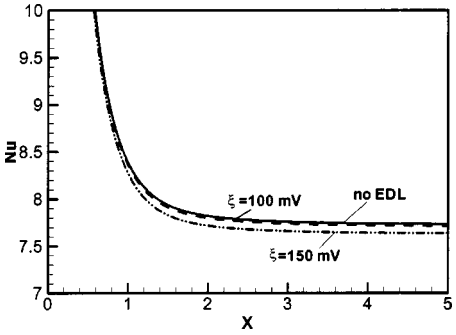

Fig. 8 Local Nusselt number distributions

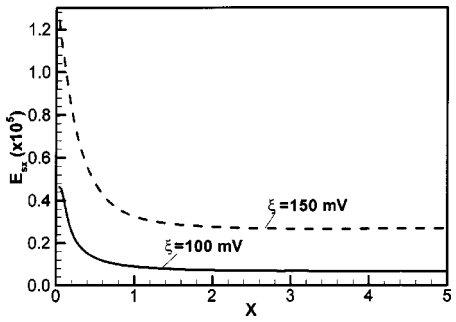

Fig. 9 Local streaming potential distributions

4.6 Local Streaming Potential. Figure 9 shows the streaming potential distribution along the axial direction for two different zeta potentials. It is seen that the zeta potential has great effect on the steaming potential, especially in the developing region. In the developing region, the streaming potentials decrease rapidly. When $X>3$ the two streaming potentials approach different constant values.

5 Concluding Remarks

In this article, a mathematical model is developed to study the electrokinetic effect on liquid developing flow in a parallel slit including the general Nernst-Planck equation describing anion and cation distributions, the Poisson equation determining the electrical potential profile, the continuity equation, and the modified Navier-Stokes equation governing the velocity field. The effects of the EDL on the hydrodynamic and thermal entry regions are investigated. The fluid properties are allowed to change with temperature. The results show that the presence of the EDL in the developing flow decreases the fluid velocities in the EDL regime, resulting in velocity distributions which deviate from the conventional patterns. Accordingly, with EDL a larger hydrodynamic friction factor *f* Re is observed. It is also demonstrated that there is a strong dependence of the *f* Re on the zeta potential. The Nu is smaller when considering the EDL effect.

Nomenclature

A_c = cross-sectional area of the channel, [m^2]
C_p = specific heat [J kg^{-1} K^{-1}]
D_h = hydraulic diameter [m]

D_+ = diffusion coefficient for n_+ [$m^2 s^{-1}$]
D_- = diffusion coefficient for n_- [$m^2 s^{-1}$]
e = elementary charge [C]
E_{sx} = streaming potential [Vm^{-1}]
f = friction factor
H = height [m]
h = heat transfer coefficient [$Wm^{-2} K^{-1}$]
L = length [m]
i_x = local electrical current density [Am^{-2}]
k = thermal conductivity [$Wm^{-1} K^{-1}$]
k_b = Boltzmann constant [$J K^{-1}$]
n_+ = concentration of positive ion [m^{-3}]
n_- = concentration of negative ion [m^{-3}]
n_0 = bulk concentration of ions [m^{-3}]
Nu = Nusselt number
p = pressure [Pa]
Re = Reynolds number
T = temperature [K]
u_1 = axial velocity [ms^{-1}]
u_2 = transverse velocity [ms^{-1}]
x_1, x = axial coordinate
x_2, y = transverse coordinate
Z_+ = valence of the positive ion
Z_- = valence of the negative ion

Greek Symbols

ε_r = dielectric constant of the fluid
ε_0 = permittivity of vacuum [$CV^{-1} m^{-1}$]
λ = electric conductivity of the fluid [$m^2 S$]
λ_+ = electric conductivity of n_+ [$m^2 Smol^{-1}$]
λ_- = electric conductivity of n_- [$m^2 Smol^{-1}$]
μ = viscosity [Pa·s]
ρ = density [$Kg m^{-3}$]
ρ_e = net electric charge density [Cm^{-3}]
ψ = electrostatic potential [V]
ζ = zeta potential [V]

Subscripts

in = inlet

References

[1] Hasegawa, T., Suganuma, M., and Watanabe, H., 1997, ''Anomaly of Excess Pressure Drops of the Flow Through Very Small Orifices,'' Phys. Fluids, **9**(1), pp. 1–3.
[2] Peng, X. F., Peterson, G. P., and Wang, B. X., 1994, ''Frictional Flow Characteristics of Water Flowing Through Rectangular Microchannels,'' Exp. Heat Transfer, **7**(4), pp. 249–264.
[3] Pfund, D., Rector, D., Shekarriz, A., Popescu, A., and Welty, J., 2000, ''Pressure Drop Measurements in a Microchannel,'' AIChE J., **46**(8), pp. 1496–1507.
[4] Urbanek, W., Zemel, J. N., and Bau, H. H., 1993, ''Investigation of the Temperature Dependence of Poiseuille Numbers in Microchannel Flow,'' J. Micromech. Microeng., **3**(4), pp. 206–208.
[5] Yang, C., and Li, D., 1998, ''Analysis of Electrokinetic Effects on the Liquid Flow in Rectangular Microchannels,'' Colloids Surf., A, **143**(2–3), pp. 339–353.
[6] Yang, C., and Li, D., 1997, ''Electrokinetic Effects on Pressure-Driven Liquid Flows in Rectangular Microchannels,'' J. Colloid Interface Sci., **194**(1), pp. 95–107.
[7] Yang, C., Li, D., and Masliyah, J. H., 1998, ''Modeling Forced Liquid Convection in Rectangular Microchannels With Electrokinetic Effects,'' Int. J. Heat Mass Transfer, **41**(24), pp. 4229–4249.
[8] Mala, G. M., Li, D. Q., and Dale, J. D., 1997, ''Heat Transfer and Fluid Flow in Microchannels,'' Int. J. Heat Mass Transfer, **40**(13), pp. 3079–3088.
[9] Ng, E. Y. K., and Poh, S. T., 2000, ''Parametric Studies of Microchannel Conjugate Liquid Flows With Zeta Potential Effects,'' J. Electronics Manufacturing, **10**(4), pp. 237–252.
[10] Ren, L., Qu, W., and Li, D., 2001, ''Interfacial Electrokinetic Effects on Liquid Flow in Microchannels,'' Int. J. Heat Mass Transfer, **44**(16), pp. 3125–3134.
[11] Ren, L., Li, D., and Qu, W., 2001, ''Electro-Viscous Effects on Liquid Flow in Microchannels,'' J. Colloid Interface Sci., **233**(1), pp. 12–22.
[12] Patankar, S. V., 1980, *Numerical Heat Transfer and Fluid Flow*, Hemisphere, Washington, DC.
[13] Hunter, R. J., 1981, *Zeta Potential in Colloid Science: Principles and Applications*, Academic Press, New York.
[14] Paluch, M., 2000, ''Electrical Properties of Free Surface of Water and Aqueous Solutions,'' Adv. Colloid Interface Sci., **84**(1–3), pp. 27–45.
[15] Masliyah, J. H., 1994, *Electrokinetic Transport Phenomena*, AOSTRA Technical Publication Series No. 12., AOSTRA, Edmonton.
[16] Mala, G. M., Li, D., Werner, G., Jacobasch, H. J., and Ning, Y. B., 1997, ''Flow Characteristics of Water Through a Microchannel Between Two Parallel Plates With Electrokinetic Effects,'' Int. J. Heat Fluid Flow, **18**(5), pp. 489–496.
[17] Incorpera, F. P., 1999, *Liquid Cooling of Electronic Devices by Single-Phase Convection*, John Wiley & Sons, Inc., New York, pp. 262–263.
[18] CRC Press, 1986, *CRC Handbook of Chemistry and Physics*, Cleveland, OH, p. E-56.
[19] Toh, K. C., Chen, X. Y., and Chai, J. C., 2002, ''Numerical Computation of Fluid Flow and Heat Transfer in Microchannels,'' Int. J. Heat Mass Transfer, **45**(26), pp. 5133–5141.

A Numerical Study of Natural Convection in Partially Open Enclosures With a Conducting Side-Wall

G. Desrayaud
INSSET,
Université de Picardie Jules Verne,
48 rue Raspail BP 422, 02109 Saint-Quentin,
France

G. Lauriat
Université de Marne-la-Vallée,
Champs-sur-Marne,
77454 Marne la Vallée Cedex 2, France

A numerical study of natural convection generated by a cold vertical wall of an enclosure with two openings on the opposite wall of finite thickness is presented. The enclosure is connected to an infinite reservoir filled with hot air. A two-dimensional laminar flow is assumed both within the enclosure and along the side of the bounding wall immersed into the reservoir. The effects of the size of the openings, spacing between the vertical walls and thermal resistance of the bounding wall are investigated. Numerical results are discussed for aspect ratios of the enclosure and Rayleigh numbers relevant to practical applications. [DOI: 10.1115/1.1643753]

Keywords: Building Heat Transfer, Computational, Conjugate, Enclosure Flows, Heat Transfer, Natural Convection

1 Introduction

Natural convection in vertical channels and within differentially heated cavities has been the subject of many analytical, numerical and experimental investigations because of its large range of applications in thermal control of electronic equipment, energy conservation in buildings, nuclear technology for safety purpose, and many others fields. Relatively few studies, however, have been directed at vertically vented enclosures. Such a geometrical configuration is encountered for example in the cooling of electronic equipment or in the passive solar heating of buildings (Trombe walls for example). According to Sefcik et al. [1] the vertical venting designation indicates that the buoyancy-driven flow and heat transfer are restricted by vent openings at the top and bottom boundary walls of the enclosure. The vented enclosure problem is generally complicated by the increase in geometrical parameters required to describe the channel and, for most applications, by the asymmetrical thermal boundary conditions. The mathematical formulation of pressure and flow fields at the entrance and exit of vertical channels requires also a special attention (see for example Nakamura et al. [2], Miayamoto et al. [3], and Martin et al. [4]). In the studies of Sparrow and Azevedo [5] and Sefcik et al. [1] the channel consisted of a heated wall maintained at constant temperature while the remaining walls were insulated. Hence, the problem formulation resembles the classical vertical plate channel whereas the flow field strongly depends on the sizes and locations of the vent openings which exert a strong influence on the flow rate. In addition, the flow structure generally reveals recirculation zones.

The purpose of the present study is to investigate a more realistic configuration for which internal and external natural convection flows interact as well as conductive heat transfer through a vertical side-wall. Figure 1 shows schematically a side view of the vertical enclosure of uniform, rectangular cross-section bounded by a cold wall and by a bounding wall connected to a plenum chamber through vent openings located at the top and bottom parts of the bounding wall. We are thus considering conjugate heat transfer on the two sides of a vertical wall separating a vented enclosure having a cold vertical wall and an infinite reservoir filled with a hot fluid (humid air). This research program was first conducted to provide an assessment of the efficiency of protective glazing used to prevent condensation of water vapor on stained-glass windows in historic buildings because inside glass pitting is the result of repeated condensations. The capability of such a device for preventing condensation depends on the flow rate in the clearance between the protective glazing and the stained-glass window and on the convective heat flux transferred from the air flow to the stained-glass window. The key geometrical parameters which control the buoyancy-driven flow and thermal efficiency of the device are the spacing between the two vertical walls, the widths of inlet and outlet openings and their locations while the buoyancy force depends strongly on the difference in temperature between the building inside and the outside, and on the thermal resistance of the bounding wall.

2 Mathematical Formulation

Since the flow and heat transfer are governed by elliptical, partial differential equations, the solution is sensitive to the assumptions used for modeling inlet and outlet flow conditions. The influence of inlet conditions on natural convection in vertically open channels were discussed in several papers for the cases where the full elliptic form of the conservation equations is kept (Sefcik et al. [1], Martin et al. [4], Chappidi and Eno [6], Marcondes and Maliska [7]) but no clear consensus came out about the best pressure boundary condition to be retained at high Grashof numbers, e.g., assumption of zero pressure defect or inviscid assumption and use of the Bernoulli equation (Nakamura et al. [2] and Miyamoto et al. [3]). In some other works (Naylor et al. [8] and Kettleborough [9] for example), the computational domain was extended to bypass the problem of prescribing the boundary conditions at the channel inlet. Similar procedures were also used for open or partially open cavities (Miyamoto et al. [3], Penot [10], Chan and Tien [11]). In the present study, extension of the computational domain far from the vent openings is required for two reasons. First, the shear stresses are not small in the regions close to the openings since the hot fluid does not penetrate axially into the channel. Second, any realistic thermal boundary condition can be applied at the outside surface of the bounding wall because large changes in the natural convection heat transfer coefficient occur from the top to the bottom. The computational domain for the solution is also shown in Fig. 1: it is closed with three ficti-

Contributed by the Heat Transfer Division for publication in the JOURNAL OF HEAT TRANSFER. Manuscript received by the Heat Transfer Division July 26, 2002; revision received October 16, 2003. Associate Editor: V. Prasad.

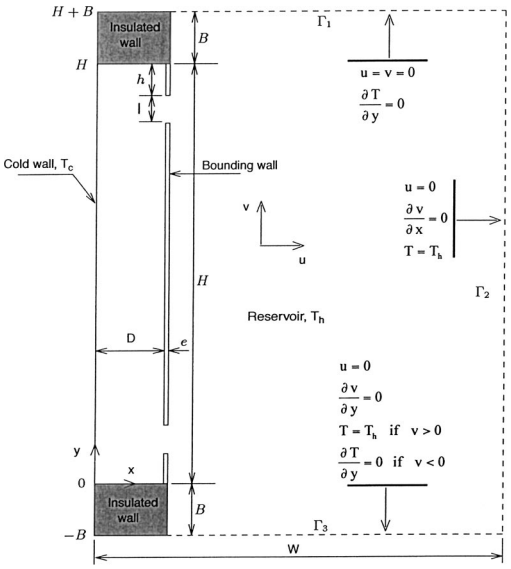

Fig. 1 Geometry of the vented slot and computational domain (dashed lines)

tious boundaries, open to allow fluid to move in and out. These boundaries have to be located far enough from the vented enclosure in order not to perturb significantly both the flow inside the enclosure and the external flow along the bounding wall. Temperatures of fluid coming into the domain are set to the hot temperature since the main flow direction is downward. On the bottom boundary, temperature gradients are set to zero for fluid going out of the domain.

2.1 Governing Equations. In order to simplify the mathematical formulation and to reduce the number of dimensionless parameters, radiative exchanges amongst surfaces are neglected at first. It is assumed that the flow is laminar, steady and that the Boussinesq approximation can be applied (i.e., the thermophysical properties of the fluid are constant except for the density in the buoyancy term). With the above assumptions, the equations in the fluid domain are cast in dimensionless form by scaling lengths, velocity, time and temperature difference $(T-T_0)$ by H, α_f/H, H^2/α_f and (T_h-T_c), respectively, where H is the height of the enclosure, α_f the thermal diffusivity of the fluid and $T_0=(T_h+T_c)/2$ is the reference temperature. For the coordinate system shown in Fig. 1, the dimensionless governing equations in the flow region can be written as

$$\frac{\partial \mathrm{U}}{\partial \mathrm{X}}+\frac{\partial \mathrm{V}}{\partial \mathrm{Y}}=0. \tag{1}$$

$$\frac{\partial U}{\partial \tau}+U\frac{\partial U}{\partial X}+V\frac{\partial U}{\partial Y}=-\frac{\partial P}{\partial X}+\mathrm{Pr}\left(\frac{\partial^2 U}{\partial X^2}+\frac{\partial^2 U}{\partial Y^2}\right) \tag{2a}$$

$$\frac{\partial V}{\partial \tau}+U\frac{\partial V}{\partial X}+V\frac{\partial V}{\partial Y}=-\frac{\partial P}{\partial Y}+\mathrm{Pr}\left(\frac{\partial^2 V}{\partial X^2}+\frac{\partial^2 V}{\partial Y^2}\right)+\mathrm{Ra}_H\mathrm{Pr}\theta \tag{2b}$$

$$\frac{\partial \theta}{\partial \tau}+U\frac{\partial \theta}{\partial X}+V\frac{\partial \theta}{\partial Y}=\left(\frac{\partial^2 \theta}{\partial X^2}+\frac{\partial^2 \theta}{\partial Y^2}\right) \tag{3}$$

In the bounding wall, the conductive heat transfer is described by

$$\frac{\partial \theta_w}{\partial \tau}=\frac{\alpha_w}{\alpha_f}\left(\frac{\partial^2 \theta_w}{\partial X^2}+\frac{\partial^2 \theta_w}{\partial Y^2}\right) \tag{4}$$

Equations (1–4) are to be solved subject to the following hydrodynamic and thermal boundary conditions:

1. Along the cold wall

$$\theta=-0.5;\quad \mathrm{U}=\mathrm{V}=0 \quad \text{at } \mathrm{X}=0 \quad \text{and} \quad 0\leqslant \mathrm{Y}\leqslant 1 \tag{5a}$$

2. At the bounding wall a balance between conduction and convection leads to the following boundary conditions

$$\left.\begin{aligned}\frac{\partial \theta}{\partial X}&=N_k\frac{\partial \theta_w}{\partial X}\\ \theta&=\theta_w\end{aligned}\right\} \quad \text{at } X=D^* \quad \text{and} \quad X=D^*+e^*$$

$$\begin{gathered}0\leqslant Y\leqslant h^*;\\ h^*+\ell^*\leqslant Y\leqslant 1-(h^*+\ell^*)\\ 1-h^*\leqslant Y\leqslant 1\end{gathered} \tag{5b}$$

3. At the adiabatic end walls of the vented enclosure

$$\frac{\partial \theta}{\partial Y}=0;\quad U=V=0 \quad \text{at } Y=0,\quad 1 \text{ and } 0\leqslant X\leqslant \mathrm{D}^* \tag{5c}$$

4. Along the boundaries of the reservoir

$$\frac{\partial \theta}{\partial X}=0;\quad U=V=0 \quad \text{at } X=D^*+e^* \quad \text{and}$$

$$-B^*\leqslant Y\leqslant 0;\quad 1\leqslant Y\leqslant 1+B^* \tag{5d}$$

5. At the boundaries of the computational domain (indicated as Γ_1, Γ_2, and Γ_3)

$$\frac{\partial \theta}{\partial Y}=0 \quad U=V=0; \quad \text{at } Y^*=1+B^* \quad \text{and}$$

$$D^*+e^*\leqslant X\leqslant D^*+e^*+W^* \tag{5e}$$

$$\theta=0.5;\quad U=0;\quad \frac{\partial V}{\partial X}=0 \quad \text{at } X=D^*+e^*+W^* \quad \text{and}$$

$$-B^*\leqslant Y\leqslant 1+B^* \tag{5f}$$

$$\frac{\partial \theta}{\partial Y}=0 \quad \text{if } V\leqslant 0 \text{ or } \theta=0.5 \quad \text{if } V>0;\quad U=\frac{\partial V}{\partial Y}=0;$$

$$\text{at } Y^*=-B^* \quad \text{and} \quad D^*+e^*\leqslant X\leqslant D^*+e^*+W^* \tag{5g}$$

In the above set of equations it can be seen that the geometry of the problem is characterized by four dimensionless lengths (D^*, e^*, h^*, and ℓ^*). B^* and W^* are only related to the size of the external computational domain, and should be taken to be sufficiently large to have a negligible influence on the numerical solution.

From a physical point of view, the relevant dimensionless parameters are the Rayleigh number based on the height of the vented enclosure, $\mathrm{Ra}_H=g\beta(T_h-T_c)H^3/\alpha\nu$, the Prandtl number, $\mathrm{Pr}=\nu/\alpha$, the height-to-length aspect ratio, $A=H/D$ or $A=1/D^*$, the dimensionless thickness of the bounding wall, e^*, the dimensionless height of the parts above and below the openings, h^*, the dimensionless width of the openings ℓ^*, and the thermal conductivity ratio, $N_k=k_w/k_f$, the ratio of the thermal conductivity of the bounding wall to that of air.

The dimensionless flow rates through the top and bottom openings are defined as

$$G_{\mathrm{in}}=-\int_{1-(h^*+\ell^*)}^{1-h^*} U\,dY \quad G_{\mathrm{out}}=\int_{h^*}^{h^*+\ell^*} U\,dY \tag{6}$$

Since the cooled and bounding walls are assumed impermeable, mass conservation implies

$$G_{in}=G_{out}=G=-\int_0^{D^*} V dX, \quad \forall Y \tag{7}$$

where G is the vertical flow rate along any horizontal line across the enclosure.

The average Nusselt numbers at the vertical walls were evaluated from

$$\overline{\mathrm{Nu}}=\overline{h}D/k_f, \quad \overline{h}=(Q/H)/(T_h-T_c)$$

where Q is the rate of heat transfer per unit-length of depth from $y=0$ to H. This presentation yields indeed a better correlation of the data as it will be discussed later.

Definitions of the average Nusselt numbers based on the cavity width along the cold and bounding walls are

$$\overline{\mathrm{Nu}}_c=\frac{\overline{h}_c D}{k_f}=D^*\int_0^1\left(\frac{\partial\theta}{\partial X}\right)_0 dY \tag{8a}$$

$$\overline{\mathrm{Nu}}_w=\frac{\overline{h}_w D}{k_f}=-\frac{D^*}{1-2\ell^*}\left[\int_0^{h^*}\left(\frac{\partial\theta}{\partial X}\right)_{D^*} dY + \int_{h^*+\ell^*}^{1-(h^*+\ell^*)}\left(\frac{\partial\theta}{\partial X}\right)_{D^*} dY + \int_{1-h^*}^{1}\left(\frac{\partial\theta}{\partial X}\right)_{D^*} dY\right] \tag{8b}$$

The dimensionless form of the heat convected through the bottom and top openings can be expressed respectively as

$$\overline{\mathrm{Nu}}_b=\frac{\overline{h}_b D}{k_f}=\frac{D^*}{\ell^*}\int_{h^*}^{h^*+\ell^*}\left[-\left(\frac{\partial\theta}{\partial X}\right)+U\theta\right]_{D^*} dY \tag{8c}$$

$$\overline{\mathrm{Nu}}_t=\frac{\overline{h}_t D}{k_f}=\frac{D^*}{\ell^*}\int_{1-(h^*+\ell^*)}^{1-h^*}\left[-\left(\frac{\partial\theta}{\partial X}\right)+U\theta\right]_{D^*} dY \tag{8d}$$

Conservation of energy in the vertical vented enclosure implies

$$\overline{\mathrm{Nu}}_c=(1-2\ell^*)\overline{\mathrm{Nu}}_w+\ell^*(\overline{\mathrm{Nu}}_t+\overline{\mathrm{Nu}}_b) \tag{9}$$

2.2 Solution Procedure. The transport equations were discretized on structured control volumes using the second-order QUICK-type scheme for the convection terms and by employing the SIMPLER pressure correction algorithm (Patankar [12]). The momentum and energy equations were cast in transient form and the time-integration was performed using a false transient scheme based on an ADI method with a much larger time step for the energy equation than for the momentum equation. When the time steps are not very small, inner iterations are required to account for the nonlinearity of the equations. In the present study, underrelaxation parameters were introduced for velocities and temperature to control the advancement of the solution field until a steady final state was obtained. The suitable values of the relaxation factors were found by experience since they depend upon a number of factors (grid resolution, Rayleigh number, width of the openings . . .). The convergence criteria to steady state included checks on the overall mass and energy balance for the vented enclosure, and relative changes between consecutive iterations.

2.3 Code Validation. The numerical code was extensively validated against benchmark problems to check its validity. Calculations were first performed for flow and heat transfer in differentially heated cavities of various aspect ratios. These comparison tests are not discussed here, except for a vertical slot. Second, partitioned enclosures were considered since this geometry is more closely related to that of the problem under consideration. Hence, Table 1 presents comparisons between the numerical results of Zimmerman and Acharya [13] in a square enclosure of height H with perfectly conducting horizontal end walls and finitely conducting vertical baffles of dimensionless thickness $e^*=0.1$ and height $h^*=0.25$. As it can be seen, the numerical results are in good agreement for various Rayleigh numbers and for two conductivity ratios, $N_k=2$ and $N_k=500$. Also the recirculation zone shown behind the baffles at high Rayleigh number in the paper of Zimmerman and Acharya [13] was also captured. In the case of a differentially heated vertical cavity with an aspect ratio $A=80$, Table 2 shows that the present Nusselt numbers can be favorably compared with those of Novak and Nowak [14] and ElSherbiny et al. [15]. In addition, a multicellular flow structure similar to the one displayed in [14] for an aspect ratio $A=30$ was obtained. Comparisons of average Nu-values for the heated wall of a open square cavity with one heated vertical wall and two insulated horizontal walls with those predicted by Chan and Tien [11] are listed in Table 3 for various Rayleigh numbers. It can be seen that the heat transfer results match very well whereas a 10% discrepancy on the volumetric flow rate through the cavity, G, was found at the highest Ra at which the mean Nusselt number approaches that for a vertical flat plate.

Accuracy of the results for the vented-slot configuration was then determined by a sequence of calculations carried out by increasing the grid resolution. The mesh was graded according to an exponential function with the smallest elements near the solid walls and in the neighborhood of the inlet and outlet vent openings. An estimate for the grid size along the vertical side walls of the enclosure was made by calculating the order of magnitude of the dimensionless boundary layer thickness ($\delta^*=A^{1.75}/\mathrm{Ra}_H^{0.25}$) and by assuring that at least four points are in the boundary layer. In the exterior computational domain, the grid was nonuniformly distributed with control volumes of much larger size in the far-field from the enclosure. The dimensionless overall energy balances and flow rates through the openings were monitored at each time step, and for all of the computations discussed in this paper the accuracy was found to be better than one percent.

Table 1 Comparisons of average Nusselt numbers at the hot wall, $A=1$, Pr=0.7 (Z. & A.: Zimmerman and Acharya [13], d^*=thickness of the baffles/dimensions of the square enclosure).

		$d^*=0.05$		$d^*=1$		$d^*=0.2$	
Ra_H	N_k	Z. & A.	present	Z. & A.	present	Z. & A.	present
10^4	2	1.25	1.25	1.22	1.22	1.18	1.18
	500	1.25	1.24	1.22	1.21	1.20	1.20
10^5	2	2.95	2.95	2.90	2.90	2.75	2.76
	500	2.74	2.73	2.69	2.69	2.52	2.57
$3.5\ 10^5$	2	4.61	4.69	4.58	4.65	4.43	4.49
	500	4.18	4.17	4.14	4.18	4.01	4.09

Table 2 Comparisons of average Nusselt numbers based on the enclosure height ($A=80$, Pr=0.7)

Ra_H	$1.4\ 10^9$	$2.1\ 10^9$
Novak and Nowak [14]	83.4	84.1
ElSherbiny et al. [15]	80.0	80.4
Present	81.7	82.5

Table 3 Comparisons of Nu and G for the open square cavity (Pr=1, $A=1$)

	Present		Chan and Tien [11]		%-discrepancy	
Ra_H	Nu	G	Nu	G	%-Nu	%-G
10^3	1.08	1.98	1.07	1.95	0.92	1.51
10^4	3.47	8.12	3.41	8.02	1.73	1.23
10^5	7.65	21.05	7.69	21.1	0.52	0.23
10^6	15.08	44.48	15.0	47.3	0.53	5.96
10^7	28.14	85.6	28.6	96.0	1.60	10.80

Table 4 Effects of the grid size on the average Nusselt number at the cold wall and on the dimensionless mass flow rate ($Ra_H = 1.1\,10^{10}$, Pr=0.71, $A=80$, $\ell/D=1$)

(NX,NY) Grids	$\overline{Nu}_c$	$\overline{Nu}_w$	G/A
60×100	1.736	1.718	2.618
60×200	1.709	1.715	2.660
80×200	1.718	1.712	2.654
100×200	1.724	1.710	2.644

Grid tests were conducted to ensure that the results were independent of both grid resolution and size of the exterior computational domain. Table 4 shows a comparison of the mean Nusselt number at the cold wall based on the cavity width and of the volumetric flow rate through the openings which were obtained for various grid sizes. As the resolution of the grid was increased above the 80×200 grid (streamwise×cross-stream directions) shown in Fig. 2, the predictions for Nu and G differed by less than 0.5%. Thus, it was determined that such a grid resolution yielded an acceptable compromise between accuracy and required computing time. From the test runs made to determine how should be tailored the exterior domain defined by B^* and W^* (Fig. 1) so that the near-field solutions, inside the enclosure and along the bounding wall, become insensitive to the distances of the outer boundaries from the openings, it was found that values of B^* and W^* larger than 0.25 and 1.25, respectively, are unnecessary.

3 Results and Discussion

All of the computations were conducted in air-filled enclosure (Pr=0.71) with the vent openings located near the top and bottom end walls ($h^*=D^*/2$) because the heat transfer rate between the bounding wall and the natural convection flow was found to be the highest for this configuration. For this reason the data for this geometry are likely of most practical interest. The Rayleigh number Ra_H, the aspect ratio A, and the ratio of the width of the openings to the interwall spacing of the vented enclosure ℓ/D are

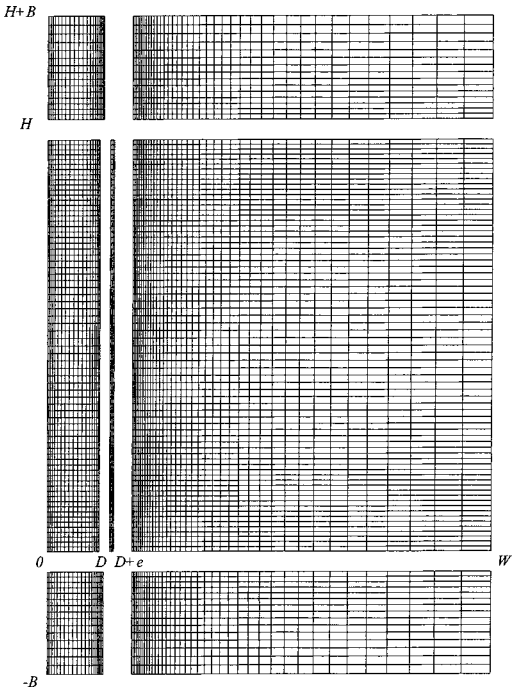

Fig. 2 Grid system

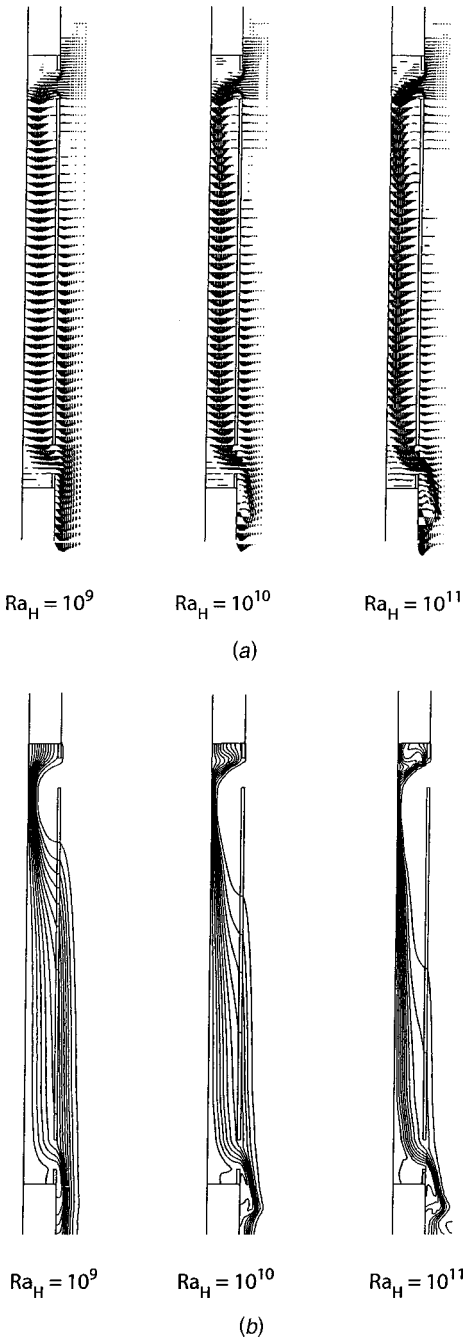

Fig. 3 Velocity vectors (a) and temperature field (b) within the vented enclosure and along the bounding-wall for three Rayleigh numbers ($A=100$, $\ell/D=1$, isothermal patterns [−0.5 (0.1) 0.5])

the primary parameters of interest in this study. Hence, the results are discussed for a fixed dimensionless width of the bounding wall, $e^*=A/1000$.

Solutions were obtained over a range of Rayleigh numbers from $Ra_H=10^8$ to $Ra_H=5.10^{11}$, aspect ratios from $A=20$ to $A=100$, for three widths of the openings ($\ell/D=0.5$, 1, and 1.5), and for a thermal conductivity ratio assigned to a value representative of window-glass material ($N_k=40$). These parameter values correspond with the practical problem under investigation (removal of condensation of humid air on historic stained-glass windows).

General Observations. Figures 3 show the velocity and temperature fields within the vented enclosure and in the near-field

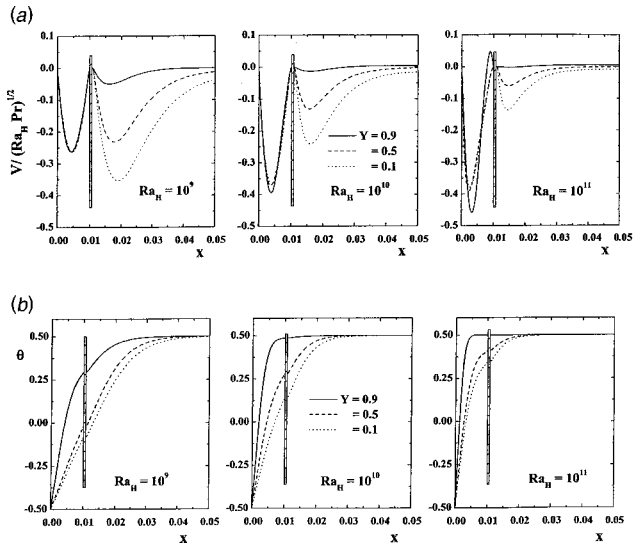

Fig. 4 Vertical velocity profiles (a) and temperature distributions (b) at three vertical locations for various Ra_H ($A=100$, $\ell/D=1$)

from the bounding wall for a tall enclosure ($A=100$), the width of the vent openings being equal to the interwall spacing ($\ell/D=1$), and for three Rayleigh numbers. It should be noted that the aspect ratio of the enclosure has been reduced to $A=15$ for graphical purpose (in order to make possible plots over the whole extent of the slot). The computations show that hot fluid penetrates into the enclosure through the upper opening and proceeds downstream (Fig. 3(a)). When the primary inlet flow approaches the bottom of the enclosure, it turns towards the outlet opening at a temperature close to that of the cold wall. Small recirculating regions are predicted along the bottom of the bounding wall at large spacings and/or high Rayleigh numbers only. However, the recirculation flow rate is rather small at the large aspect ratios considered in this study. Over most of the height, the flow characteristics are similar to the ones for the natural convective flow between vertical parallel plates heated asymmetrically. In the range of aspect ratios investigated, the flow can be considered as fully developed for $Ra_H<10^9$ and in the single-plate regime for the highest Rayleigh numbers (Sparrow and Azevedo [5]). Since the temperature of the bounding wall sets between the hot and cold temperatures, a boundary layer flow develops along its right-hand side. Thus, the thermal equilibrium of the bounding wall is determined from a conjugate problem: natural convection on both sides of the wall and heat conduction through the wall. The downward convection in the right-hand side of the bounding wall is decreased when Ra_H increases, because the strong downward convection in the cold wall creates a thin boundary-layer closer to this wall, keeping the bounding wall temperature closer to the reservoir temperature. Therefore, an increase in Ra_H in the range of values considered in the present study leads to an intensification of the flow rate within the vented enclosure and decrease in the external boundary layer flow (Fig. 3(a)). Figure 3(b) shows that the temperatures of the upper part of the bounding wall is very close to the temperature of the hot air in the reservoir whereas its lower part is cooled by the flow of cold air. The thinning down of the thermal boundary layer along the cold wall evidences the increase in the heat transfer rate as Ra_H is increased.

The profiles of the vertical component of the velocity and the temperature profiles at three vertical locations are shown in Figs. 4 where the bounding wall is schematically represented. The internal velocity profile exhibits the feature of a fully-developed channel flow at a short distance from the inlet opening (Fig. 4(a)) and presents an almost parabolic shape at $Ra_H=10^9$ because the heat transfer between the cold wall and the bounding wall is mainly by conduction, as it can be seen in Fig. 4(b) where a transversally linear temperature profile is displayed over most of the enclosure height. When increasing the Rayleigh number, the location of the velocity maximum moves towards the cold wall whereas the vertical velocity maximum along the right-hand side of the bounding wall is significantly reduced. Consequently, the temperature of the bounding wall increases with Ra_H and the slope of the temperature profile indicates that the cooling of the flow of hot air occurs mainly at the cold wall for high Rayleigh numbers. On account of the low thermal resistance of the bounding wall, the temperature difference between the two surfaces is negligible whatever Ra_H is. On the other hand, the decrease of the vertical temperature differences along the bounding wall (i.e., between $Y=0.1$ and $Y=0.9$) at high Ra_H shows that it has almost no thermal effect on the flow rate provided that the interwall spacing and width of the openings are large enough.

If the aim of the vented enclosure device is to maintain the bounding wall at a temperature as close as possible to the temperature of the reservoir, the intensity of the external boundary layer flow rate is thus a reliable indication of its efficiency.

Table 5 Average Nusselt numbers ($A=100$, Pr=0.71, $\ell/D=1$)

Ra_H	$\overline{Nu}_c$	$(1-2\ell^*)\overline{Nu}_w$	$\ell^*\overline{Nu}_t$	$\ell^*\overline{Nu}_b$	Nu	G/A
10^9	0.75	0.38	0.23	0.14	0.75	0.46
10^{10}	1.63	0.27	1.00	0.35	1.62	2.00
10^{11}	3.06	0.10	2.90	0.05	3.05	5.80

Average Nusselt Number and Mass Flow Rate. The average Nusselt number at the cold wall (Eq. 8*a*), at the bounding wall (Eq. 8*b*) and the dimensionless heat flow rate through the top and bottom openings (Eqs. 8*c* and 8*d*) are reported in Table 5. The Nusselt number at the total height of the bounding wall, Nu, is a weighted sum of the average Nusselt number at the bounding wall ($\overline{Nu}_w$) and of heat flow rates through the openings ($\overline{Nu}_t$ and $\overline{Nu}_b$) as defined by Eq. (9). When increasing the Rayleigh number, Table 5 shows that the heat transfer rates at the cold wall and through the top opening increases whereas the transfer rate decreases at the bounding wall. Hence, most of the heat convected by the hot air flowing through the top opening is transferred to the cold wall at $Ra_H=10^{11}$. At the bottom opening, the heat flow rate increases first with Ra_H and then decreases indicating that the temperature of the air stream increases

The flow rate through the vented slot is shown in Fig. 5 as a function of Ra_H for various widths of the openings. It is first observed that the increase in the flow rate is more important at low Rayleigh numbers, as depicted by the decrease in the slope of

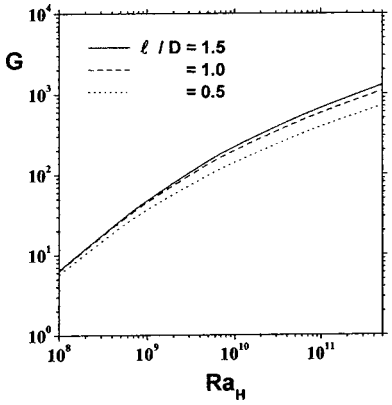

Fig. 5 Variations of the flow rate as a function of Ra_H for various sizes of the vent openings ($A=100$)

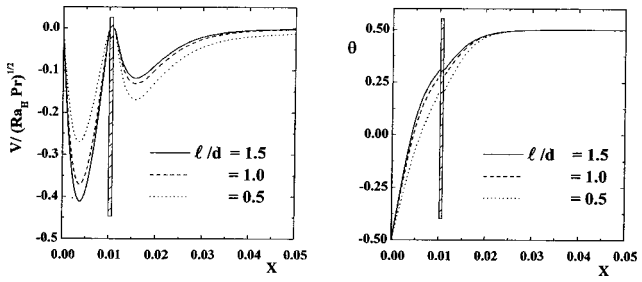

Fig. 6 Velocity and temperature profiles at mid-height for various sizes of the vent openings ($Ra_H = 10^{10}$, $A = 100$)

the curves when increasing Ra_H. On account of the aspect ratio considered, the viscous effects are dominant at low Ra_H while the head losses at the inlet and outlet openings become increasingly important at high Ra_H. For practical purpose, it should be noted here that $Ra_H = 10^{11}$ and $A = 100$ correspond, for example, to an air-filled slot of 4 m height and a temperature difference $(T_h - T_c) = 15$ K at a reference temperature $T_0 = 280$ K. Figure 5 illustrates also the effect of the width of the openings which was investigated in order to find the optimum width for a fixed interwall spacing. The results show that widths of the openings larger than the spacing are unnecessary because viscous stresses are the main cause of the reduction in the flow rate. On the other hand, the flow rate could be noticeably increased at high enough Ra_H provided that the size of the openings are of the order of the spacing and located very close to the top and bottom walls of the enclosure. Therefore, the present computations show that a ratio ℓ/D of the order of one can be considered as an almost optimal design for vented enclosures of large aspect ratio. The vertical velocity and temperature profiles displayed in Fig. 6 support such a conclusion since it is shown that the differences in flow rates and temperatures are much smaller when increasing (ℓ/D) from 1 to 1.5 than from 0.5 to 1.

Influence of the Conductivity Ratio. Few computations were carried out at $Ra_H = 10^{10}$ and 10^{11} to determine the influence of the thermal conductivity ratio, $N_k = k_w/k_f$, in order to investigate the changes in average Nusselt numbers and mass flow rate from the limiting case of a perfectly conducting bounding wall to that of an insulated wall. These limits are indeed of interest since comparisons can be made with the solution for a vertical channel formed by two isothermal plates at different temperatures and with that of a vertical channel formed by an isothermal plate and an insulated plate, respectively. The computations were for $A = 100$ and $\ell/D = 1$. It was found that the differences in the average Nusselt number at the bounding wall ($\overline{Nu}_w$) were about 5% when the thermal conductivity ratio varied from $N_k = 10^4$ (perfectly conducting wall for a thickness $e^* = A/1000$) to $N_k = 100$. On the other hand, a sharp decrease in $\overline{Nu}_w$ was obtained by decreasing the conductivity ratio from $N_k = 100$ to $N_k = 1$, value of N_k at which the bounding wall may be assumed adiabatic. The Nusselt number at the cold wall was seen to be almost constant in the whole range of the N_k values investigated due to the high values of the Rayleigh number considered. For lower Ra_H, larger decreases in $\overline{Nu}_c$ were obtained due to the non-negligible effect of heat conduction through the air layer. For example, the difference in $\overline{Nu}_c$ between $N_k = 1$ and $N_k = 10^4$ is of about 30% at $Ra_H = 10^9$.

Obviously, the mass flow rates through the openings increase when the thermal conductivity of the bounding wall is decreased, whatever the Rayleigh number is, since the boundary-layer flow along its side in contact with the reservoir of hot air is strongly reduced.

Correlations for the Average Nusselt Number and for the Flow Rate. According to the most usual form for deriving composite relations reflecting the heat transfer results for natural convection in channels, we followed the correlating procedure described by Bar-Cohen and Rohsenow [16]. The Nusselt numbers at the cooled surface and at the LHS of the bounding wall based on the interwall spacing were thus expressed in terms of the so-called "channel Rayleigh number" defined as $Ra_D^* = Ra_D/A$. This presentation yields indeed a better correlation of the data for the various aspect ratios and Rayleigh numbers investigated. That is shown in Fig. 7 where the Nusselt numbers at the cold wall and at the LHS of the bounding wall are presented as a function of Ra_D^* which spans five order of magnitude. For all of the data reported in Fig. 7, the width of the openings was kept equal to the spacing (i.e., $\ell/D = 1$). At low values of Ra_D^*, the average heat transfer rate at the bounding wall is nearly constant while it increases linearly at the cold wall. The explanation for this outcome is that conduction heat transfer dominates. The differences between $\overline{Nu}_c$ and $\overline{Nu}_w$ represent mainly the convective heat transfer at the cold wall due to the weak air-flow rate through the openings. When increasing Ra_D^*, the vertical circulation of hot air intensifies and the temperature of the bounding wall increases. Therefore $\overline{Nu}_w$ tends towards zero since in the limit $Ra_D^* \to \infty$ the bounding wall is at the reservoir temperature. In that limit, the external boundary layer flow vanishes. On the other hand, convective transfer at the cold wall increases without limit. At $Ra_D^* = 10^5$, it can be assumed that the cooling of the hot air entering through the top opening occurs at the cold wall only.

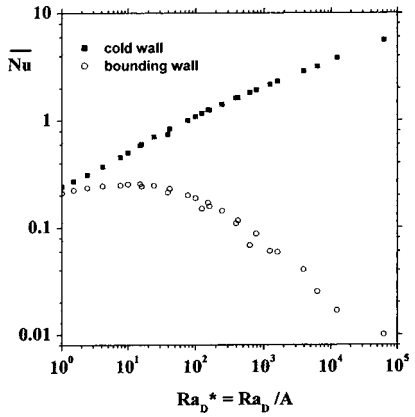

Fig. 7 Variations in average Nusselt numbers at the cooled wall and at the bounding wall as a function of the channel Rayleigh number $(\ell/D = 1)$

Obviously, the thermal resistance of the bounding wall plays an important role on the Nu-variations with Ra_D^*. Figure 8 shows the variations of the mean Nusselt number at the cold wall as a function of the channel Rayleigh number for the two limiting values of the thermal resistance of the bounding wall. For an infinite ther-

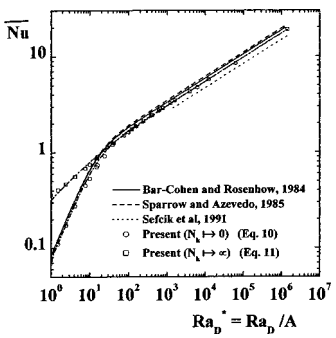

Fig. 8 Variation in average Nusselt numbers at the cooled wall as a function of the channel Rayleigh number $(\ell/D = 1)$

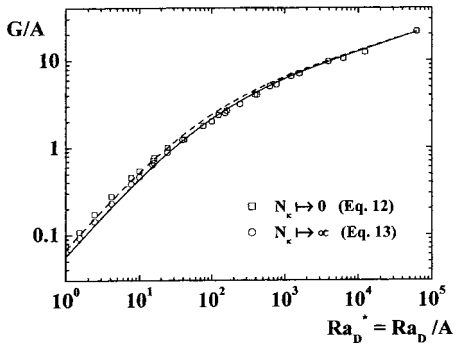

Fig. 9 Variation in the mass flow rate as a function of the channel Rayleigh number ($\ell/D=1$)

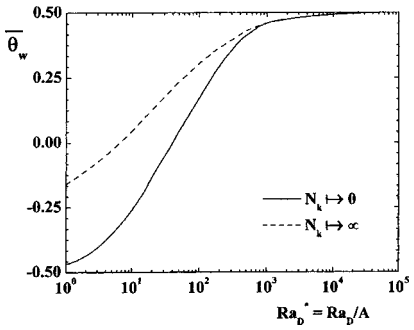

Fig. 10 Variation in the average temperature of the bounding wall as a function of the channel Rayleigh number ($\ell/D=1$)

mal resistance (i.e., adiabatic bounding wall), the solution should be close to that obtained in the case of a asymmetrically heated vertical channel which was deeply investigated in many studies published in the archival literature. We selected the papers of Sefcik et al. [1], Sparrow and Azevedo [5], and Bar-Cohen and Rohsenow [16]. Using the procedure described by Churchill and Usagi [17], the present results yield the following composite $\overline{\mathrm{Nu}}_c$ relation for $\ell/D=1$:

$$\overline{\mathrm{Nu}}_c=\left\{\left(\frac{13.33}{\mathrm{Ra}_D^*}\right)^2+\left(\frac{1}{0.546\ \mathrm{Ra}_D^{*1/4}}\right)^2\right\}^{-1/2} \quad \text{for } N_k\to 0 \tag{10}$$

It should be noted that the value of the coefficient of the second term (i.e., 0.546) is slightly less that the one suggested by Sparrow and Azevedo [5] for water whereas the correlation proposed by Sefcik et al. [1], valid for a vertically vented enclosure containing one isothermal heated wall while the remaining walls are insulated, leads to smaller Nusselt numbers. For very low thermal resistance of the bounding wall, the present results can be correlated as

$$\overline{\mathrm{Nu}}_c=\left\{\left(\frac{2.78}{\mathrm{Ra}_D^{*1/2}}\right)^{5/2}+\left(\frac{1}{0.546\ \mathrm{Ra}_D^{*1/4}}\right)^{5/2}\right\}^{-2/5} \quad \text{for } N_k\to\infty \tag{11}$$

For channel Rayleigh numbers greater than about 10^2, the thermal resistance of the bounding wall has a marginal effect and the two correlations yield almost the same value of $\overline{\mathrm{Nu}}_c$. In conclusion, the effects of the thermal resistance of the bounding wall are noticeable only if the conductive heat transfer through the layer of air within the interwall spacing is important.

Correlations of similar form were also derived for the mass flow rate both for insulated bounding wall and perfectly conducting bounding wall. Figure 9 shows variations of G/A with the channel Rayleigh number which are qualitatively similar to those of $\overline{\mathrm{Nu}}_c$: in the fully developed régime (i.e., at low values of Ra_D^*) the differences between G/A are of the order of 15% according to the asymptotic values of the thermal resistance whereas the two curves merge in the boundary layer régime (i.e., at values of Ra_D^* greater than 10^3). Therefore, the composite relations for G/A were assumed to have the same form as those derived for $\overline{\mathrm{Nu}}_c$. Thus

$$G/A=\left\{\left(\frac{13.33}{\mathrm{Ra}_D^*}\right)^{0.85}+\left(\frac{1}{1.354\ \mathrm{Ra}_D^{*1/4}}\right)^{0.85}\right\}^{-1/0.85} \quad \text{for } N_k\to 0 \tag{12}$$

$$G/A=\left\{\left(\frac{15.85}{\mathrm{Ra}_D^*}\right)^{0.8}+\left(\frac{1}{1.354\ \mathrm{Ra}_D^{*1/4}}\right)^{0.8}\right\}^{-1/0.8} \quad \text{for } N_k\to\infty \tag{13}$$

Finally, Fig. 10 shows the variations in the average temperature of the bounding wall as a function of the channel Rayleigh number for the two limiting cases. In the fully developed régime, the heat flux diffused through the bounding wall produces a significant increases in the average temperature when increasing the thermal conductivity whereas θ_w is almost independent of the thermal conductivity of the bounding wall in the single-plate régime, i.e., at $\mathrm{Ra}_H=10^{11}$ for an enclosure of aspect ratio $A=100$. Therefore, the average temperature of the bounding wall is insensitive to its thermal resistance at high Rayleigh number and tends towards that of the hot air of the reservoir for $\mathrm{Ra}_D^*>10^4$.

4 Concluding Remarks

A numerical investigation has been made of natural convection in a vertically vented enclosure of high aspect ratio with a conducting wall connected to a reservoir filled with air at a temperature higher than that of the cold wall. Results have been obtained by carrying out computations to an extended outside domain. This approach is necessary due to the interaction between the boundary-layer flow along the side of the conducting wall immersed into the reservoir and the flow within the vented enclosure. The effects of the Rayleigh number, size of the openings and thermal conductivity of the bounding wall were examined. At high Rayleigh numbers, a boundary layer is formed adjacent to the cold wall and the mean temperature of the bounding wall approaches that of the hot fluid. For the geometrical configurations investigated, vent gaps larger than the enclosure width do not significantly affect the flow rate through the vents. In the cases of perfectly conducting or adiabatic bounding wall, correlations were derived to predict the mean Nusselt number at the cold wall and the mass flow rate as a function of the channel Rayleigh number. These correlations are relevant for the design of double-glazing used to prevent condensation on single-pane windows.

Acknowledgment

This work was supported by research grants from the IDRIS-Computer Center (French National Institute for Advances in Scientific Computations, Grant no. 00 1265.)

Nomenclature

A = H/D, height-to-width aspect ratio of the vented enclosure
B = vertical extension of the computational domain, m
D = width of the vented enclosure, m
e = thickness of the bounding wall, m
g = acceleration of gravity, m/s^2
G = dimensionless volumetric flow rate
h = height of the parts above and below the vent openings, m
$\overline{h}$ = mean heat transfer coefficient, W/m^2 K
H = height of the vented enclosure, m

k = thermal conductivity, W/mK
ℓ = size of the vent openings, m
N_k = k_w/k_f, thermal conductivity ratio
Nu = average Nusselt number based on the width of the enclosure
P = dimensionless pressure defect
Pr = Prandtl number
Ra_H = $g\beta(T_h-T_c)H^3/\alpha\nu$, Rayleigh number based on the height of the enclosure
Ra_D = $g\beta(T_h-T_c)D^3/\alpha\nu$, Rayleigh number based on the width of the enclosure
Ra_D^* = $g\beta(T_h-T_c)D^4/\alpha\nu H$, channel Rayleigh number
T = fluid temperature, K
T_c = temperature of the cold wall, K
T_h = hot fluid temperature, K
T_0 = reference temperature, $T_0=(T_c+T_h)/2$
(U,V) = dimensionless velocities, $=(u,v)H/\alpha$
W = horizontal extension of the computational domain, m
(X,Y) = dimensionless coordinates, $=(x,y)/H$

Greek Symbols

α = thermal diffusivity, m^2/s
β = volumetric coefficient of thermal expansion, K^{-1}
δ = boundary layer thickness
θ = dimensionless temperature difference, $=(T-T_0)/(T_h-T_c)$
ν = kinematic viscosity, m^2/s
τ = dimensionless time, $=\alpha_f t/H^2$

Subscripts

b = bottom
c = cold wall
f = fluid
t = top
w = bounding wall

Superscripts

$*$ = dimensionless quantity

References

[1] Sefcik, D. M., Webb, B. W., and Heaton, H. S., 1991, "Natural Convection in Vertically Vented Enclosures," ASME J. Heat Transfer, **113**, pp. 912–918.
[2] Nakamura, H., Yutaka, A., and Naitou, T., 1982, "Heat Transfer by Free Convection Between Two Parallel Flat Plates," Numer. Heat Transfer, **5**, pp. 95–106.
[3] Miyamoto, M., Kuehn, T. H., Goldstein, R. J., and Katoh, Y., 1989, "Two-Dimensional Laminar Natural Convection Heat Transfer From a Fully or Partially Open Square Cavity," Numer. Heat Transfer, Part A, **15**, pp. 411–430.
[4] Martin, L., Raithby, G. D., and Yovanovich, M. M., 1991, "On the Low Rayleigh Number Asymptote for Natural Convection Through an Isothermal, Parallel-Plate Channel," ASME J. Heat Transfer, **113**, pp. 899–905.
[5] Sparrow, E. M., and Azevedo, L. F. A., 1985, "Vertical-Channel Natural Convection Spanning Between the Fully-Developed Limit and the Single-Plate Boundary-Layer Limit," Int. J. Heat Mass Transfer, **28**(10), pp. 1847–1857.
[6] Chappidi, P. R., and Eno, B., 1990, "A Comparative Study of the Effect of Inlet Conditions on a Free Convection Flow in a Vertical Channel," ASME J. Heat Transfer, **112**, pp. 1082–1085.
[7] Marcondes, F., and Maliska, C. R., 1999, "Treatment of the Inlet Boundary Conditions in Natural-Convection Flows in Open-Ended Channels," Numer. Heat Transfer, Part B, **35**, pp. 317–345.
[8] Naylor, D., Floryan, J. M., and Tarasuk, J. D., 1991, "A Numerical Study of Developing Free Convection Between Isothermal Vertical Plates," ASME J. Heat Transfer, **113**, pp. 620–626.
[9] Kettleborough, C. L., 1972, "Transient Laminar Free Convection Between Heated Vertical Plates Including Entrance Effects," Int. J. Heat Mass Transfer, **15**, pp. 883–896.
[10] Penot, F., 1982, "Numerical Calculation of Two-Dimensional Natural Convection in Isothermal Open Cavities," Numer. Heat Transfer, **5**, pp. 421–437.
[11] Chan, Y. L., and Tien, C. L., 1985, "A Numerical Study of Two-Dimensional Natural Convection in Square Open Cavities," Numer. Heat Transfer, **8**, pp. 65–80.
[12] Patankar, S. V., 1980, *Numerical Heat Transfer and Fluid Flow*, Hemisphere Publishing Corp., Washington, DC.
[13] Zimmerman, E., and Acharya, A., 1987, "Free Convection Heat Transfer in a Partially Divided Vertical Enclosure With Conducting End Wall," Int. J. Heat Mass Transfer, **30**(2), pp. 319–331.
[14] Novak, M. H., and Nowak, E. S., 1993, "Natural Convection Heat Transfer in Slender Window Cavities," ASME J. Heat Transfer, **115**, pp. 476–479.
[15] ElSherbiny, S., Raithby, G. D., and Hollands, K. G. T., 1982, "Heat Transfer by Natural Convection Across Vertical and Inclined Air Layers," ASME J. Heat Transfer, **104**, pp. 159–167.
[16] Bar-Cohen, A., and Rohsenow, W. M., 1984, "Thermally Optimum Spacing of Vertical, Natural Convection Cooled, Parallel Plates," ASME J. Heat Transfer, **106**, pp. 116–1123.
[17] Churchill, S. W., and Usagi, R., 1972, "A General Expression for the Correlation of Rates of Transfer and Other Phenomena," AIChE J., **18**(6), pp. 1121–1128.

Transient Hydrodynamic Phenomena and Conjugate Heat Transfer During Cooling of Water in an Underground Thermal Storage Tank

E. Papanicolaou
Mem. ASME
e-mail: elpapa@ipta.demokritos.gr

V. Belessiotis

"Demokritos" National Center for Scientific Research,
Solar and other Energy Systems Laboratory,
Aghia Paraskevi, Attiki, Greece, 15310

The flow and heat transfer phenomena inside an underground thermal storage tank, initially filled with hot water at an almost uniform temperature and then left to interact with the cold surroundings, are studied numerically. The purpose of the study is to gain insight into how these phenomena affect the heat losses to the surroundings, before a new charging process takes place. A two-dimensional numerical model to solve for the transient flow and thermal fields within the tank coupled with the heat transport through the tank walls and within the ground are employed. Natural convection is found to dominate at the early transients when a strong recirculation develops, with a Rayleigh number characteristic of turbulent flow. A low-Re $k-\epsilon$ turbulence model is used for the computation. As time proceeds and the temperature differences between water and surroundings decrease, the recirculation decays and the heat transfer is dominated by thermal diffusion. The ground properties are varied, mainly in order to account for different moisture contents in the ground. Comparisons are made under realistic conditions with preliminary experimental results showing satisfactory agreement. [DOI: 10.1115/1.1643907]

Keywords: Conjugate, Heat Transfer, Natural Convection, Storage, Transient

Introduction

For storage of thermal energy in the form of sensible heat, water is the most commonly used medium due to the significant advantages it offers: apart from its availability and low cost, it has the largest heat capacity of most common materials [1] and, for solar energy applications in particular, it removes the need for an intermediate transport fluid, storage and transport medium being one [2]. Heat losses from the storing medium (water) to the surroundings can be reduced by making use of underground storage. The various methods that have been available for this purpose, for a couple of decades already, have been summarized by Givoni [3] and Garg et al. [4]. One of the most simple relevant constructions is the insulated underground water tank, for which several materials have been used, such as steel, aluminum, reinforced concrete, reinforced plastic etc. [4]. The amount of heat losses from the tank clearly depends on many factors but, in order to estimate it, it is necessary to understand the heat transfer mechanisms and the flow phenomena that develop after the tank is filled with water (charged) at a temperature higher than its surroundings. Several studies have dealt with the charging phase and the mixing that occurs in this case, whereby hot (or even chilled) water is discharged into a tank already filled with water at a lower (or higher), uniform temperature or with a thermal stratification present. However, very little work has been done on the still mode of operation, i.e., the transient process of heat loss from a tank with an initially uniform temperature distribution, in the absence of water inflow into or outflow from the tank. A closely related problem was studied by Jaluria and Gupta [5] who carried out experimental and analytical work on the decay of stratification in two small, water-filled cubical tanks (of dimensions 0.6 m and 0.3 m), considering various initial temperature distributions, including the uniform one as a special case. In another relevant application, Cotter and Charles [6,7] studied numerically the cooling of warm crude oil in cylindrical storage tanks located in a cold environment. Transient cooling problems in rectangular enclosures were also considered by Nicolette et al. [8] and Robillard and Vasseur [9].

In such configurations, the problem is characterized by the pure natural convective flow and associated heat transfer in the fluid. Eventually, and if there is no new charging of the tank in between, the fluid will come to thermal equilibrium with its surroundings and therefore any natural circulation will have died out by then. It is exactly the evolution of this particular transient problem that is investigated in the present study, by using numerical methods and by comparing with some preliminary measurements of temperature in a real underground tank made of concrete walls. This has been built at the Solar and other Energy Systems Laboratory of NCSR ''Demokritos'' in Attiki, Greece and has been instrumented with an array of thermocouples monitoring the temperature at various locations within the water body as well as within the surrounding ground. The computational treatment of this configuration gives rise to a conjugate heat transfer problem, whereby besides the tank itself the computational domain extends into the concrete walls and the surrounding ground. Even though the heat transfer in the ground is mostly dominated by conduction, several nonconductive heat transfer mechanisms are present as well [4]. Considering all these would have severely complicated the modeling efforts, therefore here only the coupling of the tank phenomena with the conductive heat transfer in the surroundings will be considered. Besides, a further simplification will be necessary, by lumping the ground properties into some averaged values and treating the ground as a homogeneous medium. This is a common approach in ground heat transfer simulations in studies of basement heat loss from buildings [10–13] or soil heat exchanger-

Contributed by the Heat Transfer Division for publication in the JOURNAL OF HEAT TRANSFER. Manuscript received by the Heat Transfer Division December 27, 2002; revision received October 27, 2003. Associate Editor: K. S. Ball.

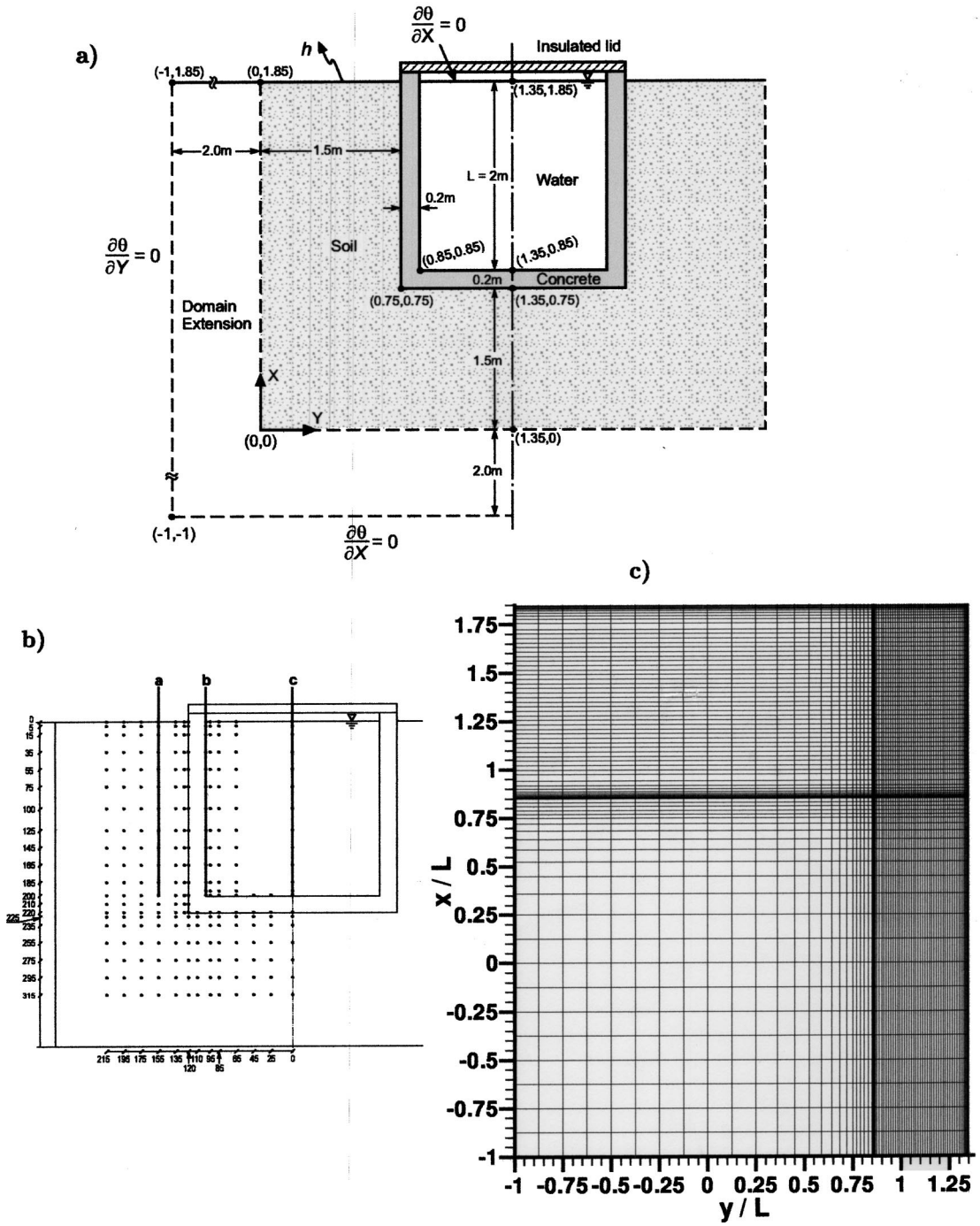

Fig. 1 Underground storage tank configuration: (*a*) instrumented region for temperature measurements (shaded area) with computational domain and boundary conditions, (*b*) temperature sensor locations, and (*c*) computational grid for the half domain

storage systems [14]. As far as underground storage tanks are concerned, ground heat transfer has been considered by Perrini et al. [15] and Inalli [16] in a cylindrical and Inalli et al. [17] in a spherical geometry.

The configuration of the cubical underground tank under investigation is shown in Fig. 1(*a*). For a first set of measurements, the tank was filled with water and effort was made to obtain a temperature as uniform as possible, at $T_i = 80°C$. Thermocouples were located over a vertical plane along the central axis of the tank, covering an area which extended up to 1.15 m below the concrete floor and 1.20 m outwards from the sidewall (Fig. 1(*b*)). Taking $T_\infty = 20°C$ yields $\Delta T = 60$ K and $T_m = 50°C$ as the mean temperature for water properties, thus a Rayleigh number equal to $Ra = 2.513 \times 10^{13}$. Therefore, considering this order of magnitude, a turbulence model has to be used in order to guarantee that the computational procedure is appropriate at all times. This is further justified by a recent study of a heat-up problem of water in a cylindrical enclosure [18], where it was found that at such orders of magnitude the natural convective boundary layer tends to become turbulent during the transients, even though it may eventually relaminarize due to the build-up of stratification. In the present cool-down problem, relaminarization is also expected eventually, due to the expected decrease of the driving temperature gradients with time.

Table 1 Diffusion coefficients Γ_ϕ and source terms S_ϕ for variable ϕ in the generic transport equation, Eq. 3

ϕ	Γ_ϕ	S_ϕ
Ω	1	$-(\mathrm{Ra/Pr})(\partial\theta/\partial Y)+S_{RS}$
θ (fluid domain)	$1/\mathrm{Pr}+\nu_t^*/\sigma_t$	0
θ (solid domain i)	$r_{d,i}(1/\mathrm{Pr})$	0
k	$1+\nu_t^*/\sigma_k$	$P_k+G_k-\epsilon$
ϵ	$1+\nu_t^*/\sigma_\epsilon$	$C_1 f_1 P_k(\epsilon/k)+C_3 G_k(\epsilon/k)-C_2 f_2(\epsilon^2/k)$

Mathematical Model

Modeling Assumptions. Due to the symmetry of the configuration and the lack of any preferred directions normal to the perimeter of the tank, it was decided that the measurements focused over a single vertical half-plane, where a good level of detail was possible to be achieved, as shown in Fig. 1(*b*). A two-dimensional model was therefore deemed adequate for the present computations as well. When considering only half of the computational domain, one has certainly to worry about potential symmetry-breaking bifurcations that occur at intermediate ranges of the Rayleigh number in several natural convection problems. However, given the very high value of the Rayleigh number of the present problem, laying in the fully turbulent regime, along with the fact that the fundamental convection problem is one due to symmetric cooling from the sides and the bottom, a situation not known to be prone to instabilities similar to the heating-from-below configurations, the use of a two-dimensional symmetric domain could be adopted with a large degree of confidence. This allowed for a good level of spatial and temporal resolution to be afforded in the present problem, characterizing at least the phenomena across a mid-plane of the tank, without resorting to unmanageable amounts of data in the measurements on one hand and to impractical computation times on the other, given the anticipated long transient process of the problem.

Model Equations. With the above considerations, and using a stream function-vorticity formulation obtained after a Reynolds averaging of the momentum equations and the Boussinesq approximation, the dimensionless equations describing continuity and conservation of momentum and energy in a Cartesian coordinate system for turbulent flow (where the overbars denote mean velocities) can be written as

Continuity.

$$\frac{\partial \overline{U}}{\partial X}+\frac{\partial \overline{V}}{\partial Y}=0 \tag{1}$$

Stream Function.

$$\frac{\partial^2 \Psi}{\partial Y^2}+\frac{\partial^2 \Psi}{\partial X^2}=-\Omega \tag{2}$$

Time-dependent transport equation for $\phi=\Omega,\ \theta,\ k,\ \epsilon$

$$\frac{\partial \phi}{\partial \tau}+\frac{\partial}{\partial X}\left[\overline{U}\phi-\Gamma_\phi\frac{\partial \phi}{\partial X}\right]+\frac{\partial}{\partial Y}\left[\overline{V}\phi-\Gamma_\phi\frac{\partial \phi}{\partial Y}\right]=S_\phi \tag{3}$$

where the diffusion coefficient Γ_ϕ and the source term S_ϕ for each variable ϕ are defined in Table 1 with $\nu_t^*=\nu_t/\nu$. In the derivation, and according to the Bousinessq eddy viscosity concept, the Reynolds stress terms and the turbulent heat fluxes have been defined as

$$-\overline{u_i' u_j'}=\Gamma_\Omega \nu_t^*\left(\frac{\partial \overline{U}_j}{\partial X_i}+\frac{\partial \overline{U}_i}{\partial X_j}\right)-\frac{2}{3}k\delta_{ij},\quad -\overline{u_i'\theta'}=\frac{\nu_t^*}{\sigma_t}\left(\frac{\partial \theta}{\partial X_i}\right) \tag{4}$$

where $X_i, X_j=(Y,X)$ and v', u' are the velocity fluctuations in the horizontal and vertical direction, respectively.[1] In the vorticity equation, written here in the form used in [19], apart from buoyancy the source term includes a contribution due to Reynolds stress gradients and this is equal to

$$S_{RS}=\Gamma_\Omega\left(\frac{\partial^2 \tau^t}{\partial X^2}-\frac{\partial^2 \tau^t}{\partial Y^2}\right)-\Gamma_\Omega\left(\frac{\partial^2 \varsigma^t}{\partial Y \partial X}\right)$$

where it has been defined for convenience

$$\tau^t\equiv\nu_t^*\left(\frac{\partial \overline{U}}{\partial Y}+\frac{\partial \overline{V}}{\partial X}\right),\quad \varsigma^t\equiv 2\nu_t^*\left(\frac{\partial^2 \overline{U}}{\partial X^2}-\frac{\partial^2 \overline{V}}{\partial Y^2}\right) \tag{5}$$

In the present study, the $k-\epsilon$ model is used and the viscosity ratio ν_t^* as well as the production terms of the turbulent kinetic energy due to shear P_k and buoyancy G_k appearing in Table 1, are given by the following expressions:

$$\nu_t^*=\Gamma_\Omega f_\mu C_\mu\frac{k^2}{\epsilon} \tag{6}$$

$$P_k=\nu_t^*\left[2\left(\frac{\partial \overline{V}}{\partial Y}\right)^2+\left(\frac{\partial \overline{U}}{\partial Y}+\frac{\partial \overline{V}}{\partial X}\right)^2+2\left(\frac{\partial \overline{U}}{\partial X}\right)^2\right],$$

$$G_k=-\frac{\mathrm{Ra}}{\mathrm{Pr}}\frac{\nu_t^*}{\sigma_t}\frac{\partial \theta}{\partial Y} \tag{7}$$

In the present computer code, several turbulence models, most belonging to the low-Reynolds $k-\epsilon$ family, have been implemented and have been tested for computations of natural convection in a previous study [18]. More specifically numerical results obtained for a differentially heated rectangular cavity of aspect ratio $A=5$ with adiabatic horizontal walls were compared against the measurements of Cheesewright et al. [20]. The overall agreement was good, even though each of the models showed better agreement for some of the selected quantities and worse for others, therefore not leading to a clear-cut preference for one of them. In this work, where laminarization is expected at some point in time, a low-Re model is clearly the best choice, let alone accuracy reasons, as the high-Re form is known to overpredict the wall heat transfer in natural convection problems [22]. Among low-Reynolds models the one by Launder and Sharma [21] has been selected here, since it was found in [18] to yield a good heat transfer curve along the heated wall, better approaching the measured values. The various functions involved in this model (Eq. 6 and Table 1) are

$$f_\mu=\exp\left[\frac{-3.4}{(1.0+\mathrm{Re}_t/50)^2}\right],\quad f_1=1.0,\quad f_2=1.0-0.3\exp(-\mathrm{Re}_t^2) \tag{8}$$

where $\mathrm{Re}_t=\Gamma_\Omega(k^2/\epsilon)$. The constants appearing in Eq. 6 and Table 1 have the following values: $C_\mu=0.09$, $C_1=1.44$, $C_2=1.92$, $\sigma_k=1.0$ and $\sigma_\epsilon=1.3$ and : $C_3=\tanh|U/V|$, the latter expression being suggested by Henkes and Hoogendoorn [22]. The value of the turbulent Prandtl number is taken as constant, equal to $\sigma_t=0.9$.

Boundary Conditions. The thermal boundary conditions are shown in Fig. 1. The adiabatic condition, used for the part of the top boundary occupied by the adiabatic lid, gives: $\partial\theta/\partial X=0$ at the top. At the ground surface next to the tank, a convective boundary condition was used, with a small Biot number, $\mathrm{Bi}=hL/\lambda_{\mathrm{ground}}=0.5$. Rather than resorting to heat transfer correlations, this value was inferred by analyzing some preliminary measurement data and approximating the slope of the temperature profile just below the ground surface next to the tank. This was found to remain fairly constant with time. The value Bi=0.5, applied to Soil 4 for instance (see Table 2), corresponds to a heat

[1] It should be noted that here X is the vertical and Y the horizontal direction, i.e., a notation typical of vertical natural convection boundary layers is used.

Table 2 Properties of concrete and ground used

Solid	λ (W/m K)	ρ (kg/m^3)	C_p (J/kg K)	ρC_p (MJ/m^3 K)[a]	$r_{d,i}$	$r_{C,i}$
Soil 1 (average) [29]	0.960	2500	836.8	2.092	3.194	0.506
Soil 2 (8% moist) [29]	0.586	1750	1004	1.757	2.292	0.425
Soil 3 (dry) [29]	0.264	1650	795	1.312	1.389	0.318
Soil 4 (well-graded sand) [11]	1.900	-	-	2.200	5.547	0.533
Concrete [11]	1.63	-	-	1.964	5.329	0.475

[a]For water at 50°C: $\rho C_p = 4.1297$ MJ/m^3 K

transfer coefficient of $h \approx 0.5$ W/m^{2}K, indicative of no significant wind activity during the measurement period and characteristic of low-Rayleigh-number natural convection. For the remaining boundary conditions, i.e., the far-field boundary conditions at the left and bottom boundaries within the ground, either constant temperature ($\theta = 0$) or zero temperature gradient may be used, as may be concluded from previous studies in ground heat transfer simulations, e.g., [12–14], [16]. Here, some experimentation was made with both conditions and with the location of the boundary and originally the constant temperature approach was adopted, but was later changed to zero gradient at both boundaries. For the vertical boundary, the constant temperature condition was found to be more restrictive, whereas zero gradient allows for a natural vertical stratification to develop as part of the computation. At the bottom boundary, $\theta = 0$ could be better justified, however, if the boundary is set sufficiently far enough, the zero gradient condition produces very similar values and is also less restrictive than the isothermal condition by allowing, again, a small horizontal gradient to develop. Therefore, both gradients were set to zero at these boundaries and this was in fact found to approximate the behavior of the real system, as obtained by the measurements, more closely at large times. As far as the final boundary locations are concerned, these were selected in such a way that any further shifting had only a local effect and did not lead to changes in the results throughout the domain.

The inner and outer walls of the tank are not treated as boundaries but as internal lines in the computational domain and special equations are solved for points located there as will be described below. From the mathematical point of view, the conditions that have to be satisfied on these locations (continuity of heat flux) are

$$r_{\lambda,1}\left(\frac{\partial\theta}{\partial n}\right)_1 = r_{\lambda,2}\left(\frac{\partial\theta}{\partial n}\right)_2 \quad \text{at solid}-\text{solid interfaces (soil}-\text{concrete)}$$

$$\left(\frac{\partial\theta}{\partial n}\right)_w = r_{\lambda,2}\left(\frac{\partial\theta}{\partial n}\right)_2 \quad \text{at fluid}-\text{solid interfaces (water}-\text{concrete)} \tag{9}$$

where n is the direction normal to the interface (either X or Y). The stream function and thus both velocity components are set to zero at the walls, whereas the wall vorticity is computed from the stream-function values in the direction normal to the wall [19], by means of an expression derived from suitable Taylor series approximations. For the turbulence variables, the wall values are specified by the choice of the turbulence model used (Launder-Sharma) and for which the corresponding conditions in dimensionless form are

$$k_w = 0, \quad \epsilon_w = 2\left(\frac{\partial\sqrt{k}}{\partial Y_n}\right)^2 = 2\frac{k_1}{Y_{n1}^2} \tag{10}$$

where k_1, Y_{n1} are, respectively, the values of k and the normal wall distance at the first point from the wall. Using the above boundary condition for ϵ removes the need for using the additional functions D_k, E_ϵ that some low-Re models use in the k and ϵ equations respectively. The applicability of these functions in buoyancy-induced flows, as pointed out by Heindel et al. [23], has yet to be confirmed.

On the axis of symmetry ($Y = 1.35$), $\psi = \Omega = V = 0$, whereas the Y-derivatives of θ, U, k, and ϵ are set to zero.

Numerical Scheme

General Description. The numerical scheme in its main features is the same one that has been described in detail by Papanicolaou and Jaluria in [19] and [24]. A time-marching procedure is followed, whereby at each time step the stream function equation, Eq. 2, is solved by the successive over-relaxation method (SOR). The computational domain is divided into a number of nonoverlapping control volumes, and over each of them the discretized, time-dependent transport equations, Eq. 3, are integrated. For the time discretization the Alternating Direction Implicit (ADI) method is used and at each half time step linear algebraic systems arise which are solved by means of the TDMA algorithm. In the present code several higher order schemes for the convective terms have been implemented and among those the Hybrid Linear Parabolic (HLPA) scheme [25] has been selected for the present computations, in the discretization of the vorticity and energy equations. For the turbulence variables k and ϵ the power-law scheme is used. The wall vorticity is computed by a first-order formula [19] which is more stable and readily applicable to nonuniform grids which will be used here.

Computational Grid. Various grid dimensions and node distributions have been considered, by varying the number of grid points especially inside the tank where the flow phenomena take place and boundary layers are present. Originally, computations were carried out over the shaded area in Fig. 1(a). For that domain, on which the fluid region grid tests were performed, the number of grid spacings that was found to be sufficient for the solid region outside the tank, where only conduction heat transfer is being simulated, was 17, both at the bottom and to the left of the tank. In the water, 43×43 spacings were originally considered, which were then increased to 60×60 yielding a total number of nodes 61×61 and 77×77 respectively. Very fine spacing was used towards the solid walls of the tank, the first grid point being located at a distance of the order of 10^{-4} from the nearest wall. Smaller stretching was used towards the axis of symmetry. An even finer grid was used, 107×107, by taking 91×91 nodes inside the tank but, as will be demonstrated in a later section, did not increase accuracy too much, while at the same time the computational effort needed to cover the relatively long time period required in this transient problem was increased significantly. Therefore, 61×61 nonuniformly spaced nodes were found to be sufficient and were chosen as the base grid within the fluid region. When the domain was later extended outwards, as shown in Fig. 1 (a), for better handling of the far-field thermal boundary condi-

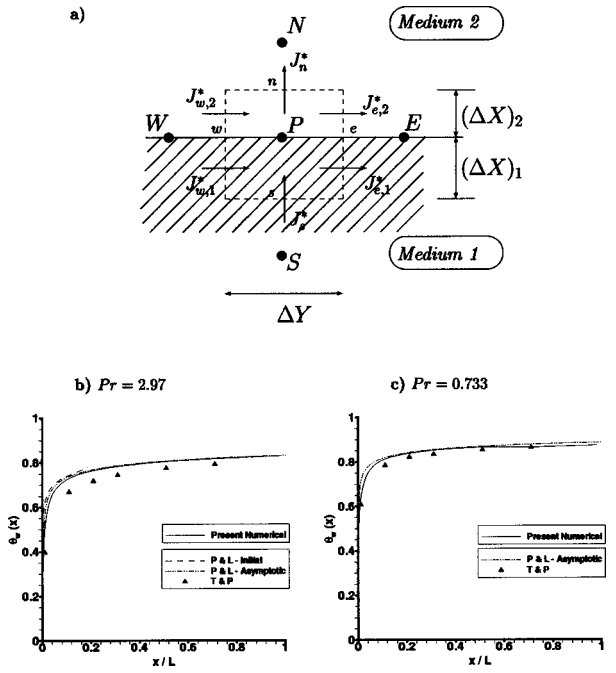

Fig. 2 (*a*) Interface control volume for derivation of the conjugate boundary condition. (*b*) and (*c*) validation for conjugate natural convection along a vertical flat plate against analytical solutions of Timma and Padet [27] and Pozzi and Lupo [28] for $Gr_l=10^9$, $\lambda_s l/\lambda_f b=500$ and at two different Prandtl numbers

tions, 22 instead of 17 grid spacings in the solid regions were required, thus the final dimensions that arose were 83×83. The latter grid is shown in Fig. 1(*c*).

Conjugate Boundary Condition. A crucial element of the present computational procedure is the conjugate boundary condition applied at the interface between fluid and solid (here water-concrete). The approach adopted is based on energy conservation principles and the basic concept has been originally presented by Papanicolaou and Jaluria [24] for a stream function-vorticity formulation in a Cartesian coordinate system. Later its applicability was also demonstrated in conjunction with a pressure-correction-based computational procedure and on a curvilinear coordinate system [26]. The basic idea is to place computational nodes exactly on the interfaces and to derive special equations for the associated control volumes such as the one shown in Fig. 2(*a*). By first splitting the control volume into two partial ones then writing the energy balance for each of them, the conditions expressed by Eq. 9 can be applied in an integral sense, i.e., as integrated heat fluxes on both sides of the interface which are forced to be equal to each other. This produces a single equation for the entire control volume of Fig. 2(*a*). For the needs of the present problem, the procedure is further generalized by similarly extending it into situations where the media on both sides of the interface may be solid materials. In accordance with the equations presented in [24] and [26]; therefore, the interface equation may more generally be written as

$$\frac{\partial\theta}{\partial\tau}(\Delta X)_2\Delta Y(r_{C,2}+r_{C,1}f_X)=a_S^*(\theta_S-\theta_P)+a_N^*(\theta_P-\theta_N)+a_W^*(\theta_W-\theta_P)+a_E^*(\theta_P-\theta_E) \tag{11}$$

where medium 1 is a solid and medium 2 may either be a fluid (in which case $r_{C,2}=1$) or a solid with the specified thermal capacity ratio $r_{C,2}$. f_X is here the local grid spacing ratio in the X dimension, equal to $f_X=(\Delta X)_1/(\Delta X)_2$, considering that faces n and s are placed here midway between nodes N, P and P, S respectively. The discretization coefficients a^*, each associated with the corresponding flux J^* shown in Fig. 2(*a*), are here defined as

$$a_S^*=r_{C,1}a_{S,1},\quad a_W^*=r_{C,1}a_{W,1}+r_{C,2}a_{W,2}$$
$$a_N^*=r_{C,2}a_{N,2},\quad a_E^*=r_{C,1}a_{E,1}+r_{C,2}a_{E,2} \tag{12}$$

i.e., a_W^*, a_E^* are *composite* coefficients and $a_{S,1}, a_{w,1}$ etc. are obtained for each medium in the standard manner. Equations of the form of Eq. 11, after a suitable time discretization (here by means of the ADI method), may be readily incorporated into the overall system of algebraic equations arising in the usual manner for all interior nodes and for all media involved, enabling thus the energy equation to be solved over the entire domain by treating the interface nodes as internal ones.

Code Validation. To validate the treatment of the conjugate boundary condition described above for natural convection, comparisons were made against analytical solutions by Timma and Padet [27] and Pozzi and Lupo [28]. In both cases solutions were obtained for conjugate natural convection along a vertical flat plate of length l and thickness b whose back side is maintained at an elevated, constant temperature and at various Prandtl numbers and coupling parameters, the latter defined in [28] as $K=\lambda_s l/\lambda_f b$. The Grashof number Gr_l based on the length of the plate was 10^9, ensuring laminar flow conditions throughout. In the present numerical computations a ratio $l/b=40$ was chosen and a non-uniform grid of 96×39 nodes (vertical $\times$ horizontal direction), suitably refined towards the leading edge and towards the surface of the plate. In Fig. 2 the computed wall temperature distribution is shown for $K=500$ and two different Prandtl numbers, Pr=0.733 (air) and Pr=2.97 (water, 60°C). As far as the validation of the turbulence model used and as mentioned earlier, several of them have been implemented in the present code and their performance was assessed in a previous study [18], by comparing with the experimental data of Cheesewright et al. [20] for a differentially heated cavity of aspect ratio $A=5$.

Results and Discussion

Input Parameters. As already mentioned, the properties of water are taken at a mean temperature of 50°C and with a $\Delta T=60$ K the value of the Rayleigh number is equal to $Ra=2.5\times 10^{13}$. The Prandtl number is equal to 3.535. With the minimum grid spacing of the order of 10^{-4} (dimensionless), the maximum time step allowed is $\Delta\tau=5\times 10^{-8}$. The computations start with the water at rest initially. As far as the turbulence variables are concerned and in accordance with [18], a 1% turbulence level is assumed initially and a dimensionless reference velocity of $U_{\text{ref}}=10^5$, so that $k_i=0.01^2\times U_{\text{ref}}^2=10^6$ and a dimensionless length scale for ϵ equal to $l_\epsilon=0.03\times D/2$, where $D=0.5$ (i.e., half the inner tank dimension). This yields the initial values $\epsilon_i=1.2\times 10^{10}$ and $\nu_{t,i}^*=7.5$ for the remaining turbulence variables. As far as the initial temperature field is concerned, the measured data at $t=0$ showed a large non-uniformity within both the water and the surroundings, due to both natural effects and those that have to do with previous chargings of the tank, before the actual set of measurements presented here was to start. Both these factors were very hard to control completely over the entire area corresponding to the computational domain. Therefore, it was decided to distinguish between two cases in the computations characterized by initial fields with (1) uniform temperature within the water, $\theta=1$, and the surroundings (concrete walls+ground), $\theta=0$ (Case 1); and (2) temperature distribution obtained by approximating as closely as possible a ''snapshot'' of the initial temperature field, i.e., the measured temperature values, at $t=0$ (Case 2).

Case 1 is an idealized case, but is of more universal value by allowing a better study of the fundamental problem posed in the

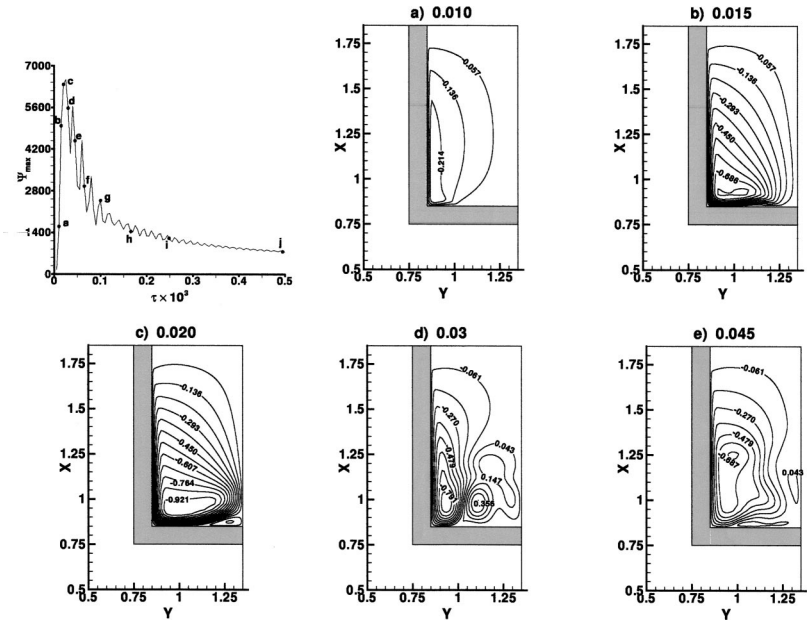

Fig. 3 Computed streamlines (normalized with the peak value of Ψ_{max}) for the underground storage tank at time instants (*a–e*) shown on the Ψ_{max} versus dimensionless time curve (15 equally spaced contour values from −1 to 0.45)

present work, focusing on the hydrodynamic phenomena in the tank and the effect of the ground properties. Case 2 is more realistic and will allow for comparisons between computations and measurements, even though the findings may inevitably lose in generality to some extent.

As far as the properties of the solid materials involved, i.e., soil and concrete, a large scattering of values exists in the literature, especially for soil, depending on its composition, porosity and moisture content. In this particular case, samples were taken from the surrounding soil at three different locations adjacent to the tank and at different depths and its composition was analyzed in a specialized laboratory. It was found that the soil consisted of a mixture of mostly sand on one hand (slightly under 50% on the average) and clay+silt on the other (slightly over 50%), with only a small percentage of gravel (1–2%). The moisture content was found to be quite high, varying between 10–15% for most of the depth. However, the full set of thermophysical properties needed here could not be deduced from this sampling, therefore values from the literature had to be sought. A good set of soil properties was given by Carslaw and Jaeger [29], for different moisture contents ranging from dry soil to average moisture content, and these are given in Table 2. In the same table a fourth set of properties is shown, taken from the study of Sobotka et al. [11] who considered values covering the range used by different standards (ASHRAE, European etc.) established for the calculation of basement wall heat loss. The particular value chosen here corresponds to a highly conducting soil thus providing a wide spectrum of soil properties for the present purposes. Properties for concrete are also provided in both [29] and [11]. Here the values given in [11] were selected, since the higher thermal conductivity of that study (referring to building basements) was found to better approximate the behavior of the present concrete as arising by the measurements. Also, this is justified by the expected large moisture content of concrete, considering the large elapsed times between construction of the tank and measurements. On the last two columns of Table 2 the thermal diffusivity and thermal capacity ratios, $r_{d,i}$ and $r_{C,i}$ respectively, for each soil type and for concrete are shown and these will be used in the following computations, using Set 4 as the base, because it is expected to lay closer to the actual moisture contents.

Main Physical Phenomena in the Tank. The study of Hyun [30] has described the basic phenomena during the adjustment process through which an initially homogeneous fluid is led to a stratified state by suddenly applying a linear temperature distribution along the vertical sidewall, considering also the case of finite thermal conductance at the wall. The main phases in this process are successively (a) the sidewall boundary layer formation, (b) the build-up of stratification through redistribution of energy, and (c) the final smoothing out of remaining disturbances towards a final equilibrium state. Such a sequence is also expected in the present cool-down process, however here there are no wall temperatures that remain fixed throughout but their values change constantly with time. From the early computations it became clear that the entire process can be divided into two major distinct phases: one where the hydrodynamic phenomena are dominant and this covers the first few hours only of the process and where the heat losses are mostly through the natural convective boundary layers (convection phase) and a second one where the natural convective flow has died out and the heat transfer from the water is mostly by conduction (diffusion phase). The latter phase theoretically extends up to the point in time when thermal equilibrium is achieved. However, the measurements here only lasted for about a month (756 hours) and, therefore, this was chosen as the time span to be covered by the computations as well.

Convection Phase. For the data corresponding to Soil 4, the computed streamlines at different time instants during the early transients (the first hour) are shown in Figs. 3 and 4, along with the typical curve of variation of the absolute value of Ψ_{max} (spatial maximum), which is a measure of the intensity of the recirculation, with time. It is observed that the maximum of this quantity in time, say $\Psi_{max,max}$, is attained between time instants *c* and *d*, corresponding to the first 2–3 minutes, as can be obtained when the values of dimensionless time τ shown, are multiplied by the appropriate multiplication factor, which is here equal to 121.06, to convert them into minutes. The contour values shown have been normalized with the absolute value of $\Psi_{max,max}$. A counterclockwise rotating recirculating flow is clearly observed, with a boundary layer developing along the vertical wall from top to bottom. At time *c* and beyond, secondary flows appear near the

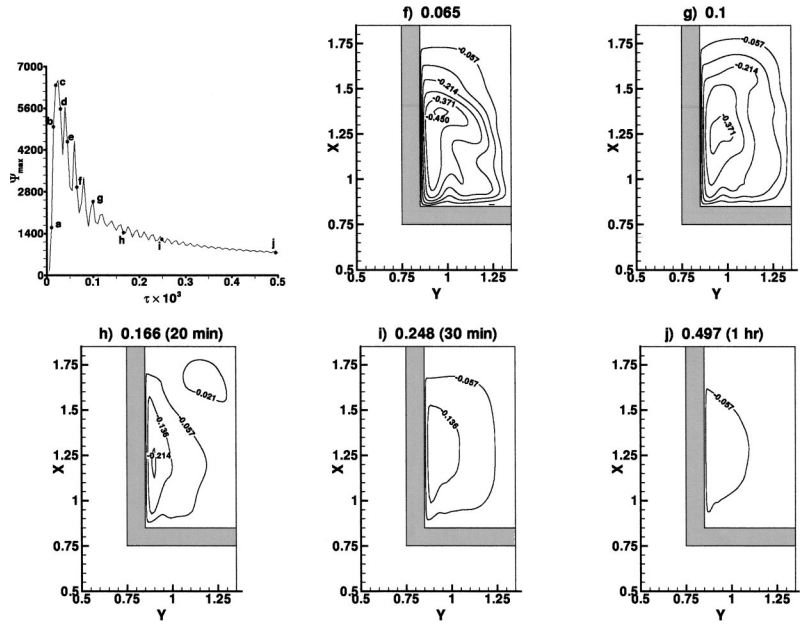

Fig. 4 Computed streamlines (normalized with the peak value of Ψ_{max}) for the underground storage tank at time instants (*f–j*) shown on the Ψ_{max} versus dimensionless time curve (15 equally spaced contour values from −1 to 0.45)

bottom of the tank and these are responsible for the oscillatory behavior observed in the corresponding section of the Ψ_{max} versus time curve. Past point *d*, the recirculation dies out rapidly but past point *g* the decrease in intensity is smoother, resulting in a weak recirculation at 1 hour of elapsed time (Fig. 4(*j*)). This pattern is maintained even at later times with decaying recirculation until a value of about 2% of $\Psi_{max,max}$ is attained and this is taken here as the termination criterion for the computation of the flow field. Beyond that time the temperature field is only computed, with a frozen flow field maintaining small values of the flow quantities. This is where the diffusion phase sets in and this will be analyzed below. The contours of the eddy viscosity ratio are shown in Figs. 5 and 6, along with the corresponding variation of the maximum value of ν_t^* with time. In accordance with the stream function behavior shown in Figs. 3 and 4, there is here also a sharp peak initially, followed by a gradual decay as the intensity of recirculation decays. The contour values are normalized with this peak value of $\nu_{t\,max}^*$. Here this peak value of ν_t^* is attained at somewhat later times than those for the peak value of the stream function, i.e., between time instants *d* and *e*. The area of increased turbulence develops in the vertical boundary layer, originally at a vertical coordinate value of 1, Fig. 5(*b–e*), then shifting upwards to about 2/3 of water depth and to mid-depth at later times, Fig. 6.

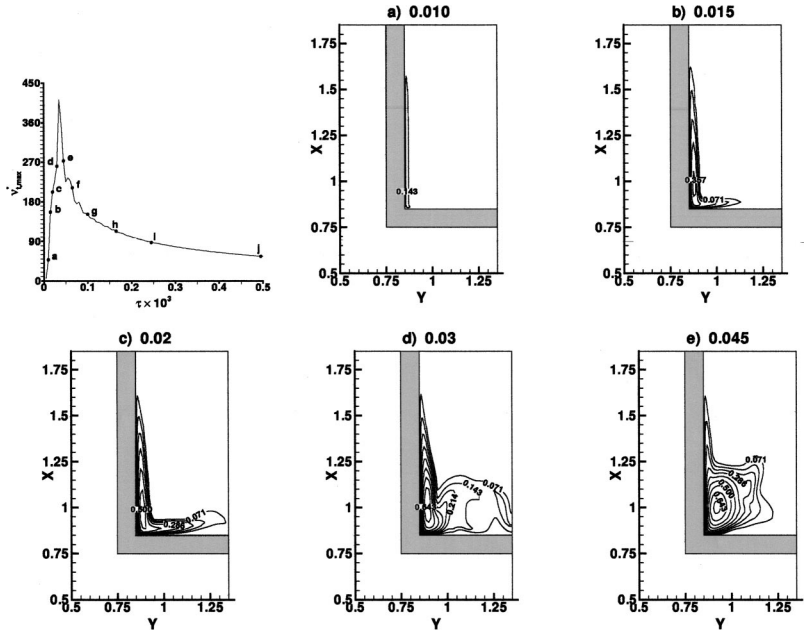

Fig. 5 Computed contours of the viscosity ratio (normalized with the peak value of $\nu_{t,max}^*$) for the underground storage tank at time instants ($\tau\times10^3$) marked as (*a–e*) on the $\nu_{t,max}^*$ versus time dimensionless curve (15 equally spaced contour values from 0 to 1)

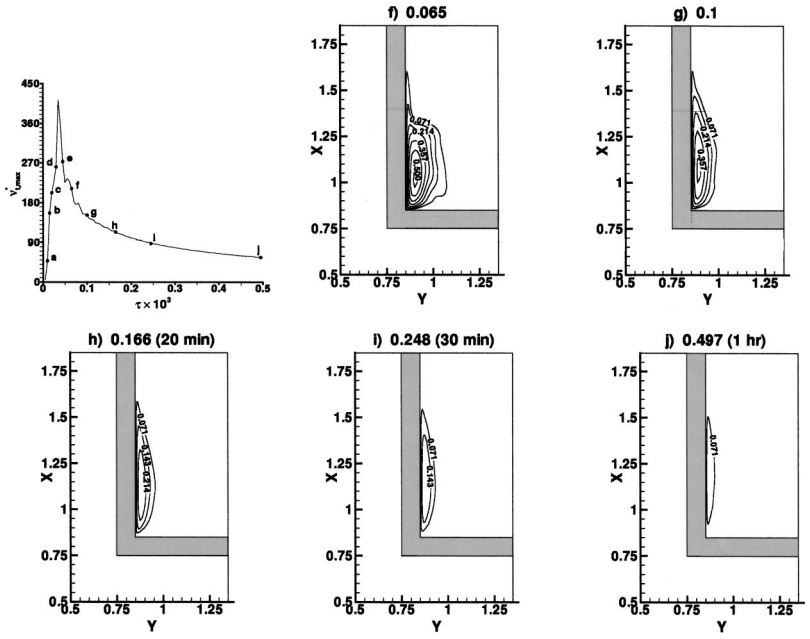

Fig. 6 Computed contours of the viscosity ratio (normalized with the peak value of $\nu^*_{t,\max}$) for the underground storage tank at time instants ($\tau\times10^3$) marked as (*f–j*) on the $\nu^*_{t,\max}$ versus time dimensionless curve (15 equally spaced contour values from 0 to 1)

The temperature field during this convection phase does not change significantly, therefore in Fig. 7, only time instants (a,c,e,h,j) are shown. There is a heat flow towards the the left wall and towards the tank bottom through the corresponding thermal boundary layers. There is still no evidence of significant stratification in the core of the tank and the cooling of the water body is almost uniform. The behavior of the vertical thermal boundary layer can be better explained by observing the local heat transfer curve, i.e., the plot of local Nusselt number Nu_x against the local Rayleigh number Ra_x. Here the coordinate x is measured from the top, downwards along the side wall. The curves of Fig. 8(*a*) correspond to time instants (a–e) of the previous figures, Figs. 3–6, while those of Fig. 8(*b*) to time instants (f–j) of the same figures. In these logarithmic plots, the curve obtained at the first time instant τ_1 exhibits a large distortion, which gradually becomes smaller and more localized at times $\tau_2-\tau_3$. This pattern is indicative of laminar-to-turbulent boundary-layer transition and very similar to the behavior observed during the transient heating of water in a cylindrical enclosure [18]. The latter study was in agreement with previously documented findings on natural convective boundary layers in water where transition was found to

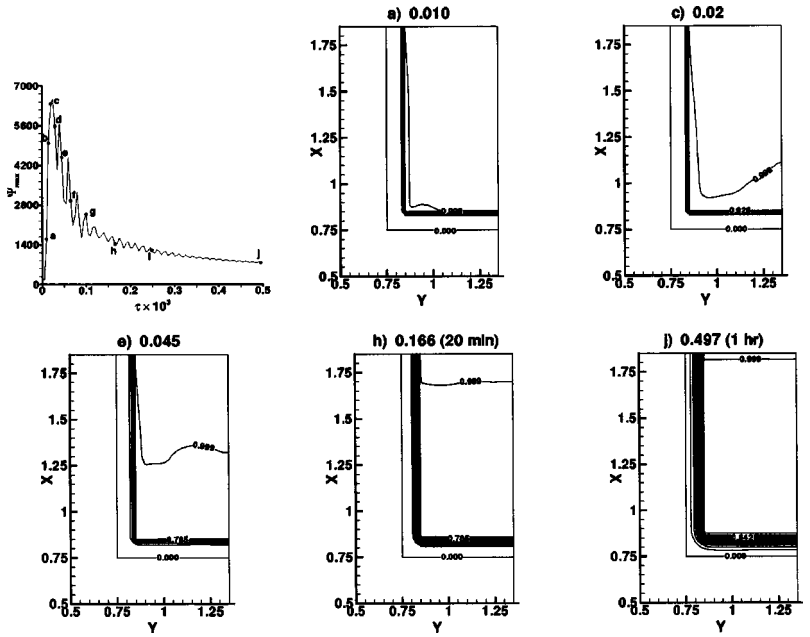

Fig. 7 Computed isotherms for the underground storage tank at selected time instants in the convection phase, among those shown on the $\Psi_{\max}$ versus dimensionless time curve

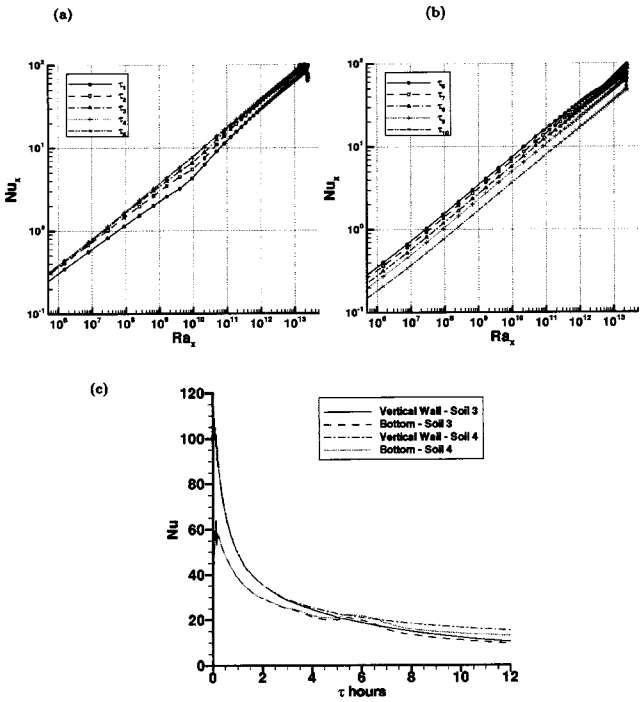

Fig. 8 (*a*) and (*b*) Local Nusselt number versus local Rayleigh number along the vertical wall (top to bottom) and for the corresponding time instants of Fig. 3 and Fig. 4 respectively, and (*c*) mean Nusselt number at the vertical wall and tank bottom for the first 12 hours and two soil types

start at values $Ra \approx 3 \times 10^{12}$ according to some authors [31] and $Ra \approx 1.2 \times 10^{13}$ according to others [32]. However, these criteria correspond to heated vertical flat surfaces and constant-heat-flux conditions and their extension to the present case of suddenly cooled surfaces cannot be granted. However, the order of magnitude of the Rayleigh number in the present case lays in the critical region according to the aforementioned studies and this fact should be taken into consideration. To the authors' knowledge, there are no experimentally or analytically obtained critical values for transition in a natural convective boundary layer during cooldown of a fluid. Here the distortion in the Nu_x versus Ra_x curve, particularly evident at times $\tau_1 - \tau_3$, may therefore only be claimed as a hint of a boundary-layer transition, which however, if true, is found to take place at much lower values than in the case of a heated surface as may be observed in Fig. 8(*a*) (order of 10^{10} for Ra_x). At later times, τ_5 and on, relaminarization is gradually established and the curves become linear and remain so throughout, with only a parallel shifting to lower values as time advances. In Fig. 8(*c*) the mean Nusselt numbers over the vertical wall and the tank bottom are plotted for the first 12 hours, times extending into the diffusion phase to be discussed below. Results for two soil types are shown, the least and the most conductive ones, Soil 3 and 4 respectively. It may be observed that during the early times (up to 5 hours approximately) the heat transfer is mostly through the vertical boundary layer and that the soil properties have a negligible influence during this period.

Diffusion Phase. The transient hydrodynamic phenomena were found to have been completed after approximately 2 hours and with them the convection phase. However, the computations of the flow field were still continued until the value of Ψ_{max} reduced to approximately 2% of its peak value, a fact which occurred at about 14 hours of physical time. During these early stages of the diffusion phase the temperature field developed as shown in Fig. 9 (top) for 4–14 hours. The form of the temperature field within the tank does not vary much over the same period,

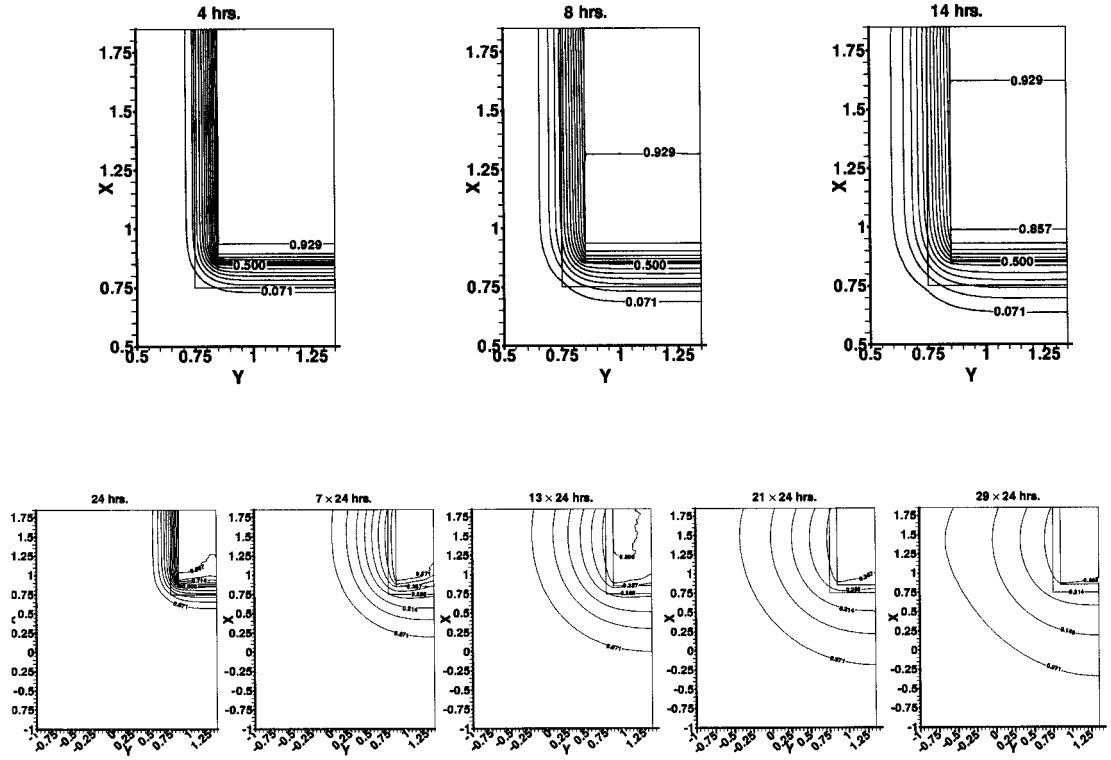

Fig. 9 Computed isotherms for the underground storage tank at the early (top, 4–14 hours) and the later (bottom, 1–29 days) stages of the diffusion phase

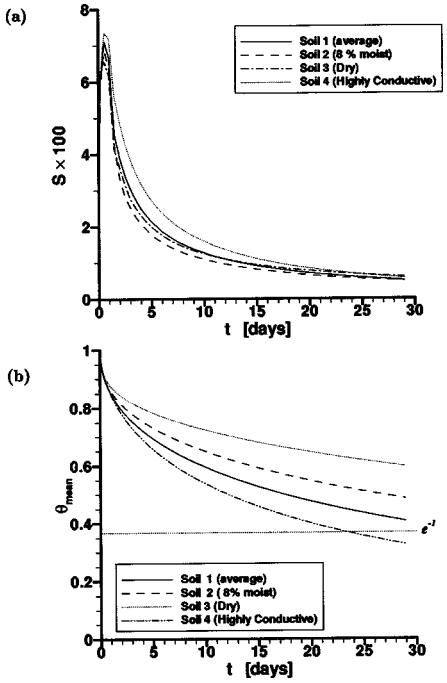

Fig. 10 Computed (*a*) stratification factor and (*b*) mean water temperature versus time for the various soil types of Table 2

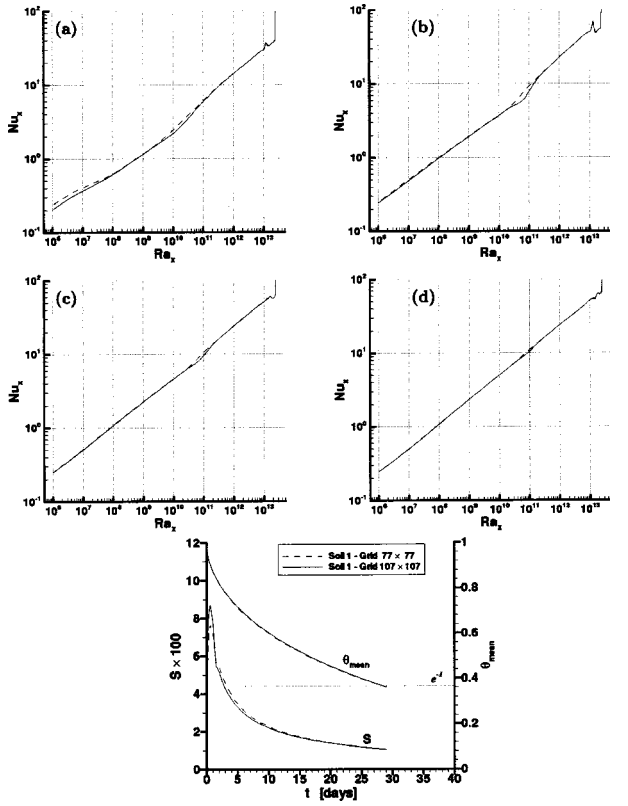

Fig. 11 Local Nusselt versus local Rayleigh number along the vertical wall for two different grid dimensions, 77×77 (dashed line) and 107×107 (solid line), and at times $\tau\times10^3=a$) 0.01, *b*) 0.02, *c*) 0.03 and *d*) 0.04. At the bottom, the transient behavior of the stratification factors and mean water temperature are also compared

however, now become more obvious both the cooling of water, gradually starting to proceed from the bottom up, as well as the development of the temperature front in the ground, to the bottom of the tank and to the left of the vertical sidewall. As observed in Fig. 8(*c*), after 5 hours the heat transfer from both surfaces is of the same order of magnitude and the thermophysical properties of soil are now beginning to have a stronger influence.

After a time period of 14 hours, the energy equation is only solved with fixed flow quantities, at the values these attained with the completion of the 14-hour period. This allows for a much larger time step to be used on the same grid ($\Delta\tau=10^{-6}$). By continuing the computations for a physical time period of about a month, the temperature field develops as shown in Fig. 9 (bottom). The small degree of stratification that develops during the first 24 hours starts decaying afterwards and the tank cools down maintaining an almost uniform temperature distribution at least within the top three quarters of it. In Fig. 10(*a*) the time evolution of the stratification factor S (multiplied by 100) is presented for the four different types of soils that have been considered. S is derived by computing the mean temperature over each horizontal line of the grid, excluding the top and bottom layers where local nonlinearities in the distribution are present, and then taking the slope of the linear fit of the mean temperature along the vertical coordinate (here X) over the remaining height of the tank (core). What may be observed is that the behavior is similar for all soils during the first day, when the convection phenomena are dominant and until the maximum of S is attained. However, at later times the decay of the stratification follows a different rate for each soil type. Interestingly enough, it appears here that, the higher the thermal conductivity of soil, the higher the rate of stratification that develops in the tank during the first two or three days of storage. However, at later times Soil 2 appears to maintain the lowest rate while asymptotically the drier soil, Soil 3, tends to maintain the highest. In Fig. 10(*b*) the mean water temperature obtained by averaging through all grid points in the tank is plotted against time. The horizontal line at an abscissa of $1/e$ is the ''e-folding time'' or ''time constant'' for the cooling process and was also used by Jaluria and Gupta [5] to determine the overall heat loss coefficient in their tank. In this figure it may be observed that the more conductive the soil, the faster the cooling process and only one of the soils, Soil 4, is shown to have an e-folding time which is shorter than the period of one month covered by the computations.

Effect of Grid Dimensions. In Fig. 11 the effect of increasing the grid dimension within the water tank is shown. This test was carried out at the early stages of developing the present model for the simulation, therefore, as explained in paragraph 3.2, the computational domain was the shaded region in Fig. 1(*a*) and the two far-field boundaries in the ground (left and bottom) were set at $\theta=0$. Nevertheless, this is a very indicative test, as the total number of nodes within the water tank is the same between this original and the actual configuration used, the differences being limited to the ground outside the tank. For the original, shaded domain of Fig. 1(*a*) the grid dimensions were equal to 77×77 (61×61 nodes in the water) and were increased to 107×107 (91×91 nodes in the water), maintaining the same pattern in the clustering of the nodes towards the solid boundaries in the tank. The local Nusselt number, obtained here for Soil 1, exhibits small discrepanies at early times (a–d) and for some locations, but as time proceeds the two grids produce identical results. Some early discrepancies may also be observed with respect to the predicted stratification factor shown at the bottom of Fig. 11, whereas the computed averaged water temperature in the tank shows a very good agreement between the two grids at all times. The efficient geometric stretching used with the 77×77 grid provided adequate accuracy (less than 2% difference in the mean Nusselt number at both the vertical wall and the bottom throughout the convection phase), while at the same time saved a significant amount of com-

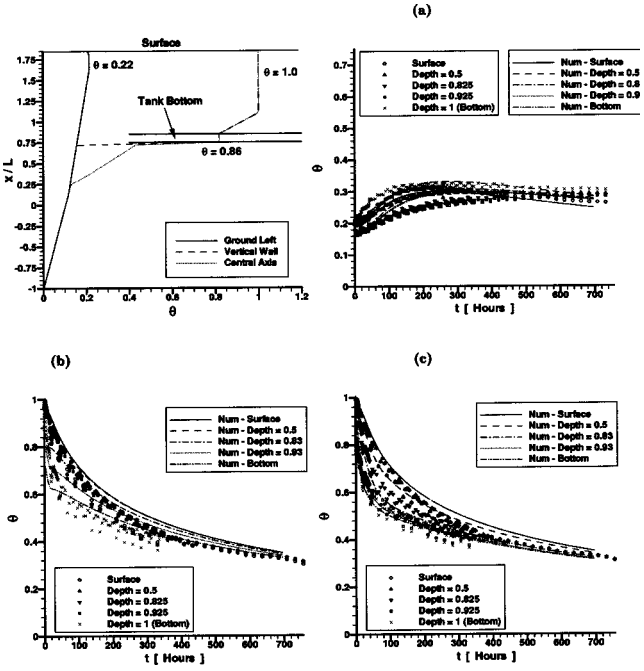

Fig. 12 Initial temperature distributions (top left) and computed temperature histories at selected depths: (*a*) within the ground and along, (*b*) vertical wall, and (*c*) central vertical tank axis, compared to measured data at the respective locations a,b,c of Fig. 1(b)

putational time for this transient problem which required a large number of time steps (CPU time per time step reduced by a factor of 3).

Comparisons With Measurements. As was discussed early in this section, in order to make comparisons with measurements in this transient problem, it is necessary to start the computations from initial conditions which are as close as possible to the actual ones. Therefore, the initial measured field was studied in detail both within the water as well as within the ground and the necessary deviations from the idealized conditions used in the previously presented computations were introduced. These are depicted at the upper part of Fig. 12. As far as the water in the tank is concerned, it was observed that due to the large time required in order to fill the tank with water at 80°C, cooling had already started at the bottom and a cold layer had already developed by the time the measurements were to start. It was concluded therefore that a linear ramp distribution, with $\theta_i=1$ at the bulk of the tank water, varying linearly within the bottom 1/4 of the height of the water and reducing to a value of $\theta_i=0.86$ at the floor of the tank would have been closer to reality as the initial condition. In the ground, a residual temperature field from previous chargings of the tank (the last of which was completed a week before the present measurements had started) could be observed, as shown in Fig. 12.

The main features of the flow field, not shown here for the sake of brevity, were somewhat modified in this case and the downward flow shown in Figs. 3 and 4, along the vertical wall was observed not to extend all the way to the bottom in this case, due to the presence of the cold layer formed initially along the bottom surface. This layer is thermally stable and therefore the recirculating flow of warmer water cannot penetrate it, being limited to the top 3/4 of the tank. This fact was also confirmed by the temperature measurements.

Among the temperature sensor locations shown in Fig. 1(*b*) the three vertical columns labeled ''a'', ''b'', and ''c'' in the same figure are selected for comparisons with the computations in the present study. These are taken in the ground to the side of the tank, along the vertical wall and along the central axis of the tank respectively. In the computations, temperature values are monitored over time at the corresponding nearest vertical and horizontal locations. The comparison is shown in Fig. 12(*a*–*c*), in terms of the dimensional temperature θ. To nondimensionalize the measured temperatures and since the ambient temperature T_∞ varied with time during the measurement period, a linear interpolation of the values during this period was used and led to the following variation with time:

$$T_\infty = -0.01745 \times t \ \ [\mathrm{Hrs}] + 23.306 \ \ [^\circ\mathrm{C}] \qquad (13)$$

In the computations, the data for Soil 4 have been originally considered, as closer representing the expected high moisture content of the present soil during the measurement period. However, as was found out, the comparisons in the ground to the side of the tank (location ''a'') were still not good enough, the measured temperature changes with time not being so rapid as in the computations, indicating a higher thermal capacity in that region. Therefore the thermal capacity ratio r_C was assigned a higher value, equal to $r_C=1.0$, in that region and the agreement as far as the temperature variations with time was very close to the measured ones. Such a value for soil can also be obtained by data encountered in the literature in ground heat transfer simulations, for instance, in [12]. On the other hand, nonhomogeneities in the ground properties are to be expected and in some studies, such as the one by Gauthier et al. [14], these have been handled by a zonal approach in modeling the ground heat transfer. In the present simulation, such a situation can be readily handled by the approach discussed in paragraph 3.3 and the ground region left of the tank and from its bottom and up was taken as a separate zone in terms of the thermophysical properties.

The overall agreement appears to be satisfactory when looking at all three locations, ''a'', ''b'', and ''c''. In the ground, along line ''a,'' the computations show the surface temperature to attain the lowest value at large times, as the measurements also show. Along the wall (line ''b''), the computed values are somewhat higher as some vertical gradient is maintained at large times, whereas the measurements show an almost uniform temperature. The same behavior can be observed on the tank axis (line ''c''), where in the numerical results a small stratification persists at large times, but otherwise the comparison is fairly good.

Note on the Use of the Boussinesq Approximation. The range of validity of the Boussinesq approximation for water is more limited compared to, for instance, air and caution therefore should be used in its application. Here a simplified analysis was pursued based on the relevant criteria outlined by Gray and Giorgini [33]. They found that the maximum value of the Rayleigh number allowed for water can be quite high (greater than 10^{19}), but the driving temperature gradient ΔT should be less than a few K. Gray and Giorgini [33] used a reference temperature $T_m=15^\circ$C and found for water $\Delta T \leqslant 1.25$ K, where ΔT in their case is a vertically applied fixed temperature gradient, giving rise to a Rayleigh-Benard problem. Assuming that their analysis is applicable to the present problem, even though the boundary conditions are quite different, and using their criteria with $T_m=50^\circ$C instead, it is found that $\Delta T \leqslant 6.92$ K≈ 7 K.

Here, however, an appropriate driving ΔT had to be found, and as such the difference between the mean water temperature, having a typical variation as shown in Fig. 10(*b*), from a mean wall temperature value (also time-dependent and referring to both vertical wall and bottom) was calculated for the convection phase. When this difference was obtained as a function of time for the results of Fig. 12, for instance, a driving ΔT in the range 5–6°K at all times was found, which is within the limit imposed for validity of the Boussinesq approximation as computed with the Gray and Giorgini criteria [33].

Conclusions

A numerical procedure has been presented to simulate the transient phenomena in water after the initial charging of an underground, rectangular storage tank, subsequently left to interact with the cold surroundings. The flow field in the tank, driven by the arising buoyancy forces at $Ra=2.5\times10^{13}$ and coupled with the ground heat transfer problem is being solved for a time period extending up to a month, under both ideal and realistic conditions. In the latter case results are compared with preliminary measurements. It was found that

1. The hydrodynamic phenomena have their own time scale which is of the order of a few hours, after which conduction heat transfer starts to become important. Therefore, similar future studies on storage tanks should make a fundamental distinction between a convection- and a diffusion-dominated phase, characterized, respectively, by a build-up and a decay of stratification in the water. The realization of this distinction allows for faster computations of the temperature field for long time periods, by switching to a mere solution of the energy equation after the convection phase is completed. The latter may have already been more accurately simulated using a turbulent flow model.
2. In the convection phase, a large peak in heat transfer takes place along the vertical wall, through a boundary layer which may initially be turbulent if the temperature difference between water and surroundings is sufficiently large, as in the present case (60 K or more) and then laminarize. In the design of actual systems, therefore, where the heat losses have to be contained, especially when the still mode between chargings of the tank is of the order of several hours (e.g., night-time), this mode of heat transfer constitutes a key mechanism of heat loss and effort should be undertaken to disrupt it.
3. Considering the uncertainties as far as ground properties and composition are concerned, the numerical model needs to interact with the measurements in order to accurately simulate the actual conditions. Once confidence is gained, however, the model may be used to examine alternative cases obtained by varying the thermophysical properties in the ground, due to internal nonhomogeneities, moisture content etc.
4. The heat transfer problem in the ground is certainly quite complex and factors such as moisture diffusion and nonconductive modes of heat transfer play also an important role. However, a lumped property approach, even though simplified, may be a useful tool in storage tank analysis, by allowing the transient hydrodynamic phenomena in the tank to be studied coupled with the thermal effects from the surroundings.

Nomenclature

C_p = specific heat under constant pressure (J/kg K)
g = magnitude of the gravitational acceleration (m/s^2)
h = local heat transfer coefficient along a solid surface, $h=-\lambda(\partial T/\partial n)_w/(T_w-T_\infty)$ (W/m^2K)
k = turbulent kinetic energy non-dimensionalized by $(\nu/L)^2$
L = characteristic dimension of the tank (m)
n = coordinate in the direction normal to the wall ($n=X$ or Y)
Nu_s = local Nusselt number varying along a solid surface ($s=X$ or Y), $Nu_s=hs/\lambda=-(1/\theta_w)(\partial\theta/\partial n)_w s$
$\overline{Nu}$ = Nusselt number averaged over a solid surface along $s=X$ or Y, $\overline{Nu}=(1/s_{max})\int_0^{s_{max}}[-(1/\theta_w)(\partial\theta/\partial n)_w]ds$
Pr = Prandtl number of water $Pr=\nu/\alpha$
$r_{C,i}$ = thermal capacity ratio for solid i, $r_{C,i}=(\rho C_p)_{s,i}/(\rho C_p)$
$r_{d,i}$ = thermal diffusivity ratio for solid i, $r_{d,i}=\alpha_{s,i}/\alpha$
$r_{\lambda,i}$ = thermal conductivity ratio for solid i, $r_{\lambda,i}=\lambda_{s,i}/\lambda$
Ra = Rayleigh number $Ra=g\beta\Delta TL^3/\nu\alpha$
y, x = horizontal and vertical coordinate distance, respectively (m)
Y, X = dimensionless horizontal and vertical coordinate distance, respectively, $Y=y/L$, $X=x/L$
t = physical time (s)
T = local temperature (K)
v,u = horizontal and vertical velocity components, respectively (m/s)
V, U = dimensionless velocity components $(V,U)=(v/(\nu/L),u/(\nu/L))$

Greek Symbols

α = thermal diffusivity (m^2/s)
α_t = eddy diffusivity for heat (m^2/s)
β = coefficient of thermal expansion of water $\beta\equiv-(1/\rho)\times(\partial\rho/\partial T)_p(K^{-1})$
ΔT = temperature scale $\Delta T=T_i$ (water)$-T_\infty$
ϵ = rate of dissipation of the turbulent kinetic energy, nondimensionalized by ν^3/L^4
θ = dimensionless temperature $\theta=(T-T_\infty)/\Delta T$
λ = thermal conductivity (W/mK)
ν = kinematic viscosity of water (m^2/s)
ν_t = turbulent viscosity (m^2/s)
ρ = density (kg/m^3)
σ_ϵ,σ_k = Prandtl number for the turbulent kinetic energy and its rate of dissipation respectively
σ_t = turbulent Prandtl number $\sigma_t=\nu_t/\alpha_t$
τ = dimensionless time $\tau=t/(L^2/\nu)$
Ψ = dimensionless stream function $V=-\partial\Psi/\partial X$, $U=\partial\Psi/\partial Y$
Ω = dimensionless vorticity $\Omega=\Omega_Z=\partial V/\partial X-\partial U/\partial Y$

Subscripts

i = initial value
w = value of a variable at the wall
∞ = ambient conditions

References

[1] *ASHRAE Handbook of Applications*, 1995, American Society of Heating, Refrigeration and Air-conditioning Engineers Inc., Atlanta, GA, Chap. 40.
[2] Duffie, J. A., and Beckman, W., 1991, *Solar Engineering of Thermal Processes*, 2nd ed., John Wiley & Sons, New York, Chap. 8.
[3] Givoni, B., 1977, "Underground Longterm Storage of Solar Energy Storage—An Overview," Sol. Energy, **19**, pp. 617–623.
[4] Garg, H. P., Mullick, S. C., and Bhargava, A. K., 1985, *Solar Thermal Energy Storage*, D. Reidel Publishing Company, Dordrecht, Holland, Chap. 5.
[5] Jaluria, Y., and Gupta, S. K., 1982, "Decay of Thermal Stratification in a Water Body for Solar Energy Storage," Sol. Energy, **28**(2), pp. 137–143.
[6] Cotter, M. A., and Charles, M. E., 1993, "Transient Cooling of Petroleum by Natural Convection in Cylindrical Storage Tanks: I—Development and Testing of a Numerical Simulator," Int. J. Heat Mass Transfer, **36**(8), pp. 2165–2174.
[7] Cotter, M. A., and Charles, M. E., 1993, "Transient Cooling of Petroleum by Natural Convection in Cylindrical Storage Tanks: II—Effect of Heat Transfer Coefficient, Aspect Ratio and Temperature-Dependent Viscosity," Int. J. Heat Mass Transfer, **36**(8), pp. 2175–2182.
[8] Nicolette, V. F., Yang, K. T., and Lloyd, J. R., 1985, "Transient Cooling by Natural Convection in a Two-Dimensional Square Enclosure," Int. J. Heat Mass Transfer, **28**(9), pp. 1721–1732.
[9] Robillard, L., and Vasseur, P., 1982, "Convective Response of a Mass of Water near 4°C to a Constant Cooling Rate Applied on its Boundaries," J. Fluid Mech., **118**, pp. 123–141.
[10] Mihalakakou, G., Santamouris, M., Asimakopoulos, D., and Argiriou, A., 1995, "On the Ground Temperature below Buildings," Sol. Energy, **55**(5), pp. 355–362.
[11] Sobotka, P., Yoshino, H., and Matsumoto, S., 1995, "The Analysis of Deep Basement Heat Loss by Measurements and Calculations," ASHRAE Trans., **101**(2), pp. 186–197.
[12] Adjali, M. H., Davies, M., Riain, C. Ni., and Littler, J. G., 2000, "In situ Measurements and Numerical Simulation of Heat Transfer beneath a Heated Ground Floor Slab," Build. Environ., **33**, pp. 75–83.
[13] Zhou, Z., Rees, S. W., and Thomas, H. R., 2002, "A Numerical and Experimental Investigation of Ground Heat Transfer Including Edge Insulation Effects," Build. Environ., **37**, pp. 67–78.
[14] Gauthier, C., Lacroix, M., and Bernier, H., 1997, "Numerical Simulation of Soil Heat Exchanger-Storage Systems for Greenhouses," Sol. Energy, **60**(6), pp. 333–346.

[15] Parrini, F., Vitale, S., and Castellano, L., 1992, ''Rational Analysis of Mass, Momentum and Heat Transfer Phenomena in Liquid Storage Tanks under Realistic Operating Conditions, 2. Application to a Feasibility Study,'' Sol. Energy, **49**(2), pp. 95–106.
[16] Inalli, M., 1998, ''Design Parameters for a Solar Heating System with an Underground Cylindrical Tank,'' Energy (Oxford), **23**(12), pp. 1015–1027.
[17] Inalli, M., Ünsal, M., and Tanyildizi, V., 1997, ''A Computational Model of a Domestic Solar Heating System with Underground Spherical Thermal Storage,'' Energy (Oxford), **22**(12), pp. 1163–1172.
[18] Papanicolaou, E., and Belessiotis, V., 2002, ''Transient Natural Convection in a Cylindrical Enclosure at High Rayleigh Numbers,'' Int. J. Heat Mass Transfer, **45**(7), pp. 1425–1444.
[19] Papanicolaou, E., and Jaluria, Y., 1995, ''Computation of Turbulent Flow in Mixed Convection in a Cavity with a Localized Heat Source,'' ASME J. Heat Transfer, **117**(3), pp. 649–658.
[20] Cheesewright, R., King, K. J., and Ziai, S., 1986, ''Experimental Data for the Validation of Computer Codes for the Prediction of Two-Dimensional Buoyant Cavity Flows,'' in *Significant Questions in Buoyancy Affected Enclosure or Cavity Flows*, J. A. C. Humphrey et al., eds., ASME, New York, HTD-Vol. 60, pp. 75–81.
[21] Launder, B. E., and Sharma, B. I., 1974, ''Application of the Energy-Dissipation Model of Turbulence to the Calculation of Flow near a Spinning Disc,'' Lett. Heat Mass Transfer, **1**, pp. 131–138.
[22] Henkes, R. A. W. M., and Hoogendoorn, C. J., 1995, ''Comparison Exercise for Computations of Turbulence Natural Convection in Enclosures,'' Numer. Heat Transfer, Part B, **28**, pp. 59–78.
[23] Heindel, T. J., Ramadhyani, S., and Incropera, F. P., 1994, ''Assessment of Turbulence Models for Natural Convection in an Enclosure,'' Numer. Heat Transfer, Part B, **26**, pp. 147–172.
[24] Papanicolaou, E., and Jaluria, Y., 1993, ''Mixed Convection from a Localized Heat Source in a Cavity with Conducting Walls: A Numerical Study,'' Numer. Heat Transfer, Part A, **23**, pp. 463–484.
[25] Zhu, J., 1991, ''A Low-Diffusive and Oscillation-Free Convection Scheme,'' Commun. Appl. Numer. Methods, **7**, pp. 225–232.
[26] Papanicolaou, E., Giebert, D., Koch, R., and Schulz, A., 2001, ''A Conservation-Based Discretization Approach for Conjugate Heat Transfer Calculations in Hot-Gas Ducting Turbomachinery Components,'' Int. J. Heat Mass Transfer, **44**(18), pp. 3413–3429.
[27] Timma, J., and Padet, J.-P., 1985, ''Etude Théorique du Couplage Convection-Conduction en Convection Libre Laminaire sur une Plaque Verticale,'' Int. J. Heat Mass Transfer, **28**(6), pp. 1097–1104.
[28] Pozzi, A., and Lupo, M., 1988, ''The Coupling of Conduction with Laminar Natural Convection along a Flat Plate,'' Int. J. Heat Mass Transfer, **31**(9), pp. 1807–1814.
[29] Carslaw, H. S., and Jaeger, J. C., 1959, *Conduction of Heat in Solids*, 2nd ed., Oxford University Press.
[30] Hyun, J. M., 1994, ''Unsteady Buoyant Convection in an Enclosure,'' *Advances in Heat Transfer*, **24**, Academic Press, San Diego, pp. 277–321.
[31] Vliet, G. C., and Liu, C. K., 1969, ''An Experimental Study of Turbulent Natural Convection Boundary Layers,'' ASME J. Heat Transfer, **91**, pp. 517–531.
[32] Qureshi, Z. H., and Gebhart, B., 1978, ''Transition and Transport in Buoyancy Driven Flow in Water Adjacent to a Vertical Uniform Flux Surface,'' Int. J. Heat Mass Transfer, **21**, pp. 1467–1479.
[33] Gray, D. D., and Giorgini, A., 1976, ''The Validity of the Boussinesq Approximation for Liquids and Gases,'' Int. J. Heat Mass Transfer, **19**, pp. 545–551.

Prediction of Nusselt Number and Flow Rate of Buoyancy Driven Flow Between Vertical Parallel Plates

Carl-Olof Olsson
ABB,
Corporate Research,
SE-721 78 Västerås,
Sweden

Literature on buoyancy driven flow in vertical channels have been reviewed in order to investigate formulas for Nusselt number and flow rate, which can be used in fast calculations of temperature rise in electrical apparatuses. The Rayleigh number range spans from fully developed duct flow to isolated plate boundary layer flow, and both uniform heat flux and uniform wall temperature boundary conditions are considered. Several heat transfer formulas are compared, and, for uniform temperature, an improved formula is presented that indicates the existence of an optimum plate separation. Flow rate formulas are proposed based on asymptotic estimates and adaptation to data available in the literature. Based on the flow rate formulas, the influence on flow rate of Rayleigh number and plate separation is discussed. [DOI: 10.1115/1.1643908]

Keywords: Channel Flow, Cooling, Heat Transfer, Laminar, Natural Convection

Introduction

Buoyancy driven flow in vertical ducts is of significance in many cooling applications. As an example, distribution transformers are cooled by air or oil flowing through straight vertical ducts in the windings. In order to calculate the temperature rise of the windings, the Nusselt numbers of the ducts are needed. For the calculation of duct outlet temperatures, also the flow rates in the ducts must be determined. Heat transfer formulas for various duct geometries have been published extensively. However, formulas for the calculation of flow rate have not received the same attention. In the present paper, results are discussed for the two-dimensional flow between vertical parallel plates.

The first reported experiments considered uniform wall temperature of vertical plate ducts [1] and of vertical ducts of various cross sections [2]. Bodoia and Osterle [3] presented numerical simulations which showed good agreement with the Elenbaas [1] data for intermediate Rayleigh numbers, Ra'. At high Rayleigh numbers the calculated Nusselt numbers were higher than the experimental data as pointed out by Novotny [4] and Miyatake and Fujii [5]. The reason is that a uniform velocity profile was assumed at the duct inlet for all Ra' which can not be justified when approaching the boundary layer regime, i.e., at high Ra'. Further numerical simulations have been reported by Aung [6], Aung et al. [7], Aihara [8], Burch et al. [9], and Kim et al. [10] for both uniform wall temperature and uniform heat flux boundary conditions. Cases of asymmetric heating were also considered. Sparrow et al. [11] and Sparrow and Azevedo [12] conducted a combined experimental and numerical investigation on the heat transfer of a vertical channel having one isothermal and one adiabatic wall.

In contrast to the numerical investigations cited above, there are numerous work reported in which the upstream volume is included in the model. Kettleborough [13], Nakamura et al. [14], and Naylor et al. [15] have reported results for uniform wall temperature including the upstream region but not the downstream region. The downstream region was included in the investigations by Chang and Lin [16], Ramanathan and Kumar [17], Shyy et al. [18], Morrone et al. [19], Campo et al. [20], and Morrone [21]. From these investigations it seems as it is acceptable to exclude the downstream region for the calculation of accurate Nusselt numbers. However, the calculated flow rate is influenced by the size of the downstream volume, and if the downstream volume is excluded the calculated flow rate at large Rayleigh numbers will be too low.

Experiments and simulations for uniform heat flux circular ducts were presented by Dyer [22] and the effect of a restricted entry was presented by Dyer [23]. Ducts with restricted entry can show reversed flow at the outlet and, in the limit of a closed entry, the duct will act as an open thermosyphon. Recently, Boudebous et al. [24] reported numerical simulations of natural convection in a vertical hyperbolic duct, and Straatman et al. [25] and Auletta et al. [26] presented results for parallel plate ducts with downstream adiabatic extensions.

The influence of conduction at the duct entrance was investigated by Martin et al. [27], and it was shown that the fully developed limit does not exist when conduction is accounted for upstream the duct. The deviation from the fully developed asymptote becomes visible for $Ra' < 1$.

Heat transfer formulas for the entire Ra' range are given by Bar-Cohen and Rohsenow [28] and by Rohsenow et al. [29]. However, when investigating the available formulas, there seem to be large differences between the predictions at intermediate and high Ra'. One reason could be that the formulas have been derived from data that do not cover the whole Ra' range. There are indications that the Nusselt numbers at intermediate Ra' are slightly higher than those obtained when extrapolating from the high Ra' range. On the other hand, when extrapolating from small and intermediate Ra', too high Nusselt numbers might be obtained at high Ra'.

The buoyancy driven flow is often not stable. Due to disturbances at the inlet and outlet the flow pattern may change with time. There is also a significant time needed for the flow pattern to adjust to changes in boundary conditions, e.g., a change in surface heat flux. As an example, the experiments carried out by Gau et al. [30] required 5 to 6 hours to reach steady state. A further discussion on stability of buoyancy driven flow in vertical ducts is given by Christov and Homsy [31]. The influence of a linearly stratified fluid on unsteady natural convection along a vertical isothermal plate is discussed by Lin et al. [32].

Contributed by the Heat Transfer Division for publication in the JOURNAL OF HEAT TRANSFER. Manuscript received by the Heat Transfer Division February 11, 2002; revision received October 30, 2003. Associate Editor: V. Prasad.

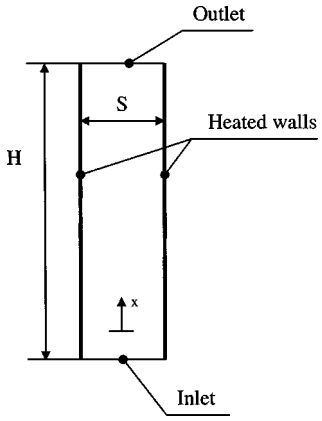

Fig. 1 Geometry of parallel plate duct. Gravity acts in negative *x*-direction.

In this paper, available heat transfer formulas are reviewed and the best formulas are pointed out. Formulas are also suggested to predict the flow rate for vertical parallel plates having uniform wall temperature or uniform heat flux boundary conditions. The formulas should be valid for Ra″ and Ra′ from 10 to 10^5.

Model Geometry

A vertical parallel plate duct is shown in Fig. 1. The vertical walls can be either isothermal for the uniform wall temperature, UWT, boundary condition or uniformly heated for the uniform heat flux, UHF, boundary condition. Due to the heated walls, a flow will be created from bottom to top, and it will be assumed that the inlet and the outlet have no constrictions influencing the flow. The flow and heat transfer will be governed by the height to width ratio H/S, the Rayleigh number, and the Prandtl number. For uniform heat flux, the following Rayleigh numbers are used:

$$\mathrm{Ra}''=\frac{g\beta q_S'' S^4}{\alpha_f \nu k_f (H/S)} \tag{1}$$

$$\mathrm{Ra}^*=\frac{g\beta q_S'' S^4}{\alpha_f \nu k_f} \tag{2}$$

$$\mathrm{Ra}_H^*=\frac{g\beta q_S'' H^4}{\alpha_f \nu k_f} \tag{3}$$

For uniform wall temperature, the following Rayleigh numbers are used:

$$\mathrm{Ra}'=\frac{g\beta(T_W-T_\infty)S^3}{\alpha_f \nu (H/S)} \tag{4}$$

$$\mathrm{Ra}=\frac{g\beta(T_W-T_\infty)S^3}{\alpha_f \nu} \tag{5}$$

$$\mathrm{Ra}_H=\frac{g\beta(T_W-T_{\mathrm{in}})H^3}{\alpha_f \nu} \tag{6}$$

The Reynolds number, using the hydraulic diameter, is

$$\mathrm{Re}=\frac{U_m(2S)}{\nu} \tag{7}$$

and the Prandtl number is defined as

$$\mathrm{Pr}=\frac{\nu}{\alpha_f} \tag{8}$$

In the following, the Prandtl number is taken to be 0.71 if no other value is indicated.

Results and Discussion

Heat transfer formulas are discussed for the UHF and UWT boundary conditions in terms of average Nusselt numbers. Subsequently, the flow rate is discussed for UHF and UWT boundary conditions and new composite formulas to predict the flow rate for a wide Rayleigh number range are derived.

Nusselt Numbers

As described by Bar-Cohen and Rohsenow [28], the Nusselt number for uniform heat flux can be estimated from

$$\mathrm{Nu}_{S,H/2}=\left(\frac{12}{Ra''}+\frac{1.88}{(Ra'')^{2/5}}\right)^{-1/2} \tag{9}$$

Here, the Nusselt number is related to the temperature difference between duct mid-height wall temperature and fluid inlet temperature, as

$$\mathrm{Nu}_{S,H/2}=\frac{q_s''}{T_{H/2}-T_{\mathrm{in}}}\frac{S}{k_f} \tag{10}$$

Equation (9) should be valid for all Ra″ provided that the duct walls are symmetrically heated with uniform heat flux. The first term is the asymptotic relation for small Ra″ while the second term is an asymptotic relation for large Ra″, i.e., when the wall boundary layers have no interaction.

The following formula for the average Nusselt number is given by Ramanathan and Kumar [17].

$$\mathrm{Nu}_{S,\mathrm{avg}}=\left(\frac{185}{(H/S)^5}+(23\mathrm{Ra}''^{-1.3}+0.5\mathrm{Ra}''^{-0.6})^{-1.25}\right)^{0.2} \tag{11}$$

The first term is in order to account for the increase in Nu due to conduction effects that can be important for small Ra″ and small H/S. In the comparison with other formulas, however, this term is set to zero corresponding to infinite H/S.

The expression recommended by Rohsenow et al. [29] is

$$\mathrm{Nu}_{S,\mathrm{avg}}=[(\mathrm{Nu}_{fd})^{-3.5}+(\mathrm{Nu}_{\mathrm{plate}})^{-3.5}]^{-1/3.5} \tag{12}$$

where

$$\mathrm{Nu}_{S,\mathrm{avg}}=\frac{q_s''}{T_{\mathrm{avg}}-T_{\mathrm{in}}}\frac{S}{k_f} \tag{13}$$

$$\mathrm{Nu}_{fd}=0.29(\mathrm{Ra}'')^{1/2} \tag{14}$$

$$\mathrm{Nu}_{\mathrm{plate}}=c\overline{H}_l(\mathrm{Ra}'')^{1/5} \tag{15}$$

$$\overline{H}_l=\frac{6}{5}\left(\frac{\mathrm{Pr}}{4+9\sqrt{\mathrm{Pr}}+10\mathrm{Pr}}\right)^{1/5} \tag{16}$$

The choice of a value for c is not evident from the reference. $c=1.15$ and $c=1.07$ are claimed to give good agreement with some experimental data, while $c=1.00$ is claimed to be the asymptotic value for an isolated vertical plate. The Nusselt numbers from Eqs. (9), (11), and (12) are shown in Fig. 2. The maximum difference at $\mathrm{Ra}''=10^5$ is 17% and at $\mathrm{Ra}''=100$ it is 20%. At lower Ra″, Eq. (11) follows a higher asymptote than the other formulas.

For large Ra″, the Nusselt number will be slightly different depending on whether the reference wall temperature is taken at the half channel height or is taken as the average wall temperature. The wall temperature rise increases with $x^{1/5}$ where x is the distance from the bottom of a vertical plate. Thus, the average wall temperature rise is

$$T_{\mathrm{avg}}-T_{\mathrm{in}}=\frac{\int_{x=0}^{H}(T_w(x)-T_{\mathrm{in}})dx}{H}=\frac{\int_{x=0}^{H}Cx^{1/5}dx}{H}=\frac{5}{6}CH^{1/5} \tag{17}$$

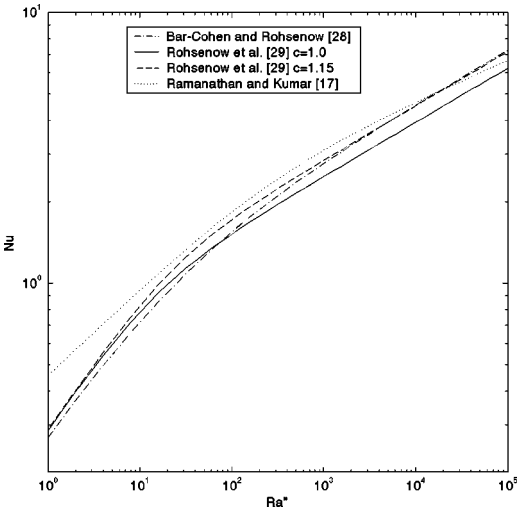

Fig. 2 Nusselt numbers for uniform heat flux

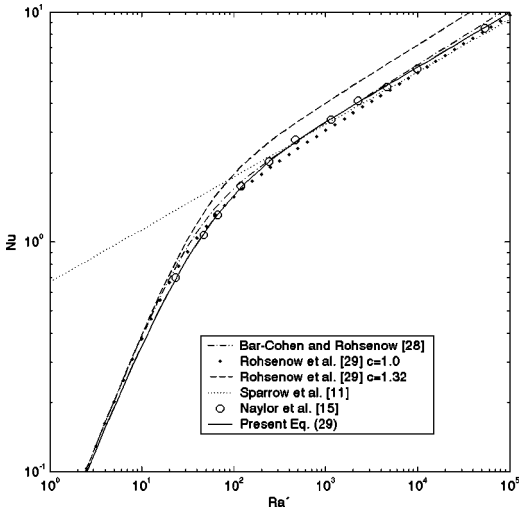

Fig. 3 Nusselt numbers for uniform wall temperature

and the ratio of average wall temperature rise and temperature rise at half height becomes

$$\frac{T_{\text{avg}}-T_{\text{in}}}{T_{H/2}-T_{\text{in}}}=\frac{\frac{5}{6}CH^{1/5}}{C(H/2)^{1/5}}=\frac{5/6}{2^{-1/5}}=0.957 \tag{18}$$

According to Rohsenow et al. [29], page 4.15, the isolated vertical plate relation with $c=1.00$ should be used with T_{avg}. As a consequence, using $T_{H/2}$ instead of T_{avg} in the Nusselt number definition would correspond to a value of c below unity since

$$\text{Nu}_{S,\text{avg}} \geqslant \text{Nu}_{S,H/2} \tag{19}$$

which follows from Eqs. (18), (10), and (13). The curve for Eq. (9) shown in Fig. 2 should, thus, be even higher at large Ra″ if it was drawn for $\text{Nu}_{S,\text{avg}}$ instead of $\text{Nu}_{S,H/2}$.

No adequate data have been found in the literature that could help to choose the best formula for the UHF boundary condition among the formulas cited above. Based on the high Ra″ asymptote, Eq. (12) using $c=1.0$ would be the best choice provided that H/S is sufficiently large that conduction effects for small Ra″ are negligible.

The formulas given above are for the uniform heat flux boundary condition. For the uniform wall temperature boundary condition another set of formulas will be given in the following. As described by Bar-Cohen and Rohsenow [28], the Nusselt number for UWT can be estimated as

$$\text{Nu}_S=\left(\frac{576}{(\text{Ra}')^2}+\frac{2.873}{(\text{Ra}')^{1/2}}\right)^{-1/2} \tag{20}$$

The Nusselt number is defined as

$$\text{Nu}_S=\frac{q_s''}{T_W-T_{\text{in}}}\frac{S}{k_f} \tag{21}$$

The expression recommended by Rohsenow et al. [29] is

$$\text{Nu}_S=[(\text{Nu}_{fd})^{-1.9}+(\text{Nu}_{\text{plate}})^{-1.9}]^{-1/1.9} \tag{22}$$

where

$$\text{Nu}_{fd}=\frac{\text{Ra}'}{24} \tag{23}$$

$$\text{Nu}_{\text{plate}}=c\overline{C}_l(\text{Ra}')^{1/4} \tag{24}$$

$$\overline{C}_l=\frac{0.671}{[1+(0.492/\text{Pr})^{9/16}]^{4/9}} \tag{25}$$

The choice of a value for c is again not evident from the reference. $c=1.32$ and $c=1.20$ are claimed to give good agreement with some experimental data, while $c=1.00$ is claimed to be the asymptotic value for an isolated vertical plate.

The experimental data of Sparrow et al. [11] were best correlated by the expression

$$\text{Nu}_S=0.667(\text{Ra}')^{0.229} \tag{26}$$

Their data ranged from $\text{Ra}'=200$ to $\text{Ra}'=80000$ and were based on the heat flux for the heated wall, the other wall being adiabatic.

The Nusselt numbers from Eqs. (20), (22), and (26) together with the data from Naylor et al. [15] are shown Figs. 3 and 4. A modified form of Eq. (22) is also included in the figure. It is seen that there is good agreement between the experimental correlation from Sparrow et al. [11] and the numerical data of Naylor et al. [15] for Ra′ from 200 to 80,000. However, the slope of the curve using Eq. (26) is different from the high Ra′ asymptote. It is therefore not possible to obtain good agreement for a large Ra′ interval using the form of Eq. (22). However, Eq. (22) can be modified to better fit the data by replacing the high Ra′ term, Eq. (24), by

$$\text{Nu}_{\text{plate}}=c\overline{C}_l(\text{Ra}')^{1/4\,f} \tag{27}$$

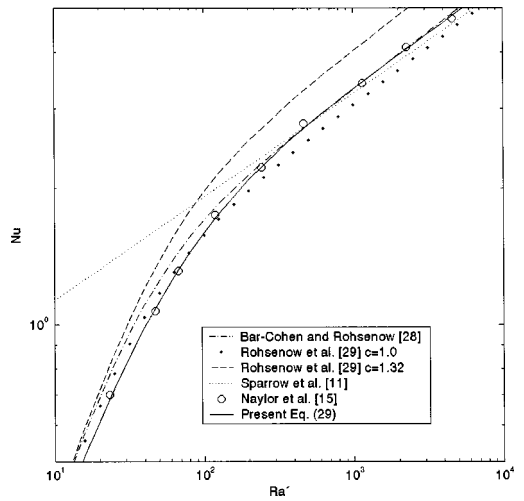

Fig. 4 Nusselt numbers for uniform wall temperature. Enlargement of Fig. 3.

$$f = 1 + (\mathrm{Ra}')^{-0.4} \tag{28}$$

where the exponent -0.4 has been chosen to give the best fit to the data. The correlation exponent of Eq. (22) was also changed from 1.9 to 1.3. The improved formula thus reads

$$\mathrm{Nu}_S = [(\mathrm{Nu}_{fd})^{-1.3} + (\mathrm{Nu}_{\mathrm{plate}})^{-1.3}]^{-1/1.3} \tag{29}$$

where

$$\mathrm{Nu}_{fd} = \frac{\mathrm{Ra}'}{24} \tag{30}$$

$$\mathrm{Nu}_{\mathrm{plate}} = c\overline{C}_l (\mathrm{Ra}')^{1/4 f} \tag{31}$$

$$f = 1 + (\mathrm{Ra}')^{-0.4} \tag{32}$$

$$\overline{C}_l = \frac{0.671}{[1 + (0.492/\mathrm{Pr})^{9/16}]^{4/9}} \tag{33}$$

One consequence of the modified formula, Eq. (29), is that a maximum heat transfer coefficient will be predicted for a certain Ra', i.e., for a given Ra_H there will be a plate separation giving maximum heat transfer. This is in contrast to the unmodified formula that predicts maximum heat transfer at the single plate limit. The optimum Ra' is depending on Pr through Eq. (33). For $\mathrm{Pr} = 0.71$, 5, and 50, the optimum Ra' are approximately 1050, 1290, and 1410, respectively.

Flow Rate. In analogy with the Nusselt number formulas presented above, formulas for the flow rate can be constructed from the asymptotic relations that hold for Ra'' approaching zero and Ra'' approaching infinity. For the uniform heat flux boundary condition, the relation for Ra'' approaching zero can be obtained as follows.

The pressure drop for fluid flow through the duct is

$$\Delta p = f_{\mathrm{app}} \frac{H}{4S^3 \rho} \dot{m}^2 \tag{34}$$

where f_{app} is the apparent Darcy friction factor, H the channel height, S the plate spacing, ρ the fluid density, and $\dot{m}$ the flow rate. This pressure drop is balanced by the buoyancy force due to the vertical density gradient in the duct. Using the Boussinesq approximation, the pressure drop should equal

$$\Delta p = \rho g \beta H \frac{(T_{\mathrm{out}} - T_{\mathrm{in}})}{2} \tag{35}$$

where g is the gravitational acceleration, β the coefficient of expansion, and T_{out} and T_{in} are the fluid bulk temperatures at the duct outlet and inlet, respectively. From a heat balance for the duct, the bulk temperature difference can be expressed as

$$T_{\mathrm{out}} - T_{\mathrm{in}} = \frac{q''_S 2H}{\dot{m} c_p} \tag{36}$$

The flow rate can now be solved from Eqs. (34)–(36), giving the expression

$$\dot{m} = \left(\frac{4\rho^2 g S^3 \beta q''_S H}{f_{\mathrm{app}} c_p} \right)^{1/3} = \rho \alpha_f \left(\frac{4\mathrm{Ra}''\mathrm{Pr}}{f_{\mathrm{app}}} (H/S)^2 \right)^{1/3} \tag{37}$$

In the second equality of Eq. (37), the channel Rayleigh number Ra'' and the Prandtl number have been introduced.

The apparent friction factor for parallel plate flow depends on Reynolds number and flow development length. According to Shah and London [33] the apparent friction factor for laminar developing flow between parallel plates can be determined from the relation

$$\frac{f_{\mathrm{app}} \mathrm{Re}}{4} = \frac{3.44}{(x^+)^{1/2}} + \frac{24 + 0.674/(4x^+) - 3.44/(x^+)^{1/2}}{1 + 0.000029(x^+)^{-2}} \tag{38}$$

where

$$x^+ = \frac{H/(2S)}{\mathrm{Re}} \tag{39}$$

Equation (37) can only be valid when the buoyancy driven flow is similar to developing duct flow, i.e., for low and moderate Ra''.

The flow rate for Ra'' approaching infinity can be derived from estimates of the boundary layer thickness and velocity scale of the momentum boundary layer of a single vertical plate. Following Bejan [34], the velocity scale is

$$v \propto \frac{\alpha_f}{H} \mathrm{Pr}^{2/5} (\mathrm{Ra}_H^*)^{2/5} \tag{40}$$

and the momentum boundary layer thickness is

$$\delta \propto H \mathrm{Pr}^{-1/5} (\mathrm{Ra}_H^*)^{-1/5} \tag{41}$$

where the modified Rayleigh number is defined according to Eq. (3). Thus, the scale of the flow rate should be

$$\dot{m} \propto \rho v \, \delta \propto \rho \alpha_f (\mathrm{Ra}_H^*)^{1/5} \mathrm{Pr}^{1/5} \tag{42}$$

Replacing Ra_H^* with Ra'' and writing on dimensionless form, we have

$$\frac{\dot{m}}{\rho \alpha_f} \propto (\mathrm{Ra}'')^{1/5} \mathrm{Pr}^{1/5} \left(\frac{H}{S} \right) \tag{43}$$

Equation (43) is the correct scale for the flow rate when $\mathrm{Pr} < 1$. For $\mathrm{Pr} > 1$, the exponent of the Prandtl number should be changed from 1/5 to 1/2. This is due to that the momentum boundary layer thickness is larger than the thermal boundary layer thickness for $\mathrm{Pr} > 1$, see Bejan [34].

Equations (37) and (43) can be used to construct a composite formula which could be used for all Ra''. We get

$$\mathrm{Re} = \frac{2}{\mathrm{Pr}} \left(\frac{1}{\left(\frac{4\mathrm{Ra}''\mathrm{Pr}}{f_{\mathrm{app}}} (H/S)^2 \right)^{2.4/3}} + \frac{1}{(1.5(\mathrm{Ra}'')^{1/5} \mathrm{Pr}^{1/5} (H/S))^{2.4}} \right)^{-1/2.4} \tag{44}$$

where the relation

$$\frac{\dot{m}}{\rho \alpha_f} = \frac{\mathrm{Re}\,\mathrm{Pr}}{2} \tag{45}$$

has been used. Equation (44) is an implicit formula for Re since the apparent friction factor depends on Re through Eqs. (38) and (39). However, using unity as start guess for f_{app}, the formula will converge after a few iterations.

The coefficient 1.5 in the second term of Eq. (44) as well as the correlation exponent 2.4 are based on the best fit to data given in Campo et al. [20] and Ramanathan and Kumar [17]. A comparison of predictions using Eq. (44) and the literature data are shown in Table 1. The general influence of Ra'' and H/S is well captured even though the formula predicts slightly too low Re at the lowest and the highest Ra'' and slightly too large Re at intermediate Ra''. It cannot be excluded that the correlation parameters would be slightly different if data for a wider range of H/S were available. Data for H/S from 0.4 to 5 can be found in Morrone et al. [19] and some of these data are included in Table 1. However, the boundary layer approximation used in the derivation of Eq. (44) is not valid for small aspect ratio ducts, and as a consequence the data of Morrone et al. [19] represent larger Reynolds numbers than those predicted by the formula.

Relations for flow rate for the uniform wall temperature boundary condition can be obtained following the same outline as for

Table 1 Comparison of Eq. (44) with literature data at uniform heat flux

Ref.	Ra″	H/S	Pr	Re	Re Eq. (44)	Diff. [%]
[20]	7.1	10	0.71	23.6	21.2	−10.3
[20]	35.5	10	0.71	46.8	46.0	−1.9
[20]	71	10	0.71	62.9	63.7	1.2
[20]	355	10	0.71	125	131	5.3
[20]	710	10	0.71	168	177	5.3
[20]	3550	10	0.71	333	335	0.7
[20]	7100	10	0.71	447	433	−3.1
[17]	100	15	0.7	107	114	6.9
[17]	400	15	0.7	200	213	6.5
[19][1]	2272	0.5	0.71	21.37	9.96	−53.4
[19][1]	710	1	0.71	22.99	14.74	−35.9
[19][1]	222	2	0.71	24.73	19.88	−19.6
[19][1]	22.7	5	0.71	20.5	18.43	−10.1

[1]Not used for adaption.

the derivation above. At Ra′ approaching zero, the buoyancy force that balances the flow resistance of Eq. (34) is

$$\Delta p = \rho g \beta H (T_W - T_{\text{in}}) \tag{46}$$

since the fluid bulk temperature in the channel is close to the wall temperature T_W. Solving for the flow rate from Eqs. (34) and (46) we obtain

$$\frac{\dot{m}}{\rho \alpha_f} = \left(\frac{4 \text{Ra}' \text{Pr}}{f_{\text{app}}} (H/S) \right)^{1/2} \tag{47}$$

For Ra′ approaching infinity, the velocity scale is

$$v \propto \frac{\alpha_f}{H} \text{Pr}^{1/2} (\text{Ra}_H)^{1/2} \tag{48}$$

and the momentum boundary layer thickness is

$$\delta \propto H \text{Pr}^{-1/4} (\text{Ra}_H)^{-1/4} \tag{49}$$

Thus, the scale of the flow rate should be

$$\dot{m} \propto \rho v \, \delta \propto \rho \alpha_f (\text{Ra}_H)^{1/4} \text{Pr}^{1/4} \tag{50}$$

After replacing Ra_H with Ra′ and writing in dimensionless form, we have

$$\frac{\dot{m}}{\rho \alpha_f} \propto (\text{Ra}')^{1/4} \text{Pr}^{1/4} (H/S) \tag{51}$$

Equation (51) is the correct scale for the flow rate when $\text{Pr} < 1$. For $\text{Pr} > 1$, the exponent of the Prandtl number should be changed from 1/4 to 1/2, see Bejan [34].

Using Eqs. (47) and (51) we can construct the composite formula, valid for all Ra′:

$$\text{Re} = \frac{2}{\text{Pr}} \left(\frac{1}{\left(\frac{4 \text{Ra}' \text{Pr}}{f_{\text{app}}} (H/S) \right)^{0.81/2}} + \frac{1}{(6.6 (\text{Ra}')^{1/4} \text{Pr}^{1/4} (H/S))^{0.81}} \right)^{-1/0.81} \tag{52}$$

The coefficient 6.6 in the second term as well as the correlation exponent 0.81 are based on the best fit to data found in Chang and Lin [16], Naylor et al. [15], and Nakamura et al. [14]. These data are given in Table 2 together with some data from Kettleborough [13], Aihara [8], and Burch et al. [9]. Again, the general influence of Ra′ and H/S is captured by the formula even though the formula predicts slightly too low Re for small Ra′. At intermediate and large Ra′ the formula seems to predict significantly lower Re than the data from Kettleborough [13] and Burch et al. [9]. However, these differences might be explained by the artificial flow

Table 2 Comparison of Eq. (52) with literature data at uniform wall temperature

Ref.	Ra′	H/S	Pr	Re	Re Eq. (52)	Diff. [%]
[16]	1600	5	0.7	231	227	−1.7
[16]	16000	5	0.7	557	577	3.6
[16]	160000	5	0.7	1260	1280	1.6
[16]	1600000	5	0.7	2670	2580	−3.4
[16]	800	10	0.7	335	327	−2.4
[16]	8000	10	0.7	909	888	−2.3
[16]	80000	10	0.7	2100	2030	−3.3
[16]	800000	10	0.7	4160	4210	1.2
[15]	1470	5	0.7	204	218	6.9
[15]	23.3	12	0.7	48.0	42.9	−10.6
[15]	4670	12	0.7	829	860	3.7
[14]	14.7	5	0.733	12.6	11.8	−6.3
[14]	1470	5	0.733	192	211	9.9
[8][1]	14.0	5	0.7	13.64	11.8	−13.5
[8][1]	1400	5	0.7	218	211	−3.2
[13][1]	14.7	5	0.733	10.9	11.8	8.3
[13][1]	1470	5	0.733	294	211	−28.2
[9][1]	7.1	5	0.71	7.65	6.58	−14.0
[9][1]	710	5	0.71	187	153	−18.2
[9][1]	710000	5	0.71	6513	2010	−69.1

[1]Not used for adaptation.

boundary conditions used by Kettleborough [13] and Burch et al. [9]. Since the velocity profile was specified on the inlet boundary, the flow rate might become too large at large Ra′.

When the flow rate formulas are available, the influence of Rayleigh number and H/S on Reynolds number can be investigated. Reynolds numbers for the UHF boundary condition are shown in Figs. 5 to 8. In Fig. 5, the influence of Ra″ on Re for fixed H/S is shown. It is seen that Re increases with increasing Ra″. In Fig. 6, it is seen that for fixed Ra″, there is a linear increase in Re with increasing H/S. In Fig. 7, Re is shown as function of H/S for fixed Ra_S^*. This condition could, e.g., represent a duct of fixed wall separation and heat flux and thus the curves show the influence of changing the duct height. Increasing the duct height corresponds to increasing Re, i.e., increasing flow rate through the duct. Finally, in Fig. 8 the influence of H/S on Re is shown for fixed Ra_H. This condition could, e.g., represent a duct of fixed height and heat flux and thus the curves show the influence of changing the wall separation. Increasing the wall separation, i.e., decreasing H/S, corresponds to increasing Re. From the asymptotic relations it can be found that the flow rate is

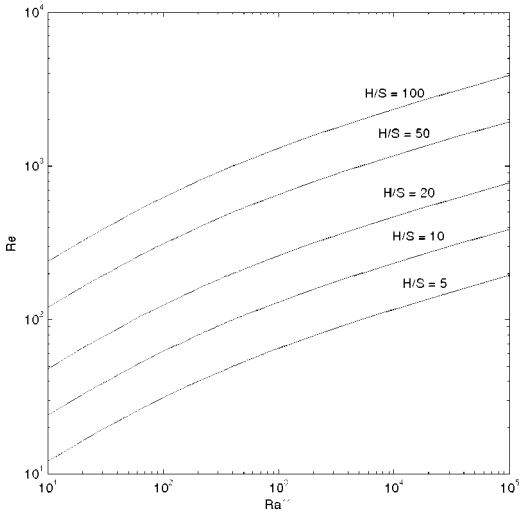

Fig. 5 Re versus Ra″ for constant *H/S* at uniform heat flux

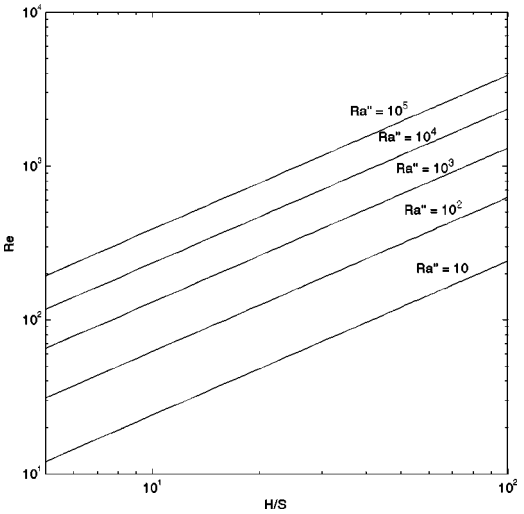

Fig. 6 Re versus H/S for constant Ra″ at uniform heat flux

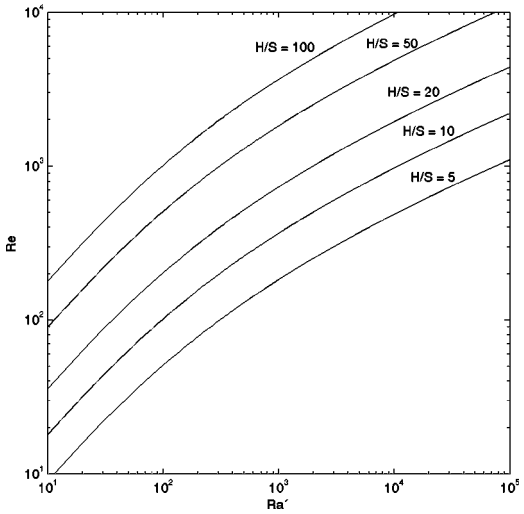

Fig. 9 Re versus Ra′ for constant H/S at uniform wall temperature

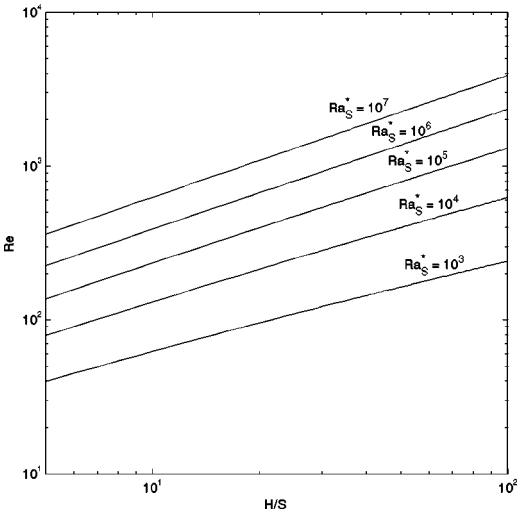

Fig. 7 Re versus H/S for constant Ra_S^* at uniform heat flux

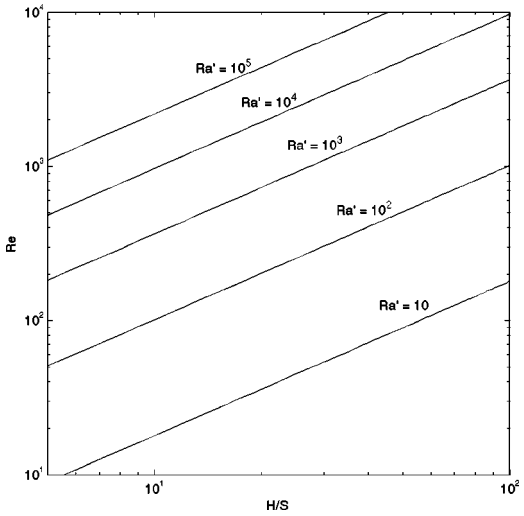

Fig. 10 Re versus H/S for constant Ra′ at uniform wall temperature

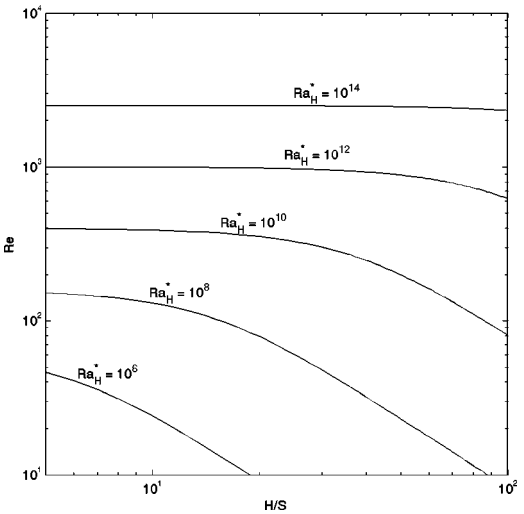

Fig. 8 Re versus H/S for constant Ra_H^* at uniform heat flux

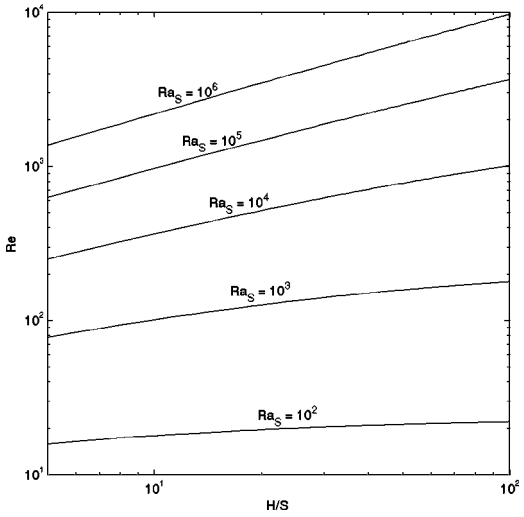

Fig. 11 Re versus H/S for constant Ra_S at uniform wall temperature

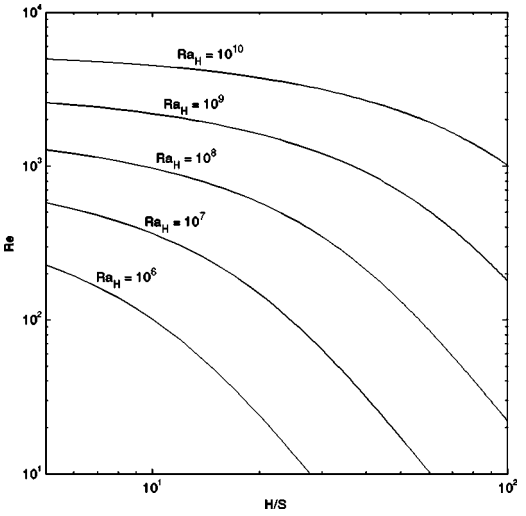

Fig. 12 Re versus H/S for constant Ra_H at uniform wall temperature

proportional to the square root of wall separation at the fully developed limit and independent of wall separation at the single plate limit.

For the UWT boundary condition, the influence of Ra' and H/S on Re is shown in Figs. 9–12 The general observations are the same as for the UHF boundary condition discussed above.

It should be noted that laminar flow is assumed throughout the analyses in this paper. If transition to turbulent flow occurs, the Nusselt number will be larger than predicted and the Reynolds number will be smaller than predicted. The Reynolds number decrease at transition is a consequence of the increasing apparent friction factor and the increasing momentum boundary layer thickness.

The present analyses are also restricted to the two-dimensional flow between infinite parallel plates. However, the formulas for both Nu and Re can be modified to provide approximate results for rectangular ducts simply by replacing the terms representing the fully developed limits with terms for the actual rectangular cross section. The single plate limits should be valid independent of the shape of the cross section.

Conclusions

Heat transfer formulas from the literature have been compared and recommended formulas are pointed out. An improved formula is suggested to better capture the Nusselt numbers at intermediate Ra' for uniform wall temperature boundary condition. From the improved formula it is found that there might be a finite wall separation giving a maximum heat transfer coefficient.

Formulas for the prediction of flow rate have been proposed based on asymptotic estimates and best fit to data found in the literature. The formulas provide good agreement with literature data for H/S greater than 5.

Nomenclature

$\overline{C_l}$ = see Eq. (25)
c_p = specific heat, J/kgK
$\overline{f}$ = see Eq. (28)
f_{app} = apparent friction factor
g = gravitational acceleration, m/s^2
H = duct height, m
$\overline{H_l}$ = see Eq. (16)
k_f = fluid thermal conductivity, W/mK
$\dot{m}$ = mass flow rate, kg/ms
Nu = Nusselt number
Nu_S = Nu for uniform wall temperature, Eq. (21)
$\text{Nu}_{S,\text{avg}}$ = Nu with average wall temperature, Eq. (13)
$\text{Nu}_{S,H/2}$ = Nu with wall temperature at half duct height, Eq. (10)
Nu_{fd} = Nusselt number at fully developed duct flow
Nu_{plate} = Nusselt number for vertical plate
Pr = Prandtl number, Eq. (8)
$q_{S''}$ = surface heat flux, W/m^2
Ra = Rayleigh number, Eq. (5)
Ra* = modified Rayleigh number, Eq. (2)
Ra' = channel Rayleigh number, Eq. (4)
Ra'' = modified channel Rayleigh number, Eq. (1)
Ra_H = Rayleigh number, Eq. (6)
Ra_H^* = modified Rayleigh number, Eq. (3)
Re = Reynolds number, Eq. (7)
S = wall distance, m
T = temperature, K
T_{avg} = average wall temperature, K
$T_{H/2}$ = wall temperature at half duct height, K
T_{in} = inlet temperature, K
T_{out} = bulk outlet temperature, K
T_w = wall temperature, K
U_{m} = mean velocity, m/s
v = boundary layer velocity scale, m/s
x = co-ordinate, m
x^+ = see Eq. (39)
α_f = fluid thermal diffusivity, m^2/s
β = coefficient of expansion, 1/K
δ = boundary layer length scale, m
ν = kinematic viscosity, m^2/s
ρ = fluid density, kg/m^3

References

[1] Elenbaas, W., 1942, "Heat Dissipation of Parallel Plates by Free Convection," Physica, **IX/1**, pp. 2–28.
[2] Elenbaas, W., 1942, "The Dissipation of Heat by Free Convection: The Inner Surface of Vertical Tubes of Different Shapes of Cross-Section," Physica, **IX/8**, pp. 865–874.
[3] Bodoia, J. R., and Osterle, J. F., 1962, "The Development of Free Convection Between Heated Vertical Plates," ASME J. Heat Transfer, **84**, pp. 40–44.
[4] Novotny, J. L., 1968, "Laminar Free Convection Between Finite Vertical Parallel Plates," in *Progress in Heat and Mass Transfer*, T. F. Irvine Jr. ed., **2**, Pergamon Press, New York, pp. 13–22.
[5] Miyatake, O., and Fujii, T., 1972, "Free Convection Heat Transfer Between Vertical Parallel Plates—One Plate Isothermally Heated and the Other Thermally Insulated," Heat Transfer-Jpn. Res., **1**, pp. 30–38.
[6] Aung, W., 1972, "Fully Developed Laminar Free Convection Between Vertical Plates Heated Asymmetrically," Int. J. Heat Mass Transfer, **15**, pp. 1577–1580.
[7] Aung, W., Fletcher, L. S., and Sernas, V., 1972, "Developing Laminar Free Convection Between Vertical Flat Plates with Asymmetric Heating," Int. J. Heat Mass Transfer, **15**, pp. 2293–2308.
[8] Aihara, T., 1973, "Effects of Inlet Boundary Conditions on Numerical Solutions of Free Convection Between Vertical Parallel Plates," Report of the Institute of High Speed Mechanics, Tohuku University, Japan, **28**, pp. 1–27.
[9] Burch, T., Rhodes, T., and Acharya, S., 1985, "Laminar Natural Convection Between Finitely Conducting Vertical Plates," Int. J. Heat Mass Transfer, **28**, pp. 1173–1186.
[10] Kim, S. H., Anand, N. K., and Aung, W., 1990, "Effect of Wall Conduction on Free Convection Between Asymmetrically Heated Vertical Plates: Uniform Wall Heat Flux," Int. J. Heat Mass Transfer, **33**, pp. 1013–1023.
[11] Sparrow, E. M., Chrysler, G. M., and Azevedo, L. F., 1984, "Observed Flow Reversal and Measured-Predicted Nusselt Numbers for Natural Convection in a One-Sided Heated Vertical Channel," ASME J. Heat Transfer, **106**, pp. 325–332.
[12] Sparrow, E. M., and Azevedo, L. F. A., 1985, "Vertical-Channel Natural Convection Spanning Between the Fully-Developed Limit and the Single-Plate Boundary-Layer Limit," Int. J. Heat Mass Transfer, **28**, pp. 1847–1857.
[13] Kettleborough, C. F., 1972, "Transient Laminar Free Convection Between Heated Vertical Plates Including Entrance Effects," Int. J. Heat Mass Transfer, **15**, pp. 883–896.
[14] Nakamura, H., Asako, Y., and Naitou, T., 1982, "Heat Transfer by Free Convection Between Two Parallel Flat Plates," Numer. Heat Transfer, **5**, pp. 95–106.
[15] Naylor, D., Floryan, J. M., and Tarasuk, J. D., 1991, "A Numerical Study of

Developing Free Convection Between Isothermal Vertical Plates,'' ASME J. Heat Transfer, **113**, pp. 620–626.
[16] Chang, T. S., and Lin, T. F., 1989, ''Transient Buoyancy-Induced Flow Through a Heated, Vertical Channel of Finite Height,'' Numer. Heat Transfer, Part A, **16**, pp. 15–35.
[17] Ramanathan, S., and Kumar, R., 1991, ''Correlations for Natural Convection Between Heated Vertical Plates,'' ASME J. Heat Transfer, **113**, pp. 97–107.
[18] Shyy, W., Gingrich, W. K., and Gebhart, B., 1992, ''Adaptive Grid Solution for Buoyancy-Induced Flow in Vertical Slots,'' Numer. Heat Transfer, Part A, **22**, pp. 51–70.
[19] Morrone, B., Campo, A., and Manca, O., 1997, ''Optimum Plate Separation in Vertical Parallel-Plate Channels for Natural Convective Flows: Incorporation of Large Spaces at the Channel Extremes,'' Int. J. Heat Mass Transfer, **40**, pp. 993–1000.
[20] Campo, A., Manca, O., and Morrone, B., 1999, ''Numerical Analysis of Partially Heated Vertical Parallel Plates in Natural Convective Cooling,'' Numer. Heat Transfer, Part A, **36**, pp. 129–151.
[21] Morrone, B., 2001, ''Natural Convection Between Parallel Plates With Conjugate Conductive Effects,'' Numer. Heat Transfer, Part A, **40**, pp. 873–886.
[22] Dyer, J. R., 1975, ''The Development of Laminar Natural Convection Flow in a Vertical Uniform Heat Flux Duct,'' Int. J. Heat Mass Transfer, **18**, pp. 1455–1465.
[23] Dyer, J. R., 1978, ''Natural Convective Flow Through a Vertical Duct With Restricted Entry,'' Int. J. Heat Mass Transfer, **21**, pp. 1341–1354.
[24] Boudebous, S., Nemouchi, Z., and Meniai, A. H., 2001, ''Numerical Study of Developing Natural Laminar Convection in a Vertical Hyperbolic Duct of a Fixed Length and with a Constant Wall Temperature,'' Numer. Heat Transfer, Part A, **40**, pp. 783–800.
[25] Straatman, A. G., Tarasuk, J. D., and Floryan, J. M., 1993, ''Heat Transfer Enhancement From a Vertical, Isothermal Channel Generated by the Chimney Effect,'' ASME J. Heat Transfer, **115**, pp. 395–402.
[26] Auletta, A., Manca, O., Morrone, B., and Naso, V., 2001, ''Heat Transfer Enhancement by the Chimney Effect in a Vertical Isoflux Channel,'' Int. J. Heat Mass Transfer, **44**, pp. 4345–4357.
[27] Martin, L., Raithby, G. D., and Yovanovich, M. M., 1991, ''On the Low Rayleigh Number Asymptote for Natural Convection Through an Isothermal, Parallel-Plate Channel,'' ASME J. Heat Transfer, **113**, pp. 899–905.
[28] Bar-Cohen, A., and Rohsenow, W. M., 1984, ''Thermally Optimum Spacing of Vertical, Natural Convection Cooled, Parallel Plates,'' ASME J. Heat Transfer, **106**, pp. 116–123.
[29] Rohsenow, W. M., Hartnett, J. P., and Cho, Y. I., eds., 1998, *Handbook of Heat Transfer*, McGraw-Hill, New York.
[30] Gau, C., Yih, K. A., and Aung, W., 1992, ''Reversed Flow Structure and Heat Transfer Measurements for Buoyancy-Assisted Convection in a Heated Vertical Duct,'' ASME J. Heat Transfer, **114**, pp. 928–935.
[31] Christov, C. I., and Homsy, G. M., 2001, ''Nonlinear Dynamics of Two-Dimensional Convection in a Vertically Stratified Slot With and Without Gravity Modulation,'' J. Fluid Mech., **430**, pp. 335–360.
[32] Lin, W., Armfield, S. W., and Morgan, P. L., 2002, ''Unsteady Natural Convection Boundary-Layer Flow Along a Vertical Isothermal Plate in a Linearly Stratified Fluid with Pr>1,'' Int. J. Heat Mass Transfer, **54**, pp. 451–459.
[33] Shah, R. K., and London, A. L., 1978, ''Laminar Flow Forced Convection in Ducts,'' *Adv. in Heat Transfer*, suppl. 1, Academic Press, New York.
[34] Bejan, A., 1995, *Convection Heat Transfer*, 2nd ed., Wiley, New York.

S. S. Sazhin
e-mail: S.Sazhin@brighton.ac.uk

W. A. Abdelghaffar

E. M. Sazhina

School of Engineering,
University of Brighton,
Cockcroft Building,
Brighton BN2 4GJ, U.K.

S. V. Mikhalovsky

S. T. Meikle

School of Pharmacy and Biomolecular Sciences,
University of Brighton,
Cockcroft Building, Brighton BN2 4GJ, U.K.

C. Bai
Ricardo Consulting Engineers Ltd.,
Bridge Works, Shoreham-by-Sea,
West Sussex BN43 5FG, U.K.

Radiative Heating of Semi-Transparent Diesel Fuel Droplets

Absorption spectra of four types of diesel fuel are studied experimentally in the range between 0.2 μm and 6 μm. The ageing process of fuels is simulated by prolonged boiling. The average absorption efficiency factor of droplets is assumed to be proportional to ar_d^b, where r_d is the droplet radius, and a and b are polynomial functions of external gas temperature. Explicit expressions for a and b are derived for diesel fuel droplets in various realistic droplet radii and external gas temperature ranges for all four types of fuel. [DOI: 10.1115/1.1643089]

1 Introduction

The models suggested so far for radiative heating of fuel droplets can be subdivided into three main groups: those which take into account the semi-transparency of droplets in the infrared range and the distribution of radiation absorption inside droplets (e.g., [1,2]), those which take into account the semi-transparency of droplets in the infrared range, but not the distribution of radiation absorption inside droplets (e.g., [3]), and those which assume that droplets are gray opaque spheres [4,5]. The second group of models provides a reasonable compromise between accuracy and computer efficiency.

The focus of this paper will be on this particular group, and more specifically on further development of the approach used in [3]. The model suggested in [3] takes into account the semi-transparency of these droplets but its formulation is considerably simpler when compared with the previously suggested models. Detailed Mie calculations were replaced by the approximation of the absorption efficiency factor for droplets with an analytical formula ar_d^b, where r_d is the droplet radius, a and b are quadratic functions of gas temperature (the authors of [3] implicitly assumed that the external gas temperature, responsible for radiative heating of droplets, is equal to the ambient gas temperature, responsible for their convective heating). The coefficients of this function were found based on the comparison with rigorous calculations for realistic diesel fuel droplets with radii in the range 5–50 μm and gas temperatures in the range 1000–3000 K. This model allowed the authors to attain a reasonable compromise between accuracy and computational efficiency. This is particularly important for the implementation of the thermal radiation model into a multidimensional computational fluid dynamics (CFD) code designed to simulate combustion processes in diesel engines.

The main objective of this paper is to investigate the applicability of the model suggested in [3] for a wider range of droplet radii, external and ambient gas temperatures and for various types of diesel fuel. We use the same types of diesel fuel as in [6], where the results of measurements of the spectral index of absorption for four samples of diesel fuels, including two samples for which the 'ageing' process of fuels was simulated by prolonged boiling, were reported. Due to experimental restrictions, these measurements were performed in the spectral ranges 0.2 μm–1.1 μm and 2μm–6 μm but not in the range 1.1 μm–2 μm. The latter range is particularly important as it corresponds to maximal intensities of thermal radiation in the range of temperatures 1449–2635 K, as follows from the Wien's law. This range is perhaps the most important for applications in diesel engines and the absence of data was rather regrettable. In this paper the measurements reported in [6] are supplemented by the measurements in the range 1 μm–3 μm using a new experimental technique. Hence the whole range 0.2 μm–6 μm is covered.

2 Optical Properties of Fuel

The index of absorption of diesel fuels was measured in the ranges 0.2 μm–1.1 μm, 1 μm–3 μm, and 2 μm–6 μm. Ultraviolet near-infrared spectra (0.2–1.1 μm) were obtained using a UV-visible spectrophotometer Shimadzu, model 1601. The spectra were recorded versus n-hexane as a background.

In the range (1–3) μm the index of absorption was measured using a Fourier Transform Infrared Spectrometer (Nicolet FT-IR Nexus). This spectrometer is designed to work in the mid-infrared or near infrared range. The experimental setup used to record the fuel spectra was optimised for analysis in the near infrared range. The program used was OMNIC E.S.P. version 5.2a set in Transmission E.S.P. experimental mode. A resolution of 4 cm^{-1} was used, recording four scans in a NaCl cell with an optical pathlength of 0.025 mm. The background was recorded as the empty NaCl cell.

Infrared spectra (2–6 μm) were obtained using FTIR (Fourier Transform Infrared) spectrometer Perkin Elmer 1720-X, at 4 cm^{-1} resolution, 4 scans, in a NaCl cell with 0.011 mm optical path length. The error of measurements of absorptance was about 5% across the whole range of wave-lengths. The lower threshold for measurements in this spectral range is higher when compared with the measurements reported in [3] where it was 1.39 μm. The use of conventional FT-IR spectrometers to measure absorptance beyond the mid-range infrared (approximately 2.5 μm or less)

Contributed by the Heat Transfer Division for publication in the JOURNAL OF HEAT TRANSFER. Manuscript received by the Heat Transfer Division March 7, 2003; revision received September 22, 2003. Associate Editor: A. F. Emery.

would result in large experimental errors, due to the detection limit of the spectrometer having been reached. This may explain some of the discrepancies in the 2–3 μm range obtained using different techniques. The results obtained by the Nicolet FT-IR Nexus spectrometer were used in this range.

Diesel fuels have relatively high absorption below 0.4 μm, exceeding the measuring limit of the instrument. In this range, the spectrum was recorded in a 1 cm quartz cell for samples diluted with n-hexane. The latter is transparent in the studied range of wavelengths. In the ranges of 3.33–3.53 μm and 6.76–6.94 μm, where absorption of the samples exceeded the instrument measuring limit, the spectra were recorded for samples diluted with chloroform. The correction for dilution was made in both cases. All measurements were carried out at room temperature. The resulting spectra are not expected to differ, until the boiling point of the fuel is reached.

Results of the measurements of the index of absorption κ are presented in Fig. 1. The plots are shown for low sulfur ESSO AF1313 diesel fuel used in cars (yellow) and BP Ford reference diesel fuel used in off road equipment in which dye was added for legislative purposes (pink). Also the plots referring to these diesel fuels after they have undergone a simulation of ageing process by prolonged (six hours) boiling are shown in the same figure. Density of the yellow fuel was experimentally determined as 816 kg/m^3 and the boiling point in the range of 458–468 K, whereas density of the pink fuel was experimentally determined as 827 kg/m^3 and boiling point in the range of 468–478 K. The density was measured at room temperature. Both parameters were measured at atmospheric pressure.

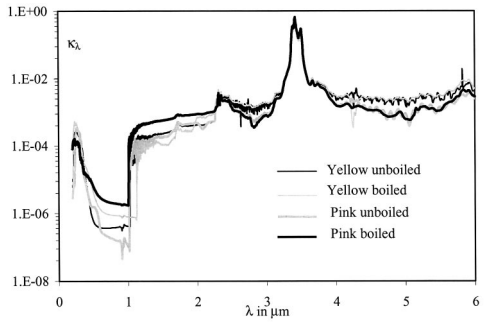

Fig. 1 Indices of absorption of four types of diesel fuel versus wavelength λ. Yellow fuel corresponds to low sulfur ESSO AF1313 diesel fuel used in cars; pink fuel corresponds to BP Ford reference diesel fuel used in off road equipment.

As can be seen in Fig. 1, the dependence of κ on the type of diesel fuel is noticeable, especially in the ranges of semi-transparency $\lambda<3$ μm and 4 μm$<\lambda<6$ μm. Peaks of absorption for all types of diesel fuel practically coincide. The values of κ in the ranges 0.2 μm–1 μm and 3 μm–6 μm coincide with those shown in Fig. 3 of [6]. The differences in the optical properties of fuels shown in Fig. 1 are expected to be transformed in different values of the absorption efficiency factors of fuel droplets as discussed in the next section.

Table 1 Values of coefficients a_i and b_i ($i=0,1,2$) in Eq. (5) for 1000 K$\leq T_{ext}\leq$ 3000 K, various types of diesel fuel and various ranges of droplet radii

Type of fuel	R_{min} (μm)	R_{max} (μm)	a_0	a_1 (K^{-1})	a_2 (K^{-2})	b_0	b_1 (K^{-1})	b_2 (K^{-2})
Yellow unboiled	5	50	0.1040	−0.05	0.008	0.4916	0.10	−0.008
Yellow unboiled	5	100	0.1689	−0.09	0.010	0.4240	0.10	−0.010
Yellow unboiled	5	200	0.1236	−0.07	0.010	0.3152	0.10	−0.010
Yellow unboiled	2	50	0.1035	−0.05	0.008	0.4959	0.09	−0.007
Yellow unboiled	2	200	0.1541	−0.09	0.010	0.3399	0.10	−0.010
Pink unboiled	5	50	0.0888	−0.05	0.007	0.4454	0.10	−0.010
Pink unboiled	5	100	0.0965	−0.05	0.007	0.4135	0.10	−0.010
Pink unboiled	5	200	0.0116	−0.06	0.009	0.3569	0.10	−0.010
Pink unboiled	2	50	0.0904	−0.05	0.007	0.4430	0.10	−0.010
Pink unboiled	2	200	0.1112	−0.06	0.009	0.3680	0.10	−0.010
Yellow boiled	5	50	0.1093	−0.06	0.008	0.5083	0.08	−0.007
Yellow boiled	5	100	0.1319	−0.07	0.010	0.4401	0.09	−0.008
Yellow boiled	5	200	0.1843	−0.10	0.020	0.3305	0.10	−0.010
Yellow boiled	2	50	0.108	−0.06	0.008	0.5133	0.08	−0.007
Yellow boiled	2	200	0.1662	−0.09	0.010	0.3555	0.10	−0.009
Pink boiled	5	50	0.0716	−0.03	0.004	0.4420	0.20	−0.020
Pink boiled	5	100	0.0779	−0.03	0.004	0.4165	0.20	−0.020
Pink boiled	5	200	0.0917	−0.04	0.004	0.3817	0.10	−0.020
Pink boiled	2	50	0.0725	−0.03	0.004	0.4422	0.20	−0.020
Pink boiled	2	200	0.0878	−0.03	0.004	0.3898	0.10	−0.020

3 Absorption Efficiency Factor of Droplets

According to the Mie theory, the absorption efficiency factor of droplets Q_a depends on droplet diffraction parameter $x=2\pi r_d/\lambda$ and complex index of refraction of the fuel $m=n-i\kappa$, where n is the index of refraction, $\kappa=a_\lambda\lambda/(4\pi)$ is the index of absorption, a_λ is the absorption coefficient. These calculations are rather complicated, especially for large droplets ($x\gg1$). This stimulated attempt to develop simplified models specifically focused on the range of parameters typical for diesel fuel droplets ([3,6–8]). The following approximation for Q_a has been suggested [7]:

$$Q_a=\frac{4n}{(n+1)^2}[1-\exp(-4\kappa x)]. \tag{1}$$

This equation gives a slightly better approximation for Q_a when compared with that used in [3].

The values of n were calculated based on subtractive Kramers-Krönig analysis [9,6]. It was shown that the results of these calculations can be accurately approximated by the following relationship [8]:

$$n=n_0+0.02\frac{\lambda-\lambda_m}{(\lambda-\lambda_m)^2+0.001}, \tag{2}$$

where $n_0=1.46$, $\lambda_m=3.4\ \mu$m, λ is the wavelength in μm. For practical calculations of κ the dependence of n on λ can be ignored, and n can be put equal to 1.46 [6].

As in [3], we assume that the dependence of radiation intensity on λ is close to that of a black body. Using Eq. (1) we calculate the averaged (over wavelengths) absorption efficiency factor of droplets as

$$\overline{Q_a}=\frac{4n}{(n+1)^2}\left\{1-\left[\int_{\lambda_1}^{\lambda_2}\frac{\exp\left(-\frac{8\pi\kappa r_d}{\lambda}\right)}{\lambda^5[\exp(C_2/(\lambda T_{\text{ext}}))-1]}d\lambda\Big/\int_{\lambda_1}^{\lambda_2}\frac{d\lambda}{\lambda^5[\exp(C_2/(\lambda T_{\text{ext}}))-1]}\right]\right\}, \tag{3}$$

where $C_2=1.439\times10^4\ \mu$m·K, T_{ext} is the external temperature responsible for radiative heating (in the case of optically thick gas this should be replaced by ambient gas temperature).

Taking into account the experimentally measured values of $\kappa(\lambda)$ it was found that the best approximation for $\overline{Q_a}$ in the ranges $5\leqslant r_d\leqslant50\ \mu$m and $1000\leqslant T_{\text{ext}}\leqslant3000$ K is provided by the function [3]

$$\Lambda_0=ar_d^b \tag{4}$$

where a and b are quadratic functions of T_{ext} approximated as

$$\left.\begin{aligned}a&=a_0+a_1(T_{\text{ext}}/1000)+a_2(T_{\text{ext}}/1000)^2\\ b&=b_0+b_1(T_{\text{ext}}/1000)+b_2(T_{\text{ext}}/1000)^2\end{aligned}\right\}. \tag{5}$$

Analysis similar to that presented in [3] has been repeated for various ranges of droplet radii and gas temperatures for all four types of diesel fuel under consideration. It has been shown that approximation (4) with a and b defined by (5) is applicable for all four types of fuel in the ranges $2\leqslant r_d\leqslant200\ \mu$m and $1000\text{ K}\leqslant T_{ext}\leqslant3000$ K, although it becomes less accurate for droplets with radii greater than 50 μm. Results of calculation of the coefficients in (5) for various ranges of r_d for all four types of fuel are shown in Table 1. As can be seen from this table, the variations of the values of the coefficients depending of the range of r_d and type of fuel are substantial and need to be taken into account.

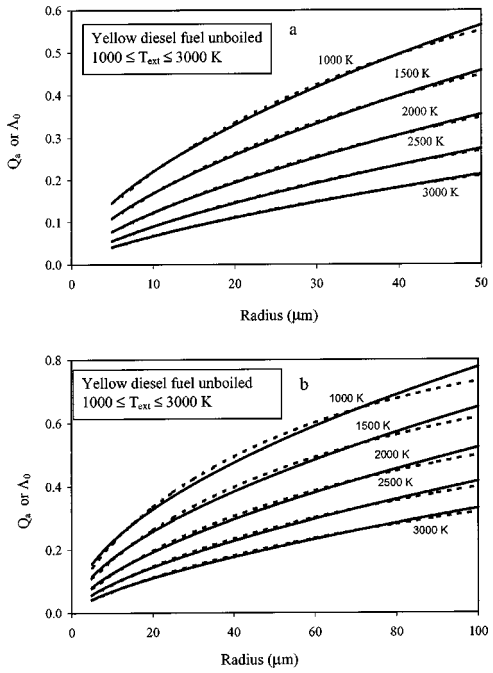

Fig. 2 Plots of $\overline{Q_a}$ versus r_d (solid) and Λ_0 versus r_d (dashed) for $T_{\text{ext}}=1000$ K, $T_{\text{ext}}=1500$ K, $T_{\text{ext}}=2000$ K, $T_{\text{ext}}=2500$ K, and $T_{\text{ext}}=3000$ K (indicated near the curves) for yellow unboiled diesel fuel. Plots shown in Fig. 2(a) are based on the values of coefficient found for external gas temperatures in the range $1000°\text{K}\leqslant T_{\text{ext}}\leqslant3000°\text{K}$ and droplet radii in the range $5\leqslant r_d\leqslant50\ \mu$m. Plots shown in Fig. 2(b) are based on the values of coefficient found for external gas temperatures in the range $1000\text{ K}\leqslant T_{\text{ext}}\leqslant3000\text{ K}$ and droplet radii in the range $5\leqslant r_d\leqslant100\ \mu$m.

The accuracy of approximation (4) with the coefficients given by Eqs. (5) and Table 1 is illustrated in Fig. 2 for the yellow unboiled fuel and two ranges of r_d. As can be seen from this figure, the approximation (5) is very good for $5\leqslant r_d\leqslant50\ \mu$m, but less accurate (although acceptable in most practical applications) for $5\leqslant r_d\leqslant100\ \mu$m.

For $500\text{ K}\leqslant T_{\text{ext}}\leqslant3000$ K approximations (5) appeared to be poor for all types of fuel under consideration. Considerably better accuracy was obtained when approximations (5) were replaced by the following approximations:

$$\left.\begin{aligned}a&=a_0+a_1(T_{\text{ext}}/1000)+a_2(T_{\text{ext}}/1000)^2+a_3(T_{\text{ext}}/1000)^3+a_4(T_{\text{ext}}/1000)^4\\ b&=b_0+b_1(T_{\text{ext}}/1000)+b_2(T_{\text{ext}}/1000)^2+b_3(T_{\text{ext}}/1000)^3+b_4(T_{\text{ext}}/1000)^4\end{aligned}\right\} \tag{6}$$

The values of coefficients in (6) for $500\text{ K}\leqslant T_{\text{ext}}\leqslant3000$ K and various ranges of r_d for all four types of fuel are shown in Table 2. As in the case of Table 1, the variation in the values of the coefficients depending on the range of r_d and type of fuel are sometimes substantial and need to be taken into account.

The contribution of external gas radiation at temperatures close to 500 K is expected to be much smaller than the contribution of radiation from gas at temperatures higher than 1000 K. Hence,

Table 2 Values of coefficients a_i and b_i $i=0,1,2,3,4$) in Eq. (6) for 500 K$\leqslant t_{ext} \leqslant$3000 K, various types of diesel fuel and various ranges of droplet radii

Type of fuel	R_{min} (μm)	R_{max} (μm)	a_0	a_1 (K^{-1})	a_2 (K^{-2})	a_3 (K^{-3})	a_4 (K^{-4})	b_0	b_1 (K^{-1})	b_2 (K^{-2})	b_3 (K^{-3})	b_4 (K^{-4})
Yellow unboiled	5	50	−0.042	0.3	−0.3	0.10	−0.01	0.967	−1.0	0.8	−0.3	0.03
Yellow unboiled	5	100	−0.044	0.3	−0.3	0.10	−0.01	0.8819	−0.9	0.8	−0.3	0.03
Yellow unboiled	5	200	−0.046	0.4	−0.4	0.10	−0.02	0.7496	−0.8	0.8	−0.3	0.03
Yellow unboiled	2	50	−0.044	0.3	−0.3	0.10	−0.01	0.9798	−1.0	0.9	−0.3	0.03
Yellow unboiled	2	200	−0.047	0.4	−0.4	0.10	−0.02	0.7824	−0.9	0.8	−0.3	0.03
Pink unboiled	5	50	−0.057	0.3	−0.3	0.09	−0.01	0.9862	−1.1	1.0	−0.3	0.04
Pink unboiled	5	100	−0.062	0.3	−0.3	0.09	−0.01	0.9636	−1.1	1.0	−0.3	0.04
Pink unboiled	5	200	−0.072	0.4	−0.3	0.10	−0.02	0.8995	−1.1	1.0	−0.3	0.04
Pink unboiled	2	50	−0.057	0.3	−0.3	0.10	−0.01	0.9681	−1.1	0.9	−0.3	0.04
Pink unboiled	2	200	−0.069	0.4	−0.3	0.10	−0.01	0.9063	−1.1	1.0	−0.3	0.04
Yellow boiled	5	50	−0.040	0.3	−0.3	0.1	−0.01	0.9387	−0.9	0.8	−0.3	0.03
Yellow boiled	5	100	−0.041	0.3	−0.3	0.1	−0.01	0.8375	−0.8	0.7	−0.2	0.03
Yellow boiled	5	200	−0.041	0.4	−0.4	0.1	−0.02	0.6954	−0.7	0.6	−0.2	0.03
Yellow boiled	2	50	−0.042	0.3	−0.3	0.1	−0.01	0.9596	−0.9	0.8	−0.3	0.03
Yellow boiled	2	200	−0.043	0.4	−0.4	0.1	−0.02	0.7331	−0.8	0.7	−0.2	0.03
Pink boiled	5	50	−0.085	0.3	−0.3	0.1	−0.01	1.4481	−2.1	2.0	−0.6	0.08
Pink boiled	5	100	−0.085	0.3	−0.3	0.1	−0.01	1.2870	−1.8	2.0	−0.6	0.07
Pink boiled	5	200	−0.091	0.4	−0.3	0.1	−0.01	1.1103	−1.5	1.0	−0.5	0.06
Pink boiled	2	50	−0.097	0.4	−0.3	0.1	−0.01	1.6235	−2.5	2.0	−0.7	0.09
Pink boiled	2	200	−0.097	0.4	−0.3	0.1	−0.01	1.2056	−1.7	1.0	−0.5	0.06

approximation (6) is less important for practical applications than approximation (5). The values of the coefficients can be chosen from Tables 1 or 2 depending on the type of fuel and the range of droplet radii and gas temperatures required.

In agreement with the previous results [3], it was shown that the effect of thermal radiation on heating and evaporation of semi-transparent diesel fuel droplets is considerably smaller when compared with the case when droplets are approximated as black opaque spheres. The effect of radiative heating of droplets was shown to be particularly strong when the effect of the difference of gas temperature responsible for droplet convective heating and flame temperature responsible for its radiative heating is taken into account (cf. [10]). The presentation of these results is beyond the scope of this note.

4 Conclusions

Results of the measurements of the index of absorption of four types of diesel fuel in the range of wavelengths 0.2 μm−6 μm are presented. The types of diesel fuel analyzed included two samples for which the ''ageing'' process of fuels was simulated by prolonged boiling.

It is shown that the approximation of the average absorption coefficient of droplets by the function ar_d^b, where r_d is the droplet radius, and a and b are polynomial functions of external gas temperature, is applicable for all types of fuel in the reasonable range of these temperatures and droplet radii. In the case when the external gas temperature range is 1000–3000 K, these polynomials are quadratic functions. In the case when this range is 500–3000 K, the polynomials are of the fourth power. The accuracy of this approximation is good for droplet radii in the range 2–50 μm, but can be worse for droplet radii in the range 5–200 μm. However, even in the latter case it can be applicable for practical engineering applications. Explicit values of the coefficients are presented for all four types of diesel fuel and for various ranges of droplet radii and gas temperatures.

Acknowledgments

The authors are grateful to Professor M Heikal for useful comments on the draft version of this paper, EPSRC (Grant GR/R82920/01) for the financial support of this project, and to Ricardo Consulting Engineers for technical support.

References

[1] Lage, P. L. C., and Rangel, R. H., 1993, ''Single Droplet Vaporization Including Thermal Radiation Absorption,'' J. Thermophys. Heat Transfer, **7**(3), pp. 502–509.
[2] Dombrovsky, L. A., and Sazhin, S. S., 2003, ''Absorption of Thermal Radiation in a Semi-Transparent Spherical Droplet: A Simplified Model,'' Int. J. Heat Fluid Flow, **24**(6), pp. 919–927.
[3] Dombrovsky, L. A., Sazhin, S. S., Sazhina, E. M., Feng, G., Heikal, M. R., Bardsley, M. E. A., and Mikhalovsky, S. V., 2001, ''Heating and Evaporation of Semi-Transparent Diesel Fuel Droplets in the Presence of Thermal Radiation,'' Fuel, **80**(11), pp. 1535–1544.
[4] Marchese, A. J., and Dryer, F. L., 1997, ''The Effect of Non-Luminous Thermal Radiation in Microgravity Droplet Combustion,'' Combust. Sci. Technol., **124**, pp. 371–402.
[5] Sazhin, S. S., Sazhina, E. M., and Heikal, M. R., 2000, ''Modelling of the Gas to Fuel Droplets Radiative Exchange,'' Fuel, **79**, pp. 1843–1852.
[6] Dombrovsky, L. A., Sazhin, S. S., Mikhalovsky, S. V., Wood, R., and Heikal,

M. R., 2003, ''Spectral Properties of Diesel Fuel Droplets,'' Fuel, **82**(1), pp. 15–22.
[7] Dombrovsky, L. A., 2002, ''A Spectral Model of Absorption and Scattering of Thermal Radiation by Diesel Fuel Droplets,'' High Temp., **40**(2), pp. 242–248.
[8] Dombrovsky, L. A., Sazhin, S. S., and Heikal, M. R., 2002, ''A Model for Computation of Radiative Characteristics of Diesel Fuel Droplets,'' *Proceedings of 3rd Russian National Heat and Mass Transfer Conference*, **6**, pp. 262–265 (in Russian).
[9] Ahrenkiel, R. K., 1971, ''Modified Kramers-Krönig Analysis of Optical Spectra,'' J. Opt. Soc. Am., **61**, pp. 1651–1655.
[10] Sazhina, E. M., Sazhin, S. S., Heikal, M. R., and Bardsley, M. E. A., 2000, ''The P-1 Model for Thermal Radiation Transfer: Application to Numerical Modelling of Combustion Processes in Diesel Engines,'' in *Proceedings of the 16th IMACS World Congress 2000 on Scientific Computation, Applied Mathematics and Simulation*, Paper 125-10, CD-ROM.

A Finite Element Formulation for the Determination of Unknown Boundary Conditions for Three-Dimensional Steady Thermoelastic Problems

Brian H. Dennis
Institute of Environmental Studies,
The University of Tokyo,
7-3-1 Hongo, Bunkyo-ku, Tokyo, Japan
113-8656
e-mail: dennis@garlic.q.t.u-tokyo.ac.jp

George S. Dulikravich
Department of Mechanical and Materials Engineering,
Florida International University,
10555 West Flagler Street,
Miami, FL 33174, USA
e-mail: dulikrav@fiu.edu

Shinobu Yoshimura
Institute of Environmental Studies,
The University of Tokyo,
7-3-1 Hongo, Bunkyo-ku,
Tokyo, Japan 113-8656
e-mail: yoshi@q.t.u-tokyo.ac.jp

A three-dimensional finite element method (FEM) formulation for the prediction of unknown boundary conditions in linear steady thermoelastic continuum problems is presented. The present FEM formulation is capable of determining displacements, surface stresses, temperatures, and heat fluxes on the boundaries where such quantities are unknown or inaccessible, provided such quantities are sufficiently over-specified on other boundaries. The method can also handle multiple material domains and multiply connected domains with ease. A regularized form of the method is also presented. The regularization is necessary for solving problems where the over-specified boundary data contain errors. Several regularization approaches are shown. The inverse FEM method described is an extension of a method previously developed by the leading authors for two-dimensional steady thermoelastic inverse problems and three-dimensional thermal inverse problems. The method is demonstrated for several three-dimensional test cases involving simple geometries although it is applicable to arbitrary three-dimensional configurations. Several different solution techniques for sparse rectangular systems are briefly discussed. [DOI: 10.1115/1.1640360]

Keywords: Finite Element, Heat Transfer, Inverse, Nonintrusive Diagnostics, Stress

Introduction

It is often difficult or even impossible to place temperature probes, heat flux probes, or strain gauges on certain parts of a surface of a solid body. This can be due to its small size, geometric inaccessibility, or a exposure to a hostile environment. With an appropriate inverse method these unknown boundary values can be determined from additional information provided at the boundaries where the values can be measured directly. In the case of steady thermal and elastic problems, the objective of the inverse problem is to determine displacements, surface stresses, heat fluxes, and temperatures on boundaries where they are unknown. The problem of inverse determination of unknown boundary conditions in two-dimensional steady heat conduction has been solved by a variety of methods [1–5]. Similarly, a separate inverse boundary condition determination problem in linear elastostatics has been solved by different methods [6]. The inverse boundary condition determination problem for steady thermoelasticity was also solved for several two-dimensional problems [4].

A three-dimensional finite element formulation is presented here that allows one to solve this inverse problem in a direct manner by over-specifying boundary conditions on boundaries where that information is available. Our objective is to develop and demonstrate an approach for the prediction of thermal boundary conditions on parts of a three-dimensional solid body surface by using FEM.

It should be pointed out that the method for the solution of inverse problems to be discussed in this paper is different from the approach based on boundary element method that has been used separately in linear heat conduction [3] and linear elasticity [6].

For inverse problems, the unknown boundary conditions on parts of the boundary can be determined by overspecifying the boundary conditions (enforcing both Dirichlet and Neumann type boundary conditions) on at least some of the remaining portions of the boundary, and providing either Dirichlet or Neumann type boundary conditions on the rest of the boundary. It is possible, after a series of algebraic manipulations, to transform the original system of equations into a system which enforces the overspecified boundary conditions and includes the unknown boundary conditions as a part of the unknown solution vector. This formulation is an adaptation of a method used by Martin and Dulikravich [7] for the inverse detection of boundary conditions in steady heat conduction.

Specifically, this work represents an extension of the conceptual work presented by the authors [4,8] by extending the original formulation from two dimensions into three dimensions.

FEM Formulation for Thermoelasticity

The Navier equations for linear static deformations u, v, w in three-dimensional Cartesian x, y, z coordinates are

$$(\lambda+G)\left(\frac{\partial^2 u}{\partial x^2}+\frac{\partial^2 v}{\partial x\partial y}+\frac{\partial^2 w}{\partial x\partial z}\right)+G\nabla^2 u+X=0 \tag{1}$$

$$(\lambda+G)\left(\frac{\partial^2 u}{\partial x\partial y}+\frac{\partial^2 v}{\partial y^2}+\frac{\partial^2 w}{\partial y\partial z}\right)+G\nabla^2 v+Y=0 \tag{2}$$

$$(\lambda+G)\left(\frac{\partial^2 u}{\partial x\partial z}+\frac{\partial^2 v}{\partial y\partial z}+\frac{\partial^2 w}{\partial z^2}\right)+G\nabla^2 w+Z=0 \tag{3}$$

where

$$\lambda=\frac{E\nu}{(1+\nu)(1-2\nu)},\quad G=\frac{E}{2(1+\nu)}$$

Contributed by the Heat Transfer Division for publication in the JOURNAL OF HEAT TRANSFER. Manuscript received by the Heat Transfer Division July 31, 2002; revision received September 8, 2003. Editor: V. K. Dhir.

Here, X, Y, Z are body forces per unit volume due to stresses from thermal expansion.

$$X = -(3\lambda + 2G)\frac{\partial \alpha \Delta \Theta}{\partial x} \tag{4}$$

$$Y = -(3\lambda + 2G)\frac{\partial \alpha \Delta \Theta}{\partial y} \tag{5}$$

$$Z = -(3\lambda + 2G)\frac{\partial \alpha \Delta \Theta}{\partial z} \tag{6}$$

This system of differential Eqs. (1–3) can be written in the following matrix form:

$$[L]^T([C][L]\{\delta\} - [C]\{\varepsilon_0\}) - \{f_b\} = 0 \tag{7}$$

where the differential operator matrix, $[L]$, is defined as

$$[L] = \begin{bmatrix} \frac{\partial}{\partial x} & 0 & 0 \\ 0 & \frac{\partial}{\partial y} & 0 \\ 0 & 0 & \frac{\partial}{\partial z} \\ \frac{\partial}{\partial y} & \frac{\partial}{\partial x} & 0 \\ \frac{\partial}{\partial z} & 0 & \frac{\partial}{\partial x} \\ 0 & \frac{\partial}{\partial z} & \frac{\partial}{\partial y} \end{bmatrix} \tag{8}$$

and the elastic modulus matrix, $[C]$, is defined as

$$[C] = \frac{\lambda}{\nu}\begin{bmatrix} 1-\nu & \nu & \nu & 0 & 0 & 0 \\ \nu & 1-\nu & \nu & 0 & 0 & 0 \\ \nu & \nu & 1-\nu & 0 & 0 & 0 \\ 0 & 0 & 0 & \frac{1-2\nu}{2} & 0 & 0 \\ 0 & 0 & 0 & 0 & \frac{1-2\nu}{2} & 0 \\ 0 & 0 & 0 & 0 & 0 & \frac{1-2\nu}{2} \end{bmatrix} \tag{9}$$

Casting the system of Eq. (7) in integral form using the weighted residual method [9,10] yields

$$\int_\Omega [V][L]^T([C][L]\{\delta\} - [C]\{\varepsilon_0\})d\Omega - \int_\Omega [V]\{f_b\}d\Omega = 0 \tag{10}$$

where the matrix, $[V]$, is the weight matrix which is a collection of test functions.

$$[V] = \begin{bmatrix} v_1 & 0 & 0 \\ 0 & v_2 & 0 \\ 0 & 0 & v_3 \end{bmatrix} \tag{11}$$

One should now integrate (10) by parts to get the weak form of (7)

$$\int_\Omega ([L][V]^T)^T[C][L]\{\delta\}d\Omega - \int_\Omega ([L][V]^T)^T[C]\{\varepsilon_0\}d\Omega - \int_\Omega [V]\{f_b\}d\Omega - \int_{\Gamma_1} [V]\{T\}d\Gamma = 0 \tag{12}$$

where $\{T\}$ is the vector of surface tractions on surface Γ_1.

$$\{T\} = [n][C][L]\{\delta\} \tag{13}$$

The matrix $[n]$ contains the Cartesian components of the unit vector normal to the surface Γ_1. The displacement field in the x, y, and z directions can now be represented with approximation functions

$$\delta_x(x,y,z) \approx \tilde{\delta}_x^e(x,y,z) = \sum_{i=1}^{n} N_i(x,y,z)u_i \tag{14}$$

$$\delta_y(x,y,z) \approx \tilde{\delta}_y^e(x,y,z) = \sum_{i=1}^{n} N_i(x,y,z)v_i \tag{15}$$

$$\delta_z(x,y,z) \approx \tilde{\delta}_z^e(x,y,z) = \sum_{i=1}^{n} N_i(x,y,z)w_i \tag{16}$$

Equations (14)–(16) can be rewritten in matrix form

$$\tilde{\delta}^e = [N]\{\delta^e\} \tag{17}$$

where $[N]$ is the interpolation matrix which contains the trial functions for each equation in the system. Also note that with Galerkin's method the weight matrix and the interpolation matrix are equal, $[N] = [V]^T$. If the matrix $[B_e]$ is defined as

$$[B_e] = [L][N] \tag{18}$$

then the substitution of the approximation functions (17) into the weak statement (12) creates the weak integral form for a finite element expressed as

$$\int_{\Omega^e} [B_e]^T[C][B_e]\{\delta^e\}d\Omega^e - \int_{\Omega^e} [B_e]^T[C]\{\varepsilon_0^e\}d\Omega^e - \int_{\Omega^e} [N]^T\{f_b^e\}d\Omega^e - \int_{\Gamma_1^e} [N]^T\{T^e\}d\Gamma^e = 0 \tag{19}$$

This can also be written in the matrix form as

$$[K^e]\{\delta^e\} = \{f^e\} \tag{20}$$

For thermal stresses, the initial elemental strain vector, ε_0^e, becomes

$$\{\varepsilon_0^e\} = \lfloor \alpha\Delta\Theta \quad \alpha\Delta\Theta \quad \alpha\Delta\Theta \quad 0 \quad 0 \quad 0 \rfloor^T \tag{21}$$

The local stiffness matrix, $[K^e]$, and the force per unit volume vector, $\{f^e\}$, are determined for each element in the domain and then assembled into the global system

$$[K]\{\delta\} = \{F\} \tag{22}$$

After applying boundary conditions, the global displacements are found by solving this system of linear algebraic equations. The stresses, $\{\sigma\}$, can then be found in terms of the displacements, $\{\delta\}$

$$\{\sigma\} = [C][L]\{\delta\} - [C]\{\varepsilon_0\} \tag{23}$$

FEM Formulation for the Thermal Problem

The temperature distribution throughout the domain can be found by solving Poisson's equation for steady linear heat conduction with a distributed steady heat source function, Q, and thermal conductivity coefficient, k.

$$-k\left(\frac{\partial^2\Theta}{\partial x^2} + \frac{\partial^2\Theta}{\partial y^2} + \frac{\partial^2\Theta}{\partial z^2}\right) = Q \tag{24}$$

Applying the method of weighted residuals to (24) over an element results in

$$\int_{\Omega^e}\left(\frac{\partial^2\Theta}{\partial x^2}+\frac{\partial^2\Theta}{\partial y^2}+\frac{\partial^2\Theta}{\partial z^2}-\frac{Q}{k}\right)v\,d\Omega^e=0 \tag{25}$$

Integrating this by parts once (25) creates the weak statement for an element

$$-\int_{\Omega^e}k\left(\frac{\partial v}{\partial x}\frac{\partial\Theta}{\partial x}+\frac{\partial v}{\partial y}\frac{\partial\Theta}{\partial y}+\frac{\partial v}{\partial z}\frac{\partial\Theta}{\partial z}\right)d\Omega^e$$
$$=\int_{\Omega^e}N_iQd\Omega^e-\int_{\Gamma^e}N_i(q\cdot\hat{n})d\Omega^e \tag{26}$$

Variation of the temperature across an element can be expressed by

$$\Theta(x,y,z)\approx\tilde{\Theta}^e(x,y,z)=\sum_{i=1}^{m}N_i(x,y,z)\Theta_i \tag{27}$$

Using Galerkin's method, the weight function v and the interpolation function for Θ are chosen to be the same. By defining the matrix $[B_T]$ as

$$[B_T]=\begin{bmatrix}\frac{\partial N_1}{\partial x} & \frac{\partial N_2}{\partial x} & \cdots & \frac{\partial N_m}{\partial x}\\ \frac{\partial N_1}{\partial y} & \frac{\partial N_2}{\partial y} & \cdots & \frac{\partial N_m}{\partial y}\\ \frac{\partial N_1}{\partial z} & \frac{\partial N_2}{\partial z} & \cdots & \frac{\partial N_m}{\partial z}\end{bmatrix} \tag{28}$$

the weak statement (26) can be written in the matrix form as

$$[K_c^e]\{\Theta^e\}=\{Q^e\} \tag{29}$$

where

$$[K_c^e]=\int_{\Omega^e}k[B_T]^T[B_T]d\Omega^e \tag{30}$$

$$\{Q^e\}=-\int_{\Omega^e}Q\{N\}d\Omega+\int_{\Gamma^e}q_s\{N\}d\Gamma^e \tag{31}$$

The local stiffness matrix, $[K_c^e]$, and heat flux vector, $\{Q^e\}$, are determined for each element in the domain and then assembled into the global system

$$[K_c]\{\Theta\}=\{Q\} \tag{32}$$

Direct and Inverse Formulations

The above equations for steady thermoelasticity were discretized by using a Galerkin's finite element method. This results in two linear systems of algebraic equations

$$[K]\{\delta\}=\{F\},\quad [K_c]\{\Theta\}=\{Q\} \tag{33}$$

The system is typically large, sparse, symmetric, and positive definite. Once the global system has been formed, the boundary conditions are applied. For a well-posed analysis (direct) problem, the boundary conditions must be known on all boundaries of the domain. For heat conduction, either the temperature, Θ_s, or the heat flux, Q_s, must be specified at each point of the boundary.

For an inverse problem, the unknown boundary conditions on parts of the boundary can be determined by over-specifying the boundary conditions (enforcing both Dirichlet and Neumann type boundary conditions) on at least some of the remaining portions of the boundary, and providing either Dirichlet or Neumann type boundary conditions on the rest of the boundary. It is possible, after a series of algebraic manipulations, to transform the original system of equations into a system which enforces the over-specified boundary conditions and includes the unknown boundary conditions as a part of the unknown solution vector. As an example, consider the linear system for heat conduction on a tetrahedral finite element with boundary conditions given at nodes 1 and 4.

$$\begin{bmatrix}K_{11} & K_{12} & K_{13} & K_{14}\\ K_{21} & K_{22} & K_{23} & K_{24}\\ K_{31} & K_{32} & K_{33} & K_{34}\\ K_{41} & K_{42} & K_{43} & K_{44}\end{bmatrix}\begin{Bmatrix}\Theta_1\\ \Theta_2\\ \Theta_3\\ \Theta_4\end{Bmatrix}=\begin{Bmatrix}Q_1\\ Q_2\\ Q_3\\ Q_4\end{Bmatrix} \tag{34}$$

As an example of an inverse problem, one could specify both the temperature, Θ_s, and the heat flux, Q_s, at node 1, flux only at nodes 2 and 3, and assume the boundary conditions at node 4 as being unknown. The original system of Eq. (34) can be modified by adding a row and a column corresponding to the additional equation for the over-specified flux at node 1 and the additional unknown due to the unknown boundary flux at node 4. The result is

$$\begin{bmatrix}1 & 0 & 0 & 0 & 0\\ K_{21} & K_{22} & K_{23} & K_{24} & 0\\ K_{31} & K_{32} & K_{33} & K_{34} & 0\\ K_{41} & K_{42} & K_{43} & K_{44} & -1\\ K_{11} & K_{12} & K_{13} & K_{14} & 0\end{bmatrix}\begin{Bmatrix}\Theta_1\\ \Theta_2\\ \Theta_3\\ \Theta_4\\ Q_4\end{Bmatrix}=\begin{Bmatrix}\Theta_s\\ Q_2\\ Q_3\\ 0\\ Q_s\end{Bmatrix} \tag{35}$$

The resulting systems of equations will remain sparse, but will be nonsymmetric and possibly rectangular (instead of square) depending on the ratio of the number of known to unknown boundary conditions.

Regularization

Three regularization methods were applied separately to the solution of the systems of equations in attempts to increase the method's tolerance for measurement errors in the over-specified boundary conditions. Here we consider the regularization of the inverse heat conduction problem.

The general form of a regularized system is given as [11]

$$\begin{bmatrix}K_c\\ \Lambda D\end{bmatrix}\{\Theta\}=\begin{Bmatrix}Q\\ 0\end{Bmatrix} \tag{36}$$

The traditional Tikhonov regularization is obtained when the damping matrix, $[D]$, is set equal to the identity matrix. Solving (36) in a least squares sense minimizes the following error function.

$$\text{error}(\Theta)=\|[K_c]\{\Theta\}-\{Q\}\|_2^2+\|\Lambda[D]\{\Theta\}\|_2^2 \tag{37}$$

This is the minimization of the residual plus a penalty term. The form of the damping matrix determines what penalty is used and the damping parameter, Λ, weights the penalty for each equation. These weights should be determined according to the error associated with the respective equation.

Method 1. This method of regularization uses a constant damping parameter Λ over the entire domain and the identity matrix as the damping matrix. This method can be considered the traditional "zeroth order" Tikhonov method. The penalty term being minimized in this case is the square of the L_2 norm of the solution vector $\{x\}$. Minimizing this norm will tend to drive the components of $\{x\}$ to uniform values thus producing a smoothing effect. However, minimizing this penalty term will ultimately drive each component to zero, completely destroying the real solution. Thus, great care must be exercised in choosing the damping parameter Λ so that a good balance of smoothness and accuracy is achieved.

Method 2. This method of regularization uses a constant damping parameter Λ only for equations corresponding to the

unknown boundary values. For all other equations $\Lambda=0$ and $[D]=[I]$ since the largest errors occur at the boundaries where the temperatures and fluxes are unknown.

Method 3. This method uses Laplacian smoothing of the unknown temperatures and displacements only on the boundaries where the boundary conditions are unknown. This method could be considered a ''second order'' Tikhonov method. A penalty term can be constructed such that curvature of the solution on the unspecified boundary is minimized along with the residual.

$$\|\nabla^2\Theta_{ub}\|_2^2 \rightarrow \min \tag{38}$$

For problems that involve unknown vector fields, such as displacements, Eq. (38) must be modified to the following:

$$\|\nabla^2(\hat{n}\cdot\{\delta_{ub}\})\|_2^2 \rightarrow \min \tag{39}$$

Here the normal component of the vector displacement field $\{\delta\}$ is minimized along the unknown surface.

Equations (38) and (39) can be discretized using the method of weighted residuals to determine the damping matrix, $[D]$.

$$\|[D]\Theta_{ub}\|_2^2 = \|[K_c]\Theta_{ub}\|_2^2 \tag{40}$$

In three-dimensional problems, $[K_c]$ is computed by integrating over surface elements on the unknown boundaries. So the damping matrix can be thought of as an assembly of boundary elements that make up the boundary of the object where the boundary conditions are unknown. The stiffness matrix for each boundary element is formed by using a Galerkin weighted residual method that ensures the Laplacian of the solution is minimized over the unknown boundary surface. The main advantage of this method is its ability to smooth the solution vector without necessarily driving the components to zero and away from the true solution.

Solution of the Linear System

In general, the resulting FEM systems for inverse thermoelastic problems are sparse, unsymmetric, and often rectangular. These properties make the process of finding a solution to the system very challenging. Three approaches will be discussed here.

The first is to normalize the equations by multiplying both sides by the matrix transpose and solve the resulting square system with common sparse solvers.

$$[K]^T[K]\{\Theta\} = [K]^T\{Q\} \tag{41}$$

This approach has been found to be effective for certain inverse problems [12]. The resulting normalized system is less sparse than the original system, but it is square, symmetric, and positive definite with application of regularization. The normalized system is solved with a direct method (Cholesky or LU factorization) or with a ILU preconditioned iterative method (preconditioned Krylov subspace). There are several disadvantages to this approach. Among them being the expense of computing $[K]^T[K]$, the large in-core memory requirements, and the roundoff error incurred during the $[K]^T[K]$ multiplication. In general, it is best to avoid methods that require the explicit of formation of $[K]^T[K]$.

Another approach is to use iterative methods suitable for least squares problems. One such method is the LSQR method, which is an extension of the well-known conjugate gradient (CG) method [13]. The LSQR method and other similar methods such as the conjugate gradient for least squares (CGLS) solve the normalized system, but without explicit computation of $[K]^T[K]$. These methods need only matrix-vector products at each iteration and therefore only require the storage of $[K]$ so they are attractive for large sized models. However, convergence rates of these methods depend strongly on the condition number of the normalized system which is the condition number of $[K]$ squared [14]. Therefore, solver performance degrades significantly as the size of the finite element model increases. Convergence can be slow when solving the systems resulting from the inverse finite element discretization since they are naturally ill-conditioned problems.

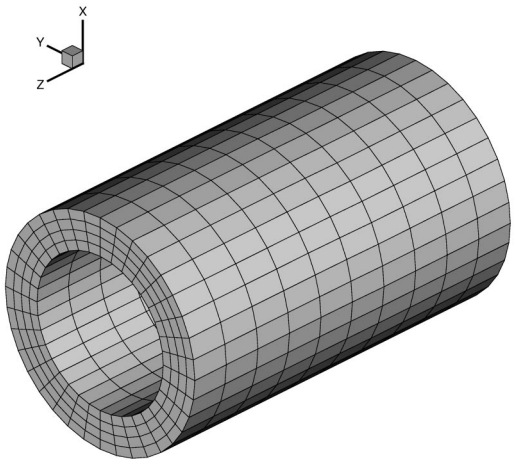

Fig. 1 Surface mesh for cylinder test case

Yet another approach is to use a non-iterative method for least squares problems such as QR factorization [15] or SVD [16]. However, sparse implementations of QR or SVD solvers are needed to reduce the in-core memory requirements for the inverse finite element problems. It is also possible to use static condensation to reduce the complete sparse system of equations into a dense matrix of smaller dimensions [5]. The reduced system involves only the unknowns on the boundary of the domain and can be solved efficiently using standard QR or SVD algorithms for dense matrices.

Numerical Results

The accuracy and efficiency of the finite element inverse formulation was tested on several simple three-dimensional problems. The method was implemented in an object-oriented finite element code written in C++. Elements used in the calculations were hexahedra with tri-linear interpolation functions. The linear systems were solved with a sparse QR factorization [15] or LSQR method [13] with column scaling. The two basic test geometries included an annular cylinder and a cylinder with multiply connected regions.

The annular cylinder geometry was tested first. The hexahedral mesh is shown in Fig. 1. The outer surface has a radius of 3.0 and the inner surface has a radius of 2.0. The mesh is composed of 1440 elements and 1980 nodes. The inner and outer boundaries each have 396 nodes. For this geometry, there is an analytical solution for heat conduction if constant temperature boundary conditions are used on the inner and outer boundaries. In a direct (well-posed) thermoelastic problem a uniform temperature of 10.0°C was enforced on the inner boundary while a temperature of -10.0°C was enforced on the outer boundary. Zero displacement was enforced on the cylinder outer boundary. A uniform pressure of 1.0 Pa was specified on the inner boundary. The following material properties were used: $E=1.0$ Pa, $\nu=0.0$, $\alpha=2.0\times10^{-2}\,\mathrm{K}^{-1}$, $\mathrm{k}=1.0\,\mathrm{W\,m^{-1}\,K^{-1}}$. Adiabatic and stress free conditions were specified at the ends of the cylinder. The computed temperature field and stress field is shown in Figs. 2 and 4. The temperature field computed with the FEM had a maximum error of less than 1.0% compared to the analytical solution.

The inverse problem was then created by over-specifying the outer cylindrical boundary with the double-precision values of temperatures, fluxes, displacements, and reaction forces on the outer boundary obtained from the direct analysis case. At the same time, no boundary conditions were specified on the inner cylindrical boundary [3]. A damping parameter of $\Lambda=0.0$ was used. The computed temperature and normal stress magnitude distributions are shown in Figs. 3 and 5. The maximum relative differences in

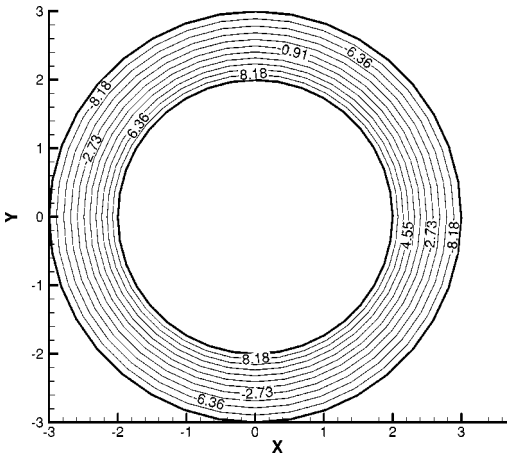

Fig. 2 Direct problem: computed isotherms when both inner and outer boundary temperatures were specified

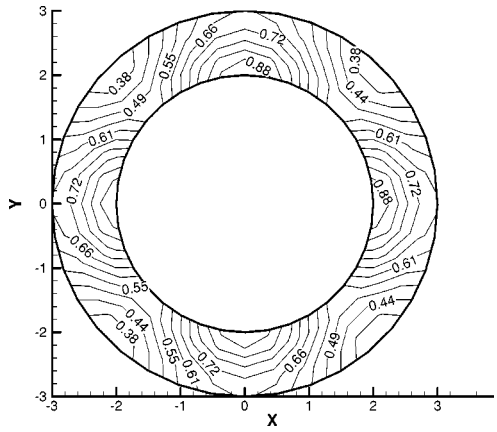

Fig. 5 Inverse problem: computed normal stress magnitude when only outer boundary conditions were specified

temperatures and displacements between the analysis and inverse results are less than 0.1% when solved using the QR factorization [15].

The above problem was repeated for the thermal problem only using boundary conditions with random measurement errors added. For these cases, regularization was used. Random errors in the known boundary temperatures and fluxes were generated using the following equations [3]:

$$\Theta = \Theta_{bc} \pm \sqrt{-2\sigma^2 \ln R} \tag{42}$$

$$Q = Q_{bc} \pm \sqrt{-2\sigma^2 \ln R} \tag{43}$$

Here R is a uniform random number between 0.0 and 1.0 and σ is the standard deviation. For each case, Eqs. (42–43) were used to generate errors in both the known boundary fluxes and temperatures obtained from the forward solution.

First, regularization method 1 was used with a wide range of damping parameters. The average percent error of the predicted temperatures on the unknown boundaries as a function of damping parameter and various levels of measurement error is shown in Fig. 6.

The inverse problem was also solved using regularization method 2 and method 3 for a wide range of damping parameters. The average percent error of the predicted temperatures on the unknown boundary as a function of damping parameter is shown in Fig. 7 for method 2 and Fig. 8 for method 3.

Results indicate that for simple three-dimensional geometries the present formulation is capable of predicting the unknown boundary conditions with errors on the same order of magnitude as the errors in the over-specified data. In other words, all regu-

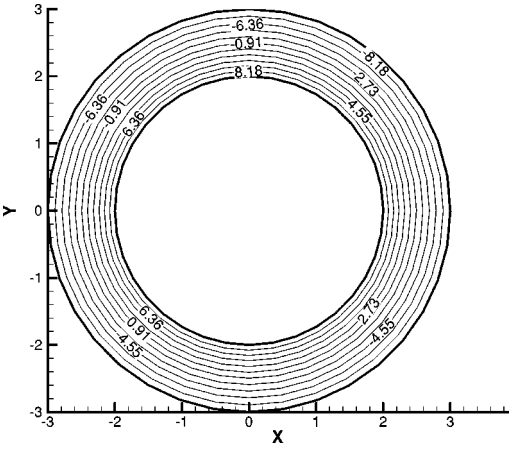

Fig. 3 Inverse problem: computed isotherms when only outer boundary temperatures and fluxes were specified

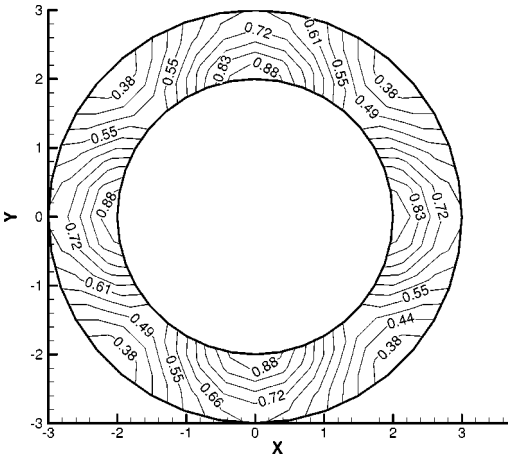

Fig. 4 Direct problem: computed normal stress magnitude when both inner and outer boundary conditions were specified

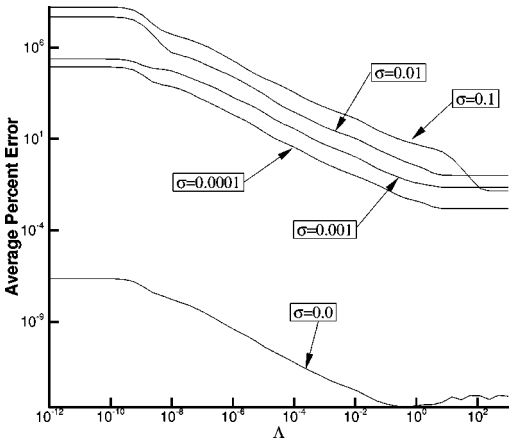

Fig. 6 Average percent error of predicted temperatures on unknown boundaries for regularization method 1 for cylinder region

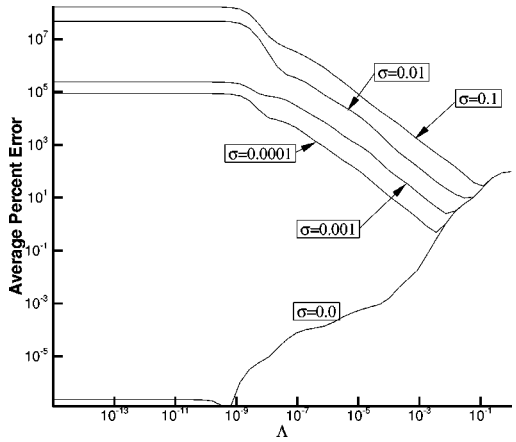

Fig. 7 Average percent error of predicted temperatures on unknown boundaries for regularization method 2 for cylinder region

larization methods prevent the amplification of the measurement errors. Regularization method 2 achieved slightly more accurate results than method 1 for all levels of random measurement error. However, method 3 produced the most accurate results overall.

The lack of error amplification with this method may only occur for simple geometries. Results in two-dimensional indicate that more sophisticated regularization techniques like method 3 are necessary for complicated geometries such as multiply connected domains [4].

The next test case involved a multiply-connected domain. Heat conduction only is considered in order to give a clear comparison of regularization methods for a more complex geometry. The geometry is composed of an outer cylinder with length 5.0 m and diameter of 2.0 m. There are four cylindrical holes that pass completely through the cylinder, each with a diameter of 1.25 m. The hexahedral mesh is shown in Fig. 9 and is composed of 1440 elements and 1980 nodes. The inner and outer boundaries each have 440 nodes. For this geometry, there is no analytical solution, even if constant temperature boundary conditions are used on the boundaries.

In the direct (well-posed) problem a uniform temperature of 10.0°C was enforced on the inner boundaries while a temperature of −10.0°C was enforced on the outer boundary. Adiabatic boundary conditions were specified at the ends of the cylinder. The computed temperature field is shown in Fig. 10.

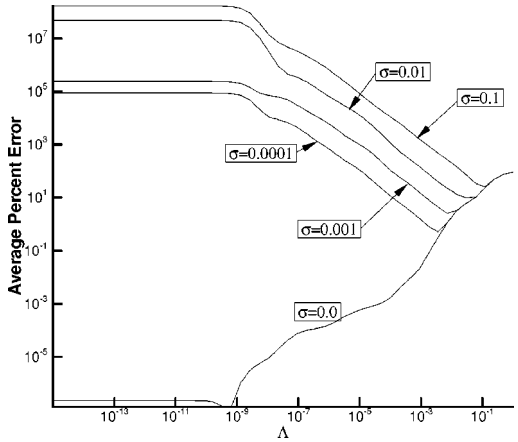

Fig. 8 Average percent error of predicted temperatures on unknown boundaries for regularization method 3 for cylinder region

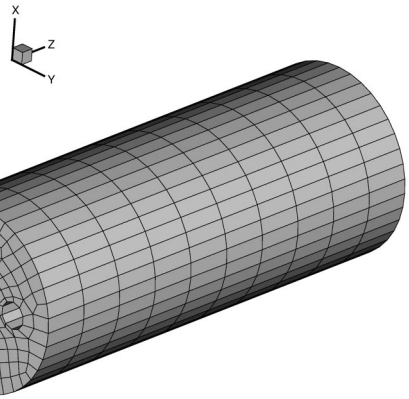

Fig. 9 Surface mesh for multiply connected domain test case

The inverse problem was then created by over-specifying the outer cylindrical boundary with the double-precision values of temperatures and fluxes obtained from the analysis case. At the same time, no boundary conditions were specified on the inner cylindrical boundaries. No errors were used in the over-specified boundary data.

A damping parameter of $\Lambda=0$ was tried first. Without regularization, the QR factorization became unstable due to the high condition number of the linear system.

The same inverse problem was repeated using regularization method 1 for a wide range of damping parameters. The lowest percent error achieved was 9.97% at damping parameter value of $\Lambda=1.75\times10^{-8}$. The resulting temperature distribution for $\Lambda=1.75\times10^{-8}$ is shown in Fig. 11.

The inverse problem was also solved using regularization method 2 for a wide range of damping parameters. The lowest percent error achieved was 2.67% at damping parameter value of $\Lambda=1.75\times10^{-8}$. The resulting temperature distribution for $\Lambda=1.75\times10^{-8}$ is shown in Fig. 12.

Finally, the inverse problem was solved using regularization method 3. A value of $\Lambda=0.1$ was used and percent error compared to the direct solution was less than 0.0001%. The resulting temperature distribution is shown in Fig. 13.

For the multiply-connected domain case only regularization method 3 worked well. These results indicate that this FEM inverse method requires regularization that is more sophisticated than the regular Tikhonov method if high accuracy is needed with multiply-connected three-dimensional geometries.

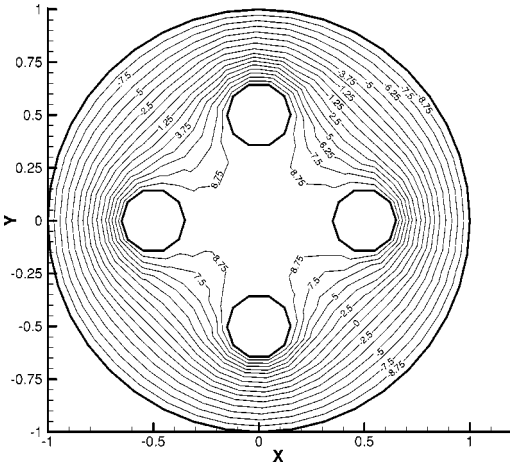

Fig. 10 Direct problem: computed isotherms when both inner and outer boundary temperatures were specified

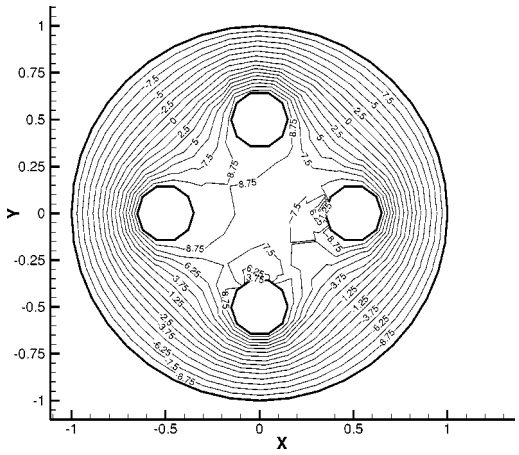

Fig. 11 Inverse problem: computed isotherms when only outer boundary temperatures and fluxes were specified and using regularization method 1

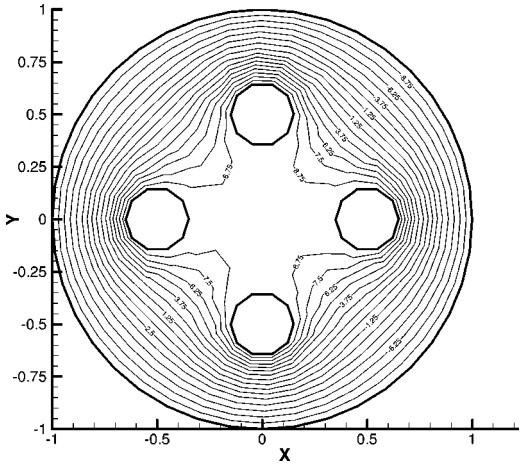

Fig. 13 Inverse problem: computed isotherms when only outer boundary temperatures and fluxes were specified and using regularization method 3 (Inverse and Direct contours plotted together)

The final test case involves solving the thermoelastic inverse problem for the multiply-connected domain in Fig. 9. This case considers thermal and elastic boundary conditions that vary in all coordinate directions thereby creating a truly three-dimensional example. The all interior boundary conditions change linearly along the *z*-axis. The exact values used are given in Table 1. On the outer cylinder the displacement was set to zero and a fixed temperature of 10°C was specified. The following material properties were used: $E=1.0\,\mathrm{Pa}$, $\nu=0.0$, $\alpha=2.0\times10^{-2}\,\mathrm{K}^{-1}$, $\mathrm{k}=1.0\,\mathrm{W\,m}^{-1}\,\mathrm{K}^{-1}$.

The inverse problem was generated by over-specifying the outer cylindrical boundary with the double-precision values of temperatures, fluxes, displacements, and surface tractions obtained from the forward analysis case. At the same time, no boundary conditions were specified on the inner cylindrical boundaries. No errors were used in the over-specified boundary data.

Regularization method 3 was used with $\Lambda=8.5\times10^{-5}$. Our experience indicates that a good value for the damping parameter, Λ, is geometry and boundary condition dependent. Currently, the damping parameter is chosen based on experience by first choosing a small value and gradually increasing it until the numerical oscillations in the unknown boundary solution are removed.

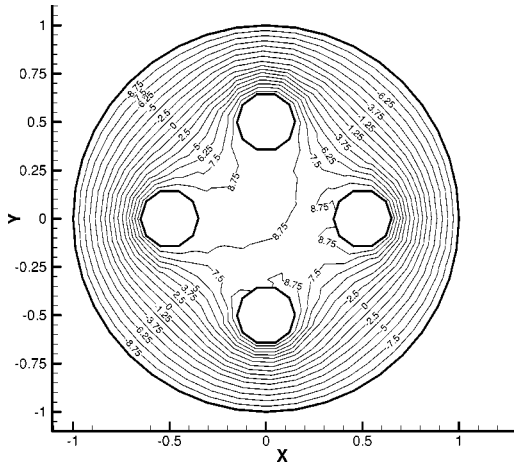

Fig. 12 Inverse problem: computed isotherms when only outer boundary temperatures and fluxes were specified and using regularization method 2

The system of equations for temperature was solved using sparse QR factorization. The linear system for displacements was too large to be solved with the sparse QR factorization code. Alternatively, the system was solved using the LSQR method with column scaling. The LSQR iterations were terminated after the Euclidean norm of the residual of the normal system was less than 1.0×10^{-6}. In this example 16805 LSQR iterations were required, which consumed about 10 min of computing time on a Pentium 4 workstation.

The average error between the inverse and direct solutions on the unknown boundaries was 0.02% for temperature and 5.6% for displacement. The direct and inverse temperature contours for three sections of the domain are shown in Figs. 14, 16, and 18. There is good agreement on all three sections between the direct and inverse temperature contours. The direct and inverse displacement magnitude contours for three sections of the domain are shown in Figs. 15, 17, and 19. For all three sections there is a noticeable difference in the direct and inverse contours in the regions far away from the outer boundary. However, the inverse solution does correctly capture the direct solution in a qualitative sense.

This thermoelastic problem was also solved using the other regularization methods over a wide range of damping parameters. In those cases the error in the inverse solution was much higher and did not match the direct solution even in a qualitative sense. The accuracy of the displacement could be increased by improving the quality of the damping matrix for the displacement field. The current damping matrix of Method 3 from Eq. (39) only includes the normal component of the displacement. Further improvements could be made by smoothing the tangential components as well. In addition, the current scheme depends on accurate surface unit normal vectors, $\hat{n}$, which are difficult to compute accurately on the nodes of flat elements on curved surfaces. So

Table 1 Temperature and pressure boundary conditions for interior surfaces

Hole	$T_{z=0}$ (°C)	$T_{z=5}$ (°C)	$P_{z=0}$ (Pa)	$P_{z=5}$ (Pa)
A	5.0	2.0	2.0	1.0
B	6.0	1.0	2.0	1.0
C	7.0	1.0	2.0	1.0
D	8.0	2.0	2.0	1.0

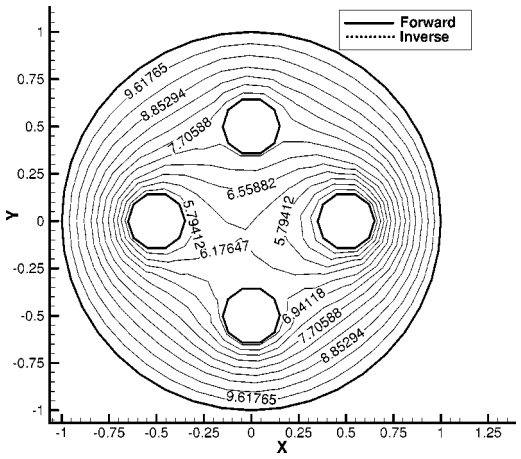

Fig. 14 Inverse problem: computed isotherms on $x-y$ plane at $z=0.5$ m when only outer boundary temperatures and fluxes were specified

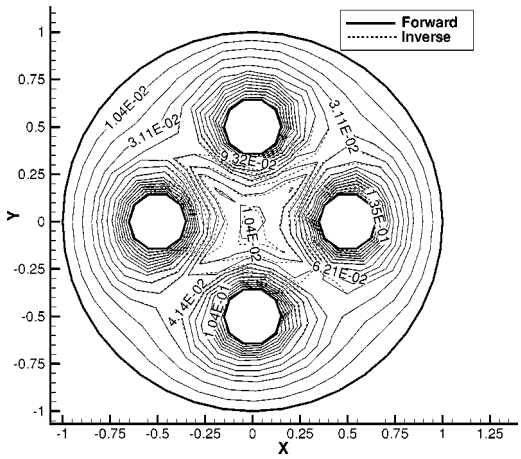

Fig. 17 Inverse problem: computed displacement magnitude on $x-y$ plane at $z=2.5$ m when only outer boundary displacements and tractions were specified

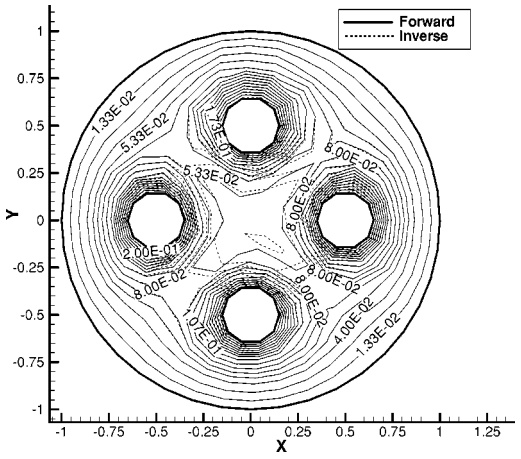

Fig. 15 Inverse problem: computed displacement magnitude on $x-y$ plane at $z=0.5$ m when only outer boundary displacements and tractions were specified

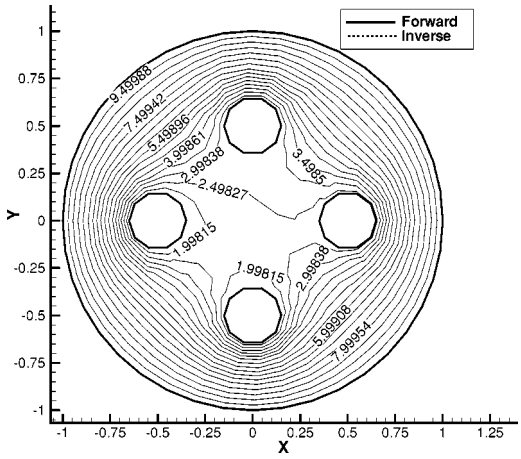

Fig. 18 Inverse problem: computed isotherms on $x-y$ plane at $z=4.5$ m when only outer boundary temperatures and fluxes were specified

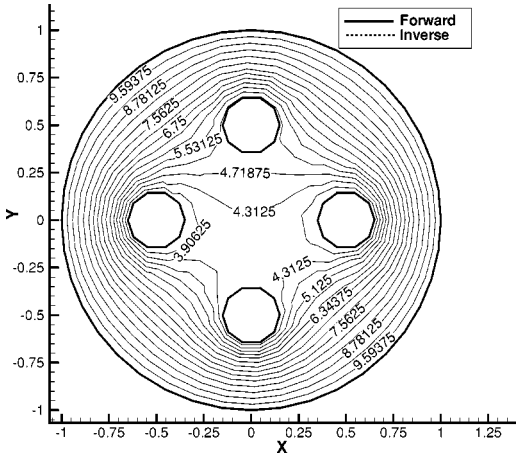

Fig. 16 Inverse problem: computed isotherms on $x-y$ plane at $z=2.5$ m when only outer boundary temperatures and fluxes were specified

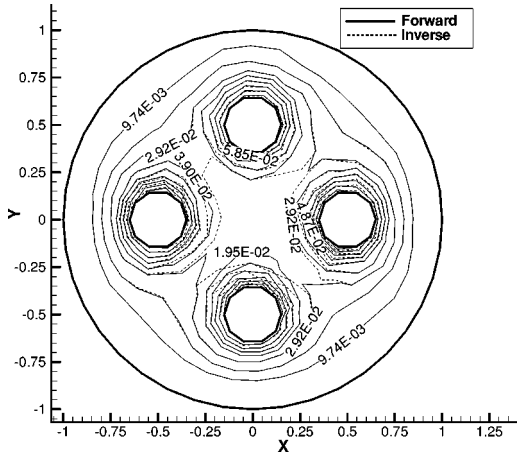

Fig. 19 Inverse problem: computed displacement magnitude on $x-y$ plane at $z=4.5$ m when only outer boundary displacements and tractions were specified

further reductions in errors could possibly be made by implementing methods that compute the surface normals with a high degree of accuracy.

The sparse QR factorization was found to provide the solution with highest accuracy in the shortest amount of computing time. However, the QR factorization requires substantial amounts of in-core memory. For the largest examples presented here, a workstation with 512 MB of memory was required. The sparse QR factorization failed for the elastic inverse problem on the multiply-connected domain that had more than 7000 unknowns. For cases where QR factorization failed or required too much memory, the LSQR method was employed. Reasonable results were obtained by LSQR with column scaling in less than 20,000 iterations for displacements and 3000 iterations for temperature. Although many iterations are required with the LSQR method, it requires much less memory and is more robust than the sparse QR factorization. The preconditioned CG method applied to the normalized equations worked well for problems with less than 100 nodes. For more than 100 nodes, this method required many iterations to converge to a solution less accurate than the QR or LSQR solution. When regularization was applied to the sparse matrix, the CG convergence improved dramatically but the QR factorization was much faster by comparison.

Conclusions

A formulation for the inverse determination of unknown steady boundary conditions in heat conduction and thermoelasticity for three-dimensional problems has been developed using FEM. The formulation has been tested numerically using an annular geometry with a known analytic solution. The formulation can predict the temperatures and displacements on the unknown boundary with high accuracy in the annular domain without the need for regularization. However, regularization was required in order to compute a good solution when measurement errors in the overspecified boundary conditions were added. Three different regularization methods were applied. All allow a stable QR factorization to be computed, but only method 3 resulted in highly accurate temperature predictions on the unknown boundaries for large values of measurement errors. However, all regularization methods prevented amplification of the measurement errors. It was shown that the FEM formulation can accurately predict unknown boundary conditions for multiply-connected domains when a good regularization scheme is used. Further research is needed to develop better regularization methods so that the present formulation can be made more robust with respect to measurement errors and more complex geometries. Further research is also needed to improve regularization for inverse problems in elasticity over complicated domains.

Acknowledgments

The primary author would like to acknowledge the support received from the ADVENTURE project sponsored by the Japanese Society for the Promotion of Science (JSPS) and the ''Frontier Simulation Software for Industrial Science (FSIS)'' project supported by IT program of Japan Ministry of Education, Culture, Sports, Science and Technology (MEXT).

Nomenclature

α = coefficient of thermal expansion
$\{\delta\}$ = displacement vector
ϵ = strain
Γ = boundary surface
λ = Lame's constant
Λ = damping parameter
ν = Poisson's ratio
$\underline{\sigma}$ = normal stress
$\overline{\sigma}$ = standard deviation
τ = shear stress
Θ = temperature
$\Delta\Theta$ = difference between local and reference temperature
$[D]$ = damping matrix
E = elastic modulus of elasticity
G = shear modulus
k = Fourier coefficient of heat conduction
Q = heat source
q = heat flux
R = uniform random number between 0 and 1
$\hat{n}$ = unit normal vector
u, v, w = deformations in the x, y, z directions
X, Y, Z = body force in x, y, z directions
x, y, z = Cartesian body axes

References

[1] Larsen, M. E., 1985, ''An Inverse Problem: Heat Flux and Temperature Prediction for a High Heat Flux Experiment,'' Technical Report, SAND-85-2671, Sandia National Laboratories, Albuquerque, NM.
[2] Hensel, E. H., and Hills, R., 1989, ''Steady-State Two-Dimensional Inverse Heat Conduction,'' Numer. Heat Transfer, **15**, pp. 227–240.
[3] Martin, T. J., and Dulikravich, G. S., 1996, ''Inverse Determination of Boundary Conditions in Steady Heat Conduction,'' ASME J. Heat Transfer, **3**, pp. 546–554.
[4] Dennis, B. H., and Dulikravich, G. S., 1999, ''Simultaneous Determination of Temperatures, Heat Fluxes, Deformations, and Tractions on Inaccessible Boundaries,'' ASME J. Heat Transfer, **121**, pp. 537–545.
[5] Olson, L. G., and Throne, R. D., 2000, ''The Steady Inverse Heat Conduction Problem: A Comparison for Methods of Inverse Parameter Selection,'' in *34th National Heat Transfer Conference-NHTC'00*, No. NHTC2000-12022, Pittsburg, PA.
[6] Martin, T. J., Halderman, J., and Dulikravich, G. S., 1995, ''An Inverse Method for Finding Unknown Surface Tractions and Deformations in Elastostatics,'' Comput. Struct., **56**, pp. 825–836.
[7] Martin, T. J., and Dulikravich, G. S., 1995, ''Finding Temperatures and Heat Fluxes on Inaccessible Surfaces in Three-Dimensional Coated Rocket Nozzles,'' in *1995 JANNAF Non-Destructive Evaluation Propulsion Subcommittee Meeting*, Tampa, FL, pp. 119–129.
[8] Dennis, B. H., and Dulikravich, G. S., 2001, ''A Three-Dimensional Finite Element Formulation for the Determination of Unknown Boundary Conditions in Heat Conduction,'' in *Proc. of Internat. Symposium on Inverse Problems in Eng. Mechanics*, M. Tanaka, ed., Nagano City, Japan.
[9] Hughes, T. J. R., 2000, *The Finite Element Method: Linear Static and Dynamic Finite Element Analysis*, Dover Publications, Inc., New York.
[10] Huebner, K. H., Thorton, E. A., and Byrom, T. G., 1995, *The Finite Element Method for Engineers*, third edition, John Wiley and Sons, New York, NY.
[11] Neumaier, A., 1998, ''Solving Ill-Conditioned and Singular Linear Systems: A Tutorial on Regularization,'' SIAM Rev., **40**, pp. 636–666.
[12] Boschi, L., and Fischer, R. P., 1996, ''Iterative Solutions for Tomographic Inverse Problems: LSQR and SIRT,'' technical report, Seismology Dept., Harvard University, Cambridge, MA.
[13] Paige, C. C., and Saunders, M. A., 1982, ''LSQR: An Algorithm for Sparse Linear Equations and Sparse Least Squares,'' ACM Trans. Math. Softw., **8**, pp. 43–71.
[14] Saad, Y., 1996, *Iterative Methods for Sparse Linear Systems*, PWS Publishing Co., Boston, MA.
[15] Matstoms, P., 1991, *The Multifrontal Solution of Sparse Least Squares Problems*, Ph.D. thesis, Linköping University, Sweden.
[16] Golub, G. H., and Van Loan, C. F., 1996, *Matrix Computations*, Johns Hopkins University Press, Baltimore, MD.

A Cost-Based Strategy to Design Multiple Shell and Tube Heat Exchangers

Raquel D. Moita

Cristina Fernandes

Henrique A. Matos
e-mail: henrimatos@ist.utl.pt

Clemente P. Nunes

Departamento de Engenharia Química,
Instituto Superior Técnico,
Av. Rovisco Pais, 1049-001 Lisboa, Portugal

Process Integration has been applied in several industrial processes mainly using standard shell and tube heat exchangers (1-1 or 1-2). The flow arrangement in 1-2 multiple shell and tube heat exchangers involves part counter-current flow and part co-current flow. This fact is accounted for in the design by introducing a F_T correction factor into the 1-1 heat exchanger design equation. To avoid some steep regions in the feasible space of heat exchangers design some authors introduce other parameters like X_P or G. Until now it was not possible to have an overall map to give some guidelines of how to choose between the several X_P approaches established in the literature. This paper summarizes the current existing criteria in a general design algorithm ($DeAl_{12}$) to show a path for the calculations of the main design variables of the heat exchanger. Also a new strategy design algorithm ($StratDeAl_{12}$) is introduced in this paper to allow the best choice between the existing X_P approaches based on the heat exchanger cost minimisation. Several examples illustrate the advantage of using the developed algorithm and the deviations obtained in the heat exchanger cost if a wrong approach was chosen.
[DOI: 10.1115/1.1643087]

Keywords: Computational, Heat Transfer, Heat Exchangers

1 Introduction

The energy optimization of the process flow diagrams is of great importance in the process industries. New process integration methodologies have been intensively developed and applied in industries in the last twenty years with considerable success. However, it is also very important that after the global process integration system has been established, the individual heat exchangers, and specially the ones that have been found to be at a very sensitive location, should be properly designed. The shell and tube heat exchanger is the most commonly used type in chemical and process industries. It can be designed to operate over a full range of pressures and temperatures and constructed from several materials. The simplest shell and tube exchanger is the 1-1 design (1 shell pass, 1 tube pass), which is the one that comes closest to pure counter-current flow (Fig. 1(*a*)). It is designed using the basic counter-current equation:

$$Q = UA\Delta T_{LM} \tag{1}$$

For a fixed duty and overall heat transfer coefficient, the 1-1 design requires the lowest surface area. There are many flow arrangements other than the 1-1 design; however, the most common is the 1-2 shell and tube heat exchanger (1 shell pass, 2 tubes passes), as shown in Fig. 1(*b*). This flow arrangement involves part counter-current and part co-current flow, therefore the effective temperature difference for the heat exchanger is reduced compared with a pure counter-current device. This decrease is accounted for in the design by introducing the F_T correction factor into the basic heat exchanger design equation:

$$A = \frac{Q}{UF_T\Delta T_{LM}} \quad \text{where} \quad 0 < F_T < 1 \tag{2}$$

Although requiring a larger area than the 1-1 design, the 1-2 design offers some practical advantages: allowance for thermal expansion, easy mechanical cleaning and good heat coefficients on the tube side (due to higher velocity) [1].

If the F_T value becomes too low it will be necessary to consider either different types of exchangers, or multiple shells arrangements (multiple 1-2 shells or of other type of shells). When multiple shells are required it is necessary to calculate the number of shells needed. This can be done either adopting a trial-and-error approach, in which the number of shells is progressively increased until a satisfactory value of F_T is reached, or using an analytical explicit approach.

In this paper an economic strategy for estimating the number of shells while designing multiple 1-2 shell and tube exchangers is developed. Applying this strategy will guarantee a feasible design, which minimizes the heat exchanger cost.

The strategy developed is fully compatible with the established design procedures. It is based on the numerical formulation given by Ahmad et al. [2] and it uses either their X_P design method, or the design criteria based on the F_T-slopes given by Shenoy [3].

2 The F_T Correction Factor

The F_T correction factor depends only on the inlet and outlet temperatures of the streams in a 1-2 heat exchanger. It is correlated in terms of two dimensionless ratios, the ratio of the heat capacity flow rates of the hot and cold streams R and the thermal effectiveness P of the heat exchanger [1]:

$$F_T = \frac{\sqrt{R^2+1}\,\mathrm{Ln}\left(\dfrac{1-P}{1-RP}\right)}{(R-1)\mathrm{Ln}\left(\dfrac{2-P(R+1-\sqrt{R^2+1})}{2-P(R+1+\sqrt{R^2+1})}\right)} \quad R \neq 1 \tag{3}$$

$$F_T = \frac{\dfrac{\sqrt{2}P}{1-P}}{\mathrm{Ln}\left(\dfrac{2-P(2-\sqrt{2})}{2-P(2+\sqrt{2})}\right)} \quad R = 1 \tag{4}$$

Contributed by the Heat Transfer Division for publication in the JOURNAL OF HEAT TRANSFER. Manuscript received by the Heat Transfer Division November 13, 2002; revision received September 8, 2003. Associate Editor: M. K. Jensen.

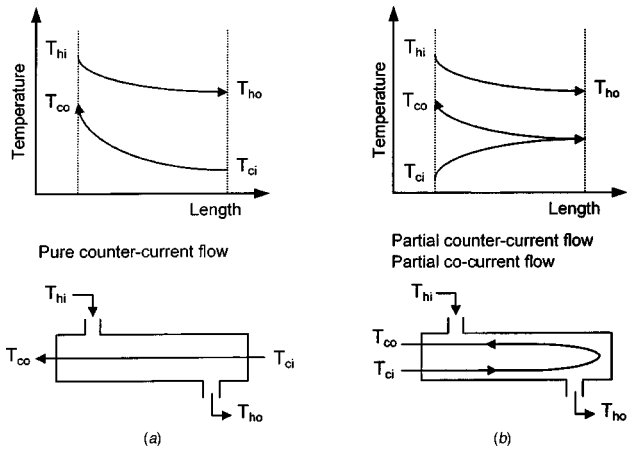

Fig. 1 (*a*) 1-1 shell and tube exchanger with pure counter-current flow; (*b*) 1-2 shell and tube exchanger with partial counter-current and partial co-current flow

where

$$R=\frac{Cp_c}{Cp_h}=\frac{T_{hi}-T_{ho}}{T_{co}-T_{ci}} \tag{5}$$

and

$$P=\frac{T_{co}-T_{ci}}{T_{hi}-T_{ci}} \tag{6}$$

Alternatively, the definitions $R'=1/R$ and $P'=RP$, instead of R and P, can be used, since $F_T(R,P)=F_T(R',P')$.

Depending on the inlet and outlet temperatures of the streams in the 1-2 exchanger, three situations can occur (Fig. 2):

1) The final temperature of the hot stream is higher than the final temperature of the cold stream. This situation is called temperature approach and is straightforward to design for with a single 1-2 shell.

2) The final temperature of the hot stream is slightly lower than the final temperature of the cold stream. This situation, which is called temperature cross, is usually straightforward to design for using a single 1-2 shell, providing the temperature cross is reduced.

3) The difference between the temperatures of the streams increases excessively and there is a large temperature cross. Local reversal of heat flow may be encountered, which is wasteful in heat transfer area. The design may even become infeasible.

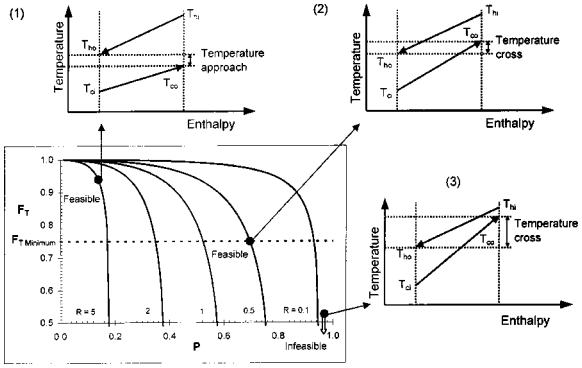

Fig. 2 Generic $F_T(R,P)$ chart and inlet/outlet temperature situations that can occur when using 1-2 heat exchangers: (1) Temperature approach; (2) Small temperature cross; (3) Large temperature cross

It is important to know how much temperature cross can be tolerated before encountering reversal of heat flow or infeasibility. A commonly used rule of thumb requires $F_T \geqslant 0.75$ for the design to be considered practical. However, this criterion can lead to poor designs if not used cautiously.

Regions of steep slope in the F_T chart should be avoided, since any violation of the simplifying assumptions adopted in the approach tends to have a particularly significant effect on those areas. Any uncertainties or inaccuracies in the design data also have a more significant effect on regions where the F_T curves approach a vertical slope, which causes the exchanger performance to become sensitive to small variations in given temperatures. Consequently, to be confident in a design, areas of steep slopes in the F_T chart should be avoided, irrespective of $F_T \geqslant 0.75$ [1,2].

2.1 The X_P Design Method. Ahmad et al. [2] proposed an alternative method to avoid regions of steep slope in the F_T chart. Their approach is based on the fact that for any value of R there is a maximum asymptotic value for P, defined as $P_{\max}$, which occurs as F_T tends to $-\infty$ and can be determined by:

$$P_{\max}=\frac{2}{R+1+\sqrt{R^2+1}} \tag{7}$$

An 1-2 heat exchanger designed for $P=P_{\max}$ will not be feasible, thus for a practical design the value of P must be limited to a fraction of $P_{\max}$:

$$P_{\text{Limit}}=X_P P_{\max} \quad 0<X_P<1 \tag{8}$$

X_P is a fraction defined by the designer, which is chosen to assure the minimum allowable F_T. They have selected X_P to be 0.9 to guarantee that $F_T \geqslant 0.75$ [2].

The F_T correction factor can be expressed as a function of R and X_P by replacing in Eqs. (3) and (4) the thermal effectiveness P by its limit value (P_{Limit}):

$$F_T=\frac{\sqrt{R^2+1}\,\text{Ln}\left[\dfrac{R+1+\sqrt{R^2+1}-2X_P}{R+1+\sqrt{R^2+1}-2RX_P}\right]}{(R-1)\text{Ln}\left[\dfrac{R+1+\sqrt{R^2+1}+X_P(\sqrt{R^2+1}-R-1)}{(R+1+\sqrt{R^2+1})(1-X_P)}\right]} \quad R\neq 1 \tag{9}$$

$$F_T=\frac{2\sqrt{2}X_P}{(2+\sqrt{2}-2X_P)\text{Ln}\left[\dfrac{2+\sqrt{2}+X_P(\sqrt{2}-2)}{(2+\sqrt{2})(1-X_P)}\right]} \quad R=1 \tag{10}$$

For any value of X_P, the F_T correction factor is minimum when R is equal to 1. So, the X_P value that guarantees a chosen $F_{T\,\text{Minimum}}$ is calculated through Eq. (10).

2.2 Design Criteria Based on F_T Slopes. An additional method of avoiding areas of steep slopes in the F_T chart is to consider a constant F_T slope. Ahmad et al. [2] have presented a constant slope criterion in a graphical form for $(\partial F_T/\partial_P)_R = -2.8$. However, their criterion, which is good to guarantee to stay away from those regions, is very complex to use and evaluate, as the authors recognized in their paper. For this reason they have proposed the simpler alternative criterion that was already discussed in Sec. 2.1.

Moreover, in order to develop a numerical, and easy-to-use, constant slope criterion Shenoy [3] has solved the nonlinear analytical equation of the F_T slope with $(\partial F_T/\partial_P)_R=-2.8$ (which is the slope at the point $F_T=0.75$ at $R=1$ given by Ahmad et al. [2]), to obtain X_P (denoted X_{PP}) for different values of R.

By plotting the $X_{PP}(R)$ data, he concluded that the choice of $X_P=0.9$ is not appropriate and can be improved, since X_{PP} varies from 1 (as $R\to 0$) to 0.777 (as $R\to\infty$). Furthermore, he stated that

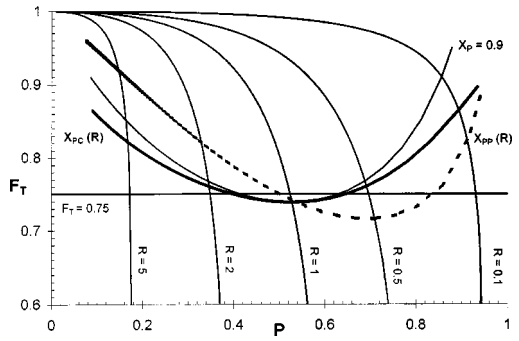

Fig. 3 Different criterions used to define the region of one shell or multiple shell heat exchangers: F_T criterion ($F_{T\,\text{Minimum}}=0.75$), X_P criterion ($X_P=0.9$), slope $(\partial F_T/\partial_P)_R$ approach (X_{PP}) and slope $(\partial F_T/\partial_{Xp})_R$ approach (X_{PC})

the X_P approach, with $X_P=0.9$, is not consistent with the constant slope approach, because it leads to the slope $(\partial F_T/\partial_P)_R$ varying between -0.86 and -8.6 (for $0.1\leqslant R\leqslant 10$).

An explicit expression for X_{PP} as function of R, was determined by curve-fitting the $X_{PP}(R)$ data (Shenoy [3]):

$$X_{PP}=1-\frac{0.223}{\left[1+\left(\frac{0.223}{0.033+0.103R}\right)^{1.4}\right]^{1/1.4}} \tag{11}$$

This equation gives an excellent approximation to the analytical expression for the slope $(\partial F_T/\partial_P)_R$, maintaining the slope close to -2.8 (the actual slope varies between -2.75 and -2.93).

Shenoy [3] has mentioned that the line of constant slope $(\partial F_T/\partial_P)_R=-2.8$ and the line of constant X_P do not have identical profiles, as stated by Ahmad et al. [2]. He noted that the constant X_P approach accepts designs that are rejected according to the constant slope approach for $R>1$, and rejects designs considered acceptable in accordance with the constant slope criteria if $R<1$ (see Fig. 3).

He stated that a criterion in terms of a constant slope $(\partial F_T/\partial_P)_R$ is inappropriate since it is not independent of the definitions used for defining R and P, as in the F_T calculation. In order to obtain equivalent points in both definitions, certain symmetry is required on the F_T chart, which implies the use of a $F_T(X_P,R)$ chart rather than the conventional $F_T(R,P)$ chart.

So, he developed a criterion based on the constant slope $(\partial F_T/\partial_{Xp})_R$. Now, $(\partial F_T/\partial_{Xp})_R$ is chosen to be -1.64 (which is the slope at $F_T=0.75$ and $R=1$), maintaining consistency with previously mentioned criteria based on constant F_T and X_P. The nonlinear equation for the slope $(\partial F_T/\partial_{Xp})_R$ is solved to obtain X_P (denoted X_{PC}) for different values of R. X_{PC} varies from 1 (as $R\to 0$ and $R\to\infty$) to 0.9 (at $R=1$). The critical value of X_P, above which the F_T slope with respect to X_P is unacceptable, is obtained by curve-fitting the X_{PC} data [3]:

$$X_{PC}=1-0.1\,\text{Exp}[-0.5(\text{Log}\,R)^2] \tag{12}$$

This equation gives an excellent approximation to the numerically computed $(\partial F_T/\partial_{Xp})_R=-1.64$ criterion and allows X_P to be explicitly expressed in terms of R [3].

2.3 An Approach Accounting for Temperature Cross. Gulyani [4] stated that neither the traditional rule of thumb $F_T\geqslant 0.75$ nor the X_P design method provided by Ahmad et al. [2] (in which $X_P=0.9$) accounts directly for temperature cross. So, he presented an approach that directly accounts for temperature cross by considering the dimensionless group G:

$$G=\frac{T_{ho}-T_{co}}{T_{hi}-T_{ci}} \tag{13}$$

When the outlet temperatures of the hot and cold fluids are equal then $G=0$, this situation is called temperature meet. Values of G positive correspond to the temperature approach situation and negative G values to the temperature cross situation. G is a more powerful parameter than either R or P, because it provides by itself more information about the temperature situation of the exchanger, and consequently about the value of the F_T correction factor, than does either R or P [5].

2.4 Analysis of the X_P Based Approaches. In Fig. 3 the different X_P based approaches are represented and compared: constant $F_T(F_{T\,\text{Minimum}}=0.75)$, constant X_P (with $X_P=0.9$), constant slope $(\partial F_T/\partial_P)_R$ (through X_{PP}) and constant slope $(\partial F_T/\partial_{Xp})_R$ (using X_{PC}). For each approach there is a division of the F_T chart in two regions: a region of preferred designs above its line, in which only one shell will be used, and a region of unacceptable designs below it, in which case multiple shells are required.

This figure shows that both the constant X_P criterion (with $X_P=0.9$) and the constant F_T slope approaches lead to values of the F_T correction factor inferiors to 0.75.

In the case of the constant X_P approach, the X_P value of 0.9, suggested by Ahmad et al. [2], leads to a F_T correction factor of 0.738682 (Eq. (10)). Thus, to assure a value of $F_{T\,\text{Minimum}}=0.75$, X_P must be set to 0.892937. If a more conservative design is required a new X_P value will be determined by Eq. (10). For instance, for $F_{T\,\text{Minimum}}=0.8$, X_P would be 0.855544.

In the case of the constant slope approaches, F_T values smaller than 0.75 are obtained due to the slope values used to determine the X_{PP} and X_{PC} expressions.

For a $F_{T\,\text{Minimum}}$ of 0.75, X_P should be 0.892937, as shown. Hence, if this X_P value was used the slope $(\partial F_T/\partial_P)_R$, determined analytically by the expression given by Shenoy [3] at $R=1$, would be -2.65076, while the slope $(\partial F_T/\partial_{Xp})_R$ would be -1.55278. If a X_P value of 0.9 is used instead, then the slopes will be -2.82341 and -1.65391, respectively (with $F_T=0.738682$).

If the $(\partial F_T/\partial_P)_R$ slope of -2.65076 is considered, instead of using -2.8 as indicated by Ahmad et al. [2] (which leads to $(\partial F_T/\partial_{Xp})_R=-1.64$), there will be a maximum decrease (at $R=0.7316$) in the heat exchanger surface area of approximately 1.38%. In the case of the slopes values, for $(\partial F_T/\partial_{Xp})_R$, of -1.64 and -1.55278 the maximum area reduction (at $R=1$) that can occur is 1.32%. These area differences are meaningless.

According to the Shenoy approach [3] the minimum value of the F_T correction factor, obtained with X_{PP} (Eq. (11)), do not occur at $R=1$ but at $R=0.537587$, with a F_T value of 0.715719, as illustrated in Fig. 3.

3 Design With Multiple 1-2 Shells

When the F_T correction factor becomes too low or the F_T slopes too large it will be necessary to consider either different types of exchangers, or multiple shells arrangements (multiple 1-2 shells or of other type of shells). In this paper only multiple shell arrangements of the 1-2 type are considered. When 1-2 shells in series are used the temperature cross in each individual shell is reduced below that for a single 1-2 shell for the same duty.

Traditionally, the number of 1-2 shells in series required would be calculated by adopting a trial-and-error approach in which the number of shells is progressively increased until a satisfactory value of F_T is reached. This will not be necessary if the design criterion given by Eq. (8) is adopted.

So, given the streams inlet and outlet temperatures in a 1-2 exchanger, if P (Eq. (6)) is lesser or equal to its limit value P_{Limit}, with X_P determined by any of the approaches discussed, only one shell will be needed and the F_T correction factor will be calculated directly by Eq. (3) or Eq. (4). When P is greater than its limit value, the number of 1-2 shells in series (N) required can be evaluated by [1,2]:

$$N=\frac{\mathrm{Ln}\left(\frac{1-RP}{1-P}\right)}{\mathrm{Ln}(W)}$$
$$W=\left(\frac{R+1+\sqrt{R^2+1}-2RX_P}{R+1+\sqrt{R^2+1}-2X_P}\right) \quad R\neq 1 \tag{14}$$

or

$$N=\left(\frac{P}{1-P}\right)\left(\frac{1+\sqrt{2}/2-X_P}{X_P}\right) \quad R=1 \tag{15}$$

The real (noninteger) value of N determined through Eq. (14) or (15) satisfies precisely the chosen value of X_P throughout the series of 1-2 shells, that is, for each 1-2 shell P will be equal to its limit value.

The number of shells needed is obtained by rounding up to the next largest integer the real value calculated by the mentioned equations. This will result in a slightly decrease of the X_P value in each shell over the originally specified value, and therefore an improvement on the F_T value [2].

So, now the value of P for each 1-2 shell (P_1) will not be equal to its limit value and must be determined. Through Eqs. (16) and (17) it is possible to obtain a relation between P_1 and the value of P over N number of 1-2 shells in series (which is calculated by Eq. (6)) [1]:

$$P_1=\frac{1-\left(\frac{1-RP}{1-P}\right)^{1/N}}{R-\left(\frac{1-RP}{1-P}\right)^{1/N}} \quad R\neq 1 \tag{16}$$

$$P_1=\frac{P}{N+P-NP} \quad R=1 \tag{17}$$

The new value for the F_T correction factor, considering the N series of 1-2 shells, can then be computed through Eq. (3) or (4), but using P_1 instead of P.

Depending on the value of R ($R\neq 1$ or $R=1$) two separated sets of equations are used. This can cause some problems when working in some models solvers where it is not possible to define equations inside an if statement. According to Santos et al. [6], it is possible to eliminate one set of equations by using only the equations for $R\neq 1$, for all values of R, but using the dummy variable given by Eq. (18) instead of R.

$$R_s=R\left[\frac{R-1}{R-0.999}\right]+1.001\left[1-\frac{R-1}{R-0.999}\right] \tag{18}$$

This equation returns $R_s\approx R$ for values of $R\neq 1$ and $R_s=1.001$ for $R=1$.

The use of this equation can lead to an approximation error in the F_T correction factor calculation. This error is inferior to 2% when R and P are such that $F_T\geqslant 0.75$ (for R greater than ≈ 0.0286). For smaller values of R it can reach almost 34% (at $R=0.001$). When $F_T<0.75$ the error increases significantly, mainly in the regions of steep slope in the F_T chart (when $P\approx P_{\max}$ it can reach 300%!), moreover this is a nonrecommended region.

The logarithmic mean temperature difference ΔT_{LM} is calculated by Eq. (19) for $R\neq 1$. If $R=1$ it will be determined through Eq. (20), which is obtained as R tends to 1.

$$\Delta T_{LM}=\frac{(T_{hi}-T_{co})-(T_{ho}-T_{ci})}{Ln\left(\frac{T_{hi}-T_{co}}{T_{ho}-T_{ci}}\right)} \quad R\neq 1 \tag{19}$$

$$\Delta T_{LM}=T_{ho}-T_{ci}=T_{hi}-T_{co} \quad R=1 \tag{20}$$

If it is necessary to use only one equation for all values of R then the logarithmic mean temperature difference ΔT_{LM} can be calculated by the Paterson approximation or by the Chen approximation given by Floudas [7]. The Paterson approximation tends to slightly underestimate the area, while the Chen approximation slightly overestimates the actual area [7].

Among other possible existing forms of capital cost laws used for a single heat exchanger, the one applied in this paper, which is the most common, is given by [1]:

$$C=a+bA^c \tag{21}$$

where A is the heat exchanger surface area (determined by Eq. (2)), and a, b, and c are cost law constants which vary according to materials of construction, pressure rating and type of exchanger.

When multiple shells are used it is assumed that the cost of the heat exchanger, which has a total surface area A and N number of shells, can be determined through Eq. (22), with all shells having the same area.

$$C=a+bN\left(\frac{A}{N}\right)^c=a+\left(\frac{b}{N^{c-1}}\right)A^c \tag{22}$$

Figure 4 presents the 1-2 design algorithm (DeAl_{12}) for obtaining the heat exchanger area and cost.

4 Influence of the Different Approaches on the Heat Exchanger Design

A 1-2 shell and tube exchanger with multiple shells could be designed through the DeAl_{12} described in Sec. 3. However, the application of that algorithm requires the knowledge of one parameter: X_P, $X_{PP}(R)$, or $X_{PC}(R)$. Then two main questions should be answered: (1) What approach should be used, since they do not have identical profiles? (2) Will there be any difference in the heat exchanger area and cost if different approaches are used?

In order to obtain some general guidelines in real applications, the approaches based on constant X_P (Sec. 2.1) and on constant F_T slopes (Sec. 2.2) presented in Table 1 will be compared in this section. Five approaches (Ap1 to Ap5) were used to illustrate the three general criteria given by the previous authors [2,3]: constant X_P value (Ap1, Ap2, and Ap3), constant F_T slope $(\partial F_T/\partial_P)_R$ (Ap4) and constant F_T slope $(\partial F_T/\partial_{Xp})_R$ (Ap5). These approaches will be applied to a set of exchangers (E1 to E7) as a test case (Table 2). The other required input data is given in Table 3, as the heat load, global transfer coefficient and the capital cost law constants.

Table 4 and Fig. 5 show the design results, for each approach, of E1, E2, and E3 heat exchangers. According to all approaches (Ap1 to Ap5), it will be required multiple shells for all the heat exchangers.

Table 5 and Fig. 6 show the design results, for each approach, of E4, E5, E6, and E7 exchangers. Depending on the criterion used, either one shell will be enough or multiple shells will be required.

As shown in Tables 4 and 5 the choice of the approach adopted is very important, since in some cases it leads to significant differences in the area and cost results. In the case of the E4 exchanger the cost divergence reaches a value of 19.8% ($\in$ 25,200). These discrepancies are only observed when N varies with the approaches, due to the X_P variation. As a consequence of this variation the P_1, the F_T, the area and the cost values are also modified. The number of shells will vary with two different approaches if:

- for one approach the heat exchanger design falls in the region of the F_T chart above its line with only one shell used and for the other approach it stays below it requiring multiple shells (e.g., E4 to E7 exchangers);

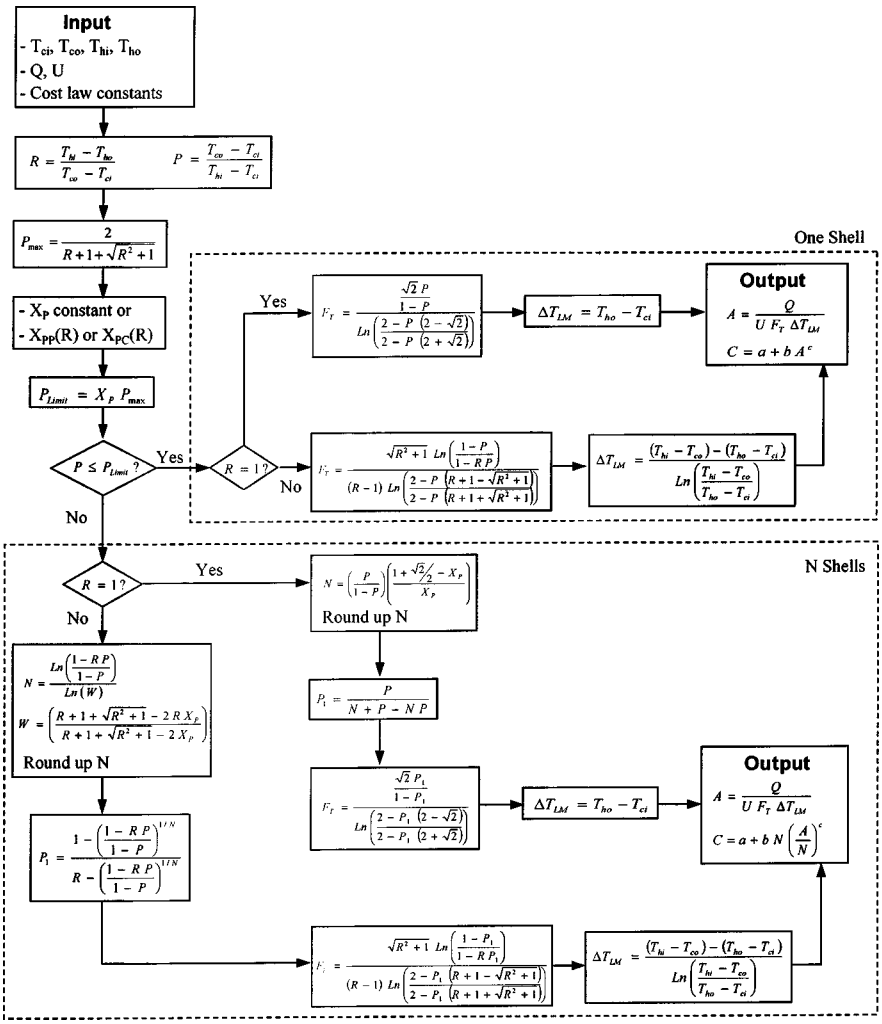

Fig. 4 Heat exchanger area and cost design algorithm (DeAl$_{12}$)

- R, P, and X_P values are such that N varies, although according to both approaches multiple shells will be necessary (e.g., E3 exchanger).

Table 1 Value of X_P and of $F_{T\,\text{Minimum}}$ at $R = R_{\text{Minimum}}$ for each approach

Approaches		X_P	$F_{T\,\text{Minimum}}$	R_{Minimum}
Constant X_P	Ap1	0.855544*	0.8	1
	Ap2	0.892937*	0.75	1
	Ap3	0.9	0.738682	1
Constant slope	Ap4	$X_{PP}(R)$	0.715719	0.537587
	Ap5	$X_{PC}(R)$	0.738682	1

*Obtained by Eq. (10) assuming the specified fixed value of $F_{T\,\text{Minimum}}$.

Table 2 Temperature data, R and P values for each exchanger

Exchanger	Thi (°C)	Tho (°C)	Tci (°C)	Tco (°C)	R	P
E1	562	92	26	120	5	0.175
E2	381.2	314	0	336	0.2	0.881
E3*	410	110	0	360	0.833	0.878
E4	560	125	1	88	5	0.156
E5	540	162	10	174	2.305	0.309
E6	388	322	0	330	0.2	0.851
E7	394	329	0	325	0.2	0.825

*Example from Ahmad et al. [2], with $P > P_{\max}$.

For E4 to E7 exchangers an increase of N led to an increase in the design cost, in spite of the area decrease. However, in the case of exchanger E3 this is not true since both area and cost decreased as N increased. So, it is necessary to know how a variation in the number of shells (N) and in the exchanger area (A) influences the exchanger cost. In order to choose the approach that minimizes the heat exchanger cost, it is also important to see how a variation in X_P affects the N and A values, and as a result the exchanger cost. This will be analyzed in Sec. 5.

The approaches $Ap1$ to $Ap5$ were also applied to the set of exchangers but using the dummy variable R_s given by Santos et al. [6] instead of R (see Sec. 3). The results obtained are approximately the same for all exchangers and approaches (Tables 4 and 5) except for exchanger E5 with approach $Ap3$ (Table 6).

In this case, for the approach adopted, when R is used $P > P_{\text{Limit}}$ and if R_s is chosen $P < P_{\text{Limit}}$. Therefore there are differ-

Table 3 Heat exchanger duty (Q), overall heat exchanger transfer coefficient (U) and capital cost law constants (a, b, and c)

		Cost law constants: $C = a + bA^c$(€)		
Q (kW)	U (kW/m^2/K)	a	b	c
2 000	0.1	0	7 000	0.65

Table 4 Design results for E1, E2, and E3 exchangers

Exchanger	N	P_1	F_T	A (m^2)	C (k€)	ΔA (%)	ΔC (%)	Approaches
E1	2	0.133	0.949	106.6	185.6	⋯	⋯	all
E2	2	0.672	0.946	152.4	234.1	⋯	⋯	all
E3	4	0.567	0.759	346.1	508.5	13.2	0.267	2, 3, 4, 5
	5	0.506	0.860	305.7	507.2	⋯	⋯	1

Note: For each approach, ΔA and ΔC represent the area and cost difference from its minimum value when considering all the approaches for a given exchanger.

ences in the number of shells, and consequently in the F_T correction factor and in the heat exchanger area and cost.

5 A Design Strategy That Minimizes the Heat Exchanger Cost

In this section an economic strategy for estimating the number of shells while designing multiple 1-2 shell and tube exchangers that minimizes the heat exchanger cost is developed. In order to do this it is important to know how a change in the X_P value, due to the use of different approaches, affects the exchanger cost.

Thus, in the first part it will be studied the influence of X_P value in the number of shells and in the area of the exchanger. In the second part it will be analyzed how these values (N and A) affect the exchanger cost. And finally, it will be developed a design strategy that minimizes the exchanger cost, which take into account the effect of X_P in the heat exchanger cost.

5.1 Influence of X_P on the Heat Exchanger Number of Shells and Total Area. The number of shells of a heat exchanger, which is determined through Eqs. (14) and (15), varies with R, P, and X_P parameters. So, to determine the influence that X_P has on N, it is necessary to differentiate those equations in order to obtain the derivative $\partial N/\partial X_P$ (Eqs. (A1) and (A2) of the appendix). Since $\partial N/\partial X_P<0$, $\forall_{R,P,X_P}$, N decreases when X_P increases.

The DeAl$_{12}$ algorithm used in the design of multiple 1-2 shell and tube exchangers (Fig. 4), shows that an alteration in the X_P value causes a variation of the exchanger area because it modifies the number of shells, and consequently the value of P for each 1-2 shell (P_1), and as a result F_T.

To evaluate the influence of X_P on the area value it is necessary to obtain the behavior of P_1 and F_T with X_P. Thus, Eqs. (16) and (17) were differentiated in order to obtain the derivatives expressions for $\partial P_1/\partial N$ (Eqs. (A3) and (A4) of the appendix). Since $\partial P_1/\partial N<0$, $\forall_{R,P,N}$, P_1 decreases when N increases.

In conclusion, an increase of the X_P value leads to a decrease of N, which causes an increase of P_1, leading to a reduction on F_T (see Fig. 3), and consequently to a greater value of the exchanger area A (see Eq. (2)), as summarized in Table 7.

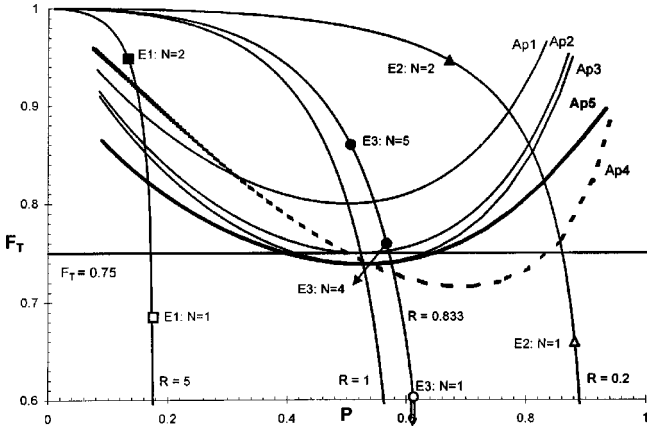

Fig. 5 Design results for E1, E2, and E3 exchangers according to approaches Ap1 to Ap5. For each criterion, above its line one shell is used and below it multiple shells are required. (△,○,□)—Infeasible points obtained with $N=1$; (▲,●,■)—Design results

5.2 Effect of the Number of Shells and Area on the Heat Exchanger Cost. To analyze how an increase of X_P influences the heat exchanger cost, two approaches were compared separately: approach 1 and 2 (Fig. 7). Choosing one approach or the other it is not the same, that is, they lead to different values of N and therefore to different area and cost values. Note that the remaining parameters (e.g., temperatures of the streams, Q, U, ...) do not change, the only modification is on X_P due to the use of different criteria. So, if X_{P1} and X_{P2} are defined as:

$$X_{P1}=X_P^{\mathrm{Api}}$$

$$X_{P2}=X_P^{\mathrm{Apj}}$$

where approaches Api and Apj, chosen from Ap1 to Ap5 presented in Table 1, are such that:

$$X_P^{\mathrm{Api}}\geqslant X_P^{\mathrm{Apn}}$$

$$X_P^{\mathrm{Apj}}\leqslant X_P^{\mathrm{Apn}} \quad \text{with} \quad n=1,\ldots,5.$$

Then,

$$X_{P1}>X_{P2}$$

$$N_1<N_2$$

$$F_{T1}<F_{T2}$$

Table 5 Design results for exchangers E4, E5, E6, and E7

Exchanger	N	P_1	F_T	A (m^2)	C (k€)	ΔA (%)	ΔC (%)	Approaches
E4	1	0.156	0.887	86.6	127.2	9.95	⋯	2, 3, 5
	2	0.109	0.976	78.7	152.4	⋯	19.8	1, 4
E5	1	0.309	0.779	105.4	144.6	22.5	⋯	5
	2	0.214	0.954	86.1	161.5	⋯	11.7	1, 2, 3, 4
E6	1	0.851	0.780	166.5	194.6	23.0	⋯	4
	2	0.629	0.959	135.4	216.8	⋯	11.4	1, 2, 3, 5
E7	1	0.825	0.832	144.5	177.4	16.2	⋯	4, 5
	2	0.597	0.966	124.3	205.1	⋯	15.6	1, 2, 3

Note: For each approach, ΔA and ΔC represent the area and cost difference from its minimum value when considering all the approaches for a given exchanger.

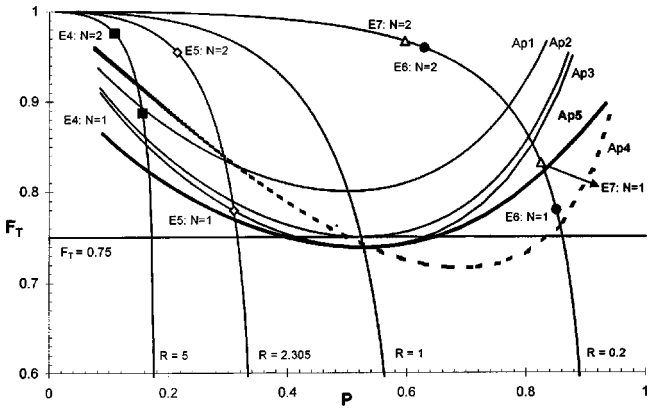

Fig. 6 Design results for E4, E5, E6, and E7 exchangers according to the approaches Ap1 to Ap5. For each criterion, above its line one shell is used and below it multiple shells are required.

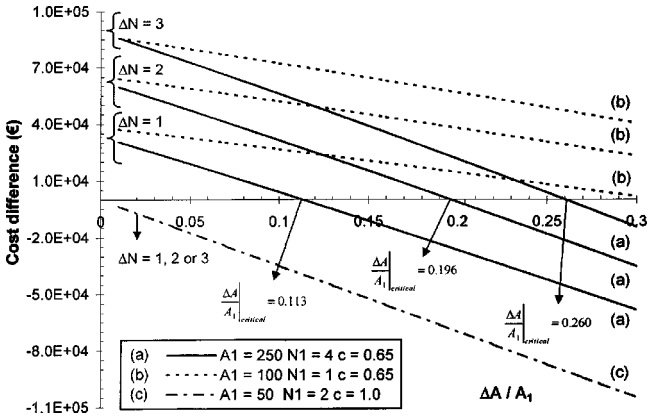

Fig. 8 Effect of the area reduction fraction ($\Delta A/A_1$) in the cost difference value (ΔC), for different A_1, N_1, ΔN and cost law constant c illustrative values, with $b=7\,000$

$$A_1 > A_2$$

The increase on the number of shells (ΔN) due to the use of different approaches is given by:

$$\Delta N = N_2 - N_1 \tag{23}$$

The area reduction fraction ($\Delta A/A_1$) is calculated through Eq. (24):

$$\frac{\Delta A}{A_1} = \frac{A_1 - A_2}{A_1} = \frac{F_{T2} - F_{T1}}{F_{T2}} \tag{24}$$

Table 6 Results for exchanger E5 and approach *Ap*3 using *R* and R_s

Results	$R=2.3049$	$R_s=2.3039$	Deviation (%)
P	0.3094	0.3094	0
$F_T(N=1)$	0.7789	0.7793	0.0531
P_{max}	0.3438	0.3439	0.0329
P_{Limit}	0.3094 ($P>P_{Limit}$)	0.3095 ($P<P_{Limit}$)	0.0329
N	2	1	50.00
P_1	0.2141	0.3094	44.50
$F_T(DeAl_{12})$	0.9543	0.7793	18.34
A (m^2)	86.06	105.4	22.46
C (k€)	161.5	144.5	10.50

Table 7 Influence of X_P on N, on P_1, on F_T and on A

X_P	N	P_1	F_T	A
↑	↓	↑	↓	↑

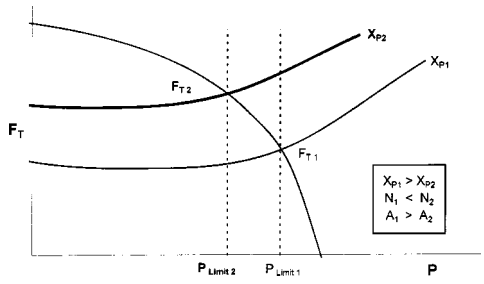

Fig. 7 Approaches 1 and 2, with X_P equal to X_{P1} and X_{P2}, respectively, which lead to different values of the number of shells and area of the exchanger

Considering that the allowed range for the F_T value is between 0.7 and 1.0, the maximum area reduction fraction allowed—$(\Delta A/A_1)_{max}$—is given by:

$$\left.\frac{\Delta A}{A_1}\right|_{max} = \frac{1-0.7}{1} = 0.3$$

Cost Difference—ΔC. The heat exchanger cost is determined by Eq. (22). So, if C_1 represents the exchanger cost when approach 1 is chosen and C_2 the cost when approach 2 is selected, then the resulting cost difference (ΔC) will be determined through Eq. (25), with N_2 and A_2 replaced by Eqs. (23) and (24), respectively.

$$\Delta C = C_2 - C_1 = [N_1 + \Delta N] b \left(\frac{A_1(1-\Delta A/A_1)}{N_1 + \Delta N} \right)^c - N_1 b \left(\frac{A_1}{N_1} \right)^c \tag{25}$$

The cost difference depends only on N_1, A_1, ΔN, and $\Delta A/A_1$ values, for each fixed set of the capital cost law constants b and c. Figure 8 presents the variation of ΔC with the area reduction fraction (until $(\Delta A/A_1)_{max}$) for the specified A_1, N_1, and ΔN values and with the constants b and c indicated.

Figure 8 shows that three situations can occur: (1) the cost difference is always positive (lines corresponding to case b); (2) it is positive until a critical value of the area reduction fraction—$(\Delta A/A_1)_{critical}$—and negative for greater values than $(\Delta A/A_1)_{critical}$ (lines corresponding to case a). This critical parameter corresponds to a cost difference value of zero; (3) the cost difference value is always negative (case c), since $(\Delta A/A_1)_{critical}$ is either equal to zero or negative.

Three distinct cases arise from this analysis (Table 8):

1. ΔC value is positive: $C_2 > C_1$, and therefore it is more advantageous to select approach 1. In this case, the area reduction is not enough to reduce the exchanger cost, that is, the effect of the increase of the number of shells prevails.
2. ΔC is negative: $C_2 < C_1$, and consequently it is more advisable to choose approach 2. Now, the effect of the area reduction in the exchanger cost prevails over the influence of the number of shells increase.

Table 8 Choice of approach 1 or 2 depending on ΔC value

ΔC value	Best approach
$\Delta C>0$	1
$\Delta C=0$	1 or 2
$\Delta C<0$	2

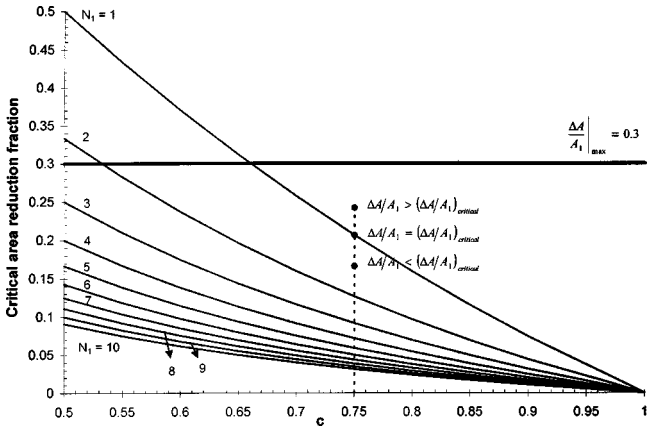

Fig. 9 Variation of the critical area reduction—$(\Delta A/A_1)_{critical}$—with the cost law constant c and the number of shells N_1, for $\Delta N=1$

3. ΔC is equal to zero and either approach 1 or 2 can be used.

Therefore, for case b illustrated in Fig. 8, approach 1 should be chosen. For case a, in order to choose the more advantageous approach the $(\Delta A/A_1)_{critical}$ value must be known. If the area reduction fraction is inferior to this value approach 1 should be used, if is superior is more advisable to choose approach 2. For case c it should be selected approach 2.

Critical Area Reduction Fraction—$(\Delta A/A_1)_{critical}$. As it was mentioned, the critical area reduction fraction—$(\Delta A/A_1)_{critical}$—corresponds to the $\Delta A/A_1$ value that leads to a cost difference (ΔC) of zero. Therefore, Eq. (26) is obtained when the nonlinear Eq. (25) is solved in order to $\Delta A/A_1$ with $\Delta C=0$.

$$\left.\frac{\Delta A}{A_1}\right|_{critical} = 1-\left[\frac{N_1+\Delta N}{N_1}\right]^{(c-1)/c} \tag{26}$$

Figure 9 shows the variation of $(\Delta A/A_1)_{critical}$ with the cost law constant c and N_1, for $\Delta N=1$.

Each line shown in Fig. 9 represents the critical area reduction fraction for a specific value of N_1, which depends on the value of the constant c. For the points above each curve presented, in which $\Delta A/A_1>(\Delta A/A_1)_{critical}$, the cost difference is negative and therefore it is more advantageous to use approach 2. For the points below it, in which $\Delta A/A_1<(\Delta A/A_1)_{critical}$, it is better to select approach 1 since $\Delta C>0$.

These results show that it is necessary to know the effective area reduction fraction due to the use of the different approaches 1 or 2, which is carried out through Eq. (26). However, this can be simplified if another area reduction fraction concept is introduced as a decision parameter.

Limit Area Reduction Fraction—$(\Delta A/A_1)_{Limit}$. The maximum area reduction that can exist due to the X_P variation (as a infeasible stopping limit) corresponds to a decrease from its initial value A_1 to its limit value $A_2=0$. Thus, the corresponding limit area reduction fraction—$(\Delta A/A_1)_{Limit}$—is:

$$\left.\frac{\Delta A}{A_1}\right|_{Limit} = \frac{A_1-0}{A_1} = 1$$

It is important to know the cost difference value when the limit area reduction fraction is reached—$\Delta C|_{\Delta A/A1=1}$ or $\Delta C|_{(\Delta A/A1)Limit}$, which is obtained by considering in Eq. (25) that $\Delta A/A_1=1$:

$$\Delta C|_{\Delta A/A_1=1} = -b\left(\frac{A_1}{N_1}\right)^c N_1 \tag{27}$$

$\Delta C|_{\Delta A/A1=1}$ is always negative, therefore the critical area reduction fraction value can always be determined, being either positive or negative or equal to zero.

Figure 10 and Table 9 summarizes the situations that can occur when using the different approaches 1 and 2. In order to choose the best approach, it is necessary to determine the critical area reduction fraction. When $(\Delta A/A_1)_{critical}>(\Delta A/A_1)_{max}$ it is not necessary to calculate the effective area reduction fraction, and it is best to use approach 1 since ΔC is positive within the operational $\Delta A/A_1$ interval: 0–0.3 (line 1). When $(\Delta A/A_1)_{critical}\leqslant 0.3$, but a positive value, it must be known the effective area reduction fraction (line 2). In this case, if $\Delta A/A_1<(\Delta A/A_1)_{critical}$ the cost difference is positive and therefore approach 1 should be chosen. If $\Delta A/A_1>(\Delta A/A_1)_{critical}$ the cost difference is negative and consequently approach 2 should be selected. If $\Delta A/A_1=(\Delta A/A_1)_{critical}$ it is indifferent the choice of the approach since $\Delta C=0$. When $(\Delta A/A_1)_{critical}\leqslant 0$ the cost difference is always negative, therefore, approach 2 should be used (line 3).

5.3 Strategy Design Algorithm (StratDeAl$_{12}$). Considering the approaches 1 and 2, in which $X_{P1}>X_{P2}$ and therefore $P_{Limit\,1}>P_{Limit\,2}$, there are three possible design situations that are represented in Fig. 11:

Situation 1: $P\leqslant P_{Limit\,2}<P_{Limit\,1}$. For both approaches the exchanger design falls in the region of preferred designs in the F_T chart and consequently only one shell will be required, with $N_1=N_2=1$ and therefore $\Delta N=\Delta A=0$.

Situation 2: $P_{Limit\,2}<P\leqslant P_{Limit\,1}$. The design falls in the F_T chart region above approach 1 line and therefore $N_1=1$, and below approach 2 line and consequently $N_2>1$. As a result $\Delta N\neq 0$ and $\Delta A\neq 0$ and it will be necessary to analyze which approach is the best choice, as discussed in Sec. 5.2.

Situation 3: $P>P_{Limit\,1}$. The exchanger design is below both approaches lines in the F_T chart, requiring more than one shell. However, for this case, depending on R, P, and X_P values, there are two possible situations: (3a) N varies with the approaches 1 and 2 (with $\Delta N\neq 0$ and $\Delta A\neq 0$) and it is necessary to choose the more advantageous approach; (3b) N is the same for both approaches $(\Delta N=\Delta A=0)$ and it is indifferent which approach is used.

The X_P values for approaches 1 and 2 (X_{P1} and X_{P2}) depend on the criteria and on the minimum allowable value for F_T. Figure 12 shows the X_P variation with R for the constant X_P criteria and the constant slope approaches presented in Table 1 of Sec. 4. Thus, X_{P1} and X_{P2} values, given in Table 10, are the X_P extreme values for the defined R decision intervals based on the approaches presented in Sec. 4.

Figure 13 illustrates the strategy design algorithm

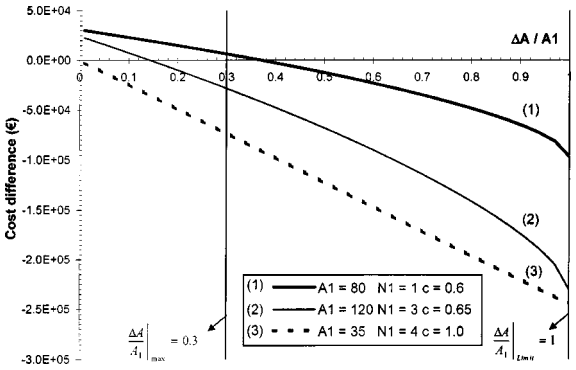

Fig. 10 Three situations that can occur due to the use of the different approaches 1 and 2, for $\Delta N=1$ and $b=7\,000$: (1) $(\Delta A/A_1)_{critical}>(\Delta A/A_1)_{max}$; (2) $0<(\Delta A/A_1)_{critical}<(\Delta A/A_1)_{max}$; (3) $(\Delta A/A_1)_{critical}\leqslant 0$

Table 9 Selection of approach 1 or 2 according to $(\Delta A/A_1)_{critical}$ and $\Delta A/A_1$ values

$(\Delta A/A_1)_{critical}$		$\Delta A/A_1$	Best approach
$(\Delta A/A_1)_{critical}>0.3$	⋯	⋯	1
$(\Delta A/A_1)_{critical}\leqslant 0.3$	$(\Delta A/A_1)_{critical}\leqslant 0$	⋯	2
	$(\Delta A/A_1)_{critical}>0$	$\Delta A/A_1<(\Delta A/A_1)_{critical}$	1
		$\Delta A/A_1=(\Delta A/A_1)_{critical}$	1 or 2
		$\Delta A/A_1>(\Delta A/A_1)_{critical}$	2

($StratDeAl_{12}$) developed. As a first decision step it should be tested if $P\leqslant P_{Limit\,2}$, which corresponds to situation 1 and therefore a single 1-2 shell is used. When $P>P_{Limit\,2}$ (situation 2, 3a, or 3b) the ΔN value must be analyzed. If $\Delta N=0$ (situation 3b) it will be determined the number of shells required, and the area and cost values, according to approach 1. A value of $\Delta N\neq 0$ corresponds either to situation 2, or to situation 3a. In both cases it is necessary to determine the more advantageous approach based on the critical area reduction fraction value, as illustrated in Table 9 (discussed in Sec. 5.2).

6 Examples

In order to illustrate the capabilities of the algorithm developed in the previous section, the $StratDeAl_{12}$ was applied to a set of five heat exchangers design cases: Ex1 to Ex5. The temperature data, the heat load (Q), the global heat transfer coefficient (U) and the capital cost law constants (a, b, and c) for the design examples considered are given in Table 11.

Figures 14 and 15 show the location in the F_T chart and the temperature situation of each design example. Example Ex1 corresponds to the temperature approach situation ($T_{ho}>T_{co}$), Ex3 to the temperature meet situation ($T_{ho}=T_{co}$) and Ex2, Ex4, and Ex5 to the temperature cross situation ($T_{ho}<T_{co}$).

Table 12 presents some parameters (as R, P, X_{P1}, X_{P2}, and $P_{Limit\,2}$) and the design results for each example problem (Ex1 to Ex5). The design example Ex1 falls in the preferred designs region of the F_T chart for approaches 1 and 2 since $P<P_{Limit\,2}$, and consequently only one shell is required.

The design example Ex2 is in the region of the F_T chart below approaches 1 and 2 lines since $P>P_{Limit\,1}$ and therefore requires more than one shell. Temperature cross is too large to use only one shell. For this case it is indifferent which approach is used because $\Delta N=0$, and consequently is selected approach 1.

In the case of example Ex3, $P>P_{Limit\,2}$ and $\Delta N=1$. It is then necessary to determine the more advantageous approach. $(\Delta A/A_1)_{critical}>0.3$ and consequently approach 1 is the best choice. The design is in the F_T chart region above approach 1 line and below approach 2 line: $P_{Limit\,2}<P<P_{Limit\,1}$. There is no temperature cross, however it is necessary more than one shell according to the more conservative approach 2. If this approach was selected the cost increase would be 14.3%.

The example design Ex4 is also in the F_T chart region above approach 1 line and below approach 2 line, however for this exchanger $(\Delta A/A_1)_{critical}=0$ and therefore approach 2 is the best choice. In this case there is a small temperature cross that is tolerated by approach 1 but not by approach 2. The choice of approach 1 would originate an increase on the exchanger cost of 23.1%.

In the last example (Ex5), the design falls in the region of the F_T chart below both approaches lines requiring more than one shell. However, for this case it is not indifferent the approach used, since $\Delta N\neq 0$. As $0<(\Delta A/A_1)_{critical}<0.3$ it is necessary to know the effective area reduction fraction. So, because $\Delta A/A_1>(\Delta A/A_1)_{critical}$ approach 2 is chosen. Selecting approach 1 would lead to a cost increase of 6.21%. This example has the largest temperature cross, and consequently requires the greatest number of shells.

The results obtained by applying the $StratDeAl_{12}$ to these five examples show how much the heat exchanger cost could be reduced if a correct approach is chosen. The literature approaches even similar could provide small differences in the heat exchanger area and number of shells with a consequent increase of the equipment cost value.

7 Conclusions

Within the overall objective of energy optimization of an industrial process, it is of great importance to improve the efficiency of individual heat exchangers.

This paper shows the several criteria to design multiple shell and tube heat exchangers based on the F_T correction factor. This factor could be obtained using the different X_P approaches already established in the literature or by the alternative G factor introduced by Gulyani [4].

For a chosen X_P based approach it was established, in this paper, a Design Algorithm ($DeAl_{12}$) showing the calculations path to obtain the needed number of shells, the final area and cost of the heat exchanger.

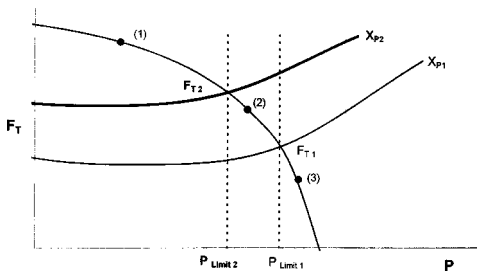

Fig. 11 Heat exchanger design situations that can occur with the approaches 1 and 2: (1) $P\leqslant P_{Limit\,2}$; (2) $P_{Limit\,2}<P\leqslant P_{Limit\,1}$; (3) $P>P_{Limit\,1}$

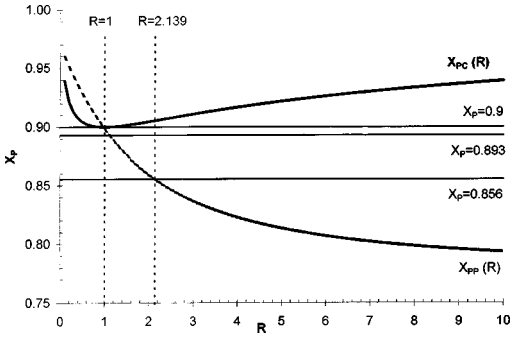

Fig. 12 X_P variation with R for the constant X_P criterions and constant slopes approaches presented in Table 1 of Sec. 4

Table 10 X_{P1} and X_{P2} values in each R interval, for the approaches presented in Table 1 of Sec. 4

	$R\leqslant 1$	$1<R\leqslant 2.139$	$R>2.139$
X_{P1}	X_{PP}(R)	X_{PC}(R)	$X_{PC}(R)$
X_{P2}	0.855544	0.855544	$X_{PP}(R)$

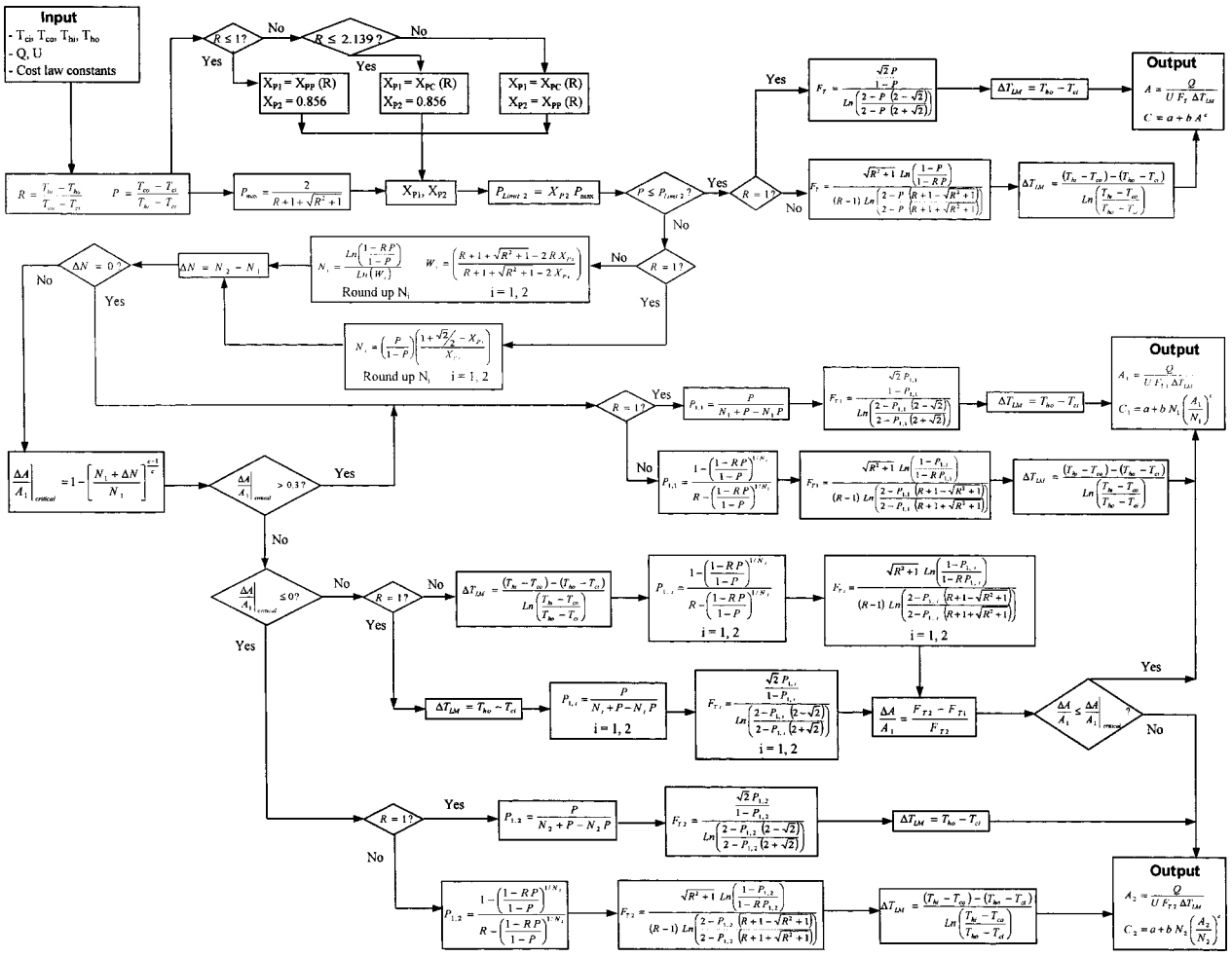

Fig. 13 Strategy design algorithm (StratDeAl$_{12}$), which minimizes the heat exchanger cost

Some design examples show significant differences (up to 20%) in the values of the heat exchanger cost using the mentioned literature X_P approaches.

This study presents a new strategy for the design of multiple shell and tube heat exchangers focused on the cost minimization. The algorithm that applies this strategy was called StratDeAl$_{12}$. It provides the best route to get a final design by introducing the concept of critical and limit area reduction fraction.

StratDeAl$_{12}$ is illustrated, in this paper, with five heat exchanger design examples. The main result is that in two of them the choice is equivalent and for the other three the cost reduction is between 6.21% and 23.1%.

Acknowledgments

The authors gratefully acknowledge financial support from the Portuguese National Team on Process Integration (GNIP-Grupo Nacional de Integração de Processos).

Table 11 Temperature data, heat exchanger duty (Q), overall heat transfer coefficient (U) and capital cost law constants (a, b, and c) for each design example (Ex1 to Ex5)

Example	Ex1	Ex2	Ex3	Ex4	Ex5[1]
Thi (°C)	500	500	570	400	410
Tho (°C)	270	130	150	320	110
Tci (°C)	40	40	50	120	0
Tco (°C)	195	180	150	330	360
Q (kW)	2 000	2 000	2 000	2 000	2 000
U (kW/m^2/K)	0.1	0.1	0.1	0.1	0.1
a[2]	0	0	0	40 000	8 600
b[2]	7 000	7 000	7 000	2 300	670
c[2]	0.65	0.65	0.65	1.0	0.83

[1]Example from Ahmad et al. [2], with $P > P_{max}$, discussed in Sec. 4 (exchanger E3)
[2]Capital cost law: $C = a + bA^c(€)$.

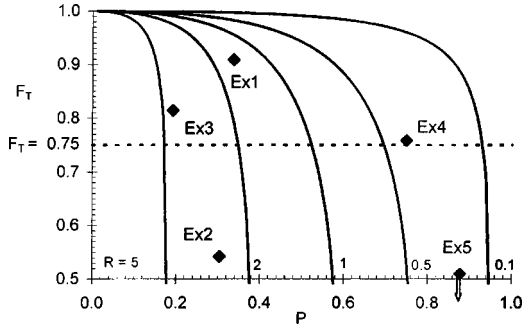

Fig. 14 Location in the $F_T(R,P)$ chart of each design example (Ex1 to Ex5)

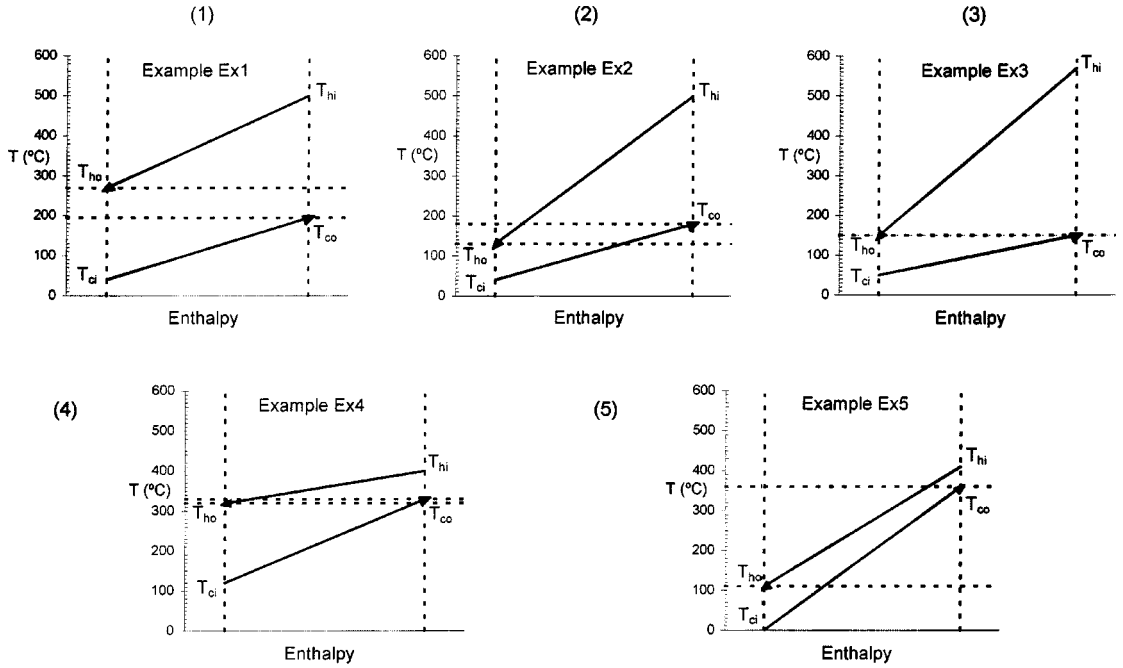

Fig. 15 Inlet/outlet temperature situations corresponding to each design example: (1) Ex1 to (5) Ex5

Nomenclature

A = heat exchanger area, m^2
C = heat exchanger capital cost, €
Cp = heat capacity flow rate, kW/°C
F_T = logarithmic mean temperature difference correction factor, dimensionless
$F_{T\ \text{Minimum}}$ = minimum allowed logarithmic mean temperature difference correction factor, dimensionless
G = parameter presented by Gulyani, dimensionless
N = number of 1-2 shells in series, dimensionless
P = heat exchanger thermal effectiveness, dimensionless
P_1 = thermal effectiveness for each 1-2 shell in the series, dimensionless
$P_{1,1}$ = thermal effectiveness of each 1-2 shell in the series for approach 1, dimensionless
$P_{1,2}$ = thermal effectiveness of each 1-2 shell in the series for approach 2, dimensionless
P_{Limit} = limit value for P, dimensionless
$P_{\max}$ = maximum (asymptotic) value of P, dimensionless
Q = heat exchanger duty, kW
R = heat capacity flow-rate ratio, dimensionless
R_s = dummy variable for R defined by Santos, dimensionless
T_{ci} = cold stream inlet temperature, °C
T_{co} = cold stream outlet temperature, °C
T_{hi} = hot stream inlet temperature, °C
T_{ho} = hot stream outlet temperature, °C
U = overall heat exchanger transfer coefficient, $kW/m^2/K$
X_P = parameter defined by Ahmad et al., dimensionless
X_{PC} = X_P expression determined by Shenoy that maintains the slope $(\partial F_T/\partial_{Xp})_R \approx -1.64$, dimensionless
X_{PP} = X_P expression determined by Shenoy that maintains the slope $(\partial F_T/\partial_P)_R \approx -2.8$, dimensionless

Greek Symbols

ΔA = heat exchanger area difference due to the use of approaches 1 and 2, m^2
$\Delta A/A_1$ = heat exchanger area reduction fraction, dimensionless

Table 12 Parameters and results obtained by applying the StratDeAl$_{12}$, described in Sec. 5, for each design example (Ex1 to Ex5)

Example	Ex1	Ex2	Ex3	Ex4	Ex5
R	1.484	2.643	4.200	0.3810	0.8333
P	0.3370	0.3043	0.1923	0.7500	0.8780
X_{P1}	X_{PC}:0.901	X_{PC}:0.908	X_{PC}:0.918	X_{PP}:0.937	X_{PP}:0.907
X_{P2}	0.856	X_{PP}:0.844	X_{PP}:0.821	0.856	0.856
$P_{\text{Limit 2}}$	0.4004	0.2609	0.1725	0.6981	0.5458
ΔN	⋯	0	1	1	1
$(\Delta A/A_1)_{\text{critical}}$	⋯	⋯	0.3115	0	0.04468
$\Delta A/A_1$	⋯	⋯	⋯	⋯	0.1168
Approach chosen	⋯	1	1	2	2
N	1	2	1	2	5
F_T	0.9089	0.9289	0.8142	0.9518	0.8599
A (m^2)	82.81	118.7	110.2	169.7	305.7
C (k€)	123.6	199.1	148.7	430.3	110.4

$(\Delta A/A_1)_{\text{critical}}$ = critical area reduction fraction, dimensionless
$(\Delta A/A_1)_{\text{Limit}}$ = limit area reduction fraction, dimensionless
$(\Delta A/A_1)_{\max}$ = maximum allowed area reduction fraction, dimensionless
ΔC = heat exchanger capital cost difference due to the use of approaches 1 and 2, €
ΔN = number shells difference due to the use of approaches 1 and 2, dimensionless
ΔT_{LM} = logarithmic mean temperature difference, °C

Subscripts

1 = approach 1
2 = approach 2
c = cold stream
h = hot stream
i = inlet
max = maximum
o = outlet

Appendix

Differential Equations of $\partial N/\partial X_P$ for $R \neq 1$ and for $R = 1$. The following derivative expressions for $\partial N/\partial X_P$ were calculated by differentiating Eqs. (14) and (15), using the software Mathematica 4.1.0.0 of the Wolfram Research Inc.:

$$\frac{\partial N}{\partial X_P} = \frac{2(R-1)\text{Ln}\left(\frac{1-RP}{1-P}\right)}{(1-P_{\text{Limit}})(1-RP_{\text{Limit}})(R+1+\sqrt{R^2+1})\left[\text{Ln}\left(\frac{1-RP_{\text{Limit}}}{1-P_{\text{Limit}}}\right)\right]^2} \quad \text{if } R \neq 1 \tag{A1}$$

where P_{Limit} is determined through Eq. (8).

$$\frac{\partial N}{\partial X_P} = \frac{(-P)(2+\sqrt{2})}{2(1-P)X_P^2} \quad \text{if } R = 1 \tag{A2}$$

The denominator of Eqs. (*A*1) and (*A*2) is always positive. The numerator of Eq. (*A*1) is the product of two expressions: one positive and one negative, and therefore it is always negative. The numerator of Eq. (*A*2) is also always negative. So, by both equations it can be concluded that $\partial N/\partial X_P < 0 \forall_{\text{R,P,X}_\text{p}}$, and therefore that N decreases when X_P increases.

Differential Equations of $\partial P_1/\partial N$ for $R \neq 1$ and for $R = 1$. The derivative expressions for $\partial P_1/\partial N$ were determined with the software Mathematica 4.1.0.0 of the Wolfram Research Inc., through Eqs. (16) and (17).

$$\frac{\partial P_1}{\partial N} = \frac{\left[\frac{1-RP}{1-P}\right]^{1/N}\left[\text{Ln}\left(\frac{1-RP}{1-P}\right)\right][R-1]}{N^2\left[R-\left(\frac{1-RP}{1-P}\right)^{1/N}\right]^2} \quad R \neq 1 \tag{A3}$$

$$\frac{\partial P_1}{\partial N} = \frac{P(P-1)}{(N+P-NP)^2} \quad R = 1 \tag{A4}$$

The denominator of Eqs. (*A*3) and (*A*4) is always positive. The numerator of Eq. (*A*3) is the product of one positive expression and one negative, and therefore it is always negative. The numerator of Eq. (*A*4) is also always negative. So, for $R = 1$ and $R \neq 1$, $\partial N < 0$, $\forall_{R,P,N}$, and, therefore, P_1 decreases when N increases.

References

[1] Smith, R., 1995, *Chemical Process Design*, McGraw-Hill, New York, Chap. 7.
[2] Ahmad, S., Linnhoff, B., and Smith, R., 1988, "Design of Multipass Heat Exchangers: An Alternative Approach," ASME J. Heat Transfer, **110**, pp. 304–309.
[3] Shenoy, U. V., 1995, *Heat Exchanger Network Synthesis—Process Optimization by Energy and Resources Analysis*, Gulf Publishing Company, Houston, pp. 255–264, Chap. 6.
[4] Gulyani, B. B., 2000, "Estimating Number of Shells in Shell and Tube Heat Exchangers: A New Approach Based on Temperature Cross," ASME J. Heat Transfer, **122**, pp. 566–571.
[5] Wales, R. E., 1981, "Mean Temperature Difference in Heat Exchangers," Chem. Eng., **88**(4), pp. 77–81.
[6] Santos, L. C., and Zemp, R. J., 2000, "Energy and Capital Targets for Constrained Heat Exchanger Networks," Braz. J. Chem. Eng., **17**(4–7), pp. 659–669.
[7] Floudas, C. A., 1995, *Nonlinear and Mixed-Integer Optimization—Fundamentals and Applications*, Oxford University Press, Oxford, UK, pp. 314–315.

Journal of Heat Transfer

Technical Notes

This section contains shorter technical papers. These shorter papers will be subjected to the same review process as that for full papers.

Augmentation of Laminar Forced Convective Heat Transfer of an Oil Flow in an Enhanced Tube by EHD Effect

Zhen-Hua Liu
e-mail: liuzhenh@sjtu.edu.cn

Jie Yi

School of Mechanical and Power Engineering, Shanghai Jiaotong University, Shanghai, 200030, P.R. China

Keywords: Convection, Electric Fields, Enhancement, Experimental, Heat Transfer, Tubes

Introduction

Heat transfer enhancement using an applied electric field has fascinating application perspective since it can realize a good enhancement effect at the expense of only a little cost of energy. Many fundamental studies have been carried out in this field and the emphasis of the study has been gradually turning to application study. The electrohydrodynamic (EHD) enhancement of the forced convective heat transfer refers to the coupling of an electric field with the fluid field in a dielectric fluid medium: The net effect is production of electrically induced secondary motions that destabilize the thermal boundary layer near the heat transfer surface.

The effect of electrohydrodynamics on the phase-change heat transfer has been under investigation for the past two decades. On the other hand, the studies of the convective heat transfer enhancement by the EHD effect are relatively little. The experimental results reported by Franke and Hogue [1] and Hasegawa et al. [2] denoted that the strong electric field could disrupt the laminar thermal boundary layer of air or refrigerants in-tube and shift the flow conformation from the laminar flow to the turbulent flow.

Compared with air and refrigerants, oil is a so viscous fluid that it keeps still the laminar flow when the external electric field is applied although the secondary flow may be aroused. It is quite meaningful to reinforce the forced convective heat transfer of oil in-tube, since it has a low heat transfer coefficient, but a widely practical perspective. In general, it is difficult to enhance the laminar forced convective heat transfer of oil in-tube. Common enhancement techniques use mainly various surface-worked tubes such as the two-dimensional or three-dimensional extended surfaces tubes (see, for example, [3]) and the helical groove tubes (see, for example, [4]), the smooth tube inserted swirl-flow devices such as the ligament or the helical steel wire coil (see, for example, [5]). In the above enhancement techniques, the smooth tube inserted a helical steel wire coil that is closely touched on the inner wall of the tube is a simple and relatively effective method. Although these enhancement techniques can effectively increase the heat transfer coefficients, while they also increase the fraction factors due to strong viscosity of oil. In general, the increase ratio of the fraction factor is greatly larger than that of the heat transfer coefficient, and hence the comprehensive effect is not good. The EHD enhancement method has a well comprehensive effect for the convective heat transfer of oil, because it not only greatly enhances the heat transfer, but also has just a little increase in the friction force. In addition, controlled heat transfer also can be conveniently implemented by means of adjustment of the electric field strength.

In the present study, an experimental investigation was performed for augmentation of the laminar forced convective heat transfer of an oil flow through an enhanced tube under a DC high-voltage electric field applied. The enhanced tube consisted of a smooth tube and a helical steel wire coil that was closely touched on the inner wall of the tube to form an internal enhanced heat-transfer surface. The effect of the applied electric field on the forced convective heat transfer of oil in the smooth and the enhanced tubes were investigated. The forced convective heat transfer characteristics of oil were obtained under various applied high voltages and the heat fluxes. In addition, the effects of the flow velocity and the oil-temperature on the enhanced heat transfer were also investigated. The present experiment reveals the influences of such factors as the applied electric voltage, the heat flux, the flow velocity and the oil temperature on the enhancement ratio of the heat transfer coefficient.

Experimental Apparatus

The experimental apparatus is not shown here for brevity's sake. The test tube was a horizontal heated copper tube with an effective heating length of 1.20 m, the inner diameter of 20 mm and the wall thickness of 3 mm. Inside of the copper tube, a helical steel wire coil was closely touched on the inner wall of the tube to form an enhanced heat-transfer surface. Three kinds of the helical steel wire coil were used in the tests. The first coil had a pitch of 5 mm and wire diameter of 1.5 mm named A coil hereafter. The second coil had a pitch of 5 mm and wire diameter of 1 mm named B coil. The last one had a pitch of 10 mm and wire diameter of 1.5 mm named C coil. The two ends of the test tube had the leading tubes made of bakelite tubes, in which the thermocouples and the pressure probes were mounted to measure the oil temperatures and the static pressures at the inlet and the outlet of the test section. Six K-type thermocouples were welded on the outside of the copper tube with an uniform distance to measure the local wall temperatures. The outside wall of the copper tube was reeled with an electric resistance wire to generate Joule heat and the interlining of mica was mounted between the copper tube and the electric resistance wire for the sake of insulation. The outmost layer of the test section was the thermal insulation layer of asbestos wire.

Contributed by the Heat Transfer Division for publication in the JOURNAL OF HEAT TRANSFER. Manuscript received by the Heat Transfer Division April 19, 2001; revision received March 21, 2002. Associate Editor: C. Th. Avedisian.

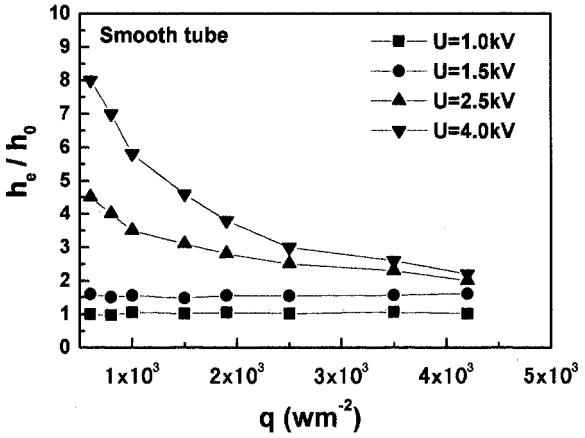

Fig. 1 The effect of the applied electric field on the enhanced heat transfer ratio for the smooth tube

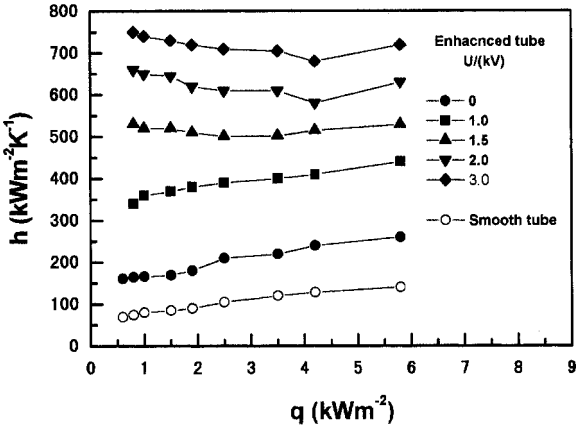

Fig. 3 The effect of the applied electric field on the enhanced heat transfer coefficient for the enhanced tube

The oil was heated in an oil tank, and circulated by the pump. The mass rate was regulated by the values and measured with a flow meter. Then, it passed through the test tube, the water cooler and finally returned to the tank. All signals from the thermocouples and the pressure probes were measured using a digital measuring system.

The cathode of the DC high-voltage was connected to the copper tube and the helical coil (both to the ground), and the anode to a stainless steel wire of dia-1 mm that was inserted along the center axis of the copper tube to apply a radial electric field between the wire electrode and the copper tube.

In each run with the applied electric field, both the mass rate and the inlet oil-temperature were fixed, a series of heat transfer characteristics were measured by changing the applied DC high voltage and the heat flux. Then, other test run was carried out at another fixed mass rate.

In the present experiment, No. 15 lubricating oil was used as the working liquid. The velocity ranged from 0.025 m/s to 0.31 m/s. The inlet oil-temperature ranged from 20°C to 52°C. The Reynolds number varied from 40 to 780.

Experimental Results and Discussion

The enhancement ratio of the heat transfer coefficient by the EHD effect (called the enhanced heat transfer ratio hereafter), h_e/h_0, is defined as the ratio of the heat transfer coefficient with the applied electric field to that without the applied electric field at the same mass rate and heat flux. Figure 1 shows the experimental results of the smooth tube by h_e/h_0 versus q curves with the experimental conditions of 0.2 m/s flow velocity and 20 °C inlet oil-temperature. It is found that the heat transfer enhancement has not occurred when the applied electric voltage is lower than 1.0 kV. However, when the applied electric voltage reaches 1.5 kV, the enhanced heat transfer ratio increases quickly and is independent of the heat flux. In the low heat flux range, the enhanced heat transfer ratio increases significantly with increasing the applied electric voltage. However, in the high heat flux range, the enhanced heat transfer ratio will gradually decrease even stop with increasing the applied electric voltage. Therefore, the enhanced heat transfer ratio is strongly dependent on both the applied electric voltage (or the electric field strength) and the heat flux. The relation among them is very complicated. In the tests, the local discharge would appear between the two electrodes when the applied electric voltage exceeded 4.0 kV.

Figure 2 shows experimental results of the smooth tube by f_e/f_o versus q curves with the same flow and heating conditions as shown in Fig. 1. Here, f_e/f_o is the ratio of the friction factor with the electric field to that without the electric field. It is found from Figs. 1 and 2 that the maximum enhanced heat transfer ratio can increase about seven times by the EHD effect. However, the friction factors increase only about two times by the EHD effect under the same flow and heating conditions. This fact shows a favorable comprehensive effect of the heat transfer enhancement in the low heat flux range by using a high voltage electric field.

It is found from the experimental results of the enhanced tubes without the applied electric field that the enhanced tube A has the

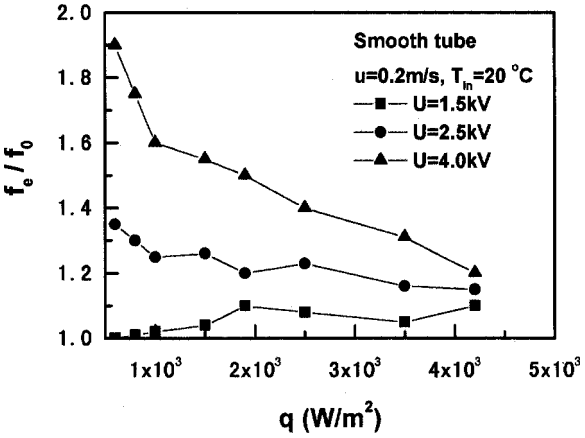

Fig. 2 The effect of the applied electric field on the increase ratio of friction factor for the smooth tube

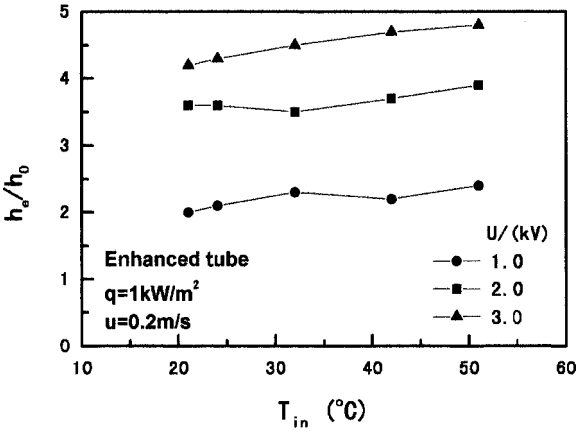

Fig. 4 The effect of oil temperature on the enhanced heat transfer ratio for the enhanced tube

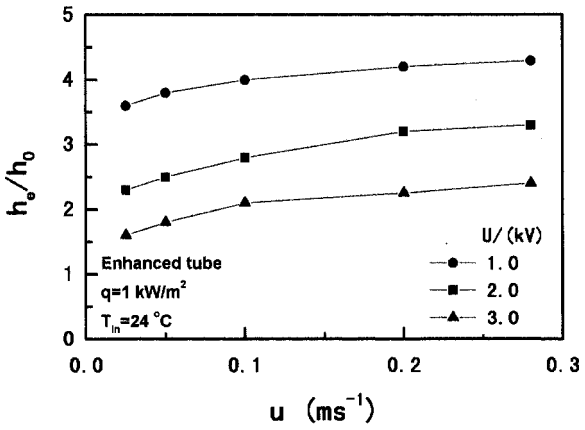

Fig. 5 The effect of flow velocity on the enhanced heat transfer ratio for the enhanced tube

best enhanced heat transfer characteristics among the three enhanced tubes. Hence, only the enhanced tube A was used for the tests using the applied electric field.

Figure 3 shows the experimental results of the enhanced tube A using the applied electric field by h versus q curves with 0.25 m/s flow velocity and 24 °C inlet oil-temperature. It is found from Fig. 3 that a relatively strong enhanced heat transfer by the EHD effect has appeared when the applied electric voltage reaches only 1 kV. The heat transfer coefficient increases quickly with increasing the applied electric voltage. The heat transfer coefficient of the enhanced tube with the applied electric field can increase three to four times than that without the applied electric field. It must be specially noted that the heat transfer coefficient is nearly independent of the heat flux. This is a significant advantage for the enhanced tube and it differs completely from that for the smooth tube. If compared with the heat transfer coefficients of the smooth tube without the applied high voltage, the total enhanced heat transfer ratio by the EHD effect and the enhanced heat-transfer surface effect will reach about eight times to ten times in the whole experimental range. It is slightly larger than the maximum value of the enhanced heat transfer ratio for the smooth tube with the applied high voltage as shown in Fig. 1. This fact means that the enhanced heat transfer ratio cannot significantly be increased by a compound enhancement technique in the low heat transfer range.

In the present experiment, it is worth noting from the measured results that the pressure drop had no change with increasing the applied electric voltage. This fact indicates that although the heat transfer coefficient is remarkably increased by the EHD effect, the fraction factors in the test section has no meaningful change with the increase in the heat transfer coefficients. This result shows a favorable comprehensive effect for the enhanced tube. The reason is presumed that the fraction force is mainly caused by the helical coil for the enhanced tube.

Figure 4 shows the effect of the inlet oil-temperature on the enhanced heat transfer ratio at a constant velocity. It is found that the enhanced heat transfer ratio some what increases with increasing the inlet oil-temperature.

Figure 5 shows the effect of the flow velocity on the enhanced heat transfer ratio at a constant inlet oil-temperature. It is found that the enhanced heat transfer ratio has a small increase with increasing the flow velocity. By comparing Figs. 4 with 5, it could be concluded that the increase of the oil-temperature will reduce the kinetic viscosity, whose effect is similar to an increase in the velocity. Both all can raise the Reynolds number, so the enhanced heat transfer ratio slowly increases with increasing the Reynolds number. The reason is estimated that it is easier to arouse turbulent flow reaction or the secondary flow with increasing the Reynolds number. However, this trend is quite slight.

The enhanced heat transfer of the forced convection by the EHD effect is mainly due to the influence of the Coulomb force caused by motions of the free electric charges in the fluid. Other EHD forces such as the dielectric force and the electrostriction force are secondary. In a dielectric fluid medium, the ionized particles, i.e., the free electric charges become more and more with increasing the applied electric voltage. These free electric charges move quickly from the anode (the central steel wire) to the cathode (the copper tube), and impact strongly the thermal boundary layer and make it thinner and more turbulent. Meanwhile, sine the radial turbulence perpendicular to the flow direction is strengthened and hence the secondary flow is inducted. Therefore, the heat transfer enhancement by the EHD effect is quite significant even in the laminar forced convective region. For the smooth tube, the influence of the heat flux on the enhanced heat transfer has not yet been able to be explained fully. It seems logical to suspect that the higher temperature gradients make the dielectric and electrostriction forces more important, because of the higher gradients in the properties.

Conclusions

An experimental study investigated the effect of a DC applied electric field on the enhanced heat transfer of the laminar forced convection for oil through a horizontal smooth tube and an enhanced tube. The experimental results are summarized as follows:

1. For the smooth tube, the enhanced heat transfer ratio is dependent on both the applied electric field strength and the heat flux. In the low heat flux range, the enhanced heat transfer ratio increases quickly with increasing the electric field strength. While, the increase ratio of the friction factor is effectively restrained. In the high heat flux range, the enhanced heat transfer is not significant.
2. For the enhanced tube, the enhanced heat transfer ratio is mainly dependent on the applied electric field strength. The enhanced heat transfer ratio increases quickly with increasing the applied electric field strength and is basically independent of the heat flux in the whole experimental range. The friction factor is nearly not change with the increase in the heat transfer coefficient. Therefore, a favorably comprehensive effect can be achieved.
3. Both the flow velocity and the oil-temperature have only a little influence on the enhanced heat transfer caused by the EHD effect.

Nomenclature

f = friction factor $[-]$
h = heat transfer coefficient $[\mathrm{Wm^{-2}\ K^{-1}}]$
q = wall heat flux $[\mathrm{Wm^{-2}}]$
T_{in} = Inlet oil-temperature [°C]
u = Flow velocity of oil $[\mathrm{ms^{-1}}]$
U = DC electric voltage [V]

Subscription

0 = without the applied electric field
e = with the applied electric field

References

[1] Franke, M. E., and Hogue, L. E., 1991, ''Electrostatic Cooling of a Horizontal Cylinder,'' ASME J. Heat Transfer, **113**, pp. 544–548.
[2] Hasegawa, M. M., Yabe, A., and Nariai, H., 1998, ''Numerical Analysis of Electro-Hydro-Dynamical Enhancement Mechanism of Forced Convection Heat Transfer in Duct Flow,'' Trans. Jpn. Soc. Mech. Eng., Ser. B, **64(620)**, pp. 228–233.
[3] Liao, Q., Zhu, X., and Xin, M. D., 2000, ''Augmentation of Turbulent Convective Heat Transfer in Tubes with Three-dimensional Internal Extended Surfaces,'' Enhanced Heat Transfer, **7**, pp. 139–151.
[4] Rabas, T. G., Webb, R. L., Thors, P., and Kim, N. K., 1993, ''Influence of Roughness Shape and Spacing on the Performance of Three-dimensional Helically Dimpled Tubes,'' Enhanced Heat Transfer, **1**, pp. 53–64.
[5] Carnavos, T. G., 1979, ''Cooling Air in Turbulent Flow With Internally Finned Tubes,'' Heat Transfer Eng., **1**(2), pp. 41–46.

On the Optimization of Circular Radiating Fins With Fin-to-Fin and Fin-to-Base Radiant Interaction

Rizos N. Krikkis
e-mail: rkrik@mie.uth.gr
Institute of Chemical Engineering and High Temperature Chemical Processes, P.O. Box 1414, Stadiou St., Platani, 26 500 Patras, Greece

Panagiotis Razelos
Mem. ASME
e-mail: razel@ath.forthnet.gr
Professor Emeritus, College of Staten Island, CUNY, New York

In the present study the optimum dimensions of circular rectangular and triangular profile fins with fin-to-fin and fin-to-base radiant interaction are determined. The basic assumptions are one-dimensional heat conduction and black surface radiation. The governing equations are formulated by means of dimensionless variables and solved numerically. The optimum fin dimensions, bore thickness and height, are presented in generalized dimensionless form and explicit correlations are provided for the dimensionless optimum parameters. The results are analyzed and reported in diagrams that give insight to the operational characteristics of the heat rejection mechanism.
[DOI: 10.1115/1.1565094]

Introduction

Radiating extended surfaces are widely used to reject heat from a spacecraft, which became very important with the advent of space exploration, in the second half of the last century. Substantial effort has been made to understand the fundamental energy exchange mechanisms involved, in order to design radiating equipment. In a pioneer work, Sparrow et al. [1] examined black radial fins of rectangular profile with fin to fin and fin to base radiant interaction. Chung and Zhang [2,3] determined the optimum dimensions of fins and fin arrays taking into consideration of fin to fin and fin to base interactions. Krishnaprakas [4] determined the optimum dimensions for fin arrays and presented his results with correlations. Schnurr and Cothran [5] developed an iterative numerical procedure for the calculation of optimum dimensions of circular assemblies with triangular profiles for black and gray surfaces. Later, Schnurr et al. [6] determined and compared the optimum dimensions of circular and straight fin arrays with rectangular and triangular profiles. The calculation of the optimum assembly environment was straightforward as a result of recasting the optimization statement in terms of a nonlinear programming problem. The solution was obtained using the Fletcher-Reeves algorithm at the initial stages and the Hooke-Reeves algorithm at the final stages of the optimization process.

In the present work we determine the optimum dimensions of rectangular and triangular profile radiating fins that includes fin to fin and fin to base radiant heat exchange. All the surfaces involved are considered black with constant thermal properties. Furthermore, a method is proposed where the optimum dimensions and distance between fins are obtained directly without any iterations and/or interpolations from diagrams.

Contributed by the Heat Transfer Division for publication in the JOURNAL OF HEAT TRANSFER. Manuscript received by the Heat Transfer Division March 5, 2002; revision received December 2, 2002. Associate Editor: G. Chen.

Statement of the Problem

Consider an annular space radiator schematically depicted schematically in Fig. 1 with uniform density radial fins. The fin is made of material with thermal conductivity k, profile $y=y(r)$, base thickness $2w_b$ and height $\ell=r_t-r_b$ (Fig. 1). The base of the fin is maintained at constant temperature T_b. Assuming one-dimensional heat conduction, no heat sources or sinks in the fin, black radiation from all surfaces according to the Stefan-Boltzmann law, the steady-state temperature and radiosity must satisfy the following dimensionless equations:

$$\left.\begin{aligned} d\Theta_1/dx&=\Theta_2/(zx)\\ d\Theta_2/dx&=x(v\beta)^2[\Theta_1^4(x)-h(x)]\end{aligned}\right\},\quad 1/\beta\leqslant x\leqslant 1 \tag{1}$$

$$h(x)=\int_{x'=1/\beta}^{1}\Theta_1^4(x')\,dF_{dx-dx'}+h_b(x) \tag{2}$$

where $v^2=h_r r_b^2/(kw_b)$ is the surface radiation/conduction parameter, $\Theta_1=\Theta$ and $\Theta_2=zx(d\Theta_1/dx)$. The boundary conditions are

$$\Theta_1(1)=1,\quad \Theta_2(\beta)=0 \tag{3}$$

The equation that describes the profile of the fin is (Razelos and Imre [8]):

$$z(x,\beta;\lambda)=1+\frac{(1-\lambda)(1-\beta x)}{\beta-1},\quad 1/\beta\leqslant x\leqslant 1 \tag{4}$$

In Eq. (4) $\lambda=1$ corresponds to the rectangular profile, and $\lambda=0.01$ to the nearly triangular. The total heat loss $q=q_f+q_b$ from the heat rejection mechanism (fin and base tube assembly) can be found by adding each component of heat losses, which in dimensionless form becomes:

$$\begin{aligned} Q&=\frac{q_f+q_b}{4\pi r_b^2 h_r T_b}\\ &=Q_f+Q_b\\ &=-\frac{1}{\beta v^2}\left.\frac{d\Theta_1}{dx}\right|_{x=1/\beta}+\frac{\gamma}{2}\left\{1-\int_{x'=1/\beta}^{1}\Theta_1^4(x')\,dF_{dA_b-dA*}\right\}\end{aligned} \tag{5}$$

It has been pointed out by Razelos and Georgiou [7] that the condition for economically justifying the use of fins is: ''the ratio of heat dissipated by the fin to be much larger in comparison with the heat that would have been dissipated from the base surface, in the absence of the fin.'' This ratio, which in the literature refers to as removal number, effectiveness or augmentation factor is equal to

$$N_r=\frac{q}{q_b^s}=\frac{q_f+q_b}{q_b^s}=\frac{2Q}{\gamma} \tag{6}$$

where $q_b^s=2\pi r_b L h_r T_b$ is the heat rejected by the single base tube (in the absence of the fin).

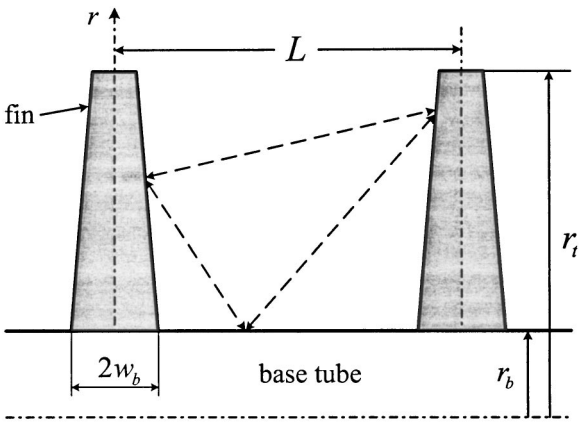

Fig. 1 Annular space radiator

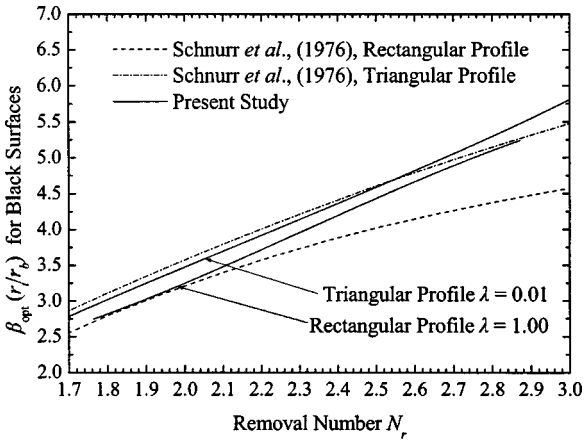

Fig. 2 β_{opt} as a function of the removal number N_r for a circular assembly

Optimization

In terms of the dimensionless variables the optimization statement is defined as, ''Given the profile of the fin, λ, r_b, and the desired removal number N_r determine the values υ, β, and γ of the fin that minimize its volume,'' Schnurr et al. [6]. Following Razelos and Imre [8] and Schnurr et al. [6], a dimensionless volume is introduced as:

$$U=\frac{kV}{4\pi h_r r_b^4(L/r_b)}=\frac{\beta^2 g(\beta;\lambda)}{\upsilon^2\gamma} \tag{7}$$

In the above equation the expression $g(\beta;\lambda)$ corresponds to the profile described by Eq. (4) and is equal to

$$g(\beta;\lambda)=\frac{(\beta-1)}{6\beta^2}[\beta(1+2\lambda)+\lambda+2)] \tag{8}$$

We may observe by inspection of From Eqs. (6,7) that the removal number and the dimensionless volume can be expressed as functions of υ, β, and γ that is $N_r=N_r(\upsilon,\beta,\gamma;\lambda)$ and $U=U(\upsilon,\beta,\gamma;\lambda)$. The problem defined by Eqs. (1) to (2), with its corresponding boundary conditions (3), is solved numerically and the optimization is performed using the nonlinear programming algorithm due to Schittkowski [9], which uses a successive quadratic programming method for the solution of the general nonlinear programming problem. The correlations used for the optimum characteristics for both the rectangular ($\lambda=1$) and the triangular ($\lambda=0.01$) profile are the following:

Table 1 Coefficients for the rectangular profile

c_i	β_{opt}	γ_{opt}	ν^2_{opt}
0	4.53626	5.55864	1.81830
1	−5.57195	−8.00277	−1.99758
2	3.47024	4.47558	0.75187
3	−0.50314	−0.70870	−0.09567

Table 2 Coefficients for the triangular profile

c_i	β_{opt}	γ_{opt}	ν^2_{opt}
0	−3.63752	−2.36673	1.18456
1	5.86823	4.36603	−1.28786
2	−1.65398	−1.55895	0.47806
3	0.24907	0.24783	−0.05976

$$z=\sum_{i=1}^{4} c_i N_r^i,\quad 1.7\leqslant N_r\leqslant 3.0,\quad z=\beta_{opt},\gamma_{opt},\upsilon^2_{opt} \tag{9}$$

The polynomial coefficients c_i in Eq. (9) can be found in Table 1 for the rectangular profile and in Table 2 for the triangular profile.

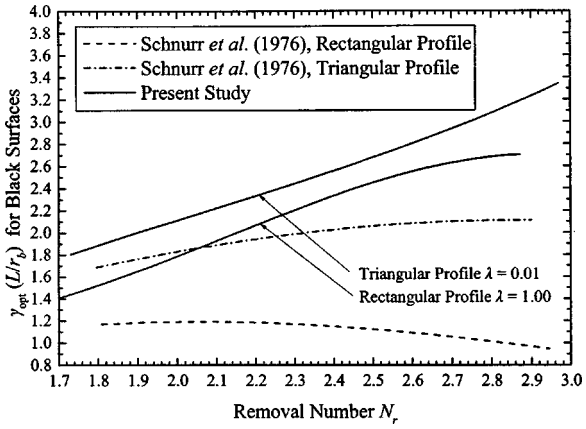

Fig. 3 γ_{opt} as a function of the removal number N_r for a circular assembly

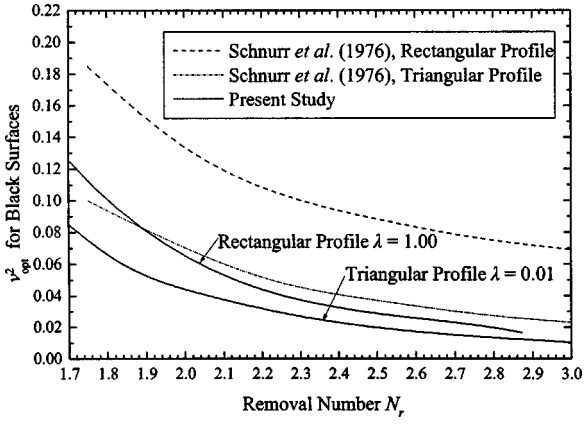

Fig. 4 ν^2_{opt} as a function of the removal number N_r for a circular assembly

Table 3 Results for the example calculations

Reference	β_{opt}	γ_{opt}	ν^2_{opt}	$(r_t)_{opt}$ mm	L_{opt} mm	$(w_b)_{opt}$ mm
Schnurr and Cothran [5]	3.00	1.50	0.105	76.2	38.1	0.0522
Schnurr et al. [6]	3.11	1.69	0.101	79.0	42.9	0.0543
Present study	3.00	1.88	0.065	76.2	47.8	0.0845

Numerical Solution

The integro-differential Eqs. (1) to (2), is solved using an iterative procedure (Modest, [11]). First a temperature distribution is calculated and then inserted into Eq. (1) and it is solved for an updated temperature distribution. The second order, two-point boundary value problem is solved using a shooting technique (Ascher et al. [13], Keller [14]). The error tolerance for the boundary condition iteration was set to 10^{-8}. The algorithm used is a variable step embedded Runge-Kutta algorithm of order 5(4), Hairer et al. [15]. The obtained discrete temperature distribution $\Theta_1(\xi_i)$, $1/\beta \leqslant \xi_i \leqslant 1$ from the ODE solver is used for the construction of a temperature interpolating piecewise polynomial of the form:

$$\Theta_1(x)=\sum_{j=1}^{k} c_{ij}(x-\xi_i)^{j-1}/(j-1)!, \quad \xi_i \leqslant x \leqslant \xi_{i+1} \qquad (10)$$

where the breakpoint sequence ξ is provided by the ordinary differential equation solver. For the interpolant constructed above $k=8$, was used (degree $k-1$) so that the right hand side of Eq. (1) has continuous derivatives. In this way full advantage is taken of the accuracy characteristics of the ordinary differential equation solver since an optimum Runge-Kutta algorithm of order 5 must agree at least with the Taylor expansion of the same order. It is therefore evident that derivative continuation is essential for an accurate and reliable solution (temperature distribution). The integral in Eq. (2) is evaluated using Eq. (10) while for the temperature distribution, a globally adaptive quadrature formula using a 21-point Gauss-Kronrod rule. The absolute error is controlled by subdivision of the integration interval so that the integral is estimated over each subinterval. The local truncation error is estimated using a 10-point Gauss quadrature rule. The absolute error tolerance used was 10^{-8}, while the corresponding relative one was 10^{-5}. It should be noted here that the fin heat dissipation is computed directly from the solution of the ordinary differential equation, Eq. (1). In this way the calculated solution is very accurate since the truncation error in the temperature derivative is of fifth order. In this way an accurate and reliable calculation of the fin heat dissipation is achieved since the computation of the constraint gradient is critical for the minimization routine. The implementation of the above mention algorithms and techniques was based on a FORTRAN code using double precision arithmetic. The expressions for the view factors required for Eq. (1) to (2) where taken from references [1] and [16]. The necessary differentiations where obtained both by analytical methods and symbolic algebra (MAPLE) and finally checked with numerical differentiation.

Results and Discussion

The temperature distributions, for the rectangular, trapezoidal, and triangular profiles have been calculated and for purpose of comparison with the results in [5], we used the same assembly characteristics (geometry) to solve these problems. At this relatively low value of the radius ratio ($\beta=2$), it has been found that the agreement is fairly good (within 1–2%). In addition the removal number as a function of the assembly geometry has been compared with the corresponding values calculated by Sparrow et al. [1]. Although a fairly good agreement has been observed for low radius ratios ($\beta=1.5\div2.0$) at intermediate ($\beta=3.0$) and higher values ($\beta=5.0$) the differences became important (i.e., up to 35%). We believe that the main reason for such large differences is due to the numerical techniques used in the present study. In Figs. 2, 3, and 4 the optimum parameters β_{opt}, γ_{opt} and υ^2_{opt} are shown as a function of the removal number. For the purpose of illustration and comparison of the results obtained by using Eq. (9) is demonstrated, for the same example given by Schnurr and Cothran [5].

Example. Determine the optimum dimensions of the black tubular radiator of Fig. 1, where the base temperature is $T_b=37.8°C$ (100°F), and the fin thermal conductivity is $k=200$ W/(m K), (aluminum). The radiator is designed to operate at $N_r=1.8$ with $r_b-25.4$ mm.

Solution. First we determined the black body heat transfer coefficient, which is equal to $h_r=\sigma T_b^3=5.67\times10^{-8}(310.9)^3=1.70$ W/(m^{2}K). From Eq. (9) and Table 2 we obtain the correlation coefficients and $\beta_{opt}=\Sigma_{i=0}^{4}c_i(1.8)^i=3.00$, $\gamma_{opt}=\Sigma_{i=0}^{4}c_i(1.8)^i=1.88$ and $\upsilon^2_{opt}=\Sigma_{i=0}^{4}c_i(1.8)^i=0.065$. The following optimum fin dimensions can be obtained as: $(w_b)_{opt}=h_r r_b^2/(k\upsilon^2_{opt})=3.05\times1.70\times(25.4\times10^{-3})^2/(200\times0.065)=0.0845$ mm, $(r_t)_{opt}=\beta_{opt}r_b=3.00\times25.4\times10^{-3}=76.2$ mm, $L_{opt}=\gamma_{opt}r_b=1.88\times25.4\times10^{-3}=47.8$ mm The results are summarized in Table 3 that for the purpose of comparison the corresponding values of previous studies [5,6] are also shown.

Conclusions

In the present study the problem of designing the optimum fin for the tubular space radiator is solved. The governing equations are formulated by means of dimensionless variables, a numerical optimization is carried out and explicit correlations are given for the description of the optimum fin environment. Comparing to the previous studies more reasonable designs are predicted since the optimum base semi thickness is substantially greater in the present study. Moreover the impact of numerical analysis on the solution of engineering problems is clearly demonstrated. Furthermore we suggest a fast and accurate procedure suitable for all practical engineering purposes.

Nomenclature

A = surface area, m^2
$F_{dr-dr'}$ = fin to fin view factor
$F_{dA-A_b^*}$ = fin to base view factor
h = $[H/(h_r T_b)]$ dimensionless irradiation
h_r = (σT_b^3) radiation heat transfer coefficient, W/(m^2 K)
H = irradiation, W/m^2
k = thermal conductivity, W/(m K)
ℓ = (r_t-r_b) fin height, m
L = fin spacing, m
N = number of fins
N_r = removal number
q = (q_f+q_b) total heat loss, W
q_b = base tube heat loss, W

q_f = fin heat loss, W
Q = dimensionless total heat dissipation
Q_b = dimensionless base tube heat dissipation
Q_f = dimensionless fin heat dissipation
r = radius, m
T = temperature, K
x = (r/r_t) dimensionless radius along fin
y = profile function (half thickness of the fin), m
v^2 = $[h_r r_b^2/(kw_b)]$ surface radiation/conduction coefficient
U = dimensionless fin volume
V = fin volume, m^3
w_b = base semi-thickness, m
z = (y/w_b) dimensionless profile

Greek Symbols

β = (r_t/r_b) radius ratio
γ = (L/r_b) fin spacing to base tube radius ratio (dimensionless)
Θ = (T/T_b) dimensionless temperature
λ = (w_t/w_b) tip to base semi-thickness ratio
σ = Stefan-Boltzmann constant

Subscripts

b = base tube
opt = optimum
t = fin tip

Superscripts

* = participating area in radiant interaction, dimensionless profile coefficients

References

[1] Sparrow, E. M., Miller, G. B., and Jonsson, V. K., 1962, "Radiating Effectiveness of Annular-Finned Space Radiators, with Mutual Irradiation Between Radiator Elements," ASCE, J. Aerosp. Eng., **29**, pp. 1291–1299.
[2] Chung, B. T. F., and Zhang, B. X., 1991, "Minimum Mass Longitudinal Fins With Radiation Interaction at the Base," J. Franklin Inst., **328**(1), pp. 143–161.
[3] Chung, B. T. F., and Zhang, B. X., 1991, "Optimization of Radiating Fin Array Including Mutual Irradiations Between Radiator Elements," ASME J. Heat Transfer, **113**, pp. 814–822.
[4] Krishnaprakas, C. K., 1997, "Optimum Design of Radiating Longitudinal Fin Array Extending From a Cylindrical Surface," ASME J. Heat Transfer, **119**, pp. 857–860.
[5] Schnurr, E. M., and Cothran, C. A., 1974, "Radiation from an Array of Gray Circular Fins of Trapezoidal Profile," AIAA J., **12**(11), pp. 1476–1480.
[6] Schnurr, E. M., Shapiro, A. B., and Townsend, M. A., 1976, "Optimization of Radiating Fin Arrays With Respect to Weight," ASME J. Heat Transfer, **98**, pp. 643–648.
[7] Razelos, P., and Georgiou, E., 1992, "Two-Dimensional Effects and Design Criteria for Convective Extended Surfaces," Heat Transfer Eng., **13**(3), pp. 38–48.
[8] Razelos, P., and Imre, K., 1980, "The Optimum Dimensions of Circular Fins With Variable Thermal Parameters," ASME J. Heat Transfer, **102**(2), pp. 420–425.
[9] Schittkowski, K., 1986, "NLPQL: A FORTRAN Subroutine Solving Constrained Nonlinear Programming Problems," *Annals of Operations Research*, Clyde L. Monma, ed., **5**, pp. 485–500.
[10] Razelos, P., 1979, "The Optimization of Convective Fins With Internal Heat Generation," Nucl. Eng. Des., **52**(2), pp. 289–299.
[11] Modest, M. F., 1993, *Radiative Heat Transfer*, McGraw-Hill, New York.
[12] Razelos, P., and Krikkis, R. N., 2001, "Optimum Design of Longitudinal Rectangular Fins with Base to Fin Radiant Interaction," Heat Transfer Eng., **22**(3), pp. 3–17.
[13] Ascher, U. M., Mattheij, R. M. M., and Russel, R. D., 1995, *Numerical Solution of Boundary Value Problems for Ordinary Differential Equations*, 2nd ed., SIAM, Philadelphia, PA.
[14] Keller, H. B., 1992, *Numerical Methods for Two-Point Boundary-Value Problems*, Dover, New York.
[15] Hairer, E., Nørsett, S. P., and G., Wanner, 1987, *Solving Ordinary Differential Equations I. Nonstiff Problems*, Springer-Verlag, New York.
[16] Sparrow, E. M., 1963, "A New and Simpler Formulation for Radiative Angle Factors," ASME J. Heat Transfer, **85**, pp. 81–88.

Solution of the Radiative Integral Transfer Equations in Rectangular Absorbing, Emitting, and Anisotropically Scattering Homogeneous Medium

Zekeriya Altaç
Professor
e-mail: zaltac@ogu.edu.tr

Mesut Tekkalmaz
e-mail: tmesut@ogu.edu.tr

Osmangazi University, Mechanical Engineering Department, School of Engineering and Architecture, 26480 Bati Meşelik, Eskişehir, Turkey

Radiative integral transfer equations for a rectangular absorbing, non-emitting, and linearly anisotropically scattering homogeneous medium are solved numerically for the incident energy and the net heat flux components using the method of "singularity subtraction." A benchmark problem is chosen as a rectangular homogeneous cold participating medium which is subject to externally uniform diffuse radiation on the bottom wall. The solutions for the incident energy and net heat flux components for selected points for a square domain are provided in tabular form for benchmarking purposes. [DOI: 10.1115/1.1578503]

Keywords: Absorption, Computational, Emitting, Heat Transfer, Participating Media, Radiation

Introduction

Radiative transfer in multidimensional rectangular geometries has numerous application areas, such as the design of combustion chambers and furnaces. If the medium is participating, the analysis gets further complicated due to scattering, absorption and emission which requires the solution of the radiative transfer equation (RTE). Over the years, a number of methods such as zonal, spherical harmonics, discrete ordinates have been developed to solve the RTE. Each method has its own advantages and disadvantages. Solution to the radiative integral transfer equation (RITE) provide us with the exact solutions for regular geometries. However, the method is not suitable to handle complex geometries. Since angular dependence of radiative transfer equation is removed through the integration of the radiation intensity over the solid angle, the RITEs contain only the spatial variables, and they are dimensionally simpler than other existing methods. However, the RITEs have singular transfer kernels, and therefore they are difficult to solve. Though RITE solutions in one-dimensional geometries are abundant in literature, there are a only few comparative studies which involve solutions of the RITE for linearly anisotropic homogeneous medium in rectangular geometries [1–4].

A technique to solve singular integral equations of this kind is the method of "singularity subtraction" or "singularity removal" which was first used by Loyalka et al. [5] to solve neutron transport problem in a rectangular geometries. The method was later used in thermal radiative transfer by Crosbie et al. [6] and comprehensive solutions in tabular form were also provided. The

Contributed by the Heat Transfer Division for publication in the JOURNAL OF HEAT TRANSFER. Manuscript received by the Heat Transfer Division September 18, 2002; revision received March 11, 2003. Associate Editor: S. T. Thynell.

method was also successfully employed to radiative transfer equations in one-dimensional RITEs in plane-parallel and cylindrical isotropic and linearly anisotropic scattering medium by Altaç [7–9]. Difficulty arises in treatment of two- and three-dimensional geometries, in problems with anisotropic scattering, and the boundaries with specular reflection; furthermore, memory requirement and computation time increase dramatically.

In the present work, the radiative integral transfer equations for a two-dimensional linearly anisotropic scattering homogeneous medium are solved using the method of ''singularity subtraction.'' Benchmark problems and solutions of at least four significant decimal places accuracy are established. The results are provided in tabular form for researchers for benchmarking purposes.

Radiative Integral Transfer Equations in Rectangular Enclosures

Crosbie and Schrenker's two-dimensional radiative transfer problem is chosen to be as a benchmark problem for linearly anisotropic scattering homogeneous medium as well [6]. The medium is cold, nonemitting, absorbing, isotropically scattering, and unbounded in the *z*-direction. Uniform diffuse radiation is incident on the bottom surface only and no loading is considered on the other surfaces (Fig. 1). All walls are cold and black.

The RITE for general geometries with linearly anisotropic scattering participating medium which are given in Ref. [9] are reduced for a rectangular domain as outlined in Ref. [6]. Then the incident energy and the net heat flux components for homogeneous rectangular medium of the present problem can be written as

$$G(x,y)=\frac{I_w}{2\pi}\int_{x'=0}^{a} y\mathbb{K}_2(\rho_w)dx' + \frac{\omega}{2\pi}\int_{x'=0}^{a}\int_{y'=0}^{b} G(x',y')\mathbb{K}_1(\rho)dx'dy' + \frac{a_1\omega}{2\pi}\int_{x'=0}^{a}\int_{y'=0}^{b}[(x-x')q_x(x',y') + (y-y')q_y(x',y')]\mathbb{K}_2(\rho)dx'dy' \quad (1)$$

$$q_x(x,y)=\frac{I_w}{2\pi}\int_{x'=0}^{a} y(x-x')\mathbb{K}_3(\rho_w)dx' + \frac{\omega}{2\pi}\int_{x'=0}^{a}\int_{y'=0}^{b} G(x',y')(x-x')\mathbb{K}_2(\rho)dx'dy' + \frac{a_1\omega}{2\pi}\int_{x'=0}^{a}\int_{y'=0}^{b}[(x-x')^2q_x(x',y') + (x-x')(y-y')q_y(x',y')]\mathbb{K}_3(\rho)dx'dy' \quad (2)$$

$$q_y(x,y)=\frac{I_w}{2\pi}\int_{x'=0}^{a} y^2\mathbb{K}_3(\rho_w)dx' + \frac{\omega}{2\pi}\times\int_{x'=0}^{a}\int_{y'=0}^{b} G(x',y')(y-y')\mathbb{K}_2(\rho)dx'dy' + \frac{a_1\omega}{2\pi}\int_{x'=0}^{a}\int_{y'=0}^{b}[(x-x')(y-y')q_x(x',y') + (y-y')^2q_y(x',y')]\mathbb{K}_3(\rho)dx'dy' \quad (3)$$

where x and y are the optical dimensions and are defined as $x=\beta X$ and $y=\beta Y$, ω is the constant scattering albedo, I_w is the uniform diffuse radiation intensity of the bottom wall, ρ and ρ_w are defined as $\rho=\sqrt{(x-x')^2+(y-y')^2}$ and $\rho_w=\sqrt{(x-x')^2+y^2}$, and the function $\mathbb{K}_n(\rho)$ is defined as $\mathbb{K}_n(\rho)=Ki_n(\rho)/\rho^n$ where $Ki_n(\rho)$ is the nth order Bickley-Naylor functions [10].

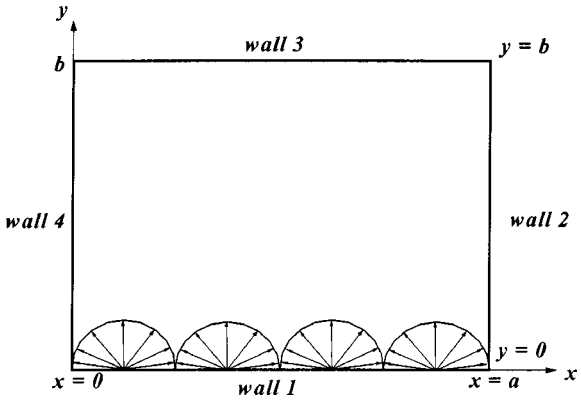

Fig. 1 Geometry and the coordinate system

Table 1 Influence of grid configuration on accuracy ($a_1=-1$, $\omega=0.5$, quantities for $(x,y)=(0.75,0)$)

a	b	N_x	N_y	G	$4q_x$	$4q_y$
1.0	1.0	40	40	0.55906	0.02920	0.88900
		80	80	0.55902	0.02920	0.88905
		100	100	0.55901	0.02920	0.88908
		120	120	0.55901	0.02920	0.88906

Numerical Solution

We divide $x\in(0,a)$ and $y\in(0,b)$ to N_x and N_y equal grid segments, respectively, and generate Simpson's integration quadratures. Adapting the procedures outlined in Refs. [5] and [6], the singularities are subtracted and double integrals are replaced by the quadrature summations. The resulting single and double integrals can be evaluated analytically [5], using the $Bis_n(x,\theta)$ and $Cis_n(x,\theta)$ special functions from their series forms [11]. Uniform diffuse radiation incident to the bottom is taken as $I_w=1$. Discretized integral equations can be rearranged to constitute a system of linear equations which need to be solved for the incident energy and the net heat flux. Direct solution of this dense system through the use of Gauss-elimination is possible if relatively small number of intervals (10 to 30) are used. In this case, the resulting dense matrice which is also computationally involved is established only once. For large number of intervals, not only computation time but also memory restrictions are to be overcome. In this case, to obtain highly accurate solutions through using large number of grids ($N>30$), an iterative algorithm was used to avoid memory restrictions mainly due to the storage of the matrices. Programming was done in double precision and run on a PC. The convergence was determined when the maximum of the two consecutive iterations of the incident energy was less than 10^{-6}.

Results and Discussions

In this study, the exact integral equation solutions for a square linearly anisotropic scattering ($a_1=-1$ and $a_1=1$) homogeneous medium for scattering albedos of $\omega=0.5$ and $\omega=0.95$ are obtained. The square enclosure considered is 1×1 in mean-free-path (mfp) dimension.

Table 2 Results for square geometry (1×1 in mfp)

	$\omega=0.5$						$\omega=0.95$					
	$a_1=-1$			$a_1=1$			$a_1=-1$			$a_1=1$		
			BOTTOM	WALL					BOTTOM	WALL		
x/a	G	$4q_x$	$4q_y$	G	$4q_x$	$4q_y$	G	$4q_x$	$4q_y$	G	$4q_x$	$4q_y$
0.50	0.56430	0.00000	0.87877	0.53677	0.00000	0.94285	0.64637	0.00000	0.72258	0.58769	0.00000	0.85389
0.60	0.56351	0.01115	0.88029	0.53637	0.00856	0.94351	0.64439	0.02680	0.72645	0.58670	0.02138	0.85572
0.75	0.55901	0.02920	0.88906	0.53413	0.02173	0.94732	0.63332	0.06910	0.74833	0.58118	0.05390	0.86600
0.90	0.54832	0.05110	0.91037	0.52907	0.03574	0.95642	0.60810	0.11745	0.79915	0.56903	0.08734	0.88953
1.00	0.53067	0.59496	0.96804	0.52126	0.52025	0.95409	0.56943	0.70208	0.92570	0.55107	0.56465	0.89114
			TOP	WALL					TOP	WALL		
x/a	G	$4q_x$	$4q_y$	G	$4q_x$	$4q_y$	G	$4q_x$	$4q_y$	G	$4q_x$	$4q_y$
0.50	0.04908	0.00000	0.15246	0.06037	0.00000	0.18617	0.07058	0.00000	0.20079	0.09644	0.00000	0.27567
0.60	0.04851	0.01226	0.15047	0.05969	0.01494	0.18370	0.06962	0.01821	0.19789	0.09528	0.02434	0.27180
0.75	0.04559	0.02912	0.14033	0.05617	0.03568	0.17102	0.06473	0.04330	0.18306	0.08923	0.05851	0.25175
0.90	0.04050	0.04228	0.12289	0.04987	0.05237	0.14870	0.05609	0.06294	0.15716	0.07804	0.08688	0.21533
1.00	0.03602	0.04539	0.10681	0.04376	0.06382	0.12972	0.04821	0.06509	0.13103	0.06626	0.11037	0.18439
			EAST	WALL					EAST	WALL		
y/b	G	$4q_x$	$4q_y$	G	$4q_x$	$4q_y$	G	$4q_x$	$4q_y$	G	$4q_x$	$4q_y$
0.10	0.21070	0.40641	0.38977	0.20962	0.40544	0.41208	0.25409	0.50253	0.35288	0.25144	0.50045	0.39382
0.25	0.15325	0.28188	0.31391	0.15772	0.28934	0.34071	0.19502	0.37487	0.30226	0.20343	0.39031	0.35155
0.50	0.09493	0.16060	0.21930	0.10282	0.17299	0.24671	0.12836	0.23352	0.23128	0.14497	0.26166	0.28327
0.75	0.05952	0.09141	0.15308	0.06800	0.10489	0.17732	0.08276	0.14032	0.17562	0.10209	0.17322	0.22446
0.90	0.04455	0.06372	0.12388	0.05280	0.07701	0.14559	0.06144	0.09796	0.14925	0.08084	0.13097	0.19544

The RITE solutions for homogeneous medium given by Crosbie et al. [6] were used to validate the computer code for various geometry and constant scattering albedo configurations. Our solutions were in excellent agreement with those of provided by Crosbie et al. [6].

In Table 1, the effect of grid configuration on the accuracy is depicted for some backward scattering cases. As a result, in square enclosures 120×120 grid configuration was used to ensure at least four-decimal places accuracy in the solutions.

In Table 2, the RITE solutions for the incident energy and the net heat flux components are tabulated for selected points on the bottom, top and east walls for 1×1 (in mfp dimensions) square enclosure of $\omega=0.5$ and $\omega=0.95$ for both backward ($a_1=-1$) and forward scattering ($a_1=1$).

Conclusion

Exact integral equation solutions for the incident energy and the net heat flux components of rectangular participating and linearly anisotropic scattering homogeneous medium are obtained using ''singularity subtraction'' method. The results for a square (1×1) enclosures with linearly anisotropic scattering ($a_1=-1$, $a_1=1$) medium having scattering albedos of $\omega=0.5$ and 0.95 are presented in tabular form for the selected points along the centerline and the enclosure walls.

Nomenclature

$G(x,y)$ = incident energy ($=\int\int_\Omega I(x,y,\mathbf{\Omega})d\mathbf{\Omega}$)
$I(x,y,\mathbf{\Omega})$ = radiation intensity
$\mathbb{K}_n(\rho)$ = function defined by $Ki_n(\rho)/\rho^n$
$Ki_n(x)$ = Bickley-Naylor functions of nth order
N = number of grid intervals
X, Y = coordinate variables
a_1 = linear anisotropy coefficient
a, b = optical dimensions of rectangular domain
$q_x(x,y)$ = net radiative heat flux in x-direction ($=\int\int_\Omega I(x,y,\mathbf{\Omega})\Omega_x d\mathbf{\Omega}$)
$q_y(x,y)$ = net radiative heat flux in y-direction ($=\int\int_\Omega I(x,y,\mathbf{\Omega})\Omega_y d\mathbf{\Omega}$)
x, y = optical coordinate variables ($x=\beta X$ and $y=\beta Y$)

Greek Symbols

$\mathbf{\Omega}, \Omega_x, \Omega_y$ = scattering direction and its components
β = extinction coefficient ($=\kappa+\sigma$)
κ = absorption coefficient
ρ = the distance between two points ($=\sqrt{(x-x')^2+(y-y')^2}$)
σ = scattering coefficient
ω = constant scattering albedo ($=\sigma/\beta$)

Subscripts

x = x-direction
y = y-direction
w = wall

Superscripts

$'$ = dummy integration variable

References

[1] Tan, Z., 1989, ''Combined Radiative and Conductive Heat Transfer in Two-Dimensional Emitting, Absorbing and Anisotropic Scattering Square Media,'' Int. Commun. Heat Mass Transfer, **16**, pp. 391–401.
[2] Tan, Z., 1989, ''Radiative Heat Transfer in Multidimensional Emitting, Absorbing, and Anisotropic Scattering Media—Mathematical Formulation and Numerical Method,'' ASME J. Heat Transfer, **111**, pp. 141–147.
[3] Wu, S. H., Wu, C. Y., and Hsu, P. F., 1996, ''Solutions of Radiative Heat Transfer in Nonhomogeneous Participating Media Using the Quadrature Method,'' ASME HTD, **332**, pp. 101–108.
[4] Hsu, P. F., Tan, Z. M., Wu, S. H., and Wu, C. Y., 1999, ''Radiative Heat Transfer in the Finite Homogeneous and Nonhomogeneous Scattering Media Exposed to Collimated Radiation,'' Numer. Heat Transfer, **31**(8), pp. 819–836.
[5] Loyalka, S. K., and Tsai, R. W., 1975, ''A Numerical Method for Solving Integral Equations of Neutron Transport-II,'' Nucl. Sci. Eng., **58**, pp. 193–202.
[6] Crosbie, A. L., and Schrenker, R. G., 1984, ''Radiative Transfer in a Two-Dimensional Rectangular Medium Exposed to Diffuse Radiation,'' J. Quant. Spectrosc. Radiat. Transf., **31**(4), pp. 339–372.

[7] Altaç, Z., 2002, "The SK_N Approximation for Solving Radiative Transfer Problems In Absorbing, Emitting, and Isotropically Scattering Plane-Parallel Medium: Part 1," ASME J. Heat Transfer, **124**, pp. 674–684.
[8] Altaç, Z., 2002, "The SK_N Approximation for Solving Radiative Transfer Problems in Absorbing, Emitting, and Linearly Anisotropically Scattering Plane-Parallel Medium: Part 2," ASME J. Heat Transfer, **124**, pp. 685–695.
[9] Altaç, Z., 2003, "Radiative Transfer in Absorbing, Emitting and Linearly Anisotropic Scattering Inhomogeneous Cylindrical Medium," J. Quant. Spectrosc. Radiat. Transf., **77**(2), pp. 177–192.
[10] Abramowitz, M., and Stegun, I. A., 1964, *Handbook of Mathematical Functions*, Dover Publications Inc., New York.
[11] Altaç, Z., 1996, "Integrals Involving Bickley and Bessel Functions in Radiative Transfer and Generalized Exponential Integral Function," ASME J. Heat Transfer, **118**(3), pp. 789–791.